An Examination of Bonding, Structure and Reactivity of Exotic Main Group Systems

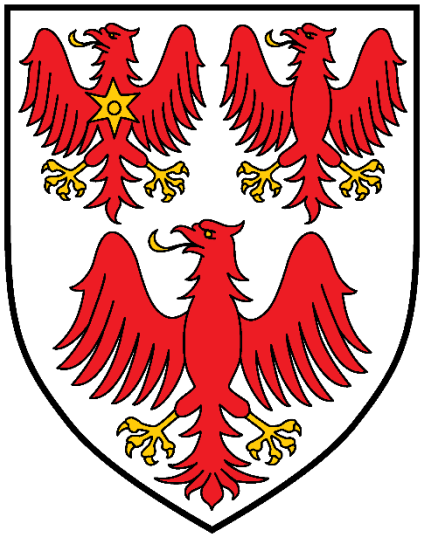



Agamemnon Elvis Crumpton

The Queen's College

Thesis submitted for the Degree of Doctor of Philosophy

April 2024

Table of contents

Abbreviations i

Abstract ii

Rational for Integrated thesis. iii

Author contributions iii

Acknowledgements iv

Thesis structure v

List of manuscripts constituting the thesis vii

List of manuscripts not included in the thesis viii

Chapter 1 - Introduction 1

Frustrated Lewis pairs 2

Group 14 systems 10

Group 13 systems 25

Group 2 systems 37

Aims of the work 47

References 49

Chapter 2 - Metathesis at $[Be–Be]^{2+}$: A Route to a Nucleophilic Beryllyl Complex 62

Author contributions 62

Abstract 62

Introduction 62

Results and Discussion 64

Conclusions 73

Characterising Data 74

References 99

Statement of Authorship 103

Chapter 3 - A Stable Hexavalent Nickel Complex 104

Author contributions 104

Abstract 104

Introduction 105

Results and Discussion 106

Conclusion 114

Characterizing data 115

References 142

Statement of Authorship 145

Chapter 4 - Synthesis of Homo-metallic Heavier Analogues of Cyclobutene and the Cyclobutadiene Dianion 146

Author contributions 146

Abstract 146

Introduction 147

Results and Discussion 149

Conclusions 156

Characterizing data 157

References 162

Statement of Authorship 164

Chapter 5 - A Planar Per-borylated Digermene 165

Author contributions 165

Abstract 165

Introduction 165

Results and Discussion 167

Conclusions 174

Characterizing data 175

References 183

Reactivity studies on 3 (unpublished): 185

Statement of Authorship 196

Chapter 6 - Coordination and Homologation of CO at Al(I): Mechanism and Chain growth, Branching, Isomerization and Reduction 197

Author contributions 197

Abstract 197

Introduction 198

Results and Discussion 201

$[C_4O_4]^{6-}$ and $[C_4O_4]^{2-}$ systems: synthesis and structural comparisons. 211

Conclusions 216

Characterizing data 217

References 240

Alternate mechanistic pathways (unpublished) 245

Statement of Authorship 251

Chapter 7 - Modulating Hydrogen Shuttling in Ammonia by Neutral and Cationic Boron-containing Frustrated Lewis Pairs (FLPs) 252

Author contributions 252

Abstract 252

Introduction 253

Results and Discussion 254

Conclusions 264

Characterization data 265

References 307

Statement of Authorship 311

Chapter 8 - Leveraging Non-Covalent Interactions for the Binding of CO by a Weakly Lewis Acidic Borane 312

Author contributions 312

Abstract 312

Introduction 314

Results and Discussion 316

Conclusions 333

Characterization data 335

References 366

Statement of Authorship 370

Chapter 9 - Summary, Outlook and Conclusions 371

Chapter 1: Metathesis at $[Be–Be]^{2+}$: A Route to a Nucleophilic Beryllyl 371

Chapter 2: A stable hexavalent nickel complex 372

Chapter 3: Synthesis of homo-metallic heavier hnalogues of cyclobutene and the cyclobutadiene dianion 374

Chapter 4: A planar per-borylated digermene 375

Chapter 5: Coordination and homologation of CO at Al(I): mechanism and chain growth, branching, isomerization and reduction 376

Chapter 6: Modulating Hydrogen Shuttling in Ammonia by Neutral and Cationic Boron-containing Frustrated Lewis Pairs (FLPs) 377

Chapter 7: Leveraging Non-Covalent Interactions for the Binding of CO by a Weakly Lewis Acidic Borane 379

References 381

Abbreviations

The following abbreviations will be employed throughout this thesis:

Ad = admantyl

Ar = aryl

BDI = beta-diketiminate

BCF = $B(C_6F_5)_3$

CAAC= Ccylic-alkyl amino carbenes

CGMT = Carter–Goddard–Malrieu–Trinquier model

Cp = cyclopentadiene

Cp* = methylcyclopentadiene

Cy = *cyclo*-hexyl

DAC = diaminocarbenes

DCD = Dewar–Chatt–Duncanson

Dep = 2,6-diethylphenyl

DFT = Density Functional Theory

Dipp = 2,6-di-*iso*-propylphenyl

DiPEP = 2,6-$CH(Et)_2$-phenyl

DMAP = 4-dimethylaminopyridine

DTB = 2,6-di-*tert*-butylphenyl

EDA = Energy decomposition analysis

ESD = estimated standard deviation

Et = ethyl

FLP = Frustrated Lewis Pair

GDP = Gross Domestic Product

Hex = hexyl

h = hour(s)

HOMO = highest occupied molecular orbital

IR = Intra-red

KIE = kinetic isotope effect

Ime^4 = $((CH_3)CN(CH_3))_2C$

I*i*PrMe = (*i*PrNC(CH3)2)2C:

*i*Pr = *iso*-propyl

LA = Lewis acid

LB = Lewis base

LUMO = lowest unoccupied molecular orbital

M = meta

Me = methyl

Mes = mesityl, 2,4,6-trimethylphenyl

NBO = Natural bonding orbitals

NHC = N-heterocyclic carbenes

NMR = nuclear magnetic resonance

NON = xanthene-based diamido-ligand

NOCV = Natural orbitals for chemical valence

O = ortho

P = para

Ph = phenyl

QTAIM = Qunatum theory of Atoms in molecules

ppm = parts per million

R = aliphatic group (unless otherwise stated)

rt = room temperature

*t*Bu = *tert*-butyl

TEMPO = 2,2,6,6-tetramethylpiperidin-1-yl)oxidanyl

THF = tetrahydrofuran

Trip = 2,4,6-tri-*iso*-propylphenyl

TMEDA = N,N,N,N,-tetramethylethylenediamine

TMS = trimethylsilyl

TMOP = 2,4,6-trimethoxyphenyl

[B]/boryl= (HCNDipp)2B

VT = Variable temperature

Abstract

This DPhil thesis ventures into the innovative domains of main group chemistry, focusing on interactions with NH_3 and CO, revealing unique bonding behaviours and stabilization mechanisms within novel chemical systems. The research showcases the hexavalent nickel complex $Ni(BeCp)_6$, with its unconventional C_{3v} geometry and aromatic stabilization, and delves into the realm of frustrated Lewis pair (FLP) and cage systems, exemplified by $(Ph_2P\text{-}xan)_3B$. These discoveries propose novel directions for main group element chemistry and FLP applications.

The thesis comprises seven chapters, each contributing significant insights and proposing future research directions. Chapter 1 expands the understanding of beryllium chemistry, introducing heteroleptic beryllium complexes and suggesting their potential in materials science and catalysis. Chapter 2's exploration of $Ni(BeCp)_6$ opens new perspectives on metal-ligand interactions due to its unique structural and electronic properties. Chapter 3 investigates heavy analogues of cyclobutene, challenging conventional notions of aromaticity in heavy element systems.

Chapter 4 reports a planar per-borylated digermene, challenging traditional geometries of dimetallenes and suggesting novel synthetic targets for further investigation. Chapter 5 focuses on CO coordination and homologation at Al(I), proposing a unique mechanism involving a transient carbene species, which could lead to innovative CO utilization methods. Chapter 6 discusses FLP systems' interaction with NH_3, uncovering mechanisms that pre-activate N-H bonds, potentially enabling novel catalytic processes.

Finally, Chapter 7 introduces novel borane xanthene phosphine-based cage systems, offering a new method for stabilizing borane carbonyls and suggesting their potential as ligands in transition metal complexes for catalytic applications. This thesis not only broadens the understanding of main group chemistry but also lays the groundwork for future studies in the synthesis, characterization, and application of novel chemical systems, with implications for materials science, catalysis, and the activation and functionalization of small molecules.

Rational for Integrated thesis.

Due to the COVID-19 pandemic, access to the laboratory was limited and such I taught myself Density functional theory (DFT), and turned to calculations to inform and direct my own research interests. I was fortunate enough to be able to apply what I had learned in my own work to help elucidate the bonding and mechanism in that of my colleagues and thus have dedicated a significant proportion of my future years to these endeavours. This has led to my computational work being published in a number of studies which are only meaningful in the context of the incredible experimental work of my colleagues and thus an integrated format allows me to showcase this work best.

Author contributions

Each chapter begins with a detailed list of each authors contributions with my contributions underlined for clarity. At the end of each chapter is a statement of authorship signed by both me and Prof. Simon Aldridge to confirm the contributions made by me in each chapter are accurate.

Acknowledgements

I am deeply grateful for the support and encouragement I received during the course of this research. First and foremost, I would like to thank my fiancée, Nicola Oldroyd, for her unwavering love, patience, and understanding, which have been my cornerstone throughout this journey.

My heartfelt thanks go to my parents, whose love and support have been endless. They have always believed in me and encouraged me to pursue my dreams, providing a foundation of strength and inspiration.

I am immensely thankful to my supervisor, Simon Aldridge, for his invaluable guidance and mentorship. His expertise and insight have greatly enriched my work. I would also like to extend my gratitude to Josef Beronski for his advice and for challenging me to push the boundaries of my research.

My labmates Lewis Wales and Aisling Roper (Perkin Warbeck) from my CDT cohort deserve special mention for their camaraderie and shared enthusiasm for our work, making my days in the lab enjoyable and fruitful. I am also thankful to Liam and Job for their kindness and good spirits, which have brightened many of my days. A special thank you to Andreas and Caitilin, whose expertise in X-ray techniques has been indispensable. Their willingness to share their knowledge and time has been crucial to my research. I am also grateful to Marcel for being a great person to share a fumehood with. His meticulousness and good humor have made our shared workspace a better place. Finally, thanks to Andy Weller for acknowledging my existence, and to Sam Altman for saving my PhD; it's the small gestures that often make a big difference.

To all of you, I extend my deepest thanks for your support and for making my PhD journey memorable.

Thesis structure

Chapter 1: Introduction

This chapter is an introduction to the emerging field of main group chemistry with emphasis placed on the reactivity of systems with CO and NH_3 along with the investigation of unusual bonding systems.

Chapter 2-3: BeCp systems

These chapters are focused on developing the chemistry of the recently reported diberyllocene, with Chapter 1 (accepted by Nature Chemistry – in press) building on the homoleptic Be-Be bond and expanding this to heteroleptic systems and investigating the effects this has on the bonding. Chapter 2 (submitted to Nature) investigates the reactivity of diberyllocene with transition metal systems generating the hexavalent nickel complex $Ni(BeCp)_6$ and investigating the unusual bonding motifs this system exhibits.

Chapter 4-5: Low valent group 14 systems featuring boryl ligands

These chapters focus on group 14 systems specifically, germanium and tin containing, featuring boryl ligands and investigating the unique bonding observed. Chapter 3 (published) investigates the aromaticity in tin derived cyclobutadiene dianions. Chapter 4 (published) investigates the per borylated planar digermene, and why this system deviates from the usual trans bent geometry. A further study (unpublished) studies the reaction of this system with CO and examines the possible mechanism for this process.

Chapter 6: Aluminyl CO homologation

Chapter 5 (published) outlines the reactivity of the NON aluminyl with CO and the homologation products observed. Quantum chemical calculations are utilised to try and rationalise these products mechanically. A further study (unpublished) refines this mechanism further by introducing the possibility for a triplet derived intermediate.

Chapter 7-8: Reactivity of xanthene derived FLP systems with CO and NH_3

These chapters look at xanthene derived FLP systems, and how the changes in the structural and electronic characteristics lead to novel reactivity. Chapter 7 (submitted to Angewandte Chemie) investigates how xanthene derived FLP systems featuring a cationic boron centre react with NH_3 and the effect of the pendant groups bound to the borane. Chapter 8 (submitted to the Journal of the American Chemical Society) investigates the tripodal FLP system and how its unusual cage like geometry facilitates binding of a number of small molecules including CO.

Chapter 9: Summary, outlook and conclusions

This chapter summarises the work completed in this thesis and suggests areas for further investigation for each of the studies presented herein.

List of manuscripts constituting the thesis

- Chapter 2: “Metathesis at [Be–Be]2+: A Route to a Nucleophilic Beryllyl” Josef T. Boronski*, Agamemnon E. Crumpton, Aisling F. Roper, Simon Aldridge*; Nat. Chem. 2024, https://doi.org/10.1038/s41557-024-01534-9
- Chapter 3: “A Stable Hexavalent Nickel Complex” Josef T. Boronski*, Agamemnon E. Crumpton, Simon Aldridge*; Submitted Nature Chemistry
- Chapter 4: “Synthesis of Homo-metallic Heavier Analogues of Cyclobutene and the Cyclobutadiene Dianion” Xiongfei Zheng, Agamemnon E. Crumpton, Andrey V. Protchenko, Mathias A. Ellwanger, Andreas Heilmann, Simon Aldridge*; Chem. Eur. J. 2023, 29, e202300006
- Chapter 5: “A planar per-borylated digermene” Xiongfei Zheng , Agamemnon E. Crumpton , Mathias A. Ellwanger and Simon Aldridge*; Dalton Trans. 2023, 52, 16591-16595
- Chapter 6: “Coordination and Homologation of CO at Al(I): Mechanism and Chain Growth, Branching, Isomerization, and Reduction” Andreas Heilmann, Matthew M. D. Roy, Agamemnon E. Crumpton, Liam P. Griffin, Jamie Hicks, Jose M. Goicoechea, and Simon Aldridge*; J. Am. Chem. Soc. 2022, 144, 28, 12942–12953
- Chapter 7: “Modulating Hydrogen Shuttling in Ammonia by Neutral and Cationic Boron-containing Frustrated Lewis Pairs (FLPs)” Agamemnon E. Crumpton, Andreas Heilmann and Simon Aldridge*; Angew. Chem. Int. Ed. 2024, e202406440.
- Chapter 7: “Leveraging Non-Covalent Interactions for the Binding of CO by a Weakly Lewis Acidic Borane” Agamemnon E. Crumpton, Caitilín McManus and Simon Aldridge*; Submitted JACS

List of manuscripts not included in the thesis

- “Alkyne insertion into Cu–Al bonds and selective functionalization to form copper acyl compounds” Caitilín McManus, Agamemnon E. Crumpton and Simon Aldridge, Chem. Commun., 2022,58, 8274-8277
- “Disproportionationand Ligand Lability in Low Oxidation State Boryl-Tin Chemistry” Xiongfei Zheng, Agamemnon E. Crumpton, Dr. Andrey V. Protchenko, Andreas Heilmann, Dr. Mathias A. Ellwanger, Prof. Simon Aldridge, Chem.Eur. J. 2023,29, e202203395.
- “Inducing Nucleophilic Reactivity at Beryllium with an Aluminyl Ligand” Josef T. Boronski, Lewis R. Thomas-Hargreaves, Mathias A. Ellwanger, Agamemnon E. Crumpton, Jamie Hicks, Deniz F. Bekiş, Simon Aldridge, and Magnus R. Buchner, J. Am. Chem. Soc. 2023, 145, 8, 4408–4413
- “Diberyllocene, a stable compound of Be(I) with a Be–Be bond” Josef T. Boronski, Agamemnon E. Crumpton, Lewis L. Wales, and Simon Aldridge, Science. 2023, 380,1147-1149
- “Boryl Ancillary Ligands: Influencing Stability and Reactivity of Amidinato-Silanone and Germanone Systems in Ammonia Activation” Yuwen Wang, Agamemnon Crumpton, Mathias Ellwanger, Caitilín McManus, Simon Aldridge, Angew. Chem. Int. Ed. 2024, e202402795.
- “Enabling nucleophilic reactivity in molecular calcium fluoride complexes” Job Struijs, Mathias Ellwanger, Agamemnon E. Crumpton, Véronique Gouverneur, Simon Aldridge ; Accepted Nature Chemistry (In-Press)

Chapter 1 - Introduction

Catalysis is an essential process in the world today, contributing over 35% of the world's gross domestic product (GDP) and accounting for greater than 80% of all manufactured goods.[1] While the importance of catalysis is incontrovertible, the majority of catalysis carried out today is heterogenous using rare earth metals as catalysts. These metals exhibit excellent catalytic ability and diverse chemistry, as a result of partially occupied d-orbitals close in energy, however the supply of these metals can be geopolitically problematic and their scarcity drives research in alternate areas of the Periodic Table to complement and substitute the existing catalytic architecture.[2] Main group compounds could provide such an alternative. For example, advances in low valent systems have overturned many long-held stereotypes, such as the assertion that main group systems are only capable of single bonds, and it has been shown that these main group systems are capable of a diverse array of so called "*transition metal like*" reactivity.[3–13] Furthermore, Frustrated Lewis Pair chemistry (FLP) has emerged over the last two decades as a new paradigm for small molecule activation and has proven capable of a wide variety of transformations and even catalytic activity.[14–23]

Two molecular substrates will be the focus of this thesis, carbon monoxide and ammonia. These substrates exemplify the very different reactivities of main group compounds compared to transition metal complexes. Transition metal carbonyl complexes have been studied exhaustively, due to their involvement in the Fischer–Tropsch process and carbonylation catalysis, particularly in hydroformylation chemistry.[24–27] The binding of CO to transition metals occurs through the Dewar–Chatt–Duncanson (DCD) model whereby the weakly antibonding lone pair centred on carbon donates into the vacant metal d-orbitals and the filled metal d-orbitals back donate into the π* orbital of CO.[28,29] In contrast, to date significantly fewer examples of carbonyl complexes have been reported for elements outside of the d-block,[30,31] due to the scarcity of systems capable of both accepting and donating electron density required for the synergistic

bonding of CO.[32] Developing systems of this type for true metallomimetic complexes represents a formidable challenge in main group chemistry.[3–5]

Hydroamination catalysis using ammonia has been described as a "*Holy Grail*" in catalysis, due to ubiquity of amines and the difficulty producing them in an efficient manner.[33] While prolific in carbonyl chemistry transition metal activation of ammonia is rare due to the competing formation of Werner complexes.[34–36] By contrast, a number of main group systems not only effect N–H bond cleavage, but reversibility in bond activation such as work by Goicoechea *et al*. with geometrically constrained phosphine systems. Given the propensity of transition metal systems to form Werner complexes, main group systems have emerged as promising targets for NH_3 functionalization, showcasing a potential that sidesteps the limitations faced by their transition metal counterparts.[37–53]

Understanding the electronic structure and bonding in low valent main group systems is *fundamental* to advancing the field of main group chemistry.[54–56] This knowledge not only unveils the intricate behaviour of these elements at the atomic and molecular levels but also lays the groundwork for predicting and rationalizing their reactivity patterns. In the realm of synthetic chemistry, insights into the electronic configurations and bonding interactions enable the design of novel compounds with tailored properties and functionalities.

Frustrated Lewis pairs

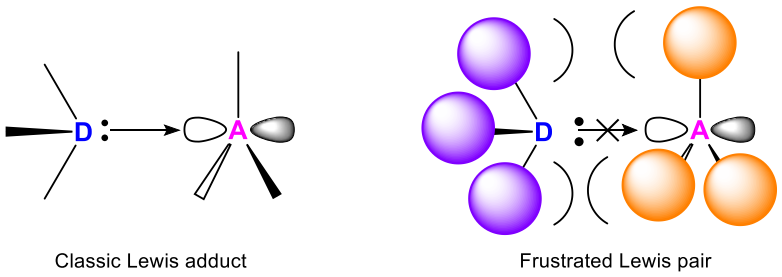

Figure 1.1: The difference between classical Lewis acid/base adducts and FLPs

Acids were defined as electron pair acceptors and bases as an electron pair donors by Lewis in 1923.[57] Classically they form adducts via donation of a lone pair from the HOMO of the Lewis

base into the empty LUMO of the Lewis acid.[58,59] 'Frustrated Lewis Pairs' (FLPs) are systems in which Lewis acid and Lewis base components are not quenched by adduct formation, usually as a result of steric encumbrance.[60–62] Frustrated systems have been known since 1942, with a report of lutidine being unable to form an adduct with BMe_3 published by Brown et al.[63] However, it was not until 2006 that the term 'Frustrated Lewis Pair' was coined, following Stephan *et al.'s* report on $(C_6H_2Me_3)_2P(C_6F_4)B(C_6F_5)_2$ (**Figure 1.2**). [64] This breakthrough in FLP research marked the beginning of a paradigm shift in metal-free bond activation chemistry, demonstrating for the first time the ability of a non-transition metal complex to reversibly activate dihydrogen. [6,23,65–68]

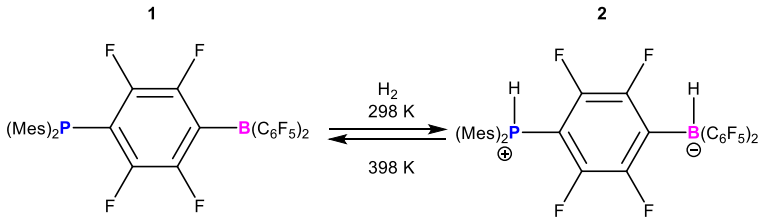

Figure 1.2: First reported FLP system, reversibly activating hydrogen

Subsequent to Stephan *et al.'s* initial discovery, a diverse array of FLP systems have been synthesized, using elements from across the Periodic Table. These systems broadly fall into two categories: intramolecular species, in which the Lewis acid and base are linked within the same molecule, and intermolecular species, featuring separate acid and base fragments.[6,23,65–68] Intramolecular FLPs typically follow a bimolecular reaction pathway, as opposed to the trimolecular interactions seen with intermolecular variants. [6,23,65–68] FLPs have been employed in reactions with a variety of small molecules—including alkynes, olefins, CO2—and have even facilitated catalytic hydrogenations with enantioselective control. [6,23,65–68]

Mechanism of Bond Activation by FLPs

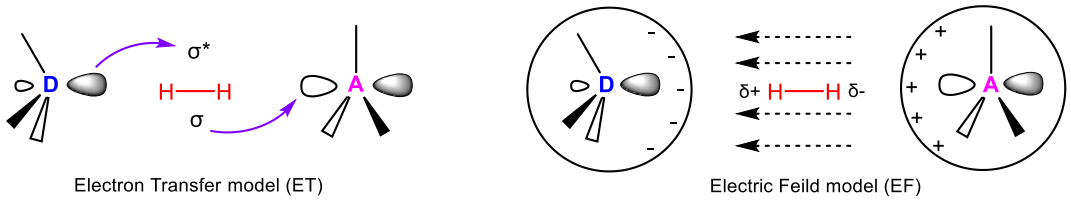

Figure 1.3: Pictorial diagram of the Electron Transfer model (ET, left) and the Electric Field model (EF, right)

Computational studies have suggested that the mechanism of H_2 activation by FLPs involved the formation of 'encounter complexes' between the Lewis acid and Lewis base in which they were positioned in close proximity, but no formal adduct was formed.[69] In 2014 NMR techniques were used to observe intermolecular interactions across an encounter complex[70] and in 2018 encounter complexes were directly observed using neutron diffraction.[71]

There has recently been much debate in the literature on the exact mode of action in bond activation by FLPs and the role of the Lewis acid and Lewis base[69,72–78] One theory is the electric field (EF) model whereby the donor and acceptor are positioned in the encounter complex such that a strong electric field exists between them leading to a barrierless cleavage of the H–H bond (**Figure 1.3**, right).[75] Electric fields are spherically orientated around the donor/acceptor, and thus the field is not positioned along the reaction pathway which would facilitate H–H bond cleavage.[74] Additionally, this model alone would be expected to ionise H_2 rather than induce cleavage. An alternate theory is the classic orbital model whereby the Lewis base donates into the H_2 σ* orbital and the H_2 σ orbital donates into the Lewis acid p-orbital to facilitate bond cleavage (ET model; **Figure 1.3**, left).[74,79] This mechanistic hypothesis is supported by the observation that the transition states of multiple systems involve the donor attacking end on, and the acceptor binding in a μ-η^2 fashion, consistent with the spatial alignment of the H_2 σ* and σ orbitals.[74] The prevailing theory is that a combination of both models occurs, with the EF model playing a larger part in early, low energy transition state processes.[80–83]

The mechanistic considerations for H_2 activation can be extrapolated to other E–H bond reactions, such as the N-H bonds in ammonia, in which bond polarity will aid the bond activation step. Gaining an understanding of the mechanism of H_2 activation by FLPs provides valuable information towards rationally designing systems to achieve diverse bond activation chemistry.

Reactivity of FLP systems with CO

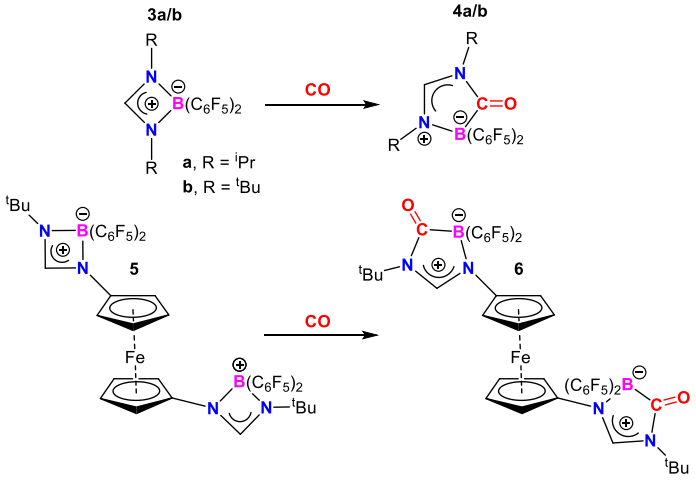

Scheme 1.1: Reaction of boron amidinate systems with CO

The capture of CO by the Lewis acid-base adduct was first reported by Stephan *et al.* with the boron amidinate systems (**Scheme 1.1**, **3a/b**).[84] These systems feature η^2 coordination of the amidinate ligand, which might preclude reactivity; even at high temperatures no evidence for η^1 binding was observed. However, both systems readily react at room temperature with 1 atm of CO forming **4a/b**. Binding of CO in **4a/b** occurs in a cooperative manner between the Lewis acidic and basic fragments. In a later report two of these amidinate fragments were tethered on a ferrocene scaffold (**5**) and the addition of two CO molecules (**6**) was demonstrated, as well as the sequential addition of one CO and one CO_2 molecule (**Scheme 1.1**). [85]

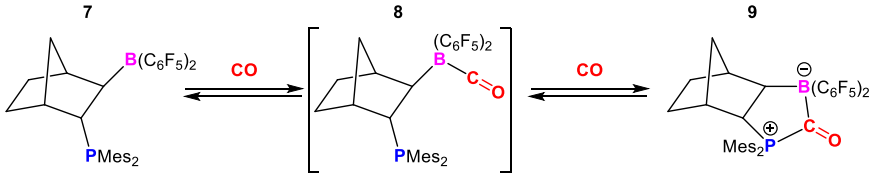

Scheme 1.2: Reaction of norbornane derived FLP **7** with CO

Erker *et al*. investigated the binding of CO to **7**, a norbornane-derived intramolecular FLP, in which a rigid backbone inherently prevents Lewis acid-base adduct formation, indicating its nature as a truly frustrated system. **7** was found to bind CO in an analogous manor to **4** with the CO sitting between the Lewis acid and base fragments (**9**); release of CO occurs at temperatures above −33°C (**Scheme 1.2**).[86] The authors proposed that the mechanism for this binding event comes from an initial coordination of CO to the boron fragment (**8**) and subsequent attack from the phosphine into the π* system of CO, reminiscent of back-donation in transition metal complexes. The initially formed adduct **8** (**Scheme 1.2**) was isolated in an argon matrix at −238 °C giving a characteristic IR CO stretch at 2196 cm^{-1}, vastly different from the CO stretch of **9** (1791 cm^{-1}).[87] The large bathochromic shift between **8** and **9** is indicative of a weakening of the C–O bond due to back-donation into the CO π* orbitals by the phosphine donor.

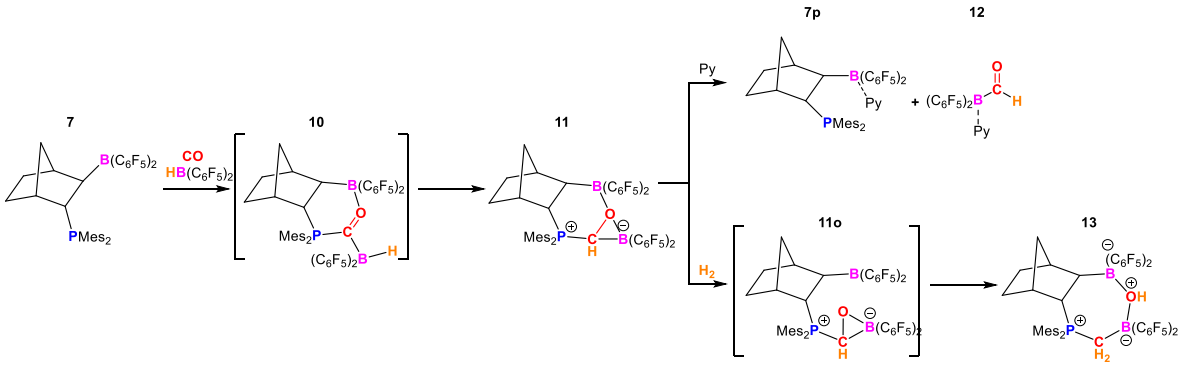

Scheme 1.3: Reaction of norbornane derived FLP **7** with CO and Piers borane and its subsequent reactivity

In a subsequent study it was found that the addition of Piers' borane to **7** in the presence of CO led to the formation of the formal hydroboration product **11** (**Scheme 1.3**).[87] This reaction occurs at room temperature, at which temperature **9** is not stable, indicating that **9** is unlikely to be an intermediate in the reaction. DFT calculations suggest instead that the reaction pathway involves initial formation of a Piers' borane carbonyl complex, which then reacts cooperatively with the FLP (**10**), followed by a subsequent 1,2-proton shift to yield **11**. This mechanism was later supported by the isolation of the Piers borane carbonyl complex and its structural

characterisation by SCXRD.[87] In a subsequent study, it was discovered that adding pyridine to compound **11** resulted in the release of formylborane **12** and the regeneration of compound **7**, now coordinated with pyridine **7p** (**Scheme 1.3**).[88] This process evidences CO reduction mediated by a FLP system. Additionally, it was observed that compound **11** could react with H_2 at room temperature, yielding a seven-membered cyclic product **13** (**Scheme 1.3**). This reaction was hypothesized to proceed via the open form of **11**, involving the cleavage of the B–O bond (**11o**), activation of H_2 across the O/B system, and subsequent rearrangement, leading to the formation of **13**. The structural motifs represented by **9**, **11**, and **13** have become hallmarks of numerous FLP systems reported thereafter, establishing themselves as quintessential products of FLP/CO reactions.[89–96]

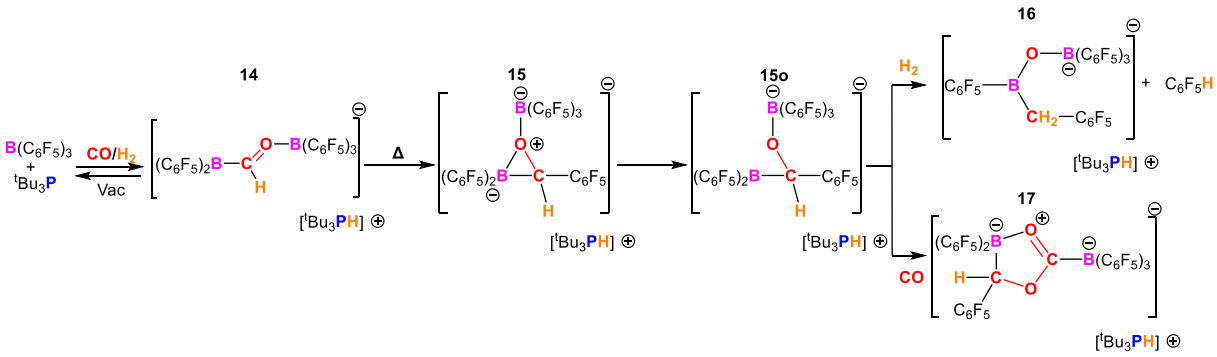

Scheme 1.4: Reaction of BCF/^{t}Bu$_3$P with syn-gas

Concurrently with the studies performed by Erker *at al.*, Stephan *et al.* explored Fischer–Tropsch-like reactivity in FLPs by investigating the reaction of intermolecular FLP systems with syn-gas (H_2/CO).[97] The reaction of a combination of ^{t}Bu$_3$P and B(C_6F_5)$_3$ (BCF) in a 1:2 ratio with 4 atm syn-gas led to the quantitative formation of the formyl borate species **14** (**Scheme 1.4**). The authors report the reversibility of this reaction on exposure to vacuum overnight, liberating CO and regenerating a phosphine borane mixture, as well as the H_2 activation products. Upon heating **14**, migration of a C_6F_5 group from the borane to the carbon atom occurs, leading to complete conversion to the cyclic product **15**, a structural motif reminiscent of **11**. Upon exposure to H_2, **15** releases C_6F_5H and forms the borane-oxy-borate salt **16** (**Scheme 1.4**). This reaction is proposed to occur via the "*open*" complex **15o**, in which the B–O bond is broken, and

FLP reactivity is unquenched, allowing activation of H_2 and subsequent rearrangement to yield **16**. **15** was also found to react with a further CO molecule leading to the cyclic product **17**, which is proposed to be formed through activation across the open form **15o**, with migration of the coordinated BCF (**Scheme 1.4**). **17** could therefore be seen as a masked carbene coordinated to a BCF moiety. In the reaction of $^{t}Bu_3P$/BCF with syn-gas the FLP must first react with hydrogen, a well-established chemistry for FLP's, then activate CO across the P–H/B–H moiety. This report has propagated studies of a wealth of systems featuring pre-installed neutral P–H/B–H fragments with CO in order to better study this Fischer–Tropsch type reactivity.[98–107]

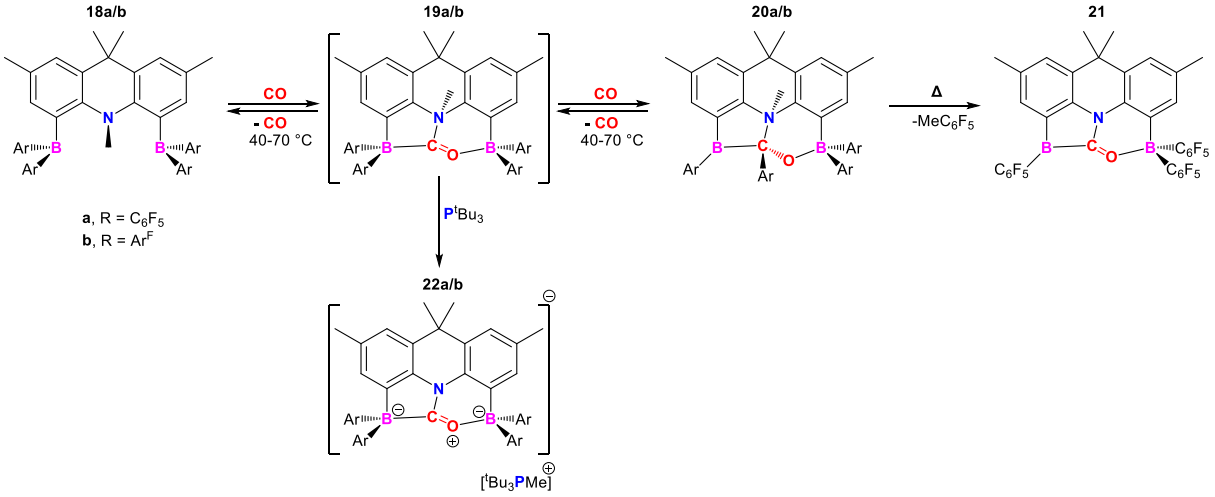

Scheme 1.5: Reaction of BNB acridan based BNB FLP **18a/b** with CO

More recently Aldridge *et al.* applied FLP systems to sensor chemistry, in the form of an acridan based BNB FLP (**18/b**).[108] Exposure of **18a/b** to CO leads to formation of the C–B bonded product **20a/b**, and a colour change from orange to colourless. This process is reported to be reversible for **20b** upon heating to between 40-70 °C and regenerates the free FLP **19b**. (**Scheme 1.5**). By contrast, heating **20a** leads instead to the elimination of MeC_6F_5. This divergent reactivity is attributed to the more Lewis acidic nature of the C_6F_5 group leading to decomposition before release of CO. The reaction of **18a/b** to **20a/b** is proposed to go via the CO sequestered intermediate **19a/b**. This intermediate is stabilized by the addition of the soft base $^{t}Bu_3P$, leading to the elimination of $[^{t}Bu_3PMe]^{+}$ and the trapping of the CO adduct **22a/b** (**Scheme 1.5**). This work unveils intriguing alternative applications for FLP CO complexes,

showcasing their potential as colorimetric CO sensors, thanks to the dramatic colour transition triggered by CO activation.

Reactivity of FLP systems with NH_3

FLP systems have been used to effect many chemical transformations with a variety of substrates, however, there is a dearth of reactions with NH_3. Stephan *et al.* reported inter- and intramolecular hydroamination of terminal alkynes using secondary aryl amines with BCF.[109,110] This process uses the BCF/terminal amine as the Frustrated Lewis Pair, cooperatively activating the alkyne, and facilitating the formation of functionalized amine products. Tangential to these investigations, FLP systems have also been used in the dehydrogenation of ammonia borane.[111–113]

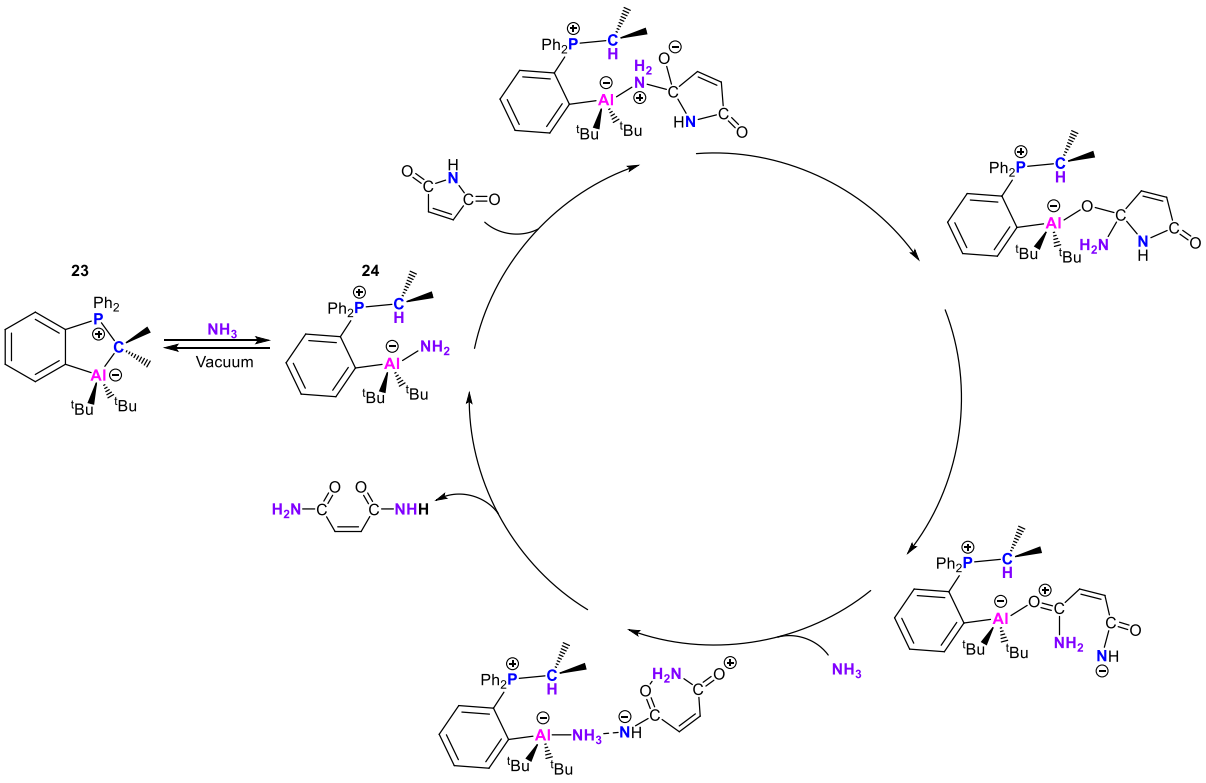

Figure 1.4: Catalytic cycle of NH_3 transfer of aluminium Lewis acid and the phosphorus ylide base **23**.

Reactions directly with NH_3 are limited to a single report by Breher *et al*. whereby catalytic transfer of NH_3 to an organic electrophile was achieved by an FLP system containing an

aluminium Lewis acid and a phosphorus ylide base (**Figure 1.4**, **23**).[40] In the solid-state **23** adopts a closed adduct configuration, and DFT calculations indicate that the opening of the adduct is energetically unfavourable (by 37.5 kcal mol^{-1}). Uptake of NH_3 is however facile at room temperature, leading to the formation of the N–H activated product **24**. Exposure to vacuum leads to regeneration of **23**. Given the reversibility of this process, the authors sought to apply it to NH_3 transfer reactions. Indeed, catalytic turnover of a number of ring-opening reactions, including that of maleimide (**Figure 1.4**), was demonstrated. DFT calculations were performed to shed light on the mechanism for catalytic ammonia transfer by **24**. These indicate that the reaction proceeds via initial amide attack on the carbonyl group, with a subsequent shift from Al–N to Al–O coordination. This is followed by ring opening of the maleimide and subsequent proton transfer from ammonia to regenerate **24**, as confirmed by ^1H NMR studies. These findings extend the utility of FLP systems to NH_3 reactions, illustrating a catalytic cycle based on practical reversibility and providing a mechanistic framework for future FLP mediated ammonia reactivity.

Group 14 systems

Carbenes

Carbenes are divalent carbon species characterised by having two non-bonding electrons, which may pair as a singlet to form a single-centre ambiphile, or remain unpaired as a diradicaloid triplet.[114–120] The ground state of the simplest carbene, CH_2, is a triplet, attributed to the narrow gap between its frontier molecular orbitals and wide H–C–H angle.[119] However, triplet carbenes exhibit extreme reactivity, rendering their isolation challenging. More recently, N-heterocyclic carbenes (NHCs) have been developed, providing strategies for the stabilisation of singlet carbene species. The first is leveraging adjacent nitrogen atoms for π-donation to increase the energy of the lowest occupied molecular orbital (LUMO). [120–123] Secondly the greater electronegativity of nitrogen compared to carbon reduces the energy of the highest occupied molecular orbital (HOMO). Additionally, the cyclic structure of NHCs, often augmented by bulky

groups to impede dimerisation, enforces a narrower bending angle, which further expands the HOMO-LUMO gap, stabilising the singlet state and facilitating the isolation of NHCs (**Figure 1.5**). Over the past three decades, N-heterocyclic carbenes (NHCs) have experienced a renaissance owing to their excellent σ-donating and π-accepting properties. As a result, they have been widely applied in stabilizing diverse systems across the Periodic Table.[114,115,117–120]

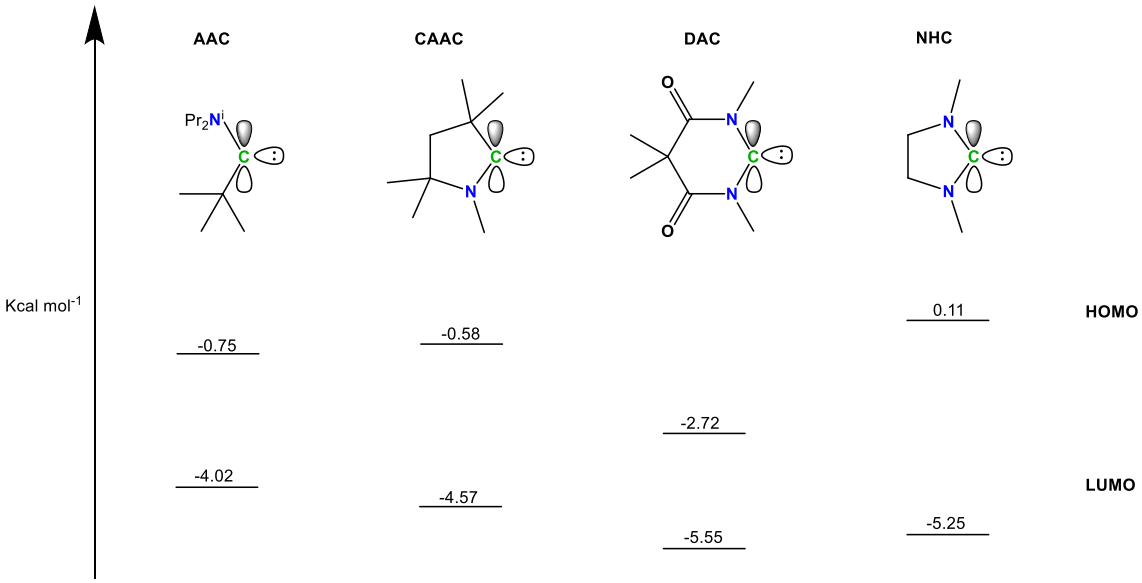

Figure 1.5: Comparison of the HOMO and LUMO energies of representative carbenes

Since 1991, the development of isolable carbenes has targeted a fine balance in terms of the HOMO-LUMO gap, widening it enough for isolation while narrowing it to enhance Lewis acidity and basicity.[124,125] Bertrand *et al*. pioneered the synthesis of cyclic alkyl amino carbenes (CAACs), in which one of the NHC's α-nitrogen donors is replaced by with an alkyl group. [126] This adjustment reduces π-donation to carbon and, overall, the HOMO-LUMO gap (**Figure 1.5**). CAACs therefore demonstrate increased nucleophilicity and electrophilicity relative to NHCs, facilitating the isolation of low-valent systems and exhibiting unique reactivities, such as the activation of H_2, NH_3, and CO, capabilities not previously observed with NHCs.[116,126,127]

Reactivity of carbene systems with CO

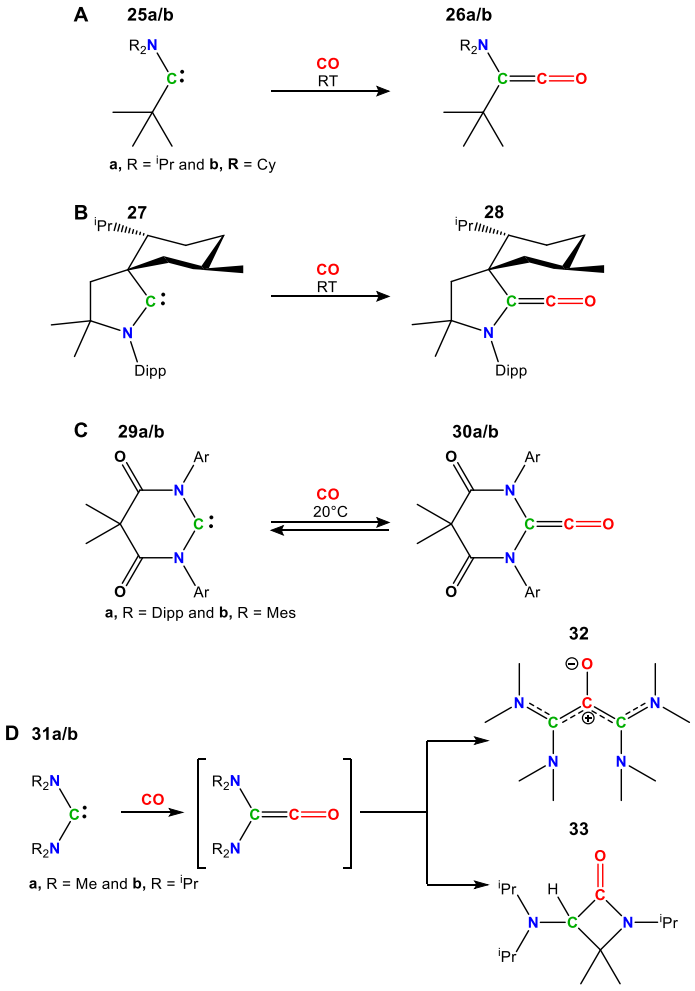

Scheme 1.6: Reactivity of selected carbenes with CO

A number of other carbene systems display reactivity towards CO; reversible trapping was even demonstrated by Bielawski *et al*. by employing diaminocarbenes (DACs, **29a/b**; **Scheme 1.6, C**).[128–131] While most reactivity towards carbenes yields the corresponding ketene, onward reactivity has been observed yielding products with two carbene fragments stabilising the zwitterion C^{+}–O^{-}, as in the case of **32** (**Scheme 1.6, D**). The latter have been of interest in generating carboxy radicals.[132–134] These zwitterionic products are extremely reactive leading to intermolecular C–H activation as reported with **33**. Remarkably Bertrand *et al*. found $CAAC^{Dipp}$ **27** to be capable of the catalytic carbonylation of o-quinone at 60 °C under 4 atm of CO. The reaction mechanism was studied both using DFT and experimentally and is proposed to proceed

by initial formation of the ketene and a concerted [4+2] cycloaddition to the spirolactone **34**, which is proposed to be the resting state of the system (**Figure 1.6**). [127]

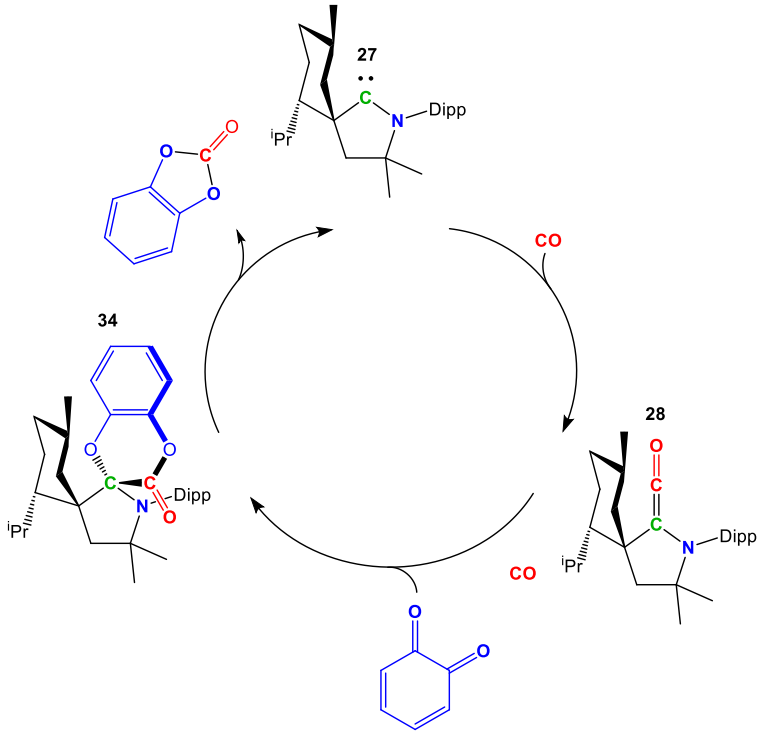

Figure 1.6: Catalytic cycle of carbonylation of quinone derivative with a CAAC

Reactivity of carbenes with NH_3

A number of carbene systems have been shown to activate ammonia. These reactions are hypothesised to proceed via electrophilic or nucleophilic asynchronous pathways (**Figure 1.7**).[126,128,129,134,135] The nucleophilic route begins with the partial deprotonation of NH_3, enhancing its nucleophilicity through polarisation of the N–H bond. Conversely, the electrophilic mechanism involves initial coordination, increasing proton acidity, followed by deprotonation facilitated by the lone pair. These pathways exploit the amphiphilic nature of carbenes, with the predominant route influenced by the dominant characteristic of the given carbene, which, in the case of **29b**, was identified as electrophilic through KIE and Hammett analysis using para-substituted anilines. This research also revealed partially reversible ammonia activation by an NHC (**35**), something that had previously been thought to be impossible.[135]

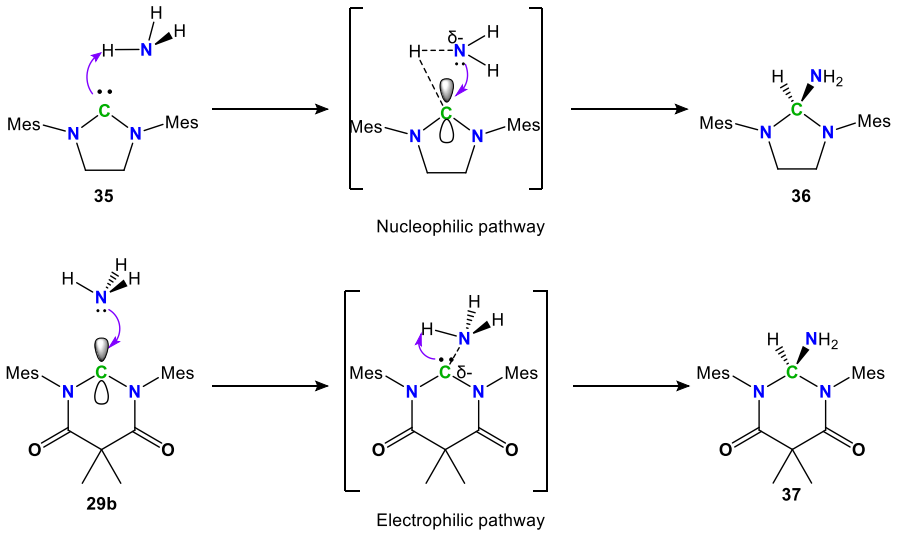

Figure 1.7: Proposed asynchronous pathways for ammonia activation, nucleophilic pathway (top) electrophilic pathway (bottom)

Tetrylenes

The heavier group 14 analogues of carbenes, known as tetrylenes, depart somewhat from the lighter carbenes. The inert pair effect increasingly favours the +II oxidation state, reflected in the bench stability of Ge, Sn, and Pb dichlorides.[136–139] Simple molecular, these tetrylenes display an increasing singlet-triplet gap on descending group 14 (**Figure 1.8**). Concurrently, decreasing s/p orbital mixing, due to poor overlap of orbital size match, results in a smaller R-E-R angle (approaching 90°) as the E-R bonds gain p-character.[136] This shift in bonding influences reactivity, skewing the heavier tetrylenes towards Lewis acidity while reducing their Lewis basicity as the lone pair gains s-character.[136,137]

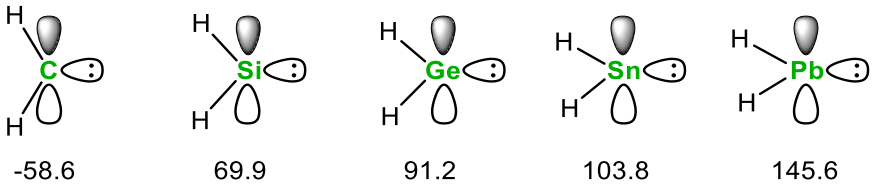

Figure 1.8: Calculated singlet-triplet gaps of the EH_2 species (E = C-Pb) in kcal mol^{-1}, a negative singlet-triplet gap indicates the triplet state is lower in energy.

The increased stability of tetrylenes with respect to carbenes, due to the inert pair effect, leads to ligands being selected in order to decrease the HOMO-LUMO gap and kinetically stabilise these systems, preventing dimerisation. Boryl ligands has been used to great effect with

the boron centre being more electropositive than carbon. Combined with the lack of any π donor properties, this results in narrow HOMO-LUMO gaps and offsetting of the inherent greater stability of the heavier tetrylenes.[140–146] Boryl ligands also provides a large steric profile in order to prevent dimerisation of these species. Si{B(NDippCH)$_2$}{N(SiMe$_3$)Dipp} (**1.4.17**), an acyclic silylene, was found to activate dihydrogen at ambient conditions (even as low as 0 °C) demonstrating the increased reactivity afforded by the boryl ligand and highlighting the departure from the stabilising effects inherent in NHCs.[146]

Reactivity of tetrylenes with CO

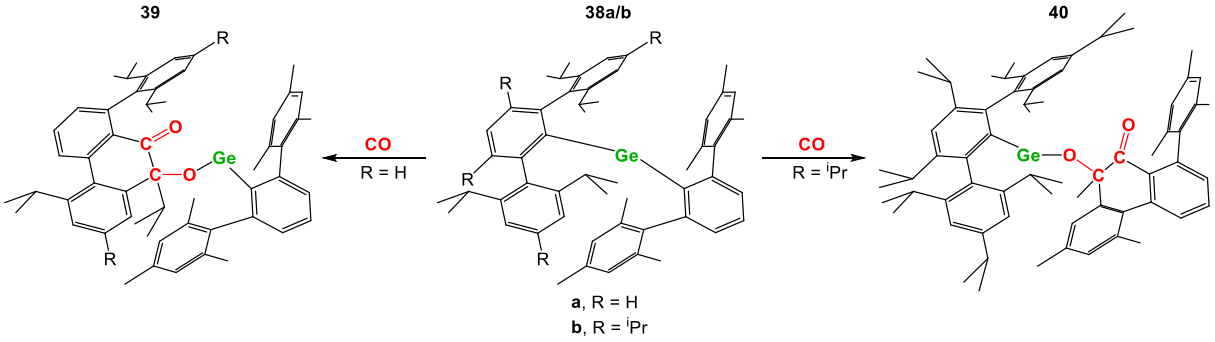

Scheme 1.7: Reaction of digermenes **36a/b** with CO

While terylenes in general possess increased HOMO-LUMO gaps relative to carbenes, they also display reactivity towards both CO and NH_3. Unlike carbenes, tetrylenes tend not to form ketene products instead forming Lewis adducts.[147] This difference stems from the larger singlet triplet gap ($\Delta E_{S\text{-}T}$) and weaker π bonding along with the increase Lewis acidity as the group is descended. In 2009 Power *et al.* reported the first example of a tetrylene which reacts with CO under ambient conditions. A germylene, employing bulky terphenyl ligands, reacts with CO to form the doubly inserted product **39**/**40** (**Scheme 1.7**).[148] DFT calculations were used to help elucidate the mechanism of the reaction of **38a**/**b** with CO, which is proposed to go via the Lewis adduct products, followed by insertion into the Ge–Ar bond (**Figure 1.9**). The germylene then coordinates a second CO molecule and inserts once again to form a 1,2-dicarbonyl species that rearranges to form a carbene which undergoes internal attack on the terphenyl ^{i}Pr group.

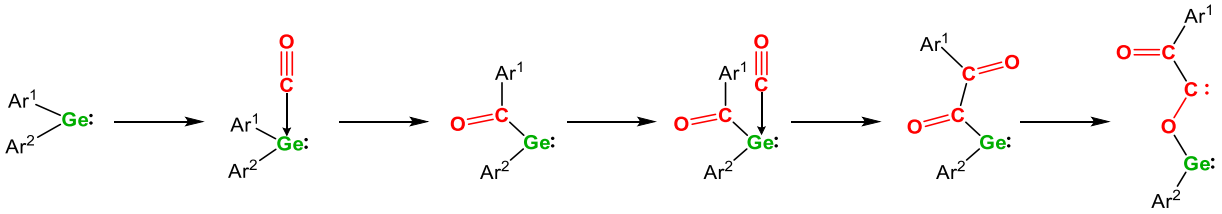

Figure 1.9: Mechanism of insertion of CO into germylenes **36a/b**

In 2018 Aldridge *et al*. reported the reaction of acyclic silylene (**41**) with CO to produce the homologated product **42** featuring the ethynediolate dianion $[OCCO]^{2-}$ moity (**Scheme 1.8**, **A**).[149] In the same year Driess *et al*. utilised bis *N*-heterocyclic silylenes (bis-NHSis) featuring either xanthene (**43**) or ferrocene bridges in reactions with CO (**Scheme 1.8**, **B**).[150,151] These reactions result in the homocoupling of carbon monoxide (**44**) via cooperative binding of two CO molecules, followed by C–C bond formation and culminates in the breaking of the C–O bond. The same group also showed that the carborane-bridged bis-NHSis **45**, reacts with CO form the polycyclic CO coupling product **46** (**Scheme 1.8, C**).[152] This enhanced reactivity was ascribed to the steric hindrance and rigidity of the o-carborane backbone.

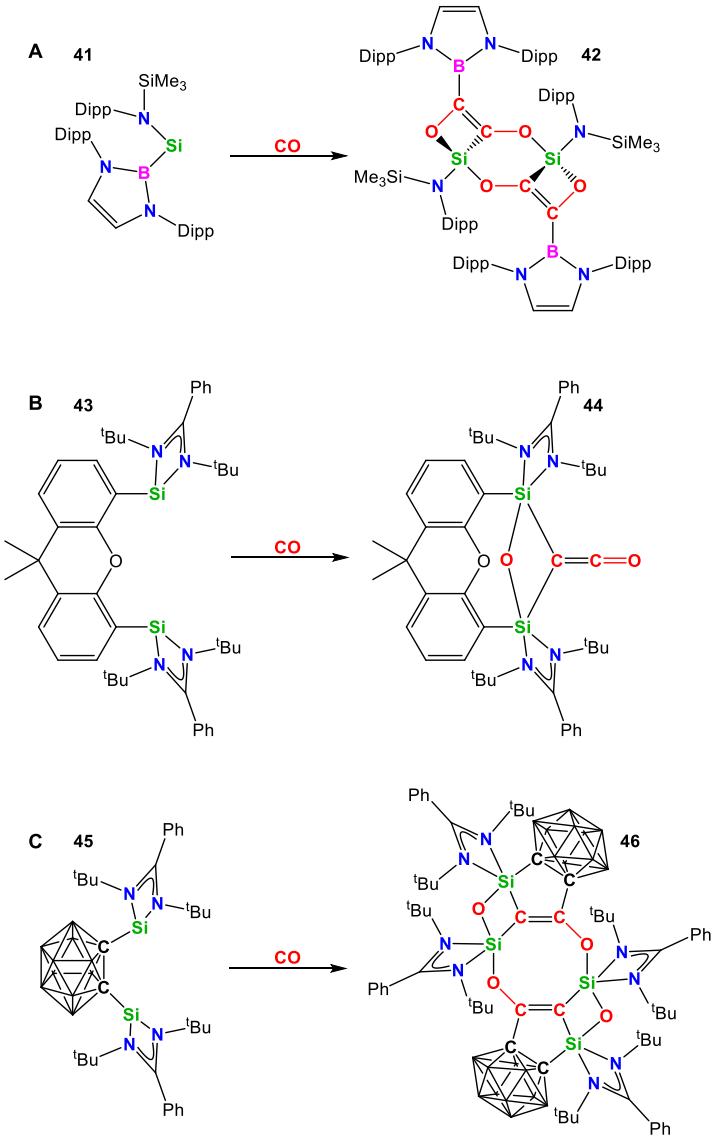

Scheme 1.8: Reaction of Silylenes with CO to form homologation products.

It was not until 2020 that a crystallographically characterised tetrylene carbonyl complex was reported.[153–155] The first example was from Schulz *et al*. who demonstrated that the electron rich transient silylene $[L(Br)Ga]_2Si$ (L = $HC[C(Me)N(2,6\text{-}iPr_2\text{-}C_6H_3)]_2$, **47**) reacted with CO at 1 atm to form the Lewis adduct **48** (**Scheme 1.9**, **A**).[155] The IR stretch ($\nu_{Si\text{-}CO}$ 1,945 cm^{-1}) is bathochromically shifted indicating a large degree of backdonation that is consistent with an electron rich silicon centre and corroborated by DFT calculations. Shortly after this report Inoue *et al*. reported the binding of CO to a second transient silylene (**49**) to form the silicon carbonyl complex (**50**), that reversibly releases CO upon heating to 130 °C or photolysis (**Scheme 1.9**, **B**). **50** also demonstrated a significant bathochromic shift in the IR stretch ($\nu_{Si\text{-}O}$ 1,903 cm^{-1})

indicating the importance of back bonding in order to stabilise these terylene carbonyl complexes. [153,154]

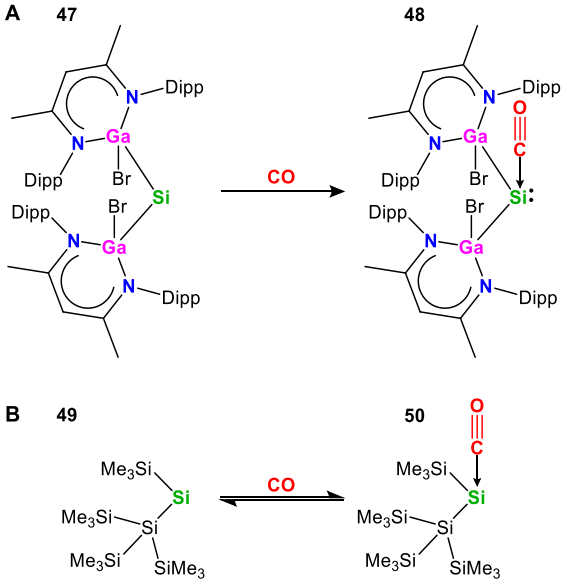

Scheme 1.9: Reaction of Silylene to form carbonyl complexes

Reactivity of tetrylenes with NH_3

Ammonia activation has been achieved by a number of terylenes, with N–H bond cleavage proceeding via different reaction pathways.[47–50,140,156–163] The most straightforward 1,1 addition, as seen in carbene systems, has been investigated by Aldridge *et al*. among others with the bisboryl stannylene **51** (**Scheme 1.10**, **A**).[140] These systems are proposed to undergo 1,1 additions through initial coordination into the vacant p orbital on the tetrylene with subsequent proton shuttling through a second ammonia molecule to give **52**.[140,162,163] **52** can react further undergoing protonolysis and dimerization leading to the bridged structure, a structural motif seen by Power *et al*. with Mes- supported terphenyl stannylenes **53** to **54** (**Scheme 1.10**, **B**).[49,162] Activation of NH_3 has also been achieved in a cooperative manner reminiscent of FLP chemistry with the basic sites on NacNac ligands and Lewis acid tetrylenes **55** to **56** (**Scheme 1.10**, **C**).[156]

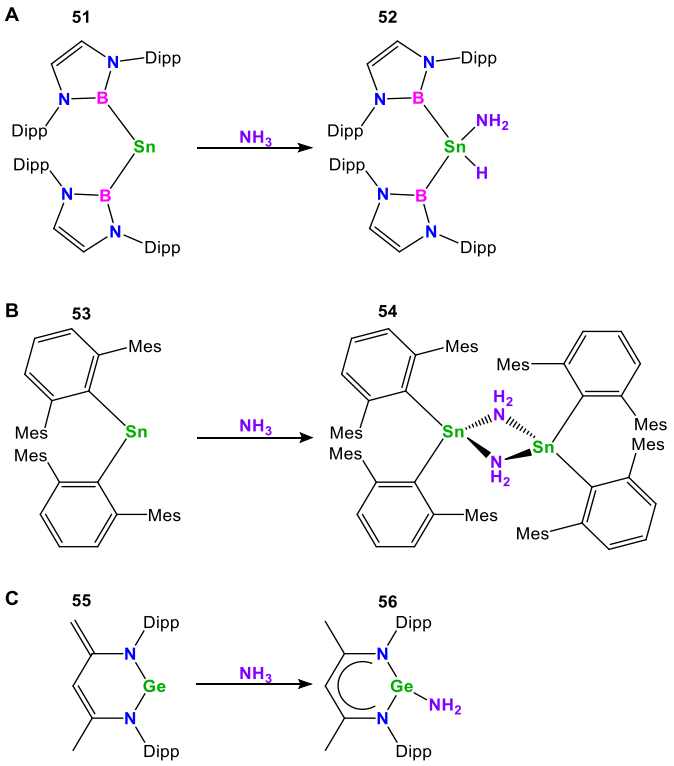

Scheme 1.10: Reaction of select tetrylenes with NH_3

Dimetallenes

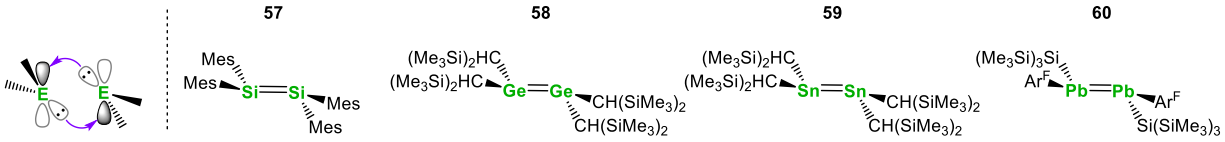

Figure 1.10: The CGMT model for dimetallenes binding (left) and the first characterised dimetallenes for each of Si-Pb (right)

Dimetallenes are the heavier analogues of alkenes, first structurally characterised by Lappert *et al*. in 1973 with the breakthrough report of $[(Me_3Si)_2CH]_2SnSn[CH(SiMe_3)_2]_2$ (**59**, **Figure 1.10**).[164] This species, along with the analogues Ge system (**58**), were found to be in an equilibrium such that in the solid state they existed as the dimetallene, and in solution dissociation occurs to the component tetrylenes. Unlike their lighter congeners, these dimetallenes are not planar but instead adopt a trans bent geometry.[10] The first silicon (**57**) and lead analogues (**60**) were synthesised by West *et al*. and Grützmacher *et al*. respectively, with the degree of trans-bending (deviation from planarity defined by the angle the plane of the R groups make to the E–E plane) increasing down the group from 18° to 41°.[11,165] The departure from traditional models of

bonding established for carbon, has been rationalised through two models. The first description involves a pseudo second-order Jahn–Teller mixing of the π and σ* and σ and π* orbitals (**Figure 1.11**). As π bonding becomes less favourable down the group, the energy gap between the π and σ* and σ and π* orbitals becomes smaller increasing the magnitude of the Jahn-Teller distortion by enhancing the degree of secondary orbital mixing.[4,9,166] With the increased trans bending the E-E bond develops less double bond character and has more nonbonding character.

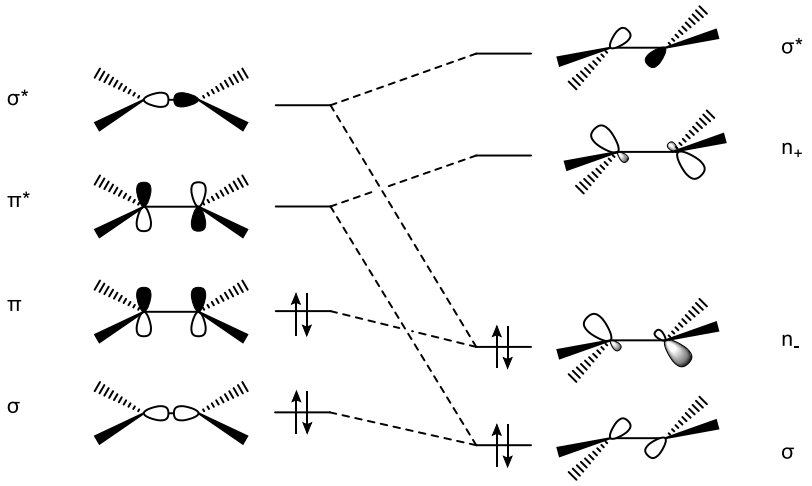

Figure 1.11: Orbital diagram for the second-order Jahn–Teller mixing

The alternative description of bonding in dimetallenes is as a donor acceptor interaction between two singlet carbenic fragments (**Figure 1.10**). With the Carter–Goddard–Malrieu–Trinquier model (CGMT) was developed based on the combining of singlet or triplet fragments, in order to predict whether a R_2EER_2 system will be planar or trans-bent.[136] This model relates the calculated singlet triplet gap for the two ER_2 fragments ($\sum E_{S-T}$), that is necessarily negative, to half the dissociation energy ($E_{\sigma+\pi}$) of the E–E bond. If $\sum E_{S-T} > \frac{1}{2} E_{\sigma+\pi}$ then the system is predicted to be trans-bent and if $\sum E_{S-T} < \frac{1}{2} E_{\sigma+\pi}$ then the system is predicted to be planar.

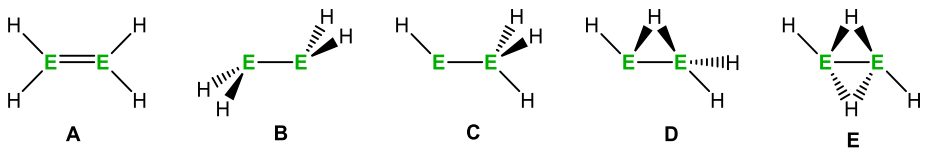

Figure 1.12: Different isomers of H_2EEH_2

Computational studies performed on H_2EEH_2 systems have demonstrated that a variety of alterative isomers are energetically accessible (within 20 kcal mol^{-1}, **Figure 1.12**).[167–173] While ethene-like isomer (**A**, **Figure 1.12**) is the most stable conformation for carbon, it is the least stable isomer for all of the heavier analogues. Bridged conformations (**D** and **E**; **Figure 1.12**) are also calculated to be stable with bridged hydric structures being structurally characterised by Power *et al*. Structural moiety **C** (**Figure 1.12**) has also been observed by Power *et al*. upon stabilisation with PMe_3 and using the bulky terphenyl ligands.[174,175]

Reactivity of dimetallenes with CO

While there are numerous examples of reactivity with carbene systems towards CO, there are comparatively few for the dimetallenes. This can be rationalised using the CGMT model, in which the amphiphilic nature is partially quenched by the donor/acceptor binding. Dimetallenes are however more reactive than alkenes, and as such, have shown reactivity towards CO. Scheschkewitz *et al*. demonstrated that silicon based dimetallene **61** can reductively couple 4 equivalents of CO to form the highly unsymmetrical product **62**. [176] The authors proposed that this transformation proceeds through a silylenoid intermediate that then dimerises to form a 1,3-disiladioxetane intermediate (**Scheme 1.11**, **A**). Subsequent addition of two additional equivalents of the silylene led, through a [2+1] cycloaddition and an oxidative addition, to the unsymmetrical product **62**. However, the authors note that the calculated barriers for this process exceed those that could occur readily at room temperature. The same group also reported the reaction of CO with a cyclotrisilene (**63**), a cyclopropane analogue.[177] The product of this reaction was shown to be the tricyclic bis-silene (**64**), formed from the dimerisaion of two transient silylene–CO adducts. These were later trapped with both an NHC and BCF (**65**, **66; Scheme 1.11, B**).[177,178]

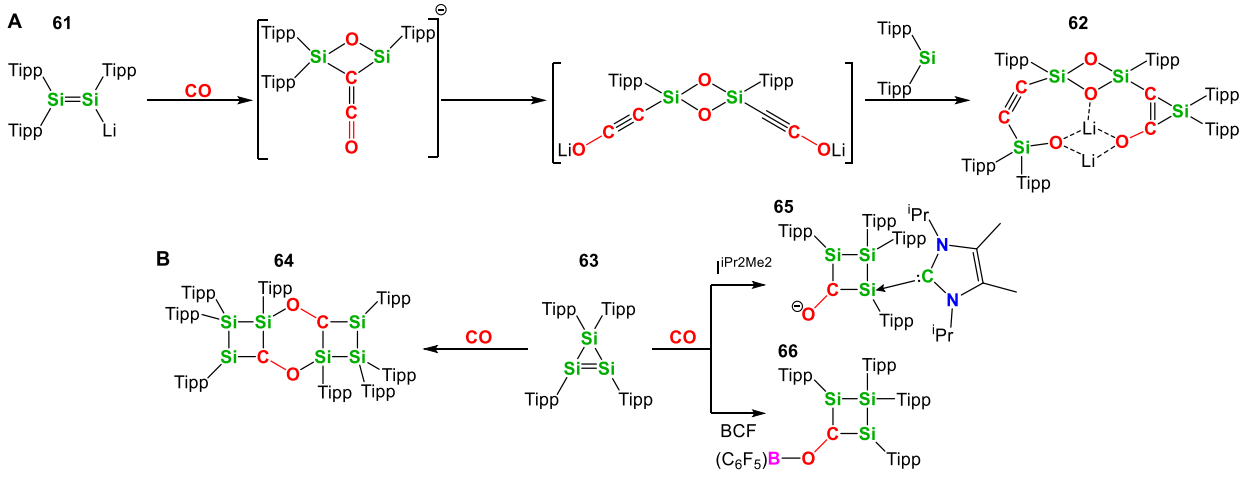

Scheme 1.11: Reactivity of dimetallenes with CO

Reactivity of dimetallenes with NH_3

The first report of a dimetallene reacting with ammonia was in 2001 by Weidenbruch *et al*. who used the conjugated tetrasilabuta-1,3-diene (**68**; **Scheme 1.12**, **B**).[46] The cyclic product **69** was the results from two 1,2 additions of ammonia with the 7 membered ring being completed of a hydrogen bond between the two NH_2 groups. Remarkably the parent disilene **67** was not able to activate ammonia (**Scheme 1.12**, **A**), demonstrating the increased reactivity that conjugation affords the system. Subsequently Scheschkewitz *et al*. reacted the 2,4,6-trimethoxyphenyl (TMOP) protected disilenide (**70**) with ammonia, with the TMOP protecting group results in a highly polarised Si=Si bond which helps to facilitating this reactivity (**Scheme 1.12**, **C**).[45] The iminodisilene **72** was found to activate NH_3 to form the anti-addition product **74** at -78 °C (**Scheme 1.12, D**).[44,179] It was observed that when performed at 25 °C the reaction proceeded to the oxidative addition product **73**.

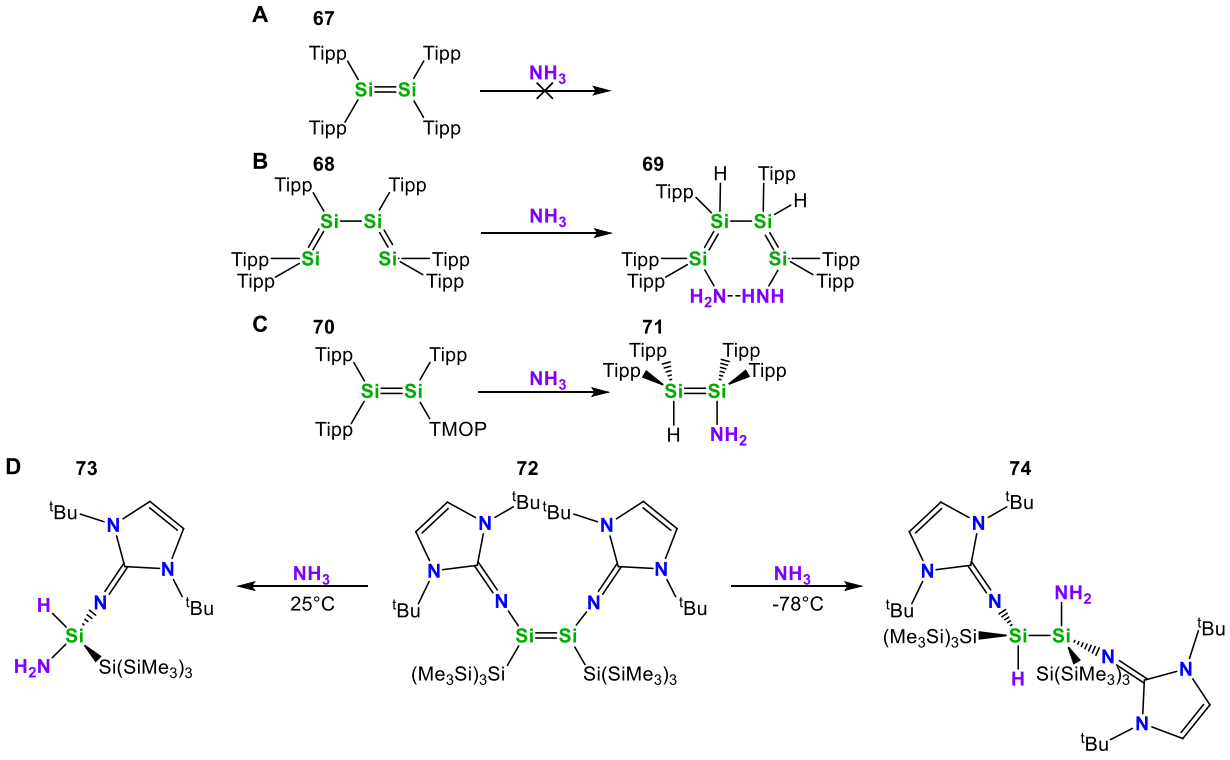

Scheme 1.12: Reactivity of dimetallenes with NH_3

Dimetallynes

Dimetallynes are the heavier analogues to alkynes which, like dimetallenes, exhibit trans-bent geometries which can either be rationalised by a second-order Jahn–Teller distortion or by the CGMT models although, the CGMT model deteriorates somewhat for lead systems).[180–184] Dimetallynes can be prepared by the reduction of halometallynes or by the dehydrogenative coupling of the metallylene hydride.[185] As with dimetallenes, the degree of trans-bending increase down the group with a corresponding decrease in multiple bond character and increase in lone pair character.[4,5] This renders these systems capable of activating a diverse array of substrates including alkenes. However, they have not been found to react with either NH_3 or CO.[4,5,9,180]

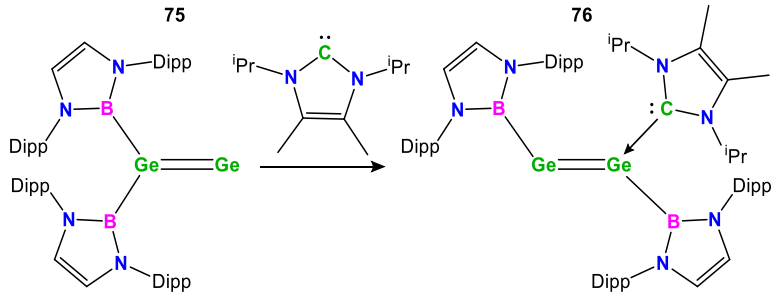

Scheme 1.13: reaction of vinylidene **74** with a carbene to generate the digermyne **75**

A number of heavier isomers of ethyne have been investigated using DFT methods, revealing a number of energetically accessible configurations.[186–188] For E_2H_2 systems these calculations predict, as with the ethene analogues, that bridged systems are the energetic minimum but also predict the vinylic geometry to be a stable isomer. Aldridge *et al*. the isolated a stable digermanium vinylidene (**75**), with the more traditional trans-bent geometry being accessible through the addition of an NHC (**76, Scheme 1.13**).[189] This is remarkable as it further highlights the ability of heavier main group systems to adopt geometries not accessible to thier lighter congeners.

Dimetallyne systems have been reduced further to the formal 0 or +0.5 oxidation states by Power *et al*.[190] Reduction of these alkyne analogues leads to an increase in the bond lengths and a greater trans-bending, particularly in the case of the dianion. The dimerisation of the radical cation, for Power's systems while not observed, could lead to a aromatic 2π cyclobutadiene (CBD) type systems.[191] Anionic systems of the $[CBD]^{2-}$ type have been synthesised for silicon and germanium via reduction of the corresponding neutral cyclic precursors **77a**/**b** (**Figure 1.13**).[192] These systems do not display planar geometries and nucleus independent chemical shift (NICS) calculations indicated no diatropic ring current. The mixed CBD **78** also demonstrated significant charge localisation which implies minimal aromaticity. The related $In_4\{B(NDippCH)_2\}_4]^{2-}$ CBD^{2-} system was synthesised by Aldridge *et al*. which did demonstrate moderate aromatic character based on NICS calculation and a near planer In_4 core.[193]

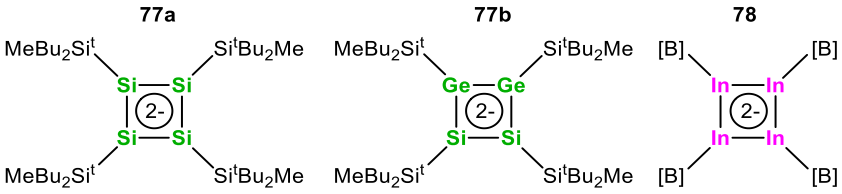

Figure 1.13: Reported heavier CDB analogues

Group 13 systems

This thesis centers on the study of boron and aluminium from group 13, chosen for their widespread availability and minimal toxicity. These elements are particularly notable for their inherently higher reactivity relative to heavier group 13 counterparts, a phenomenon commonly ascribed to the inert pair effect.

Boranes

Trivalent boranes equipped with electron withdrawing substituents have been used extensively as Lewis acids due to their formally vacant p orbital and high electropositivity and Lewis acidity.[13,194,195] These systems commonly form adducts with Lewis bases, which curtails their effectiveness in N-H activation.

Reactivity of boranes with CO

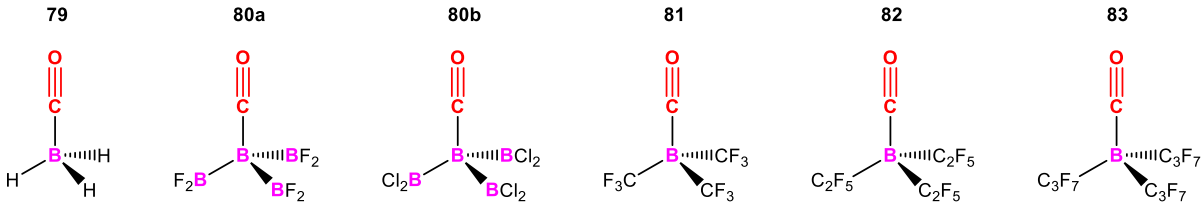

Figure 1.14: A selection of simple borane carbonyl complexes

A number of borane-carbonyl complexes have been structurally characterised, with the simplest BH_3·CO being first reported in 1937. However, due to the inherent instability of these compounds it was not until much later that the first of these systems could be structurally characterised by SCXRD (**Figure 1.14**).[196–199] Timms *et al*. reported the structure of $(BX_2)_3B$·CO (X = F or Cl) (**Figure 1.14**, **80a/b**) in 2000 featuring the electron withdrawing BCl_2 and BF_2 groups.[200,201] These compounds give rise to IR stretching frequencies that are hypsochromically

shifted (**80a**, 2162 cm^{-1}; **80b**, 2176 cm^{-1}) with respect to free CO (2143 cm^{-1}), indictive of strengthening of the C-O bond and an interaction that is dominated by σ donation from the CO with minimal back-donation.[202] Berke and Erker *et al*. performed DFT calculations and carried out energy decomposition analysis (EDA) on the $B(C_6F_5)_3$·CO adduct which concluded that the magnitude of the σ interaction was 5 times greater than that of the π back-bonding component.[203] Given the importance of the σ interaction, increasing the Lewis acidity of the boron centre through increasingly electron withdrawing groups would be expected to lead to more stable boron carbonyl complexes. Consistency, compounds **81-83** (**Figure 1.14**)[204,205] feature fluorinated alkyl groups, enhancing the Lewis acidity and resulting in greater hypsochromically shifted CO stretching frequencies (**81**, 2252 cm^{-1}; **82**, 2263 cm^{-1}; **83**, 2249 cm^{-1}). It should be noted that these compounds cannot be synthesised through direct addition of CO to the borane, but through solvolysis of a borate anion.

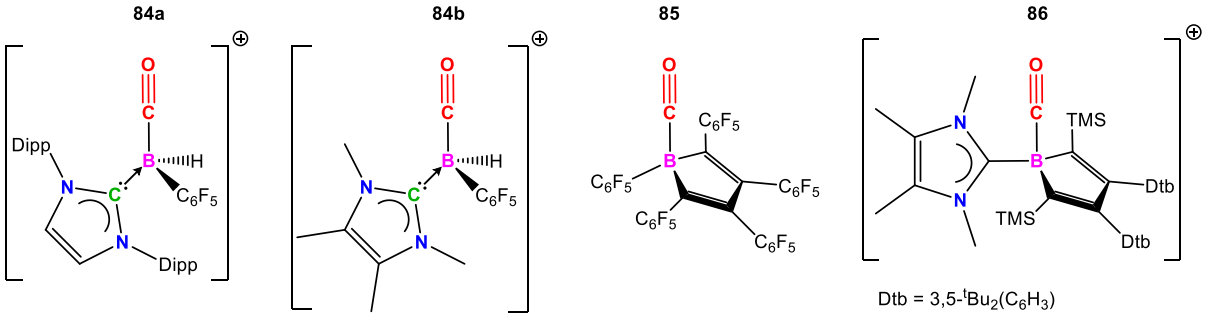

Figure 1.15: Borane carbonyl complexes employing borenium cations (**1.2.6a/b**) and borroles (**1.2.7, 1.2.8**)

In order to further increase the Lewis acidity, Erker *et al*. employed a borenium cations (i.e a boron cation stabilised by a Lewis base) to access cationic boron carbonyl complexes **84/b** from the reaction of the parent borenium species with 1 bar of CO at room temperature (**Figure 1.15**).[206,207] Both species were found to be stable with respect to reduction by the adjacent B-H moity. Moreover Piers *et al*. synthesised complex **85**, which was found to release CO upon heating or expose to vacuum.[208] **85** features highly electron withdrawing C_6F_5 groups along with the an antiaromatic borole framework, which loses its antiaromatic character upon coordination of a CO, creating a strong driving force for forming the carbonyl complex.[209] Sindlinger *et al*.

combined these approaches using the cationic borole to form **86** that reversibly binds CO.[210] Unlike all previous examples of borane carbonyl complexes the CO stretching frequency is bathochromicly shifted to 2128 cm^{-1} indicating there is a greater degree of back-bonding in this system. EDA using the natural orbitals for chemical valence (NOCV) method was carried on this system which revealed that the π system of the borole was responsible for the increase in back bonding interactions.

Borylenes

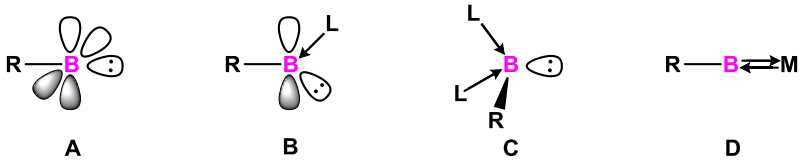

Figure 1.16: Orbital morphologies of different borylenes

Borylenes are mono-coordinated species with boron in a formal +1 oxidation sate. They are regarded as analogues of carbenes with two vacant orthogonal p orbitals and a filled non-bonding orbital (**Figure 1.16**, **A**).[211–213] Mono-coordinate borylenes (**Figure 1.16**, **A**) have not been isolated and additional stabilisation is invariably required to generate isolable compounds.[213] Stabilisation can occur though the addition of one or two donor ligands (**Figure 1.16**, **B** or **C**) that can quench one or both of the vacant p orbitals or though coordination to transition metals, analogous to Fischer carbene complexes (**Figure 1.16**, **D**). The first tricoordinate borylene was synthesised by Bertrand *et al*. and featured two CAAC ligands bound to a BH fragment.[214] While the tricoordinate borylenes are remarkable, their orbital morphology is not conducive to binding free CO or activating N-H bonds.

Reactivity of borylenes with CO

A number of examples of borylene systems reacting with CO have been reported. The tricoordinate borylene CO complex **88**, reported by Xie *et al*., was prepared via substitution of bromide with a CO molecule originating from $W(CO)_6$ (**Scheme 1.14**, **A**).[215,216] This CO complex shows a highly bathochromicly shifted CO stretch (2021 cm^{-1}) indicating a large degree of back

bonding from the filld p orbital on the boron centre. Bertrand *et al*. prepared the dicoordinate borylene **89** stabilised by a $CAAC^{cy}$ moiety.[217] The calculated minimum structure demonstrates a near linear arrangement of the C=B=N unit (175.48 °) due to the nitrogen lone pair donating into the vacant p orbital on boron and the filled p orbital on boron donating into the π* orbital on the CAAC. Scanning the energetic surface reveals a low barrier to bending (**89a-b** = +5.7 kcal mol^{-1}) allowing the filled and vacant orbitals on boron to become active in bonding, and facilitating the reaction with a molecule of CO (**Scheme 1.14**, **B**). The IR stretching frequency of the CO group in **90** is 1956 cm^{-1} indicating a significant degree of π back-bonding, i.e. much more than in **88** presumably due to the presence of three π accepting ligands vs two π accepting ligands in **90** so the electron density on boron is shared between fewer back-donation interactions. Braunschweig *et al*. reported the $CAAC^{dipp}$ stabilised arylborylene **92**, which was synthesised from the transition metal stabilised borylene **91** through the addition of $CAAC^{dipp}$ (**Scheme 1.14**, **C**).[218] This system displays a bathochromically shifted CO stretching frequency (1942 cm^{-1}), lower than that of **88**, and is accompanied by an increase in the C–O bond length (**92,** 1.158(2) Å; **88**, 1.091(3) Å) indicating a greater degree of back-bonding in this system. Upon photolysis the OC–B bond is broken, releasing CO and leaving the highly reactive dicoordinate borylene which subsequently undergoes intramolecular C–H activation. The Braunschweig group also reported the first multiple complexation of CO at a main group centre, utilising the bulky Tripp- supported terphenyl ligand with two CO molecules bound (**94**; **Scheme 1.14**, **D**).[219] This system was synthesised from the molybdenum carbonyl stabilised borylene (**93**) under a CO atmosphere at 80 °C with accompanying formation of $Mo(CO)_6$. Two IR stretching bands are at 1942 cm^{-1} and 2060 cm^{-1} due to the symmetric and asymmetric stretches, as commonly seen in transition metal cis-dicarbonyl complexes. The bathochromically shifted IR stretch is indicative of a large degree of back-bonding. While this reactivity is remarkable, it must be noted that all borylene systems but **90** were synthesised from transition metal complexes.

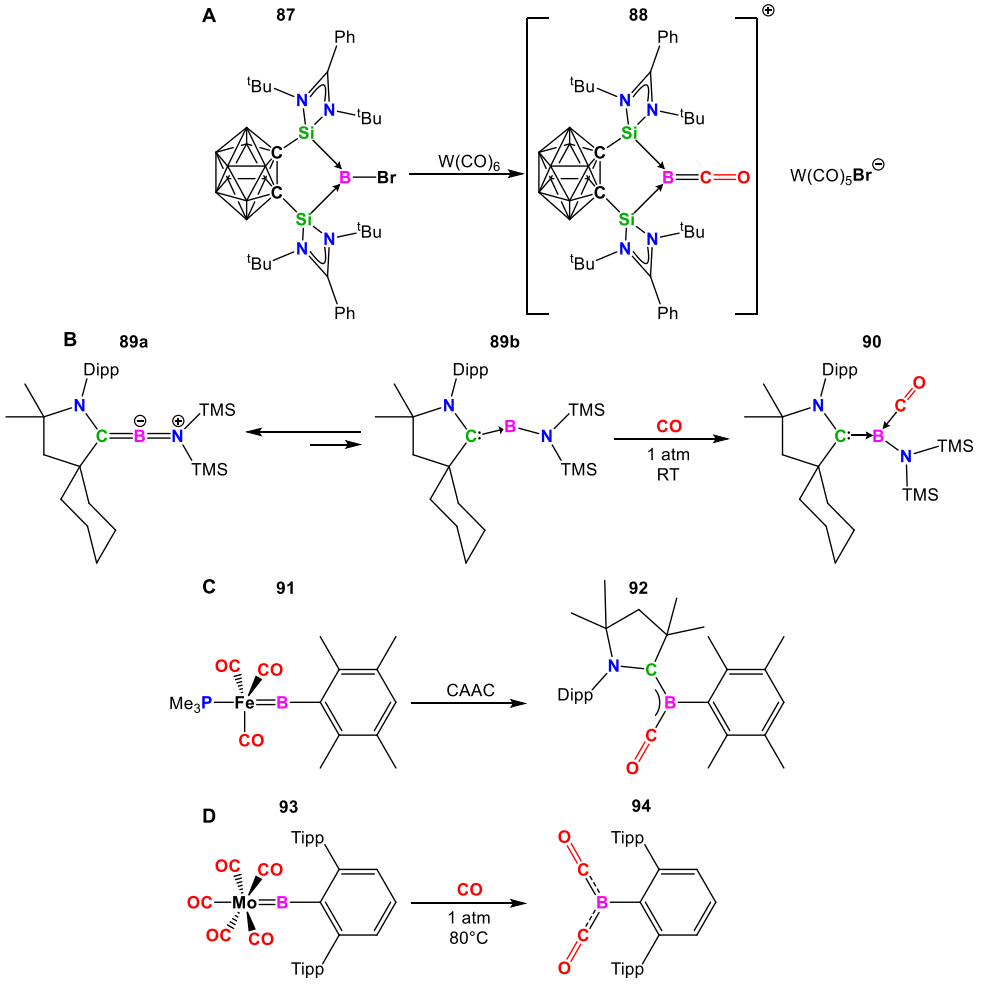

Scheme 1.14: Reactivity of borylenes with CO

Aluminium

Aluminium makes up 8.2% of the Earth's crust by mass, making it the third most abundant element and the most abundant metal.[220] Much like boron, aluminium trihalides are used as Lewis acids in synthetic chemistry, while organoaluminium compounds are used as alkylating agents and used in Zeiger Natta catalysis for the polymerisation of olefins.[221–223]

Aluminium(I)

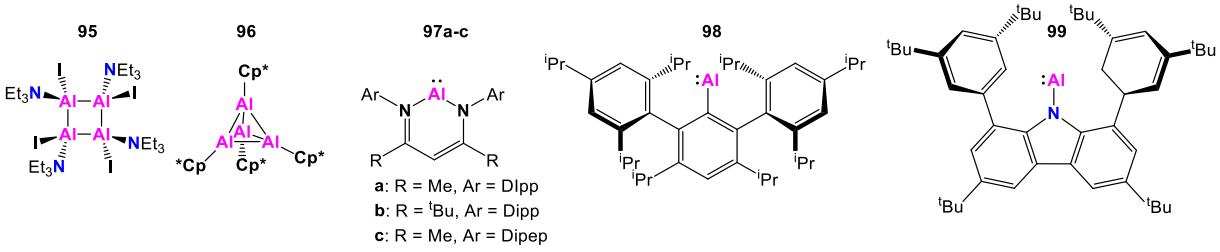

Figure 1.17: A selection of neutral aluminium(I) systems

Aluminium in the +1 oxidation state has become an area of significant interest in the past decade.[224–227] While simple aluminium species in the +1 oxidation state are prone to disproportionation, the tetrameric binary halides have been structurally characterised when coordinated with amine donors (**95**, **Figure 1.17**).[228–230] In 1991 Schnöckel *et al*. synthesised the first stable organo-aluminium(I) species $(Cp^*Al)_4$, (**96**, **Figure 1.17**), that adopts a tetrahedral geometry with η^5-Cp* ligands capping the vertices.[231] **96** was originally synthesised by the reaction of metastable AlCl with $MgCp^*_2$ but a more accessible synthesis involving the reduction of Cp^*AlCl_2 with potassium metal has since been reported by Roesky *et al*. **96** dissociates into monomeric AlCp* units at elevated temperatures which propagates much of the onwards reactivity of **96**. Efforts to stabilise monomeric species have led to an array of cyclopentadienyl aluminum systems featuring increasing steric bulk.[232–234] In 2000 Roesky *et al*. reported the synthesis of a monomeric aluminium species featuring a bulky beta-diketiminate (BDI) ligand (**97a**, **Figure 1.17**).[235] This species was synthesised via the reduction of the corresponding di-iodide with potassium. Since the initial synthesis two other derivatives have been reported, **97b** by substituting the backbone methyl groups for t-Butyl groups and **97c** substituting the Dipp groups for extremely bulky diisopentylphenyl (Dipep) groups.[236,237] More recently Power *et al*. synthesised the first mono-coordinate or free aluminylene (**98**, **Figure 1.17**), a heavier analogue of a borylene, featuring bulky terphenyl ligands that shroud the reactive aluminium centre.[238] A second "*free*" aluminylene (**99**, **Figure 1.17**) was reported independently by both the Hinz *et al*. and Liu *et al*. and is stabilised in a similar manner to **98** by shrouding the aluminium centre with bulky aryl groups derived from a carbazolyl ligand.[239,240] While this class of free aluminylene species is in its infancy reactivity towards H_2, olefins and alkynes has been shown however thus far no reactivity towards NH_3 or CO has been reported.[227,241]

Reactivity of neutral aluminium*(I) compounds with CO*

The majority of the reactivity of neutral aluminium(I) systems with CO revolves around BDI-supported complex **97a**, and insertion reactions into the C-Al bond (**Scheme 1.14**). However, directly adding CO to **97a** does not result in any reaction. [242] Crimmin *et al*. reported that the

addition of CO in the presence of $W(CO)_6$ results in a bicyclic CO homologation product being formed **100** (**Scheme 1.15**, **A**). [242] Moreover addition of further CO to complex **100** led to the chain growth from C_3 to C_4 (**101**) with the additional CO molecule inserting into the C–Al bond. This insertion step was confirmed through a ^{13}C labelling experiment to allow for the identification of which CO moiety originated on the $W(CO)_6$ and which originated from the trapped gaseous CO (**Scheme 2a**). In both **100** and **101** the tungsten is bound by a carbenic carbon, but this carbon centre is not involved in the chain growth mechanism as shown experimentally and theoretically. Cui *et al*. reported the insertion of CO into the Al-C bond of the strained aluminacyclopropene ring of **102** to form the metallocyclobutenone system **103** (**Scheme 1.15**, **B**).[243] This system was found to further insert a single oxygen atom into the Al-C bond when exposed to O_2, to form the aluminacyclopentene, leading to further relief of ring strain. A further CO insertion into the Al-C bond of **97a** was reported by Crimmin *et al*. (**Scheme 1.15**, **C**).[244] The unsaturated [2.2.1] metallobicyclic compound **104** is formed by the [4+1] cycloaddition of 1,3-cyclohexadiene with **97a**. Exposing **104** to 1 atm of CO at 25 °C, furnishes the [2.2.2] metallocycle **105** through Al–C insertion. Moreover on heating **105** to 100 °C, **104** is regenerated with release of CO, consistent with a reversible insertion. In contrast, the saturated metallocycle **106**, formed from **97a** and bicyclo[2.2.1]hept-2-ene, reacts with CO irreversibly. This contrasting reactivity was studied theoretically (via DFT calculation) and experimentally (with Eyring analysis) indicating the reaction from **104** to **105** is less exergonic than the conversion of **106** to **107**.

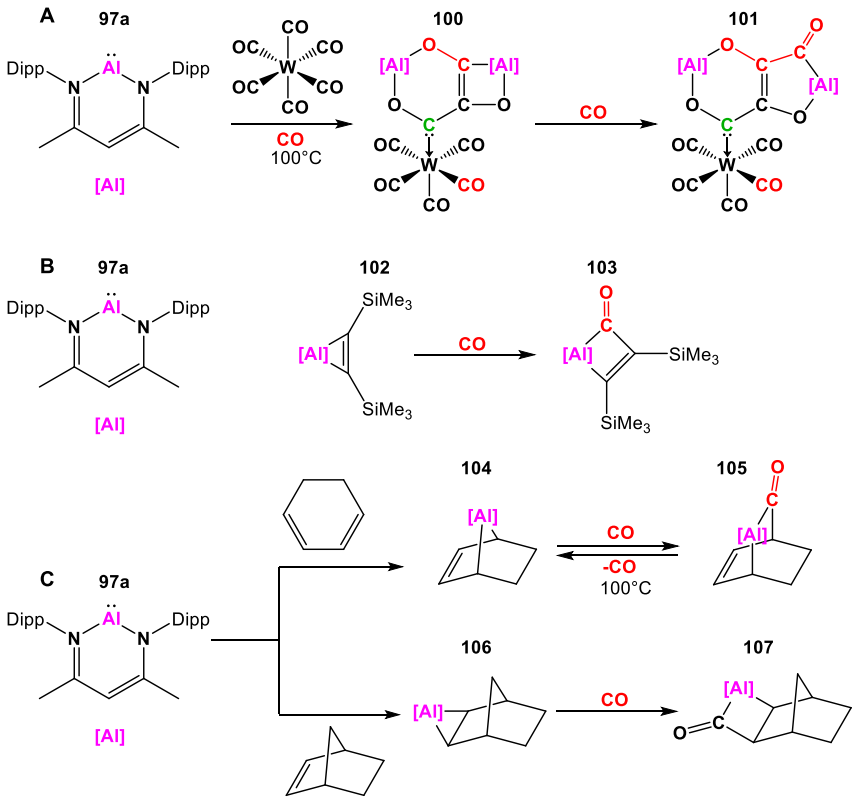

Scheme 1.15: Reactivity of neutral aluminium(I) compounds with CO

Aluminyl compounds

Anionic aluminium(I) systems, aluminyl anions, challenge the conventional understanding that categorises group 13 elements as electrophiles. Aldridge *et al*. reported the first aluminyl compound **108** (**Figure 1.18**) in 2018, supported by the xanthene-based diamido-ligand (NON).[245] **108** was synthesised via a KC_8 reduction of the corresponding Al(III) compound (NON)AlI; reducing agents with lower reduction potentials yeild the Al(II) dialumane $[(NON)Al]_2$ instead. Interestingly attempts to further reduce the dialumane $[(NON)Al]_2$ failed, indicating it is not an intermediate in the synthesis of **108**. SCXRD of **108** revealed a dimeric structure held together with potassium-arene interactions, with a very large Al-Al distance (6.627(1) Å) indicating no significant covalent interaction. A weak O–Al interaction (2.28(2) Å) is observed, believed to potentially be a weakly destabilising interaction on the lone pair of aluminium. The dimeric structure of **108** is found not to be just be a crystallographic packing artifact, with DOSY NMR measurements determining the hydrodynamic raidii to be much greater than that of the monomeric (NON)AlI. This dimeric structure can however, be disrupted through the

sequestration of the potassium cation using cryptand-222, therefore forming the "*naked*" aluminyl analogue **108*** with the structure having no close K···Al interactions.[246] Umpolung nucleophilic reactivity of **108** was predicted by DFT calculations indicating a HOMO which is found at a notably higher in energy than that of the neutral Al(I) complex **97a** (0.6 eV for **97a** and 3.65 eV for **108***) and was experimentally verified by the reaction with MeI from which the product was shown to be (NON)Al-Me.

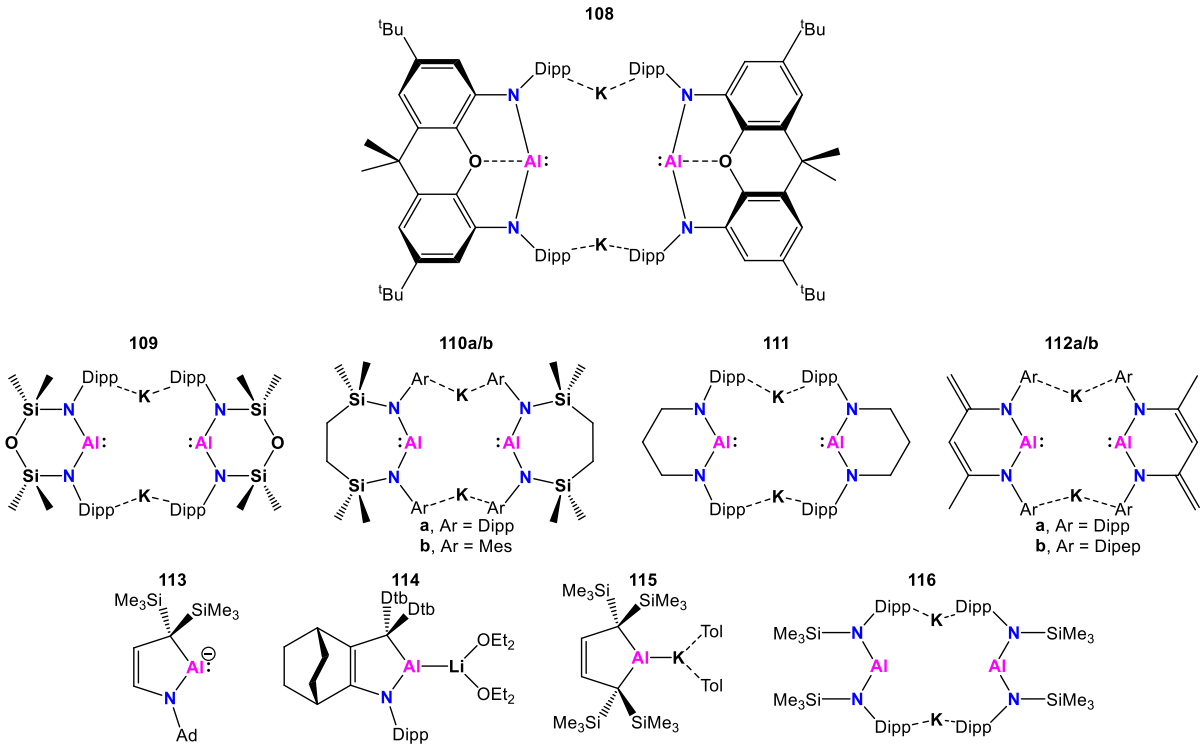

Figure 1.18: Aluminyl anions documented in the literature

Since the initial report of **108** a number of other alumniyls compounds have been synthesised with different ligand architectures. Six subsequent aluminyl compounds featuring diamido-ligand have been reported, all of which exist as potassium dimers in the solid state (**Figure 1.18**). The first of these was reported by Coles *et al*. in 2019 featuring the ^{Si}NON ligand (**109**).[247] The closely related aluminyls **110a/b** were reported by Hill *et al.* utilising a 7 membered variant of the ^{Si}NON ligand.[248,249] Yamashita *et al.* subsequently reported aluminyl compound **111** featuring simple 1,3-propanediamide ligand.[250] The first acyclic aluminyl systems was reported by Hicks and Liptrot *et al.* utilizing the bulky DippN(SiMe$_3$) ligands (**116**).[251] **109-111,116** were all synthesised in an analogous manner to **108** via reduction of the corresponding aluminium iodide

compound. Harder *et al.* utilised a different synthetic approach, exploiting the well-established BDI aluminium(I) compound (**97a**/**c**) and KHMDS, which led to protonation of the backbone and generation of aluminyl **112a**/**b**.[252,253] The N–Al–N angle can be employed to compare aluminyl systems that utilize common diamido-based ligands, in a manner similar to carbene systems, in which a closer approach to linearity leads to a smaller HOMO-LUMO gap (**Table 1**).[4,225] The largest N–Al–N angle is counter-intuitively achieved by **108** with the acyclic aluminyl (**116**) having a significantly narrower angle. **110a**/**b** unsurprisingly has a larger angle due to the 7 membered ring than **109** with **111** and **112a**/**b** having the narrowest angles.

Table 1: Table of N-Al-N Angles in the structures of **109-111** and **116**

	N-Al-N Angle (°)	
108	128.1(1)	
109	103.89(8)	
110a	108.84(9)	108.77(9)
110b	109.73(11)	
111	98.46(16)	98.42(15)
112A	96.05	
116	116.33(16)	116.61(17)

Mirroring the evolution of carbenes, the groups of Kinjo and Yamashita *et al.* have pioneered the use of less stabilising alkyl-amino and alkyl substituents in the synthesis of aluminyl compounds (**113-115**).[254–256] These systems are generated by the reduction of the corresponding dialumanes, offerning a contrast with **108** where this synthetic strategy is not possible. In a departure from the diamido-systems, none of **113-115** exist as the potassium dimer, instead they are isolated as the monomeric aluminyl species on reaction with a sequestering agent in the case of **113** (12-crown-4), or with a direct metal aluminium bond (**114**/**115**).

A DFT study has compared the frontier molecular orbitals of the dialkyl (**115**), alkylamido (**113**) and diamido (**108**) aluminyl systems (**Figure 1.19**).[225] The HOMO energies follow the expected trend with **115** being the highest in energy but very close to that of **113** and a significant gap of 0.5 eV to diamido-substituted **108**. The LUMOs of the aluminyl systems are not always the vacant p orbital centred at aluminium due to the presence of extended π systems that result in low lying π* orbitals. In order to compare like-for-like the vacant p orbital energies

(LUMO*) were considered showing that the diamido aluminyl has the lowest energy orbital. This is attributed to the geometric constraints of the ligand preventing orbital overlap with the lone pairs on the aluminium adjacent nitrogen atoms. This leads to the HOMO-LUMO* gaps being very close (**108**, 3.58; **113**, 3.42; **115**, 3.72 eV), with **113** having the smallest gap.

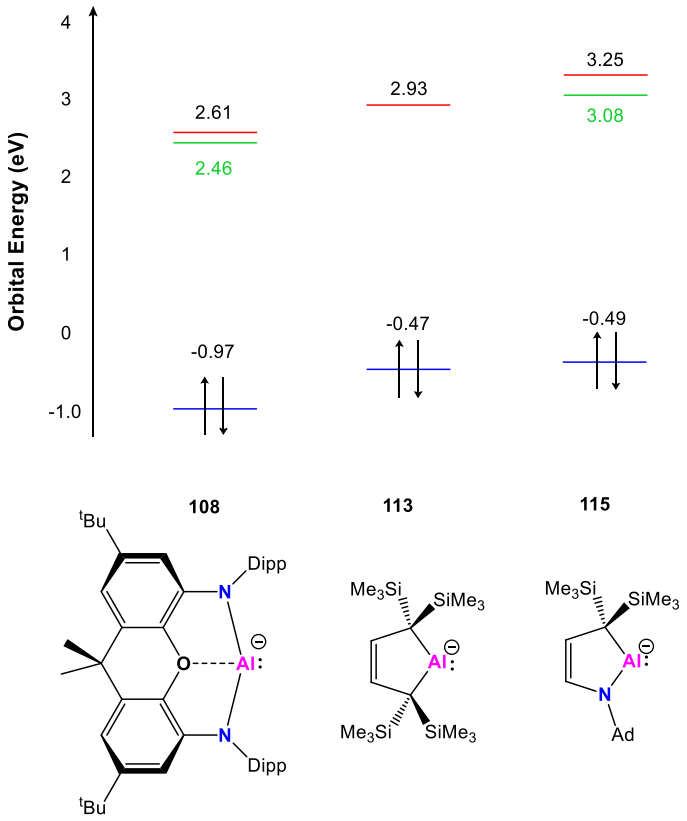

Figure 1.19: Frontier molecular orbital energies for **108**, **113** and **115**. Blue represents the HOMO, green represents the LUMO and red represents the vacant p orbital centred at Al

Reactivity of aluminium*(I) compounds with CO*

In a study published at the same time as work described in this thesis, Coles *et al.* reported the reaction of **109** with CO (**Scheme 1.16**).[257] It had previously been reported that the addition of tetramethylethylenediamine (TMEDA) breaks up the dimeric structure of **109**.[258] When subsequently exposed to CO, the homologation product **117**, which contains the $[C_4O_4]^{4-}$ fragment, is formed over a period of 4 days. This $[C_4O_4]^{4-}$ fragment, featuring C=O units in a syn arrangement, is reminiscent of the work by Crimmin *et al.*[244] (**101**). Heating an isolated sample of **117** under an atmosphere of CO for 2 days resulted in the isomerisation of the $[C_4O_4]^{4-}$ fragment. The direct interaction of CO with compound **109** resulted in the formation of a

product that could not be isolated. Subsequent addition of TMEDA facilitated the isolation of compound **119**, which incorporates the novel $[C_5O_5]^{5-}$ fragment, albeit with exceedingly low yields. The authors suggest that the $[C_5O_5]^{5-}$ fragment is more delocalized than the $[C_4O_4]^{4-}$ fragment, based on solely on crystallographically determined bonding parameters. However, the differences in these parameters are not statistically significant, rendering this claim spurious. While this report shows the remarkable CO homologation by an aluminium centre, no attempt was made either experimentally or theoretically to explain the mechanism for this process.

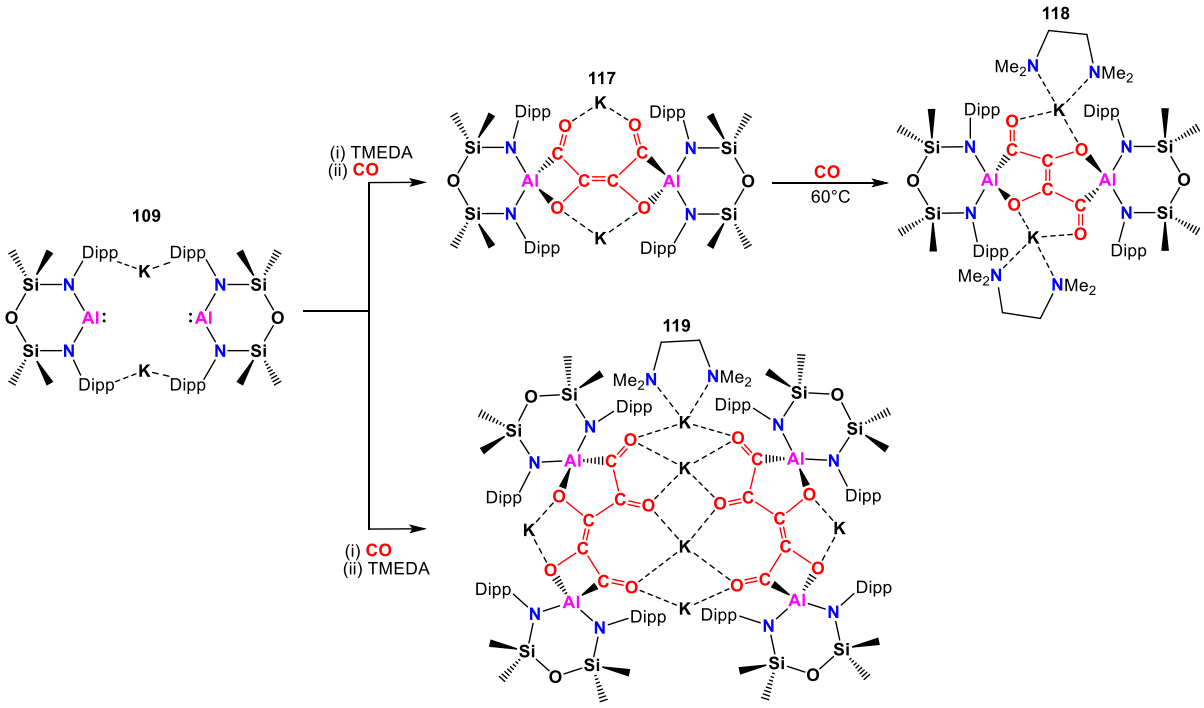

Scheme 1.16: Reactivity of **109** with CO

In addition to the direct reactivity of Aluminyl compounds with CO, aluminyl derivatives have shown to react cooperatively with CO.[224,225] Aldridge *et al.* demonstrated the aluminyl amide (**120**) reacts rapidly with four equivalents of CO to generate the C_2 homologated product **121** (**Scheme 1.17**, **A**).[259] The mechanism for this process was examined by DFT calculations and a pathway found involving an initial cooperative activation process across the Al–N bond followed by a rearrangement of the isocyanate ligand so generated and a second cooperative activation across the DippNC adduct of the aluminium oxide. In both cases, the aluminium centre is acting as an electrophilic fragment in an FLP type process. Coles *et al.* reported the uptake of

CO by the aluminyl derivatives **122**/**125** in conjunction with ethene uptake (**Scheme 1.17**, **B**).[260] The reaction of **109** with ethene leads to the formation of ethene activation products, resulting in either the dimeric structure **125** or the monomeric structure **122** when 12-crown-4 sequesters the potassium. **122** reacts in an analogous manor to **102**, **104** and **106** with insertion into the Al–C bond expanding to the metallocyclobutanone **123**. Upon heating a ring expansion then occurs to the aluminacycle **124**, in order to relieve ring strain. Conversely the dimeric structure **125** reacts with CO to form the asymmetric product **126**, with an ethyl ligand and a $[C_3H_3O]^{-3}$ moity. The mechanism, as calculated using DFT, for the production of **126** was proposed to go via a metallocyclobutanone intermediate with initial Al–C insertion and subsequent proton transfer and rearrangement. Neither of these examples demonstrates CO capture at the aluminium centre, nor do they exhibit the nucleophilic nature of aluminium.

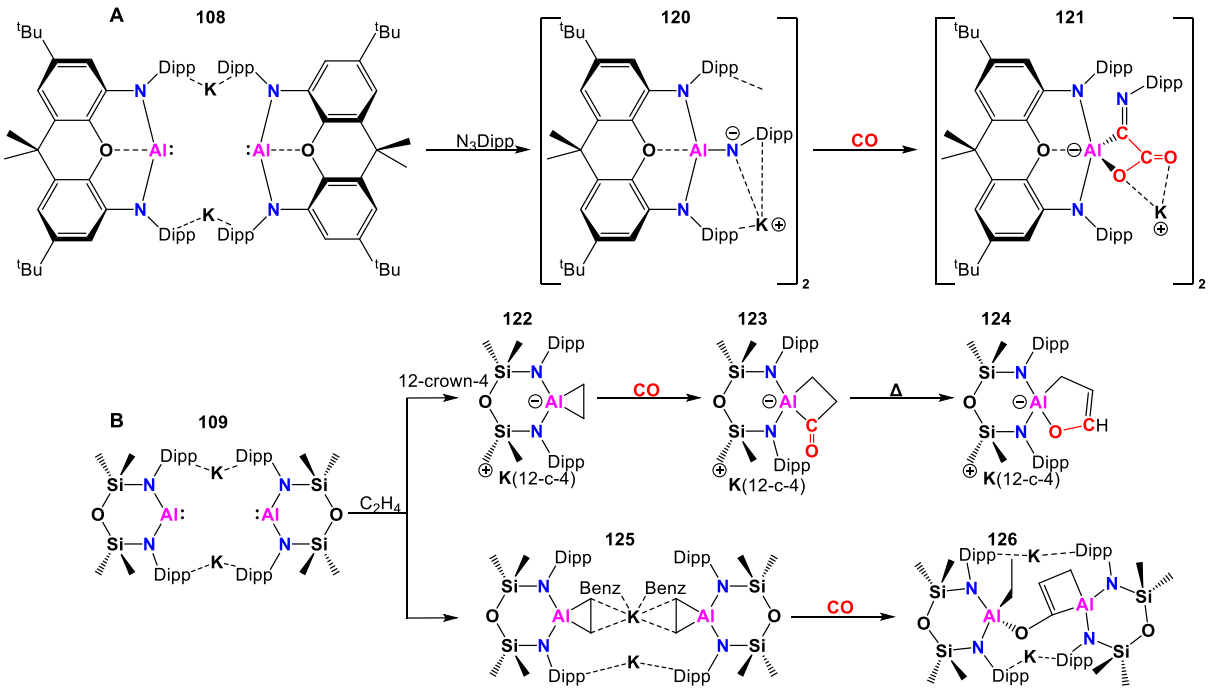

Scheme 1.17: Reactivity of Aluminyl systems and then onwards reactivity with CO

Group 2 systems

The series of alkaline earth metals manifests a considerable diversity in physicochemical properties across the group. Notably, magnesium and calcium, with terrestrial abundances of approximately 2.3% and 4.2% respectively, are distinguished by their ready availability and

essential roles in various geological and biological processes. [220,261,262] Conversely, beryllium and radon are characterized by their relative scarcity within the Earth's crust, with the former's involvement in nuclear fusion reactions further contributing to its rarity, and the latter, devoid of stable isotopes, representing the ephemeral nature of certain elements within this group.[263,264]

This disparity in abundance and accessibility is mirrored in the variation observed in the ionic and atomic radii down the group, transitioning from Be^{2+}, which exhibits the highest charge density of any element in the periodic table and a propensity for covalent bonding, to Ba^{2+}, characterized by one of the least charge densities on the periodic table and a predisposition towards ionic interactions.[265,266] Such variations are indicative of the complex interplay between electron configuration and resultant chemical behaviour, illustrating the nuanced relationship between atomic structure and bonding propensity within the alkaline earth metals.

The group oxidation state is +2 for the alkaline earth metals, which is heavily favoured due to the large negative reduction potentials downs the group (Be, −1.85; Mg, −2.37; Ca, −2.87; Sr, −2.90; Ba, −2.91 eV).[265] This leads to the metals themselves being strong reducing agents, surpassed only by the alkali metals and renders the isolation of the low oxidation state species Ae^{+1}/Ae^{0} a synthetic challenge.[265] The key breakthrough in synthesizing low oxidation state Group 2 systems came in 2007 with the seminal work by Jones *et al.*, who successfully isolated the first magnesium(I) compound (**127** and **129c**; **Figure 1.20**).[267] This pioneering discovery paved the way for the subsequent isolation and characterisation of various related systems, as detailed below.

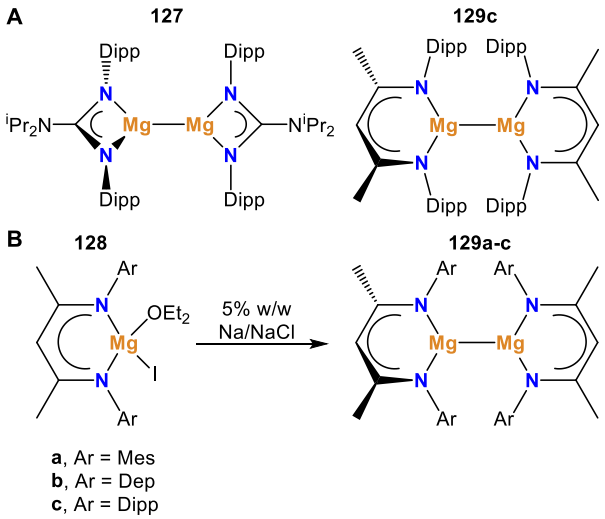

Figure 1.20: **A** The first structurally characterised Mg(I) dimers, **B** Large scale synthesis of **129a-c**

Magnesium

First synthesised by Jones *et al.*, the systems **127** and **129c** featuring bulky guanidinate (Priso) and bulky BDI ligands respectively have been unambiguously characterised as magnesium(I) dimers (**Figure 1.20**, **A**).[267] These systems were originally synthesised via a reduction with potassium in toluene on moderate scales, and yields were impacted by the poor surface area of the reductant.[268] However, a large-scale synthesis was subsequently reported using a novel reducing agent possessing a high surface area. The use of Na dispersed on finely ground NaCl (Na/NaCl), allows the synthesis of these Mg(I) compounds on multigram scale (**Figure 1.20**, **B**).[269] Remarkably **127** and **129a-c** exhibit exceptional thermal stability, being stable as crystalline solids up to 200 °C, a property which is unusual for low valent main group systems.[267,268] These systems have also been studied by DFT techniques using QTAIM revealing a (3, −3) critical point between the Mg atoms, referred to as a non-nuclear attractors (NNA).[270,271] NNAs correspond to large regions of negative Laplacian, a descriptor used to define the nuclear positions of atoms in the QTAIM framework. This leads to the bonding being described as two Mg atoms bonded to a pseudo-atom (or NNA), with the electron density associated with this pseudo-atom being visible in the residual electron density map in the SCXRD data.[271–274] NNAs have presented themselves in theoretical studies of metal-metal bonding in non-isolable systems, but in these systems have they profound effects on the observable chemical properties. The electron density

linked to the NNA in Mg(I) dimers permits the facile release of electrons, rendering them potent "*quasi-universal*" reducing agents.[268]

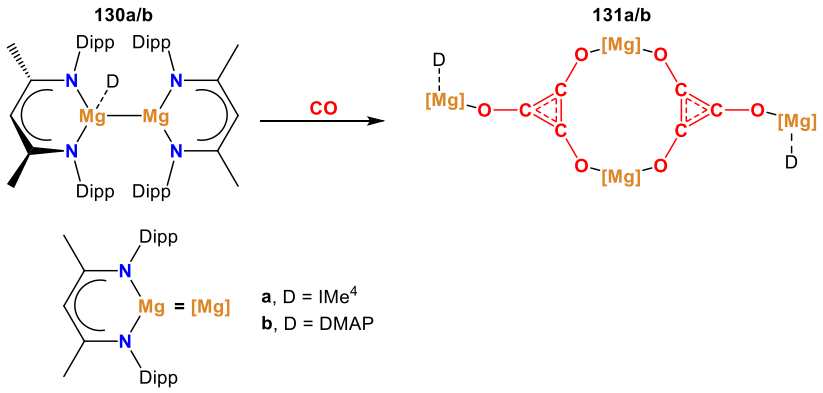

Scheme 1.18: Reaction of **130a/b** with CO

Since the initial discovery in 2007, a wide variety of novel Mg(I) dimers have been synthesised, yet the synthesis of monomeric radical species remains unsuccessful.[265,268,274,275] Attempts to stabilise a monomeric Mg(I) species have involved the use of, strong σ donating ligands coordinated to a variety of Mg(I) dimers leading to the systems of the type $(RMgL)_2$.[275–280] While breaking of the Mg–Mg bond under these conditions has not yet been observed, elongation of the Mg–Mg bond was observed to an increasing effect with increasing steric bulk of the donors.[275] The elongated Mg–Mg bond might be expected to lead to an increase in reactivty however, the addition of two ligands coordinatively saturates both Mg centres and thereby inhibits reactivity kinetically. Jones *et al.* made use of a single DMAP or tetramethyl carbene (IMe_4) ligand bound to the $(^{Dipp}NacnacMg)_2$ unit (**130a/b**) which led to increased reactivity allowing for the homologation of CO to **130a/b**, a mode of reactivity not possible with the "*free*" Mg(I) dimer (**Scheme 1.18**).[276,277] In a related reaction, **129a** was found to hexamerize CO to give a Mg benzenehexolate complex in the presence of a $Mo(CO)_6$ catalyst.[281]

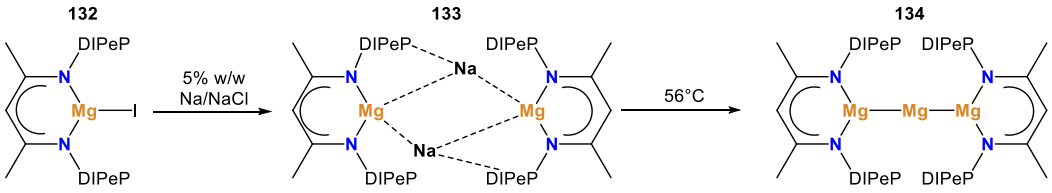

Scheme 1.19: Synthesis of Mg(0) complexes **133** and **134**

A Mg(0) complex was not reported until 2021 work by Harder *et al.*, who reported a synthesis involving reduction of the extremely bulky ^{DIPeP}NacNacMgI (**132**) with Na/NaCl to generate (^{DIPep}NacnacMgNa)$_2$ species **133** (**Scheme 1.19**).[282] The structure of **133** is likened to the aluminyl species (**108-112**) with two formally anionic [NacnacMg]$^{-1}$ fragments bridged by two [Na]$^+$ atoms. **133** is isoelectronic with the BDI aluminium species (**97a**). The structure of **133** reveals long Mg–Mg distances (5.7792(5) Å) precluding any direct bonding interaction. The Mg-Na distances, however, are relatively short (3.2116(7) and 3.4529(7) Å), being close to the sum of the covalent radii (3.19 Å). Natural population analysis (NPA) carried out on **133** calculated a BDI ligand charge of -1.07, indicating no significant metal to ligand charge transfer, with the magnesium and sodium both having a charge close to 0.5 (Al, 0.57; Na, 0.50). The authors suggest this fragment might be better described as $Mg_2Al_2^{2+}$ cluster, as NPA indicates transfer of electron density from Mg to Na. Upon standing, compound **133** gradually decomposes into ^{DIPeP}NacNacNa and a novel species featuring a Mg_3 unit **134** (**Scheme 1.19**). Analysis using QTAIM on **134** disclosed two NNAs bridging adjacent Mg-Mg atoms, mirroring the original Mg(I) dimers. Challenges in determining oxidation states through charges arise due to each NNA having 0.64 electrons in its associated basin. Opting for a pragmatic approach, the authors distribute the electrons in each NNA equally between the two neighbouring atoms, resulting in the charges Mg(0.90)-Mg(0.36)-Mg(0.90) and suggesting an oxidation state of Mg(I)-Mg(0)-Mg(I). Although this designation is convenient, the existence of NNAs between the Mg centres suggests a bonding scenario more intricate than this straightforward model might imply. It is proposed that the structural motif in **134** could act as a potential intermediate in the synthesis of Grignard reagents. Unlike Mg(I) dimers, both **133** and **134** exhibit reactivity towards H_2, highlighting the enhanced reactivity of these more extensively reduced fragments.

Beryllium

Beryllium's notable biotoxicity and scarcity render it less accessible for extensive research, contributing to its relatively underdeveloped chemistry among the non-radioactive elements.

[266,283,284] Despite these challenges, beryllium's exceptional charge density and inclination towards covalent bonding make it an intriguing subject for fundamental studies of bonding and mechanism.[265,266,283–286] Investigating the unique properties of beryllium could yield insights with implications extending throughout the Group 2 elements and across the Periodic Table, potentially enhancing our understanding of theories of chemical bonding.

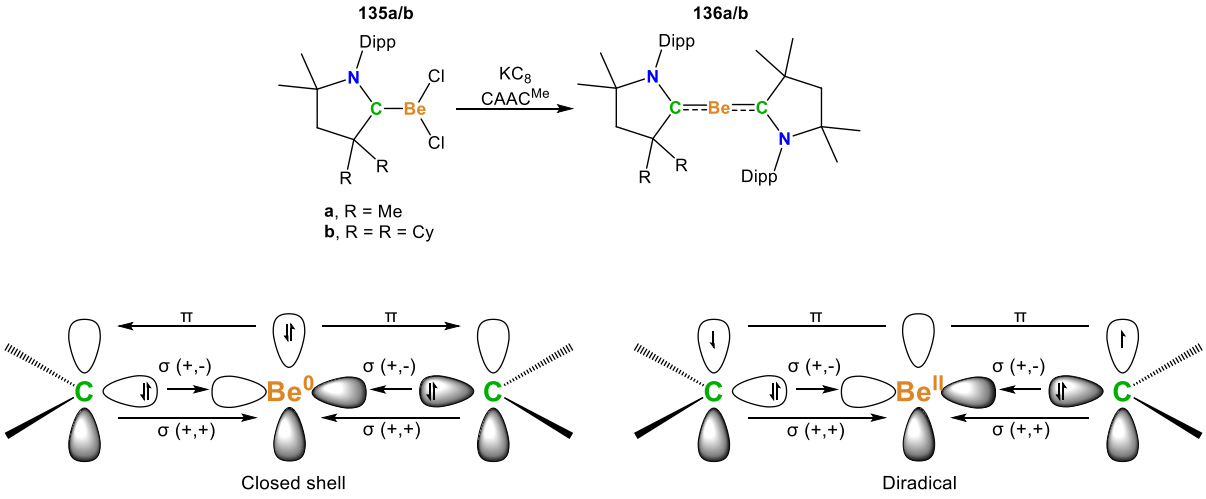

Figure 1.21: (top) synthesis of **136a/b** (bottom) different descriptions of the bonding in **136a/b**

The first purported example of low valent beryllium came from Braunschweig *et al.* in 2016 with the beryllium bis-CAAC complex **136a/b**.[287] This complex was synthesised, much like other CAAC stabilised low valent systems, via the reduction of the CAAC beryllium chloride (**Figure 1.21**, top; **136a/b**) with KC_8 in the presence of a second equivalent of CAAC.[288] This system was touted by the authors as the first isolated Be(0) system as determined by DFT calculations, but has subsequently been contested by a number of subsequent studies.[289–293] At the heart of this dispute is the role of the CAAC ligand and its highly π accepting nature, leading to an alternative bonding description of a diradicaloid singlet with the electron density instead residing in the CAAC p orbitals i.e as a Be^{2+} complex featuring two $[CAAC]^{\bullet-}$ ligands (**Figure 1.21**, bottom). While the truth may lie between these two divergent descriptions, the isolation of **136a/b** demonstrates an unusual bonding motif that could better help explain bonding in the heavier group 2 systems.

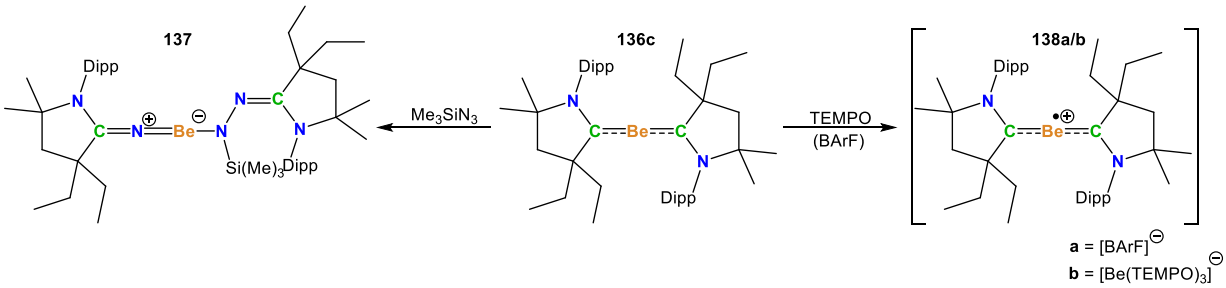

Scheme 1.20: Reactivity of **136c** with Me_3SiN_3 (left) and TEMPO (right)

Gilliard *et al.* further developed the chemistry of bis-CAAC beryllium complexes with the synthesis of **136c** in an analogous manor to **136a/b** but using the small CAAC ligand, $CAAC^{Et}$. [294] **136c** proved to be an effective reducing agent, enabling the isolation of the Bi(I) species CAAC-Bi(Ph) from its reaction with $(CAAC^{Et})BiCl_2(Ph)$. Notably, this species could not be directly obtained by reducing $(CAAC^{Et})BiCl_2(Ph)$ with alkali metals. In a later report Gilliard *et al.* demonstrated the isolation of the first Ae=N double bond via the reaction of **136c** with two equivalents of $TMSN_3$ (**Scheme 1.20**, left).[295] This reaction is proposed to proceed via the insertion into a CAAC=N_3-$SiMe_3$ intermediate, a species previously reported to be viable for CAAC systems. [296]

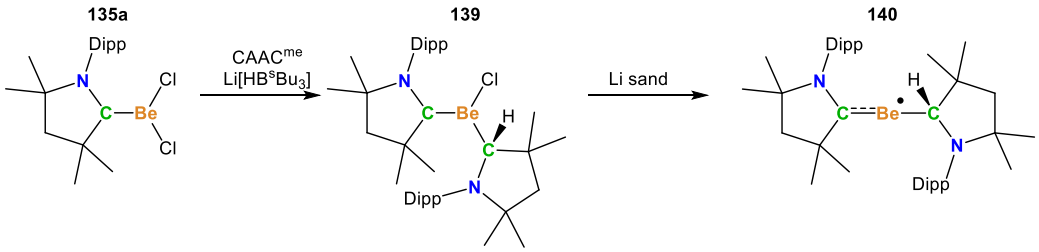

Scheme 1.21: Synthesis of the neutral Be radical **140**

Beryllium in the +1 oxidation state has been a target for much computational study in the last 50 years, centred around the Be(I)-Be(I) bond.[273,297–305] Gilliard *et al.* reported the oxidation of **136c** with TEMPO to generate the radical cation **138b,** with subsequent anion exchange to generate the BArF analogue **138a** (**Scheme 1.20**, right)**.**[306] This species was characterised by EPR spectroscopy, but showed no hyperfine coupling to the ^{9}Be nuclei, only to the ^{14}N nuclei of the CAAC ligand. The lack of coupling to the ^{9}Be nucleus was attributed to

diethyl ether solvent coordination, leading to reduced interaction with the ^{9}Be nucleus, overshadowed by the dominant ^{14}N nuclei coupling. It could however be also rationalised that the radical character is in fact mostly located on the CAAC ligands as found with related transition metal systems.[307] The authors report a DFT calculated spin density of 38% on the Be centre, with the rest of the spin density spread across the CAAC ligands supporting the idea that the radical character is mostly derived from the CAAC ligands. Given the ambiguity of the assignment of oxidation state of **136a-c,** the assignment of the Be(I) oxidation state of **138a/b** by the authors has to be brought into question. Following this report, Braunschweig *et al.* synthesised the neutral radical species **140** through a two-step synthesis.[308] The initial step proceeded through the reaction of **150a** with an additional CAAC ligand and L-selectride generating the CAAC(CAACH)BeCl **139** (**Scheme 1.21**). This species was then subsequently reduced with lithium sand. EPR spectroscopy was used to characterise **140**, revealing discernible hyperfine coupling associated with ^{9}Be. Despite the observation that only approximately 23% of the spin density was localized on the beryllium centre, and the majority residing on the CAAC ligand system, the authors nonetheless attributed an oxidation state of +1 to the beryllium centre.

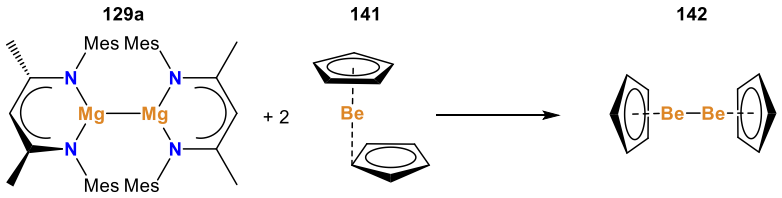

Scheme 1.22: Synthesis of diberyllocene **142**

While the reports of Be(I) systems by Gilliard and Braunschweig *et al.* are ambiguous, an unequivocal Be(I) compound, diberyllocene (**142**) was synthesised by the Aldridge group in 2023.[309] This marked the first stable compound with a Be(I)-Be(I) bond. Diberyllocene was synthesised through the reduction of $BeCp_2$ (**141**) in toluene with **129a**, and purification by sublimation (**Scheme 1.22**). **142** features a Be-Be bond length of 2.0545(18) Å, very close to the bond lengths predicted by previously reported theoretical studies.[273,298,299] Through DFT

investigation by the authors, employing the QTAIM method, a NNA is observed between the Be-Be bond. This is reminiscent of the heavier Mg-Mg bonded species **129a-c** and **127** and highlights the similarities in this type of bonding in group 2. The reactivity of **142** as a reducing agent was studied, drawing analogies from the widespread use of magnesium(I) as reducing agents. The reduction of (NON)AlI with **142** afforded (NON)Al–BeCp (**143**), transferring the BeCp fragment to the aluminium and centre and yielding a rare Al–Be bond (**Scheme 1.23**, left).[310] **143** had previously being synthesised in the reverse fashion from the reduction of **141** with the NON aluminyl compound **108**.[311] DFT analysis suggests that the Be–Al bond is best described in terms of a Al(II)–Be(I) species on the basis of natural population analysis in conjunction with Bader charges; the Be–Al bond also displays a NNA between the Al and Be units. The reduction of BDI zinc iodide with **142** afforded the ^{Dipp}NacnacZnBeCp, containing the first structurally characterised example of a Be–Zn bond (**Scheme 1.23**, right). DFT calculations on this species indicate that this species has a great deal of covalency in the bonding and is also best described as a Be(I)Zn(I) species. The reactivity of the diberyllocene as a reducing agent and as a source of Be(I)Cp, opens avenues into the possibility of making new Be-E bonds across the Periodic Table.

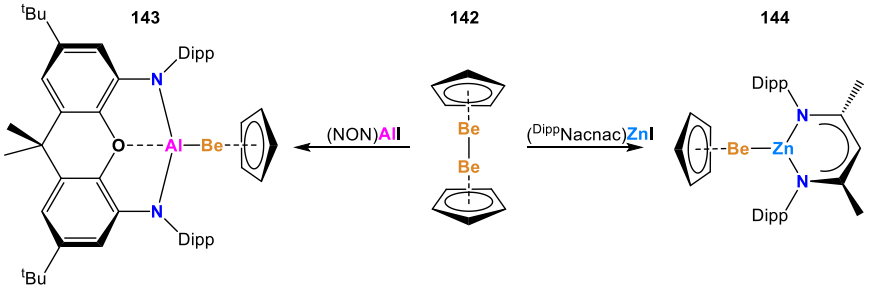

Scheme 1.23: Reactivity of **142** with NONAlI (left) and ^{Dipp}NacnacZnI (right)

Calcium and below

There are relatively few examples of low valent calcium complexes, due to the low (calculated) Ca-Ca bond dissociation energy, and inherent instability with respect to disproportionation.[265,272,285,312] In 2009 Westerhausen *et al.* reported the reverse sandwich complex, with 1,3,5-tris(phenyl)benzene (TPB) bound by two Ca atoms each capped by 3 THF ligands (**146**).[313] This complex is formed from the addition of activated calcium to a mixture of

TBP and catalytic amounts of $Ph_3C_6H_2Br$ in THF, resulting in the reduction of TBP and formation of **146** (**Scheme 1.24**). In a further study it was proposed that the catalytic $Ph_3C_6H_2Br$ generates the heavy Grignard **145** in situ which is important mechanistically for this transformation.[314] In order to unambiguously characterise **146**, the authors sought to prove no hydride, oxide or bromide was present. The latter two are obviously absent from the SCXRD structural characterisation, with the addition of D_2O generating exclusively D_2 and precluding the existence of hydrides. DFT calculations in concert with EPR spectroscopy on **146** led to the assignment by the authors of the Ca(I) centre with a doubly reduced TBP leading to a triplet ground state. This assignment has been disputed in the literature, instead suggesting that a Ca(II) with a quad-anionic TBP might be a more appropriate designation.[315]

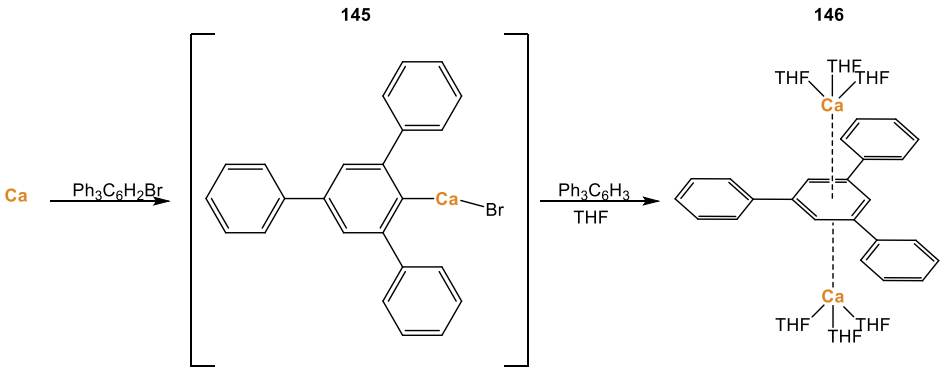

Scheme 1.24: Synthesis of **146** from TPB and activated calcium

More recently Harder *et al.* attempted the synthesis of a Ca(I)-Ca(I) species using bulky BDI ligands, as they have been used to great effect in the isolation of low valent group 2 systems.[315] Upon reduction of the $(^{DIpeP}NacnacCaI)_2$ (**147**) with KC_8 in aromatic solvents, formation of the dimeric calcium complex **148a-c** with the puckered $[Ar]^{-2}$ anion bonded between the calcium centres is observed (**Scheme 1.25**). Given the incompatibility of the reduced Ca systems with aromatic solvents, the reduction was instead carried out in methylcyclohexane under a argon atmosphere, which resulted in the Ca(II) decomposition product **149** with the unusual $\eta_2\eta_1$ BDI binding attributed to the steric bulk of the flanking DIPep groups (**Scheme 1.25**). When the reduction of **147** was performed in a N_2 atmosphere the extremely rare group 2 dinitrogen complex **150** was formed (**Scheme 1.25**). The authors report

a significantly elongated N-N bond (**1.3.14**; 1.268(2), 1.258(3) and 1.268(3) Å; N_2, 1.098 Å) alongside a bathochromically shifted Raman N-N stretch, designating the dinitrogen as a $[N_2]^{-2}$ fragment consistent with highly activated transition metal complexes. Remarkably N_2 reduction was shown to be reversible through an exchange experiment with $^{14}N_2$, however no evidence of a Ca(I)-Ca(I) intermediate was found. DFT studies using EDA-NOCV on **150** tentatively indicate the binding of N_2 could involve partially filled d orbitals, but this is a highly controversial topic in the current literature.[316–318] While the work reported by Harder *et al.* demonstrates the exceptional reductive potential of Ca(I), a Ca(I)-Ca(I) species remains elusive.

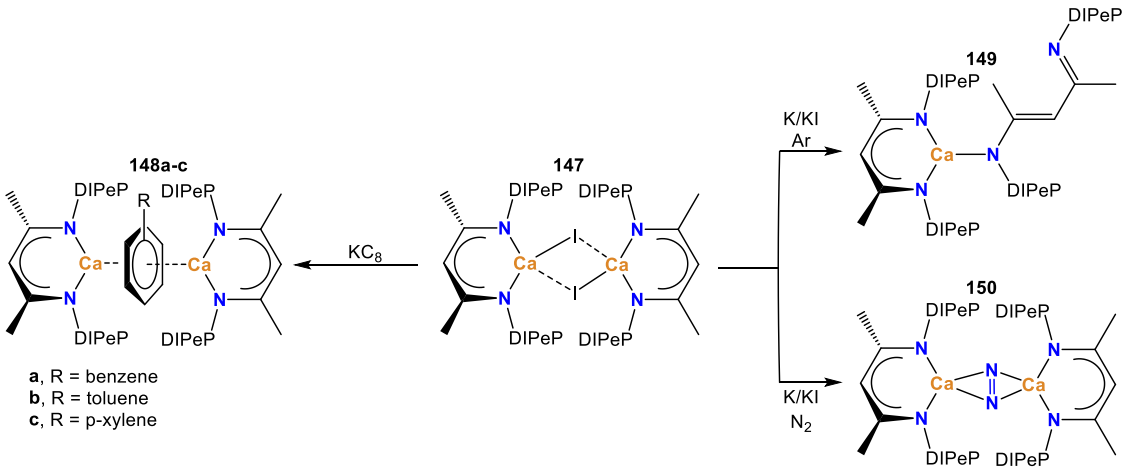

Scheme 1.25: Reduction products of **147**

Beyond calcium, there are no isolable low valent complexes reported.[265,285] Heavier low valent group 2 compounds could be observed through neon matrix isolation. $Ae(CO)_8$ species (Ca, Sr Ba) could be characterised by IR at -261 °C but these species could not be isolated.[316] Computational studies on these compounds indicate an octahedral ground state and the involvement of partially filled d orbitals in the bonding, sparking much debate into the validity of this claim.[317,318] This study further highlights the instability of low valent heavier group 2 elements and the differences in their bonding.

Aims of the work

The aims of this work are twofold. The primary objective is to explore the reactivity of xanthene-based Frustrated Lewis Pair (FLP) systems with NH_3 and CO. Xanthene-based FLP systems are

known for their reversible activation of dihydrogen, attributed to the P–B distance, which is similar to that in calculated encounter complexes.[319] This research leverages the structural flexibility of the xanthene backbone to optimize the interaction of these systems with NH_3 and CO. Given the significance of the cumulative Lewis acidity and basicity of the borane and phosphine fragments in activation, this study targets cationic borane systems to enhance the reactivity of xanthene-derived systems.

The secondary aims involve employing quantum chemical calculations to elucidate the bonding and reaction pathways of various main group systems. Following our group's report on diberyllocene, numerous BeCp-derived complexes have been synthesized.[309] Given the contentious nature of bonding in previously reported group 2 systems, these low-valent beryllium systems require rigorous and objective analysis to ensure the reliability of compound reports. Additionally, our group has explored boryl-stabilized group 14 systems to increase the reactivity of tetrylene systems.[320] Computational calculations will aid in understanding the origins of the novel reactivity and bonding observed for these systems. Lastly, the group has demonstrated the capability of the aluminyl system **108** to homologate CO under ambient conditions.[321] While remarkable, a deeper understanding of this process could guide future research and potentially enable Fischer–Tropsch-like reactivity from aluminium centres.

References

1. Richard Catlow, C., Davidson, M., Hardacre, C. & Hutchings, G. J. Catalysis making the world a better place. *Philosophical Transactions of the Royal Society A: Mathematical, Physical and Engineering Sciences* **374**, (2016).
2. Fan, J. H., Omura, A. & Roca, E. Geopolitics and rare earth metals. *Eur J Polit Econ* **78**, 102356 (2023).
3. Légaré, M. A., Pranckevicius, C. & Braunschweig, H. Metallomimetic Chemistry of Boron. *Chem Rev* **119**, 8231–8261 (2019).
4. Power, P. P. Main-group elements as transition metals. *Nature* **463**, 171–177 (2010).
5. Weetman, C. & Inoue, S. The Road Travelled: After Main-Group Elements as Transition Metals. *ChemCatChem* **10**, 4213–4228 (2018).
6. Stephan, D. W. Frustrated Lewis pair chemistry of CO. *Chem Soc Rev* **52**, 4632–4643 (2023).
7. Fujimori, S. & Inoue, S. Carbon Monoxide in Main-Group Chemistry. *J Am Chem Soc* **144**, 2034–2050 (2022).
8. Hanusch, F., Groll, L. & Inoue, S. Recent advances of group 14 dimetallenes and dimetallynes in bond activation and catalysis. *Chem Sci* **12**, 2001–2015 (2021).
9. Rivard, E. Group 14 inorganic hydrocarbon analogues. *Chem Soc Rev* **45**, 989–1003 (2016).
10. Power, P. P. Homonuclear multiple bonding in heavier main group elements. *J. Chem. Soc., Dalton Trans.* 2939–2951 (1998)
11. West, R. Isolable compounds containing a silicon-silicon double bond. *Science* **225**, 1109–1114 (1984).
12. Freeman, L. A., Walley, J. E. & Gilliard, R. J. Synthesis and reactivity of low-oxidation-state alkaline earth metal complexes. *Nature Synthesis* **1**, 439–448 (2022).
13. Worku, A. K., Yemata, T. A., Worku, A. K. & Yemata, T. A. Lewis Acidic Boron Reagents: Recent Advancement and Applications. (2023)
14. Lam, J., Szkop, K. M., Mosaferi, E. & Stephan, D. W. FLP catalysis: main group hydrogenations of organic unsaturated substrates. *Chem Soc Rev* **48**, 3592–3612 (2019).
15. Stephan, D. W. & Erker, G. Frustrated lewis pairs: metal-free hydrogen activation and more. *Angew. Chem. Int. Ed.* 49 46–76 (2009)
16. Stephan, D. W. The broadening reach of frustrated Lewis pair chemistry. *Science* **354**, 7229–7229 (2016).
17. Stephan, D. W. *et al.* Metal-free catalytic hydrogenation of polar substrates by frustrated Lewis pairs. *Inorg Chem* **50**, 12338–12348 (2011).
18. Erker, G. Organometallic frustrated Lewis pair chemistry. *Dalton Trans.* 40 7475–7483 (2011).
19. Stephan, D. W. 'Frustrated Lewis pair' hydrogenations. *Organic and Biomolecular Chemistry* 10 5740–5746 (2012).
20. Stephan, D. W. & Erker, G. Frustrated Lewis Pair Chemistry: Development and Perspectives. *Angew. Chem. Int. Ed.***54**, 6400–6441 (2015).
21. Paradies, J. Frustrated Lewis pair catalyzed hydrogenations. *Synlett* **24**, 777–780 (2013).
22. Stephan, D. W. & Erker, G. Frustrated Lewis Pair Chemistry: Development and Perspectives. *Angew. Chem. Int. Ed.***54**, 6400–6441 (2015).
23. Stephan, D. W. Frustrated Lewis Pairs: From Concept to Catalysis. *Acc Chem Res* **48**, 306–316 (2015).
24. Cotton, F. A. Proposed Nomenclature for Olefin-Metal and Other Organometallic Complexes. *J. Am. Chem. Soc.* 90 6230–6232 Preprint at (1968).
25. Spessard, G. O. & Miessler, G. L. *Organometallic Chemistry SECOND EDITION*. (2010).
26. Klerk, A. de. Fischer–Tropsch Process. *Kirk-Othmer Encyclopedia of Chemical Technology* 1–20 (2013).
27. Dry, M. E. The Fischer–Tropsch process: 1950–2000. *Catal Today* **71**, 227–241 (2002).
28. Chatt, J. & Duncanson, L. A. Olefin co-ordination compounds. Part III. Infra-red spectra and structure: Attempted preparation of acetylene complexes. *Journal of the Chemical Society* 2939–2947 (1953).
29. Chatt, J., Duncanson, L. A. & Venanzi, L. M. Directing effects in inorganic substitution reactions. Part I. A hypothesis to explain the trans-effect. *Journal of the Chemical Society (Resumed)* 4456–4460 (1955)
30. Atkins, D. F. S. and P. W. *Inorganic Chemistry*. (Oxford University Press, 2001).

31. Brown, Z. D. & Power, P. P. Mechanisms of Reactions of Open-Shell, Heavier Group 14 Derivatives with Small Molecules: n−π* Back-Bonding in Isocyanide Complexes, C−H Activation under Ambient Conditions, CO Coupling, and Ancillary Molecular Interactions † The treatment of Ge(Ar $Me_6)_2$ (Ar Me_6 = C_6H_3-2,6(C 6 H 2-2,4,6-$Me_3)_2$) with MeNC or Bu t. (2013)
32. Ramler, J. *et al.* Carbon monoxide insertion at a heavy p-block element: unprecedented formation of a cationic bismuth carbamoyl. *Chem Sci* **10**, 4169–4176 (2019).
33. Streiff, S. & Jérôme, F. Hydroamination of non-activated alkenes with ammonia: a holy grail in catalysis. *Chem Soc Rev* **50**, 1512–1521 (2021).
34. Werner, A. Coordination chemistry. *Z. Anorg. Chem.* **3**, 267–300 (1893).
35. Morgan, E., MacLean, D. F., McDonald, R. & Turculet, L. Rhodium and iridium amido complexes supported by silyl pincer ligation: Ammonia N-H bond activation by a [PSiP]Ir complex. *J Am Chem Soc* **131**, 14234–14236 (2009).
36. Salomon, M. A., Jungton, A. K. & Braun, T. Activation of ethylene and ammonia at iridium: C–H versus N–H oxidative addition. *Dalton Trans.* 7669–7677 (2009).
37. Abbenseth, J. *et al.* Thermoneutral N−H Bond Activation of Ammonia by a Geometrically Constrained Phosphine. *Angew. Chem. Int. Ed.***60**, 23625–23629 (2021).
38. Wang, Y. *et al.* Activation of Ammonia by a Carbene-Stabilized Dithiolene Zwitterion. *J Am Chem Soc* **144**, 16325–16331 (2022).
39. Yang, X. *et al.* Radical Activation of N-H and O-H Bonds at Bismuth(II). *J Am Chem Soc* **144**, 16535–16544 (2022).
40. Krämer, F., Paradies, J., Fernández, I. & Breher, F. A crystalline aluminium–carbon-based ambiphile capable of activation and catalytic transfer of ammonia in non-aqueous media. *Nature Chemistry* **16**, 63–69 (2023).
41. Cui, J. *et al.* Metal-free σ-bond metathesis in ammonia activation by a diazadiphosphapentalene. *J Am Chem Soc* **136**, 16764–16767 (2014).
42. Robinson, T. P., De Rosa, D. M., Aldridge, S. & Goicoechea, J. M. E–H Bond Activation of Ammonia and Water by a Geometrically Constrained Phosphorus(III) Compound. *Angew. Chem. Int. Ed.***54**, 13758–13763 (2015).
43. Wang, Y. *et al.* Activation of Ammonia by a Carbene-Stabilized Dithiolene Zwitterion. *J Am Chem Soc* **144**, 16325–16331 (2022).
44. Wendel, D. *et al.* Precise Activation of Ammonia and Carbon Dioxide by an Iminodisilene. *Angew. Chem. Int. Ed.***57**, 14575–14579 (2018).
45. Meltzer, A., Majumdar, M., White, A. J. P., Huch, V. & Scheschkewitz, D. Potential protecting group strategy for disila analogues of vinyllithiums: Synthesis and reactivity of a 2,4,6-trimethoxyphenyl-substituted disilene. *Organometallics* **32**, 6844–6850 (2013).
46. Boomgaarden, S., Saak, W., Weidenbruch, M. & Marsmann, H. Ammonia and chlorine additions to a tetrasilabuta-1,3-diene: Conglomerate versus racemate crystallization. *Z Anorg Allg Chem* **627**, 349–352 (2001).
47. Wang, W., Inoue, S., Yao, S. & Driess, M. Reactivity of N-heterocyclic germylene toward ammonia and water. *Organometallics* **30**, 6490–6494 (2011).
48. Zhou, X. *et al.* Cooperative N–H bond activation by amido-Ge(II) cations. *Dalton Trans.* **49**, 9495–9504 (2020).
49. Peng, Y., Ellis, B. D., Wang, X. & Power, P. P. Diarylstannylene activation of hydrogen or ammonia with arene elimination. *J Am Chem Soc* **130**, 12268–12269 (2008).
50. Jana, A., Schulzke, C. & Roesky, H. W. Oxidative addition of ammonia at a silicon(II) center and an unprecedented hydrogenation reaction of compounds with low-valent group 14 elements using ammonia borane. *J Am Chem Soc* **131**, 4600–4601 (2009).
51. Zhu, Z. *et al.* Addition of Hydrogen or Ammonia to a Low-Valent Group 13 Metal Species at 25 °C and 1 Atmosphere. *Angew. Chem. Int. Ed.***48**, 2031–2034 (2009).
52. Beachley, O. T., Pazik, J. C. & Noble, M. J. Facile reactions for the preparation of $[(Me_3CCH_2)2GaNH_2]_2$ and of GaN. *Organometallics* **17**, 2121–2123 (1998).
53. B Abdalla, J. A. *et al.* Cooperative Bond Activation and Catalytic Reduction of Carbon Dioxide at a Group 13 Metal Center. *Angew. Chem. Int. Ed.***54**, 5098–5102 (2015).
54. Zhao, L., Pan, S., Holzmann, N., Schwerdtfeger, P. & Frenking, G. Chemical Bonding and Bonding Models of Main-Group Compounds. *Chem Rev* **119**, 8781–8845 (2019).
55. Weetman, C. Main Group Multiple Bonds for Bond Activations and Catalysis. *Chem. Eur. J.* **27**, 1941–1954 (2021).

56. Cotton, F. A., Cowley, A. H. & Feng, X. The use of density functional theory to understand and predict structures and bonding in main group compounds with multiple bonds. *J Am Chem Soc* **120**, 1795–1799 (1998).
57. Lewis, G. N. *Valence and the Structure of Atoms and Molecules,*. (New York, 1923).
58. Stephan, D. W. & Erker, G. Frustrated lewis pairs: metal-free hydrogen activation and more. *Angew. Chem. Int. Ed.* 49, 46–76 (2010).
59. Stephan, D. W. The broadening reach of frustrated Lewis pair chemistry. *Science* **354**, 7229–7229 (2016).
60. Stephan, D. W. & Erker, G. Frustrated Lewis Pair Chemistry: Development and Perspectives. *Angew. Chem. Int. Ed.* **54**, 6400–6441 (2015).
61. Hounjet, L. J. *et al.* Combinations of ethers and $B(C_6F_5)_3$ function as hydrogenation catalysts. *Angew. Chem. Int. Ed.* **52**, 7492–7495 (2013).
62. Lam, J., Szkop, K. M., Mosaferi, E. & Stephan, D. W. FLP catalysis: main group hydrogenations of organic unsaturated substrates. *Chem Soc Rev* **48**, 3592–3612 (2019).
63. Brown, H. C., Schlesinger, H. I. & Cardon, S. Z. Studies in Stereochemistry. I. Steric Strains as a Factor in the Relative Stability of Some Coördination Compounds of Boron. *J Am Chem Soc* **64**, 325–329 (1942).
64. Welch, G. C., San Juan, R. R., Masuda, J. D. & Stephan, D. W. Reversible, metal-free hydrogen activation. *Science* **314**, 1124–1126 (2006).
65. Jupp, A. R. & Stephan, D. W. New Directions for Frustrated Lewis Pair Chemistry. *Trends Chem* **1**, 35–48 (2019).
66. Li, N. & Zhang, W. Frustrated Lewis Pairs: Discovery and Overviews in Catalysis. *Chin J Chem* **38**, 1360–1370 (2020).
67. Stephan, D. W. & Erker, G. Frustrated lewis pairs: metal-free hydrogen activation and more. *Angew. Chem. Int. Ed.* 49 46–76, (2010).
68. Stephan, D. W. The broadening reach of frustrated Lewis pair chemistry. *Science* **354**, 7229–7229 (2016).
69. Rokob, T. A., Hamza, A., Stirling, A., Soós, T. & Pápai, I. Turning frustration into bond activation: A theoretical mechanistic study on heterolytic hydrogen splitting by frustrated Lewis pairs. *Angew. Chem. Int. Ed.* **47**, 2435–2438 (2008).
70. Rocchigiani, L., Ciancaleoni, G., Zuccaccia, C. & MacChioni, A. Probing the association of frustrated phosphine-borane Lewis pairs in solution by NMR spectroscopy. *J Am Chem Soc* **136**, 112–115 (2014).
71. Brown, L. C. *et al.* Frustrated Lewis pairs in ionic liquids and molecular solvents-a neutron scattering and NMR study of encounter complexes. *Chem. Commun.* **54**, 8689–8692 (2018).
72. Brown, L. C. *et al.* Frustrated Lewis pairs in ionic liquids and molecular solvents-a neutron scattering and NMR study of encounter complexes. *Chem. Commun.* **54**, 8689–8692 (2018).
73. Pé, P. *et al.* A computational and conceptual DFT study on the mechanism of hydrogen activation by novel frustrated Lewis pairs †. *Phys. Chem. Chem. Phys* **17**, 10715 (2015).
74. Rokob, T. A., Bakó, I., Stirling, A., Hamza, A. & Pápai, I. Reactivity Models of Hydrogen Activation by Frustrated Lewis Pairs: Synergistic Electron Transfers or Polarization by Electric Field? *J Am Chem Soc* **135**, 4425–4437 (2013).
75. Mück-Lichtenfeld, C. & Grimme, S. Theoretical analysis of cooperative effects of small molecule activation by frustrated Lewis pairs. *Dalton Trans.* **41**, 9111 (2012).
76. Grimme, S., Kruse, H., Goerigk, L. & Erker, G. The mechanism of dihydrogen activation by frustrated lewis pairs revisited. *Angew. Chem. Int. Ed.* **49**, 1402–1405 (2010).
77. Rokob, T. A., Hamza, A., Stirling, A. & Pápai, I. On the mechanism of $B(C_6F_5)_3$-catalyzed direct hydrogenation of imines: Inherent and thermally induced frustration. *J Am Chem Soc* **131**, 2029–2036 (2009).
78. Rokob, T. A., Hamza, A. & Pápai, I. Rationalizing the reactivity of frustrated Lewis pairs: Thermodynamics of H_2 activation and the role of acid-base properties. *J Am Chem Soc* **131**, 10701–10710 (2009).
79. Rokob, T. A., Hamza, A., Stirling, A., Soós, T. & Pápai, I. Turning frustration into bond activation: A theoretical mechanistic study on heterolytic hydrogen splitting by frustrated Lewis pairs. *Angew. Chem. Int. Ed.* **47**, 2435–2438 (2008).
80. Berke, H. Conceptual Approach to the Reactivity of Dihydrogen. *ChemPhysChem* **11**, (2010).
81. Stephan, D. W. & Erker, G. Frustrated lewis pairs: metal-free hydrogen activation and more. *Angew. Chem. Int. Ed.* 49, 46–76 (2010).

82. Travis, A. L. *et al.* Small molecule activation by frustrated Lewis pairs. *Dalton Trans.* **42**, 2431–2437 (2013).
83. Skara, G., De Vleeschouwer, F., Geerlings, P., De Proft, F. & Pinter, B. Heterolytic Splitting of Molecular Hydrogen by Frustrated and Classical Lewis Pairs: A Unified Reactivity Concept. *Sci Rep* **7**, 1–15 (2017).
84. Dureen, M. A. & Stephan, D. W. Reactions of boron amidinates with CO_2 and CO and other small molecules. *J Am Chem Soc* **132**, 13559–13568 (2010).
85. Esarte Palomero, O. & Jones, R. A. Ferrocene tethered boramidinate frustrated Lewis pairs: stepwise capture of CO_2 and CO. *Dalton Trans.* **51**, 6275–6284 (2022).
86. Sajid, M. *et al.* Carbonylation reactions of intramolecular vicinal frustrated phosphane/borane lewis pairs. *J Am Chem Soc* **135**, 18567–18574 (2013).
87. Sajid, M. *et al.* Facile Carbon Monoxide Reduction at Intramolecular Frustrated Phosphane/Borane Lewis Pair Templates. *Angew. Chem. Int. Ed.***52**, 2243–2246 (2013).
88. Sajid, M., Kehr, G., Daniliuc, C. G. & Erker, G. Formylborane Formation with Frustrated Lewis Pair Templates. *Angew. Chem. Int. Ed.***53**, 1118–1121 (2014).
89. Wang, L. *et al.* An Ethylene-Bridged Phosphane/Borane Frustrated Lewis Pair Featuring the -B(Fxyl)2 Lewis Acid Component. *Chem. Eur. J.* **22**, 11015–11021 (2016).
90. Elmer, L. M. *et al.* The Chemistry of a Non-Interacting Vicinal Frustrated Phosphane/Borane Lewis Pair. *Chem. Eur. J.* **23**, 6056–6068 (2017).
91. Ye, K. Y., Daniliuc, C. G., Dong, S., Kehr, G. & Erker, G. Frustrated Lewis Pair Behavior of an Open, Noninteracting Phosphane/Borane Pair at a Rigid Organic Framework: Exploring Decisive Factors for FLP Activity. *Organometallics* **36**, 5003–5012 (2017).
92. Ye, K. Y. *et al.* Coupling of Carbon Monoxide with Nitrogen Monoxide at a Frustrated Lewis Pair Template. *Angew. Chem. Int. Ed.* **55**, 9216–9219 (2016).
93. Jian, Z. *et al.* CO-Reduction Chemistry: Reaction of a CO-Derived Formylhydridoborate with Carbon Monoxide, with Carbon Dioxide, and with Dihydrogen. *J Am Chem Soc* **139**, 6474–6483 (2017).
94. Ye, K. Y. *et al.* Reversible formylborane/SO2 coupling at a frustrated Lewis pair framework. *Chem. Commun.* **53**, 633–635 (2017).
95. Manankandayalage, C. P., Unruh, D. K. & Krempner, C. Carbon monoxide bond cleavage mediated by an intramolecular frustrated Lewis pair: access to new B/N heterocycles via selective incorporation of single carbon atoms. *Chem. Commun.* **57**, 12528–12531 (2021).
96. Wang, T. *et al.* CO/CO and NO/NO coupling at a hidden frustrated Lewis pair template. *Chem Sci* **8**, 2457–2463 (2017).
97. Dobrovetsky, R. & Stephan, D. W. Stoichiometric metal-free reduction of CO in syn-gas. *J Am Chem Soc* **135**, 4974–4977 (2013).
98. Sun, Q., Daniliuc, C. G., Kehr, G. & Erker, G. Reaction of carbon oxides with an ethylene-bridged PH/B Lewis pair. *Dalton Trans.* **50**, 3523–3528 (2021).
99. Wang, L. *et al.* Formation of macrocyclic ring systems by carbonylation of trifunctional P/B/B frustrated Lewis pairs. *Chem Sci* **9**, 1544–1550 (2018).
100. Wang, L. *et al.* Cooperative carbon monoxide to formyl reduction at a trifunctional PBB frustrated Lewis pair. *Chem. Commun.* **53**, 5499–5502 (2017).
101. Yu, J., Kehr, G., Daniliuc, C. G. & Erker, G. Cooperative reaction chemistry derived from a borata-diene framework. *Chem. Commun.* **52**, 1393–1396 (2016).
102. Yu, J. *et al.* Direct synthesis of a geminal zwitterionic phosphonium/hydridoborate system – developing an alternative tool for generating frustrated Lewis pair hydrogen activation systems. *Org Biomol Chem* **13**, 5783–5792 (2015).
103. Sun, Q. *et al.* Reductive Cleavage of the CO Molecule by a Reactive Vicinal Frustrated PH/BH Lewis Pair. *J Am Chem Soc* **142**, 17260–17264 (2020).
104. Li, J., Mück-Lichtenfeld, C., Daniliuc, C. G., Kehr, G. & Erker, G. Using the Secondary PH/BH Functional Groups of an Active Geminal Frustrated Lewis Pair for Carbon Monoxide Reduction and Reactions with Nitriles and Isonitriles. *Angew. Chem. Int. Ed.* **59**, 12477–12483 (2020).
105. Sun, Q., Daniliuc, C. G., Bergander, K., Kehr, G. & Erker, G. Carbon Monoxide Coupling Reactions via a Frustrated Lewis Pair-Derived η2-Formyl Borane. *J Am Chem Soc* **143**, 14992–14997 (2021).
106. Škoch, K., Daniliuc, C. G., Kehr, G. & Erker, G. Alkyne 1,1-Hydroboration to a Reactive Frustrated P/B-H Lewis Pair. *Angew. Chem. Int. Ed.* **60**, 6757–6763 (2021).
107. Li, J., Daniliuc, C. G., Kehr, G. & Erker, G. Preparation of the Borane (Fmes)BH_2 and its Utilization in the FLP Reduction of Carbon Monoxide and Carbon Dioxide. *Angew. Chem. Int. Ed.* **58**, 6737–6741 (2019).

108. Zheng, X., Zulkifly, I., Heilmann, A., McManus, C. & Aldridge, S. Colorimetric Metal-Free Detection of Carbon Monoxide: Reversible CO Uptake by a BNB Frustrated Lewis Pair. *Angew. Chem. Int. Ed.* **60**, 16416–16419 (2021).
109. Mahdi, T. & Stephan, D. W. Stoichiometric and Catalytic Inter- and Intramolecular Hydroamination of Terminal Alkynes by Frustrated Lewis Pairs. *Chem. Eur. J.* **21**, 11134–11142 (2015).
110. Mahdi, T., Stephan, D. W., Mahdi, T & Stephan, D. W. Frustrated Lewis Pair Catalyzed Hydroamination of Terminal Alkynes. *Angew. Chem. Int. Ed.* **52**, 12418–12421 (2013).
111. Ma, G., Song, G. & Li, Z. H. Designing Metal-Free Frustrated Lewis Pairs Catalyst for the Efficient Dehydrogenation of Ammonia Borane. *Chem. Eur. J.* **24**, 13238–13245 (2018).
112. Zhang, L. *et al.* Catalytic Dehydrogenation of Ammonia Borane Mediated by a Pt(0)/Borane Frustrated Lewis Pair: Theoretical Design. *ChemPhysChem* **21**, 2573–2578 (2020).
113. Mo, Z., Rit, A., Campos, J., Kolychev, E. L. & Aldridge, S. Catalytic B-N Dehydrogenation Using Frustrated Lewis Pairs: Evidence for a Chain-Growth Coupling Mechanism. *J Am Chem Soc* **138**, 3306–3309 (2016).
114. Nesterov, V. *et al.* NHCs in Main Group Chemistry. *Chem Rev* **118**, 9678–9842 (2018).
115. Sau, S. C., Hota, P. K., Mandal, S. K., Soleilhavoup, M. & Bertrand, G. Stable abnormal N-heterocyclic carbenes and their applications. *Chem Soc Rev* **49**, 1233–1252 (2020).
116. Soleilhavoup, M. & Bertrand, G. Cyclic (alkyl)(amino)carbenes (CAACs): Stable carbenes on the rise. *Acc Chem Res* **48**, 256–266 (2015).
117. Flanigan, D. M., Romanov-Michailidis, F., White, N. A. & Rovis, T. Organocatalytic Reactions Enabled by N-Heterocyclic Carbenes. *Chem Rev* **115**, 9307–9387 (2015).
118. Hopkinson, M. N., Richter, C., Schedler, M. & Glorius, F. An overview of N-heterocyclic carbenes. *Nature* **510**, 485–496 (2014).
119. Huynh, H. V. Electronic Properties of N-Heterocyclic Carbenes and Their Experimental Determination. *Chem Rev* **118**, 9457–9492 (2018).
120. Bellotti, P., Koy, M., Hopkinson, M. N. & Glorius, F. Recent advances in the chemistry and applications of N-heterocyclic carbenes. *Nature Reviews Chemistry* **5**, 711–725 (2021).
121. Arduengo, A. J., Dias, H. V. R., Harlow, R. L. & Kline, M. Electronic Stabilization of Nucleophilic Carbenes. *J Am Chem Soc* **114**, 5530–5534 (1992).
122. Arduengo, A. J., Harlow, R. L. & Kline, M. A Stable Crystalline Carbene. *J Am Chem Soc* **113**, 361–363 (1991).
123. Arduengo, A. J., Goerlich, J. R. & Marshall, W. J. A Stable Diaminocarbene. *J Am Chem Soc* **117**, 11027–11028 (1995).
124. Nakano, R., Jazzar, R. & Bertrand, G. A crystalline monosubstituted carbene. *Nature Chemistry* **10**, 1196–1200 (2018).
125. Kumar Kushvaha, S., Mishra, A., Roesky, H. W. & Chandra Mondal, K. Recent Advances in the Domain of Cyclic (Alkyl)(Amino) Carbenes. *Chem Asian J* **17**, e202101301 (2022).
126. Frey, G. D., Lavallo, V., Donnadieu, B., Schoeller, W. W. & Bertrand, G. Facile splitting of hydrogen and ammonia by nucleophilic activation at a single carbon center. *Science* **316**, 439–441 (2007).
127. Peltier, J. L. *et al.* Realizing metal-free carbene-catalyzed carbonylation reactions with CO. *J Am Chem Soc* **142**, 18336–18340 (2020).
128. Hudnall, T. W. & Bielawski, C. W. An N,N'-diamidocarbene: Studies in C-H insertion, reversible carbonylation, and transition-metal coordination chemistry. *J Am Chem Soc* **131**, 16039–16041 (2009).
129. Hudnall, T. W., Moerdyk, J. P. & Bielawski, C. W. Ammonia N–H activation by a N,N'-diamidocarbene. *Chem. Commun.* **46**, 4288–4290 (2010).
130. Peltier, J. L. *et al.* Realizing metal-free carbene-catalyzed carbonylation reactions with CO. *J Am Chem Soc* **142**, 18336–18340 (2020).
131. Lavallo, V., Canac, Y., Donnadieu, B., Schoeller, W. W. & Bertrand, G. CO fixation to stable acyclic and cyclic alkyl amino carbenes: Stable amino ketenes with a small HOMO-LUMO gap. *Angew. Chem. Int. Ed.* **45**, 3488–3491 (2006).
132. Martin, D., Moore, C. E., Rheingold, A. L. & Bertrand, G. An air-stable oxyallyl radical cation. *Angew. Chem. Int. Ed.* **52**, 7014–7017 (2013).
133. Schulz, T. *et al.* Carbonylation of the simplest persistent diaminocarbene. *Chem. Commun.* **49**, 6834–6836 (2013).
134. Siemeling, U. *et al.* N-heterocyclic carbenes which readily add ammonia, carbon monoxide and other small molecules,. *Chem Sci* **1**, 697–704 (2010).

135. Moerdyk, J. P., Blake, G. A., Chase, D. T. & Bielawski, C. W. Elucidation of carbene ambiphilicity leading to the discovery of reversible ammonia activation. *J Am Chem Soc* **135**, 18798–18801 (2013).
136. Driess, M. & Grützmacher, H. Main Group Element Analogues of Carbenes, Olefins, and Small Rings. *Angewandte Chemie (International Edition in English)* **35**, 828–856 (1996).
137. Mizuhata, Y., Sasamori, T. & Tokitoh, N. Stable heavier carbene analogues. *Chem Rev* **109**, 3479–3511 (2009).
138. Nechaev, M. S. Tetrylenes: Electronic Structure, Stability, Reactivity, and Ligand Properties - A Comparative DFT Study. *Organometallics* **40**, 3408–3423 (2021).
139. Denk, M. K., Khan, M., Lough, A. J. & Shuchi, K. Redetermination of the germanium dichloride complex with 1,4-dioxane at 173 K. *Acta Crystallogr C* **54**, 1830–1832 (1998).
140. Protchenko, A. V. *et al.* Enabling and Probing Oxidative Addition and Reductive Elimination at a Group 14 Metal Center: Cleavage and Functionalization of E-H Bonds by a Bis(boryl)stannylene. *J Am Chem Soc* **138**, 4555–4564 (2016).
141. Wendel, D. *et al.* From Si(II) to Si(IV) and Back: Reversible Intramolecular Carbon− Carbon Bond Activation by an Acyclic Iminosilylene. J. Chem. Soc. **139** 1834-8137 (2017)
142. Driess, M. Breaking the limits with silylenes. *Nature Chemistry* **4**, 525–526 (2012).
143. Segawa, Y., Yamashita, M. & Nozaki, K. Boryllithium: Isolation, characterization, and reactivity as a boryl anion. *Science* **314**, 113–115 (2006).
144. Segawa, Y., Suzuki, Y., Yamashita, M. & Nozaki, K. Chemistry of boryllithium: Synthesis, structure, and reactivity. *J Am Chem Soc* **130**, 16069–16079 (2008).
145. Duan, C. & Cui, C. Boryl-substituted low-valent heavy group 14 compounds. *Chem Soc Rev* **53**, 361–379 (2024).
146. Protchenko, A. V. *et al.* A stable two-coordinate acyclic silylene. *J Am Chem Soc* **134**, 6500–6503 (2012).
147. Goedecke, C., Leibold, M., Siemeling, U. & Frenking, G. When does carbonylation of carbenes yield ketenes? A theoretical study with implications for synthesis. *J Am Chem Soc* **133**, 3557–3569 (2011).
148. Wang, X. *et al.* Room-temperature reaction of carbon monoxide with a stable diarylgermylene. *J Am Chem Soc* **131**, 6912–6913 (2009).
149. Protchenko, A. V. *et al.* Reduction of Carbon Oxides by an Acyclic Silylene: Reductive Coupling of CO. *Angew. Chem. Int. Ed.* **58**, 1808–1812 (2019).
150. Wang, Y. *et al.* Silicon-Mediated Selective Homo- and Heterocoupling of Carbon Monoxide. *J Am Chem Soc* **141**, 626–634 (2019).
151. Shan, C., Yao, S. & Driess, M. Where silylene–silicon centres matter in the activation of small molecules. *Chem Soc Rev* **49**, 6733–6754 (2020).
152. Xiong, Y., Yao, S., Szilvási, T., Ruzicka, A. & Driess, M. Homocoupling of CO and isocyanide mediated by a C,C′-bis(silylenyl)-substituted ortho-carborane. *Chem. Commun.* **56**, 747–750 (2020).
153. Fujimori, S. & Inoue, S. Main group carbonyl complexes. *Communications Chemistry 2020 3:1* **3**, 1–4 (2020).
154. Reiter, D., Holzner, R., Porzelt, A., Frisch, P. & Inoue, S. Silylated silicon–carbonyl complexes as mimics of ubiquitous transition-metal carbonyls. *Nature Chemistry* **12**, 1131–1135 (2020).
155. Ganesamoorthy, C. *et al.* A silicon–carbonyl complex stable at room temperature. *Nature Chemistry* **12**, 608–614 (2020).
156. Jana, A., Objartel, I., Roesky, H. W. & Stalke, D. Cleavage of a N-H bond of ammonia at room temperature by a germylene. *Inorg Chem* **48**, 798–800 (2009).
157. Meltzer, A., Inoue, S., Präsang, C. & Driess, M. Steering S-H and N-H bond activation by a stable N-heterocyclic silylene: Different addition of H_2S, NH_3, and organoamines on a Silicon(II) ligand versus its Si(II)→Ni(CO)$_3$ complex. *J Am Chem Soc* **132**, 3038–3046 (2010).
158. Alberto, M. E., Russo, N. & Sicilia, E. EH_3 (E=N, P, As) and H_2 Activation with N-Heterocyclic Silylene and Germylene Homologues. *Chem. Eur. J.* **19**, 7835–7846 (2013).
159. Stoelzel, M., Inoue, S., Meltzer, A. & Driess, M. Metal-Free Activation of EH_3 (E=P, As) by an Ylide-like Silylene and Formation of a Donor-Stabilized Arsasilene with a HSiAsH Subunit. *Angew. Chem. Int. Ed.* **49**, 10002–10005 (2010).
160. Xiong, Y., Yao, S., Müller, R., Kaupp, M. & Driess, M. Activation of ammonia by a Si - O double bond and formation of a unique pair of sila-hemiaminal and silanoic amide tautomers. *J Am Chem Soc* **132**, 6912–6913 (2010).

161. Wang, W., Inoue, S., Yao, S. & Driess, M. Reactivity of N-heterocyclic germylene toward ammonia and water. *Organometallics* **30**, 6490–6494 (2011).
162. Peng, Y. *et al.* Reaction of hydrogen or ammonia with unsaturated germanium or tin molecules under ambient conditions: Oxidative addition versus arene elimination. *J Am Chem Soc* **131**, 16272–16282 (2009).
163. Usher, M. *et al.* A Systematic Study of Structure and E−H Bond Activation Chemistry by Sterically Encumbered Germylene Complexes. *Chem. Eur. J.* **22**, 11685–11698 (2016).
164. Goldberg, D. E., Harris, D. H., Lappert, M. F. & Thomas, K. M. *A New Synthesis of Divalent Group 4B Alkyls M[CH(SiMe,),], (M=Ge or Sn), and the Crystal and Molecular Structure of the Tin Compound? J. Chem. Soc., Chem. Commun.* 261-262 (1976)
165. Klinkhammer, K. W., Fässler, T. F. & Grützmacher, H. The Formation of Heteroleptic Carbene Homologues by Ligand Exchange - Synthesis of the First Plumbanediyl Dimer. *Angew. Chem. Int. Ed.* **37**, 124–126 (1998).
166. Power, P. P. Silicon, germanium, tin and lead analogues of acetylenes. *Chem. Commun.* **3**, 2091–2101 (2003).
167. Lein, M., Krapp, A. & Frenking, G. Why do the heavy-atom analogues of acetylene E2H2 (E = Si-Pb) exhibit unusual structures? *J Am Chem Soc* **127**, 6290–6299 (2005).
168. Landis, C. R. & Weinhold, F. Origin of trans-bent geometries in maximally bonded transition metal and main group molecules. *J Am Chem Soc* **128**, 7335–7345 (2006).
169. Aldridge, S. & Downs, A. J. Hydrides of the main-group metals: New variations on an old theme. *Chem Rev* **101**, 3305–3365 (2001).
170. Wang, X. & Andrews, L. Infrared spectra of group 14 hydrides in solid hydrogen: Experimental observation of Pbh4, Pb2H2, and Pb2H4. *J Am Chem Soc* **125**, 6581–6587 (2003).
171. Trinquier, G. Double Bonds and Bridged Structures in the Heavier Analogues of Ethylene. *J Am Chem Soc* **112**, 2130–2137 (1990).
172. Trinquier, G. Singly Bridged Arrangements on Group 14 X2H4 Potential Surfaces. *J Am Chem Soc* **113**, 144–151 (1991).
173. Windus, T. L. & Gordon, M. S. π-Bond Strengths of H2X:YH2: X = Ge, Sn, Y = C, Si, Ge, or Sn. *J Am Chem Soc* **114**, 9559–9568 (1992).
174. Richards, A. F., Phillips, A. D., Olmstead, M. M. & Power, P. P. Isomeric forms of divalent heavier group 14 element hydrides: Characterization of Ar'(H)GeGe(H)Ar' and Ar'$(H)_2$GeGeAr'·PME_3 (Ar' = C_6H_3-2,6-$Dipp_2$; Dipp = C_6H_3-2,6-Pri_2). *J Am Chem Soc* **125**, 3204–3205 (2003).
175. Rivard, E. *et al.* Isomeric forms of heavier main group hydrides: Experimental and theoretical studies of the $[Sn(Ar)H]_2$ (Ar = terphenyl) system. *J Am Chem Soc* **129**, 16197–16208 (2007).
176. Majumdar, M. *et al.* Reductive Cleavage of Carbon Monoxide by a Disilenide. *Angew. Chem. Int. Ed.* **54**, 8746–8750 (2015).
177. Cowley, M. J. *et al.* Carbonylation of cyclotrisilenes. *Angew. Chem. Int. Ed.* **52**, 13247–13250 (2013).
178. Cowley, M. J., Huch, V. & Scheschkewitz, D. Donor-acceptor adducts of a 1,3-disila-2-oxyallyl zwitterion. *Chemistry - A European Journal* **20**, 9221–9224 (2014).
179. McOnie, S. L., Özpinar, G. A., Bourque, J. L., Müller, T. & Baines, K. M. NH bond activation of ammonia and amines by ditetrelenes: key insights into the stereochemistry of nucleophilic addition. *Dalton Trans.* **50**, 17734–17750 (2021).
180. Power, P. P. Bonding and reactivity of heavier group 14 element alkyne analogues. *Organometallics* **26**, 4362–4372 (2007).
181. Lai, T. Y., Tao, L., Britt, R. D. & Power, P. P. Reversible Sn-Sn Triple Bond Dissociation in a Distannyne: Support for Charge-Shift Bonding Character. *J Am Chem Soc* **141**, 12527–12530 (2019).
182. Wiberg, N., Vasisht, S. K., Fischer, G. & Mayer, P. Disilynes. III [1]: A relatively stable disilyne RSi=SiR (R = SiMe$(SitBu_3)_2$). *Z Anorg Allg Chem* **630**, 1823–1828 (2004).
183. Ko, S. Y. *et al.* A stable compound containing a silicon-silicon triple bond. *Science* **305**, 1755–1757 (2004).
184. Stender, M., Phillips, A. D., Wright, R. J. & Power, P. P. Synthesis and characterization of a digermanium analogue of an alkyne. *Angew. Chem. Int. Ed.* **41**, 1785–1787 (2002).
185. Pu, L., Twamley, B. & Power, P. P. Synthesis and characterization of 2,6-$Trip_2H_3C_6PbPbC_6H_3$-2,6-Trip2 (Trip = C_6H_2-2,4,6-i-Pr_3): A stable heavier group 14 element analogue of an alkyne [2]. *J Am Chem Soc* **122**, 3524–3525 (2000).
186. Lischka, H. & Kohler1, H.-J. *Ab Initio Investigation on the Lowest Singlet and Triplet State of Si_2H_2. J. Am. Chem. Soc* 05 (1983).

187. Binkley, J. S. *Theoretical Study of the Relative Stabilities of C_2H_2 and Si_2H_2 Conformers*". *J. Am. Chem. Soc.* 106 (1984).
188. Snyder, L. C., Wasserman, Z. R. & Moskowitz, J. W. Stability and bonding of disilyne and its isomers: A generalized valence bond-effective potential study. *Int J Quantum Chem* **21**, 565–579 (1982).
189. Rit, A., Campos, J., Niu, H. & Aldridge, S. A stable heavier group 14 analogue of vinylidene. *Nature Chemistry* **8**, 1022–1026 (2016).
190. Cui, C., Olmstead, M. M., Fettinger, J. C., Spikes, G. H. & Power, P. P. Reactions of the heavier group 14 element alkyne analogues Ar'EEAr' (Ar' = C_6H_3-2,6(C_6H_3-2,6-Pri2)2; E = Ge, Sn) with unsaturated molecules: Probing the character of the EE multiple bonds. *J Am Chem Soc* **127**, 17530–17541 (2005).
191. Sekiguchi, A., Matsuo, T. & Watanabe, H. Synthesis and characterization of a cyclobutadiene dianion dilithium salt: Evidence for aromaticity. *J Am Chem Soc* **122**, 5652–5653 (2000).
192. Lee, V. Y., Takanashi, K., Matsuno, T., Ichinohe, M. & Sekiguchi, A. Cyclobutadiene Dianions Consisting of Heavier Group 14 Elements: Synthesis and Characterization. *J Am Chem Soc* **126**, 4758–4759 (2004).
193. Protchenko, A. V *et al.* Electronic Delocalization in Two and Three Dimensions: Differential Aggregation in Indium "Metalloid" Clusters. *Angew. Chem. Int. Ed.* **56**, 15098–15102 (2017).
194. Nori, V., Pesciaioli, F., Sinibaldi, A., Giorgianni, G. & Carlone, A. Boron-Based Lewis Acid Catalysis: Challenges and Perspectives. *Catalysts 2022, 12, Page 5* **12**, 5 (2021).
195. Sivaev, I. B. & Bregadze, V. I. Lewis acidity of boron compounds. *Coord Chem Rev* **270–271**, 75–88 (2014).
196. Rathke, J. & Schaeffer, R. Bis(carbonyl)diborane(4). *Inorg Chem* **13**, 760–761 (1974).
197. Glore, J. D., Rathke, J. W. & Schaeffer, R. Studies of Boranes. XXXVII. Some Reactions of Triborane(7) and the Structure of Triborane(7)-Carbonyl. *Inorg Chem* **12**, 2175–2178 (1973).
198. Burg, A. B. & Schlesinger, H. I. Hydrides of Boron. VII. Evidence of the Transitory Existence of Borine (BH_3): Borine Carbonyl and Borine Trimethylammine. *J Am Chem Soc* **59**, 780–787 (1937).
199. Spielman, J. R. & Burg, A. B. Further Studies of the Tetraborane Carbonyl B_4H_8CO. *Inorg Chem* **2**, 1139–1145 (1963).
200. Timms, P. L. Boron-Fluorine Chemistry. I. Boron Monofluoride and Some Derivatives. *J Am Chem Soc* **89**, 1629–1632 (1967).
201. Jeffery, J. C., Norman, N. C., Pardoe, J. A. J. & Timms, P. L. Synthesis and structures of carbonyl adducts of the boranes $B(BX_2)_3$ (X = F, Cl). *Chem. Commun.* 2367–2368 (2000).
202. Lupinetti, A. J., Frenking, G. & Strauss, S. H. Nonclassical metal carbonyls: Appropriate definitions with a theoretical justification. *Angew. Chem. Int. Ed.* **37**, 2113–2116 (1998).
203. Jacobsen, H. *et al.* Lewis Acid Properties of Tris(pentafluorophenyl)borane. Structure and Bonding in L-B(C6F5)3 Complexes. *Organometallics* **18**, 1724–1734 (1999).
204. Gerken, M., Pawelke, G., Bernhardt, E. & Willner, H. Syntheses and Characterization of $(C_2F_5)_3BCO$ and $(C_3F_7)_3BCO$. *Chem. Eur. J.* **16**, 7527–7536 (2010).
205. Finze, M. *et al.* Tris(trifluoromethyl)borane carbonyl, $(CF_3)_3BCO$ - Synthesis, physical, chemical and spectroscopic properties, gas phase, and solid state structure. *J Am Chem Soc* **124**, 15385–15398 (2002).
206. Chen, C. *et al.* The [(NHC)B(H)C_6F_5]+ Cations and Their [B](H)−CO Borane Carbonyls. *Angew. Chem. Int. Ed.* **59**, 21460–21464 (2020).
207. Piers, W. E., Bourke, S. C. & Conroy, K. D. Borinium, borenium, and boronium ions: Synthesis, reactivity, and applications. *Angew. Chem. Int. Ed.* 44, 5016–5036 (2005).
208. Fan, C., Piers, W. E. & Parvez, M. Perfluoropentaphenylborole. *Angew. Chem. Int. Ed.* **48**, 2955–2958 (2009).
209. Braunschweig, H. & Kupfer, T. Recent developments in the chemistry of antiaromatic boroles. *Chem. Commun.* **47**, 10903–10914 (2011).
210. Heitkemper, T. & Sindlinger, C. P. A Cationic NHC-Supported Borole. *Chem. Eur. J.* **26**, 11684–11689 (2020).
211. Soleilhavoup, M. & Bertrand, G. Borylenes: An Emerging Class of Compounds. *Angew. Chem. Int. Ed.* **56**, 10282–10292 (2017).
212. Braunschweig, H., Dewhurst, R. D. & Gessner, V. H. Transition metal borylene complexes. *Chem Soc Rev* **42**, 3197–3208 (2013).
213. Légaré, M. A., Pranckevicius, C. & Braunschweig, H. Metallomimetic Chemistry of Boron. *Chem Rev* **119**, 8231–8261 (2019).
214. Kinjo, R., Donnadieu, B., Celik, M. A., Frenking, G. & Bertrand, G. Synthesis and characterization of a neutral tricoordinate organoboron isoelectronic with amines. *Science* **333**, 610–613 (2011).

215. Wang, H., Wu, L., Lin, Z. & Xie, Z. Transition-Metal-Like Behavior of Monovalent Boron Compounds: Reduction, Migration, and Complete Cleavage of CO at a Boron Center. *Angew. Chem. Int. Ed.* **57**, 8708–8713 (2018).
216. Wang, H., Wu, L., Lin, Z. & Xie, Z. Synthesis, structure and reactivity of a borylene cation [(NHSi)2B(CO)]+ stabilized by three neutral ligands. *J Am Chem Soc* **139**, 13680–13683 (2017).
217. Dahcheh, F., Martin, D., Stephan, D. W. & Bertrand, G. Synthesis and reactivity of a CAAC-aminoborylene adduct: A hetero-allene or an organoboron isoelectronic with singlet carbenes. *Angew. Chem. Int. Ed.* **53**, 13159–13163 (2014).
218. Braunschweig, H. *et al.* Main-group metallomimetics: Transition metal-like photolytic CO substitution at boron. *J Am Chem Soc* **139**, 1802–1805 (2017).
219. Braunschweig, H. *et al.* Multiple complexation of CO and related ligands to a main-group element. *Nature* **522**, 327–330 (2015).
220. *CRC Handbook of Chemistry and Physics* . (CRC Press, Boca Raton, Fl, 2016).
221. Cecchin, G., Morini, G. & Piemontesi, F. Ziegler-Natta Catalysts. *Kirk-Othmer Encyclopedia of Chemical Technology* (2003)
222. Ooi, T. & Maruoka, K. Achiral Al(III) Lewis Acids. *Lewis Acids in Organic Synthesis* 191–281 (2008)
223. Saito, S. Aluminum in Organic Synthesis. *Main Group Metals in Organic Synthesis* 189–306 (2004)
224. Coles, M. P. & Evans, M. J. The emerging chemistry of the aluminyl anion. *Chem. Commun.* **59**, 503–519 (2023).
225. Hicks, J., Vasko, P., Goicoechea, J. M. & Aldridge, S. The Aluminyl Anion: A New Generation of Aluminium Nucleophile. *Angew. Chem. Int. Ed.* **60**, 1702–1713 (2021).
226. Zhong, M., Sinhababu, S. & Roesky, H. W. The unique β-diketiminate ligand in aluminum(I) and gallium(I) chemistry. *Dalton Trans.* **49**, 1351–1364 (2020).
227. Mian He, Chaopeng Hu, Rui Wei, Xin-Feng Wang & Leo Liu, L. Recent advances in the chemistry of isolable carbene analogues with group 13–15 elements. *Chem Soc Rev* (2024)
228. Ecker, A. & Schnöckel, H. Donorstabilisiertes Aluminium(I)-iodid. *Z Anorg Allg Chem* **622**, 149–152 (1996).
229. Mocker, M., Robl, C. & Schnöckel, H. Donor-Stabilized Aluminum(I) Bromide. *Angew. Chem. Int. Ed. in English* **33**, 1754–1755 (1994).
230. Tacke, M. & Schnöckel, H. Metastable AlCl as a Solid and in Solution. *Inorg Chem* **28**, 2895–2896 (1989).
231. Dohmeier, C., Robl, C., Tacke, M. & Schnöckel, H. The Tetrameric Aluminum(I) Compound [{Al(η5-C5Me5)}4]. *Angew. Chem. Int. Ed. in English* **30**, 564–565 (1991).
232. Sitzmann, H., Lappert, M. F., Dohmeier, C., Üffing, C. & Schnöckel, H. Cyclopentadienylderivate von Aluminium(I). *J Organomet Chem* **561**, 203–208 (1998).
233. Hofmann, A., Tröster, T., Kupfer, T. & Braunschweig, H. Monomeric Cp3tAl(I): synthesis, reactivity, and the concept of valence isomerism. *Chem Sci* **10**, 3421–3428 (2019).
234. Dohmeier, C., Baum, E., Ecker, A., Köppe, R. & Schnöckel, H. Pentabenzylcyclopentadienides of lithium. *Organometallics* **15**, 4702–4706 (1996).
235. Cui, C. *et al.* Synthesis and Structure of a Monomeric Aluminum(i) Compound [{HC(CMeNAr) 2 }Al] (Ar ˆ 2,6-iPr 2 C 6 H 3): A Stable Aluminum Analogue of a Carbene**. *Angew. Chem. Int. Ed* **39**, (2000).
236. Grams, S., Mai, J., Langer, J. & Harder, S. Synthesis, Structure, and Reactivity of a Superbulky Low-Valent β-Diketiminate Al(I) Complex. *Organometallics* **41**, 2862–2867 (2022).
237. Li, X., Cheng, X., Song, H. & Cui, C. Synthesis of HC[(CBut)(NAr)]$_2$Al (Ar = 2,6-Pr$_2$ C$_6$H$_3$) and its reaction with isocyanides, a bulky azide, and H2O. *Organometallics* **26**, 1039–1043 (2007).
238. Queen, J. D., Lehmann, A., Fettinger, J. C., Tuononen, H. M. & Power, P. P. The Monomeric Alanediyl: AlAriPr8(AriPr8= C$_6$H-2,6-(C$_6$H$_2$-2,4,6-Pr i3)2-3,5-Pr$_2$): An Organoaluminum(I) Compound with a One-Coordinate Aluminum Atom. *J Am Chem Soc* **142**, 20554–20559 (2020).
239. Hinz, A. & Müller, M. P. Attempted reduction of a carbazolyl-diiodoalane. *Chem. Commun.* **57**, 12532–12535 (2021).
240. Zhang, X. & Liu, L. L. A Free Aluminylene with Diverse σ-Donating and Doubly σ/π-Accepting Ligand Features for Transition Metals**. *Angew. Chem. Int. Ed.* **60**, 27062–27069 (2021).
241. Zhang, X. *et al.* Free Aluminylenes: An Emerging Class of Compounds. *Chem. Eur. J.* **28**, e202202102 (2022).
242. Kong, R. Y. & Crimmin, M. R. Carbon Chain Growth by Sequential Reactions of CO and CO 2 with [W(CO)$_6$] and an Aluminum(I) Reductant. *J Am Chem Soc* **140**, 13614–13617 (2018).
243. Li, X., Ni, C., Song, H. & Cui, C. Formation of aluminacyclobutenes via carbon monoxide and isocyanide insertion. *Chem. Commun.* 1763–1765 (2006)

244. Kong, R. Y. & Crimmin, M. R. Reversible insertion of CO into an aluminium–carbon bond. *Chem. Commun.* **55**, 6181–6184 (2019).
245. Hicks, J., Vasko, P., Goicoechea, J. M. & Aldridge, S. Synthesis, structure and reaction chemistry of a nucleophilic aluminyl anion. **557**, 92–95 (2018).
246. Hicks, J., Vasko, P., Goicoechea, J. M. & Aldridge, S. Reversible, room-Temperature c-c bond activation of benzene by an isolable metal complex. *J Am Chem Soc* **141**, 11000–11003 (2019).
247. Schwamm, R. J., Anker, M. D., Lein, M. & Coles, M. P. Reduction vs. Addition: The Reaction of an Aluminyl Anion with 1,3,5,7-Cyclooctatetraene. *Angew. Chem. Int. Ed.* **58**, 1489–1493 (2019).
248. Schwamm, R. J. *et al.* A Stable Calcium Alumanyl. *Angew. Chem. Int. Ed.* **59**, 3928–3932 (2020).
249. Schwamm, R. J. *et al.* Seven-Membered Cyclic Potassium Diamidoalumanyls. *Chem. Eur. J.* **27**, 14971–14980 (2021).
250. Feng, G., Chan, K. L., Lin, Z. & Yamashita, M. Al-Sc Bonded Complexes: Synthesis, Structure, and Reaction with Benzene in the Presence of Alkyl Halide. *J Am Chem Soc* **144**, 22662–22668 (2022).
251. Jackson, R. A. *et al.* An acyclic aluminyl anion. *Chem. Commun.* **59**, 5277–5280 (2023).
252. Grams, S., Eyselein, J., Langer, J., Färber, C. & Harder, S. Boosting Low-Valent Aluminum(I) Reactivity with a Potassium Reagent. *Angew. Chem. Int. Ed.* **59**, 15982–15986 (2020).
253. Grams, S., Mai, J., Langer, J. & Harder, S. Synthesis, Structure, and Reactivity of a Superbulky Low-Valent β-Diketiminate Al(I) Complex. *Organometallics* **41**, 2862–2867 (2022).
254. Yan, C., Kinjo, R., Yan, [C & Kinjo, R. A Three-Membered Diazo-Aluminum Heterocycle to Access an Al=C π Bonding Species. *Angew. Chem. Int. Ed.* **61**, e202211800 (2022).
255. Koshino, K. & Kinjo, R. Construction of σ-Aromatic AlB2Ring via Borane Coupling with a Dicoordinate Cyclic (Alkyl)(Amino)Aluminyl Anion. *J Am Chem Soc* **142**, 9057–9062 (2020).
256. Kurumada, S., Takamori, S. & Yamashita, M. An alkyl-substituted aluminium anion with strong basicity and nucleophilicity. *Nature Chemistry* **12**, 36–39 (2019).
257. Evans, M. J., Gardiner, M. G., Anker, M. D. & Coles, M. P. Extending chain growth beyond C1 → C4 in CO homologation: aluminyl promoted formation of the $[C_5O_5]^{5-}$ ligand. *Chem. Commun.* **58**, 5833–5836 (2022).
258. Evans, M. J., Anker, M. D., Gardiner, M. G., McMullin, C. L. & Coles, M. P. Controlling Al- M Interactions in Group 1 Metal Aluminyls (M = Li, Na, and K). Facile Conversion of Dimers to Monomeric and Separated Ion Pairs. *Inorg Chem* **60**, 18423–18431 (2021).
259. Heilmann, A., Hicks, J., Vasko, P., Goicoechea, J. M. & Aldridge, S. Carbon Monoxide Activation by a Molecular Aluminium Imide: C−O Bond Cleavage and C−C Bond Formation. *Angew. Chem. Int. Ed.* **59**, 4897–4901 (2020).
260. Evans, M. J., Neale, S. E., Anker, M. D., McMullin, C. L. & Coles, M. P. Potassium Aluminyl Promoted Carbonylation of Ethene. *Angew. Chem. Int. Ed.* **61**, e202117396 (2022).
261. Lu, J. *et al.* High-precision magnesium isotope analysis of carbonates by laser ablation MC-ICP-MS using wet and dry conditions. *J Anal At Spectrom* **37**, 1665–1674 (2022).
262. Berg, R. D., Solomon, E. A. & Teng, F. Z. The role of marine sediment diagenesis in the modern oceanic magnesium cycle. *Nature Communications* **10**, 1–10 (2019).
263. Vangioni-Flam, E. & Cassé, M. Cosmic Lithium-Beryllium-Boron Story. *Astrophysics and Space Science* **265**, 77–86 (1999).
264. White, F. D., Thiele, N. A., Simms, M. E. & Cary, S. K. Structure and bonding of a radium coordination compound in the solid state. *Nature Chemistry* **16**, 168–172 (2023).
265. Freeman, L. A., Walley, J. E. & Gilliard, R. J. Synthesis and reactivity of low-oxidation-state alkaline earth metal complexes. *Nature Synthesis* **1**, 439–448 (2022).
266. Naglav, D., Buchner, M. R., Bendt, G., Kraus, F. & Schulz, S. Off the Beaten Track—A Hitchhiker's Guide to Beryllium Chemistry. *Angew. Chem. Int. Ed.* **55**, 10562–10576 (2016).
267. Green, S. P., Jones, C. & Stasch, A. Stable magnesium(I) compounds with Mg-Mg bonds. *Science* **318**, 1754–1757 (2007).
268. Jones, C. Dimeric magnesium(I) β-diketiminates: a new class of quasi-universal reducing agent. *Nature Reviews Chemistry* **1**, 1–9 (2017).
269. Hicks, J., Juckel, M., Paparo, A., Dange, D. & Jones, C. Multigram Syntheses of Magnesium(I) Compounds Using Alkali Metal Halide Supported Alkali Metals as Dispersible Reducing Agents. *Organometallics* **37**, 4810–4813 (2018).
270. Azizi, A., Momen, R., Xu, T., Kirk, S. R. & Jenkins, S. Non-nuclear attractors in small charged lithium clusters, Limq (m = 2–5, q = ±1), with QTAIM and the Ehrenfest force partitioning. *Physical Chemistry Chemical Physics* **20**, 24695–24707 (2018).

271. Platts, J. A., Overgaard, J., Jones, C., Iversen, B. B. & Stasch, A. First experimental characterization of a non-nuclear attractor in a dimeric magnesium(I) compound. *J. Phys. Chem. A.* **115**, 194–200 (2011).
272. Gosch, M. A. & Wilson, D. J. D. Heteronuclear and Homonuclear Bimetallic Metallocenes of Alkaline Earths and Zinc. *Organometallics* **42**, 2185–2196 (2023).
273. Li, X. *et al.* Metal-metal and metal-ligand bonds in $(\eta5\text{-}C_5H_5)_2M_2$ (M = Be, Mg, Ca, Ni, Cu, Zn). *Organometallics* **32**, 1060–1066 (2013).
274. Jones, C. Open questions in low oxidation state group 2 chemistry. *Communications Chemistry 2020 3:1* **3**, 1–4 (2020).
275. Rösch, B. & Harder, S. New horizons in low oxidation state group 2 metal chemistry. *Chem. Commun.* **57**, 9354–9365 (2021).
276. Yuvaraj, K., Douair, I., Jones, D. D. L., Maron, L. & Jones, C. Sterically controlled reductive oligomerisations of CO by activated magnesium(I) compounds: deltate vs. ethenediolate formation. *Chem Sci* **11**, 3516–3522 (2020).
277. Yuvaraj, K., Douair, I., Paparo, A., Maron, L. & Jones, C. Reductive Trimerization of CO to the Deltate Dianion Using Activated Magnesium(I) Compounds. *J Am Chem Soc* **141**, 8764–8768 (2019).
278. Yuvaraj, K., Carpentier, A., Smith, C. D., Maron, L. & Jones, C. C-N and C-H Activation of an N-Heterocyclic Carbene by Magnesium(II) Hydride and Magnesium(I) Complexes. *Inorg Chem* **60**, 6065–6072 (2021).
279. Green, S. P., Jones, C. & Stasch, A. Stable Adducts of a Dimeric Magnesium(I) Compound. *Angew. Chem. Int. Ed.* **47**, 9079–9083 (2008).
280. Stasch, A. & Jones, C. Stable dimeric magnesium(I) compounds: from chemical landmarks to versatile reagents. *Dalton Trans.* **40**, 5659–5672 (2011).
281. Paparo, A. *et al.* Reductive Hexamerization of CO Involving Cooperativity Between Magnesium(I) Reductants and $[Mo(CO)_6]$: Synthesis of Well-Defined Magnesium Benzenehexolate Complexes**. *Angew. Chem. Int. Ed.* **60**, 630–634 (2021).
282. Rösch, B. *et al.* Strongly reducing magnesium(0) complexes. *Nature* **592**, 717–721 (2021).
283. Buchner, M. R. Beryllium coordination chemistry and its implications on the understanding of metal induced immune responses. *Chem. Commun.* **56**, 8895–8907 (2020).
284. Puchta, R. A brighter beryllium. *Nature Chemistry* 416–416 (2011).
285. Boronski, J. T. Alkaline earth metals: homometallic bonding. *Dalton Trans.* **53**, 33–39 (2023).
286. Hill, M. S., Liptrot, D. J. & Weetman, C. Alkaline earths as main group reagents in molecular catalysis. *Chem Soc Rev* **45**, 972–988 (2016).
287. Arrowsmith, M. *et al.* Neutral zero-valent s-block complexes with strong multiple bonding. *Nature Chemistry* **8**, 890–894 (2016).
288. Gilliard, R. J. *et al.* Carbene-stabilized beryllium borohydride. *J Am Chem Soc* **134**, 9953–9955 (2012).
289. Jędrzkiewicz, D. *et al.* Access to a Labile Monomeric Magnesium Radical by Ball-Milling. *Angew. Chem. Int. Ed.* **61**, e202200511 (2022).
290. Gimferrer, M. *et al.* The oxidation state in low-valent beryllium and magnesium compounds. *Chem Sci* **13**, 6583–6591 (2022).
291. Ponec, R. & Cooper, D. L. Insights from domain-averaged Fermi hole (DAFH) analysis and multicenter bond indices into the nature of Be(0) bonding. *Struct Chem* **28**, 1033–1043 (2017).
292. Gimferrer, M. *et al.* Reply to the 'Comment on "The oxidation state in low-valent beryllium and magnesium compounds"' by S. Pan and G. Frenking, Chem. Sci., 2022, 13, *Chem Sci* **14**, 384–392 (2023).
293. Gimferrer, M. *et al.* Comment on "The oxidation state in low-valent beryllium and magnesium compounds" by M. Gimferrer, S. Danés, E. Vos, C. B. Yildiz, I. Corral, A. Jana, P. Salvador and D. M. Andrada, Chem. Sci. 2022, 13, 6583. *Chem Sci* **14**, 379–383 (2023).
294. Wang, G. *et al.* Isolation of Cyclic(Alkyl)(Amino) Carbene–Bismuthinidene Mediated by a Beryllium(0) Complex. *Chem. Eur. J.* **25**, 4335–4339 (2019).
295. Wang, G. *et al.* s-Block Multiple Bonds: Isolation of a Beryllium Imido Complex. *Angew. Chem. Int. Ed.* **60**, 9407–9411 (2021).
296. Goettel, J. T., Gao, H., Dotzauer, S. & Braunschweig, H. MeCAAC=N−: A Cyclic (Alkyl)(Amino)Carbene Imino Ligand. *Chem. Eur. J.* **26**, 1136–1143 (2020).
297. Yuan, C. *et al.* Ultrashort Beryllium−Beryllium Distances Rivalling Those of Metal−Metal Quintuple Bonds Between Transition Metals. *Angew. Chem. Int. Ed.* **55**, 15651–15655 (2016).

298. Xie, Y., Schaefer, H. F. & Jemmis, E. D. Characteristics of novel sandwiched beryllium, magnesium, and calcium dimers: $C_5H_5BeBeC_5H_5$, $C_5H_5MgMgC_5H_5$, and $C_5H_5CaCaC_5H_5$. *Chem Phys Lett* **402**, 414–421 (2005).
299. Velazquez, A., Fernández, I., Frenking, G. & Merino, G. Multimetallocenes. A theoretical study. *Organometallics* **26**, 4731–4736 (2007).
300. Saha, R., Pan, S., Merino, G. & Chattaraj, P. K. Unprecedented Bonding Situation in Viable $E_2(NHBMe)_2$ (E=Be, Mg; NHBMe=$(HCNMe)_2B$) Complexes: Neutral E2 Forms a Single E−E Covalent Bond. *Angew. Chem. Int. Ed.* **58**, 8372–8377 (2019).
301. Brea, O., Mó, O., Yáñez, M., Alkorta, I. & Elguero, J. On the existence of intramolecular one-electron Be–Be bonds. *Chem. Commun.* **52**, 9656–9659 (2016).
302. Bondybey, V. E. Electronic structure and bonding of Be_2. *Chem Phys Lett* **109**, 436–441 (1984).
303. De, S. & Parameswaran, P. Neutral tricoordinated beryllium(0) compounds – isostructural to BH3 but isoelectronic to NH_3. *Dalton Trans.* **42**, 4650–4656 (2013).
304. Merritt, J. M., Bondybey, V. E. & Heaven, M. C. Beryllium dimer-caught in the act of bonding. *Science* **324**, 1548–1551 (2009).
305. Couchman, S. A., Holzmann, N., Frenking, G., Wilson, D. J. D. & Dutton, J. L. Beryllium chemistry the safe way: a theoretical evaluation of low oxidation state beryllium compounds. *Dalton Trans.* **42**, 11375–11384 (2013).
306. Wang, G. *et al.* A Stable, Crystalline Beryllium Radical Cation. *J Am Chem Soc* **142**, 4560–4564 (2020).
307. Epping, R. F. J., Vesseur, D., Zhou, M. & de Bruin, B. Carbene Radicals in Transition-Metal-Catalyzed Reactions. *ACS Catal* **13**, 5428–5448 (2023).
308. Czernetzki, C. *et al.* A Neutral Beryllium(I) Radical. *Angew. Chem. Int. Ed.* **60**, 20776–20780 (2021).
309. Boronski, J. T., Crumpton, A. E., Wales, L. L. & Aldridge, S. Diberyllocene, a stable compound of Be(I) with a Be–Be bond. *Science* **380**, 1147–1149 (2023).
310. Paparo, A., Smith, C. D. & Jones, C. Diagonally Related s- and p-Block Metals Join Forces: Synthesis and Characterization of Complexes with Covalent Beryllium–Aluminum Bonds. *Angew. Chem. Int. Ed.* **58**, 11459–11463 (2019).
311. Boronski, J. T. *et al.* Inducing Nucleophilic Reactivity at Beryllium with an Aluminyl Ligand. *J Am Chem Soc* **145**, 4408–4413 (2023).
312. Bonyhady, S. J. *et al.* β-Diketiminate-Stabilized Magnesium(I) Dimers and Magnesium(II) Hydride Complexes: Synthesis, Characterization, Adduct Formation, and Reactivity Studies. *Chem. Eur. J.* **16**, 938–955 (2010).
313. Krieck, S., Görls, H., Yu, L., Reiher, M. & Westerhausen, M. Stable 'Inverse' sandwich complex with unprecedented organocalcium(I): Crystal structures of [(thf)Mg(Br)-CH-2,4,6-Ph] and [(thf)Ca{μ-CH-1,3,5-Ph}Ca(thf)]. *J Am Chem Soc* **131**, 2977–2985 (2009).
314. Krieck, S., Görls, H. & Westerhausen, M. Mechanistic elucidation of the formation of the inverse Ca(I) sandwich complex $[(thf)_3Ca(\mu\text{-}C6H3\text{-}1,3,5\text{-}Ph_3)Ca(thf)_3]$ and stability of aryl-substituted phenylcalcium complexes. *J Am Chem Soc* **132**, 12492–12501 (2010).
315. Rösch, B. *et al.* Dinitrogen complexation and reduction at low-valent calcium. *Science* **371**, 1125–1128 (2021).
316. Wu, X. *et al.* Observation of alkaline earth complexes $M(CO)_8$ (M = Ca, Sr, or Ba) that mimic transition metals. *Science* **361**, 912–916 (2018).
317. Zhao, L., Pan, S., Zhou, M. & Frenking, G. Response to Comment on "Observation of alkaline earth complexes M(CO)8 (M = Ca, Sr, or Ba) that mimic transition metals". *Science* **365**, 2024 (2019).
318. Landis, C. R., Hughes, R. P. & Weinhold, F. Comment on "Observation of alkaline earth complexes M(CO)8 (M = Ca, Sr, or Ba) that mimic transition metals". *Science* **365**, 2024 (2019).
319. Mo, Z. *et al.* Facile Reversibility by Design: Tuning Small Molecule Capture and Activation by Single Component Frustrated Lewis Pairs. *J Am Chem Soc* **137**, 12227–12230 (2015).
320. Zheng, X. *et al.* Disproportionation and Ligand Lability in Low Oxidation State Boryl-Tin Chemistry**. *Chem. Eur. J.* **29**, e202203395 (2023).
321. Heilmann, A. *et al.* Coordination and Homologation of CO at Al(I): Mechanism and Chain Growth, Branching, Isomerization, and Reduction. *J Am Chem Soc* **144**, 12942–12953 (2022).

Chapter 2 - Metathesis at $[Be–Be]^{2+}$: A Route to a Nucleophilic Beryllyl Complex

Josef T. Boronski*, Agamemnon E. Crumpton, Aisling F. Roper, Simon Aldridge*

Published in Nature Chemistry: Nat. Chem. 2024, https://doi.org/10.1038/s41557-024-01534-9

Author contributions

Josef T. Boronski: Synthesised the novel compound, collected characterisation data and corresponding author.

Agamemnon E. Crumpton: Performed the quantum chemical calculations and was lead crystallographer.

Aisling F. Roper: Crystallographer.

Simon Aldridge: Corresponding author.

Manuscript was written by Josef T. Boronski with contribution to the discussion by Simon Aldridge and Agamemnon E. Crumpton.

Abstract

The ligand metathesis chemistry of diberyllocene (**1**; CpBeBeCp) – a stable complex with a Be–Be bond – has been investigated. These studies yield two new complexes with Be–Be bonds: Cp*BeBeCp (**2**) and $[K\{(HCDippN)_2BO\}_2]BeBeCp$ (**3**; Dipp = 2,6-diisopropylphenyl). Quantum chemical calculations reveal that the unsymmetrical coordination environment at the beryllium centres in **2** and **3** leads to a polarization of the Be–Be. The bond polarization in **3** is of sufficient magnitude that the complex could be formulated as a mixed-valence Be^0/Be^{II} complex. In support of this formulation, it is demonstrated that **3** can transfer the "beryllyl" anion, $[BeCp]^-$, to an organic substrate, by analogy with the reactivity of sp^2-sp^3 diboranes. Indeed, this work reveals striking similarities between the homo-elemental bonding linkages of beryllium and boron, despite the respective metallic and non-metallic natures of these elements.

Introduction

The properties of the very lightest elements (i.e., those with principal quantum numbers of 1 or 2) form the basis for fundamental models of chemical bonding and reactivity.[1] It is notable, however, that the chemistry of the Periodic Table's fourth element, beryllium, is very poorly developed due to its extreme toxicity. [2–5] One essential aspect of the element's properties which

long remained unexplored in the condensed phases was the chemistry of the homo-elemental Be–Be bond.[6–11] In 1930, Herzberg unsuccessfully attempted to prepare diberyllium (Be_2) in the gas phase; this diatomic species (with a formal bond order of zero) was first spectroscopically identified in 2009.[12–14] Moreover, despite numerous synthetic endeavours over the past 50 years, only in 2023 was the first example of a stable complex with a Be–Be bond – diberyllocene (CpBeBeCp, **1**) – structurally characterised.[15–19] Complex **1** also represents the first unambiguous low oxidation state beryllium species.[9,20] Indeed, several recent studies have reported low-coordinate beryllium complexes bearing redox non-innocent carbene ligands.[21–26] Although these have been formulated as "low-valent" beryllium complexes by some, such descriptions have been rejected by more recent theoretical studies.[20,27–30]

In contrast to the recent discovery of **1**, stable complexes with Mg–Mg bonds were first reported in 2007.[31,32] Attempts to prepare direct beryllium analogues of N-ligated magnesium(I) dimers were plagued by the formation of ligand- and solvent-activation products.[15–19] Also of relevance are diborane(4) compounds, which feature B–B bonds and are isoelectronic with **1**.[33] The first diborane(4) derivative, B_2Cl_4, was prepared in 1925 and such species have subsequently found myriad applications in synthesis and catalysis. Quaternization of one of the boron centres of diborane(4) species by coordination of a nucleophile yields an sp^2–sp^3 diborane, with a polarized (sp^2, δ–; sp^3, δ+) B–B bond.[34,35] As such, these species have been used for the metal-free delivery of the boryl $[BR_2]^-$ anion to organic substrates.

Here we investigate the metathesis chemistry of the $[Be–Be]^{2+}$ core of **1** and report two new complexes with Be–Be bonds: Cp*BeBeCp (**2**) and $[K\{(HCDippN)_2BO\}_2]$BeBeCp (**3**; Dipp = 2,6-diisopropylphenyl). These complexes are both unsymmetrical and, as a result, possess Be–Be bonds which are polarized, albeit to vastly differing degrees. [34] In the case of **3**, quantum chemical calculations suggest that the uneven distribution of electron density could be rationalised in terms of a mixed-valence Be^0/Be^{II} formalism. This is supported by experimental studies, which reveal that **3** acts as a source of "beryllyl" anions (formally featuring beryllium in

the 0-oxidation state). Indeed, complex **3** is shown to transfer $[BeCp]^-$ to carbon electrophiles in a manner analogous to boryl anion, $[BR_2]^-$, transfer by sp^2-sp^3 diboranes.[33,34,36]

Results and Discussion

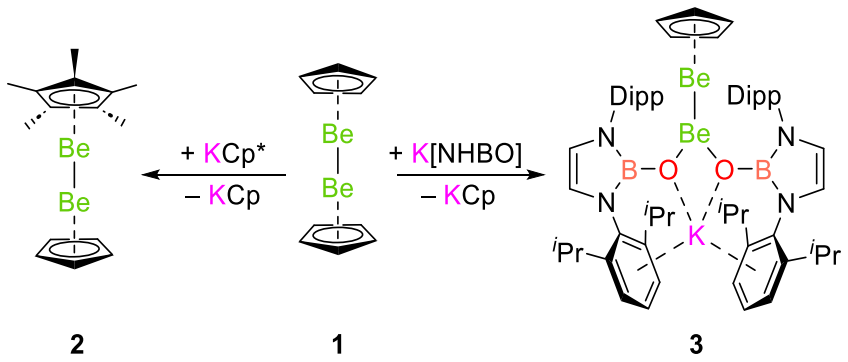

Scheme 2.1: Synthesis of the complexes Cp*BeBeCp (**2**) and $[K(NHBO)_2]$BeBeCp (**3**) via metathesis reactions with diberyllocene (1).

Diberyllocene (**1**) and decamethyldizincocene, Cp*ZnZnCp* (**A**), are both calculated to feature robust homometallic bonds (homolytic bond dissociation energy for CpMMCp: M = Be, 71.7 kJ mol^{-1}; M = Zn, 70.3 kJ mol^{-1}).[6,10,37] Indeed, **A** has been found to participate in ligand metathesis reactions which leave the Zn–Zn bond intact.[38–43] Thus, we decided to investigate whether a salt metathesis approach would enable the substitution of the cyclopentadienyl ligands of **1**.[18,44] Heating **1** and an excess of KCp* in benzene for four days leads to the quantitative formation of Cp*BeBeCp (**2**) and KCp (**Scheme 2.1**); no evidence for further substitution of the remaining Cp ligand was obtained even under forcing conditions. By contrast, reaction of **1** with two equivalents of the potassium salt of N-heterocyclic boryloxy (NHBO) ligand $K[(HCDippN)_2BO]$ (Dipp = 2,6-diisopropylphenyl) is rapid, yielding $[K(NHBO)_2]$BeBeCp (**3**), again with the concomitant formation of KCp (**Scheme 2.1**).[45] Both **2** and **3** could be crystallised from hexane and their molecular structures determined by single crystal X-ray diffraction (SCXRD) (**Figure 2.1** and **Figure 2.2**, respectively).

Complex **2**, like **1**, is a dimetallocene, consisting of two beryllium half-sandwich units – in this case one BeCp* and one BeCp – linked by a Be–Be bond.[37] There are two Cp*BeBeCp molecules in the asymmetric unit of **2**. Of these two independent molecules, one exhibits a

slightly staggered conformation of cyclopentadienyl ligands, whereas in the other complex these carbocyclic ligands are almost perfectly eclipsed, as they are in **1**. The Be–Be distances measured for the two independent Cp*BeBeCp units are 2.065(3) Å and 2.045(3) Å, which are statistically indistinguishable from the Be–Be bond of **1** (2.0545(18) Å). Unlike in **1**, the orientations of the cyclopentadienyl ligands of the two molecules of **2** deviate somewhat from a parallel alignment, with interplanar angles of 8.71(9)° and 12.84(10)°.[46] Additionally, the Be-Cp_{cent} distances are 1.528(4) and 1.521(4) Å, respectively, and the Be-Cp^*_{cent} distances are 1.501(4) and 1.491(5) Å, respectively. Hence, the Be-Cp_{cent} distances in **2** are comparable to the analogous metric measured for **1** (1.519(3) Å).[18]

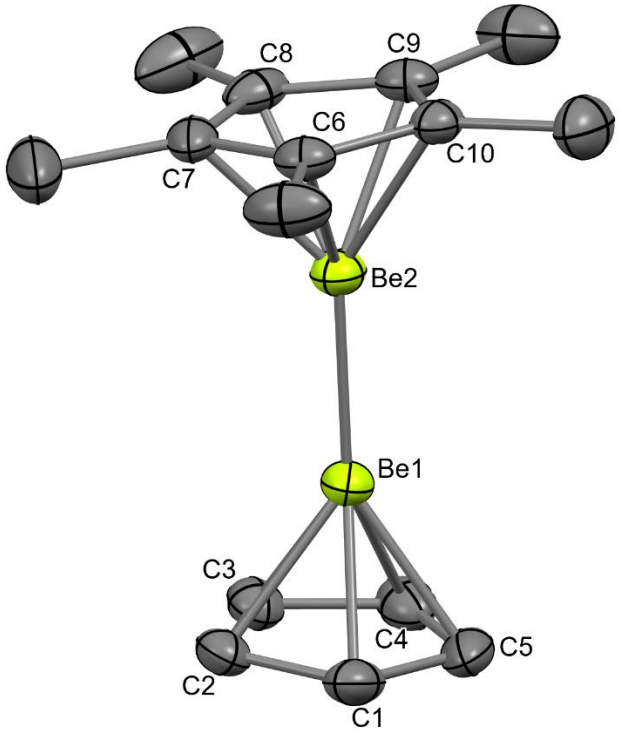

Figure 2.1: Molecular structure of **2** in the solid state, as determined by X-ray crystallography. Thermal ellipsoids set at 50% probability and hydrogen atoms omitted format for clarity.

Complex **3** also features a BeCp unit, in addition to a $[K(NHBO)_2]Be$ moiety, with two NHBO ligands coordinated to one Be centre through Be–O bonds.[45] The two beryllium centres of **3** are connected to one another via a Be–Be bond. The two NHBO ligands of **3** also coordinate a potassium cation via K···(η^6-$C_6H_3{}^iPr_2$) and K···O interactions, thereby forming a four-membered BeO_2K ring. The Be1–Be2 distance within **3** (2.135(3) Å) is markedly longer than those measured

for **1** and **2** (2.0545(18) and 2.045(3)/2.065(3) Å, respectively).[18] In addition, the Be-Cp_{cent} distance measured for **3** (1.578(2) Å) is considerably longer than the corresponding metrics for **1** and **2** (1.519(3) and 1.528(4) Å, respectively), suggesting that Be2 in **3** is highly electron rich. The Be1–O1 and K1···O1 distances are 1.5639(14) and 2.6561(8) Å, respectively. This Be–O distance is somewhat longer than those reported for the three-coordinate beryllium(II) aryloxide complexes $Be(ODipp)_2(SIPr)$ (1.497(3)/1.507(3); SIPr = 1,3-diisopropyl-4,5-dimethylimidizol-2-ylidine) and $Be(OMes^*)_2(Et_2O)$ (1.481(2) Å; Mes* = 2,4,6-^{t}Bu$_3$C$_6$H$_2$), as well as for the homoleptic two-coordinate NHBO complex $Be(NHBO)_2$ (**4**; 1.4266(8) Å; *vide infra*), likely due to the greater ionic radius of Be^I compared with Be^{II}.[18,47,48] The O1–Be1–O1' angle in **3** is 107.88(7)° and the sum of the angles at Be1 is 360.00(16)°, consistent with a trigonal planar geometry for this beryllium centre. This mirrors the trigonal planar geometry of the boron centres within diborane(4) derivatives.[33]

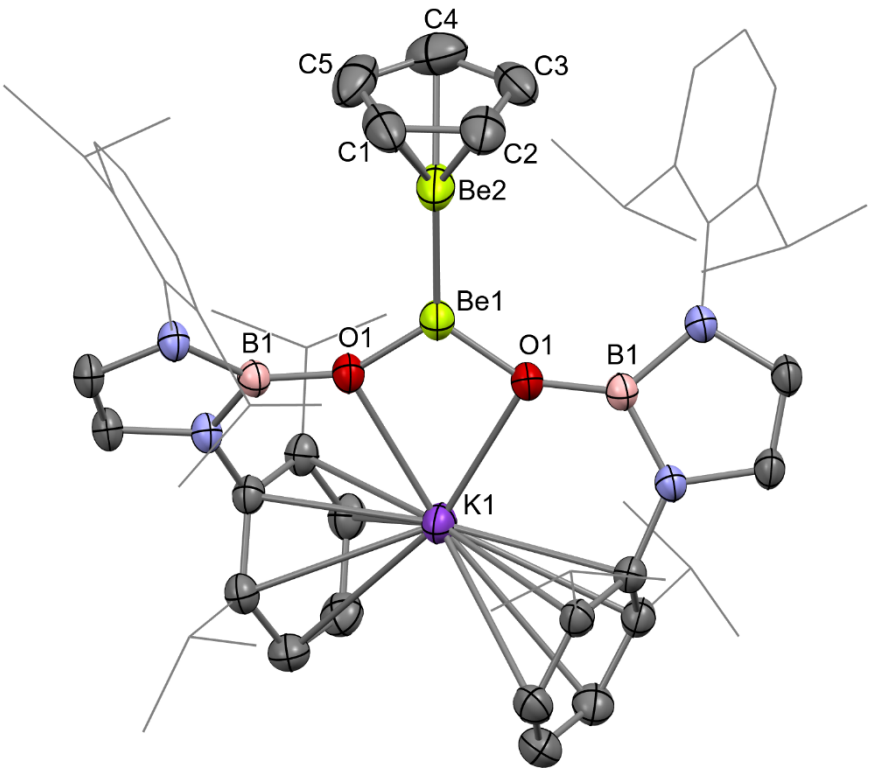

Figure 2.2: Molecular structure of **3** in the solid state as determined by X-ray crystallography. Thermal ellipsoids set at 50% probability; selected substituents shown in wireframe format and hydrogen atoms omitted for clarity.

It should be noted that ligand metathesis at a $[Mg–Mg]^{2+}$ unit has not previously been reported.[32] Moreover, all structurally characterised magnesium(I) dimers feature supporting ligands with N-donor groups. Juxtaposing this, a variety of supporting ligands have been found to be suitable for stabilizing the Zn–Zn bond, including halides, aryloxides, and even simple Lewis bases (e.g. DMAP, THF).[38–41,43] The lability of **1** with respect to ligand metathesis (i.e., the retention of the homo-metallic linkage) provides further experimental evidence for the theoretically predicted chemical similarities between the $[Zn–Zn]^{2+}$ and $[Be–Be]^{2+}$ moieties.[6,10]

Complexes **2** and **3** were characterized by multinuclear NMR spectroscopy. Perhaps most informative are the ^{9}Be NMR chemical shifts measured for these complexes.[49,50] The ^{9}Be NMR spectrum of complex **2** features resonances at –28.6 and –21.7 ppm, attributable to the Cp-coordinated beryllium centre (Be_{Cp}) and Cp*-coordinated beryllium centre (Be_{Cp*}), respectively. These ^{9}Be NMR chemical shifts are very similar to those measured for the Be centres of **1** and $BeCp*_2$ (–27.6 ppm and –21.7 ppm, respectively).[18,51] By contrast, in the case of **3** disparate ^{9}Be NMR resonances are observed at –29.8 and +9.5 ppm, which correspond to Be_{Cp} and the NHBO-coordinated beryllium centre (Be_{NHBO}), respectively. The upfield resonance has the lowest chemical shift of any reported ^{9}Be NMR signal and indicates that Be_{Cp} is a highly electron-rich low-oxidation state beryllium centre (Table **ST 2.2** and Figure **S 2.3**).[18,44,49,50] The ^{9}Be NMR resonance corresponding to Be_{NHBO} is similar to that measured for the beryllium(II) complex $Be(NHBO)_2$ (**4**, +5.1 ppm; *vide infra*), and is extremely broad (full width half maximum ($w_{1/2}$): 380 Hz) as is typically found for low-coordinate, electron-poor beryllium centres.[49] For comparison, the $w_{1/2}$ of the ^{9}Be resonance measured for **1** is 33.4 Hz.[18] No evidence of measurable Be–Be coupling could be observed in the ^{9}Be NMR spectra of either **2** or **3**.

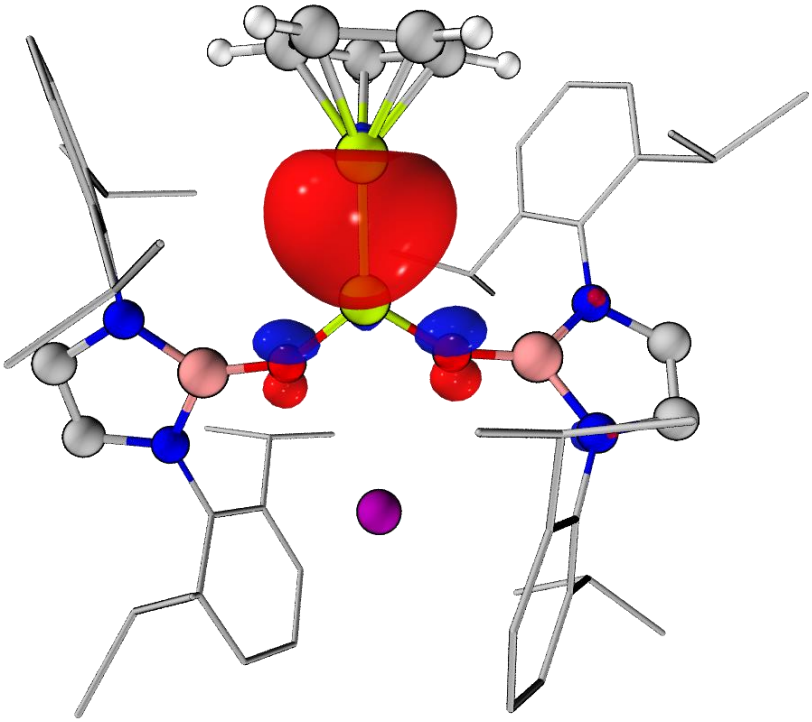

Figure 2.3: Highest occupied molecular orbital of compound **3** (0.05 a.u.).

To gain further insight into the electronic structure and bonding of **2** and **3**, both complexes were investigated using quantum chemical calculations. The structures of complexes **2** and **3** (and for comparative purposes, **1**) were optimised with the r^{2}SCAN-3c composite method and a single point calculation was performed on this optimised geometry using the ωB97X-D4 functional with the def2-QZVPP basis set. The highest occupied molecular orbital (HOMO) of all three complexes corresponds to a Be–Be bonding orbital of σ-symmetry.[18] In the case of **1** and **2**, the HOMO is distributed equally between both beryllium centres (Figure **S 2.4** and **S 2.5**). However, the HOMO of complex **3** has a hemispherical profile, with a greater proportion of the electron density localised on Be_{Cp} than on Be_{NHBO}, thus indicating that the Be–Be interaction in this complex is polarized (**Figure 2.3**).[1]

To provide further evidence for this observation, quantum theory of atoms in molecules (QTAIM) and electron localisation function (ELF) calculations were performed on **1**, **2**, and **3**. In the case of **1** and **2**, QTAIM calculations find a (3, −3) critical point, or non-nuclear attractor (NNA), in addition to two (3, –1) bond critical points (BCPs), for the Be–Be interactions in both complexes (Figure **S 2.8** and **S 2.9**). This is consistent with previous calculations on **1** and with

experimental/theoretical studies of magnesium(I) dimers.[10,18,52] By contrast, complex **3** is not calculated to feature a NNA, indicating fundamental differences between the Be–Be interaction in this complex and that in **1** and **2** (**S 2.10**).[53] The Bader charges calculated for the Be centres within **1** (+1.42) and **2** (Be_{Cp}, +1.39; Be_{Cp*}, +1.43) are very similar, with the NNA bearing a large negative charge in both cases (**1**, –1.17; **2**, –1.15). Indeed, the Be–Be bond of **2** is clearly only very slightly polarized. In the case of **3**, however, the charge distribution at the beryllium centres is highly uneven (Be_{Cp}, +0.19; Be_{NHBO}, +1.62). The Bader charge for Be_{Cp} in **3** implies that this beryllium centre is extremely electron rich and is consistent with the upfield ^{9}Be NMR resonance and long Be-Cp_{cent} distance measured for this complex.[54,55] This charge distribution also aligns with the composition of the ELF basin associated with the Be–Be interaction in **3**, which features a much greater contribution from Be_{Cp} (1.67 e^{-}) than the Be_{NHBO} (0.24 e^{-}).[56,57] Combined, these data imply that complex **3** could be considered a mixed valence Be_{Cp}^{0}/Be_{NHBO}^{II} complex with a $Be^{0}\rightarrow Be^{II}$ donor-acceptor bond.[56,57]

Natural bond order (NBO) and natural population analysis (NPA) calculations also indicate that the Be–Be interaction in **3** is highly polarized; NPA charges of +0.64 for Be_{Cp} and +1.15 for Be_{NHBO} were calculated (Figure **S 2.18** –**S 2.20**, Table **ST 2.6** and

ST 2.7). In similar fashion to the ELF calculations, NBO analysis indicates starkly different contributions to the Be–Be interaction from the two beryllium centres in **3**, with 62% of the electron density donated by Be_{Cp} and 38% by Be_{NHBO}.[56,57] The populations of the valence 2s- and 2p-orbitals of the two beryllium centres also evidence the greater degree of electron density at Be_{Cp} (1.34 e^{-}) compared with BeNHBO (0.85 e^{-}).

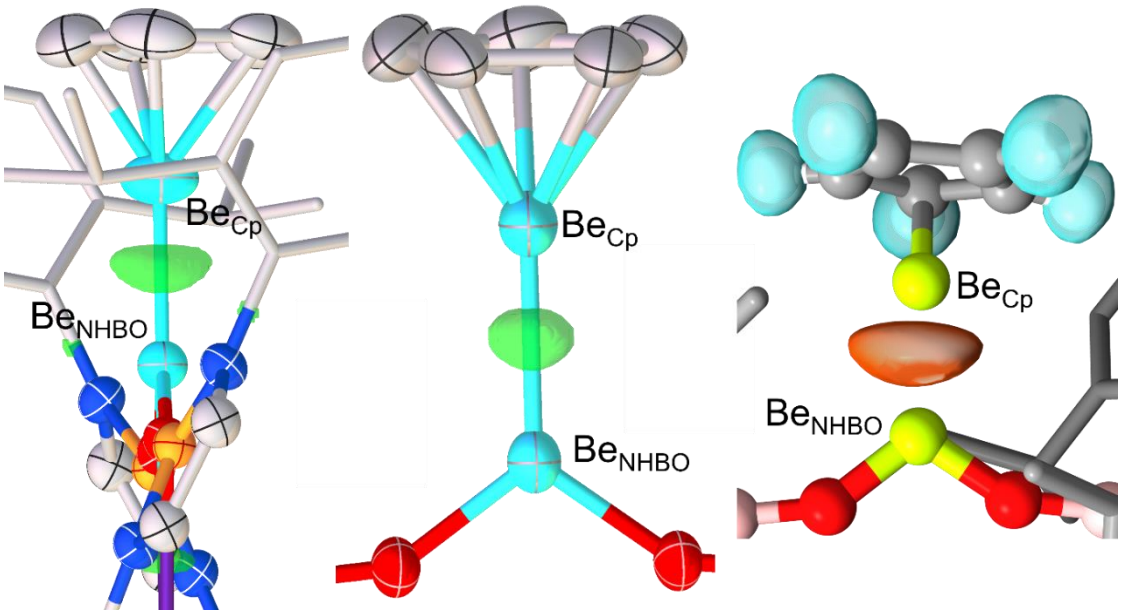

Figure 2.4: Two orientations of SCXRD-derived residual electron density plot for complex **3** (left and centre) and ELF isosurface for the Be–Be interaction in **3** (right; orange; 0.7 a.u.).

In order to obtain futher evidence for the polairised nature of the Be–Be interaction in **3**, the SCXRD-derived residual electron density map for this complex (refined using non-spherical atomic form factors) was examined.[52,58,59] There is a resemblance between the residual electron density in this plot and the profile of the ELF isosurface corresponding to the Be–Be bonding basin (**Figure 2.4**). Indeed, in both cases, the electron density appears to be polarised, with a hemispherical lobe directed from Be_{Cp} towards Be_{NHBO}. In order to benchmark the ELF data for **3**, the isosurfaces corresponding to the B–B bond of sp^2–sp^3 diborane $[(pin)B–B(F)(pin)]^-$ (**B**; pin = $[\{OC(Me)_2\}_2]^{2-}$) and the archetypal donor-acceptor N–B bond of H_3NBH_3 (**C**) were plotted using the same method (Figure **S 2.16** and **S 2.17**).[35] Visually, these two ELF isosurfaces, and that of the Be–Be interaction in **3**, have similar hemispherical profiles, with the electron density directed from the Lewis basic moiety towards the Lewis acidic centre. This topology is typical of the forms of ELF isosurfaces for donor-acceptor interactions.[56–58] It should be noted that the ELF isosurfaces for the Be–Be interaction **1** and **2** (as well as a range of polarized/non-polarized C–C bonds) have symmetrical, pancake-like profiles, which are typical of covalent-type bonds and are therefore markedly different from that of **3** (Figure **S 2.11** and **S 2.12**, **S 2.17**).[58]

To further examine the nature of the Be–Be interaction in **3** computationally, energy decomposition analysis (EDA) calculations were performed on this complex, as well as **1**, **2**, **B** and **C**. It has previously been found (by ourselves and others) that natural energy decomposition analysis (NEDA) is effective for probing the nature of bonding in main group element-containing molecules; thus we employed this technique here (Table **ST 2.8** - **ST 2.12**).[60,61] The most representative bonding model for a given molecule can be determined by the fragments that yield the lowest magnitude of the orbital interaction energy (E_{orb}) upon recombination.[20,27,28,62–64] Indeed, in the case of **3**, $|E_{orb}|$ for a donor-acceptor recombination ([CpBe]→[Be(NHBO)$_2$K], –217 kcal mol^{-1}) is lower than that of the (homolytic) radical recombination of the Be–Be linkage (–282 kcal mol^{-1}). This mirrors calculations performed on **B** and **C**, for which $|E_{orb}|$ for the donor-acceptor recombination ([(pin)B→B(F)(pin)]$^-$, –411 kcal mol^{-1}; H_3N→BH_3, –216 kcal mol^{-1}) is lower, in each case, than the respective homolytic radical recombinations (–521 kcal mol^{-1} and –532 kcal mol^{-1}, respectively). This contrasts with the corresponding analysis on **2**, for which a homolytic radical Be–Be recombination is favoured (E_{orb} = –224 kcal mol^{-1}), compared with both donor-acceptor formulations for the complex ([CpBe]→[BeCp*], –275 kcal mol^{-1}; [Cp*Be]→[BeCp], –276 kcal mol^{-1}). Hence, NEDA also indicates that a donor-acceptor, Be^0/Be^{II} formalism could be used to describe the electronic configuration of **3**.[27]

EDA coupled with natural orbitals for chemical valence (EDA-NOCV) calculations were also performed on **1**, **2** and **3**.[1] The $|E_{orb}|$ for the (homolytic) biradical fragmentation of the Be–Be linkage of **3** (–70.1 kcal mol^{-1}; Figure S45 and S46) is lower than the corresponding $|E_{orb}|$ for a pure donor-acceptor fragmentation ([CpBe]→[Be(NHBO)$_2$K], –116 kcal mol^{-1}; Figure S47). Nonetheless, in the case of homolytic fragmentation, the eigenvalues for the α_1- and β_1-pair densities are highly dissimilar ([CpBe]→[Be(NHBO)$_2$K], 0.36; [CpBe]←[Be(NHBO)$_2$K], 0.29), thereby indicating that there is a large net movement of electrons from Be_{Cp} to Be_{NHBO} (Table **ST 2.15**). Again, this evidences the highly polarised nature of the Be–Be linkage in **3**. For reference, EDA-NOCV calculations were also performed on a range of other molecules with polar and non-polar homo-elemental (B–B and C–C) bonds (Table **ST 2.14** - **ST 2.16**, Figure **S 2.21** - **S 2.26**). Of

all these examples, homolytic fragmentation of the Be–Be bond of **3** was calculated to lead to the greatest net movement of electrons. Thus, the Be–Be linkage of **3** could be described as the most polarized bond of all those studied here.

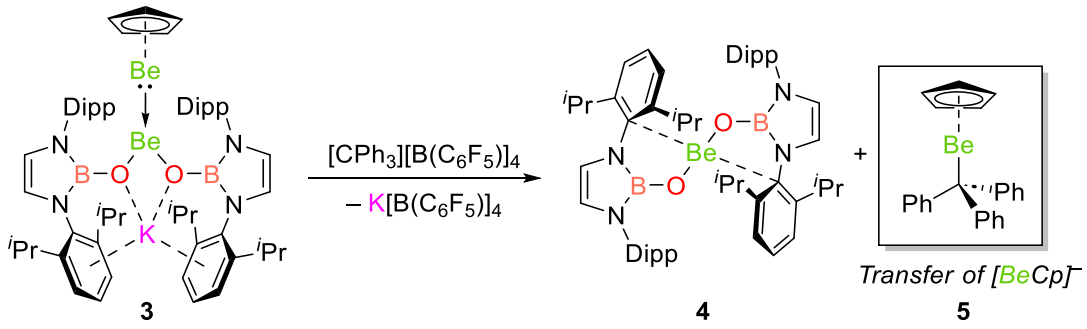

Scheme 2.2: Reactivity of complex **3** with $[CPh_3][B(C_6F_5)_4]$, a source of the organic electrophile $[CPh_3]^+$.

When complexes of the form $[Be(cAAC)_2]$ (**D**; cAAC = cyclic(alkyl)(amino)carbene) were initially reported they were described as comprising a neutral beryllium(0) centre and two neutral carbene ligands.[21] However, cAAC ligands are known to be redox non-innocent and several subsequent theoretical studies indicate that **D** is instead best described as a beryllium(II) complex featuring two anionic cAAC ligands.[20,29] Indeed, this is consistent with our own calculations on **D**, which yield Bader and NPA charges of +1.50 and +1.47, respectively, for the beryllium centre within this complex. These values are much greater than the same metrics calculated for Be_{Cp} in **3** (+0.19 and +0.64, respectively). In broader terms, the formal oxidation state assignment for a particular element centre is only meaningful in the context of its chemical behaviour. Indeed, although **D** has been used as a reducing agent, this reactivity may be ascribed to the anionic nature of the carbene ligands within this complex.[25] As far as we are aware there are no reported data that unequivocally show that **D** reacts as a source of low-valent beryllium.

In order to obtain experimental evidence for the possible Be^0/Be^{II} formulation for **3**, the reactivity of this complex was examined. In this context, the reaction of **3** with $[CPh_3][B(C_6F_5)_4]$ is informative: the process leads to the formation of previously unreported complexes

$Be(NHBO)_2$ (**4**; Figure **S 2.1**) and $CpBe(CPh_3)$ (**5**; Figure **S 2.2**), as well as $K[B(C_6F_5)_4]$. This reaction involves the transfer of a nucleophilic "beryllyl" anion, $[CpBe]^-$, (which features a formal beryllium(0) centre) from **3** to the electrophilic trityl cation, forming a Be–C bond and yielding **5**, leaving the beryllium(II)-containing fragment **4**.[44] This reactivity is analogous to that of sp^2–sp^3 diboranes, which feature highly polarized B–B bonds and act as a source of the boryl anion, $[BR_2]^-$, which is closely related to the beryllyl anion.[33–36] As such, the observed reactivity of **3** provides evidence that this species could be considered a mixed-oxidation state Be^0/Be^{II} complex, and is a rare example of a nucleophilic *s*-block complex.

Conclusions

In conclusion, we have prepared two complexes with Be–Be bonds through ligand metathesis reactions of diberyllocene (CpBeBeCp, **1**). These new complexes – Cp*BeBeCp (**2**) and $[K\{(HCDippN)_2BO\}_2]$BeBeCp (**3**) – have been studied by quantum chemical methods, which imply that **3** is could be formulated as a Be^0/Be^{II} complex. This assignment is supported by quantum chemical calculations and residual electron density plots, which are derived from single crystal X-ray diffraction measurements. Further experimental evidence for this claim has been obtained through transfer of the beryllyl anion, $[CpBe]^-$, to an electrophilic organic substrate and isolation of both beryllium-containing products. Fundamentally, this reactivity can be likened to that of sp^2–sp^3 diboranes, revealing that the reactivities of homo-elemental bonds of beryllium and boron have parallels, despite the respective metallic and non-metallic natures of these elements. Hence, this work reveals that bonding trends across period 2 are more continuous than may previously have been appreciated. We continue to investigate the chemical relationships between beryllium and its neighbouring elements in order to test models of chemical bonding.

Characterising Data

General Considerations

Health warning: beryllium and its compounds are extremely toxic and can cause irreversible health effects through inhalation or skin contact. The work with beryllium-containing materials described herein was carried out by trained operators, with strict adherence to local and national rules/regulations.[5]

All manipulations were carried out using Schlenk line or glovebox techniques under an atmosphere of argon or dinitrogen. Solvents were dried by passage through activated alumina towers, dried with NaK_2 and degassed before use. Solvents were stored over NaK_2. NMR spectra were measured in C_6D_6 which was dried over NaK_2, with the solvent being distilled under reduced pressure, degassed by three freeze-pump-thaw-cycles and stored under argon in a Teflon valve ampoule. NMR samples were prepared under argon in 5 mm Wilmad 507-PP tubes fitted with J. Young Teflon valves. NMR spectra were measured on a Bruker Avance III HD Nanobay 400 MHz NMR spectrometer equipped with a 9.4 T magnet, Bruker Avance III 500 MHz NMR spectrometer equipped with a 11.75 T magnet, or a Bruker Avance III NMR 500 MHz NMR spectrometer equipped with a 11.75 T magnet and a ^{13}C detect cryoprobe. ^{1}H and ^{13}C NMR spectra were referenced internally to residual protio-solvent (^{1}H) or solvent (^{13}C) resonances and are reported relative to tetramethylsilane (δ = 0 ppm). ^{9}Be NMR spectra were referenced to a 0.43 M solution of $BeSO_4{\cdot}4H_2O$ in D_2O (δ = 0 ppm). Chemical shifts are quoted in δ (ppm) and coupling constants in Hz. Elemental analyses were carried out by London Metropolitan University. The compounds diberyllocene (**1**), $[(HCDippN)_2BO]K$ (K-NHBO), KCp*, and $[CPh_3][B(C_6F_5)_4]$ were prepared as described previously. [18,45,65]

Synthesis of Novel Compounds

*Synthesis of Cp*BeBeCp (2):*

To an ampoule fitted with a Teflon valve and equipped with a glass-coated stirrer bar was added a solid mixture of **1** (4.0 mg, 0.027 mmol) and KCp* (19 mg, 0.11 mmol, 4.0 equ.). Benzene (1 mL) was condensed into the vessel *in vacuo* at –196 °C. The colourless suspension was allowed to warm to room temperature and stirred at 80 °C for four days. Volatiles were removed *in vacuo* at 0 °C leaving a white powder. Complex **2** is volatile, so prolonged drying should be avoided. Soluble material was dissolved in hexane (0.5 mL), filtered, and concentrated (0.2 mL). Standing overnight led to the formation of colourless crystals, which were carefully dried *in vacuo*. Yield: 4.0 mg, 68%. Single crystals of **2** suitable for X-ray diffraction experiments were obtained by slow evaporation of a concentrated hexane solution in a sealed glass λ-type tube. Anal. Calcd for $C_{15}H_{20}Be_2$: C, 82.51; H, 9.23. Found: C, 81.96; H, 9.16. ^{1}H NMR (400 MHz, C_6D_6, 298 K): δ = 1.90 (s, 15H, $C_5(CH_3)_5$), 5.68 (s, 5H, C_5H_5); ^{9}Be NMR (42 MHz, C_6D_6): δ = –28.6 ($w_{1/2}$ = 49.3 Hz; Cp*Be*), –21.7 ($w_{1/2}$ = 39.9 Hz; Cp**Be*); ^{13}C{^{1}H} NMR 101 MHz, C_6D_6): δ = 10.3 ($C_5(CH_3)_5$), 102.3 (C_5H_5), 108.2 ($C_5(CH_3)_5$).

Synthesis of [K{(HCDippN)$_2$BO}$_2$]BeBeCp (3):

To an ampoule fitted with a Teflon valve and equipped with a glass-coated stirrer bar was added a solid mixture of **1** (4.0 mg, 0.027 mmol) and K-NHBO (23 mg, 0.054 mmol, 2.0 equ.). Benzene (1 mL) was condensed into the vessel *in vacuo* at –196 °C. The pale-yellow suspension was allowed to warm to room temperature and stirred for one hour. Subsequently, volatiles were removed *in vacuo*, and soluble material was dissolved in hexane (0.5 mL). The suspension was filtered and concentrated (0.2 mL). Standing overnight led to the formation of colourless crystals, which were dried *in vacuo*. Yield: 18 mg, 73%. Single crystals of **2** suitable for X-ray diffraction experiments were obtained by slow evaporation of a concentrated hexane solution in a sealed glass λ-type tube. Anal. Calcd for $C_{57}H_{77}B_2Be_2KN_4O_2$: C, 73.69; H, 8.35; N, 6.03. Found: C, 73.32; H, 8.11; N, 5.85. ^{1}H NMR (400 MHz, C_6D_6, 298 K): δ = 1.20 (2 x d, 48H, $CH(CH_3)_2$), 3.49

(sept, $^{3}J_{HH}$= 6.8 Hz, 8H, C*H*$(CH_3)_2$), 5.49 (s, 5H, C_5H_5), 5.93 (s, 4H, C*H*), 7.06 (m, 12H, Ar*H*); ^{9}Be NMR (42 MHz, C_6D_6): δ = –29.8 ($w_{1/2}$ = 94.7 Hz; Cp*Be*), 9.5 ($w_{1/2}$ = 380 Hz; O_2*Be*); ^{11}B NMR (128 MHz, C_6D_6): δ = 20.5; ^{13}C{^{1}H} NMR (101 MHz, C_6D_6): δ = 23.7 (CH(*C*$H_3)_2$), 24.6 (CH(*C*$H_3)_2$), 28.3 (*C*H$(CH_3)_2$), 102.7 (C_5H_5), 116.5 (N*C*H), 123.7 (Dipp-*m*-*C*H), 126.4 (Dipp-*p*-*C*H), 141.9 (Dipp-*i*-*C*), 147.4 (Dipp-*o*-*C*).

Synthesis of Be(NHBO)2 (4) and CpBe(CPh3) (5):

To an ampoule fitted with a Teflon valve and equipped with a glass-coated stirrer bar was added a solid mixture of **3** (8.0 mg, 0.0086 mmol) and [CPh_3][$B(C_6F_5)_4$] (7.9 mg, 0.0086 mmol). Benzene (1 mL) was condensed into the vessel *in vacuo* at –196 °C. The yellow solution was allowed to warm to room temperature and stirred for one hour. Subsequently, volatiles were removed *in vacuo*, soluble material was dissolved in hexane (0.5 mL), and the suspension was filtered. Slow concentration of the resulting solution in a sealed glass λ-type tube led to the formation of colourless crystals (**4**) and bright yellow crystals (**5**), which were manually separated. Yield of **4**: 3.8 mg, 54%. Yield of **5**: 2.1 mg, 76%. Compound **4**: anal. calcd for $C_{52}H_{72}B_2BeN_4O_2$: C, 76.56; H, 8.90; N, 6.87. Found: C, 76.39; H, 8.86; N, 6.74. ^{1}H NMR (400 MHz, C_6D_6, 298 K): δ = 1.03 (d, $^{3}J_{HH}$= 7.1 Hz, 24H, CH(C*H*$_3)_2$),1.18 (d, $^{3}J_{HH}$= 6.8 Hz, 24H, CH(C*H*$_3)_2$), 3.16 (sept, $^{3}J_{HH}$= 7.5 Hz, 8H, C*H*$(CH_3)_2$), 5.86 (s, 4H, C*H*), 7.09 (m, 12H, Ar*H*); ^{9}Be NMR (42 MHz, C_6D_6): δ = 5.1 ($w_{1/2}$ = 727.4 Hz); ^{11}B NMR (128 MHz, C_6D_6): δ = 20.6; ^{13}C{^{1}H} NMR (101 MHz, C_6D_6): δ = 24.0 (CH(*C*$H_3)_2$), 24.4 (CH(*C*$H_3)_2$), 28.6 (*C*H$(CH_3)_2$), 116.0 (N*C*H), 123.5 (Dipp-*m*-*C*H), 127.4 (Dipp-*p*-*C*H), 137.8 (Dipp-*i*-*C*), 146.8 (Dipp-*o*-*C*). Compound **5**: anal. calcd for $C_{24}H_{20}$Be: C, 90.81; H, 6.35. Found: C, 90.48; H, 6.32. ^{1}H NMR (400 MHz, C_6D_6, 298 K): δ = 5.61 (s, 5H, C_5H_5), 7.03 (t, $^{3}J_{HH}$ = 7.1, 6H, *o*-C_6H_5), 7.10 (t, $^{3}J_{HH}$ = 7.3, 6H, *m*-C_6H_5), 7.36 (d, $^{3}J_{HH}$ = 7.6, 3H, *p*-C_6H_5); ^{9}Be NMR (42 MHz, C_6D_6): δ = –18.0 ($w_{1/2}$ = 29.4 Hz); ^{13}C{^{1}H} NMR (101 MHz, C_6D_6): 102.7 (C_5H_5), 131.0 (C_6H_5), 137.9 (C_6H_5), 141.5 (C_6H_5), 145.0 (C_6H_5); 187.3 (*C*Ph_3).

Crystallographic Data

Crystallographic data for **2**, **3**, **4**, and **5** were collected using an Oxford Diffraction/Agilent SuperNova or Rigaku XtaLAB Synergy-R. Crystals were selected under Paratone-N or perfluorinated oil, mounted on MiTeGen Micromount loops and quench-cooled using an Oxford Cryosystems open flow N_2 cooling device.[65] Selected details of data collection are given in Table Equivalent reflections were merged and diffraction patterns processed with the CrysAlisPro suite. Structures were solved *ab initio* from the integrated intensities using SHELXT and refined on F2 using SHELXL with the graphical interface OLEX2.69-70 In the case of complex **3,** the NoSpherA2 method was employed for refinement using non-spherical form factors.[59] In this case, R2SCAN def2-SVP was used in the iterative improvement of the fit of the model (followed by a single point calculation; R2SCAN def2-TZVP) using ORCA version 5.0.4.71-75 Crystallographic data is given in the supplementary deposited CIF files (CCDC 2324714 – 2324717) and can be obtained free of charge from the Cambridge Crystallographic Data Centre *via* http://www.ccdc.cam.ac.uk/data_request/cif. Structures of **3** and **5** feature disorder of the cyclopentadienyl groups over special positions. This was treated using Part –1 and fractional occupancy in both cases. Further details of how crystallographic disorder was treated can be found in the CIF files.

ST 2.1. Data collected were processed using the CrysAlisPro package, including unit cell parameter refinement and inter-frame scaling (which was carried out using SCALE3 ABSPACK within CrysAlisPro).[68] Equivalent reflections were merged and diffraction patterns processed with the CrysAlisPro suite. Structures were solved *ab initio* from the integrated intensities using SHELXT and refined on F2 using SHELXL with the graphical interface OLEX2.[69-70] In the case of complex **3**, the NoSpherA2 method was employed for refinement using non-spherical form factors.[59] In this case, R2SCAN def2-SVP was used in the iterative improvement of the fit of the model (followed by a single point calculation; R2SCAN def2-TZVP) using ORCA version 5.0.4.[71-75] Crystallographic data is given in the supplementary deposited CIF files (CCDC 2324714 – 2324717) and can be obtained free of charge from the Cambridge Crystallographic Data Centre *via* http://www.ccdc.cam.ac.uk/data_request/cif. Structures of **3** and **5** feature disorder of the cyclopentadienyl groups over special positions. This was treated using Part –1 and fractional occupancy in both cases. Further details of how crystallographic disorder was treated can be found in the CIF files.

ST 2.1: Selected X-ray data collection and refinement parameters

	2	**3**	**4**	**5**
Formula	$2(C_{15}H_{20}Be_2)$	$C_{57}H_{77}B_2Be_2KN_4O_2$	$C_{52}H_{72}B_2\ BeN_4O_2$	$2(C_{24}H_{20}Be)$
Fw (g mol^{-1})	436.66	928.96	815.76	634.82
Cell setting	triclinic	monoclinic	orthorhombic	trigonal
Space group	$P\bar{1}$	$C2/c$	$Pccn$	$R\bar{3}$
a (Å)	8.6287(4)	24.6183(4)	15.63010(10)	11.23020(10)
b (Å)	12.8408(6)	12.9582(2)	18.58010(10)	11.23020(10)
c (Å)	13.2334(5)	18.3627(3)	16.80210(10)	23.9227(2)
α (°)	98.098(4)	90	90	90
β (°)	97.174(3)	110.923(2)	90	90
γ (°)	96.751(4)	90	90	120
V (Å^{-3})	1426.57(11)	5471.60(17)	4879.48(5)	2612.86(5)
Z	2	4	4	3
ρ_{calc} (g cm^{-3})	1.017	1.128	1.110	1.210
Radiation, λ (Å)	1.54184	1.54184	1.54184	1.54184
μ (mm^{-1})	0.391	1.169	0.502	0.502
$R_{(int)}$	0.0515	0.0391	0.0360	0.0248
Parameters	317	360	306	107
R_1 (all data/I >2σ(I))	0.0496	0.0445	0.0393	0.0348
ωR_2 (all data/I >2σ(I))	0.1463	0.1295	0.1011	0.0876
GooF	1.034	1.032	1.051	1.076
T (K)	150.0(2)	100.0(2)	100.0(2)	100.0(2)
CCDC Deposition No.	2324716	2324715	2324717	2324714

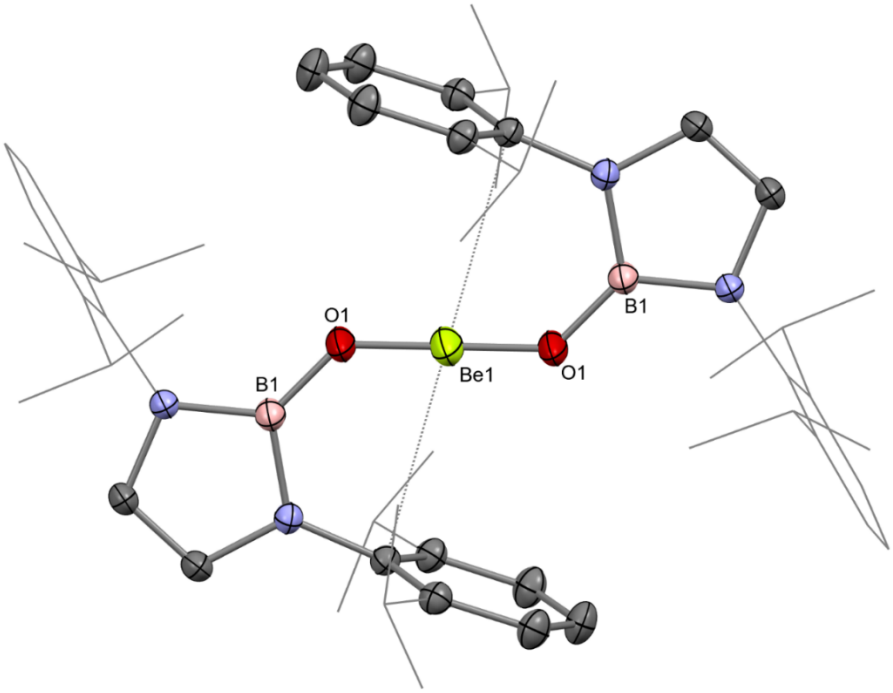

S 2.1: Molecular structure of 4 in the solid state as determined by X-ray crystallography. Thermal ellipsoids set at 50% probability; hydrogen atoms omitted and selected substituents shown in wireframe format for clarity.

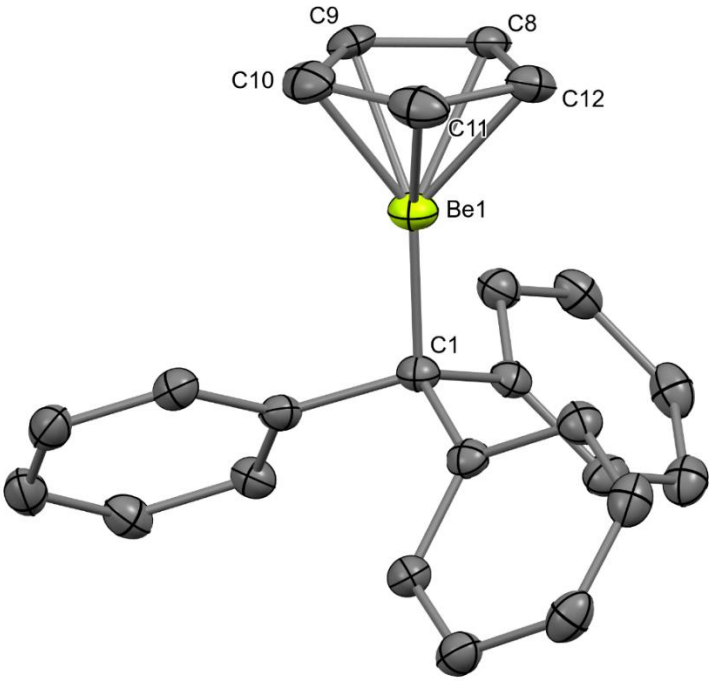

S 2.2: Molecular structure of 5 in the solid state as determined by X-ray crystallography. Thermal ellipsoids set at 50% probability; hydrogen atoms omitted for clarity.

^{9}Be NMR Chemical Shifts – CpBeR Complexes

^{9}Be NMR chemical shift is very sensitive to the degree of electron density at a particular beryllium centre.[49-50] Of relevance here is the ^{9}Be NMR chemical shift of a cyclopentadienyl-coordinated beryllium centre. Increasingly upfield ^{9}Be NMR signals correspond to beryllium centres which are more electron-rich/reduced.[44] Indeed, the data for a series a series of (otherwise geometrically identical) compounds of the type CpBeX are presented in Table **ST 2.2**. It could be proposed that the assignment of formal oxidation state gradually changes from Be(II) to Be(I) on transitioning from electronegative X-groups (e.g. X = Cl), to electropositive X-groups (e.g. X = aluminyl), with the unambiguous extension of this being X = CpBe (i.e., the *bona fide* Be(I) compound **1**). Indeed, the NMR data illustrates the step-wise formal reduction of beryllium, from the less powerful sigma donors (chloride/methyl), to intermediate (silyl- or gallyl-ligands), to aluminyl complex, and to **3**, in which Be_{Cp} can be considered to be in the 0-oxidation state.

ST 2.2: ^{9}Be NMR chemical shifts (in C_6D_6) for a range of CpBeR species and the Pauling electronegativity of the atom from each group which is bonded to beryllium.10

R-Group (CpBeR)	$\delta_{^{9}Be}$ / ppm	Pauling Electroneg. of Donor Atom
$[K(NHBO)_2]$Be (**3**)	–29.8	1.57
[(NON)Al]	–28.8	1.61
Cp*Be (**2**)	–28.6	1.57
(^{Dipp}Nacnac)Zn	–27.7	1.65
Me_3Si	–27.7	1.90
CpBe (**1**)	–27.6	1.57
$[Me_2(SiMe_3)Si]$	–27.2	1.90
[(NON)Ga]	–26.9	1.81
[{NON}Al{$(N^{i}Pr)_2C$}]	–24.6	2.55
Me	–20.5	2.55
Cl	–19.5	3.16
Br	–19.5	2.96
Ph_3C (**5**)	–18.0	2.55

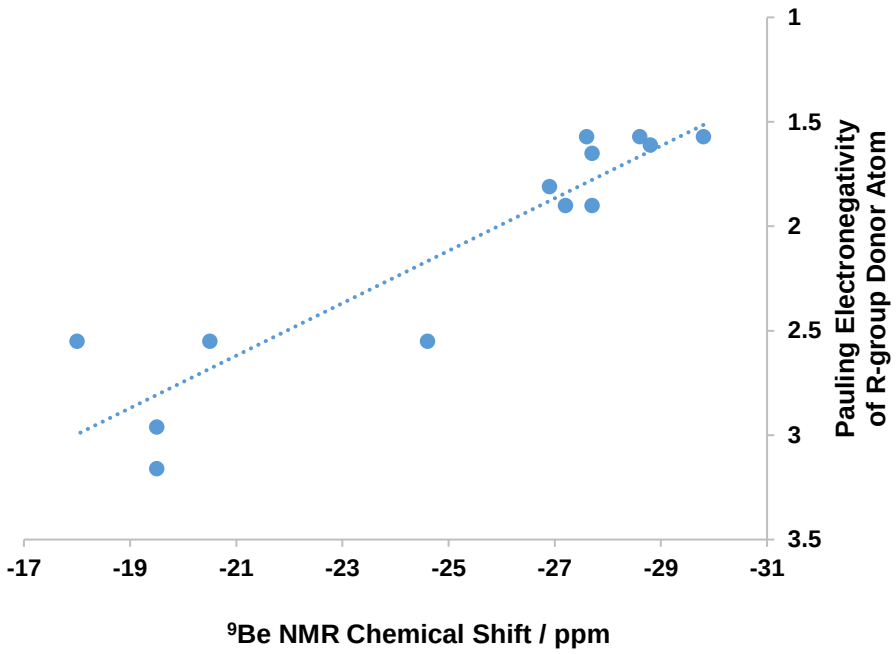

S 2.3: Plot of 9Be NMR chemical shifts for a range of CpBeR species vs the Pauling electronegativity of the atom from each group which is bonded to beryllium.

Computational Details

The structures of complexes **1**, **2**, **3**, **3'** (compound **3** without potassium cation [{(HCDippN)$_2$BO}$_2$]BeBeCp]$^-$), **B**, **C**, and **D** were optimised using ORCA (Revision 5.0.4).[71,72] Specifically, R2-SCAN was used,[73-74] in conjunction with the Def2-TZVPPm basis set with the D4 dispersion correction,[75] employing the geometrical counterpoise correction gCP (together known as the R2SCAN-3c method) and CPCM solvent (benzene) modelling.[76,77] Subsequently, a single point calculation was performed on this optimised structure with the ωB97X range-separated hybrid functional,[78-79] in conjunction with the Def2-QZVPP basis set[80,81] and the D4 dispersion correction.[75] The nature of the stationary points (minima) was confirmed by full frequency calculations, and are characterized by zero imaginary frequencies. Natural bond orbital was performed on the ORCA wavefunction using NBO 7.0.[82] Quantum Theory of Atoms in Molecules calculations were performed using the ORCA wavefunctions for the respective complexes, and were generated using Multiwfn 3.8 and AIMALL.[83,84] Electron localisation function calculations were performed using the ORCA wavefunctions for the respective

complexes, generated using Multiwfn 3.8.[85] All energy decomposition analysis was performed using Gaussian16 (RevisionC.01) at the M062x- Def2-TZVP level.[86]

Relevant Molecular Orbitals

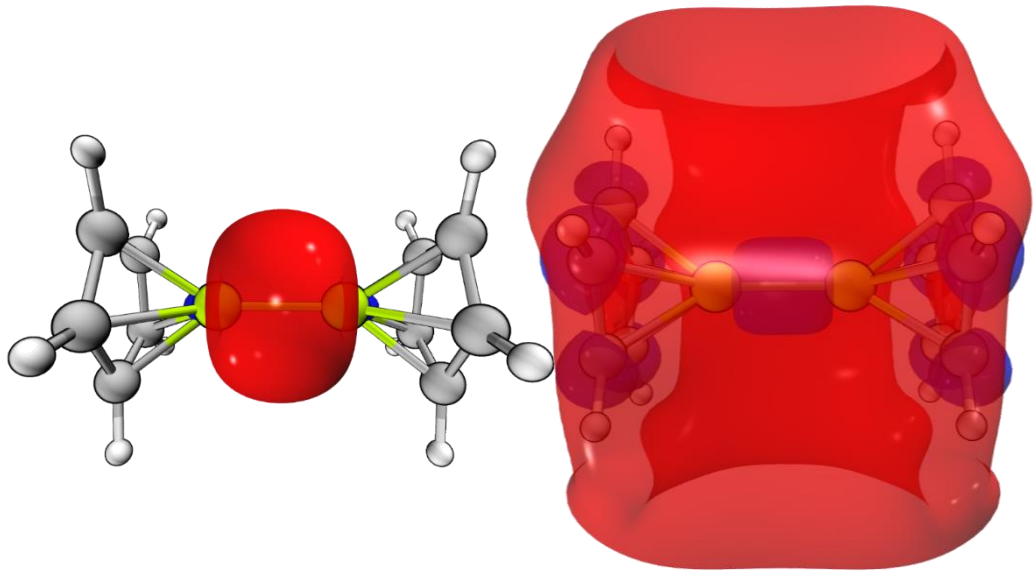

S 2.4: HOMO (left) and LUMO (right) of compound **1** (0.05 a.u.).

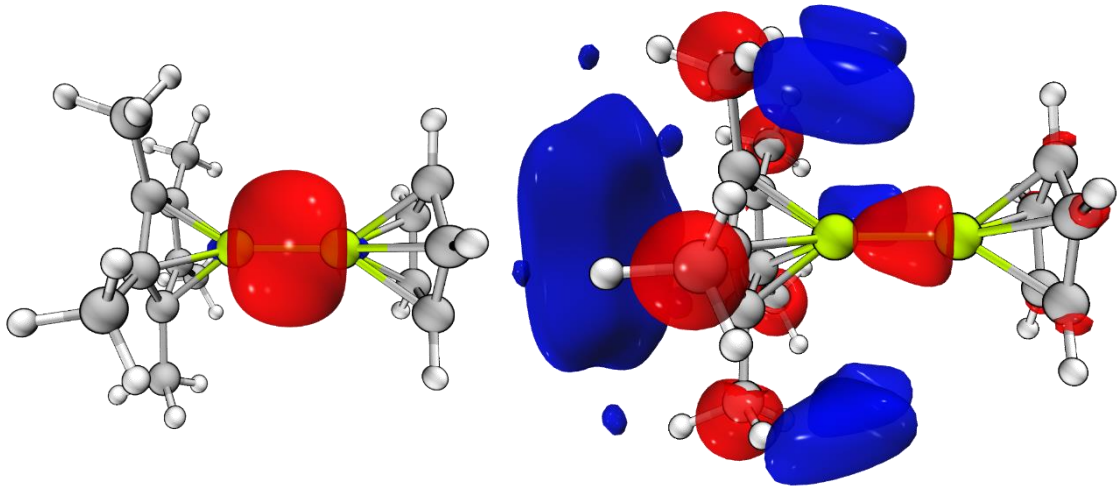

S 2.5: HOMO (left) and LUMO (right) of compound **2** (0.05 a.u.).

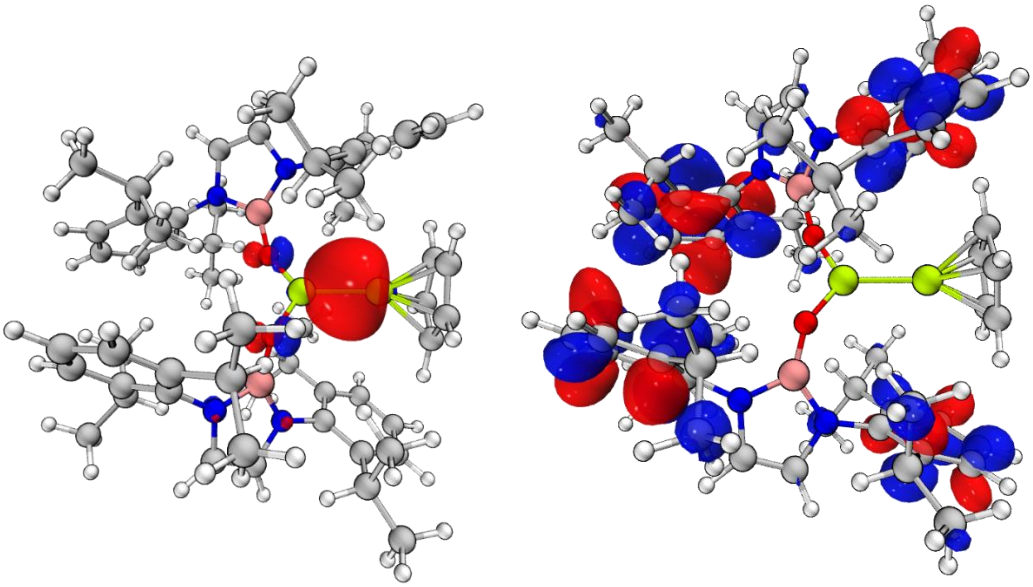

S 2.6: HOMO (left) and LUMO (right) of anion **3'** (0.05 a.u.).

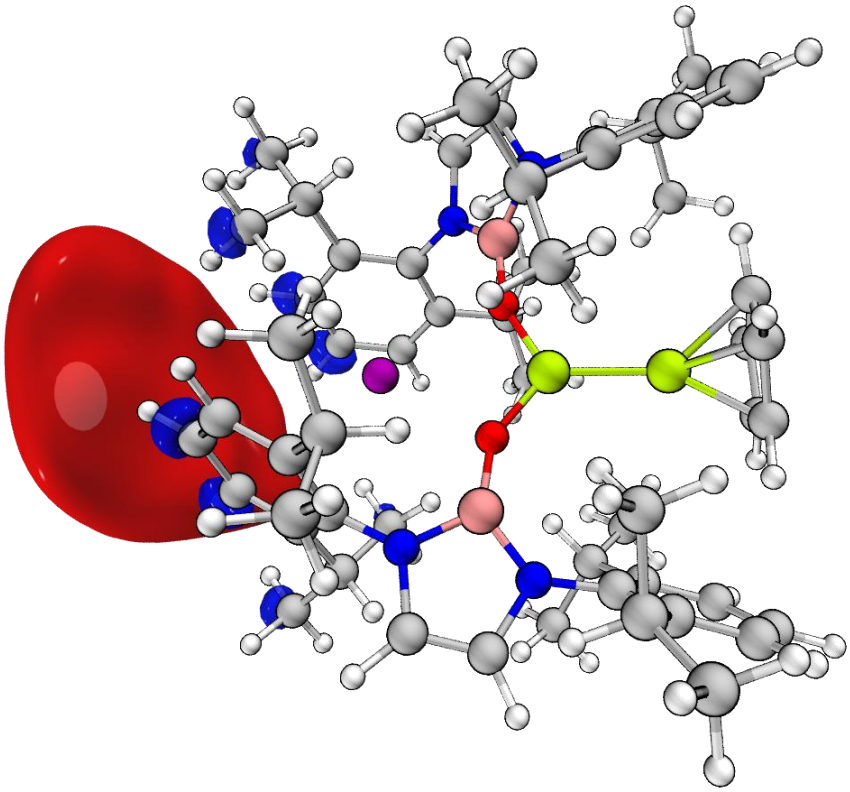

S 2.7: LUMO of compound **3** (0.05 a.u.).

Quantum Theory of Atoms in Molecules Calculations

ST 2.3: Summary of QTAIM data generated for **1 – 3**. All values in a.u..

	1		2			3
Critical Point	**Be_{Cp}-NNA**	**NNA**	**Be_{Cp}-NNA**	**Be_{Cp*}-NNA**	**NNA**	**Be-Be**
ρ_{bcp} / e^- $Bohr^{-3}$	0.067	0.068	0.067	0.066	0.067	0.060
KE (L)	0.020	0.002	0.018	0.021	0.003	0.019
KE (H)	0.039	0.031	0.039	0.037	0.033	0.034
V	-0.059	-0.033	-0.057	-0.059	-0.035	-0.052
E	-0.039	-0.031	-0.039	-0.037	-0.033	-0.034
$\nabla^2\rho_{bcp}$ / e^- $Bohr^{-5}$	-0.076	-0.116	-0.085	-0.064	-0.119	-0.059
ELF	0.716	0.996	0.758	0.671	0.992	0.663
LOL	0.614	0.942	0.639	0.588	0.917	0.584

ST 2.4: Charge distribution data (Bader) and contributions to disynaptic basin corresponding to Be-Be bond (ELF) for compounds **1** and **2**.

Compound 1			**Compound 2**		
	Bader Charge	Contribution to Disynaptic Basin		Bader Charge	Contribution to Disynaptic Basin
NNA	-1.17456	1.16844	NNA	-1.148042	1.14387
Be	1.420623	0.42623	Be_{Cp}	1.391892	0.45831
Be	1.42052	0.43131	Be_{Cp*}	1.427303	0.40704

ST 2.5: Charge distribution data (Bader) and contributions to disynaptic basin corresponding to Be-Be bond (ELF) for compounds **3** and **3'**.

Compound 3			**Compound 3'**		
	Bader charge	Contribution to Disynaptic Basin		Bader Charge	Contribution to Disynaptic Basin
NNA	N/A	N/A	NNA	N/A	N/A
Be_{NHBO}	1.622375	0.24004	Be_{NHBO}	1.645432	1.68654
Be_{Cp}	0.188163	1.66613	Be_{Cp}	0.175772	0.21141

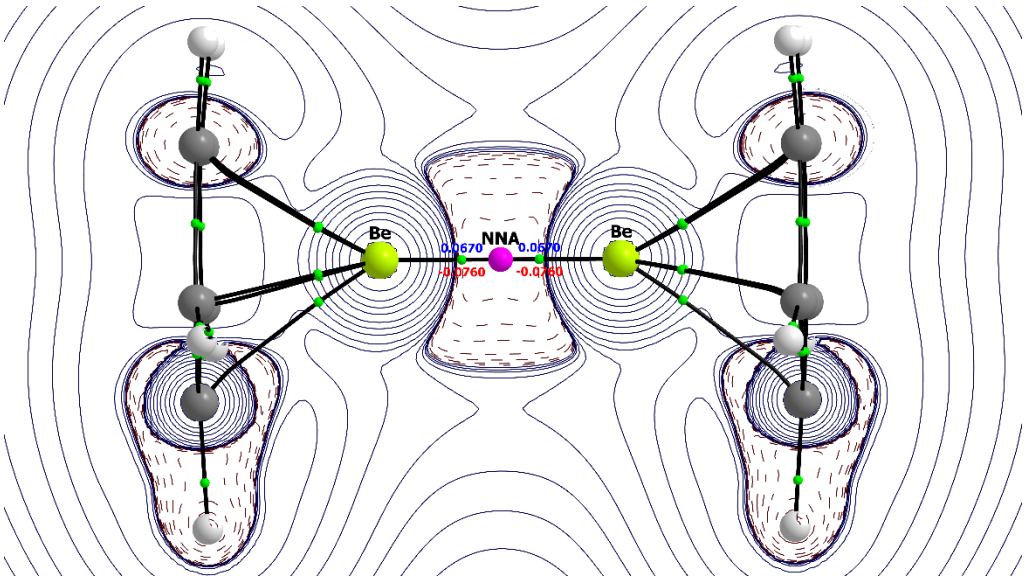

S 2.8: Plot of QTAIM data generated for **1.** Bond paths (BPs) in black and bond critical points (BCPs) in green. Contour map of is of Laplacian (∇2ρbcp). Values in red are ∇2ρbcp (e– Bohr–5) and values in blue are ρbcp (electron density; e– Bohr–3) at the respective BCP. Ring critical points and prismatic critical points are omitted for clarity.

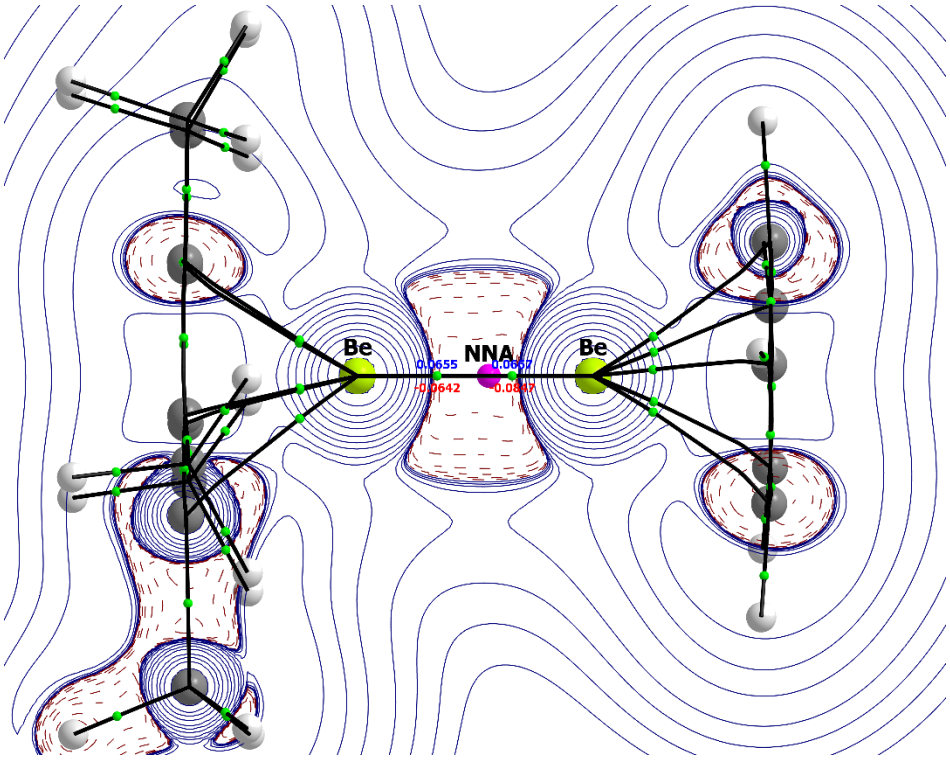

S 2.9: Plot of QTAIM data generated for **2**. Bond paths (BPs) in black and bond critical points (BCPs) in green. Contour map of is of Laplacian (∇2ρbcp). Values in red are ∇2ρbcp (e– Bohr–5) and values in blue are ρbcp (electron density; e– Bohr–3) at the respective BCP. Ring critical points and prismatic critical points are omitted for clarity.

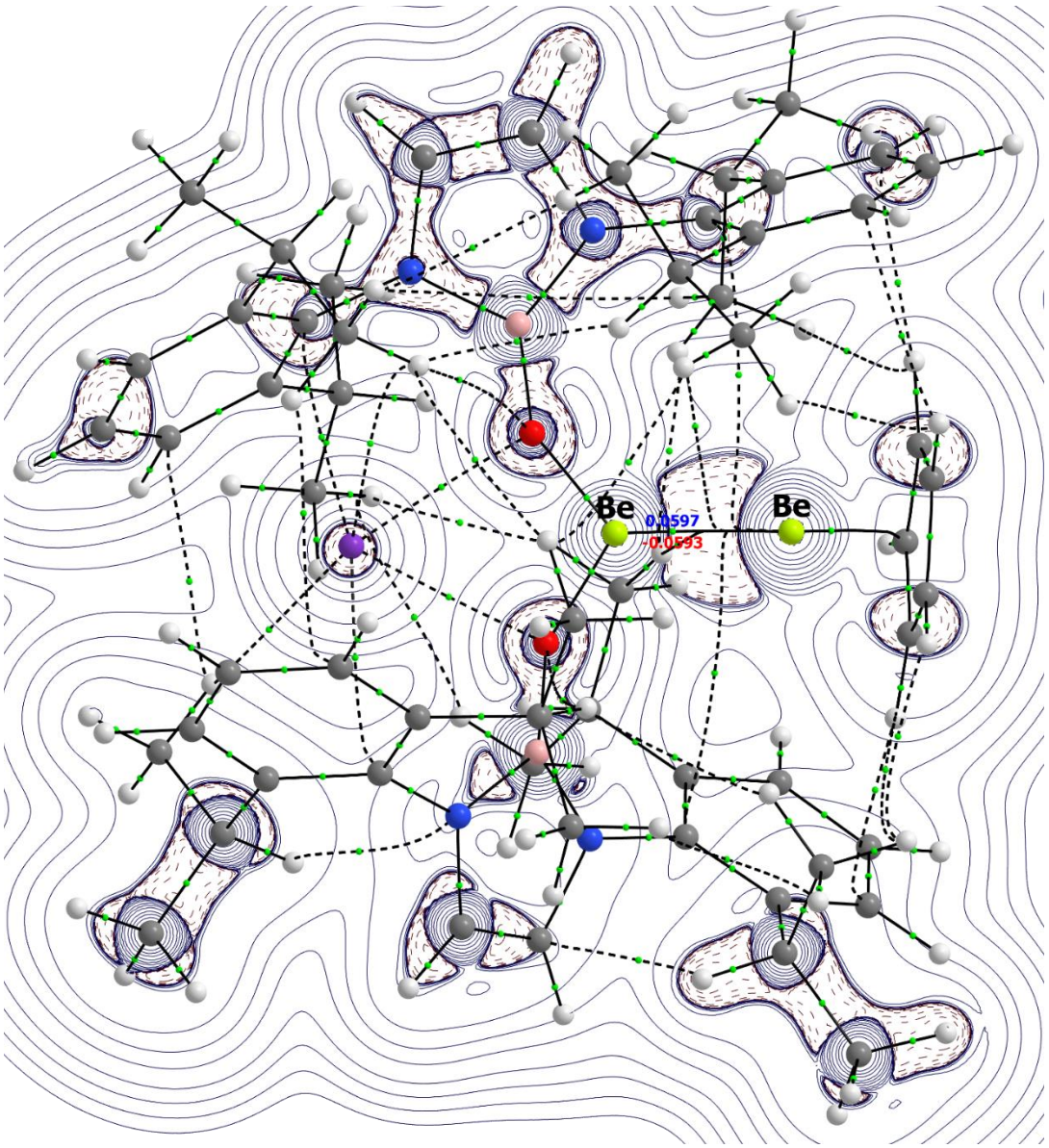

S 2.10: Plot of QTAIM data generated for **3**. Bond paths (BPs) in black and bond critical points (BCPs) in green. Contour map of is of Laplacian (∇2ρbcp). Values in red are ∇2ρbcp (e– Bohr–5) and values in blue are ρbcp (electron density; e– Bohr–3) at the respective BCP. Ring critical points and prismatic critical points are omitted for clarity.

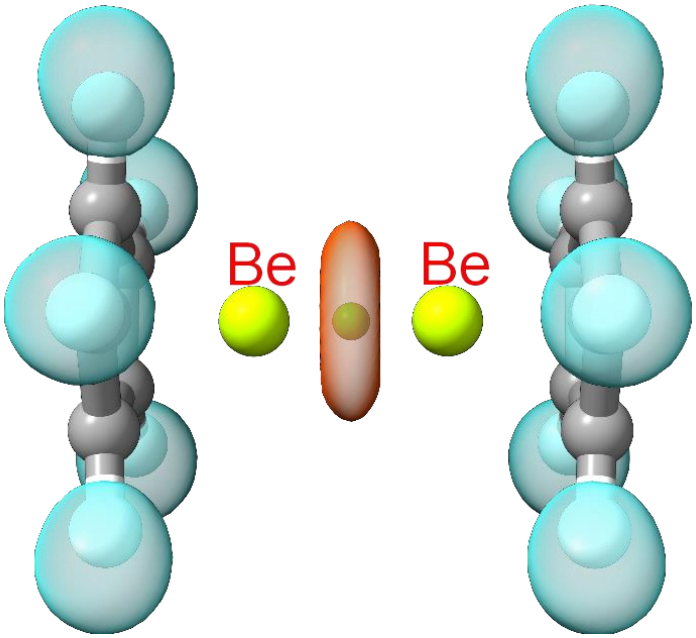

S 2.11: ELF isosurface for **1** (0.7 a.u.). Blue represents the isosurfaces associated with the Cp ligands. Orange represents the isosurface associated with the Be–Be bonding basin.

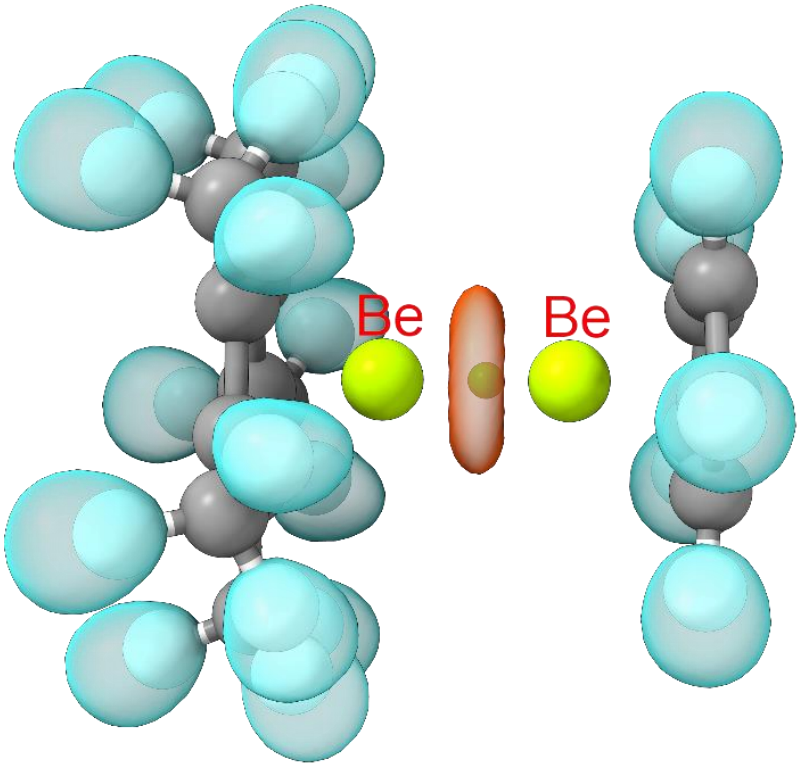

S 2.12: ELF isosurface for **2** (0.7 a.u.). Blue represents the isosurfaces associated with the ligands. Orange represents the isosurface associated with the Be–Be bonding basin.

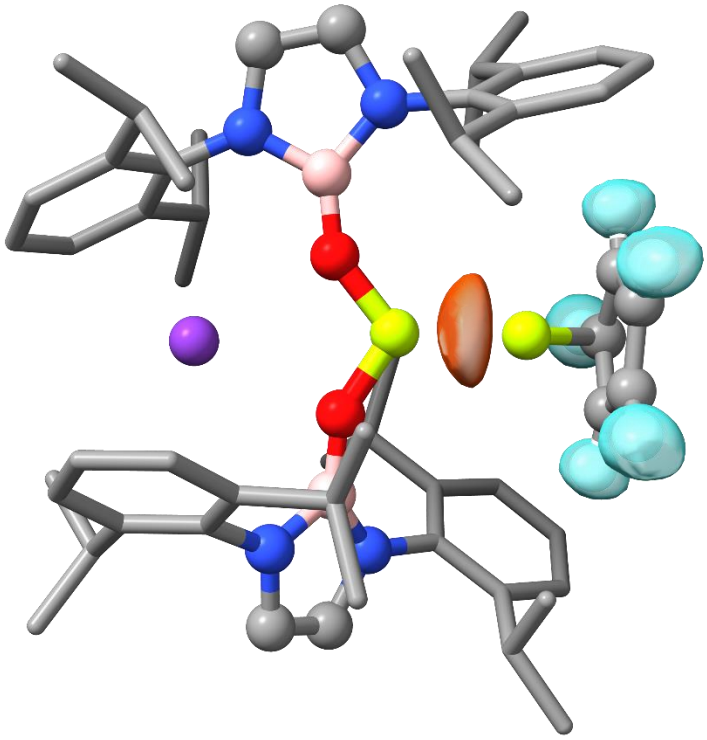

S 2.13: ELF isosurface for **3** (0.7 a.u.). Blue represents the isosurfaces associated with the Cp ligand. Orange represents the isosurface associated with the Be–Be bonding basin.

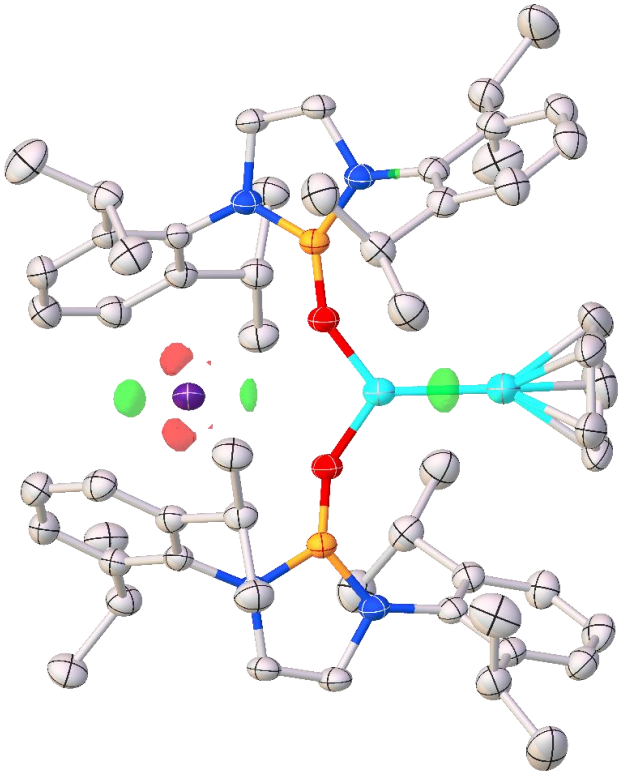

S 2.14: Residual electron density map for **3** derived from SCXRD data. Threshold: ±0.31 e Å–3

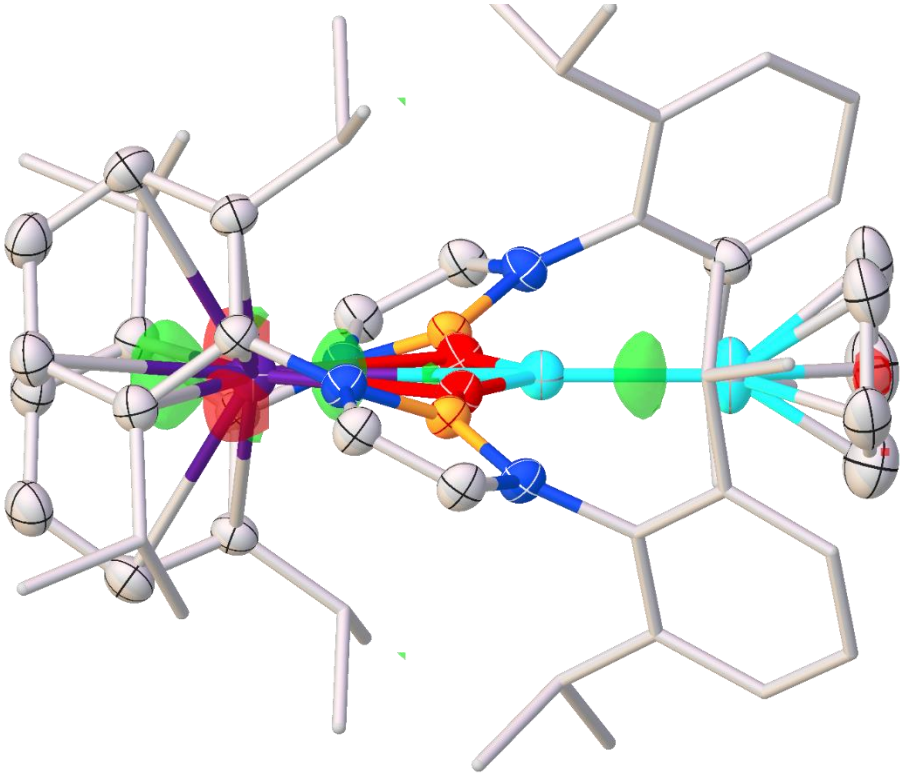

S 2.15: Residual electron density map for **3** derived from SCXRD data (side on). Threshold: ±0.31 e Å–3

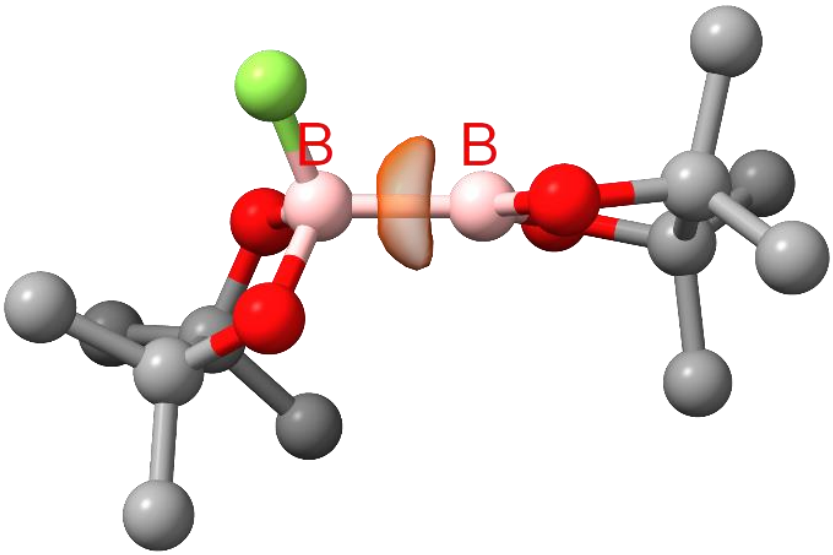

S 2.16: ELF isosurface for **B** (0.7 a.u.). Orange represents the isosurface associated with the B–B bonding basin.

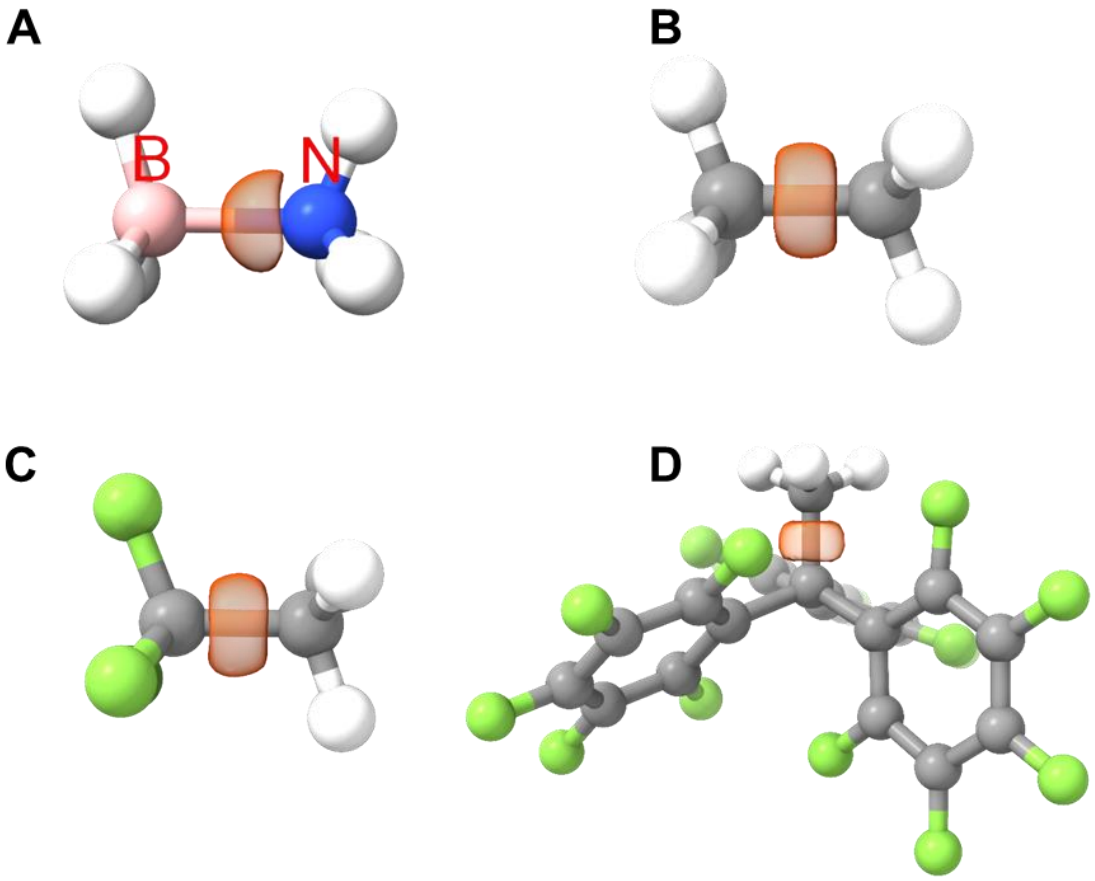

S 2.17: ELF isosurface for $NH_3{\cdot}BH_3$ (**A**), $H_3C–CH_3$ (**B**), $F_3C–CH_3$ (**C**) and $(C_6F_5)_3C–CH_3$ (**D**) at 0.7 a.u. Orange represents the isosurface associated with the B–N bonding basin.

Natural Bond Orbital and Natural Population Analysis Calculations

ST 2.6: Charge distribution (NPA) and Wiberg bond index (WBI) data for compounds **1** and **2**.

Compound 1		**Compound 2**	
	NPA Charge		**NPA Charge**
Be_{Cp}	0.85063	**Be_{Cp}**	0.85911
Be_{Cp}	0.85036	**Be_{Cp*}**	0.86709
WBI (Be-Be)	0.8933	**WBI (Be-Be)**	0.8962

ST 2.7: Charge distribution (NPA) and Wiberg bond index (WBI) data for compounds **3** and **3'**.

Compound 3		**Compound 3'**	
	NPA Charge		**NPA Charge**
Be_{Cp}	1.15137	**Be_{Cp}**	1.17501
Be_{NHBO}	0.63978	**Be_{NHBO}**	0.60071
WBI (Be-Be)	0.8054	**WBI (Be-Be)**	0.7873

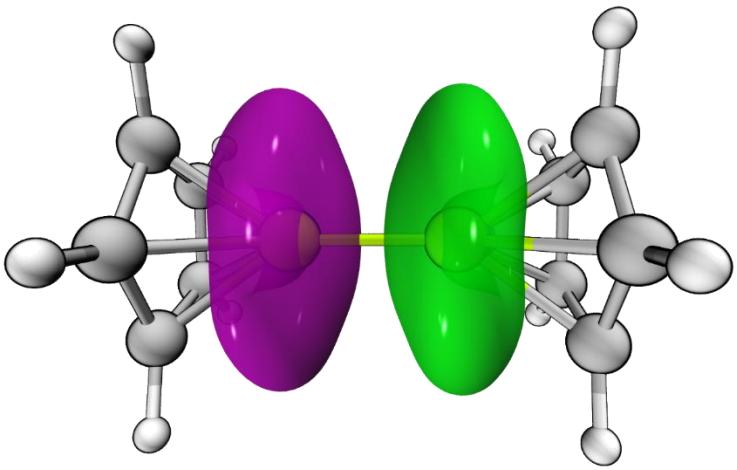

S 2.18: NBO for the Be–Be interaction of **1** (0.05 a.u.). Contribution (BeCp:BeCp) to Be-Be bond: 50:50. Wiberg bond index: 0.89. Natural population analysis charges (BeCp, BeCp): 0.85, 0.85.

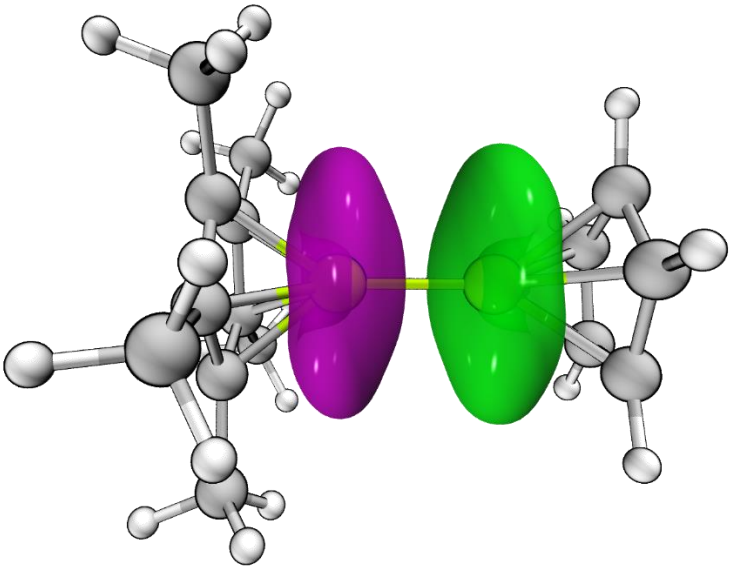

S 2.19: NBO for the Be–Be interaction of **2** (0.05 a.u.). Contribution (BeCp:BeCp*) to Be-Be bond: 50:50. Wiberg bond index: 0.90. Natural population analysis charges (BeCp, BeCp*): 0.86, 0.87.

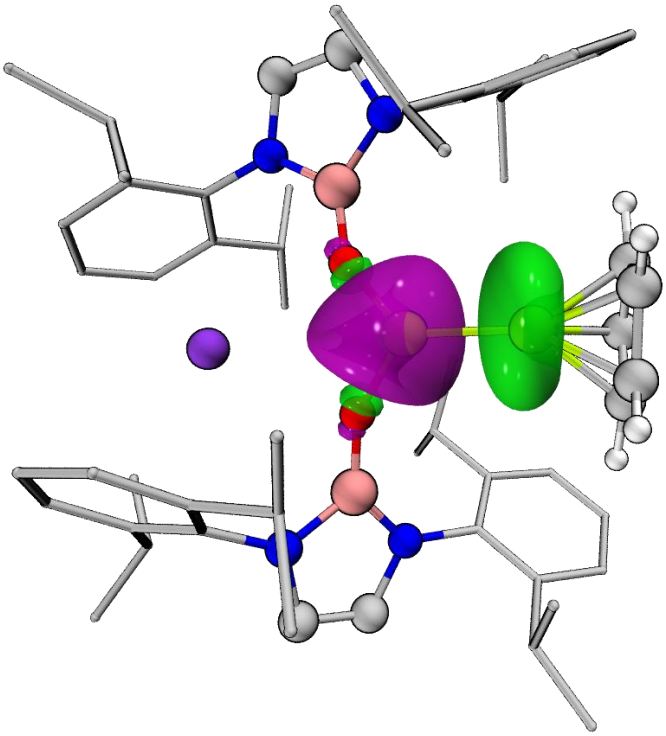

S 2.20: NBO for the Be–Be interaction of **2** (0.05 a.u.). Contribution (BeCp:BeNHBO) to Be-Be bond: 62:38. Wiberg bond index: 0.81. Natural population analysis charges (BeCp, BeNHBO): 0.64, 1.15.

Natural Energy Decomposition Analysis Calculations

ST 2.8: NEDA data for complex **1**. All values in kcal mol-1. Radical recombination of Be-Be bond is homolytic.

	Complex 1	
	[CpBe]→[BeCp]	**Radical Recombination**
E_{elstat}	-169.765	-40.524
$E_{orb/ct}$**EDA**	-272.364	-216.053
E_{core}	213.596	187.655
E_{int}	-228.533	-68.922

ST 2.9: NEDA data for complex **2**. All values in kcal mol-1. Radical recombination of Be-Be bond is homolytic.

	Complex 2		
	[CpBe]→[BeCp*]	**[Cp*Be]→[BeCp]**	**Radical Recombination**
E_{elstat}	-166.506	-147.681	-40.379
$E_{orb/ct}$**EDA**	-274.929	-275.965	-223.654
E_{core}	225.446	199.065	195.823
E_{int}	-215.989	-224.581	-68.21

ST 2.10: NEDA data for complex **3**. All values in kcal mol-1. Radical recombination of Be-Be bond is homolytic

	Complex 3		
	[CpBe]→[Be(NHBO)$_2$K]	**[K(NHBO)$_2$Be]→[BeCp]**	**Radical Recombination**
E_{elstat}	-203.066	-64.235	-69.911
$E_{orb/ct}$EDA	-216.848	-510.96	-282.486
E_{core}	241.376	336.078	282.709
E_{int}	-178.538	-239.117	-69.688

ST 2.11: NEDA data for complex **B**. All values in kcal mol-1. Radical recombination of B-B bond is homolytic. Calculations for the opposite donor-acceptor combination (i.e., [(F)(pin)B→B(pin)]–) collapse.

	Complex B	
	[(pin)B→B(F)(pin)]$^-$	**Radical Recombination**
E_{elstat}	-117.941	-75.608
$E_{orb/ct}$EDA	-411.471	-520.936
E_{core}	410.891	497.963
E_{int}	-118.521	-98.581

ST 2.12: NEDA data for complex **C**. All values in kcal mol-1. Radical recombination of N-B bond is homolytic. Calculations for the opposite donor-acceptor combination (i.e., H3B→NH3) collapse.

	Complex C	
	$H_3N→BH_3$	**Radical Recombination**
E_{elstat}	-75.659	-223.392
$E_{orb/ct}$EDA	-216.432	-532.4
E_{core}	246.564	367.755
E_{int}	-45.527	-388.038

Energy Decomposition Analysis with Natural Orbitals for Chemical Valence Calculations

ST 2.13: EDA-NOCV data for compounds **2** and **3**. All values in kcal mol-1. Radical fragmentation (0 2,0 –2) of the bond under investigation is homolytic.

	Compound 2		Compound 3	
	[CpBe]→[BeCp*]	**Radical**	**[CpBe]→[Be(NHBO)$_2$K]**	**Radical**
E_{orb} Total	-117.62	-61.73	-115.67	-70.08
E_{orb1}	-93.49	-57.75	-86.05	-60.52
E_{orb2}	-5.88	-1.18	-4.01	-1.25

ST 2.14: EDA-NOCV data for compounds **B** and **C**. All values in kcal mol-1. Radical fragmentation (B: 0 2, –1 –2; C: +1 2, –1 –2) of the bond under investigation is homolytic.

3	Compound B		Compound C	
	[(pin)B→B(F)(pin)]$^-$	Radical	**H_3N→BH_3**	**Radical**
E_{orb} Total	-205.05	-142.2	-78.76	-334.64
E_{orb1}	-176.93	-101.01	-65.43	-258.93
E_{orb2}	-9.39	-3.03	-2.83	-43.23

ST 2.15: EDA-NOCV eigenvalue data for compounds **1**, **3**, and **B** and their respective fragments.

		Compound 1	Compound 3	Compound B
Total (α_1+β_1)	**E /** kcal mol^{-1}	-59.7	-60.52	-131.01
	Eigenvalue	0.60224	0.64854	0.73067
Pair α_1	**E /** kcal mol^{-1}	-29.85	-27.25	-53.24
	Eigenvalue	0.30111	0.28546	0.32795
	% of Total	49.99833953	44.01578931	44.88346312
Pair β_1	**E /** kcal mol^{-1}	-29.85	-33.27	-77.77
	Eigenvalue	0.30113	0.36308	0.40272
	% of Total	50.00166047	55.98421069	55.11653688
Difference		0.001660468	5.984210689	5.116536877

ST 2.16: EDA-NOCV eigenvalue data for selected organic compounds and their respective fragments.

		H_3C–CH_3	**F_3C–CH_3**	**$(C_6F_5)_3C$–CH_3**
Total (α_1+β_1)	**E /** kcal mol^{-1}	-229.48	-245.5	-240.24
	Eigenvalue	0.931	0.92518	1.02008
Pair α_1	**E /** kcal mol^{-1}	-114.74	-110.42	-138.54
	Eigenvalue	0.4655	0.42801	0.55771
	% of Total	50	46.26235	54.67316
Pair β_1	**E /** kcal mol^{-1}	-114.74	-135.08	-101.7
	Eigenvalue	0.4655	0.49717	0.46237
	% of Total	50	53.73765	45.32684
Difference		0	3.737651	4.673163

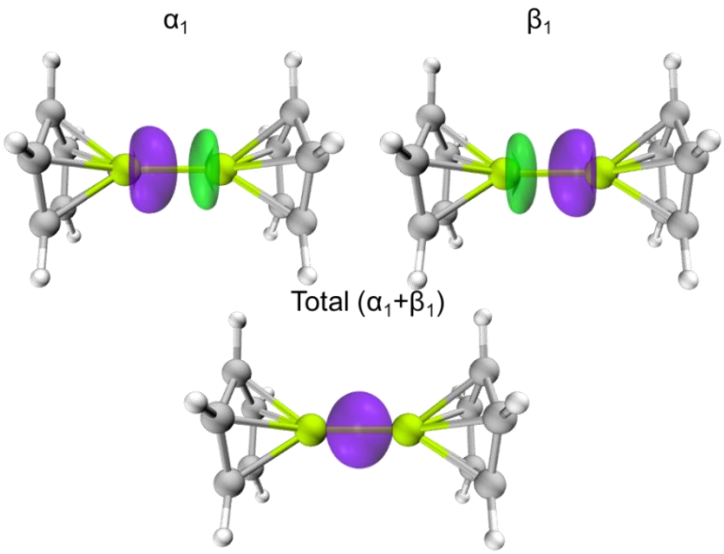

S 2.21: Visualisation of EDA-NOCV deformation density. Compound **1**; Pair α_1 (top left), Pair β_1 (top right) and Total (α1+β1) (bottom).

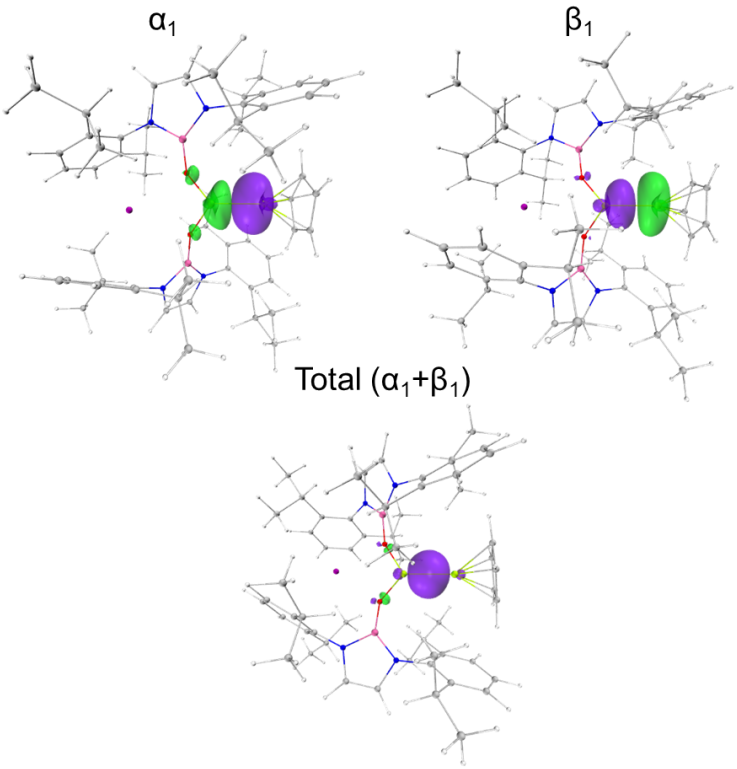

S 2.22: Visualisation of EDA-NOCV deformation density. Compound **3**; Pair α_1 (top left), Pair β_1 (top right) and Total (α1+β1) (bottom).

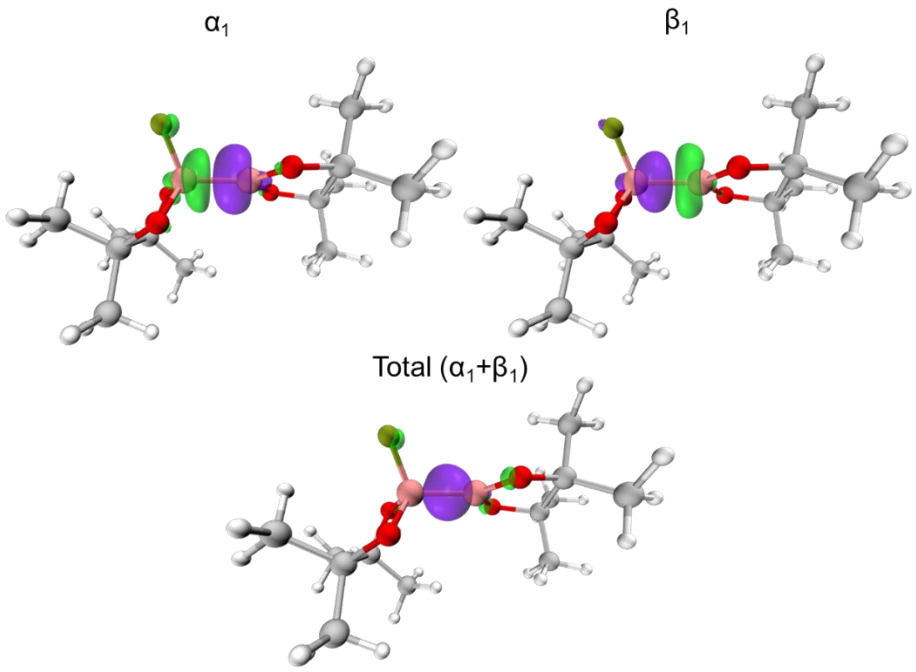

S 2.23: Visualisation of EDA-NOCV deformation density. Compound **B**; Pair α_1 (top left), Pair β_1 (top right) and Total (α1+β1) (bottom).

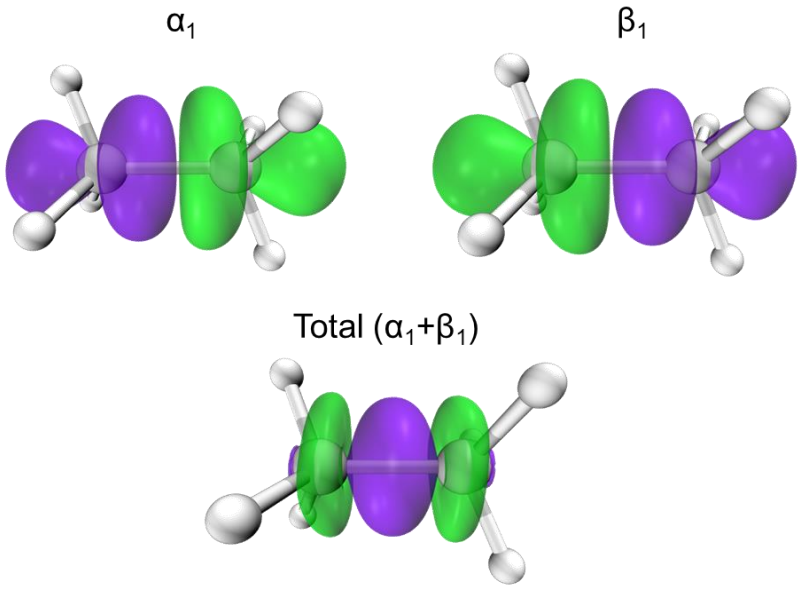

S 2.24: Visualisation of EDA-NOCV deformation density. H_3CCH_3; Pair α_1 (top left), Pair β_1 (top right) and Total (α1+β1) (bottom).

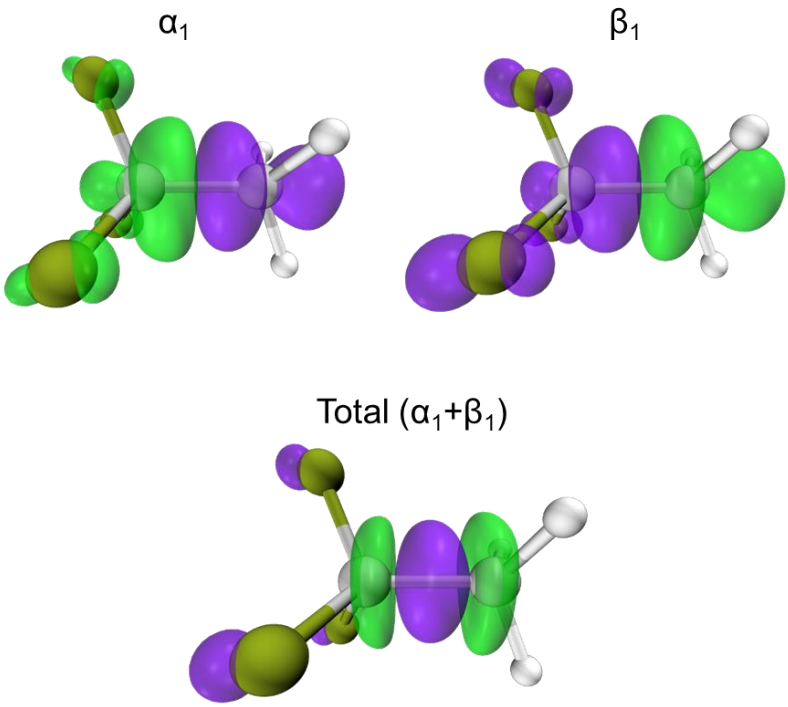

S 2.25: Visualisation of EDA-NOCV deformation density. F_3CCH_3; Pair α_1 (top left), Pair β_1 (top right) and Total (α1+β1) (bottom).

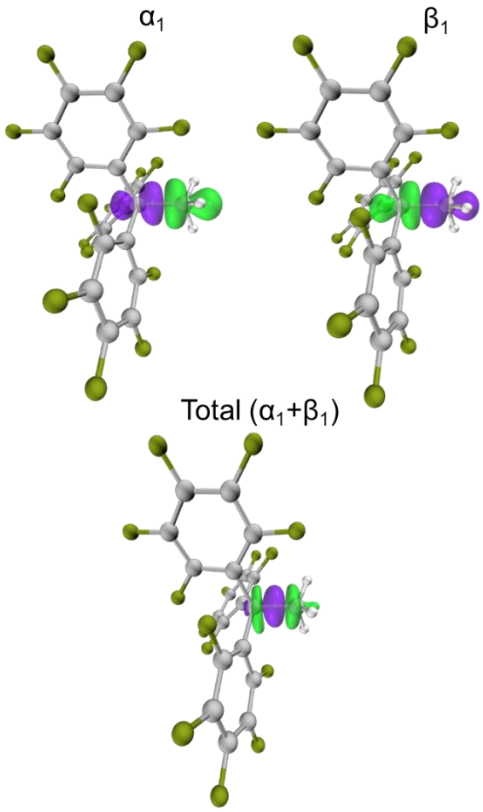

S 2.26: Visualisation of EDA-NOCV deformation density. $(C_6F_5)_3CCH_3$; Pair α_1 (top left), Pair β_1 (top right) and Total (α1+β1) (bottom).

References

1. Zhao, L., Pan, S., Holzmann, N., Schwerdtfeger, P. & Frenking, G. Chemical Bonding and Bonding Models of Main-Group Compounds. *Chem. Rev.* **119**, 8781–8845 (2019).
2. Buchner, M. R. Recent Contributions to the Coordination Chemistry of Beryllium. *Chem. - A Eur. J.* **25**, 12018–12036 (2019).
3. Buchner, M. R. Beryllium coordination chemistry and its implications on the understanding of metal induced immune responses. *Chem. Commun.* **56**, 8895–8907 (2020).
4. Naglav, D., Buchner, M. R., Bendt, G., Kraus, F. & Schulz, S. Off the Beaten Track—A Hitchhiker's Guide to Beryllium Chemistry. *Angew. Chemie - Int. Ed.* **55**, 10562–10576 (2016).
5. Buchner, M. R. & Müller, M. Handling Beryllium, the Safe Way. *ACS Chem. Heal. Saf.* **30**, 36–43 (2023).
6. Velazquez, A., Fernández, I., Frenking, G. & Merino, G. Multimetallocenes. A theoretical study. *Organometallics* **26**, 4731–4736 (2007).
7. Xie, Y., Schaefer, H. F. & Jemmis, E. D. Characteristics of novel sandwiched beryllium, magnesium, and calcium dimers: C5H5BeBeC5H5, $C_5H_5MgMgC_5H_5$, and $C_5H_5CaCaC_5H_5$. *Chem. Phys. Lett.* **402**, 414–421 (2005).
8. Kalemos, A. The nature of the chemical bond in Be_2^+, Be_2, Be_2^-, and Be_3. *J. Chem. Phys.* **145**, (2016).
9. Couchman, S. A., Holzmann, N., Frenking, G., Wilson, D. J. D. & Dutton, J. L. Beryllium chemistry the safe way: A theoretical evaluation of low oxidation state beryllium compounds. *Dalt. Trans.* **42**, 11375–11384 (2013).
10. Gosch, M. A. & Wilson, D. J. D. Heteronuclear and Homonuclear Bimetallic Metallocenes of Alkaline Earths and Zinc. *Organometallics* **42**, 2185–2196 (2023).
11. Tague, T. J. & Andrews, L. Reactions of beryllium atoms with hydrogen. Matrix infrared spectra of novel product molecules. *J. Am. Chem. Soc.* **115**, 12111–12116 (1993).
12. Herzberg, G. Zum Aufbau der zweiatomigen Molekele. *Zeitschrift for Phys.* **57**, 601–630 (1929).
13. Merritt, J. M., Bondybey, V. E. & Heaven, M. C. Beryllium dimer-caught in the act of bonding. *Science.* **324**, 1548–1551 (2009).
14. Patkowski, K., Špirko, V. & Szalewicz, K. On the Elusive Twelfth Vibrational State of Beryllium Dimer. *Science.* **326**, 1382–1384 (2009).
15. Bonyhady, S. J. *et al.* β-Diketiminate-Stabilized Magnesium(I) Dimers and Magnesium(II) Hydride Complexes: Synthesis, Characterization, Adduct Formation, and Reactivity Studies. *Chem. - A Eur. J.* **16**, 938–955 (2010).
16. Pearce, K. G., Hill, M. S. & Mahon, M. F. Beryllium-centred C–H activation of benzene. *Chem. Commun.* **59**, 1453–1456 (2023).
17. Arrowsmith, M. *et al.* Three-coordinate beryllium β-diketiminates: Synthesis and reduction chemistry. *Inorg. Chem.* **51**, 13408–13418 (2012).
18. Boronski, J. T., Crumpton, A. E., Wales, L. L. & Aldridge, S. Diberyllocene, a stable compound of Be(I) with a Be–Be bond. *Science.* **380**, 1147–1149 (2023).
19. Boronski, J. T. Alkaline earth metals: homometallic bonding. *Dalt. Trans.* **53**, 33–39 (2024).
20. Gimferrer, M. *et al.* The oxidation state in low-valent beryllium and magnesium compounds. *Chem. Sci.* **13**, 6583–6591 (2022).
21. Arrowsmith, M. *et al.* Neutral zero-valent s-block complexes with strong multiple bonding. *Nat. Chem.* **8**, 890–894 (2016).
22. Czernetzki, C. *et al.* A Neutral Beryllium(I) Radical. *Angew. Chemie - Int. Ed.* **60**, 20776–20780 (2021).
23. Czernetzki, C., Arrowsmith, M., Endres, L., Krummenacher, I. & Braunschweig, H. Tricoordinate Beryllium Radicals and Their Reactivity. *Inorg. Chem.* **63**, 2670–2678 (2024).
24. Wang, G. *et al.* A Stable, Crystalline Beryllium Radical Cation. *J. Am. Chem. Soc.* **142**, 4560–4564 (2020).
25. Freeman, L. A., Walley, J. E. & Gilliard, R. J. Synthesis and reactivity of low-oxidation-state alkaline earth metal complexes. *Nat. Synth.* **1**, 439–448 (2022).
26. Parveen, D., Yadav, R. K. & Roy, D. K. Recent progress in beryllium organometallic chemistry. *Chem. Commun.* **60**, 1663–1673 (2024).
27. Pan, S. & Frenking, G. Comment on "The oxidation state in low-valent beryllium and magnesium compounds" by M. Gimferrer, S. Danés, E. Vos, C. B. Yildiz, I. Corral, A. Jana, P. Salvador and D. M. Andrada, Chem. Sci. 2022, 13, 6583. *Chem. Sci.* **14**, 379–383 (2023).

28. Gimferrer, M. *et al.* Reply to the 'Comment on "The oxidation state in low-valent beryllium and magnesium compounds"' by S. Pan and G. Frenking, Chem. Sci. , 2022, 13 , DOI: 10.1039/D2SC04231B. *Chem. Sci.* **14**, 384–392 (2023).
29. Jędrzkiewicz, D. *et al.* Access to a Labile Monomeric Magnesium Radical by Ball-Milling. *Angew. Chemie Int. Ed.* **61**, (2022).
30. Parkin, G. Impact of the coordination of multiple Lewis acid functions on the electronic structure and v n configuration of a metal center. *Dalt. Trans.* **51**, 411–427 (2022).
31. Green, S. P., Jones, C. & Stasch, A. Stable magnesium(I) compounds with Mg-Mg bonds. *Science.* **318**, 1754–1757 (2007).
32. Jones, C. Dimeric magnesium(I) β-diketiminates: a new class of quasi-universal reducing agent. *Nat. Rev. Chem.* **1**, 0059 (2017).
33. Neeve, E. C., Geier, S. J., Mkhalid, I. A. I., Westcott, S. A. & Marder, T. B. Diboron(4) Compounds: From Structural Curiosity to Synthetic Workhorse. *Chem. Rev.* **116**, 9091–9161 (2016).
34. Dewhurst, R. D., Neeve, E. C., Braunschweig, H. & Marder, T. B. sp 2 –sp 3 diboranes: astounding structural variability and mild sources of nucleophilic boron for organic synthesis. *Chem. Commun.* **51**, 9594–9607 (2015).
35. Pietsch, S. *et al.* Synthesis, Structure, and Reactivity of Anionic sp 2 –sp 3 Diboron Compounds: Readily Accessible Boryl Nucleophiles. *Chem. – A Eur. J.* **21**, 7082–7098 (2015).
36. Pécharman, A.-F. *et al.* Easy access to nucleophilic boron through diborane to magnesium boryl metathesis. *Nat. Commun.* **8**, 15022 (2017).
37. Resa, I., Carmona, E., Gutierrez-Puebla, E. & Monge, A. Decamethyldizincocene, a stable compound of Zn(I) with a Zn-Zn bond. *Science.* **305**, 1136–1138 (2004).
38. Hicks, J., Underhill, E. J., Kefalidis, C. E., Maron, L. & Jones, C. A Mixed-Valence Tri-Zinc Complex, [LZnZnZnL] (L=Bulky Amide), Bearing a Linear Chain of Two-Coordinate Zinc Atoms. *Angew. Chemie Int. Ed.* **54**, 10000–10004 (2015).
39. Schulz, S. *et al.* Structural Characterization of a Base-Stabilized $[Zn_2]^{2+}$ Cation. *Angew. Chemie Int. Ed.* **48**, 5748–5751 (2009).
40. Freitag, K. *et al.* Cp* as a removable protecting group: low valent Zn(i) compounds by reductive elimination, protolytic and oxidative cleavage of Zn–Cp*. *Dalt. Trans.* **42**, 10540 (2013).
41. Banh, H., Gemel, C., Seidel, R. W. & Fischer, R. A. A solvated zinc analogue of the calomel-dication. *Chem. Commun.* **51**, 2170–2172 (2015).
42. Schulz, S., Schuchmann, D., Westphal, U. & Bolte, M. Dizincocene as a Building Block for Novel Zn-Zn-Bonded Compounds *Organometallics* **28**, 1590–1592 (2009).
43. Carrasco, M. *et al.* Zn-Zn-bonded compounds that contain monoanionic oxygen-donor ligands. *Chem. - A Eur. J.* **16**, 9754–9757 (2010).
44. Boronski, J. T. *et al.* Inducing Nucleophilic Reactivity at Beryllium with an Aluminyl Ligand. *J. Am. Chem. Soc.* **145**, 4408–4413 (2023).
45. Loh, Y. K., Ying, L., Ángeles Fuentes, M., Do, D. C. H. & Aldridge, S. An N-Heterocyclic Boryloxy Ligand Isoelectronic with N-Heterocyclic Imines: Access to an Acyclic Dioxysilylene and its Heavier Congeners. *Angew. Chemie Int. Ed.* **58**, 4847–4851 (2019).
46. Grirrane, A. *et al.* Zinc−Zinc Bonded Zincocene Structures. Synthesis and Characterization of Zn 2 (η 5 -C_5Me_5) 2 and Zn_2 (η 5 -C_5Me_4Et) 2. *J. Am. Chem. Soc.* **129**, 693–703 (2007).
47. Walley, J. E., Wong, Y., Freeman, L. A., Dickie, D. A. & Gilliard, R. J. N-Heterocyclic Carbene-Supported Aryl- and Alk- oxides of Beryllium and Magnesium. *Catalysts* **9**, 934 (2019).
48. Ruhlandt-Senge, K., Bartlett, R. A., Olmstead, M. M. & Power, P. P. Synthesis and structural characterization of the beryllium compounds [Be(2,4,6-$Me_3C_6H_2)_2(OEt_2)$], [Be{O(2,4,6-tert-$Bu_3C_6H_2)\}_2(OEt_2)$], and [Be{S(2,4,6-tert-$Bu_3C_6H_2)\}_2$(THF)].cntdot.PhMe and determination of the structure of $[BeCl_2(OEt_2)_2]$. *Inorg. Chem.* **32**, 1724–1728 (1993).
49. Buchanan, J. K. & Plieger, P. G. 9Be nuclear magnetic resonance spectroscopy trends in discrete complexes: An update. *Zeitschrift fur Naturforsch. - Sect. B J. Chem. Sci.* **75**, 459–472 (2020).
50. Plieger, P. G. *et al.* Predicting 9Be nuclear magnetic resonance chemical shielding tensors utilizing density functional theory. *J. Am. Chem. Soc.* **126**, 14651–14658 (2004).
51. del Mar Conejo, M. *et al.* Synthesis, Solid-State Structure, and Bonding Analysis of the Beryllocenes [Be($C_5Me_4H)_2$], [Be($C_5Me_5)_2$], and [Be(C_5Me_5)(C_5Me_4H)]. *Chem. – A Eur. J.* **9**, 4452–4461 (2003).
52. Platts, J. A., Overgaard, J., Jones, C., Iversen, B. B. & Stasch, A. First experimental characterization of a non-nuclear attractor in a dimeric magnesium(I) compound. *J. Phys. Chem. A* **115**, 194–200 (2011).

53. Liu, H.-Y. *et al.* Reductive Dimerization of CO by a Na/Mg(I) Diamide. *J. Am. Chem. Soc.* **143**, 17851–17856 (2021).
54. Timoshkin, A. Y. & Schaefer, H. F. Donor−Acceptor Sandwiches of Main-Group Elements. *Organometallics* **24**, 3343–3345 (2005).
55. Jansen, G. *et al.* Unsupported Ti-Co and Zr-Co bonds in heterobimetallic complexes: A theoretical description of metal-metal bond polarity. *J. Am. Chem. Soc.* **120**, 7239–7251 (1998).
56. Dang, Y., Meng, L., Qin, M., Li, Q. & Li, X. Stability and donor-acceptor bond in dinuclear organometallics $CpM_1–M_2Cl_3$ (M_1, M_2 = B, Al, Ga, In; Cp = η 5–C_5H_5). *J. Mol. Model.* **24**, 7 (2018).
57. Huo, S., Meng, D., Zhang, X., Meng, L. & Li, X. Bonding analysis of the donor–acceptor sandwiches CpE–MCp (E = B, Al, Ga; M = Li, Na, K; Cp = η 5-C_5H_5). *J. Mol. Model.* **20**, 2455 (2014).
58. Bianchi, R., Gervasio, G. & Marabello, D. Experimental electron density analysis of Mn2(CO)10: Metal-metal and metal-ligand bond characterization. *Inorg. Chem.* **39**, 2360–2366 (2000).
59. Kleemiss, F. *et al.* Accurate crystal structures and chemical properties from NoSpherA2. *Chem. Sci.* **12**, 1675–1692 (2021).
60. Zheng, X., Crumpton, A. E., Ellwanger, M. A. & Aldridge, S. A planar per-borylated digermene. *Dalt. Trans.* **52**, 16591–16595 (2023).
61. Li, T.-L. & Lu, W.-C. Energy decomposition analysis of cationic carbene analogues with group 13 and 16 elements as a central atom: a comparative study. *Phys. Chem. Chem. Phys.* **24**, 8970–8978 (2022).
62. Hermann, M. & Frenking, G. Carbones as Ligands in Novel Main-Group Compounds $E[C(NHC)_2]_2$ (E=Be, B^+, C^{2+}, N^{3+}, Mg, Al^+, Si^{2+}, P^{3+}): A Theoretical Study. *Chem. – A Eur. J.* **23**, 3347–3356 (2017).
63. Zhang, Q. *et al.* Formation and Characterization of the Boron Dicarbonyl Complex $[B(CO)_2]^-$. *Angew. Chemie Int. Ed.* **54**, 11078–11083 (2015).
64. Scharf, L. T., Andrada, D. M., Frenking, G. & Gessner, V. H The Bonding Situation in Metalated Ylides. Chemistry. **23** 4422–4434. (2017)
65. Bahr, S. R. & Boudjouk, P. Trityl tetrakis[3,5-bis(trifluoromethyl)phenyl]borate: a new hydride abstraction reagent. *J. Org. Chem.* **57**, 5545–5547 (1992).
66. Cosier, J. & Glazer, A. M. A nitrogen-gas-stream cryostat for general X-ray diffraction studies. *J. Appl. Crystallogr.* **19**, 105–107 (1986).
67. CrysAlisPro v.1.171.42.70a, Agilent Technologies 2011.
68. Sheldrick, G. M. Crystal structure refinement with SHELXL. *Acta Crystallogr. Sect. C Struct. Chem.* **71**, 3–8 (2015).
69. Sheldrick, G. M. SHELXT – Integrated space-group and crystal-structure determination. *Acta Crystallogr. Sect. A Found. Adv.* **71**, 3–8 (2015).
70. Dolomanov, O. V., Bourhis, L. J., Gildea, R. J., Howard, J. A. K. & Puschmann, H. OLEX2 : a complete structure solution, refinement and analysis program. *J. Appl. Crystallogr.* **42**, 339–341 (2009).
71. Neese, F. The ORCA program system. *WIREs Comput. Mol. Sci.* **2**, 73–78 (2012).
72. Neese, F. Software update: the ORCA program system, version 4.0. *WIREs Comput. Mol. Sci.* **8**, (2018).
73. Grimme, S., Hansen, A., Ehlert, S. & Mewes, J.-M. r2SCAN-3c: A “Swiss army knife” composite electronic-structure method. *J. Chem. Phys.* **154**, (2021).
74. Furness, J. W., Kaplan, A. D., Ning, J., Perdew, J. P. & Sun, J. Accurate and Numerically Efficient $_{r2}$SCAN Meta-Generalized Gradient Approximation. *J. Phys. Chem. Lett.* **11**, 8208–8215 (2020).
75. Caldeweyher, E., Mewes, J.-M., Ehlert, S. & Grimme, S. Extension and evaluation of the D4 London-dispersion model for periodic systems. *Phys. Chem. Chem. Phys.* **22**, 8499–8512 (2020).
76. Kruse, H. & Grimme, S. A geometrical correction for the inter- and intra-molecular basis set superposition error in Hartree-Fock and density functional theory calculations for large systems. *J. Chem. Phys.* **136**, (2012).
77. Barone, V. & Cossi, M. Quantum Calculation of Molecular Energies and Energy Gradients in Solution by a Conductor Solvent Model. *J. Phys. Chem. A* **102**, 1995–2001 (1998).
78. Mardirossian, N. & Head-Gordon, M. ωB97X-V: A 10-parameter, range-separated hybrid, generalized gradient approximation density functional with nonlocal correlation, designed by a survival-of-the-fittest strategy. *Phys. Chem. Chem. Phys.* **16**, 9904 (2014).
79. Najibi, A. & Goerigk, L. DFT-D4 counterparts of leading meta-generalized-gradient approximation and hybrid density functionals for energetics and geometries. *J. Comput. Chem.* **41**, 2562–2572 (2020).

80. Weigend, F. & Ahlrichs, R. Balanced basis sets of split valence, triple zeta valence and quadruple zeta valence quality for H to Rn: Design and assessment of accuracy. *Phys. Chem. Chem. Phys.* **7**, 3297 (2005).
81. Weigend, F. Accurate Coulomb-fitting basis sets for H to Rn. *Phys. Chem. Chem. Phys.* **8**, 1057 (2006).
82. Glendening, E. D. *et al.* NBO 7.0. (2018).
83. Todd, K. A. AIMAll (Version 19.10.12). at aim.tkgristmill.com (2019).
84. Lu, T. & Chen, F. Multiwfn: A multifunctional wavefunction analyzer. *J. Comput. Chem.* **33**, 580–592 (2012).
85. Silvi, B. & Savin, A. Classification of chemical bonds based on topological analysis of electron localization functions. *Nature* **371**, 683–686 (1994).
86. Frisch, M. J.; Trucks, G. W.; Schlegel, H. B.; Scuseria, G. E.; Robb, M. A.; Cheeseman, J. R.; Scalmani, G.; Barone, V.; Petersson, G. A.; Nakatsuji, H.; Li, X.; Caricato, M.; Marenich, A. V.; Bloino, J.; Janesko, B. G.; Gomperts, R.; Mennucci, B.; Hratch, D. J. Gaussian 16. (2016)

Statement of Authorship

Title of Paper	Metathesis at $[Be–Be]^{2+}$: A Route to a Nucleophilic Beryllyl
Publication Status	Accepted for Publication
Publication Details	Submitted for publication in Nature Chemistry, 12/01/2024, Revised manuscript submitted to Nature Chemistry 21/02/2024.

Student Confirmation

Student Name:	Agamemnon Elvis Crumpton	
Contribution to the Paper	Performed DFT calculations on the structures within the manuscript, was lead crystallographer and contributed to the discussion of the quantum chemical calculations and single crystal X-ray diffraction residual electron density in the manuscript.	
Signature 		Date 15/04/2024

Supervisor Confirmation

Supervisor name and title: Professor Simon Aldridge	
Supervisor comments I can confirm that the candidate's contribution to this paper is as described above.	
Signature 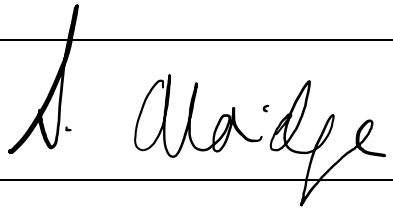	Date 18/4/2024

Chapter 3 - A Stable Hexavalent Nickel Complex

Josef T. Boronski*, Agamemnon E. Crumpton, Simon Aldridge*

Submitted to Nature Chemistry

Author contributions

Josef T. Boronski: synthesised the novel compound, collected characterisation data and corresponding author.

Agamemnon E. Crumpton: performed the quantum chemical calculations and was lead crystallographer.

Simon Aldridge: Corresponding author.

Manuscript was written by Josef T. Boronski with contribution to the discussion by Simon Aldridge and Agamemnon E. Crumpton.

Abstract

The abundance of nickel in the Earth's crust presents it as an attractive alternative to its scarce (and toxic) congeners, palladium and platinum, which are central to numerous current catalytic processes [1]. Known oxidation states for nickel span the range –2 to +4, but the +2 state predominates under ambient conditions [2–5]. Higher valence states (tri- and tetra-valent) have been invoked as key intermediates in nickel-catalysed carbon-carbon and carbon-heteroatom cross-couplings, carbon-hydrogen bond functionalisations, and in the biochemical activity of metalloenzymes [6–12]. In order to account for all mechanistic avenues in nickel catalysed reactions and unlock the full chemical potential of this element, a comprehensive knowledge of the range of accessible valence states is crucial [5,9]. Here we report a stable, crystalline hexavalent nickel complex, $Ni(BeCp)_6$ (1; Cp = cyclopentadienyl anion), formed by the oxidative addition of three Be–Be bonds at zerovalent nickel [13]. Crystallographic, spectroscopic, and quantum chemical studies suggest that a closed-shell C_{3v} structure is the ground state and that the complex exhibits an inverted ligand field [14,15]. In addition, computational methods and X-ray diffraction studies indicate that σ-aromaticity contributes to the stability of this complex [16]. Societal reliance upon nickel will undoubtedly increase in the coming decades, and our results are highly relevant both to the chemical processes in which this element is utilised and to its future applications

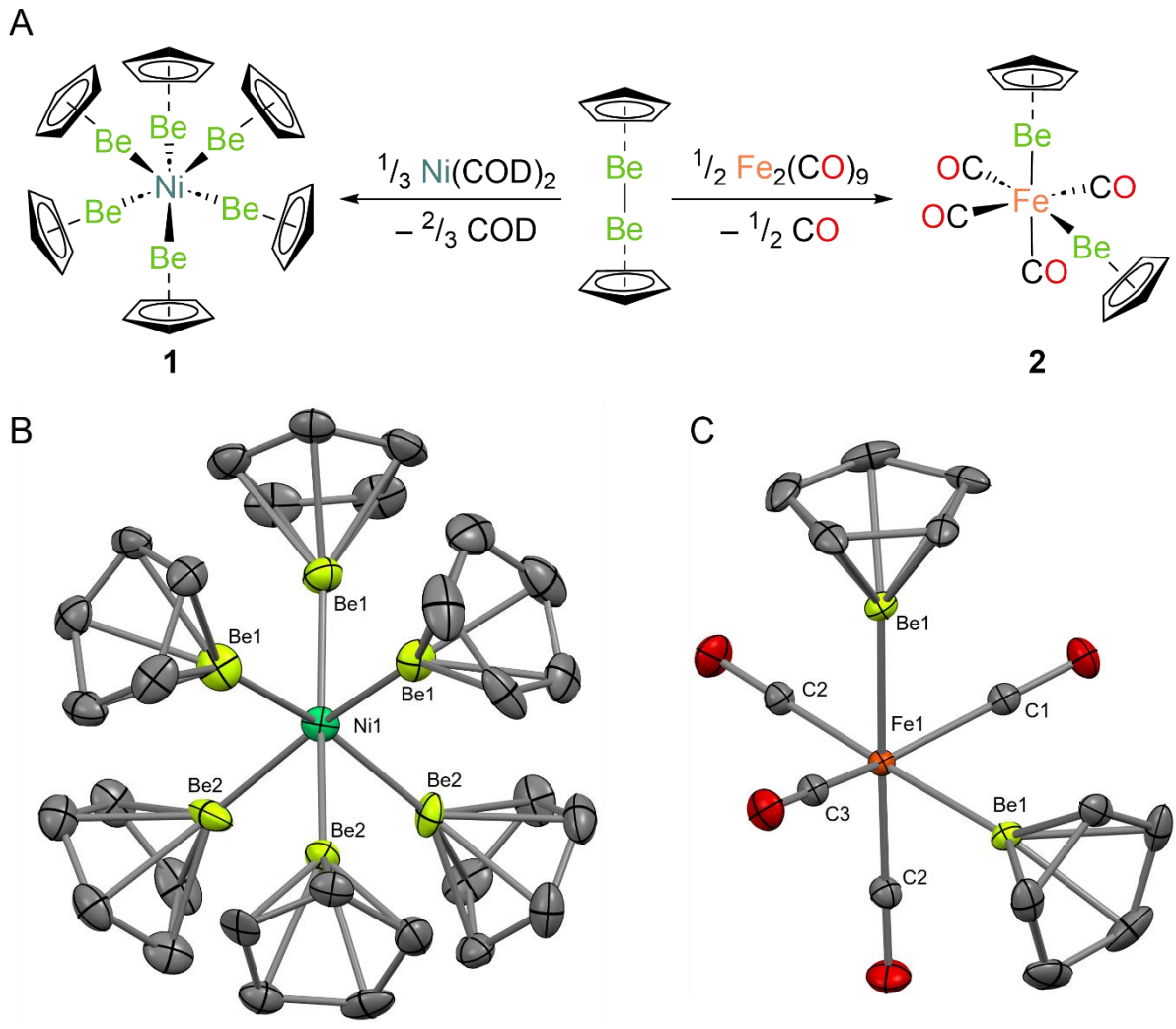

Figure 3.1: A) Synthesis of $Ni(BeCp)_6$ (1) and cis-$Fe(BeCp)_2(CO)_4$ (2Be) through oxidative addition of Be–Be bonds. (B) Molecular structure of 1 in the solid state, as determined by X-ray crystallography. (C) Molecular structure of 2Be in the solid state, as determined by X-ray crystallography. Hydrogen atoms in B and C are omitted for clarity.

The oxidative addition of H–H and B–B bonds by transition metals (yielding metal complexes featuring hydride $[H]^-$ or boryl $[BR_2]^-$ ligands, respectively) has been widely studied both from the viewpoint of structure and bonding, and within the context of hydrogenation/borylation catalysis [17,18]. We recently reported diberyllocene (CpBeBeCp; Cp = cyclopentadienyl anion), a stable complex with a Be–Be bond [13]. Given that beryllium is adjacent to boron in the Periodic Table, we envisaged that a Be–Be bond might similarly undergo oxidative addition to electron-rich metal centres, yielding two "beryllyl" $[BeR]^-$ ligands. Considering the very low electronegativity of beryllium (1.57 on the Pauling scale; cf. boron, 2.04), we hypothesised that

these X-type beryllyl ligands might be even more potently electron releasing than their boryl counterparts, which are known to be very strongly σ-donating [19].

Results and Discussion

Reaction of two equivalents of diberyllocene with $Fe_2(CO)_9$ in benzene led to the formation of two equivalents of the 18-electron, diamagnetic bis(beryllyl) complex *cis*-$Fe(BeCp)_2(CO)_4$ (**2Be**), isolated in 66% yield (**Figure 3.1 A**, right). Pale yellow crystals of **2Be** suitable quality for single-crystal X-ray diffraction (SC XRD) experiments could be obtained from concentrated hexane solutions (**Figure 3.1 C**). In the solid state, **2Be** exhibits a distorted octahedral geometry featuring two mutually *cis*-BeCp groups. The carbonyl ligands *cis* to the beryllyl groups bend out of the axial plane towards the beryllium centres (C1-Fe1-C3 angle = 137.21(7)°). This distortion is more pronounced than that observed for the mutually *trans* carbonyl ligands in the isostructural iron-bis(boryl) complex *cis*-$Fe(BCat^*)_2(CO)_4$ (**2B**; BCat* = $BO_2C_6H_3$-4-^{t}Bu; 166.0(4)°) and -bis(hydride) complex *cis*-$Fe(H)_2(CO)_4$ (**2H**; 148.5(1.5)°), indicating the even more potent σ-donor properties of the BeCp ligand [20–22]. The Fe–Be distance in **2Be** (2.1884(14) Å) is consistent with the sum of the single bond covalent radii of the elements (2.18 Å) [23]. Notably, the Fe–C1 and –C3 distances, associated with the mutually *trans* carbonyl ligands (1.7625(17) and 1.7680(16) Å, respectively) are markedly shorter than the Fe-C2 distance (1.7886(11) Å) for the carbonyl ligands *trans* to BeCp. This geometric feature is also consistent with the strongly σ-electron donating properties of the beryllyl metallo-ligand [21].

Complex **2Be** was probed by multinuclear nuclear magnetic resonance (NMR) spectroscopy. In the ^{1}H NMR spectrum, a single resonance at 5.76 ppm is measured for the protons of the cyclopentadienyl ligands, i.e., in the region typical of beryllium-coordinated cyclopentadienyl ligands (cf. diberyllocene, 5.73 ppm) [13]. The ^{9}Be NMR spectrum of **2Be** consists of a single resonance at –18.0 ppm, which is shifted markedly downfield compared with that measured for diberyllocene (−27.6 ppm). ^{9}Be NMR shifts are highly sensitive to the electron density at a given beryllium centre, particularly in the case of CpBeX species [24]. For example, CpBeCl and

CpBe($SiMe_3$) exhibit resonances at −19.5 and −27.7 ppm, respectively [24]. The low-field shift for **2Be** is indicative that the beryllium centres are relatively electron poor, consistent with a high degree of Be→Fe σ-donation. The ^{13}C NMR spectrum of **2Be** consists of a resonance at 105.8 ppm, corresponding to the carbon atoms of the Cp ligands, as well as resonances at 211.4 and 212.1 ppm, associated with the carbonyl ligands. These resonances for **2Be** are shifted downfield compared to those associated with the carbonyl ligands in the bis(boryl) analogue **2B** (204.3 and 202.2 ppm) [21].

To further scrutinise the electronic properties of the beryllyl ligand, attenuated total reflection infrared (ATR IR) measurements were carried out on **2Be**. The stretching frequencies of ancillary carbonyl ligands are a widely-employed probe of the electron-donating properties of the other ligands coordinated to the same metal centre. Four IR-active carbonyl stretching bands for **2Be** are measured at 2010, 1983, 1887, 1870 cm^{-1}, consistent both with local C_{2v} symmetry and with the pattern of bands in the simulated IR spectrum of **2Be** (Appendix Figure **A 3.7** - **A 3.8**). Critically, these carbonyl stretches are measured at much lower frequencies than those of isostructural complexes such as **2B** (2117, 2050, 2036, 2000 cm^{-1}) and *cis*-$Fe(SiMe_3)_2(CO)_4$ (**2Si**; 2069, 2006, 2000, 1979 cm^{-1}) [21,25]. These data provide further support for the hypothesis that BeCp is an extremely strongly σ-electron releasing ligand, showing it to be even more potent than boryl and silyl donors.

Having established the unprecedented σ-donor capabilities of BeCp as a covalently-bound ligand, we sought to exploit these electron-releasing capabilities in the synthesis of 3*d*-metal complexes featuring hitherto unknown (high) valence states. Hence, we investigated the reaction of diberyllocene with bis(cyclooctadiene)nickel(0) (**Figure 3.1 A**). Analysis of the benzene reaction mixture by multinuclear NMR spectroscopy indicated that three equivalents of the beryllium starting material had been consumed and that free cyclooctadiene was generated. Colourless needle-like crystals formed readily at room temperature, which SC XRD revealed to be the 16-electron, hexavalent nickel complex $Ni(BeCp)_6$ (**1; Figure 3.1 1B**), isolated

in 91% yield. Access to the hexavalent state of Ni in **1** can be attributed to the electronic (and steric) properties of the beryllyl ligands [26–28].

Homoleptic complex **1** exhibits a C_{3v} geometry, featuring a six-coordinate Ni centre ligated exclusively by BeCp metallo-ligands. When viewed perpendicular to the C_3 axis (**Figure 3.1 1B**), there are two 'decks' of three Be atoms, one with narrower Be1-Ni1-Be1 angles (81.6(3)°), and one with wider Be2-Ni1-Be2 angles (101.9(2)°). Within **1**, the Ni1–Be1 and Ni1–Be2 distances are 2.090(8) and 2.117(13) Å, respectively, which are statistically indistinguishable by the 3σ-criterion, and comparable to the sum of the covalent radii for these elements (2.12 Å). Crucially, all Be–Be distances are >2.7 Å, i.e., significantly greater than (i) the sum of the single-bond covalent radii for beryllium (2.04 Å) [23]; (ii) the Be–Be bond in diberyllocene (2.0545(18) Å) [13]; and even (iii) the Be–Be distance in diatomic Be_2 (2.45 Å), which features a Be–Be bond order of zero [29]. These separations also approach the sum of the van der Waals radii for Be (3.06 Å) [30]. Therefore, these data imply that **1** does not feature any Be–Be bonding, a point further evidenced by NMR spectroscopy and quantum chemical calculations carried out on **1** (see below).

Structurally, complex **1** bares superficial resemblance to $Pt(ZnCp^*)_6$ (**3**; Cp* = pentamethylcyclopentadienyl anion), which exhibits D_{2h} geometry at platinum [31]. Additionally, considering that the nickel centre in **1** is ligated entirely by metallo-ligands, comparisons with the multi-metallic clusters $\{[(Cp^*)Ni](\mu\text{-}ZnMe)_4[Ni(ZnCp^*)_2(ZnMe)_2]\}$ (**4**) and $\{[(C_6H_5Me)Ni](\mu\text{-}ZnMe)_4[Ni(ZnCp^*)_2(ZnMe)_2]\}$ (**4'**), can also be drawn [32].

The ^{1}H NMR spectrum of **1** features a single resonance at 5.71 ppm, corresponding to the protons of the Cp ligands, which is comparable to the ^{1}H NMR shift of **2Be** (5.76 ppm) [13]. The ^{9}Be NMR spectrum for **1** features a single resonance at −16.7 ppm, which is the most downfield of any reported CpBeX complex [24]. Aromatic ring currents may explain the deshielding of the six beryllium centres in **1** (see below). Notably, this chemical shift further evidences the absence of Be–Be bonding in **1**, as this is known to lead to high electron density at Be and high-field ^{9}Be

NMR chemical shifts (cf., diberyllocene, −27.6 ppm). Complex **1** exhibits a single resonance at 105.7 ppm in its ^{13}C NMR spectrum, associated with the Cp carbon atoms, which is near-identical to the corresponding signal in the ^{13}C NMR spectrum of **2Be** (105.8 ppm).

Quantum chemical calculations were employed in order to gain a deeper understanding of the electronic structure and geometry **1**. The geometry of the complex was optimised at the ωB97X-D4 DEF2-QZVPP level, yielding a complex with C_{3v} symmetry, which closely resembles the crystallographically determined structure of **1**. The structure of $Ni(BeCp)_6$ with the $NiBe_6$ core constrained in O_h geometry (**1'**) was also optimised, showing the complex to be significantly higher in energy than **1** (ΔE = +46.0 kcal mol^{-1}).

Within homoleptic **1**, Ni (Pauling electronegativity, 1.91) is ligated exclusively by Be-centred donors (Pauling electronegativity, 1.57); and hence, has an inverted ligand field (**Figure 3.2**) [15]. As predicted by Hoffmann, in this regime high-lying orbitals should have a large degree of ligand character, whereas lower energy orbitals are mainly metal centred [15]. As such, all Ni *d*-orbitals in **1** are fully occupied, and their ordering is the inverse of that expected from a 'classical' transition metal complex. In addition, the lowest unoccupied molecular orbital (LUMO), highest occupied molecular orbital (HOMO), and HOMO−1 comprise large contributions from beryllium (see below). The electronic structure of **1**, therefore, supports the hypothesis that powerfully σ-electron releasing metallo-ligands can induce this electronic structuring [15]. Interestingly, there have been previous suggestions that other high-valent Ni^{IV} complexes feature an inverted ligand field, which has been computationally demonstrated to influence their reactivity in C–C bond-forming reactions [6,14,33].

To better understand the electronic structure of **1**, we undertook a qualitative comparison of the frontier orbitals of this complex and hypothetical octahedral complex **1'** (**Figure 3.2**). Projecting the *z*-axis parallel to the molecular C_3 axis, calculations on **1** indicated that the highest energy nickel-based valence *d*-orbital is the non-bonding d_{z^2} orbital (HOMO−2). The next highest energy nickel *d*-orbitals are the pseudo-degenerate d_{xz} and d_{yz} (HOMO−3 and

HOMO−4, respectively), which, due to their alignment along the *z*-direction, are also not able to overlap effectively with Be-based orbitals. The lowest energy Ni *d*-orbitals are the pseudo-degenerate $d_{x^2-y^2}$ and d_{xy} orbitals (HOMO−5 and HOMO−6, respectively), which engage in constructive overlap with the 2*s*-orbitals of four and two Be centres, respectively. The higher energy Ni 4p_x and 4p_y orbitals (HOMO and HOMO−1) are pseudo-degenerate, with the former overlapping constructively with two pairs of Be 2*s*-orbitals and the latter with all six Be 2*s*-orbitals. The high ligand character of these orbitals is consistent with an inverted ligand field (Table **ST 3.7**) [15]. The LUMO of **1** corresponds to the Ni 4p_z orbital (also high in Be 2*s* character; **ST 3.7**), which lies much higher in energy (HOMO−LUMO energy gap = 8.2 eV). Hence, for **1** we postulate that the stabilization of the p_x- and p_y-orbitals, and destabilization of p_z-orbital (enabled by descent to C_{3v} symmetry), plays a significant role in determining the (diamagnetic) singlet ground state of 16-electron complex **1**. The nickel 4*s* orbital is also engaged in a significant bonding interaction with the beryllyl ligands, contributing to the HOMO−19. Strikingly, this delocalised molecular orbital is toroidal in shape, occupying the 'equatorial' region between the two 'decks' of three beryllium atoms when viewed perpendicular to the C_3 axis. This orbital is composed of the in-phase combination of the Ni 4*s*-orbital with the six Be 2*s*-orbitals. In contrast to closed shell complex **1**, hypothetical complex **1'** is a triplet with two unpaired electrons in the three degenerate Ni *p*-orbitals (t_{1u} set). Due to the inverted ligand field, the triply degenerate t_{2g} set (d_{xy}, d_{xz} and d_{yz}) are the highest energy Ni valence *d*-orbitals and the doubly degenerate e_g set (d_{z^2} and $d_{x^2-y^2}$) are the lowest energy Ni *d*-orbitals (**Figure 3.2** and **S 3.7**: Qualitative molecular orbital scheme for **1'** (O_h) and **1** (C_{3v}) with corresponding molecular orbitals calculated for both complexes.) [15].

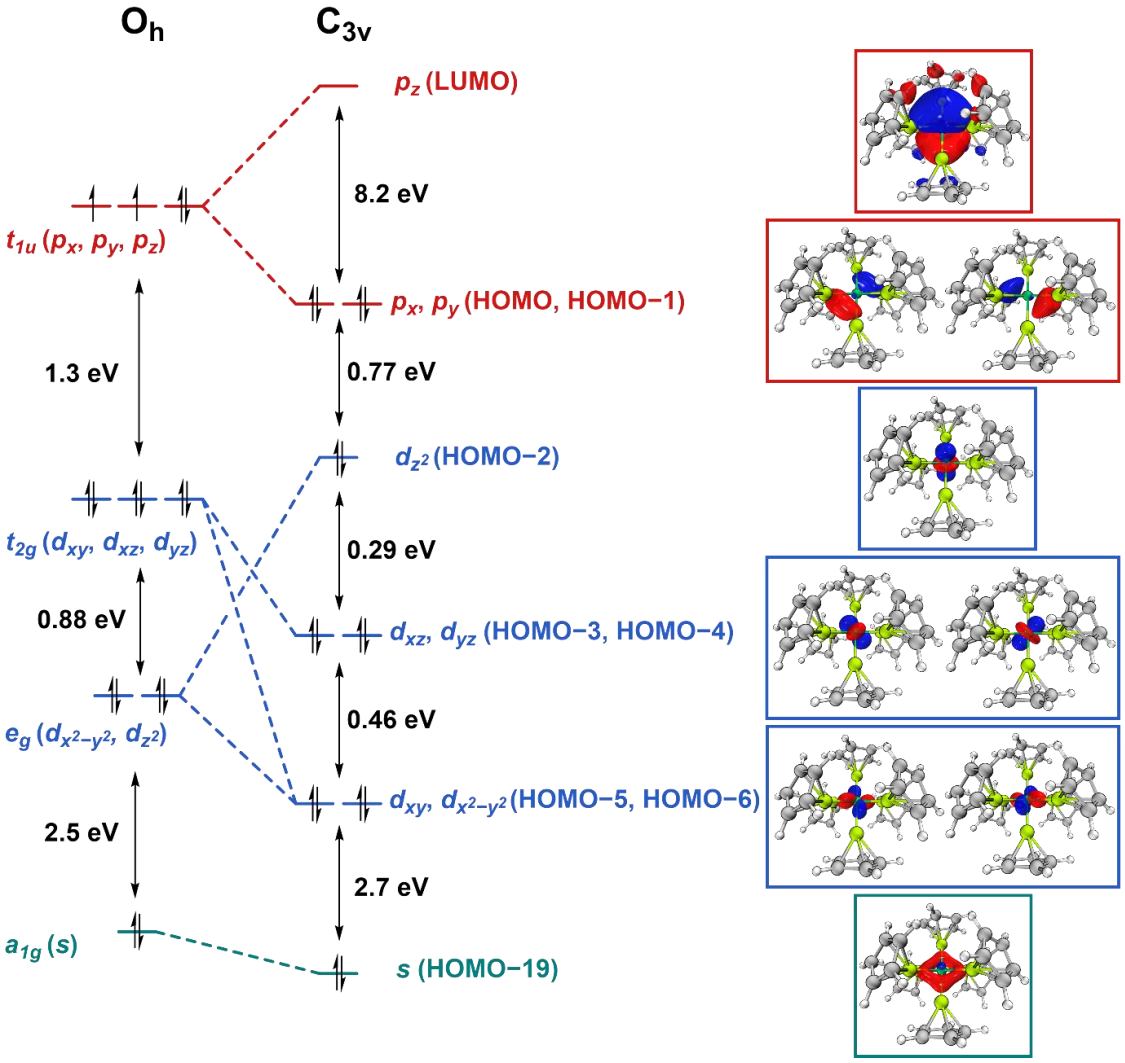

Figure 3.2: (Left) Qualitative molecular orbital scheme for 1′ (Oh) and 1 (C3v); Right) corresponding molecular orbitals (0.075 a.u) calculated for 1

Quantum theory of atoms in molecules (QTAIM) calculations were employed to examine the Ni–Be bonding and charge distribution within **1** (Figure **S 3.12; ST 3.2**). Bond paths (BPs) and bond critical points (BCPs) are located for all of the Ni–Be interactions. Topological parameters (Be–Ni ρ_{bcp} = 0.061 e$^-$ Bohr^{-3}; $\nabla^2\rho_{bcp}$ = –0.014 e$^-$ Bohr^{-5}) are typical of Be–M interactions (e.g., Be–Ga ρ_{bcp} = 0.063 e$^-$ Bohr^{-3}; $\nabla^2\rho_{bcp}$ = –0.0066 e$^-$ Bohr^{-5}) and indicative that the Be–Ni bonding in **1** is weakly covalent in nature [34]. Deconvolution of the Ni–Be BCPs reveals that the principal contributing orbitals to these interactions are the HOMO−19 in combination with the HOMO−5/HOMO−6. Decisively, no BPs or BCPs corresponding to Be···Be interactions are located by these calculations. This finding provides further evidence for the hexavalent nature of the Ni centre in **1**, which is bonded to six discrete X-type Be ligands, and not to L-type Be–Be σ-bonds

[35]. QTAIM basin analysis of **1** returns charges of –3.98 for the Ni centre and +1.50 for all Be atoms, indicating that the Ni atom is extremely charge rich due to the coordination of the powerfully σ-electron-releasing BeCp ligands. QTAIM calculations also detect a network of BCPs between the hydrogen atoms of Cp ligands. Hence, the fact that **1** can even be isolated may arise, in part, from the stabilizing dispersion interactions between Cp ligands, in addition to the steric shielding these organic groups afford the $[NiBe_6]^{6+}$ core [36].

The electron localization function (ELF) was calculated for **1**. Inspection of the isosurface reveals a delocalised, σ-symmetry toroidal region of electron density, which occupies a space between the two 'decks' of three beryllium atoms, perpendicular to the C_3 axis – thus, resembling the HOMO−19 of **1** in both its position and profile (**Figure 3.3**, **3B**). This delocalised bonding is reflected in the multicentre bond order calculated for the $NiBe_6$ moiety of **1** (0.023; cf., that for benzene 2.8 x 10^{-4}). Additionally, electron density of delocalised bonds (EDDB) calculations indicate that, aside from the 36 delocalised electrons associated with the Cp ligands, approximately two electrons are completely delocalised across the $NiBe_6$ unit [37].

Given the delocalised nature of the $NiBe_6$ bonding in **1**, we performed nucleus-independent chemical shift (NICS) calculations on the complex [16]. As the Ni centre occupies the site at the centre of the ring in **1**, NICS(0) (the negative of the isotropic magnetic shielding at the centre of the ring) is uninformative. However, the NICS(1) value (the negative of the isotropic magnetic shielding 1 Å perpendicularly above and below the toroidal ring centre; –17.6 ppm) for **1** is consistent with an aromatic system (NICS(1) for benzene = –10.0 ppm). Aromaticity in **1** is also evidenced by inspection of the $NICS_{zz}$ scan – the variation of the out-of-plane zz component of the shielding tensor (Figure **S 3.25:** NICSzz plot for complex **1.** R is the distance along the C3 axis from the Ni centre.). In the region between +0.5 and +2.5 (and –0.5 and –2.5), $NICS_{zz}$ values are negative and decay rapidly with respect to the perpendicular distance from the ring centroid, which is also indicative of σ-aromaticity [16].

Ring current analysis was also performed on **1** [38]. This reveals **1** to feature a substantial diamagnetic ring current in the region associated with the delocalised seven-centre two-electron bond (**Figure 3.3**, **C**). Around the inner rim of this ring, directly encircling the Ni centre, a paramagnetic ring current is observed. Both features are mirrored in benzene and are indicative of aromaticity in **1** [16,38]. Similarly, QTAIM magnetizability analysis was performed on **1**. The out-of-plane component of the atomic and bond magnetizability (χ_{zz}^{Atom} and $\chi_{zz}^{(X|Y)}$, respectively) are useful probes for ring currents. In the case of **1**, χ_{zz}^{Atom} Ni is –46.0 ppm, and average $\chi_{zz}^{(Be|Ni)}$ is –2.4 ppm. For reference, χ_{zz}^{Atom} for the C atoms of benzene is –3.4 ppm and $\chi_{zz}^{(C|C)}$ is –5.1 ppm. Again, this further evidences the diamagnetic currents at Ni and Be and the aromaticity of **1** [38].

The anisotropy of induced current density (ACID) was also used to assess the aromaticity of **1** [39]. The ACID plot represents a visualization of the density and the direction of the ring current induced when an external magnetic field is applied perpendicularly to the delocalised bonding system (**Figure 3.3 D**). The direction of the current density vectors (clockwise) is the same for the (aromatic) Cp ligands and the delocalised $NiBe_6$ bonding, which provides further evidence for σ-aromaticity in **1** [39]. Aromatic deshielding may explain the downfield shift of the ^{9}Be NMR resonance observed for **1**. Remarkably, there is experimental evidence for this calculated electronic feature. The residual electron density map, derived from SC XRD measurements on **1** at a range of temperatures, shows a clear toroidal band of electron density in the same region that the ELF isosurface is calculated to occupy (**Figure 3.3**, **A**).

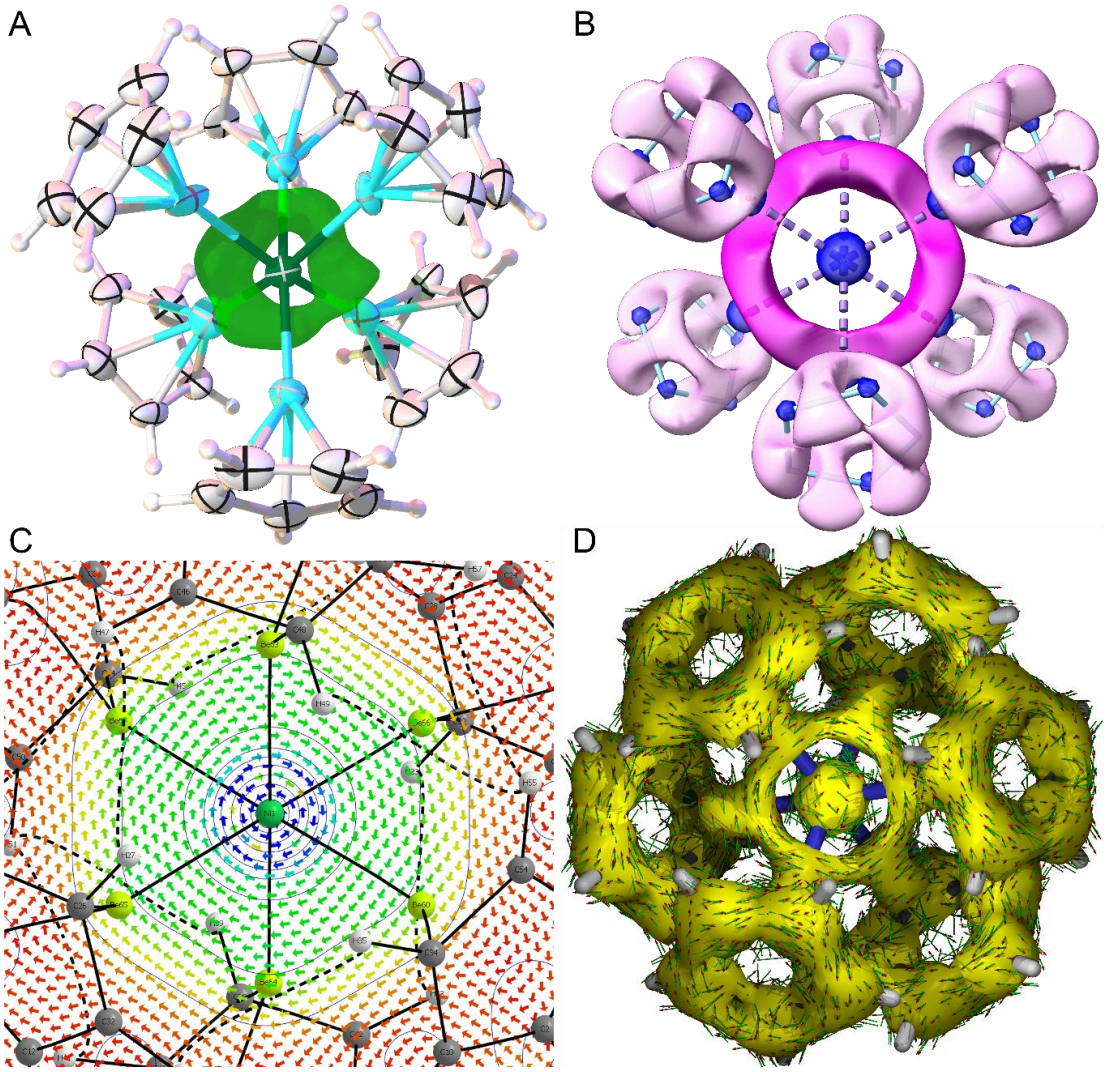

Figure 3.3: A) SC XRD residual electron density map for 1, with green ring representing an area of residual density; B) ELF isosurface for 1 (hydrogen atoms omitted for clarity; 0.7 a.u.); C) Profile of current density within 1 in the plane of the NiBe6 toroidal HOMO−19. The blue to red colour scale indicates strong (J(r) ≥ 0.001 a.u.) to weak currents (J(r) = 0.0000). A clockwise (diamagnetic) current can clearly be seen; D) ACID plot for 1 at 0.05 a.u. isosurface value. The clockwise direction of the induced current (illustrated by red arrow heads) indicates aromatic delocalisation.

Conclusion

In summary, a hexavalent nickel complex, $Ni(BeCp)_6$ (**1**), has been structurally characterised. We postulate that the complex adopts C_{3v} geometry as this yields a large HOMO-LUMO gap, through the splitting of the t_{1u} (Ni 4*p*) orbitals. Quantum chemical analysis indicates that the complex features seven-centre two-electron delocalised bonding across the $NiBe_6$ core, which is aromatic in nature.

Characterizing data

General considerations

All manipulations were carried out using Schlenk line or glovebox techniques under an atmosphere of argon or dinitrogen. Solvents were dried by passage through activated alumina towers, dried with NaK_2 and degassed before use. Solvents were stored over NaK_2. NMR spectra were measured in C_6D_6 which was dried over NaK_2, with the solvent being distilled under reduced pressure, degassed by three freeze-pump-thaw-cycles and stored under argon in a Teflon valve ampoule. NMR samples were prepared under argon in 5 mm Wilmad 507-PP tubes fitted with J. Young Teflon valves. NMR spectra were measured on a Bruker Avance III HD Nanobay 400 MHz NMR spectrometer equipped with a 9.4 T magnet or a Bruker Avance III NMR 500 MHz NMR spectrometer equipped with a 11.75 T magnet and a ^{13}C detect cryoprobe. ^{1}H and ^{13}C NMR spectra were referenced internally to residual protio-solvent (^{1}H) or solvent (^{13}C) resonances and are reported relative to tetramethylsilane (δ = 0 ppm). ^{9}Be NMR spectra were referenced to a 0.43 M solution of $BeSO_4{\cdot}4H_2O$ in D_2O (δ = 0 ppm). Chemical shifts are quoted in δ (ppm) and coupling constants in Hz. FTIR spectra were recorded on a Bruker Alpha spectrometer with Platinum-ATR module. Elemental analyses were carried out by London Metropolitan University. Diberyllocene was prepared as described previously [13]. Transition metal precursors $Fe_2(CO)_9$ and $Ni(COD)_2$ were used as received.

Health warning: beryllium and its compounds are extremely toxic and can cause irreversible health effects through inhalation or skin contact. The work with beryllium-containing materials described herein was carried out by trained operator(s), with strict adherence to local and national rules/regulations [39].

Synthesis of Novel Compounds

Synthesis of cis-Fe(BeCp)2(CO)4 (2Be):

To a Schlenk flask equipped with a glass-coated stirrer bar was added a solid mixture of diberyllocene (10.0 mg, 0.067 mmol) and $Fe_2(CO)_9$ (12.3 mg, 0.034 mmol, 0.5 equiv.). Benzene (1 mL) was condensed into the vessel *in vacuo* at –196 °C. The orange solution was allowed to warm to room temperature and stirred for 96 hours. Solvent was removed from the solution *in vacuo*, yielding a brown solid. Soluble material was extracted with hexane (2 x 2 mL) and the solution was filtered. The pale orange solution was transferred to a λ-crystallization tube (fitted with a J. Young PTFE valve), frozen, and placed under a static vacuum. Slow concentration of the solution over the course of 16 hours led to the formation of a crop of pale yellow rod-like crystals of **2Be**, which were dried *in vacuo*. Yield: 14 mg, 66%. Single crystals of **2Be** suitable for X-ray diffraction experiments were obtained by slow concentration of a hexane solution in a λ-crystallization tube. Anal. Calcd for $C_{14}H_{10}Be_2FeO_4$: C, 53.20; H, 3.19. Found: C, 53.11; H, 3.09. ^{1}H NMR (400 MHz, C_6D_6, 298 K): δ = 5.76 (s, 10H, C_5H_5); ^{9}Be NMR (42 MHz, C_6D_6): δ = –18.0 ($w_{1/2}$ = 7.5 Hz); $^{13}C\{^1H\}$ NMR (101 MHz, C_6D_6): δ = 105.8 (C_5H_5), 211.4 (*C*O), 212.1 (*C*O). ATR-IR υ/cm^{-1}: 626 (s), 696 (w), 794 (m), 855 (m), 938 (m), 1014 (w), 1254 (w), 1870 (s), 1887 (m), 1983 (m), 2010 (m).

*Synthesis of Ni(BeCp)$_6$ (**1**):*

To a Schlenk flask equipped with a glass-coated stirrer bar was added a solid mixture of diberyllocene (15.0 mg, 0.10 mmol) and $Ni(COD)_2$ (9.3 mg, 0.034 mmol, 0.33 equiv.). Benzene (1 mL) was condensed into the vessel *in vacuo* at –196 °C. The yellow solution was allowed to warm to room temperature and stirred for 10 minutes. The solution was then allowed to stand at room temperature for 5 hours, leading to the formation of a large crop of colourless needle-like crystals. The mother liquor was decanted by filtration, the crystalline material was washed with hexane (3 x 2 mL), and dried *in vacuo*. Yield: 15 mg, 91%. Single crystals of **1** suitable for X-ray diffraction experiments were obtained by allowing a benzene solution (0.5 mL) of diberyllocene

(15.0 mg, 0.10 mmol) and $Ni(COD)_2$ (9.3 mg, 0.034 mmol, 0.33 equiv.) to stand undisturbed for 16 hours. Anal. Calcd for $C_{30}H_{30}Be_6Ni$: C, 71.59; H, 6.01. Found: C, 71.55; H, 5.92. ^1H NMR (400 MHz, C_6D_6, 298 K): δ = 5.71 (s, 30H, C_5H_5); ^9Be NMR (42 MHz, C_6D_6): δ = –16.7 ($w_{1/2}$ = 25.1 Hz); $^{13}C\{^1H\}$ NMR (101 MHz, C_6D_6): δ = 105.7.

Crystallographic Data

Data for **1** and **2Be** were collected using an Oxford Diffraction/Agilent SuperNova. Crystals were selected under Paratone-N or perfluorinated oil, mounted on MiTeGen Micromount loops and quench-cooled using an Oxford Cryosystems open flow N_2 cooling device [40]. Selected details of data collection are given in **ST 3.1**. Data collected were processed using the CrysAlisPro package, including unit cell parameter refinement and inter-frame scaling (which was carried out using SCALE3 ABSPACK within CrysAlisPro) [41]. Equivalent reflections were merged and diffraction patterns processed with the CrysAlisPro suite. Structures were solved *ab initio* from the integrated intensities using SHELXT and refined on F2 using SHELXL with the graphical interface OLEX2 [42–44]. Crystallographic data is given in the supplementary deposited CIF files (CCDC 2297401- 2297404) and can be obtained free of charge from the Cambridge Crystallographic Data Centre *via* http://www.ccdc.cam.ac.uk/data_request/cif.

High-quality SC XRD data for **1** was collected at both 100 and 250 K. At both temperatures the same crystallographic parameters are observed. Given the marginally higher quality of the data collected at 100 K (R-factor = 4.78, *vs* 4.81 at 250 K), data discussed in the manuscript are for this structure. Refinement of data at 100 K (without SQUEEZE) is also presented, demonstrating the disorder of the benzene over a special position and leading to poorer agreement with crystallographic data.

ST 3.1: Selected X-ray data collection and refinement parameters.

	1	**1 (w/o SQUEEZE)**	**1**	**2Be**
Formula	C30 H30 Be6 Ni, 3(C6 H6)	C30 H30 Be6 Ni, 3(C6 H6)	C30 H30 Be6 Ni, 3(C6 H6)	C14 H10 Be2 Fe O4
Fw (g mol^{-1})	737.63	737.63	737.63	316.09
Cell setting	hexagonal	hexagonal	hexagonal	orthorhombic
Space group	P 63 m c	P 63 m c	P 63 m c	-P 2ac 2n
***a* (Å)**	16.0196(7)	16.0196(7)	16.25577(16)	12.7042(2)
***b* (Å)**	16.0196(7)	16.0196(7)	16.25577(16)	17.3016(3)
***c* (Å)**	9.1995(3)	9.1995(3)	9.30619(8)	6.44850(10)
***α* (°)**	90	90	90	90
***β* (°)**	90	90	90	90
***γ* (°)**	120	120	120	90
***V* (Å^{-3})**	2044.55(19)	2044.55(19)	2129.69(5)	1417.40(4)
Z	2	2	2	4
ρ_{calc} (g cm^{-3})	1.198	1.198	1.150	1.481
Radiation, λ (Å)	Mo K_α, 0.71073	Mo K_α, 0.71073	Cu K_α, 1.54184	Cu K_α, 1.54184
μ (mm^{-1})	0.506	0.506	0.865	8.611
$R_{(int)}$	9.37	9.37	3.14	4.82
Parameters	98	183	137	149
R_1 (all data/I >2σ(I))	0.0487/0.0479	0.0556/0.0545	0.0497/0.0481	0.0196/0.0196
ωR_2 (all data/I >2σ(I))	0.1395/0.1402	0.1344/0.1350	0.01387/0.1411	0.0510/0.0510
GooF	1.127	1.098	1.107	1.075
***T* (K)**	100.01(10)	100.01(10)	249.99(10)	150.01(10)
CCDC Deposition No.	2297403	2297404	2297402	2297401

Computational Details

General details

Compounds **1** and **2Be** were optimised using ORCA (Revision 5.0.4) [45,46]. The ωB97X range-separated hybrid functional [47,48] was employed in conjunction with the Def2-QZVPP basis set [49,50] with the D4 dispersion correction [51]. The nature of the stationary points (minima) was confirmed by full frequency calculations, and are characterized by zero imaginary frequencies.

The hypothetical compound **1'** was optimised as a triplet with ORCA (Revision 5.0.4) [45,46] with the meta-generalized-gradient approximation (mGGA) functional R2-SCAN [52,53] was employed in conjunction with the Def2-TZVPPm basis set with the D4 dispersion correction [51], and employing the geometrical counterpoise correction gCP [54] (together known as the R2SCAN-3c method) [52]. In order to maintain an Octahedral geometry, constraints were applied such that all the Be-Ni-Be angles were held at 90° and Cp-Be -Ni (Cp = centroid of the Cp ring) angle was held at 180°. A single point calculation was then performed using the ωB97X range-separated hybrid functional [47,48] in conjunction with the Def2-QZVPP basis set [49,50] with the D4 dispersion correction.

In order to facilitate further analysis, single point calculations were performed using Gaussian16 (RevisionC.01) [55] using the ωB97XD [56] range-separated hybrid functional in conjunction with the Def2-QZVPP basis set [49,50] (unless otherwise specified).

The xyz coordinates for the calculated structures of **1**, **1'**, and **2Be** are available at the Dryad repository [57].

Molecular Orbitals Calculated for 1

Molecular orbitals were generated using ORCA wavefunction for the respective complex.

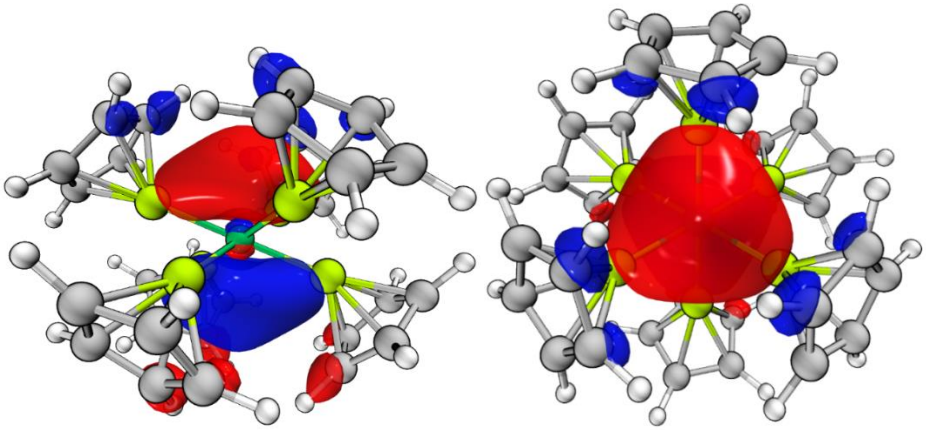

S 3.1: LUMO (0.025 a.u.) of **1** viewed perpendicular to z-axis (left) and along z-axis (right).

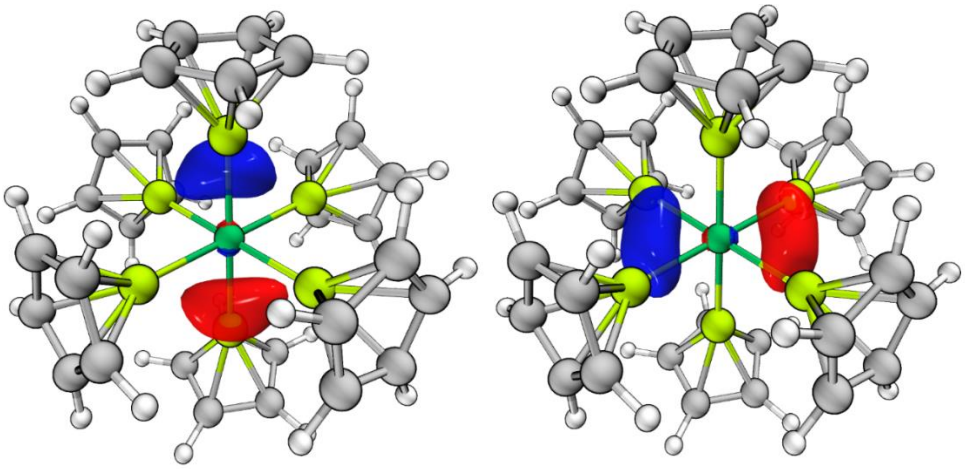

S 3.2: HOMO (left) and HOMO–1 (right) (0.075 a.u.) of complex **1**.

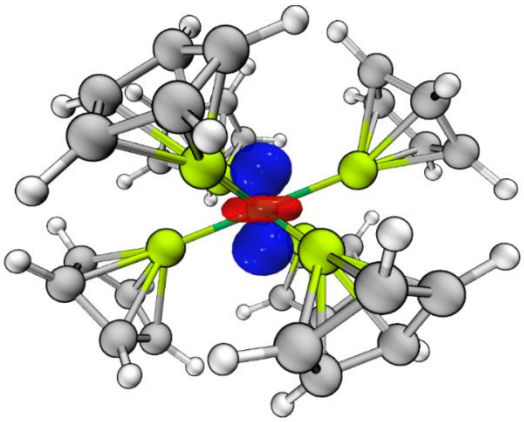

S 3.3: HOMO–2 (0.075 a.u.) of complex **1**.

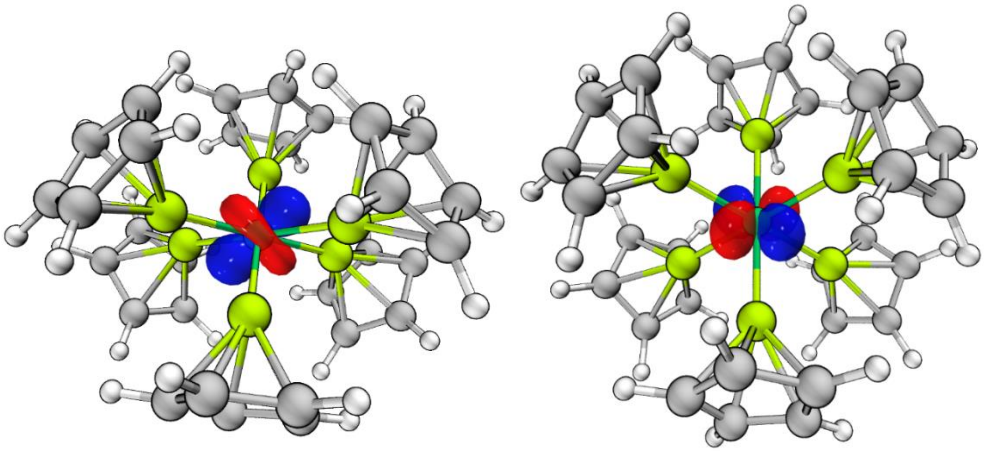

S 3.4: HOMO–3 (left) and HOMO–4 (right) (0.075 a.u.) of complex **1**.

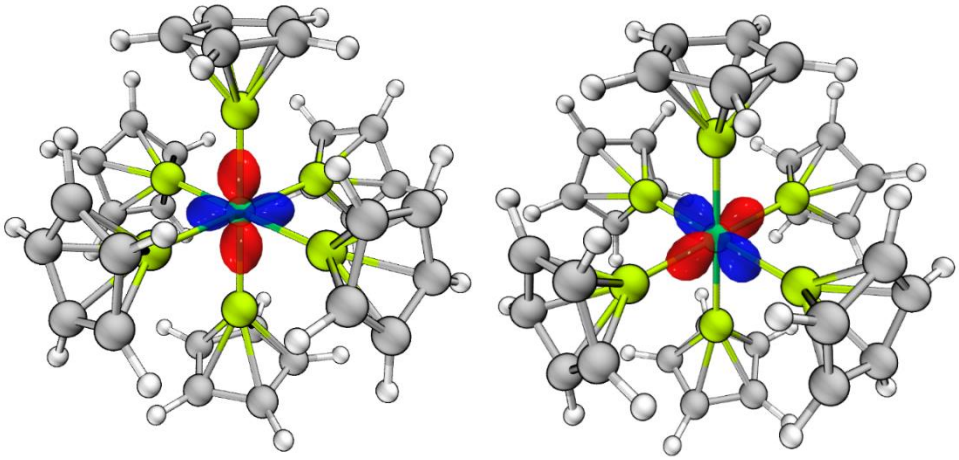

S 3.5: HOMO–5 (left) and HOMO–6 (right) (0.075 a.u.) of complex **1**.

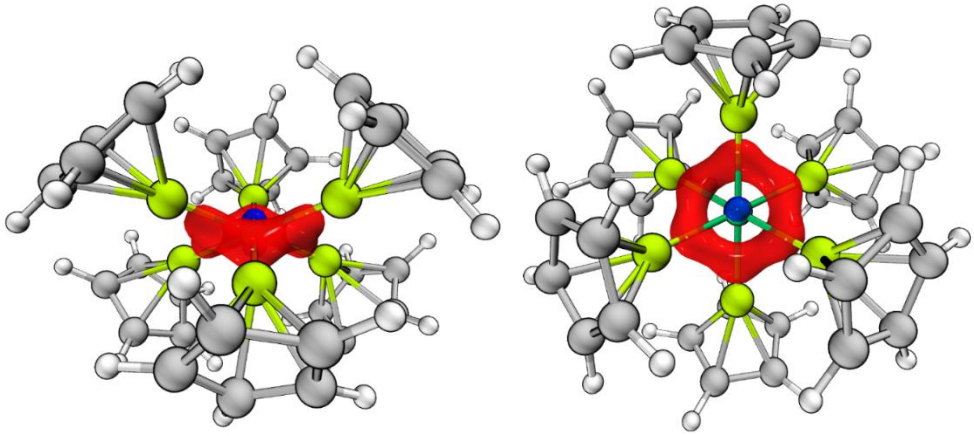

S 3.6: HOMO–19 (0.075 a.u.) of complex **1** viewed perpendicular to z-axis (left) and along z-axis (right)

Qualitative Molecular Orbital Diagram for 1 and 1':

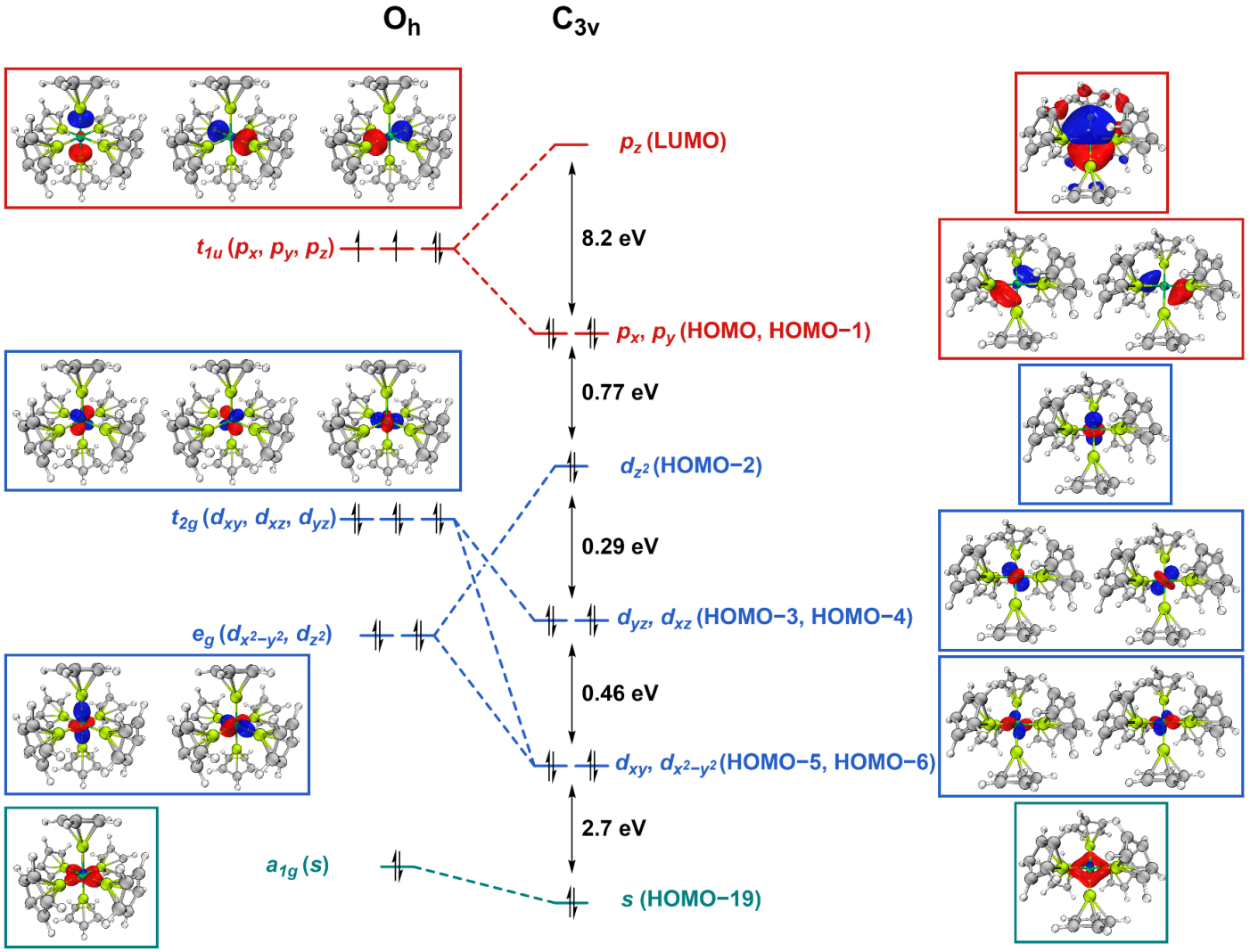

S 3.7: Qualitative molecular orbital scheme for **1'** (O_h) and **1** (C_{3v}) with corresponding molecular orbitals calculated for both complexes.

Molecular Orbitals Calculated for 2Be

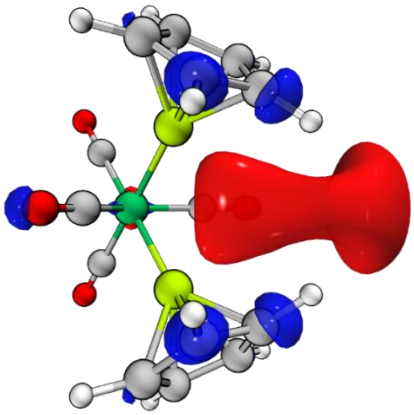

S 3.8: LUMO (0.025 a.u.) of complex **2Be**.

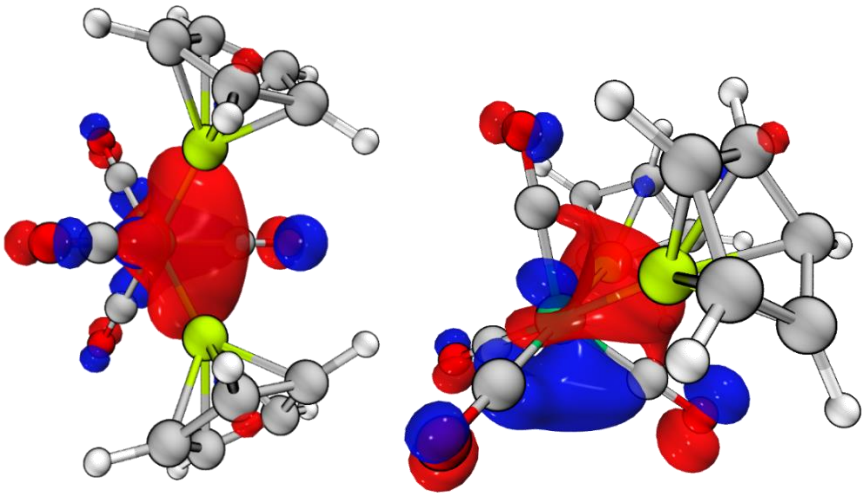

S 3.9: HOMO (0.05 a.u.) of complex **2Be** viewed with the Fe–Be bonds in the plane (left) and from the side (right).

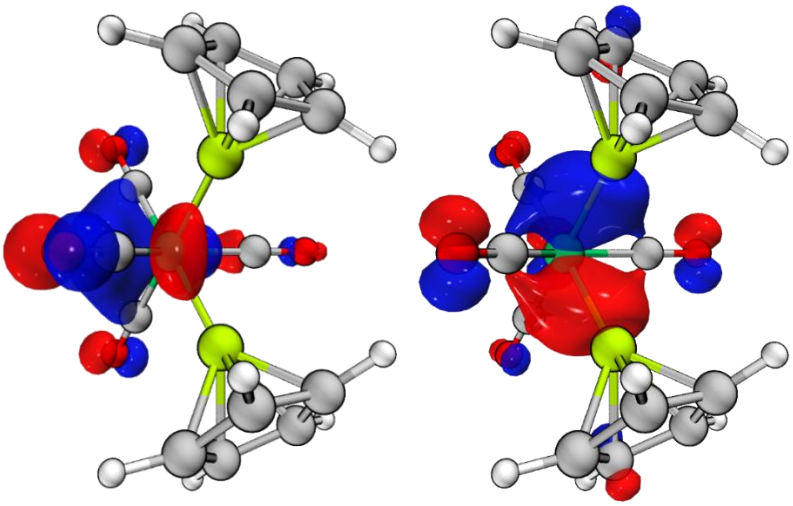

S 3.10: HOMO–1 (left) and HOMO–2 (right) (0.05 a.u.) of complex **2Be**.

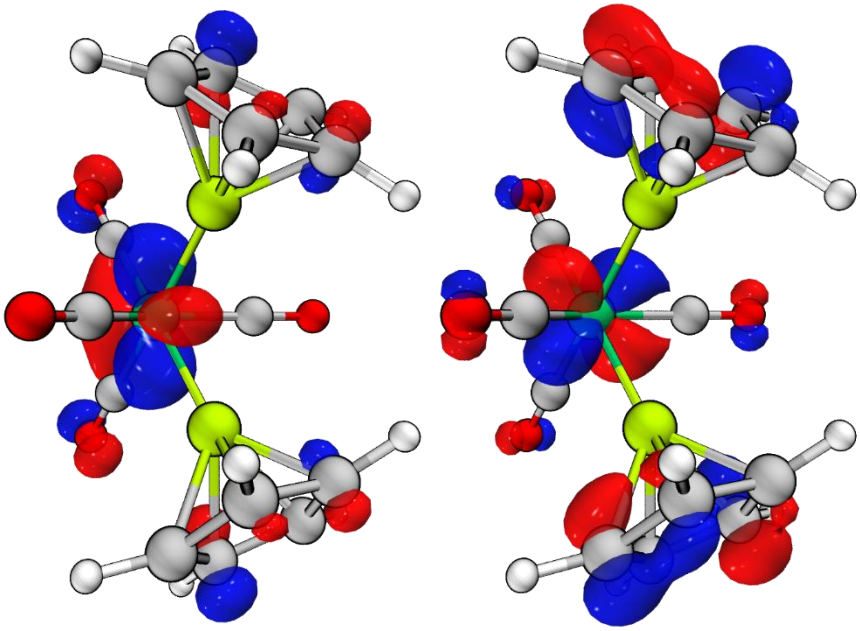

S 3.11: HOMO–3 (left) and HOMO–4 (right) (0.05 a.u.) of complex **2Be**.

Quantum Theory of Atoms in Molecules (QTAIM)

QTAIM was preformed using the AIMALL programme [58]. Calculations were performed using the ORCA wavefunctions for the respective complexes.

ST 3.2: Summary of QTAIM data generated for **1**. All values in a.u., unless specified. ELF and LOL are unit-less.

Ni–Be BCP	101	124	128	138	142	164	Average
ρ_{bcp} / e$^-$ Bohr^{-3}	0.06078	0.06097	0.06093	0.06091	0.06092	0.06073	0.06087
KE (L)	0.02944	0.02982	0.02967	0.02958	0.02971	0.02944	0.02961
KE (H)	0.03316	0.03330	0.03327	0.03327	0.03327	0.03313	0.03323
V	-0.06260	-0.06311	-0.06294	-0.06284	-0.06297	-0.06257	-0.06284
E	-0.03316	-0.03330	-0.03327	-0.03327	-0.03327	-0.03313	-0.03323
$\nabla^2\rho_{bcp}$ / e$^-$ Bohr^{-5}	-0.01489	-0.01392	-0.01443	-0.01475	-0.01424	-0.01475	-0.01450
ELF	0.45622	0.45247	0.45446	0.45572	0.45366	0.45565	0.45470
LOL	0.47815	0.47626	0.47727	0.47790	0.47687	0.47787	0.47739

ST 3.3: Summary of QTAIM data generated for **1'**. All values in a.u., unless specified. ELF and LOL are unit-less.

Ni–Be BCP	101	124	128	138	142	164	Average
ρ_{bcp} / e$^-$ Bohr^{-3}	0.05208	0.05215	0.06735	0.05610	0.05600	0.06712	0.05847
KE (L)	0.03286	0.03299	0.03917	0.04136	0.04114	0.03865	0.03770
KE (H)	0.02763	0.02766	0.03790	0.02952	0.02948	0.03779	0.03166
V	-0.06049	-0.06065	-0.07707	-0.07088	-0.07062	-0.07643	-0.06936
E	-0.02763	-0.02766	-0.03790	-0.02952	-0.02948	-0.03779	-0.03166
$\nabla^2\rho_{bcp}$ / e$^-$ Bohr^{-5}	0.02092	0.02134	0.00509	0.04738	0.04666	0.00344	0.02414
ELF	0.32562	0.32462	0.40047	0.27826	0.27936	0.40421	0.33542
LOL	0.40992	0.40937	0.44975	0.38307	0.38371	0.45167	0.41458

ST 3.4: Summary of QTAIM data generated for **2Be**. All values in a.u., unless specified. ELF and LOL are unit-less.

	Axial CO		Equatorial CO		Be	
Fe-L BCP	**49**	**50**	**48**	**52**	**46**	**54**
ρ_{bcp} / e$^-$ Bohr^{-3}	0.16516	0.16539	0.15294	0.15294	0.05628	0.05628
KE (L)	0.22287	0.22206	0.21159	0.21159	0.03279	0.03278
KE (H)	0.09010	0.09051	0.07464	0.07464	0.02866	0.02866
V	-0.31298	-0.31257	-0.28623	-0.28623	-0.06145	-0.06145
E	-0.09010	-0.09051	-0.07464	-0.07464	-0.02866	-0.02866
$\nabla^2\rho_{bcp}$ / e$^-$ Bohr^{-5}	0.53108	0.52621	0.54783	0.54783	0.01651	0.01649
ELF	0.29086	0.29336	0.26048	0.26048	0.34360	0.34365
LOL	0.39042	0.39186	0.37246	0.37246	0.41986	0.41989

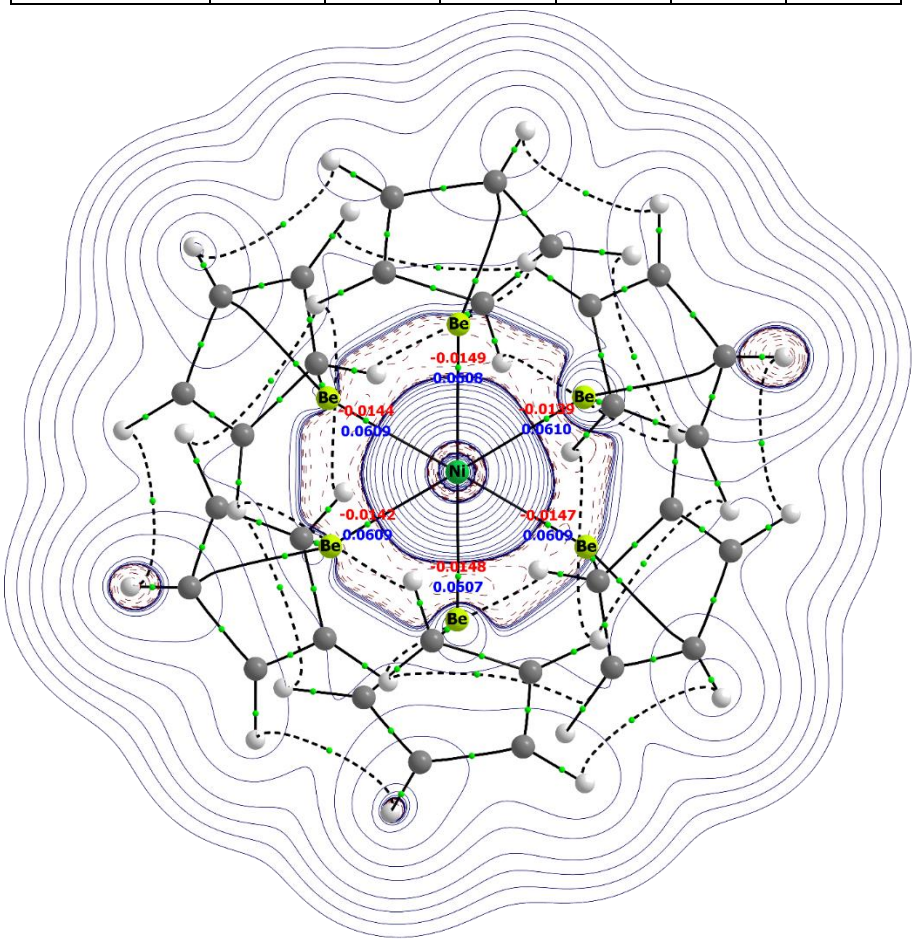

S 3.12: Plot of QTAIM data generated for **1**. Bond paths (BPs) in black and bond critical points (BCPs) in green. Contour map of is of Laplacian ($\nabla^2\rho_{bcp}$). Values in red are $\nabla^2\rho_{bcp}$ (e$^-$ Bohr^{-5}) and values in blue are ρ_{bcp} (electron density; e$^-$ Bohr^{-3}) at the respective BCP. The negative $\nabla^2\rho_{bcp}$ values are indicative of covalent Ni–Be bonding, which contrasts with **1'** (see below). Ring critical points and prismatic critical points are omitted for clarity.

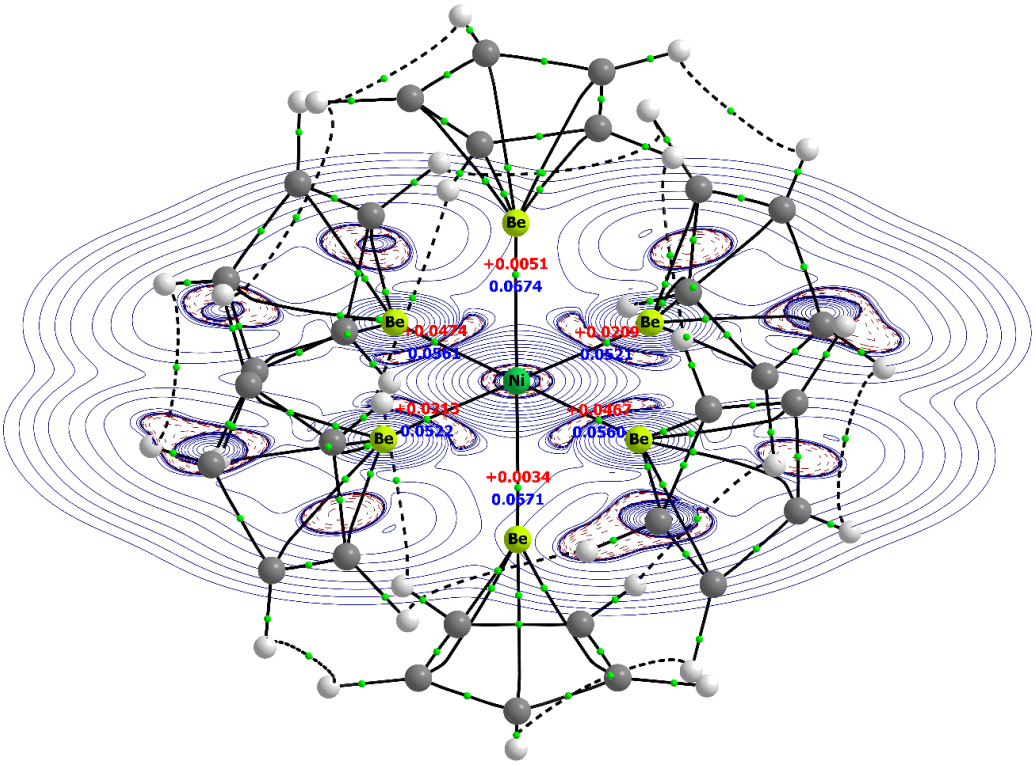

S 3.13: Plot of QTAIM data generated for **1'**. Bond paths (BPs) in black and bond critical points (BCPs) in green. Contour map of is of Laplacian ($\nabla^2\rho_{bcp}$). Values in red are $\nabla^2\rho_{bcp}$ (e^- $Bohr^{-5}$) and values in blue are ρ_{bcp} (electron density; e^- $Bohr^{-3}$) at the respective BCP. The positive values of $\nabla^2\rho_{bcp}$ are indicative that the bonding is ionic in nature. Ring critical points and prismatic critical points are omitted for clarity.

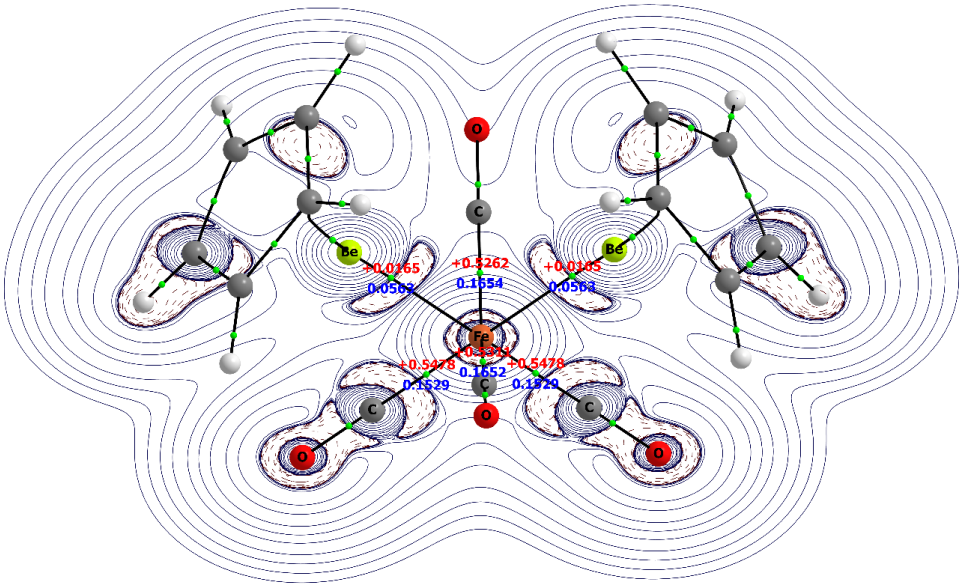

S 3.14: Plot of QTAIM data generated for **2Be**. Bond paths (BPs) in black and bond critical points (BCPs) in green. Contour map of is of Laplacian ($\nabla^2\rho_{bcp}$). Values in red are $\nabla^2\rho_{bcp}$ (e^- $Bohr^{-5}$) and values in blue are ρ_{bcp} (electron density; e^- $Bohr^{-3}$) at the respective BCP. Ring critical points and prismatic critical points are omitted for clarity.

Localised Orbital Locator (LOL) and Electron Localisation Function (ELF) Calculations

Calculations were performed using the ORCA wavefunctions for the respective complexes, generated using Multiwfn 3.8 [59–61]. The toroidal feature in the ELF isosurface for **1** comprises six adjacent $NiBe_2$ tri-synaptic basins. The co-variance values support delocalisation across these six basins [62]. The sum of the electrons across these basins is approximately 10 electrons, as would be expected from the five Ni–Be bonding orbitals (2 x 3*d*, 2 x 4*p*, 1 x 4*s*). LOL calculations yield a similar picture to that of the ELF calculations.

ST 3.5: Summary of ELF data for **1**.

Attractors	**20(t)**	**21(t)**	**22(t)**	**37(t)**	**41(t)**	**45(t)**
population	1.3946	1.4142	1.3946	1.4109	1.4151	1.3977
volume	8.693	8.881	8.731	8.865	8.884	8.736
LI[a]	0.43995	0.45094	0.43917	0.44909	0.45072	0.44132
DI[b]	0.27963049	0.27963049	0.27972373	0.2794927	0.2799513	0.27972162
(X,Y)	20,21	21,20	22,21	37,20	41,22	45,37
DI[b]	0.2794927	0.27972373	0.2799513	0.27972162	0.28016953	0.28016953
(X,Y)	20,37	21,22	22,41	37,45	41,45	45,41

a) LI = localization index; b) DI = delocalization index.

ST 3.6: Summary of LOL data for **1**.

Attractors	**35**	**37**	**38**	**39**	**40**	**41**
integration	1.568249953	1.607928229	1.560850544	1.571359302	1.613237857	1.606682995
volume	66.690216	68.773752	66.451104	67.000824	69.1362	68.545872
LI[a]	0.49347	0.51676	0.48912	0.4942	0.51948	0.51624
DI[b]	0.31480287	0.31480287	0.31481624	0.31570007	0.31591996	0.31520429
(X,Y)	35,37	37,39	38,40	39,37	40,35	41,38
DI[b]	0.31591996	0.31570007	0.31520429	0.3155519	0.31481624	0.3155519
(X,Y)	35,40	37,39	38,41	39,41	40,38	41,39

a) LI = localization index; b) DI = delocalization index.

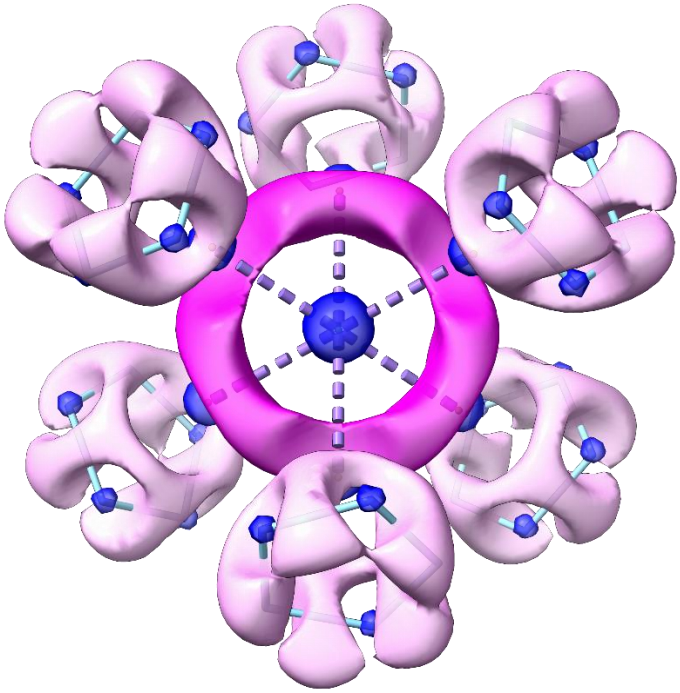

S 3.15: ELF isosurface for **1** (with H atoms omitted for clarity) (0.7 a.u.). Pink represents the isosurfaces associated with the Cp ligands. Magenta represents the isosurface associated with the Be–Ni tri-synaptic basins, which contain an average 1.37 electrons (Ni:Be:Be 74:13:13).

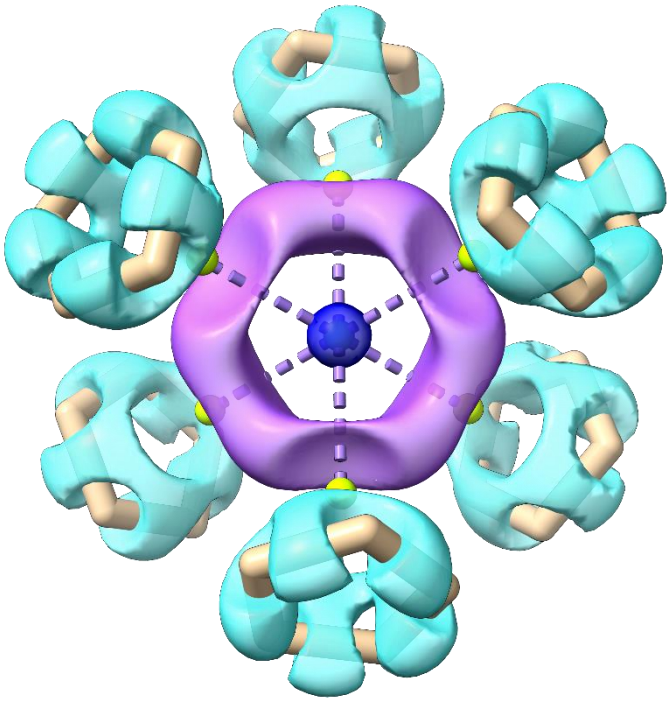

S 3.16: LOL isosurface for **1** (with H atoms omitted for clarity), viewed along z-axis (0.5 a.u.). Cyan represents the isosurfaces associated with Cp ligand basins. Be–Ni tri-synaptic basins contain an average 1.52= electrons (Ni:Be:Be 74:13:13).

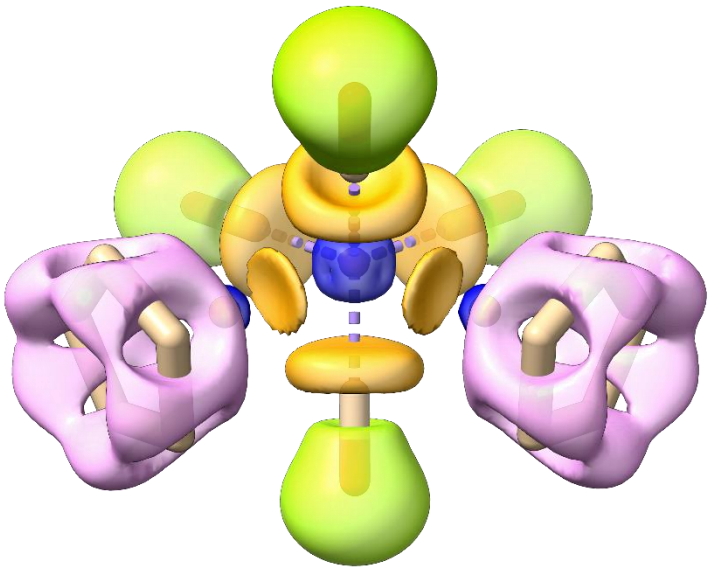

S 3.17: ELF isosurface for **2Be** (with H atoms omitted for clarity) (0.7 a.u.). Pink represents the isosurfaces associated with the Cp ligands. Orange represents the Fe–ligand disynaptic basin isosurfaces. Dark blue are isosurfaces of the core basins. Fe–Be disynaptic basins each contain 1.07 electrons (Fe:Be 79:21).

Natural Bond Orbital (NBO) Analysis

NBO calculations were performed on the ORCA wavefunction for **1** using NBO 7.0 [63] to compliment QTAIM and ELF/LOL calculations. Although Be–Ni bonds are not found by this programme, Wiberg bond indices of 0.27 for the six Be–Ni bonds are calculated. Natural charges for Ni (–1.14) and the six Be centres (+1.04) are consistent with charge transfer from Be to Ni.

Selected Adaptive natural density partitioning (AdNDP) orbitals

Adaptive natural density partitioning (AdNDP) analysis of the wavefunction produced by Gaussian 16 was performed on **1** using the Multiwfn code [64,65]. This technique, which is effective at describing electron delocalisation, has been widely employed for the examination of aromaticity in organic and inorganic systems. Aside from the expected bonding interactions associated with the Cp σ- and π-bonding frameworks and other Be–Ni σ-bonding combinations (**S 3.18-S 3.22**), AdNDP returns a delocalised $NiBe_6$ σ-symmetry bonding orbital (**S 3.23**).

ST 3.7: Summary of AdNDP orbital composition for **1**.

	orbital	1	2	3	4	5	6	7	8	9
Ni	d_{xy}	3.4%	5.6%		44.9%	43.3%				
	d_{xz}	62.1%	27.8%		1.8%	7.8%				
	d_{yz}	27.7%	62.5%		7.4%	1.9%				
	$d_{x^2-y^2}$	5.8%	3.1%		43.5%	44.7%				
	d_{z^2}			99.3%						
	4_p							56.0%	56.0%	71.2%
	$4s$						49.9%			
	Total Ni	99.1%	99.1%	99.3%	97.8%	97.7%	49.9%	56.0%	56.0%	71.2%
Be	**1: 2*s***						8.3%	11.0%	3.7%	4.8%
	2: 2*s*				0.5%		8.3%	10.6%	4.1%	4.8%
	3: 2*s*						8.3%	11.0%	3.6%	4.8%
	4: 2*s*				0.5%		8.3%	10.6%	4.0%	4.8%
	5: 2*s*					0.5%	8.5%		14.3%	4.8%
	6: 2*s*					0.6%	8.4%		14.3%	4.8%
	Total Be				1.0%	1.1%	50.1%	43.3%	44.0%	28.8%
	O.N.	2.00	2.00	2.00	2.00	2.00	1.99	1.97	1.97	0.32
	energy / eV	-7.90	-7.88	-7.52	-7.94	-7.94	-18.36	-9.70	-9.70	-14.32

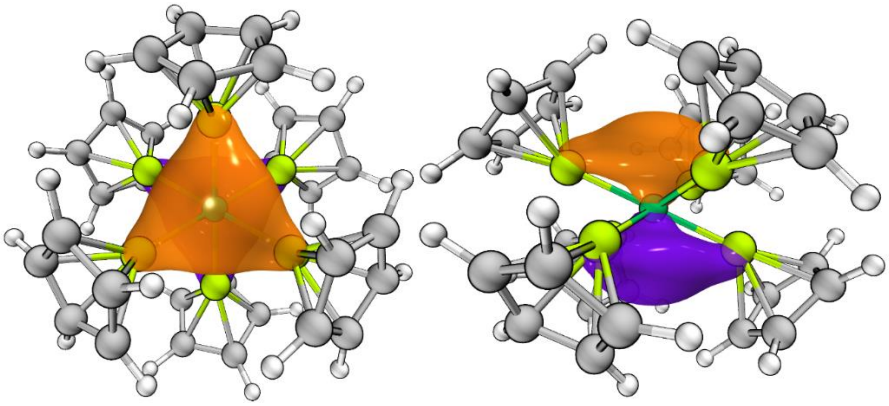

S 3.18: AdNDP orbital 9 for **1** viewed along the z-axis (left) and perpendicular to the z-axis (right) (0.5 a.u.).

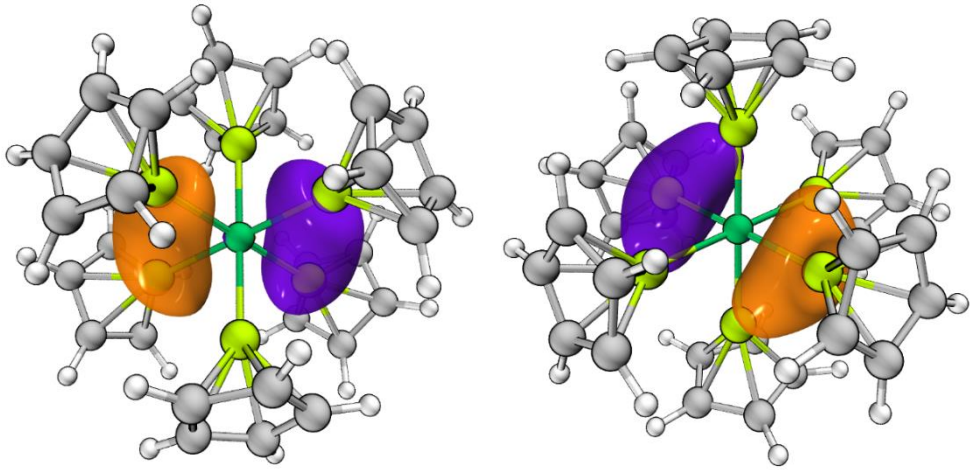

S 3.19: AdNDP orbital for **1** (7, left) (8, right) (0.5 a.u.).

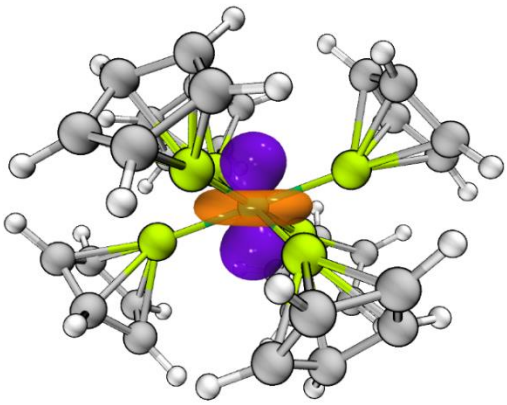

S 3.20: AdNDP orbital 3 for **1** (O.N. = 1.9) (0.5 a.u.).

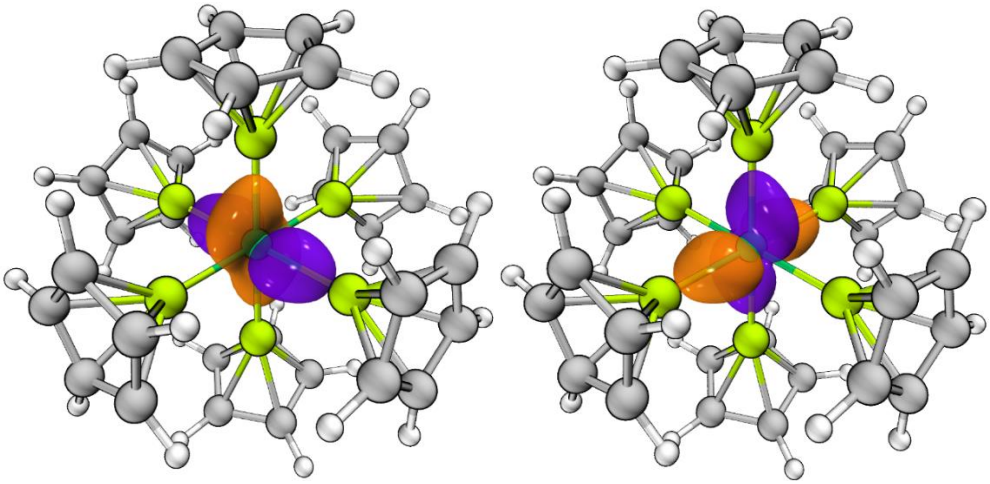

S 3.21: AdNDP orbital for **1** (1, left) (2, right) (0.5 a.u.).

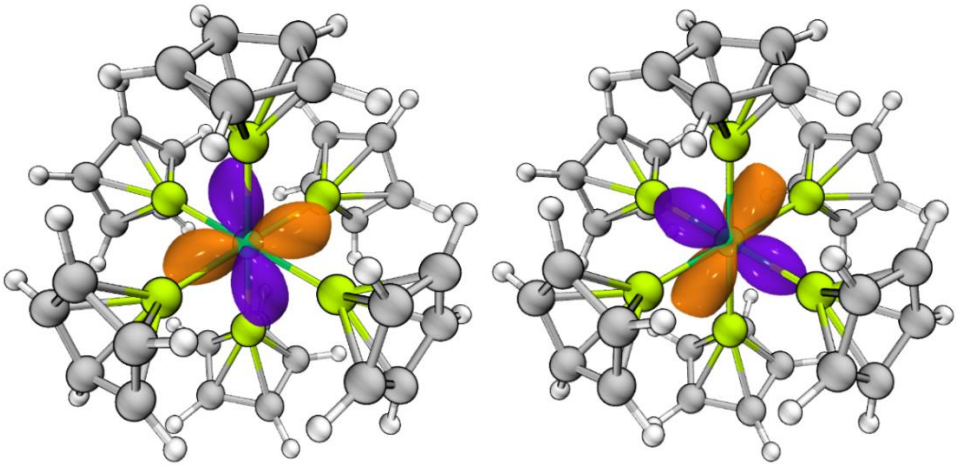

S 3.22: AdNDP orbitals for **1** (4, left) (5, right) (0.5 a.u.).

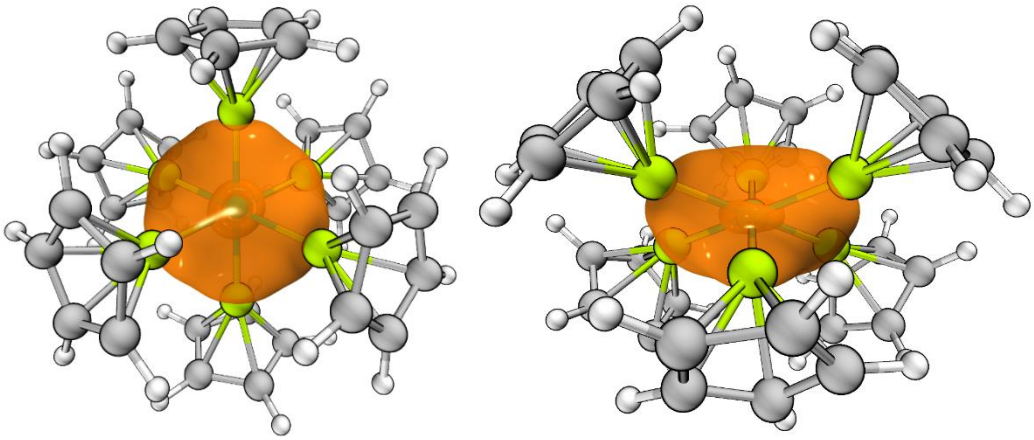

S 3.23: AdNDP orbital 6 for **1** viewed along the z-axis (left) and perpendicular to the z-axis (right) (O.N. = 1.9) (0.5 a.u.). This orbital comprises contributions from the Ni 4s-orbital (49.9%) and each of the 2s-orbitals of the six beryllium atoms (8.26 – 8.47% from each).

Electron Density of Delocalised Bonds (EDDB) Analysis:

EDDB analysis of the wavefunction produced by Gaussian 16 was performed on **1** using the RunEDDB code [36]. A global search finds 38.9928 delocalised electrons of 262.0000 NPA electrons (Table S8).

ST 3.8: Summary of EDDB data for electron delocalisation across the $NiBe_6$ unit.

Atom	Be	Be	Be	Be	Be	Be	Ni
Number of delocalised electrons	0.2709	0.2700	0.2704	0.2706	0.2705	0.2701	1.6321

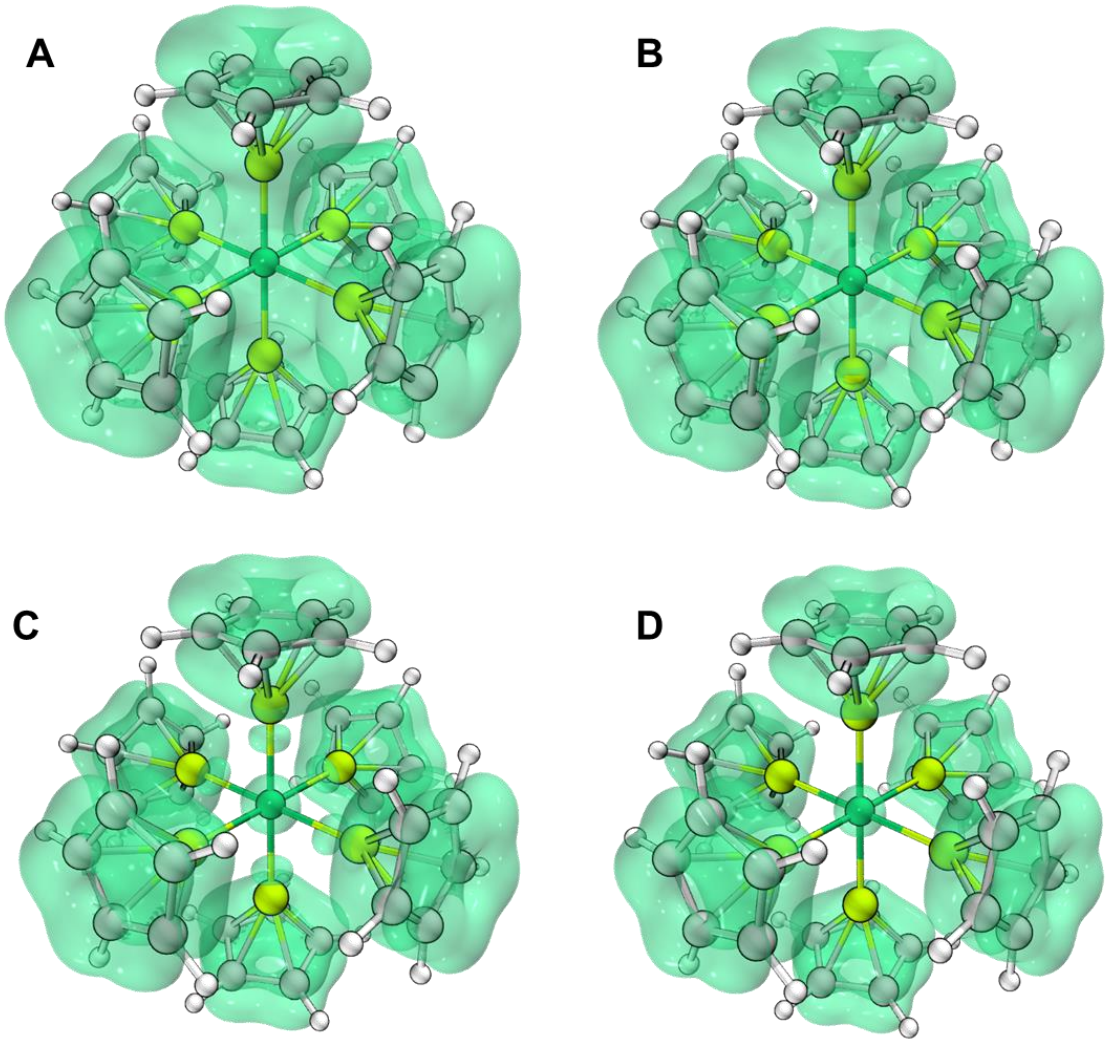

S 3.24: EDDB isosurface for **1** (**A**, 0.02.; **B**, 0.015; **C**, 0.01; **D**, 0.000125 a.u.)

Nucleus-Independent Chemical Shift (NICS) Analysis

NICS analysis was performed in Gaussian 16 (Gaussian wavefunction) using the GIAO method [66]. Isochemical shielding surface (ICSS) analysis was performed using the M06-2x hybrid functional with Def2-TZVP [49,50].

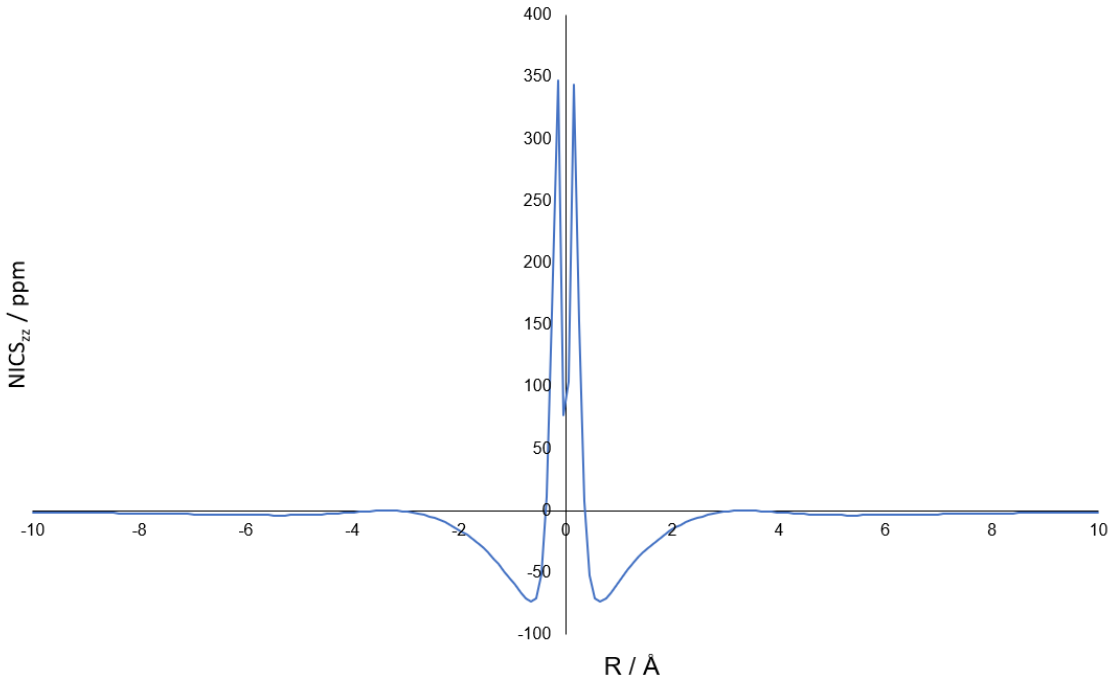

S 3.25: $NICS_{zz}$ plot for complex **1**. R is the distance along the C_3 axis from the Ni centre.

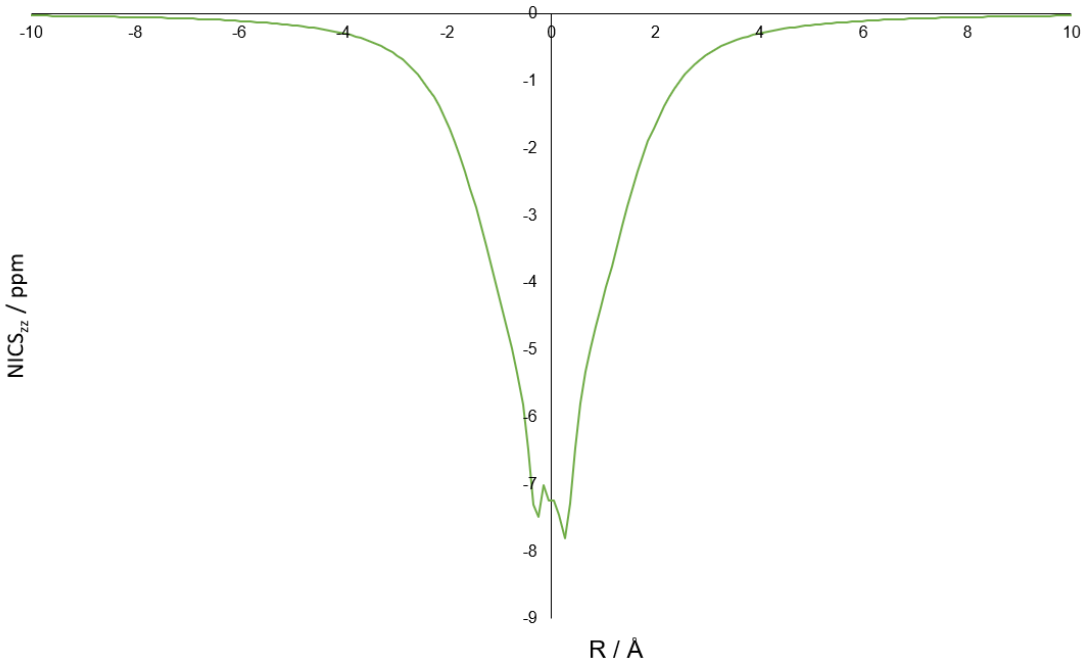

S 3.26: $NICS_{zz}$ plot for the HOMO−19 of complex **1**. R is the distance along the C_3 axis from the Ni centre.

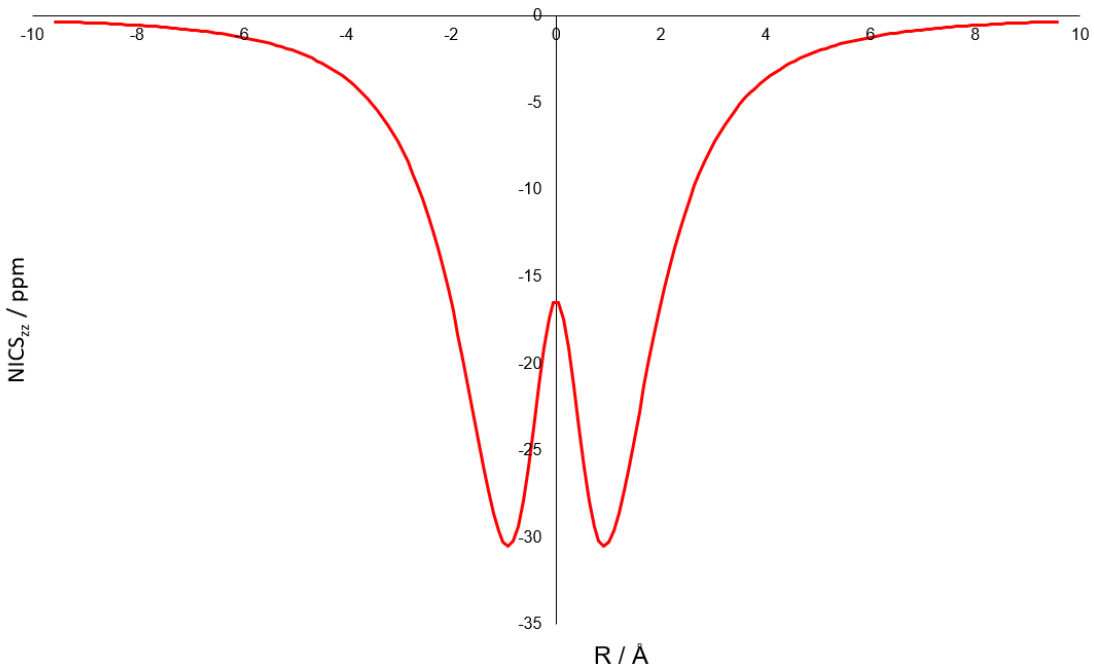

S 3.27: $NICS_{zz}$ plot for benzene. R is the perpendicular distance from the C_6 ring centroid.

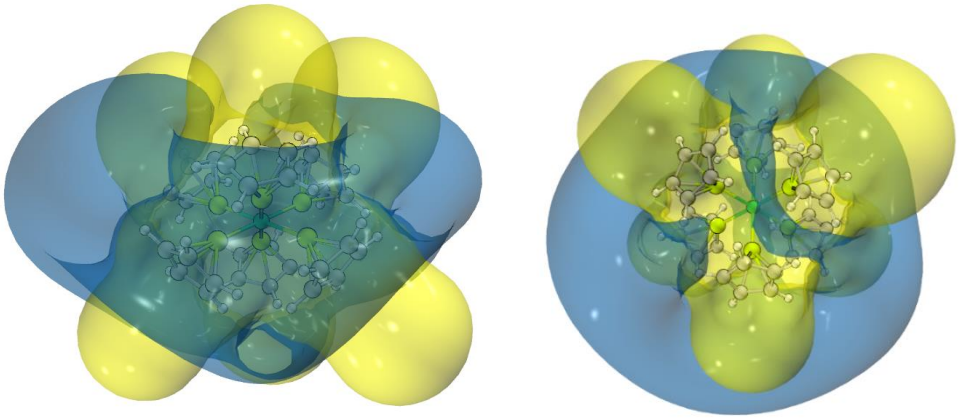

S 3.28: Isotropic isochemical shielding surface plots for **1** viewed perpendicular to the z-axis (left) and along the z-axis (right) (0.75 ppm).

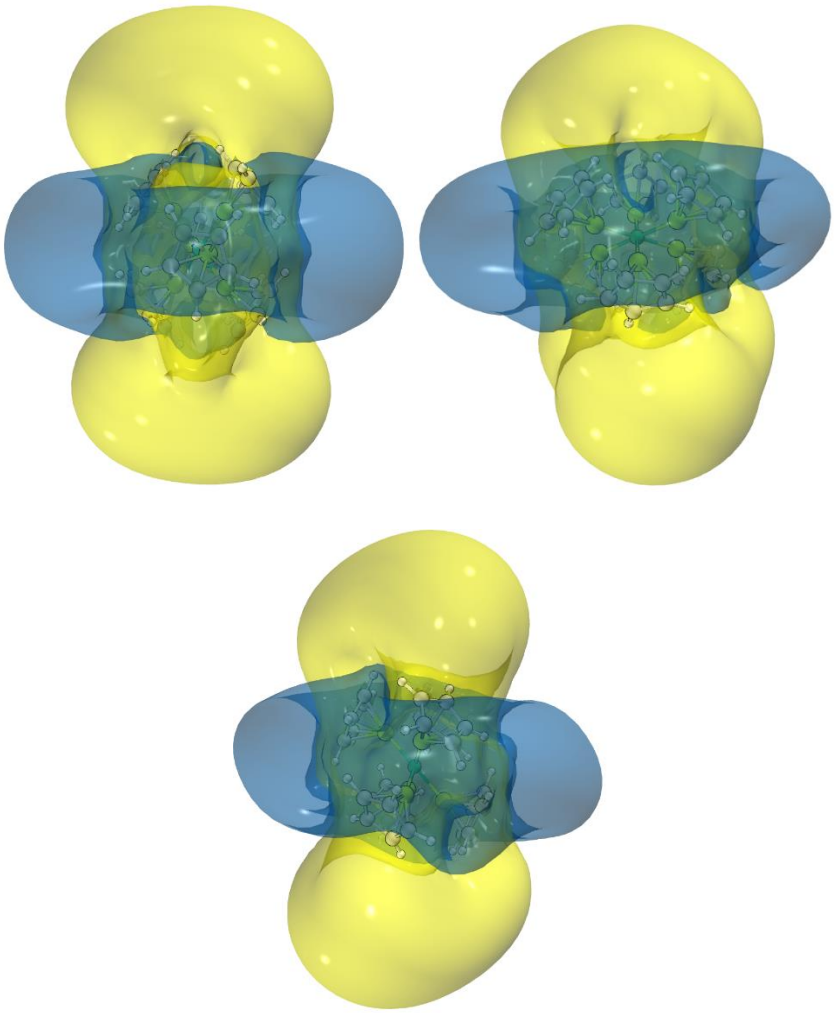

S 3.29: Isochemical shielding surface plots for **1**, $ICSS_{xx}$ (left), $ICSS_{yy}$ (centre), $ICSS_{zz}$ (right) (1 ppm).

QTAIM Magnetic Analysis

Magnetic analysis was performed using AIMALL using the wavefunction generated by Gaussian 16 (GIAO method) [58].

ST 3.9: Magnetizability data calculated for **1**. Units of χ are ppm.

Atom	χ^{iso}Intra	χ^{iso}Bond	χ^{iso}	χ^{zz}Intra	χ^{zz}Bond	χ^{zz}
Ni	-24.65	-5.55	-30.20	-45.98	-9.95	-55.93
Be	-0.36	-0.20	-0.56	-0.14	-0.72	-0.87
Be	-0.36	-1.41	-1.77	-0.14	-2.20	-2.34
Be	-0.36	-2.16	-2.52	-0.14	-2.50	-2.65
Be	-0.36	-0.90	-1.26	-0.14	-0.13	-0.27
Be	-0.36	-1.62	-1.98	-0.14	-1.21	-1.36
Be	-0.36	-0.61	-0.97	-0.14	-0.14	-0.28
Av. Be	-0.36	-1.15	-1.51	-0.14	-1.15	-1.29

It should be noted that χ_{zz}^{Atom} for Be would be expected to be smaller than those of benzene as the Be centres are not within the space defined by the delocalised ELF isosurface.

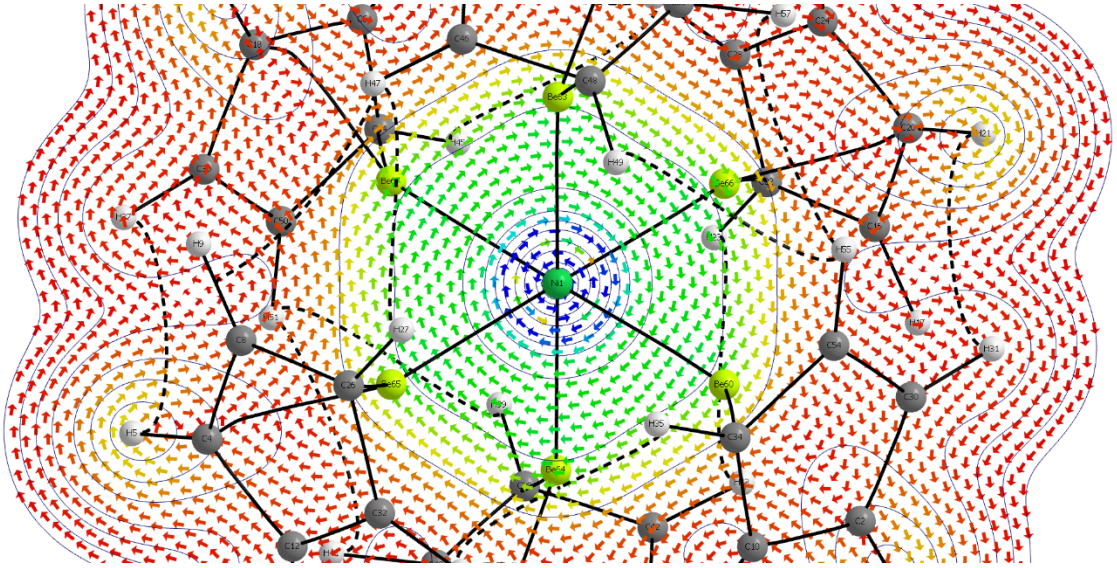

S 3.30: Ring current plot for **1**. A clockwise (diamagnetic) current can clearly be seen. Counter-clockwise currents towards the inner rim of the diamagnetic region can also be seen. This is analogous to benzene (Figure. **S 3.32**). The blue to red colour scale indicates strong (J(r) ≥ 0.001 a.u.) to weak currents (J(r) = 0.0000)

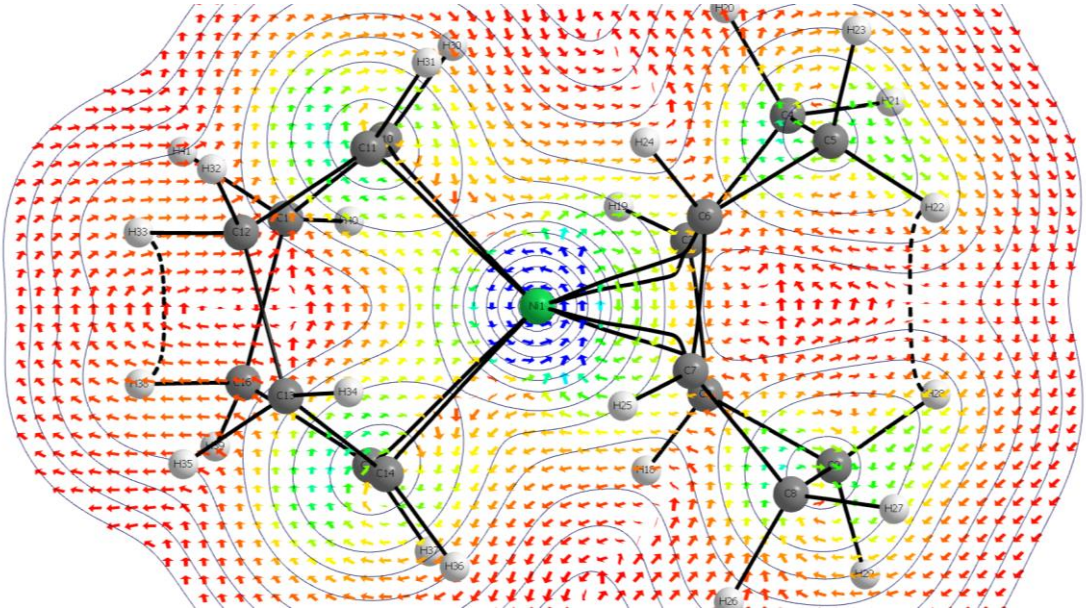

S 3.31: Ring current plot for $Ni(COD)_2$. Only local paramagnetic currents can be seen surrounding the Ni centre, which is typical of a metal. The blue to red colour scale indicates strong ($J(r) \geq 0.001$ a.u.) to weak currents ($J(r) = 0.0000$)

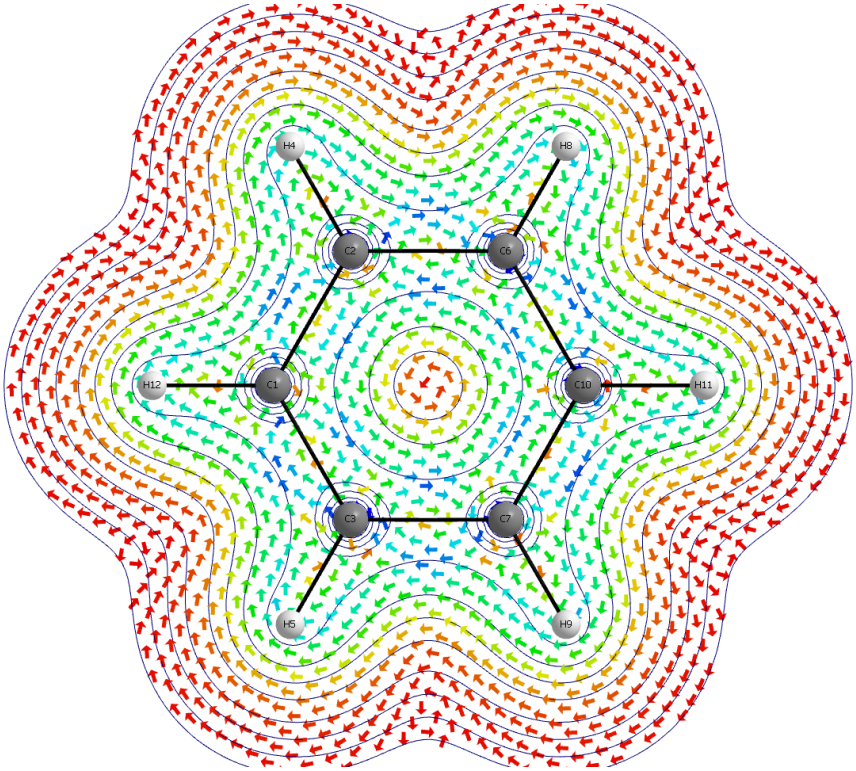

S 3.32: Ring current plot for benzene. A clockwise (diamagnetic) current can clearly be seen around the outside of the C_6 ring. Counter-clockwise currents around the inner rim of the C_6 ring can also be seen. The blue to red colour scale indicates strong ($J(r) \geq 0.001$ a.u.) to weak currents ($J(r) = 0.0000$)

Anisotropy of Induced Current Density (ACID) Analysis

Anisotropy of Induced Current Density (ACID) was performed with the code provided to us by the research group of Prof. Herges, from the wavefunction generated by Gaussian 16 (CSGT method) [38,67].

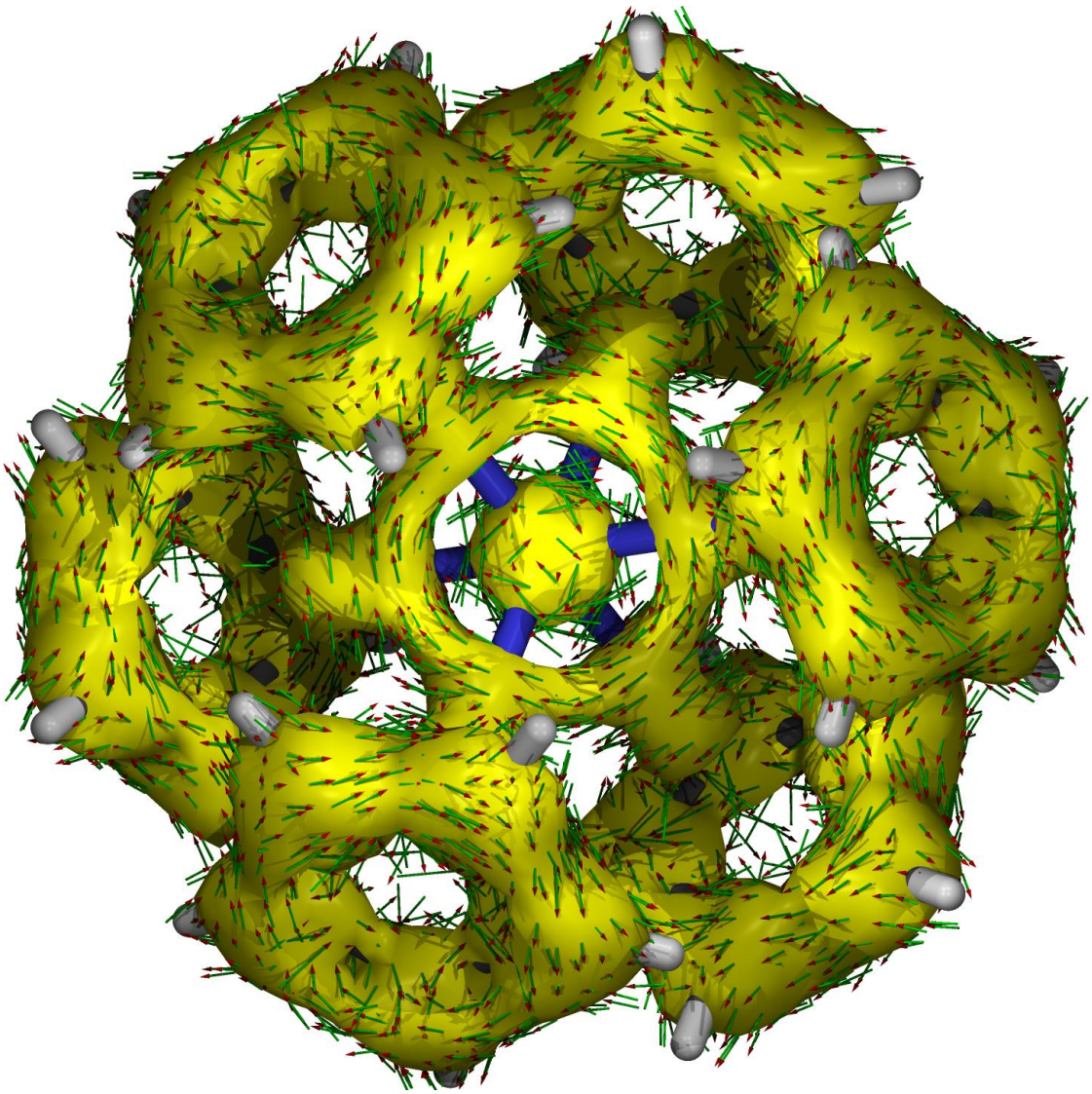

S 3.33: ACID plot for **1** at 0.05 a.u. isosurface value. The clockwise direction of the induced current (illustrated by red arrow heads) indicates aromatic delocalisation.

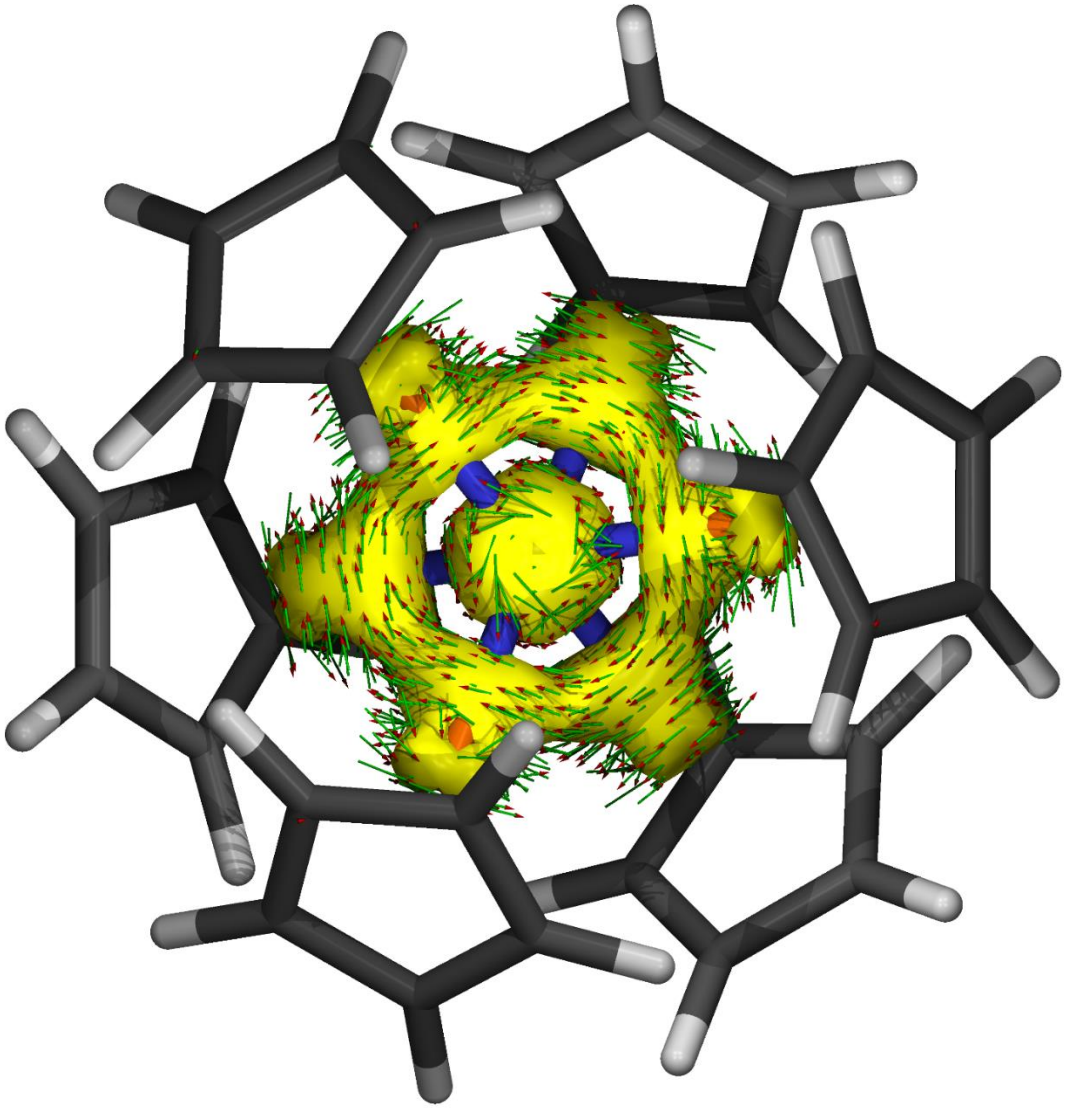

S 3.34: ACID plot of the $NiBe_6$ bonding orbitals of **1** at 0.05 a.u. isosurface value. The clockwise direction of the induced current (illustrated by red arrow heads) indicates aromatic delocalisation.

References

1. Kettler, P. B. Platinum Group Metals in Catalysis: Fabrication of Catalysts and Catalyst Precursors. *Org. Process Res. Dev.* **7**, 342–354 (2003).
2. Ellis, J. E. Adventures with Substances Containing Metals in Negative Oxidation States. *Inorg. Chem.* **45**, 3167–3186 (2006).
3. Lin, C.-Y. & Power, P. P. Complexes of Ni(I): a "rare" oxidation state of growing importance. *Chem. Soc. Rev.* **46**, 5347–5399 (2017).
4. Riedel, S. & Kaupp, M. The highest oxidation states of the transition metal elements. *Coord. Chem. Rev.* **253**, 606–624 (2009).
5. Malischewski, M. *Very High Oxidation States in Organometallic Chemistry*. *Comprehensive Organometallic Chemistry IV: Volume 1-15* vols 1–15 (Elsevier Ltd., 2022).
6. D'Accriscio, F. *et al.* C−H Bond Trifluoromethylation of Arenes Enabled by a Robust, High-Valent Nickel(IV) Complex. *Angew. Chemie - Int. Ed.* **56**, 12898–12902 (2017).
7. Roy, P., Bour, J. R., Kampf, J. W. & Sanford, M. S. Catalytically Relevant Intermediates in the Ni-Catalyzed C(sp 2)–H and C(sp 3)–H Functionalization of Aminoquinoline Substrates. *J. Am. Chem. Soc.* **141**, 17382–17387 (2019).
8. Camasso, N. M. & Sanford, M. S. Design, synthesis, and carbon-heteroatom coupling reactions of organometallic nickel(IV) complexes. *Science* **347**, 1218–1220 (2015).
9. Diccianni, J. B. & Diao, T. Mechanisms of Nickel-Catalyzed Cross-Coupling Reactions. *Trends Chem.* **1**, 830–844 (2019).
10. Sheng, Y. *et al.* Superoxide Dismutases and Superoxide Reductases. *Chem. Rev.* **114**, 3854–3918 (2014).
11. Lubitz, W., Ogata, H., Rüdiger, O. & Reijerse, E. Hydrogenases. *Chemical Reviews* 114 4081–4148 (2014).
12. Kulka-Peschke, C. J. *et al.* Reversible Glutamate Coordination to High-Valent Nickel Protects the Active Site of a [NiFe] Hydrogenase from Oxygen. *J. Am. Chem. Soc.* **144**, 17022–17032 (2022).
13. Boronski, J. T., Crumpton, A. E., Wales, L. L. & Aldridge, S. Diberyllocene, a stable compound of Be(I) with a Be–Be bond. *Science.* **380**, 1147–1149 (2023).
14. DiMucci, I. M. *et al.* Scrutinizing formally Ni IV centers through the lenses of core spectroscopy, molecular orbital theory, and valence bond theory. *Chem. Sci.* **14**, 6915–6929 (2023).
15. Hoffmann, R. *et al.* From Widely Accepted Concepts in Coordination Chemistry to Inverted Ligand Fields. *Chem. Rev.* **116**, 8173–8192 (2016).
16. Boldyrev, A. I. & Wang, L.-S. All-Metal Aromaticity and Antiaromaticity. *Chem. Rev.* **105**, 3716–3757 (2005).
17. Hartwig, J. F. Regioselectivity of the borylation of alkanes and arenes. *Chem. Soc. Rev.* **40**, 1992–2002 (2011).
18. Labinger, J. A. Tutorial on Oxidative Addition. *Organometallics* **34**, 4784–4795 (2015).
19. Segawa, Y., Yamashita, M. & Nozaki, K. Boryllithium: Isolation, characterization, and reactivity as a boryl anion. *Science.* **314**, 113–115 (2006).
20. McNeill, E. A. & Scholer, F. R. Molecular Structure of the Gaseous Metal Carbonyl Hydrides of Manganese, Iron, and Cobalt. *J. Am. Chem. Soc.* **99**, 6243–6249 (1977).
21. He, X. & Hartwig, J. F. Boryls Bound to Iron Carbonyl. Structure of a Rare Bis(boryl) Complex, Synthesis of the First Anionic Boryl, and Reaction Chemistry That Includes the Synthetic Equivalent of Boryl Anion Transfer. *Organometallics* **15**, 400–407 (1996).
22. Uddin, J., Boehme, C. & Frenking, G. Nature of the chemical bond between a transition metal and a group-13 element: Structure and bonding of transition metal complexes with terminal group-13 diyl ligands ER (E = B to Tl; R = Cp, N(SiH3)2, Ph, Me). *Organometallics* **19**, 571–582 (2000).
23. Pyykkö, P. Additive covalent radii for single-, double-, and triple-bonded molecules and tetrahedrally bonded crystals: A summary. *J. Phys. Chem. A* **119**, 2326–2337 (2015).
24. Plieger, P. G. *et al.* Predicting 9Be nuclear magnetic resonance chemical shielding tensors utilizing density functional theory. *J. Am. Chem. Soc.* **126**, 14651–14658 (2004).
25. Vancea, L., Bennett, M. J., Jones, C. E., Smith, R. A. & Graham, W. A. G. Stereochemically Nonrigid Six-Coordinate Metal Carbonyl Complexes. 1. Polytopal Rearrangement and X-Ray Structure of Tetracarbonylbis(trimethylsilyl) iron. *Inorg. Chem.* **16**, 897–902 (1977).

26. Hicks, J., Mansikkamäki, A., Vasko, P., Goicoechea, J. M. & Aldridge, S. A nucleophilic gold complex. *Nat. Chem.* **11**, 237–241 (2019).
27. Protchenko, A. V. *et al.* Stable GaX2, InX2 and TlX2 radicals. *Nat. Chem.* **6**, 315–319 (2014).
28. Nakamoto, M., Yamasaki, T. & Sekiguchi, A. Stable mononuclear radical anions of heavier group 13 elements: [($^{t}Bu_2MeSi)_3E\bullet$-]·[K +(2.2.2-cryptand)] (E = Al, Ga). *J. Am. Chem. Soc.* **127**, 6954–6955 (2005).
29. Merritt, J. M., Bondybey, V. E. & Heaven, M. C. Beryllium dimer-caught in the act of bonding. *Science (80-.).* **324**, 1548–1551 (2009).
30. Mantina, M., Chamberlin, A. C., Valero, R., Cramer, C. J. & Truhlar, D. G. Consistent van der Waals radü for the whole main group. *J. Phys. Chem. A* **113**, 5806–5812 (2009).
31. Hidalgo, N., Romero-Pérez, C., Maya, C., Fernández, I. & Campos, J. Reactivity of [Pt($P^{t}Bu_3)_2$] with Zinc(I/II) Compounds: Bimetallic Adducts, Zn–Zn Bond Cleavage, and Cooperative Reactivity. *Organometallics* **40**, 1113–1119 (2021).
32. Molon, M. *et al.* Hume-rothery phase-inspired metal-rich molecules: Cluster expansion of [Ni($ZnMe)_6(ZnCp_2$] by face capping with Ni0(η6-toluene) and NiI(η5-Cp). *Inorg. Chem.* **53**, 10403–10411 (2014).
33. Steen, J. S., Knizia, G. & Klein, J. E. M. N. σ-Noninnocence: Masked Phenyl-Cation Transfer at Formal NiIV. *Angew. Chemie - Int. Ed.* **58**, 13133–13139 (2019).
34. Boronski, J. T. *et al.* Inducing Nucleophilic Reactivity at Beryllium with an Aluminyl Ligand. *J. Am. Chem. Soc.* **145**, 4408–4413 (2023).
35. Liptrot, D. J. & Power, P. P. London dispersion forces in sterically crowded inorganic and organometallic molecules. *Nat. Rev. Chem.* **1**, 0004 (2017).
36. Szczepanik, D. W. *et al.* The electron density of delocalized bonds (EDDB) applied for quantifying aromaticity. *Phys. Chem. Chem. Phys.* **19**, 28970–28981 (2017).
37. Foroutan-Nejad, C. Interatomic Magnetizability: A QTAIM-Based Approach toward Deciphering Magnetic Aromaticity. *J. Phys. Chem. A* **115**, 12555–12560 (2011).
38. Geuenich, D., Hess, K., Köhler, F. & Herges, R. Anisotropy of the Induced Current Density (ACID), a General Method To Quantify and Visualize Electronic Delocalization. *Chem. Rev.* **105**, 3758–3772 (2005).
39. Buchner, M. R. & Müller, M. Handling Beryllium, the Safe Way. *ACS Chem. Heal. Saf.* **30**, 36–43 (2023).
40. Cosier, J. & Glazer, A. M. A nitrogen-gas-stream cryostat for general X-ray diffraction studies. *J. Appl. Crystallogr.* **19**, 105–107 (1986).
41. CrysAlisPro v.1.171.42.70a, Agilent Technologies 2011.
42. Sheldrick, G. M. Crystal structure refinement with SHELXL. *Acta Crystallogr. Sect. C Struct. Chem.* **71**, 3–8 (2015).
43. Sheldrick, G. M. SHELXT – Integrated space-group and crystal-structure determination. *Acta Crystallogr. Sect. A Found. Adv.* **71**, 3–8 (2015).
44. Dolomanov, O. V., Bourhis, L. J., Gildea, R. J., Howard, J. A. K. & Puschmann, H. OLEX2 : a complete structure solution, refinement and analysis program. *J. Appl. Crystallogr.* **42**, 339–341 (2009).
45. Neese, F. The ORCA program system. *WIREs Comput. Mol. Sci.* **2**, 73–78 (2012).
46. Neese, F. Software update: the ORCA program system, version 4.0. *WIREs Comput. Mol. Sci.* **8**, (2018).
47. Mardirossian, N. & Head-Gordon, M. ωB97X-V: A 10-parameter, range-separated hybrid, generalized gradient approximation density functional with nonlocal correlation, designed by a survival-of-the-fittest strategy. *Phys. Chem. Chem. Phys.* **16**, 9904 (2014).
48. Najibi, A. & Goerigk, L. DFT-D4 counterparts of leading meta-generalized-gradient approximation and hybrid density functionals for energetics and geometries. *J. Comput. Chem.* **41**, 2562–2572 (2020).
49. Weigend, F. & Ahlrichs, R. Balanced basis sets of split valence, triple zeta valence and quadruple zeta valence quality for H to Rn: Design and assessment of accuracy. *Phys. Chem. Chem. Phys.* **7**, 3297 (2005).
50. Weigend, F. Accurate Coulomb-fitting basis sets for H to Rn. *Phys. Chem. Chem. Phys.* **8**, 1057 (2006).
51. Caldeweyher, E., Mewes, J.-M., Ehlert, S. & Grimme, S. Extension and evaluation of the D4 London-dispersion model for periodic systems. *Phys. Chem. Chem. Phys.* **22**, 8499–8512 (2020).

52. Grimme, S., Hansen, A., Ehlert, S. & Mewes, J.-M. r2SCAN-3c: A “Swiss army knife” composite electronic-structure method. *J. Chem. Phys.* **154**, (2021).
53. Furness, J. W., Kaplan, A. D., Ning, J., Perdew, J. P. & Sun, J. Accurate and Numerically Efficient r 2 SCAN Meta-Generalized Gradient Approximation. *J. Phys. Chem. Lett.* **11**, 8208–8215 (2020).
54. Kruse, H. & Grimme, S. A geometrical correction for the inter- and intra-molecular basis set superposition error in Hartree-Fock and density functional theory calculations for large systems. *J. Chem. Phys.* **136**, (2012).
55. Frisch, M. J.; Trucks, G. W.; Schlegel, H. B.; Scuseria, G. E.; Robb, M. A.; Cheeseman, J. R.; Scalmani, G.; Barone, V.; Petersson, G. A.; Nakatsuji, H.; Li, X.; Caricato, M.; Marenich, A. V.; Bloino, J.; Janesko, B. G.; Gomperts, R.; Mennucci, B.; Hratch, D. J. Gaussian 16. (2016).
56. Chai, J.-D. & Head-Gordon, M. Long-range corrected hybrid density functionals with damped atom–atom dispersion corrections. *Phys. Chem. Chem. Phys.* **10**, 6615 (2008).
57. Boronski, J. T., Crumpton, A. E. & Aldridge. A Hexavalent Nickel Complex: xyz coordinates of optimised structures. *Dryad* (2023).
58. Todd, K. A. AIMAll (Version 19.10.12). aim.tkgristmill.com (2019).
59. Lu, T. & Chen, F. Multiwfn: A multifunctional wavefunction analyzer. *J. Comput. Chem.* **33**, 580–592 (2012).
60. Silvi, B. & Savin, A. Classification of chemical bonds based on topological analysis of electron localization functions. *Nature* **371**, 683–686 (1994).
61. Jacobsen, H. Localized-orbital locator (LOL) profiles of chemical bonding. *Can. J. Chem.* **86**, 695–702 (2008).
62. Michalski, M., Gordon, A. J. & Berski, S. Topological analysis of the electron localisation function (ELF) applied to the electronic structure of oxaziridine: the nature of N-O bond. *Struct. Chem.* **30**, 2181–2189 (2019).
63. Glendening, E. D. *et al.* NBO 7.0. (2018).
64. Zubarev, D. Y. & Boldyrev, A. I. ”Developing paradigms of chemical bonding: adaptive natural density partitioning. *Phys. Chem. Chem. Phys.* **10**, 5207 (2008).
65. Tkachenko, N. V. & Boldyrev, A. I. Chemical bonding analysis of excited states using the adaptive natural density partitioning method. *Phys. Chem. Chem. Phys.* **21**, 9590–9596 (2019).
66. Ab initio calculation of the anisotropy effect of multiple bonds and the ring current effect of arenes—application in conformational and configurational analysis. *J. Chem. Soc. Perkin Trans. 2* 1893–1898 (2001)
67. Herges, R. & Geuenich, D. Delocalization of Electrons in Molecules. *J. Phys. Chem. A* **105**, 3214–3220 (2001).

Statement of Authorship

Title of Paper	A Stable Hexavalent Nickel Complex
Publication Status	Submitted for Publication
Publication Details	Submitted for publication in Nature, 19/10/2023

Student Confirmation

Student Name:	Agamemnon Elvis Crumpton	
Contribution to the Paper	Performed DFT calculations on the structures within the manuscript, was lead crystallographer and contributed to the discussion of the quantum chemical calculations and single crystal X-ray diffraction residual electron density in the manuscript.	
Signature 		Date 15/04/2024

Supervisor Confirmation

Supervisor name and title: Professor Simon Aldridge	
Supervisor comments I can confirm that the candidate's contribution to this paper is as described above.	
Signature 	Date 18/4/2024

Chapter 4 - Synthesis of Homo-metallic Heavier Analogues of Cyclobutene and the Cyclobutadiene Dianion

Xiongfei Zheng, Agamemnon E. Crumpton, Andrey V. Protchenko, Mathias A. Ellwanger, Andreas Heilmann, Simon Aldridge*

Published in Chemistry - A European Journal: Chem. Eur. J. 2023, 29, e202300006

Author contributions

Xiongfei Zheng: Synthesised the novel compounds and collected characterisation data.

Agamemnon E. Crumpton: Performed the quantum chemical calculations

Andrey V. Protchenko: Advised in synthetic chemistry and crystallised novel compounds.

Mathias A. Ellwanger: Lead crystallographer.

Andreas Heilmann: Crystallographer

Simon Aldridge: Corresponding author.

Manuscript was written by Simon Aldridge on the basis of the thesis chapter written by Xiongfei Zheng with contribution to the discussion of the quantum chemical calculations by Agamemnon E. Crumpton.

Abstract

The reduction of the boryl-substituted SnII bromide {(HCDippN)$_2$B}Sn(^{i}PrMe)Br with 1.5 equivalents of potassium graphite leads to the generation of the cyclic tetratin tetraboryl system $K_2[Sn_4\{B(NDippCH)_2\}_4]$, a homo-metallic heavier analogue of the cyclobutadiene dianion. This system is non-aromatic as determined by Nucleus Independent Chemical Shift Calculations (NICS(0) = −0.28, NICS(1) = −3.17), with the primary contributing resonance structures shown by Natural Resonance Theory (NRT) to involve a Sn=Sn double bond and 1,2-localized negative charges. Abstraction of the K+ cations or oxidation leads to contraction or cleavage of the Sn4 unit, respectively, while protonation generates the neutral dihydride 1,2-$Sn_4\{B(NDippCH)_2\}_4H_2$ (a heavier homologue of cyclobutene) in a manner consistent with the predicted charge distribution in the $[Sn_4\{B(NDippCH)_2\}_4]^{2-}$ dianion.

Introduction

The concept of aromaticity is a key tool in understanding structure and reactivity in organic chemistry.[1] Extrapolation to the heavier elements of group 14 brings with it additional challenges relating not only to synthetic strategy, but also to the rationalization of geometric data in terms of electronic structure.[2] At a superficial level, Huckel's rule predicts that both the dianion and dication of cyclobutadiene (CBD) should be aromatic with 6π and 2π electrons, respectively. However, the potential aromaticity of these systems has attracted significant debate; doubly anionic 6π cyclic systems have been predicted to behave quite differently from neutral and singly charged analogues because of additional Coulombic repulsion.[3,4] A folded $[CBD]^{2-}$ structure with one localized and one allylic delocalized negative charge,[5] a trapezoid structure with 1,2-localized negative charges and a C=C double bond,[6] and a planar delocalized structure stabilized by the coordination of two Li cations,[7,8] have all been evaluated via quantum chemical methods. Experimentally, there have been studies on the transient cyclobutadiene dianion[7] and its derivatives stabilized by ester or phenyl groups.[10,11] The first cyclic system featuring a delocalized 6π-electron system was characterized crystallo-graphically by Sekiguchi *et al*. in 2000 (**I**, **Figure 4.1**).[12] Subsequently in 2004, the same group isolated $[CBD]^{2-}$ derivatives of the heavier group 14 elements ($[R_4Si_4]^{2-}$, **II**, and $[R_4Si_2Ge_2]^{2-}$, **III**; R = $SiMe^tBu_2$)[13] in which the central four-membered ring is significantly folded, and features two η^2-1,3-coordinated potassium cations. These systems are thought to be non-aromatic on the basis of nucleus-independent chemical shift (NICS) calculations.

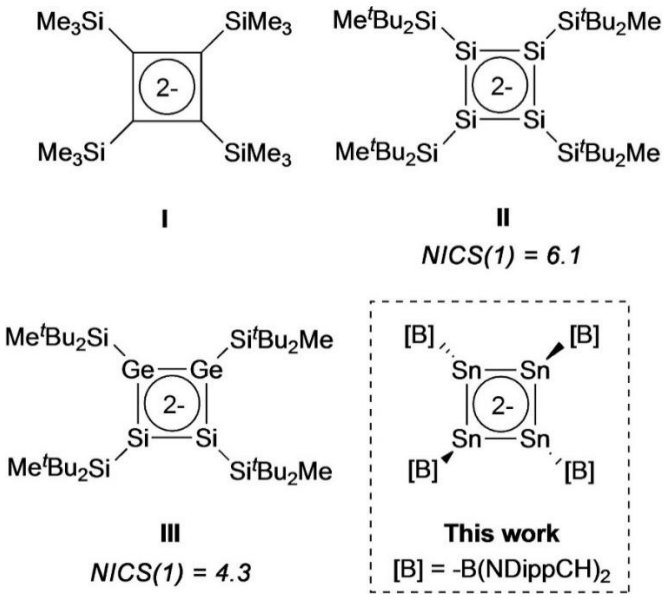

Figure 4.1: Dianionic derivatives of cyclobutadiene and their heavier analogues of relevance to the current study.

We have recently been interested in the use of strongly σ-donating and sterically encumbered boryl ligands, -B(NDippCH)$_2$ for the stabilization of main group systems featuring unusual electronic or geometric structure, and unprecedented modes of reactivity.[14] These include a germanium analogue of vinylidene {(HCDippN)$_2$B}$_2$Ge=Ge,[14h] and a 2π-electron tetra-indium dianion [In$_4${B(NDippCH)$_2$}$_4$]$^{2-}$ (**IV**, as the dipotassium salt) which shows a moderate degree of aromatic character.[14j] Here we show that a superficially similar tin compound K$_2$[Sn$_4${B(NDippCH)$_2$}$_4$] can be accessed via controlled (stoichiometric) reduction of a boryltin(II) precursor. This system represents the first tin-containing analogue of [CBD]$^{2-}$, but in contrast to its indium counterpart, is non-aromatic in nature.

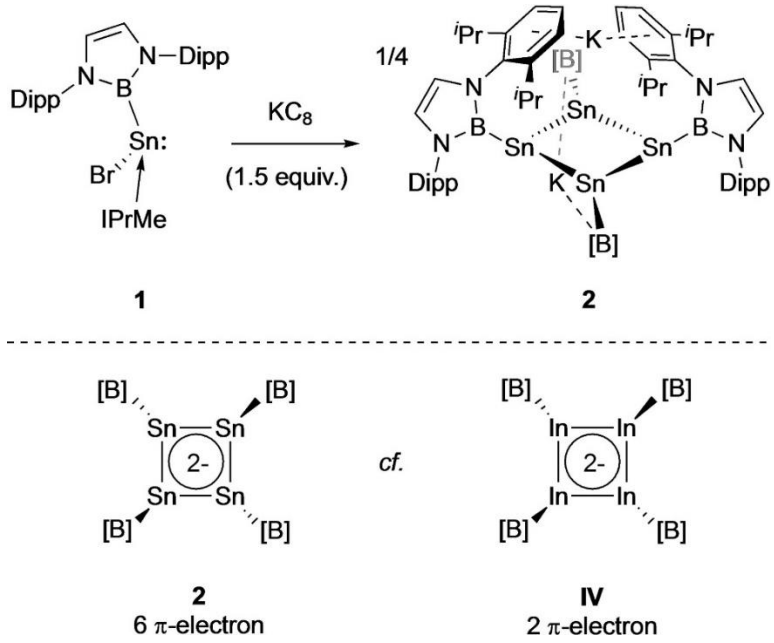

Scheme 4.1: Reduction of NHC-supported boryl-tin bromide **1** with 1.5 equiv of potassium graphite to generate cyclic tetratin tetraboryl system $K_2[Sn_4\{B(NDippCH)_2\}_4]$ (**2**). ([B] = $\{B(NDippCH)_2\}$; Dipp = $C_6H_3{}^{i}Pr_2$-2,6).

Results and Discussion

The reduction of $\{(HCDippN)_2B\}Sn(IPrMe)Br$ (**1**; Dipp = 2,6-$^{i}Pr_2C_6H_3$; IPrMe = $C\{(N^{i}PrCMe)_2\}$)[15] with 1.5 equiv. of potassium graphite leads to the formation of a diamagnetic product characterized by a single ^{11}B NMR resonance at δ_B = 49 ppm. The ^{1}H NMR spectrum suggests a lower symmetry for the ligand scaffold, showing four ^{i}Pr CH_3 doublets and two CH septets, in addition to two mutually coupled doublets for the CH groups of the boryl heterocycle. Black crystals grown from toluene/pentane solution allow definitive characterization of the product to be achieved by X-ray crystallography, and shows that it is the cyclic tetratin tetraboryl system $K_2[Sn_4\{B(NDippCH)_2\}_4]$ (**2**) (**Figure 4.1** and **Scheme 4.1**).

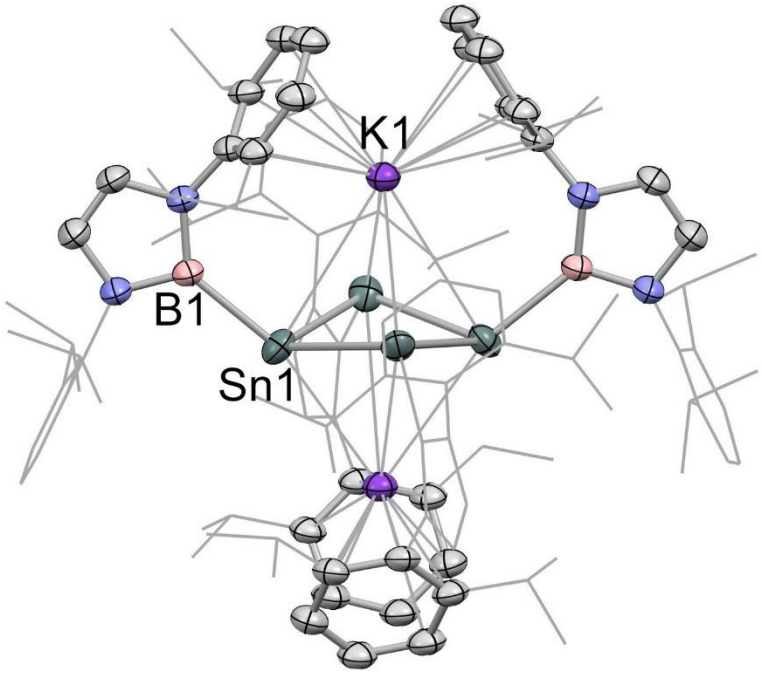

Figure 4.2: Molecular structure of $K_2[Sn_4\{B(NDippCH)_2\}_4]$ (**2**) in the solid state as determined by X-ray crystallography. Hydrogen atoms omitted and selected groups shown in wireframe format for clarity; thermal ellipsoids drawn at the 40% probability level. Key bond lengths (Å) and angles (°): Sn–Sn 2.9018(9), 2.9010(6); Sn–B 2.306(5); Sn···K 3.915, 3.510; Sn–Sn–Sn 88.41(3); centroid-Sn-B 132.8.

The solid-state structure of **2** features an approximately square array of four (symmetry-related) tin atoms, with each metal centre being additionally bound to a single terminal boryl ligand (*d*(Sn–Sn) = 2.9018(9), 2.9010(6) Å, *d*(Sn–B) = 2.306(5) Å), and the internal Sn–Sn–Sn angles being close to 90° (88.41(3)°). The structure is completed by two K^+ counter-ions positioned above and below the Sn_4 unit (K···Sn distances: 3.915 and 3.510 Å), which are sandwiched between the flanking Dipp aryl rings of diagonally opposite boryl ligands (with K···arene contacts in the range 3.088–3.413 Å). The Sn_4 unit is puckered, with each tin atom lying 0.24 Å out of the least-squares plane, such that the Sn_4 centroid-Sn-B angles are non-linear (132.8°), and alternate boron atoms are positioned above/below the approximate Sn_4 plane. As a consequence each tin centre is pyramidalized, with the sum of the Sn–Sn–Sn and Sn–Sn–B angles being 318.6°. By means of comparison, the corresponding angles in tetra-silicon system **II** reported by Sekiguchi and co-workers sum to 341/326° (for the two distinct silicon centres).[13]

In a broader sense, **2** represents the formal dimer of the radical anion $[Sn_2\{B(NDippCH)_2\}_2]^{\cdot-}$, the terphenyl analogue of which, $[Sn_2Ar^{Dipp}{}_2]^{\cdot-}$, has been reported by Power and co-workers ($Ar^{Dipp} = C_6H_3Dipp_2$-2,6).[16] From a synthetic perspective, it is noteworthy that **2** can also be formed by one-electron oxidation of $[Sn_2\{B(NDippCH)_2\}_2]^{2-}$ [15] using trityl oxidants. From a structural viewpoint, the underlying difference between tetranuclear **2**, and the dimeric terphenyl systems presumably relates to the smaller steric profile of the boryl ligand. The longer Sn–B bond (*cf.* Sn–C) and five- (rather than six-) membered central heterocycle cause the pendant Dipp groups to exert a smaller steric profile at the tin centre.

Geometrically, the structure of **2** bears a close resemblance to the corresponding indium compound $K_2[In_4\{B(NDippCH)_2\}_4]$ (**IV**, **Scheme 4.1**), which possesses four electrons fewer within a less puckered $[In_4\{B(NDippCH)_2\}_4]^{2-}$ unit.[14j] In the indium system, the four (symmetry-equivalent) metal centres are less significantly displaced from the least-squares plane (0.12 Å), and Nucleus Independent Chemical Shift calculations are consistent with moderately aromatic character attributable to the two π-electrons within the cyclic manifold. The corresponding unit in **2** could also give rise to Hückel aromaticity on the basis of the six π-electron count, and we therefore set out to examine the electronic structure of **2** by quantum chemical methods.

CASSCF calculations (Figure **S 4.1** and Table **ST 4.3**) are consistent with the singlet ground state implied experimentally for **2** (with a singlet-triplet gap of 0.50 eV); the associated HOMO-LUMO separation is 1.29 eV. DFT calculations (r^2-scan def2-TZVP level) reveal that π-symmetry orbitals in **2** are primarily defined by the in-phase HOMO-5 (analogous to Π_1 for $[CBD]^{2-}$) and by a near-degenerate pair (HOMO and HOMO-1) of essentially equivalent form reminiscent of Π_2/Π_3 for $[CBD]^{2-}$, but twisted due to the non-planar nature of the Sn_4 unit (**Figure 4.3**). The highest energy molecular orbital possessing Sn−Sn σ-bonding character is the HOMO-2. Nucleus independent chemical shift (NICS) values have been calculated for **2** (NICS(0) = −0.28, NICS(1) = −3.17) and can be compared with the values calculated using the same method for 'moderately

aromatic' $K_2[In_4\{B(NDippCH)_2\}_4]$ (**IV**; NICS(0) = −7.52, NICS(1) = −8.61), implying that the degree of aromatic character in **2** is minimal. This finding is consistent with the non-aromatic nature of the 6π-electron silicon and germanium systems **II** and **III**, and presumably reflects the markedly pyramidal nature of the tin centres in **2**. The contrasting signs of the curvature of the *z*-component of the electron density at the ring critical points (RCPs) in tetra-indium system **IV** (-0.087 e $Å^{-5}$) and tetra-tin compound **2** (+0.024 e $Å^{-5}$) also provide further evidence for their aromatic/non-aromatic nature.

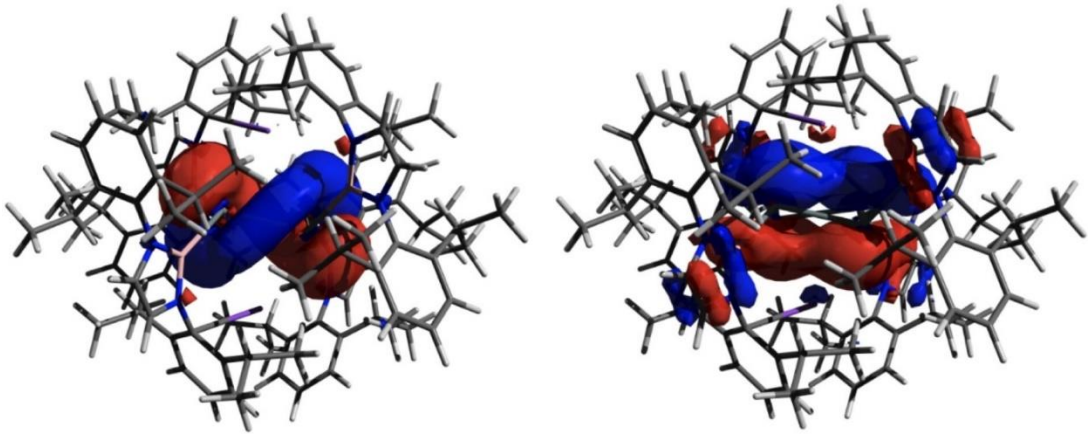

Figure 4.3: Electron density surfaces of key molecular orbitals for $K_2[Sn_4\{B(NDippCH)_2\}_4]$ (**2**) calculated by DFT (r^2-scan def2-TZVP level): (left) HOMO; (right) HOMO-5.

Given the potential structural role of the K^+ ions in **2** (and related systems such as **II** and **III**) we wanted to probe the consequences of cation abstraction. As such, the reaction of **2** with two equiv. of 2.2.2-cryptand in benzene-d_6 solution was investigated. The product (**3**) precipitates as deep purple crystals and can be shown by X-ray crystallography to consist of a tetrahedral Sn_4 cluster $[Sn_4\{B(NDippCH)_2\}_2]^{2-}$ featuring two boryl ligands bridging opposite Sn–Sn edges, together with two $[K(2.2.2\text{-crypt})]^+$ counter-cations (**Scheme 4.2** and **Figure 4.4**). **3** can be viewed as a *nido* cluster based on the Wade-Mingos cluster electron counting rules (6 PSEPs), and results from the loss of two (formally charge neutral) boryl ligands - which are observed *in situ* (by ^1H NMR) as $(HCDippN)_2BD$. The formation of **3** from **2** under these conditions implies that the inclusion of the K^+ cations is essential to the structural integrity of **2**. At a broader level,

this finding is consistent with computational studies of the $[CBD]^{2-}$ system, which suggest that electron loss should be extremely facile for the gas-phase (cation-free) species.[3]

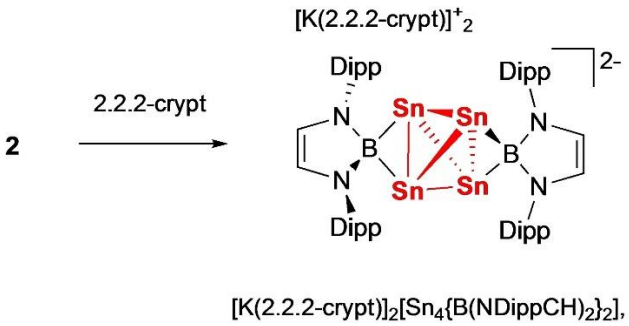

Scheme 4.2: Cation abstraction from **2** by 2.2.2-crypt leading to formation of the nido cluster $[K(2.2.2\text{-crypt})]_2[Sn_4\{B(NDippCH)_2\}_2]$ (**3**).

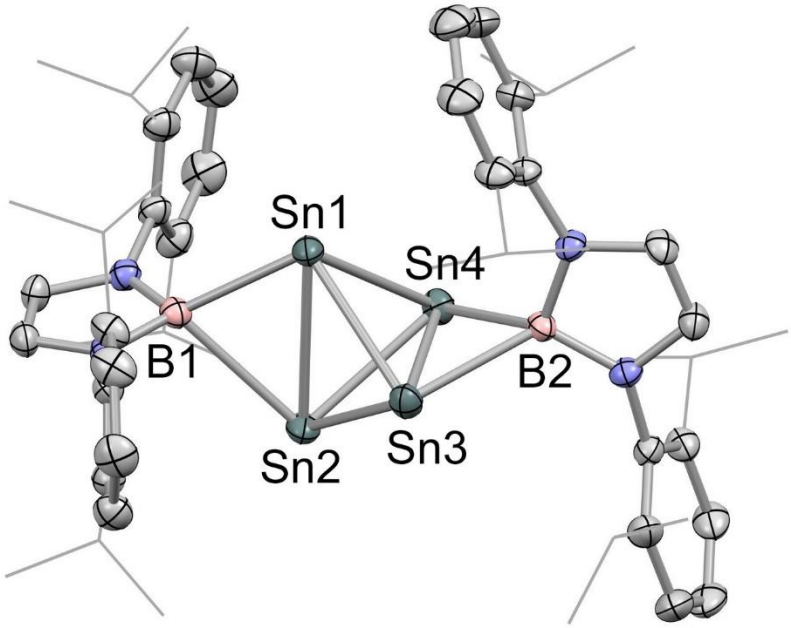

Figure 4.4: Molecular structure of the dianionic component of $[K(2.2.2\text{-crypt})]_2[Sn_4\{B(NDippCH)_2\}_2]$ (**3**) in the solid state as determined by X-ray crystallography. Cations and hydrogen atoms omitted and selected groups shown in wireframe format for clarity; thermal ellipsoids drawn at the 40% probability level. Key bond lengths (Å): Sn–Sn 3.1279(6), 2.8911(7), 2.8729(7), 2.8184(6), 2.8414(6), 3.1108(8); Sn–B1 2.737(6), 2.370(6); Sn–B2 2.618(5), 2.468(5).

The oxidation of **2** was also examined with the possibility of accessing related neutral (or even cationic) Sn_4 systems. However, in line with other reports of charge neutral systems of the stoichiometry $[Sn\{B(NDippCH)_2\}]_n$[15] (and in contrast to the related germanium systems, for which the digermavinylidene, $\{(HCDippN)_2B\}_2GeGe$, can be isolated),[14h] disproportionation is

observed in the presence of a range of oxidizing agents, leading to the formation of a 1:2 mixture of the cluster $Sn_6\{B(NDippCH)_2\}_4$ and the bis(boryl)stannylene (**Scheme 4.3**).[14f]

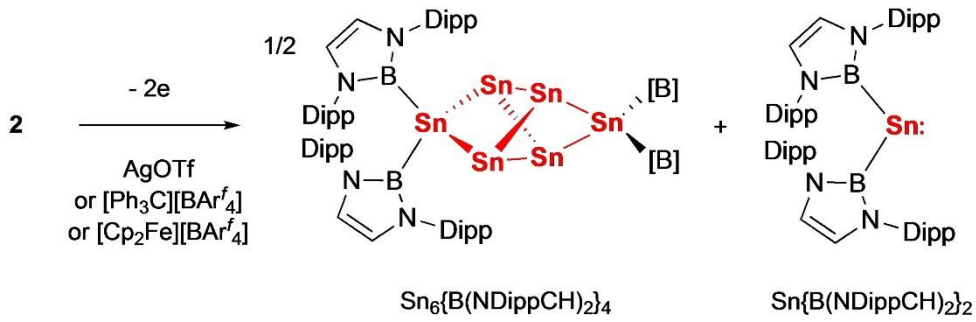

Scheme 4.3: Oxidation of **2** leading to formation of a 1:2 mixture of $Sn_6\{B(NDippCH)_2\}_4$ and $Sn\{B(NDippCH)_2\}_2$.[15]

Finally, we examined the behaviour of **2** in the presence of protic reagents, with a view to providing a route to the parent neutral cyclobutene analogue, and also as a probe of sites of electron density within the dianionic $[Sn_4\{B(NDippCH)_2\}_4]^{2-}$ framework. Reaction of **2** with benzoic acid in benzene solution leads to the formation of dark purple crystals of the doubly protonated product $Sn_4\{B(NDippCH)_2\}_4H_2$ (**4**) in good (ca. 60 %) yield. **4** has been characterized by NMR spectroscopy and X-ray crystallography (**Scheme 4.4** and **Figure 4.5**). The (single) hydride signal appears at 4.25 ppm with two sets of satellites being resolved due to coupling to the ^{119}Sn and ^{117}Sn nuclei ($J_{119Sn-H}$ = 53.9 Hz, $J_{117Sn-H}$ = 45.6 Hz). The solid state structure shows a short Sn(1)–Sn(2) distance (2.6737(7) Å) and three longer Sn–Sn distances (2.8045(7), 2.8232(5), 2.8333(5) Å), consistent with a structure featuring a formal Sn=Sn double bond and three single bonds, respectively (**Figure 4.5**). The B(1)Sn(1)Sn(2)B(2) unit approaches coplanarity (torsion angle = 28.1°), while the B(3)Sn(3)Sn(4)B(4) unit features a much wider torsion angle of 125.0°. While the location of the tin-bound hydrogen atoms by X-ray crystallography must be viewed critically, the alignment of the boryl groups at Sn(3) and Sn(4) is consistent with the projection of the two Sn–H bonds either side of the Sn_4 plane, and with the overall C_2 symmetry implied by solution phase NMR measurements.

From a synthetic perspective, protonation in this (1,2-*trans*) fashion is consistent (i) with a 1,2-localization of negative charge in **2** in a manner similar to that proposed by Sekiguchi and co-workers for Si_2Ge_2 system **III**,[12,13] and (ii) with the steric bulk of the boryl substituents favouring an anticlinal rather than eclipsed conformation about the Sn(3)–Sn(4) bond. Consistently, Natural Resonance Theory (NRT) calculations show that the primary resonance contributions (>80 %) involve a Sn=Sn double bond and 1,2-localized negative charges (**Scheme 4.4** and Figure **S 4.2**); this model of electronic structure also provides a rationale for the non-aromatic character of **2** determined by the NICS calculations.

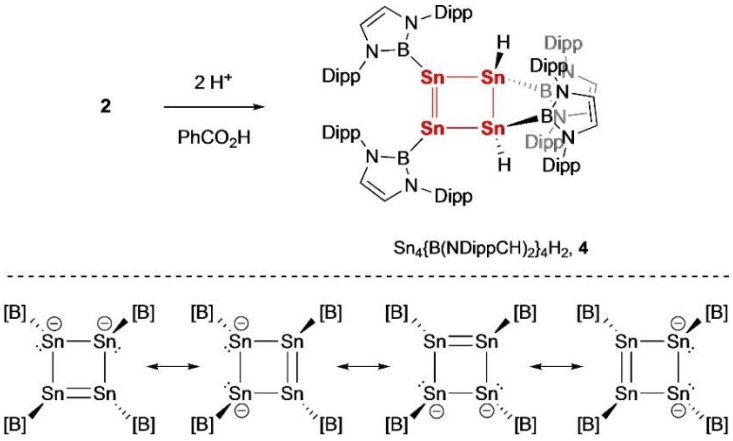

Scheme 4.4: (upper) Protonation of the tin core of $K_2[Sn_4\{B(NDippCH)_2\}_4]$ (**2**), yielding $Sn_4\{B(NDippCH)_2\}_4H_2$ (**4**). (lower) Major contributing resonance structures for $[Sn_4\{B(NDippCH)_2\}_4]^{2-}$.

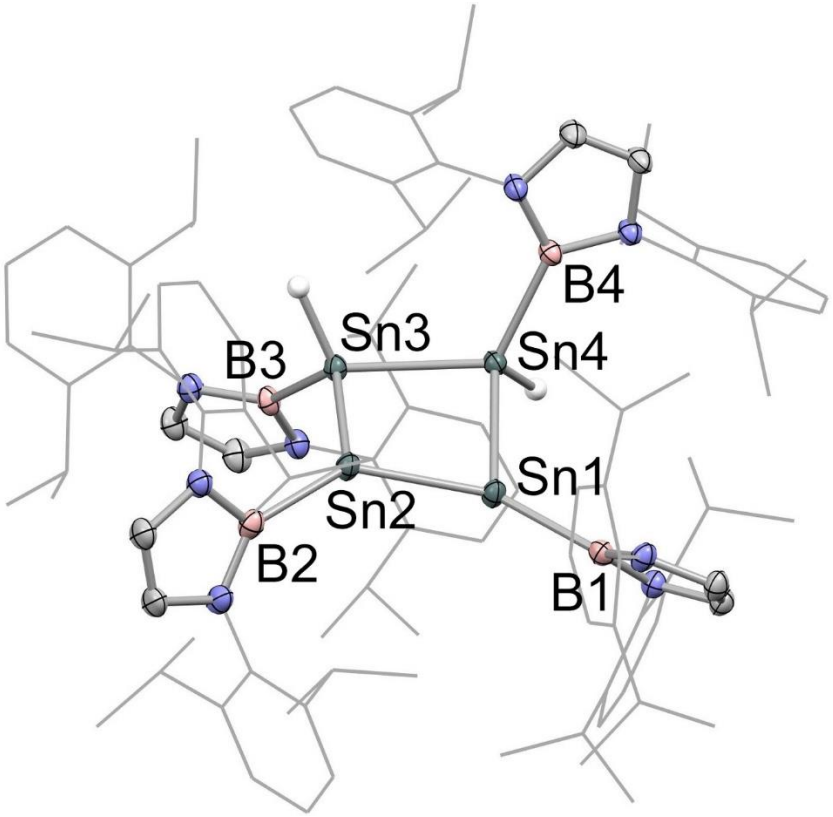

Figure 4.5: Molecular structure of $Sn_4\{B(NDippCH)_2\}_4H_2$ (**4**) in the solid state as determined by X-ray crystallography. Most hydrogen atoms omitted and selected groups shown in wireframe format for clarity; thermal ellipsoids drawn at the 40% probability level. Key bond lengths (Å), angles (°) and torsions (°): Sn–Sn 2.6737(7), 2.8232(5), 2.8045(7), 2.8333(5); Sn–B 2.280(4), 2.273(3), 2.269(3), 2.262(4); Sn–Sn–Sn 91.01(2), 89.12(2), 88.18(2), 86.77(2); B1–Sn1–Sn2–B2 28.1; B3–Sn3–Sn4–B4 125.0.

Conclusions

In conclusion, we have shown that the controlled reduction of the boryl-substituted SnII precursor {(HCDippN)$_2$B}Sn-(IPrMe)Br with 1.5 equivalents of potassium graphite leads to the generation of the cyclic tetra-tin tetra-boryl system $K_2[Sn_4\{B(NDippCH)_2\}_4]$, a homo-metallic heavier analogue of the cyclobutadiene dianion. This system is non-aromatic, with the primary contributing resonance structures involving a Sn=Sn double bond and 1,2-localized negative charges. Attempted abstraction of the K+ cations or oxidation lead to contraction or cleavage of the Sn4 unit, respectively, while protonation generates the neutral dihydride 1,2-$Sn_4\{B(NDippCH)_2\}_4H_2$ in a manner consistent with the predicted charge distribution. Interestingly, although the 6π-system $[Sn_4\{B(NDippCH)_2\}_4]^{2-}$, and 2π-electron systems $[In_4\{B(NDippCH)_2\}_4]^{2-}$ and (hypothetical) $[Sn_4\{B(NDippCH)_2\}_4]^{2+}$ conform to the Hückel 4n+2

stipulation for aromaticity, only the two-electron systems appear to show aromatic character (for the $[Sn_4\{B(NDippCH)_2\}_4]^{2+}$ dication: NICS(0) = -9.46; NICS(1) = -11.76 (1)).17 Such a finding is consistent with the key electronic structure-defining role predicted for enhanced Coulombic repulsions in 6π electron systems bearing a double negative charge.[3,18]

Characterizing data

Synthesis of Novel Compounds

*K2[Sn4{B(NDippCH)2}4] (**2**):*

A mixture of $\{(HCDippN)_2B\}Sn(IPrMe)Br$ (0.20 g, 0.26 mmol) and KC_8 (0.055 g, 0.41 mmol) was dissolved/suspended in toluene (5 mL) at room temperature. The reaction mixture was stirred and monitored by NMR until most of the starting material turned into the desired product. The reaction mixture was then filtered into a Schlenk tube and concentrated. Pentane (5 mL) was then added and the tube was stored at 4 °C overnight to give black crystals suitable for X-ray crystallography, which were isolated, washed with small amount of cold (-20 °C) pentane and dried in vacuo. Yield: 0.051 g (36.4 %).

Spectrocopic data: ^{1}**H** NMR (400 MHz, C_6D_6, 298 K): δ_H 0.64 (d, J_{HH} = 6.8 Hz, 12H, CH(C*H*$_3$)$_2$ of Dipp), 1.15 (d, J_{HH} = 6.8 Hz, 12H, CH(C*H*$_3$)$_2$ of Dipp), 1.39 (d, J_{HH} = 6.8 Hz, 12H, CH(C*H*$_3$)$_2$ of Dipp), 1.62 (d, J_{HH} = 6.8 Hz, 12H, CH(C*H*$_3$)$_2$ of Dipp), 3.45 (sept, J_{HH} = 6.8 Hz, 4H, C*H*(CH$_3$)$_2$ of Dipp), 3.60 (sept, J_{HH} = 6.8 Hz, 4H, C*H*(CH$_3$)$_2$ of Dipp), 6.04 and 6.36 (d, J_{HH} = 2.2 Hz, 4H, C*H* of boryl), 6.73-6.81 (m, 6H, Ar*H* of Dipp···K), 7.20-7.32 (m, 6H, Ar*H* of Dipp).^{11}**B{^{1}H}** NMR (128 MHz, C_6D_6, 298 K): δ_B 49.4.^{13}**C** NMR (126 MHz, C_6D_6, 298 K) δ_C 24.8, 25.3, 25.8 and 26.2 (CH(*C*H$_3$)$_2$ of Dipp), 28.6 and 28.8 (*C*H(CH$_3$)$_2$ of Dipp), 122.6 (*C*H of boryl), 123.5 and 123.6 (*m*-Ar of Dipp), 123.7 and 123.8 (*p*-Ar of Dipp), 144.1 and 144.2 (*o*-Ar of Dipp), 147.0 and 148.7 (*i*-Ar of Dipp). **Elemental microanalysis:** $C_{52}H_{72}B_2KN_4Sn_2$ Calc: C 59.41 %, H 6.90 %, N 5.33 %; Meas: C 59.58 %, H 7.27 %, N 5.34 %. **UV-Vis** (methylcyclohexane): λ_{max} = 432 nm, ε = 10,100 L mol^{-1} cm^{-1}.

*[K(2.2.2-crypt)]2[Sn4{B(NDippCH)2}2] (**3**):*

To a mixture of **2** (5 mg, 0.002 mmol) and 2,2,2-cryptand (1.8 mg, 0.004 mmol) was added C_6D_6 (0.3 mL). The colour of the solution immediately turned pale and dark purple crystals precipitated, which were suitable for X-ray crystallography. The crystals were isolated, washed with a small amount of pentane and dried in vacuo. Yield: 2.5 mg, (50.5 %). **3** is resolutely insoluble in compatible solvents, so NMR spectra could not be obtained.

*Sn4{B(NDippCH)2}4H2 (**4**):*

To a mixture of **2** (20 mg, 0.019 mmol) and $PhCO_2H$ (2.3 mg, 0.019 mmol) was added benzene (5 mL). The solution was stirred for 10 min and dried under vacuum to remove all volatiles. The residues were then extracted into pentane and concentrated to about half of the original volume, stored at – 30 °C to afford dark purple small crystals which were suitable for crystallography. Yield: 12 mg (62.3 %).

Spectrocopic data: **^{1}H** NMR (500 MHz, C_6D_6, 298 K): δ_H 0.40 (d, J_{HH} = 6.8 Hz, 6H, CH(C*H*$_3$)$_2$ of Dipp), 0.57 (d, J_{HH} = 6.8 Hz, 6H, CH(C*H*$_3$)$_2$ of Dipp), 0.99 (d, J_{HH} = 6.8 Hz, 6H, CH(C*H*$_3$)$_2$ of Dipp), 1.10 (dd, J_{HH} = 6.8, 2.0 Hz, 12H, CH(C*H*$_3$)$_2$ of Dipp), 1.21 (m, 48H, CH(C*H*$_3$)$_2$ of Dipp), 1.31 (d, J_{HH} = 6.8 Hz, 6H, CH(C*H*$_3$)$_2$ of Dipp), 1.38 (dd, J_{HH} = 6.8, 2.0 Hz, 12H, CH(C*H*$_3$)$_2$ of Dipp), 2.53, 2.76, 2.78, 2.93, 3.09, 3.14, 3.31 and 3.48 (sept, J_{HH} = 6.8 Hz, 2H, C*H*(CH$_3$)$_2$ of Dipp), 4.25 (t, J_{HSn119} = 53.9 Hz, J_{HSn117} = 45.6 Hz, 2H, Sn*H*), 6.03, 6.15, 6.16 and 6.24 (d, J_{HH} = 2.0 Hz, 2H, C*H* of boryl), 6.85 (d, J_{HH} = 7.6 Hz, 2H, *p*-Ar*H*), 7.07-7.19 (m, 6H, *p*-Ar*H*), 7.21-7.35 (m, 16H, *m*-Ar*H*). **^{11}B{^{1}H}** NMR (128 MHz, C_6D_6, 298 K): δ_B 32.2 ([B]SnH), 44.9 ([B]Sn).

^{13}C{^{1}H} NMR (126 MHz, C_6D_6, 298 K): δ_C 23.8, 23.9, 24.4, 24.5, 25.0, 25.2, 25.4 and 25.6 (CH(<u>C</u>H$_3$)$_2$ of Dipp), 25.9, 26.2, 26.6, 26.7, 26.8, 27.0, 27.3, 27.5, 27.9, 27.9, 28.1, 28.4, 28.5, 28.6, 28.7 and 29.3, (<u>C</u>H(CH$_3$)$_2$ of Dipp), 119.8, 122.8, 123.1 and 123.4 (<u>C</u>H of boryl), 123.6, 123.7, 123.8, 123.9, (*p*-Ar of Dipp), 124.0, 124.1, 124.2 and 125.1 , (*m*-Ar of Dipp), 139.8, 140.0, 140.2, 141.4, (*o*-Ar

of Dipp), 145.5, 145.7, 145.9, 146.2, 146.6, 146.8, 147.1 and 147.1 (*i*-Ar of Dipp). **UV-Vis** (methylcyclohexane): λ_{max} = 529 nm, ε = 2,240 L mol^{-1} cm^{-1}.

Computational Details

General details:

All computational work reported here was performed using ORCA (Revision 5.0.3).[19] The meta-generalized-gradient approximation (mGGA) functional R2-SCAN[20] was employed in conjunction with the Def2-TZVPPm[21] basis set with the D4 dispersion correction,[22] and employing the geometrical counterpoise correction gCP[23] (together known as the R2SCAN-3c method).[21] The nature of the stationary points (minima) was confirmed by full frequency calculations, and are characterized by zero imaginary frequencies.

Aromaticity indices

Nuclear independent chemical shift (NICS[24] calculations where performed with the R2-SCAN functional in conjunction with the Def2-TZVP basis set and D4 dispersion correction.[25] Ring Critical Point (RCP) properties;[26] electron density (ρ) and curvature perpendicular to the ring ($\lambda_{\sigma 3}$), and Multicentre Index (MCI) calculations [27] were carried out using the optimised electronic structure from the R2-SCAN-3C method using the Multiwfn program.[28] RCP properties are strictly not comparable between rings of different elements however the Sn rings can all be compared to one another.[29] Larger values of ρ and negative $\lambda_{\sigma 3}$ have been shown to correspond to aromatic species. MCI is necessarily ring size depended however has been normalised such that it is comparable to benzene by the expression $-|MCBO|^{1/n}$.[30]

ST 4.1: Aromaticity indices in a.u.

	NICS(ppm)		RCP		MCI	
	0	**1**	**ρ**	**$\lambda_{\sigma 3}$**	**MCI**	**Normalised MCI**
K_2Sn_4	-3.167	-0.275	0.091729116	0.023823206	-0.0282983972	-0.4101478691
K_2In_4	-7.523	-8.608	0.096298004	-0.086809507	0.0601362506	0.4952039347
$[Sn_4]^{2+}$	-9.460	-11.760	0.095304494	-0.10364191	0.0153103166	0.3517596679
H_2Sn_4	-4.989	-4.826	0.097114984	-0.036569265	0.0040599670	0.2524239897
C_6H_6	-7.813	-9.813	0.137790173	-0.404925105	0.0823792309	0.6596338827

CASSCF calculations

The small HOMO-LUMO gap (0.8454 eV) calculated using the R2-SCAN-3c method led us to explore multi-configurational methods to probe further the electronic structure of **2**. CASSCF (6,4) was performed on the Hückel type *p* orbitals based on the natural MP2 orbitals of system **2** using the geometry from the R2-SCAN-3c method. Orbitals **A**-**D** show the CASSCF orbitals; significant population of the complete out-of-phase orbital D (1.32 e) was found with 15.3% of the ground state seeing this orbital filled. The CASSF "HOMO-LUMO gap" (the difference in energy between **C** and **D**) is 1.2898 eV.

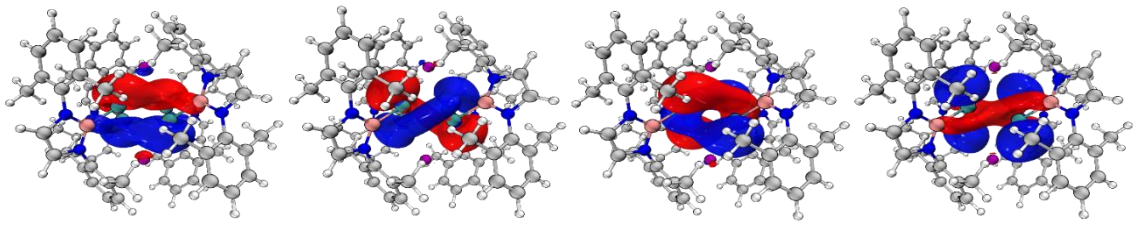

S 4.1: CASSF active orbitals with iso-values of 0.02.

ST 4.2: CASSCF density matrix.

	A	B	C	D
A	1.759837	0	0	0
B	0	1.513581	0	0
C	0	0	1.399572	0
D	0	0	0	1.327010

ST 4.3: Root 0 composition of CASSCF calculation.

%	A	B	C	D
84.352	2	2	2	0
8.115	2	2	0	2
7.185	2	0	2	2

NRT calculations

Natural resonance theory calculations were performed using the NBO7 program,[31] using the R2-SCAN-3c methodology. A model system was used to allow convergence of the NRT module (in which the B-bound Dipp groups were replaced by methyl groups) and employing a constrained optimisation fixing the K, Sn, B, N positions.

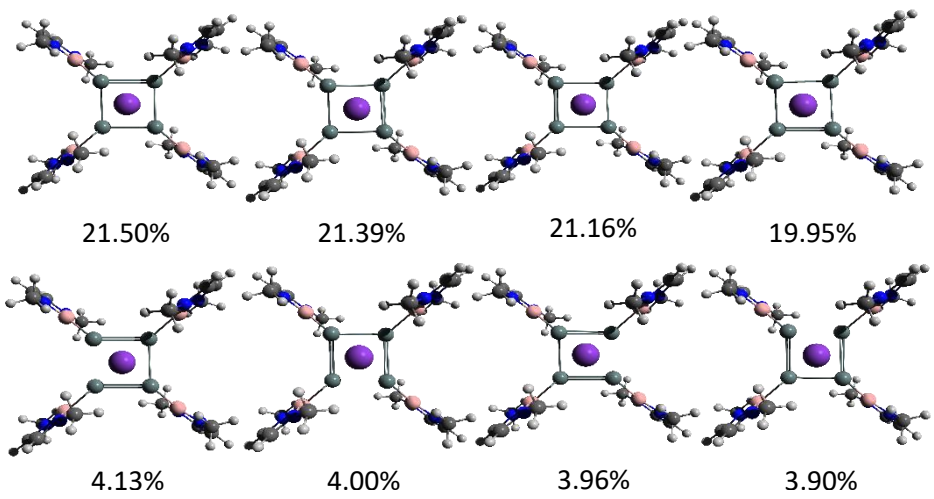

S 4.2: Composition of the NRT resonance forms and their relative contributions.

References

1 P. V. S. Schleyer *Chem. Rev.,* **2001**, *101*, volume 5.

2 K. Ota, R. Kinjo, *Chem. Soc. Rev.* **2021**, *50*, 10594-10673.

3 T. Sommerfeld, *J. Am. Chem. Soc.* **2002**, *124*, 1119-1124.

4 S. Feuerbacher, L. S. Cederbaum, *J. Am. Chem. Soc.* **2003**, *125*, 9531-9537.

5 B. A. Hess, C. S. Ewig, L. J. Schaad, *J. Org. Chem.* **1985,** *50*, 5869-5871.

6 G. Van Zandwijk, R. A. J. Janssen, H. M. Buck, *J. Am. Chem. Soc.* **1990**, *112*, 4155-4164.

7 A. J. Kos, P. v. R. Schleyer, *J. Am. Chem. Soc.* **1980**, *102*, 7928-7929.

8 M. Balci, M. L. McKee, P. v. R. Schleyer, *J. Phys. Chem. A* **2000**, *104*, 1246-1255.

9 J. S. McKennis, L. Brener, J. R. Schweiger, R. Pettit, *J. Chem. Soc., Chem. Commun.* **1972**, 365-366.

10 P. J. Garratt, R. Zahler, *J. Am. Chem. Soc.* **1978**, *100*, 7753-7754.

11 G. Boche, H. Etzrodt, M. Marsch, W. Thiel, *Angew. Chem. Int. Ed. Engl.* **1982**, *21*, 132-133.

12 A. Sekiguchi, T. Matsuo, H. Watanabe, *J. Am. Chem. Soc.* **2000**, *122*, 5652-5653.

13 V. Y. Lee, K. Takanashi, T. Matsuno, M. Ichinohe, A. Sekiguchi, *J. Am. Chem. Soc.* **2004**, *126*, 4758-4759.

14 (a) A. V. Protchenko, K. H. Birjkumar, D. Dange, A. D. Schwarz, D. Vidovic, C. Jones, N. Kaltsoyannis, P. Mountford, S. Aldridge, *J. Am. Chem. Soc.* **2012**, *134*, 6500-6503; (b) A. V. Protchenko, D. Dange, J. Harmer, C. Y. Tang, A. D. Schwarz, M. J. Kelly, N. Phillips, K. H. Birjkumar, C. Jones, N. Kaltsoyannis, P. Mountford, S. Aldridge, *Nature Chem.* **2014**, *6*, 315-319; (c) A. V. Protchenko, D. Dange, A. D. Schwarz, M. P. Blake, C. Jones, P. Mountford, S. Aldridge, *J. Am. Chem. Soc.* **2014**, *136*, 10902-10905; (d) A. V. Protchenko, M. P. Blake, A. D. Schwarz, C. Jones, P. Mountford, S. Aldridge, *Organometallics* **2015**, 34, 2126-2129; (e) D. Dange, A. Davey, J. A. B. Abdalla, S. Aldridge, C. Jones, *Chem. Commun.* **2015**, *51*, 7128-7131; (f) A. V. Protchenko, J. I. Bates, L. M. A. Saleh, M. P. Blake, A. D. Schwarz, E. L. Kolychev, A. L. Thompson, C. Jones, P. Mountford, S. Aldridge, *J. Am. Chem. Soc.* **2016**, *138*, 4555-4564; (g) M. Usher, A. V. Protchenko, A. Rit, J. Campos, E. L. Kolychev, R. Tirfoin, S. Aldridge, *Chem.-Eur. J.* **2016**, *22*, 11685-11698; (h) A. Rit, J. Campos, H. Niu, S. Aldridge, *Nature Chem.* **2016**, *8*, 1022-1026; (i) D. Dange, C. P. Sindlinger, S. Aldridge, C. Jones, *Chem. Commun*. **2017**, *53*, 149-152; (j) A. V. Protchenko, J. Urbano, J. A. B. Abdalla, J. Campos, D. Vidovic, A. D. Schwarz, M. P. Blake, P. Mountford, C. Jones, S. Aldridge, *Angew. Chem. Int. Ed.* **2017**, *56*, 15098-15102; (k) A.V. Protchenko, P. Vasko, D. C. H. Do, J. Hicks, M. Á. Fuentes, C. Jones, S. Aldridge, *Angew. Chem. Int. Ed*. **2019**, *58*, 1808-1812; (l) A. V. Protchenko, P. Vasko, M. Á. Fuentes, J. Hicks, D. Vidovic, S. Aldridge, *Angew. Chem. Int. Ed*. **2021**, *60*, 2064-2068.

15 X. Zheng, A. E. Crumpton, A. V. Protchenko, A. Heilmann, M. A. Ellwanger, S. Aldridge, *Chem. Eur. J.* **2023**, 29, e202203395.

16 L. Pu, A. D. Phillips, A. F. Richards, M. Stender, R. S. Simons, M. M. Olmstead, *J. Am. Chem. Soc.* **2003**, *125*, 11626-11636.

17 Recent examples of heavier group 14 analogues of $[CBD]^{2+}$: (a) S. Inoue, J. D. Epping, E. Irran, M. Driess, *J. Am. Chem. Soc.* **2011**, *133*, 8514-8517; (b) X. Sun, T. Simler, R. Yadav, R. Köppe, P. W. Roesky, *J. Am. Chem. Soc.* **2019**, *141*, 14987-14990.

18 Deposition numbers 2216379 (for **2**), 2216380 (for **3**) and 2216381 (for **4**) contain the supplementary crystallographic data for this paper. These data are provided free of charge by the joint Cambridge Crystallographic Data Centre and Fachinformationszentrum Karlsruhe. https://www.ccdc.cam.ac.uk/services/structures?id=doi:10.1002/chem.202300006

19 (a) F. Neese, *WIREs Computational Molecular Science* **2012**, *2*, 73-78; (b) F. Neese, F. Wennmohs, U. Becker, C. Riplinger, *J. Chem. Phys.* **2020**, *152*, 224108; (c) F. Neese, *WIREs Computational Molecular Science* **2018**, *8*, e1327.

20 (a) J. W. Furness, A. D. Kaplan, J. Ning, J. P. Perdew, J. Sun, *J. Phys. Chem. Lett.* **2020**, *11*, 8208-8215; (b) J. W. Furness, A. D. Kaplan, J. Ning, J. P. Perdew, J. Sun, *J. Phys. Chem. Lett.* **2020**, *11*, 9248-9248.

21 S. Grimme, A. Hansen, S. Ehlert, J.-M. Mewes, *J. Chem. Phys.* **2021**, *154*, 064103.

22 (a) E. Caldeweyher, C. Bannwarth, S. Grimme, *J. Chem. Phys.* **2017**, *147*, 034112; (b) E. Caldeweyher, S. Ehlert, A. Hansen, H. Neugebauer, S. Spicher, C. Bannwarth, S. Grimme, *J. Chem. Phys.* **2019**, *150*, 154122.

23 H. Kruse, S. Grimme, *J. Chem. Phys.* **2012**, *136*, 154101.

24 P. V. R. Schleyer, C. Maerker, A. Dransfeld, H. Jiao, N. J. R. Van Eikema Hommes, *J. Am. Chem. Soc.* **1996**, *118*, 6317-6318.
25 (a) F. Weigend, *Phys. Chem. Chem. Phys.* **2006**, *8*, 1057; (b) F. Weigend, R. Ahlrichs, *Phys. Chem. Chem. Phys.* **2005**, *7*, 3297; (c) S. Ehlert, U. Huniar, J. Ning, J. W. Furness, J. Sun, A. D. Kaplan, J. P. Perdew, J. G. Brandenburg, *J. Chem. Phys.* **2021**, *154*, 061101.
26 S. T. Howard, T. M. Krygowski, *Can. J. Chem.* **1997**, *75*, 1174-1181.
27 (a) M. Giambiagi, M. S. De Giambiagi, K. C. Mundim, *Struct. Chem.* **1990**, *1*, 423-427; (b) M. Giambiagi, M. Segre De Giambiagi, C. D. Dos Santos Silva, A. Paiva De Figueiredo, *Phys. Chem. Chem. Phys.* **2000**, *2*, 3381-3392.
28 T. Lu, F. Chen, *J. Comp. Chem.* **2012**, *33*, 580-592.
29 S. Noorizadeh, E. Shakerzadeh, *Phys. Chem. Chem. Phys.* **2010**, *12*, 4742.
30 E. Matito, *Phys. Chem. Chem. Phys.* **2016**, *18*, 11839-11846.
31 J. K. B. E. D. Glendening, A. E. Reed, J. E. Carpenter, C. M. M. A. Bohmann, P. Karafiloglou, C. R. Landis, and F. Weinhold, Theoretical Chemistry Institute, University of Wisconsin Madison, **2018**.

Statement of Authorship

Title of Paper	Synthesis of Homo-metallic Heavier Analogues of Cyclobutene and the Cyclobutadiene Dianion
Publication Status	Published
Publication Details	X. Zheng, A. E. Crumpton, A. V. Protchenko, M. A. Ellwanger, A. Heilmann, S. Aldridge, *Chem. Eur. J.* 2023, 29, e202300006.

Student Confirmation

Student Name:	Agamemnon Elvis Crumpton	
Contribution to the Paper	Performed DFT calculations on the structures within the manuscript, investigated the aromaticity of these compounds and contributed to the discussion of the quantum chemical calculations in the manuscript.	
Signature 		Date 15/04/2024

Supervisor Confirmation

Supervisor name and title: Professor Simon Aldridge	
Supervisor comments I can confirm that the candidate's contribution to this paper is as described above.	
Signature 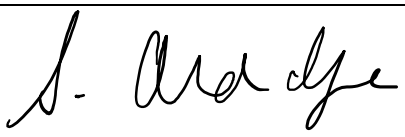	Date 18/4/2024

Chapter 5 - A Planar Per-borylated Digermene

Xiongfei Zheng , Agamemnon E. Crumpton , Mathias A. Ellwanger and Simon Aldridge*

Published in Chemical Communications: Dalton Trans. 2023, 52, 16591-16595

Author contributions

Xiongfei Zheng: Synthesised the novel compounds and collected characterisation data

Agamemnon E. Crumpton: Performed the quantum chemical calculations and solved the X-ray structure in the unpublished work

Mathias A. Ellwanger: Lead crystallographer.

Simon Aldridge: Corresponding author.

Manuscript was written by Simon Aldridge on the basis of the thesis chapter written by Xiongfei Zheng with contribution to the discussion of the quantum chemical calculations by Agamemnon E. Crumpton. Unpublished work written by Agamemnon E. Crumpton.

Abstract

A tetraboryl digermene synthesized by the reaction between a dianionic digermanide nucleophile and a boron halide electrophile is dimeric both in the solid state and in hydrocarbon solution. It features both a planar 'alkene-like' geometry for the Ge_2B_4 core, and an exceptionally short Ge=Ge double bond. These structural features are consistent with the known electronic properties of the boryl group, and with lowest energy (*in silico)* fragmentation into two triplet bis(boryl)germylene fragments.

Introduction

Carbenes and their heavier group 14 analogues (tetrylenes) have received considerable recent attention, not least because of their ability to activate small molecules such as H_2, CO and alkenes in 'transition-metal like' fashion.[1,2] The ambiphilic nature of two-coordinate systems of the type EX_2 (E = C-Pb), and the availability of frontier orbitals of both σ and π symmetry allow the possibility for synergistic interactions with small molecules which have both donor and acceptor properties.[3] As with *d*-block systems, the extent of such inter-actions is influenced significantly by the energies of the frontier orbitals, which in turn reflect factors such as the

identity of the group 14 element E, the X–E–X angle, and the electronic properties of the X-substituents. X groups featuring highly electronegative donor atoms and/or strong π-donor capabilities tend to lead to a stabilised σ symmetry orbital (typically the HOMO), a destabilised π orbital (often the LUMO, or an orbital close to it), and consequently a wide HOMO-LUMO energy gap.[3] On the other hand, boryl substituents (i.e. X = BR_2) offer the opposite scenario - namely a narrow HOMO-LUMO gap, brought about by the electropositive and non π-donor nature of the donor atom.[4] As such, boryl-substituted tetrylenes have shown unusually high levels of reactivity in the activation of molecules, being implicated in the first examples of both silylenes and stannylenes to oxidatively add H_2 (**I**-Si and **II**-Sn; Figure 5.1).[5,6]

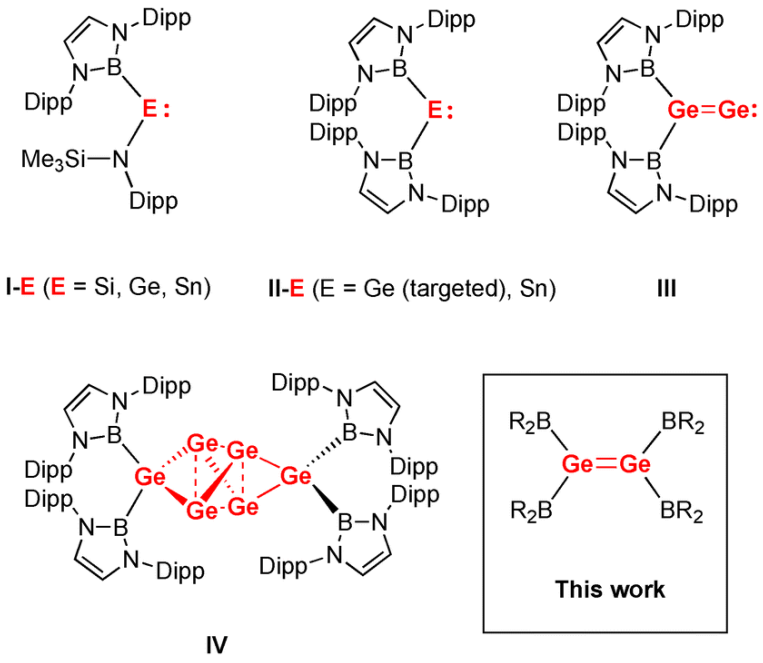

Figure 5.1: Boryl-substituted tetrylene and related systems of relevance to the current study.

Steric factors are also important in tetrylene systems - not only in influencing the magnitude of the X–E–X angle, but also their tendency towards dimerization to give ditetrelenes, X_2EEX_2.[7] These heavier alkene analogues typically adopt *trans*-bent C_{2h} skeletal geometries, which can formally be regarded as being constructed by the dimerization of two singlet EX_2

fragments (which become increasing stabilized with respect to the corresponding triplet state on descending group 14).[8]

Results and Discussion

Given the heightened reactivity shown by bis(boryl)-stannylene **II**, and the accessibility of digermavinylidene **III**,[9] we were interested here to explore strategies for the synthesis of the corresponding bis(boryl)germylene, **II**-Ge (**Figure 5.1**). In the event, the combination of an energetically accessible triplet state for the Ge(boryl)$_2$ fragment, allied to steric limitations in the boryl groups available synthetically, led to the isolation of the corresponding (planar) tetraboryl-digermene.

While the germanium (and silicon) analogues of the heteroleptic (amido)(boryl)stannylene Sn{N(SiMe$_3$)Dipp}(boryl) (**I**-Sn), are readily accessible,[5] attempts to synthesize Ge(boryl)$_2$ (**II**-Ge) via reactions of GeCl$_2$·L (L = dioxane, NHC) or Ge{N(SiMe$_3$)$_2$}$_2$ with two or more equivalents of (boryl)Li(thf)$_2$[10] proved unsuccessful in our hands (where boryl = -B(NDippCH)$_2$). In addition, the reaction of the hexa-germanium system Ge$_6$(boryl)$_4$ (**IV**)[11] with reducing agents such as KC$_8$, targeting Ge(boryl)$_2$ by liberation of the known tetrahedral cluster *nido*-[Ge$_4$]$^{4-}$,[12] also did not lead to the isolation of the desired germylene product. With this in mind, we turned our attention to an umpolung synthetic strategy, via the use of nucleophilic sources of the [(boryl)Ge]$^-$ fragment, with the idea of assembling a second Ge–B bond by reaction of M$_2$Ge$_2$(boryl)$_2$ (M = Group 1 metal)[9] with a boron-centred electrophile.

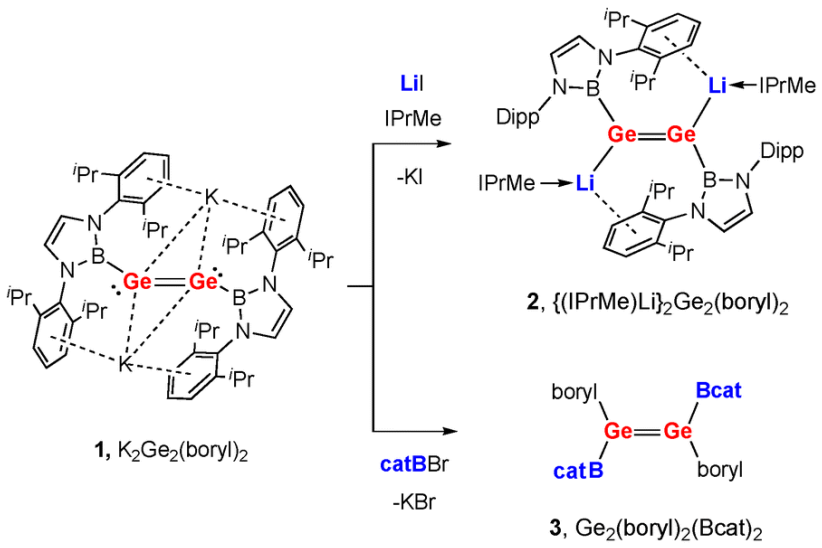

Scheme 5.1: Synthesis of lithiated and borylated derivatives of $K_2Ge_2(boryl)_2$ (**1**) via metathesis processes with LiI/IPrMe and CatBBr, respectively. (IPrMe = C{N(^{i}Pr)CMe}$_2$)

$K_2Ge_2(boryl)_2$ (**1**) is available via the exhaustive reduction of (boryl)Ge(IPrMe)Cl using KC_8,[9] and we sought to expand the range of nucleophilic group 1 metal digermanide derivatives by synthesizing a related lithium compound. However, rather than a reductive protocol starting from (boryl)Ge(IPrMe)Cl, the dilithium species $\{(IPrMe)Li\}_2Ge_2(boryl)_2$ (**2**) is most conveniently prepared from **1** by a salt metathesis reaction with lithium iodide, in the presence of the carbene IPrMe (**Scheme 5.1** and **Figure 5.2**).[‡] **2** can be obtained via this route in ca. 30% yield after recrystallization from toluene/hexane. Its solid-state structure, determined by X-ray crystallography, is based around a Ge_2 unit featuring two boryl groups arranged in 1,2-fashion (and *trans* to one another), with each germanium centre being additionally bound to a single lithium atom. Each lithium centre is also coordinated by a single NHC donor (*d*(Li–C) = 2.133(5) Å), and engages in weaker contacts with two of the carbon atoms of a Dipp group associated with the boryl ligand attached to the other germanium centre (*d*(Li···C) = 2.702(7), 2.743(7) Å). In contrast to the solid-state structure of **1** (and related terphenyl-ligated systems) in which the alkali metal cation sits above the centre of the Ge_2 unit and is further encapsulated by π-interactions with the flanking aryl rings,[9,13] the positioning of the lithium atoms in **2** suggests greater directionality in the Ge–Li interactions. The associated Ge–Li distances (2.541(7) Å) are

slightly greater than the sum of the respective covalent radii (1.20 + 1.28 Å),[14] and the geometry at each germanium centre defined by the proximal boron, germanium and lithium centres is trigonal planar (Σ(angles at Ge) = 358.8(3)°).

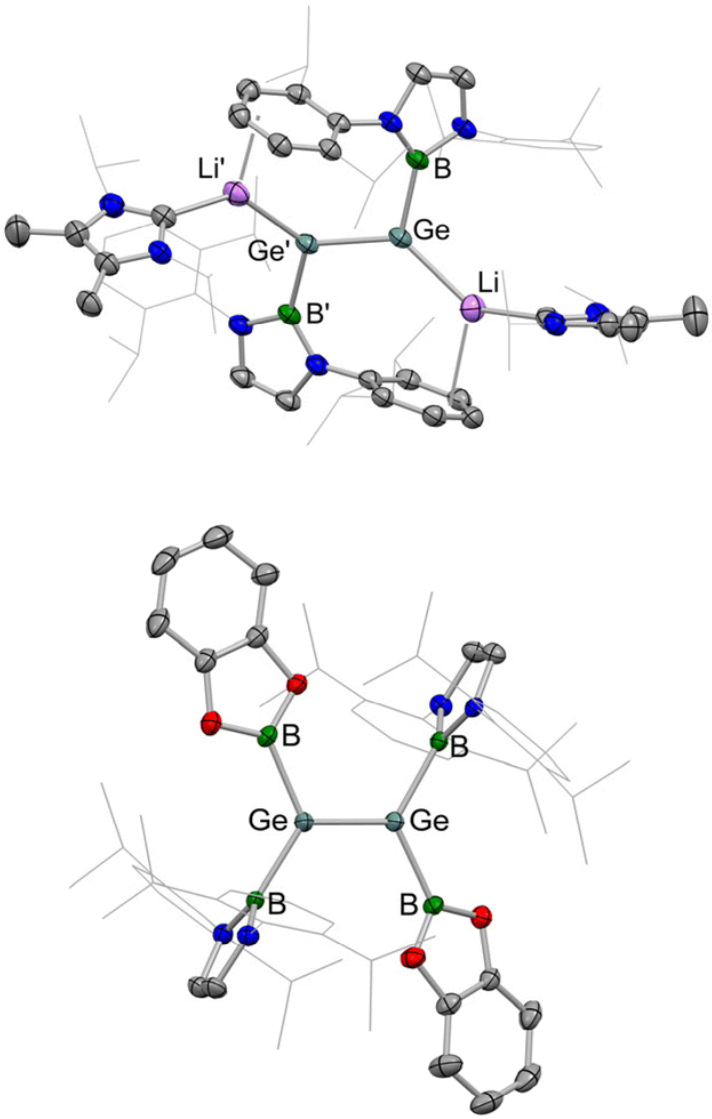

Figure 5.2: Molecular structures of (upper) {(IPrMe)Li}$_2$Ge$_2$(boryl)$_2$ (as the pentane solvate, **2**·C$_5$H$_{12}$) and (lower) of one of the (four) components of the asymmetric unit of Ge$_2$(boryl)$_2$(Bcat)$_2$ (**3**) in the solid state as determined by X-ray crystallography. Hydrogen atoms and solvate molecules omitted, and certain carbon atoms depicted in wireframe format for clarity; thermal ellipsoids set at the 25% probability level. Key bond lengths (Å) and angles (°): (for **2**) Ge–Ge 2.3453(5), Ge–B 2.091(3), Ge–Li 2.541(7), Li–C$_{NHC}$ 2.133(5), Li–C$_{aryl}$ 2.702(7), 2.743(7), B–Ge–Ge–B 166.7(1); (for **3**) Ge–Ge 2.234(1), 2.235(1), 2.235(1), 2.238(1); Ge–B$_{Bcat}$ 2.022(3), 2.025(3), 2.026(3), 2.026(3), 2.028(3), 2.028(3), 2.031(3), 2.033(3), Ge–B$_{boryl}$ 2.023(2), 2.025(2), 2.025(3), 2.027(2), 2.027(2), 2.028(3), 2.028(3), 2.028(3); B–Ge–Ge–B 180.0(1), 177.3(1), 179.6(1), 180.0(1).

The straightforward substitution of the K$^+$ cations in **1** by Li$^+$ in the reaction with LiI/IPrMe led us to investigate its reactivity towards boron-based electrophiles, with the aim of

generating a diborylgermylene. However, neither **1** or **2** reacts with (boryl)Br to give a species of empirical composition Ge(boryl)$_2$ under any conditions examined - presumably due to the excessive steric demands of the boryl Dipp substituents and relatively low electrophilicity of (boryl)Br enforced by the presence of two α-amido π donors. With this in mind we turned to the less sterically demanding boron electrophile, catBBr (cat = 1,2-$O_2C_6H_4$) as has previously been employed by Cui in related silicon chemistry.[15] Reaction with **1** leads to clean conversion in ca. 65 % yield (after recrystallization from pentane), to yield the unsymmetrical *trans*-1,2-tetraboryl digermene, Ge_2(boryl)$_2$(Bcat)$_2$ (**3**; **Scheme 5.1**).‡ **3** is characterized by two ^{11}B signals at δ_B = 28.9 and 43.6 ppm, and its dimeric structure in the solid state, together with the relative arrangement of the two different sets of boryl ligands has been confirmed by X-ray crystallography (**Figure 5.2**).

The solid-state structure of **3** contains four molecules within the asymmetric unit, and reveals an exceptionally short Ge–Ge separation (2.234(1) - 2.238(1) Å). This distance can be compared to 2.4 Å for the sum of the (single bond) covalent radii,[14] 2.347(2) Å for the digermene $Ge_2\{CH(SiMe_3)_2\}_4$,[16] and 2.285(1) Å for the digermyne $Ge_2Ar^{Dipp}_2$ (where Ar^{Dipp} = 2,6- $C_6H_3Dipp_2$).[17] Moreover, in contrast to the *trans*-bent structures observed for digermenes such as $Ge_2\{CH(SiMe_3)_2\}_4$, **3** adopts a planar geometry at each germanium centre (Σ(angles at germanium) = 358.2 - 360.0°) with an inter-planar angle (between the least-squares planes defined by the two GeB_2 units) in the range 0 - 4.8°.

The Ge–Ge distance measured for **3** (2.236 Å (mean)) is successively shorter than those determined for dilithium compound **2** (2.3453(5) Å) and dipotassium species **1** (2.392(1) Å).[9] Notwithstanding the predominantly non-bonding nature of the (a_g, n_+) HOMO in doubly reduced digermyne species such as **1**,[13] this sequential shortening presumably reflects a reduction in the partial negative charge at each germanium centre on assimilation of the Li(NHC) and (particularly) the more covalently bound Bcat fragment. In a broader context, the 'alkene-like'

form of **3** is reminiscent of the geometries determined for tetrasilyldigermenes, which also evidence near-planar structures with very small *trans*-bending and inter-planar angles.[18] The Ge=Ge distances measured for **3**, are however, even shorter than those measured for silyl-substituted systems, and are among the shortest measured for any digermene.[19]

Viewing **3** as having a geometric structure closer to a conventional alkene than the *trans* bent geometry typical of heavier group 14 E_2R_4 species, implies that it can be formally constructed by combining two triplet (rather than singlet) germylene fragments. Dimerization via 'conventional' σ and π bond formation rather than a two-way donor-acceptor interaction offers a rationale for the structural features observed for **3** and related silyl-substituted systems.[7,8] This in turn is consistent with the influence of the strongly electro-positive boryl (and silyl) substituents at germanium, which are known to lead to a small HOMO-LUMO energy gaps (and low-lying triplet states) for tetrylene systems of the type $E(boryl)_2$. By means of comparison, singlet-triplet energy separations of -0.3, 17.9 and 39.2 kJ mol^{-1} have previously been calculated for the tetrylene systems $E(boryl)_2$ (where E = Si, Ge and Sn, respectively).[5]

With this in mind, we examined computationally the fragmentation of a range of digermenes, Ge_2X_4, into both singlet and triplet germylenes (GeX_2) by ETS-NOCV methods (**Table 5.1**).[†] In the cases of **3** and $Ge_2(SiMe_2{}^tBu)_4$,[18b] cleavage into triplet germylene fragments clearly represents the lowest energy fragmentation pathway (e.g. ΔE_{orb} = +155.4 vs. +299.2 kJ mol^{-1} for **3**). On the other hand, the cleavage of Lappert's tetraalkyl digermene is most easily accomplished to give singlet $Ge\{CH(SiMe_3)_2\}_2$ fragments (ΔE_{orb} = +157.0 vs. +142.6 kJ mol^{-1}), consistent with the observed *trans* bent structure of the digermene.[16] Only in the case of the *trans* bent, but twisted system $Ge_2Trip_3(SiPh_3)$ (among the digermene systems examined),[20] were the two fragmentation pathways found to be of comparable energy (ΔE_{orb} = +159.1 and +160.5 kJ mol^{-1}, respectively).

Table 5.1: Structural and electronic properties of **3**, $Ge_2(SiMe_2{}^tBu)_4$, $Ge_2\{CH(SiMe_3)_2\}_4$ and $Ge_2Trip_3(SiPh_3)$.[16,18b,20]

	***d*(Ge–Ge) (Å)**	**Σ(angles at Ge)**	***Trans*-bending angle, (θ°)**	**Inter-planar angle (°)** [a]	**ΔE_{orb} (triplet) kJ mol^{-1}**	**ΔE_{orb} (singlet) kJ mol^{-1}**
$Ge_2(boryl)_2(Bcat)_2$ (**3**)[a]	2.234(1) 2.235(1) 2.235(1) 2.238(1)	359.2(3), 359.2(3) 360.0(3), 360.0(3) 360.0(3), 359.9(3) 359.2(3), 358.2(3)	4.0, 4.0 8.5, 8.5 2.8, 5.3 14.6, 9.3	0 0 3.1 4.8	155.4	299.2
$Ge_2(SiMe_2{}^tBu)_4$[c]	2.270(1)	360.0(1)	1.3	7.5	139.4	227.9
$Ge_2\{CH(SiMe_3)_2\}_4$[c]	2.347(2)	348.5	32.8	0	157.0	142.6
$Ge_2Trip_3(SiPh_3)$[c]	2.328(1)	345.3(2), 346.5(2)	34.6, 35.1	13.6	159.1	160.5

[a] Defined as the angle between the two least squares GeXX' planes. [b] The crystal structure of **3** contains four independent molecules in the asymmetric unit. [c] Metrical data taken from current study and from CIFs JORGIJ, LIGTAY and CENWAT (CCDC).[16,18b,20]

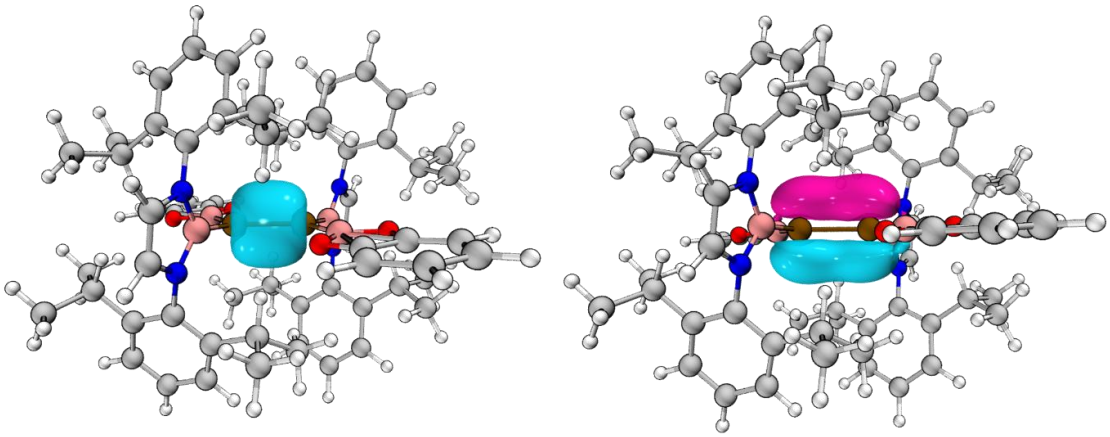

Figure 5.3: Localized Molecular Orbitals (LMOs) contributing significantly to the electron density (left) at the bond critical point (BCP) and (right) 1 Å above the BCP (and above the Ge_2B_4 plane) for $Ge_2(boryl)_2(Bcat)_2$, **3**. The π-type LMO accounts for 91% of the electron density at the BCP and 48% at 1 Å above the BCP; the π-type LMO accounts for 44% of the electron density at 1 Å above the BCP.

An alternative approach to probe the nature of the Ge=Ge bonds in planar and *trans*-bent cases (exemplified by **3** and $Ge_2\{CH(SiMe_3)_2\}_4$), involves the use of localised molecular orbitals (LMOs) to visualise the primary interactions between the two metal centres.[†] In the case of **3** the LMOs which account for significant electron density at the bond critical point (BCP) and 1 Å above the BCP (**Figure 5.3**) resemble classical σ- and π-type bonding orbitals. By contrast, in the case of $Ge_2\{CH(SiMe_3)_2\}_4$, two essentially equivalent LMOs each account for 48 % of the

electron density at the BCP (**Figure 5.4**), and are of a form consistent with the 'slipped' π-bond description, distorted in each case towards one of the two germanium centres.[7,18]

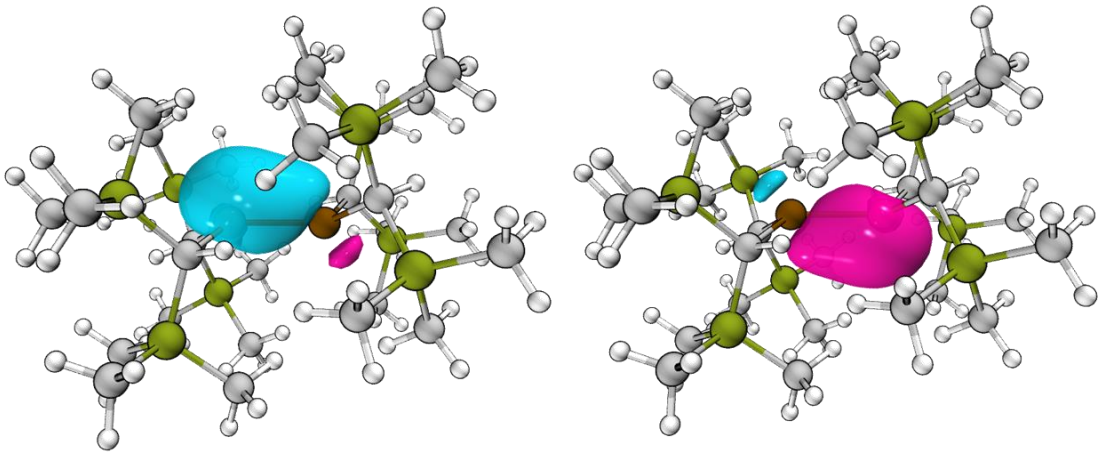

Figure 5.4: Localized Molecular Orbitals (LMOs) contributing significantly to the electron density at the BCP for $Ge_2\{CH(SiMe_3)_2\}_4$ (48% of the electron density, in each case).

The speciation of **2** and **3** in hydrocarbon solution was also investigated. Most informatively, the UV-Vis spectrum of **2** in methylcyclohexane and **3** in pentane feature strong bands at 423 and 431 nm, respectively, i.e. similar to those measured for species containing Ge=Ge double bonds (e.g. 455 nm for $[Ge(IDipp)]_2$,[21] and 434 nm for (boryl)Ge=Ge(IPrMe)(boryl)).[9] In the case of **3**, the assignment of the band at 431 nm is aided by the results of TD-DFT calculations. The first strongly absorbing band is attributed to the S_3 absorption (2.971 eV, 417 nm) which is predominantly due to a Ge=Ge π to π* transition, being composed of 93 % NTOd_S3 -> NTOa_S3 (Figure **S 5.6**) with a minor contribution from the digermene σ to σ* orbitals (4 %; Figure **S 5.7**). The features at 300 nm in the UV-Vis spectrum are predominantly due to the $S_{10/11}$ transitions (3.409ev, 363 nm ; 3.423 eV, 362 nm) also accessing the Ge=Ge π* orbital, in this case from the boryl ligand π-system (99 %; Figure **S 5.8**, **S 5.9**)

Spectroscopic and quantum chemical evidence is therefore consistent with retention of the dimeric structure of **3** in hydrocarbon solution at room temperature. We also investigated whether the speciation of **3** might be temperature dependent. However, while heating a

solution in benzene-d_6 over a period of 5 days, did lead to the formation of a single major new species, this could be shown by X-ray crystallographic studies to be the unsymmetrical diboron(4) species catBB(NDippCH)$_2$ (**4**; Figure **S 5.1**),[22] formed by reductive B–B bond formation. Despite repeated attempts, we were unable to ascertain the nature of the germanium-containing species formed under these conditions - which according to *in situ* NMR measurements is only very sparingly soluble in benzene-d_6 solution.

Conclusions

In conclusion, we have explored a range of synthetic routes to systems of the type [Ge(boryl)$_2$]$_n$, with the reaction between a dianionic digermanide nucleophile and a boron halide electrophile proving to be the most viable. The tetraboryl digermene so generated is dimeric both in the solid state and in hydrocarbon solution and features both a planar 'alkene-like' geometry for the Ge_2B_4 core, and an exceptionally short Ge=Ge double bond. These structural features are consistent with the known electronic properties of the boryl group, and with conceptual fragmentation into two triplet bis(boryl)-germylene fragments.

Characterizing data

Synthesis of novel compounds

*Compound **2**:*

A mixture of (Boryl)Ge(IPrMe)Cl (0.20 g, 0.29 mmol) and excess KC_8 (0.21 g, 1.6 mmol) was dissolved/suspended in toluene (5 mL) at room temperature. The reaction mixture was sonicated for 2 h with occasional manual stirring, resulting in a brown coloured solution. The reaction mixture was then filtered into another Schlenk flask containing LiI (0.04 g, 0.29 mmol) and stirred for 20 min at room temperature. After filtration, the filtrate was concentrated and layered with hexane (3 mL). Storage at 277 K overnight gave a dark red crystals of **2** suitable for X-ray crystallography, which were isolated, washed with small amount of cold hexane and dried in vacuo.

Yield: 0.053 g (28 %).

Spectroscopic data: ^{1}**H** NMR (400 MHz, C_6D_6, 298 K): δ_H 1.24 (d, J_{HH} = 6.9 Hz, 12H, CH(C*H*$_3$)$_2$ of Dipp), 1.29 (24H, CH(C*H*$_3$)$_2$ of Dipp overlapping with CH(C*H*$_3$)$_2$ of carbene), 1.70 (s, 6H, CC*H*$_3$ of carbene), 3.75 (sept, J_{HH} = 6.9 Hz , 4H, C*H*(CH$_3$)$_2$ of Dipp), 3.89 (sept, J_{HH} = 6.8 Hz , 2H, C*H*(CH$_3$)$_2$ of carbene), 6.53 (s, 2H, C*H* of boryl), 7.03 (m, 6H, Ar*H* of Dipp).^{11}**B{^{1}H}** NMR (128 MHz, C_6D_6, 298 K): δ_B 43.6. ^{13}**C{^{1}H}** (151 MHz, C_6D_6, 298 K): δ_C 8.9 (C<u>C</u>H$_3$ of carbene), 24.4 (CH(<u>C</u>H$_3$)$_2$ of Dipp), 24.5 (CH(<u>C</u>H$_3$)$_2$ of carbene), 25.1 (CH(<u>C</u>H$_3$)$_2$ of Dipp), 28.7 (<u>C</u>H(CH$_3$)$_2$ of Dipp), 49.2 (<u>C</u>H(CH$_3$)$_2$ of carbene), 120.0 (<u>C</u>H of boryl), 122.7 (*m*-Ar of Dipp), 125.3 (*p*-Ar of Dipp), 145.8 (*o*-Ar of Dipp), 148.8 (*i*-Ar of Dipp), carbene carbon not observed. **UV-Vis** (methylcyclohexane): λ_{max} = 423 nm, ε = 1440 L mol^{-1}cm^{-1}.

Compound **2** is extremely air- and moisture sensitive and we were unable to obtain reliable elemental microanalysis, despite repeated attempts.

*Compound **3**:*

A mixture of **1** (20 mg, 0.04 mmol) and catBBr (8.0 mg, 0.04 mmol) in benzene (5 mL) was stirred at room temperature for 1 h. After removal of all volatiles in vacuo, the residual solid was extracted with pentane (10 mL) and filtered. Concentration of the filtrate and storage at 243 K overnight yielded **3** as yellow crystals suitable for X-ray crystallography. Yield: 0.014 g (65 %).

Spectroscopic data: ^{1}**H** NMR (400 MHz, C_6D_6, 298 K): δ_H 0.95 (d, J_{HH} = 6.9 Hz, 24H, CH(CH_3)$_2$ of Dipp), 1.18 (d, J_{HH} = 6.9 Hz, 24H, CH(CH_3)$_2$ of Dipp), 3.50 (sept, J_{HH} = 6.7 Hz, 8H, C*H*(CH_3)$_2$ of Dipp), 6.41 (s, 4H, C*H* of boryl), 6.84 (m, 4H, *p*-Ar*H* of Dipp), 6.98 (m, 8H, *m*-Ar*H* of Dipp), 7.06 (m, 8H, Ar-*H* of BCat). ^{11}**B{^{1}H}** NMR (128 MHz, C_6D_6, 298 K): δ_B 28.9, 43.6. ^{13}**C{^{1}H}** (151 MHz, C_6D_6, 298 K): δ_C 23.2 (CH(*C*H$_3$)$_2$ of Dipp), 26.2 (CH(*C*H$_3$)$_2$ of Dipp), 28.5 (*C*H(CH_3)$_2$ of Dipp), 112.6 (OCH*C*H of BCat), 122.6 (*C*H of boryl), 123.0 (*p*-Ar of Dipp), 123.5 (*m*-Ar of Dipp), 127.7 (OC*C*H of BCat), 139.7 (*i*-Ar of Dipp), 146.3 (*o*-Ar of Dipp), 148.9 (O*C* of BCat), carbene carbon not observed. **UV-Vis** (pentane): λ_{max} = 431 nm, ε = 4470 L mol^{-1} cm^{-1}.

Crystallographic Data:

ST 5.1: Selected crystallographic and refinement data for **2**, **3** and **4**.

	2·(C_5H_{12})	**3**	**4**
Formula	$C_{79}H_{124}B_2Ge_2Li_2N_8$	$C_{64}H_{80}B_4Ge_2N_4O_4$	$C_{32}H_{40}B_2N_2O_2$
Formula weight	1366.53	1157.74	506.28
Crystal System	Monoclinic	Triclinic	Monoclinic
Space Group	I 2/a	P-1	P 2_1/c
Wavelength/Å	1.54184	1.54184	1.54184
a/Å	21.8726(8)	11.9393(2)	16.5820(2)
b/Å	16.5014(3)	22.4852(2)	11.08990(10)
c/Å	25.3097(7)	36.1463(5)	16.7948(2)
α/°	90	99.1440(10)	90
β/°	114.994(4)	94.3580(10)	105.5900(10)
γ/°	90	92.4280(10)	90
Volume/Å^3	8279.5(5)	9538.1(2)	2974.82(6)
Z	4	6	4
Temperature/K	150(2)	150(2)	150(2)
Reflections collected	8516	39407	6152
$2\vartheta_{max}$	148.542	135.368	152.268
R_{int}	0.0557	0.0403	0.0225
Goodness of fit	1.018	1.055	1.038
$R[F^2>2\sigma]$, F	0.0469	0.0477	0.0408
R_w(all data), F^2	0.1248	0.1261	0.1105
CCDC reference	2300941	2300942	2300943

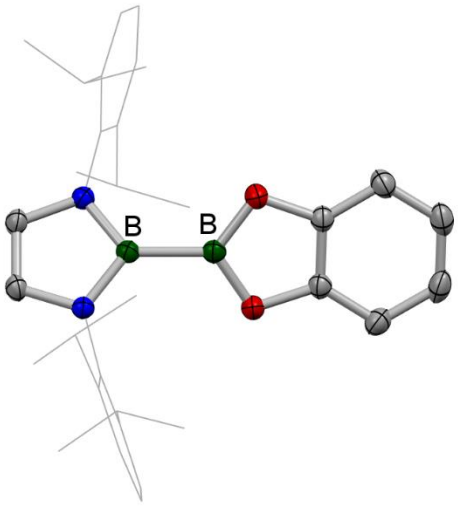

S 5.1: Molecular structure of **4** in the solid state, as determined by X-ray crystallography. Thermal ellipsoid plots are set at the 40% probability level; hydrogen atoms are omitted and Dipp groups are drawn in a wireframe format for clarity.

Computational details

General methods

All computational work reported here was performed using ORCA (Revision 5.0.3) unless otherwise specified.[23] All geometries were first optimised using the meta-generalized-gradient approximation (mGGA) functional R2-SCAN,[24] which was employed in conjunction with the Def2-TZVPPm basis set,[25] with the D4 dispersion correction,[26] and the employing the geometrical counterpoise correction gCP[27] (together known as the R2SCAN-3c method).[25] Alongside this, the Conductor-like Continuum Polarization Model (CPCM) was used to approximate benzene solvation.[28] The nature of the stationary points (minima) was confirmed by full frequency calculations, and are characterized by zero imaginary frequencies.

Time dependent density functional theory (TDFT) was performed with the optimized coordinates with the hybrid M062x functional,[29] in conjunction with the Def2-TZVP basis set,[30] with D3 dispersion correction;[31] Natural transition orbitals (NTO) were generated by the ORCA program. Investigations into the wavefunctions of the calculated species were performed using

the Multiwfn program[32] (including LMO, ETS-NOCV, and topology investigations) and the NBO7 program[33] (utilising the NEDA fragmentation analysis and WBI).

*Electronic structure of monomeric germylene derived from **3***

The lowest energy singlet and triplet state germylenes were optimised as above. A singlet-triplet energy gap of -9.699 kcal mol^{-1} (triplet ground state) was obtained.

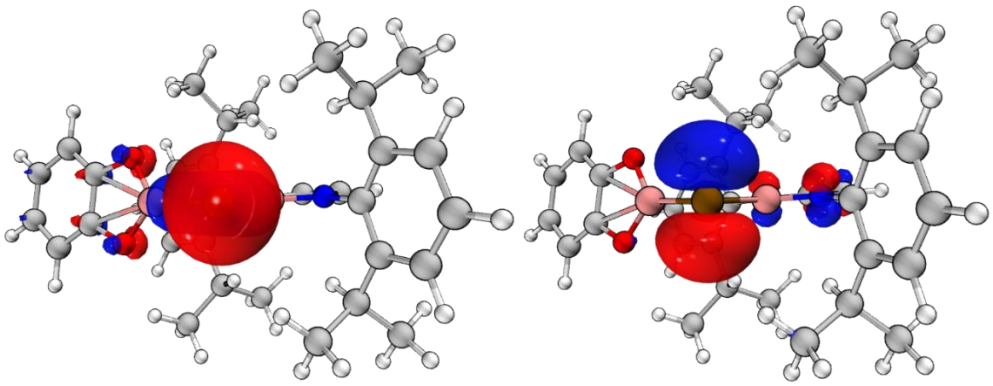

S 5.2: Singlet germylene: (left) HOMO at -5.017 eV; (right) LUMO at -3.340 eV (1.677 eV gap).

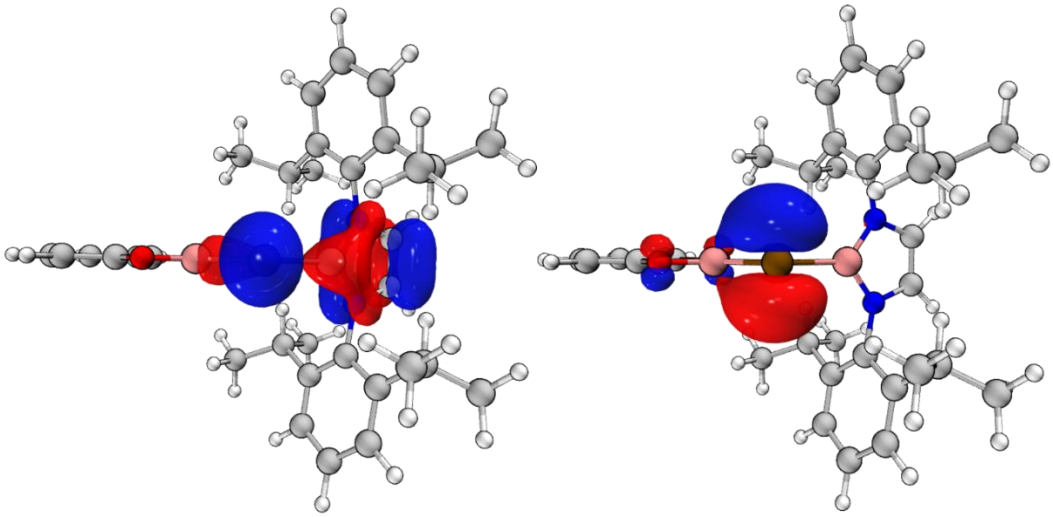

S 5.3: Triplet germylene: (left) HSOMO+1 at -4.955 eV; (right) HSOMO at -4.510 eV (0.445eV gap).

Fragmentation and bonding Analysis of digermenes

ST 5.2: Fragmentation and bonding properties of selected digermenes.

		AgT			AgT1		AgT2		AgT3		AgT5
		SS	TT	SS	TT	SS	TT	SS	TT	SS	TT
ETS-NOCV	Eorb1 (Kcal)	-210.47	-19.3	-260.71	-21.25	-125.05	-39.26	-194.49	-17.07	-101.83	-43.66
	Eorb2 (Kcal)	-14.33	-45.6	-20.22	-46.94	-24.11	-30.47	-14.59	-44.61	-22.92	-27.62
	Eorb (Kcal)	-251.17	-156.95	-293.8	-151.06	-161.99	-155.44	-222.48	-135.57	-134.55	-153.75
NEDA	CT (Kcal)	-365.98	-310.19	-433.99	-310.68	-331.30	-336.14	-328.44	-280.94	-288.77	-318.21
WBI		1.6623			1.658		1.5935		1.7238		1.5605
Epliticity		0.179552			0.323723		0.334113		0.313263		0.335091

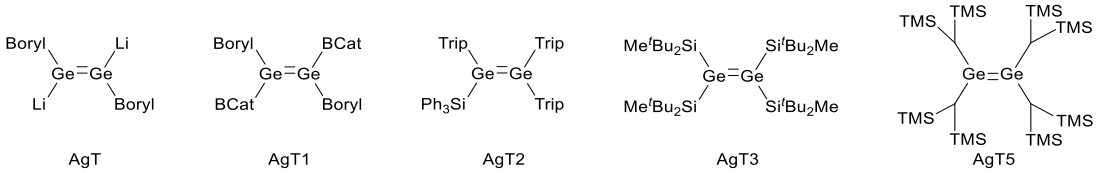

S 5.4: Key to for the designation of AgT1-5 to their respective structures

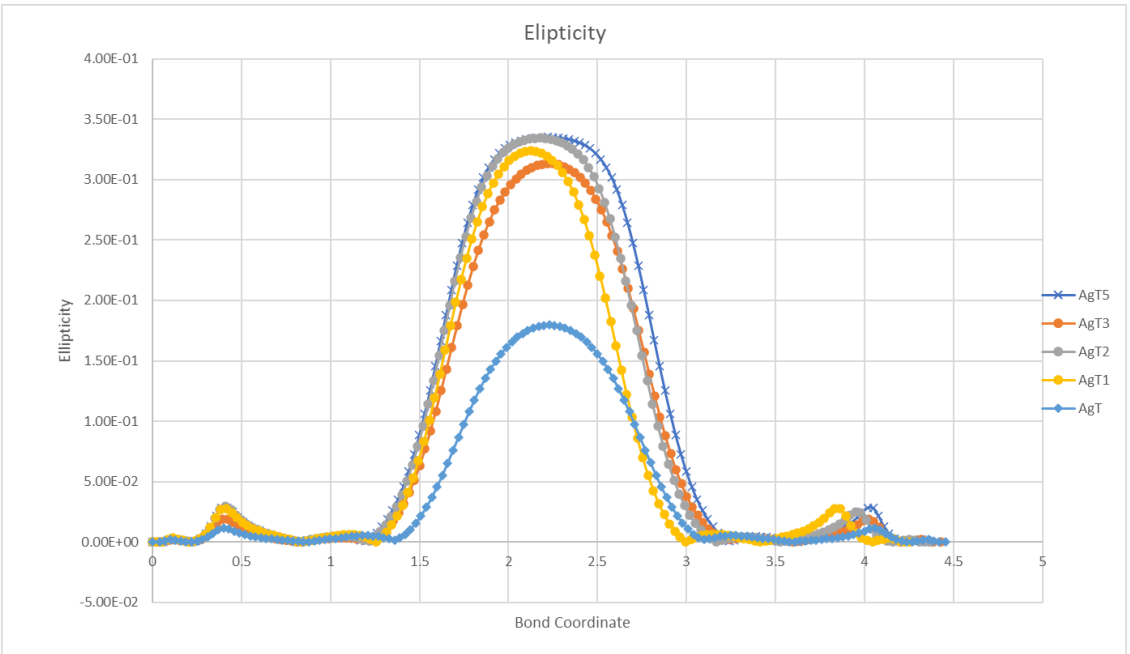

S 5.5: Ellipticities across the bond path for selected digermenes.

TD-DFT; NTO's

Time dependent DFT was performed in order to probe the excited states of **3**, at the R2-SCAN-3c composite method for the first 50 excited states. The natural transition orbitals (NTO) can be used to show the chemically intuitive orbitals associated with the excitation.

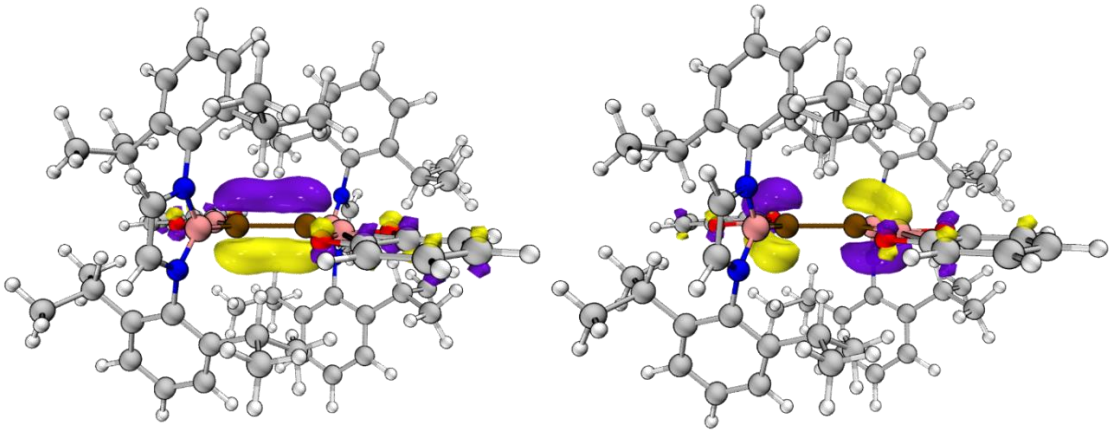

S 5.6: Primary (94%) NTO orbitals for the S_3 transition, with the Ge-Ge π bonding donor orbitals (left) and Ge-Ge π* acceptor orbitals (right)

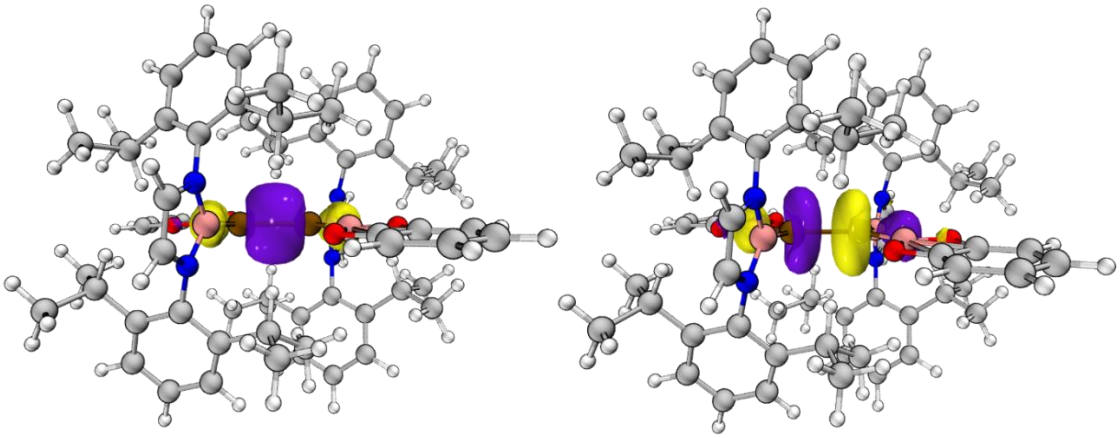

S 5.7: Secondary (4%) NTO orbitals for the S_3 transition, with the Ge-Ge σ bonding donor orbitals (left) and Ge-Ge σ* acceptor orbitals (right)

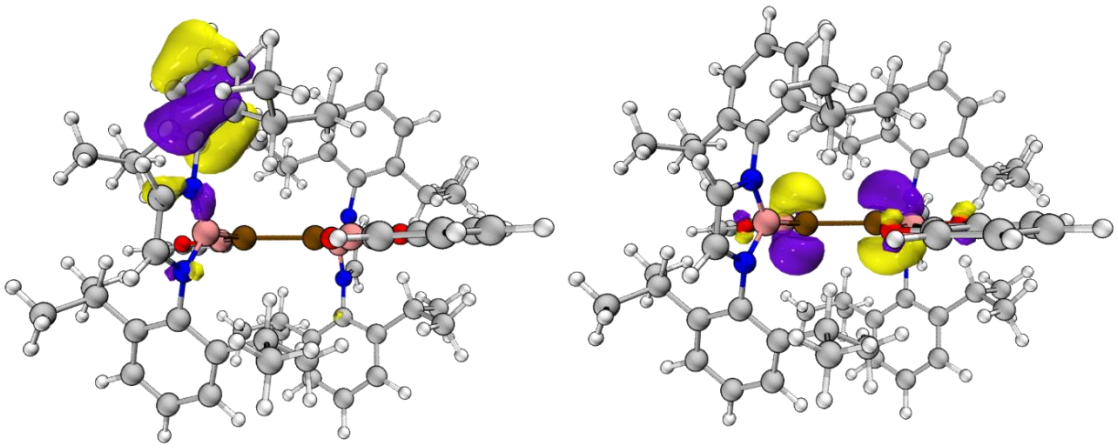

S 5.8: NTO orbitals for the S_{10} transition, with the π type ligand donor orbitals (left) and Ge-Ge π* acceptor orbitals (right)

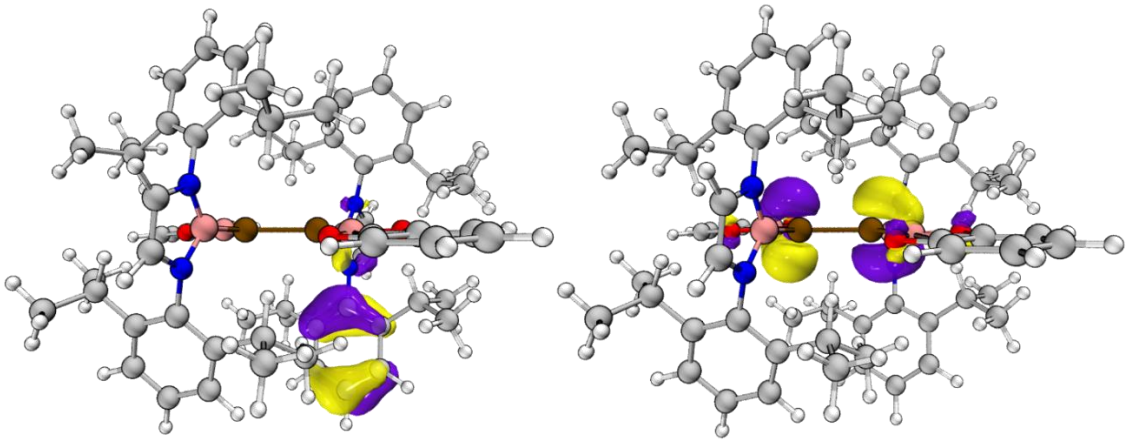

S 5.9: NTO orbitals for the S_{11} transition, with the π type ligand donor orbitals (left) and Ge-Ge π* acceptor orbitals (right).

References

1. P. P. Power, *Nature*, 2010, **463**, 171. See also: b) C. Weetman and S. Inoue, *ChemCatChem*, 2018, **10**, 4213-4228.
2. See, for example: (a) Y. Mizuhata, T. Sasamori and N. Tokitoh, *Chem. Rev.*, 2009, **109**, 3479. (b) D. Martin, M. Soleilhavoup and G. Bertrand, *Chem. Sci.*, 2011, **2**, 389. (c) M. Asay, C. Jones, M. Driess, *Chem. Rev.*, 2011, **111**, 354. (d) T. Chu and G.I. Nikonov, *Chem. Rev.*, 2018, **118**, 3608.
3. D. Bourissou, O. Guerret, F. P. Gabbaï and G. Bertrand, *Chem. Rev.*, 2000, **100**, 39.
4. M. Usher, A. V. Protchenko, A. Rit, J. Campos, E. Kolychev, R. Tirfoin and S. Aldridge, *Chem.-Eur. J.*, 2016, **22**, 11685.
5. A. V. Protchenko, K. H. Birjkumar, D. Dange, A. Schwarz, D. Vidovic C. Jones, N. Kaltsoyannis, P. Mountford and S. Aldridge, *J. Am. Chem. Soc.*, 2012, **134**, 6500.
6. A. V. Protchenko, J. I. Bates, L. M. A. Saleh, M. P. Blake, A. D. Schwarz, E. L. Kolychev, A. L. Thompson, C. Jones, P. Mount-ford and S. Aldridge, *J. Am. Chem. Soc.*, 2016, **138**, 4555.
7. (a) P. P. Power, *Chem. Rev.*, 1999, **99**, 3463. (b) R. C. Fischer and P. P. Power, *Chem. Rev.*, 2010, **110**, 3877. (b) F. Hanusch, L. Groll, S. Inoue, *Chem. Sci.*, 2021, **12**, 2001.
8. (a) G. Trinquier, J. P. Malrieu and P. Rivière, *J. Am. Chem. Soc.*, 1982, **104**, 4529. (b) G. Trinquier and J. P. Malrieu, *J. Am. Chem. Soc.*, 1987, **109**, 5303. (c) G. Trinquier, *J. Am. Chem. Soc.*, 1990, **112**, 2130. (d) H. B. Wedler, P. Wendelboe and P. P. Power, *Organometallics*, 2018, **37**, 2929.
9. A. Rit, J. Campos, H. Niu and S. Aldridge, *Nature Chem*., 2016, **8**, 1022.
10. Y. Segawa, M. Yamashita and K. Nozaki, *Science* 2006, **314**, 113.
11. X. Zheng, A. E. Crumpton, A. V. Protchenko, A. Heilmann, M. A. Ellwanger and S. Aldridge, *Chem.-Eur. J.*, 2023, **29**, e202203395.
12. See, for example: C. Liu and Z.-M. Sun, *Coord. Chem. Rev.*, 2019, 382, 32.
13. L. Pu, A. D. Phillips, A. F. Richards, M. Stender, R. S. Simons, M. M. Olmstead, P. P. Power, *J. Am. Chem. Soc.*, 2003, **125**, 11626.
14. B. Cordero, V. Gómez, A. E. Platero-Prats, M. Revés, J. Echeverría, E. Cremades, F. Barragán and S. Alvarez, *Dalton Trans*., 2008, 2832.
15. M. Tian, J. Zhang, L. Guo and C. Cui, *Chem. Sci.*, 2021, **12**, 14635.
16. P. B. Hitchcock, M. F. Lappert, S. J. Miles and A. J. Thorne, *J. Chem. Soc., Chem. Commun.*, 1984, 480.
17. M. Stender, A. D. Phillips, R. J. Wright and P. P. Power, *Angew. Chem. Int Ed.*, 2002, **41**, 1785.
18. (a) M. Kira, T. Iwamoto, T. Maruyama, C. Kabuto and H. Sakurai, *Organometallics*, 1996, **15**, 3767. (b) T. Iwamoto, J. Okita, N. Yoshida and M. Kira, *Silicon*, 2010, **2**, 209.
19. The only comparably short Ge=Ge bonds among non-cyclic systems are those found in two tetraaryl systems: (a) J. T. Snow, S. Murakami, S. Masamune and D. J. Williams, *Tetrahedron Lett.*, 1984, **25**, 4191. (b) H. Schafer, W. Saak and M. Weidenbruch, *Organometallics*, 1999, **18**, 3159.
20. L. Klemmer, Y. Kaiser, V. Huch, M. Zimmer and D. Scheschkewitz, *Chem.-Eur. J.*, 2019, **25**, 12187.
21. A. Sidiropoulos, C. Jones, A. Stasch, S. Klein and G. Frenking, *Angew. Chem. Int. Ed.* 2009, **48**, 9701.
22. W. Oschmann, C. Borner and C. Kleeberg, *Dalton Trans.*, 2018, **47**, 5318.
23. (a) F. Neese, *WIREs Computational Molecular Science*, 2012, **2**, 73-78; (b) F. Neese, F. Wennmohs, U. Becker and C. Riplinger, *J. Chem. Phys.*, 2020, **152**, 224108; (c) F. Neese, *WIREs Computational Molecular Science*, 2018, **8**, e1327.
24. (a) J. W. Furness, A. D. Kaplan, J. Ning, J. P. Perdew, J. Sun, *J. Chem. Phys. Lett.*, 2020, **11**, 8208; (b) J. W. Furness, A. D. Kaplan, J. Ning, J. P. Perdew, J. Sun, *J. Chem. Phys. Lett.*, 2020, **11**, 9248.
25. S. Grimme, A. Hansen, S. Ehlert and J.-M. Mewes, *J. Chem. Phys.*, 2021, **154**, 064103.
26. (a) E. Caldeweyher, C. Bannwarth and S. Grimme, *J. Chem. Phys.*, 2017, **147**, 034112; (b) E. Caldeweyher, S. Ehlert, A. Hansen, H. Neugebauer, S. Spicher, C. Bannwarth and S. Grimme, *J. Chem. Phys.*, 2019, **150**, 154122.
27. H. Kruse and S. Grimme, *J. Chem. Phys.*, 2012, **136**, 154101.
28. V. Barone and M. Cossi, *J. Phys. Chem. A.*, 1998, **102**, 1995.
29. F. Weigend and R. Ahlrichs, *Phys. Chem. Chem. Phys*., 2005, **7**, 3297.

30. F. Weigend, *Phys. Chem. Chem. Phys*., 2006, **8**, 1057.
31. S. Grimme, J. Antony, S. Ehrlich and H. Krieg, *J. Chem. Phys*., 2010, **132**, 154104.
32. Lu, T. and Chen, F. J. Comput. Chem. 2012, **33**, 580-592
33. NBO 7.0. E. D. Glendening, J, K. Badenhoop, A. E. Reed, J. E. Carpenter, J. A. Bohmann, C. M. Morales, P. Karafiloglou, C. R. Landis, and F. Weinhold, Theoretical Chemistry Institute, University of Wisconsin, Madison (2018).

Reactivity studies on 3 (unpublished):

The planar nature of **3** implies that it may not be able to demonstrate novel reactivity towards CO as it is iso-electronic and iso-structural with an alkene which typically do not react with CO. Since publication, however, **3** was found to react with CO, undergoing conversion to **5** (**Figure 5.5**, **Scheme 5.2**). This transformation is unexpected and interesting because it demonstrates a formal reduction of the Ge centre and oxidation of CO to CO_2. Intriguingly it was also found that the vinylidene compound **III** reacts with CO at low temperature (-78°C) to form **5**, with a different, unidentified product formed from this same reaction at high temperature. This leads us to propose that **3** is reduced under these reaction conditions and forms a common vinylic intermediate with **III**.[1] In order to probe this process DFT calculations were carried out to assess the mechanistic feasibility of a common intermediate and examine the energetic landscape of the processes leading to the formation of **5**.

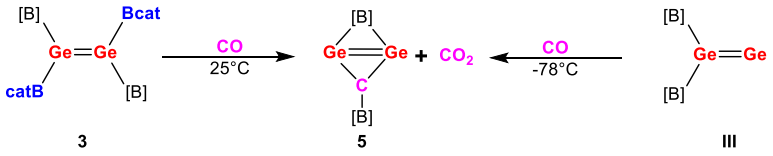

Scheme 5.2 Reaction of **3** and **III** with CO to form **5**

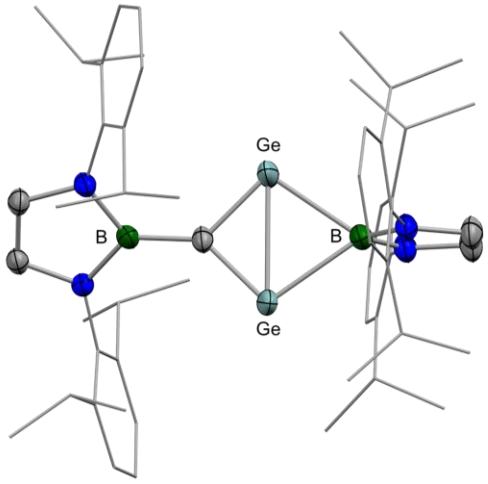

Figure 5.5: Molecular structures of **5** in the solid state as determined by X-ray crystallography. Hydrogen atoms and solvate molecules omitted, and certain carbon atoms depicted in wireframe format for clarity; thermal ellipsoids set at the 25% probability level.

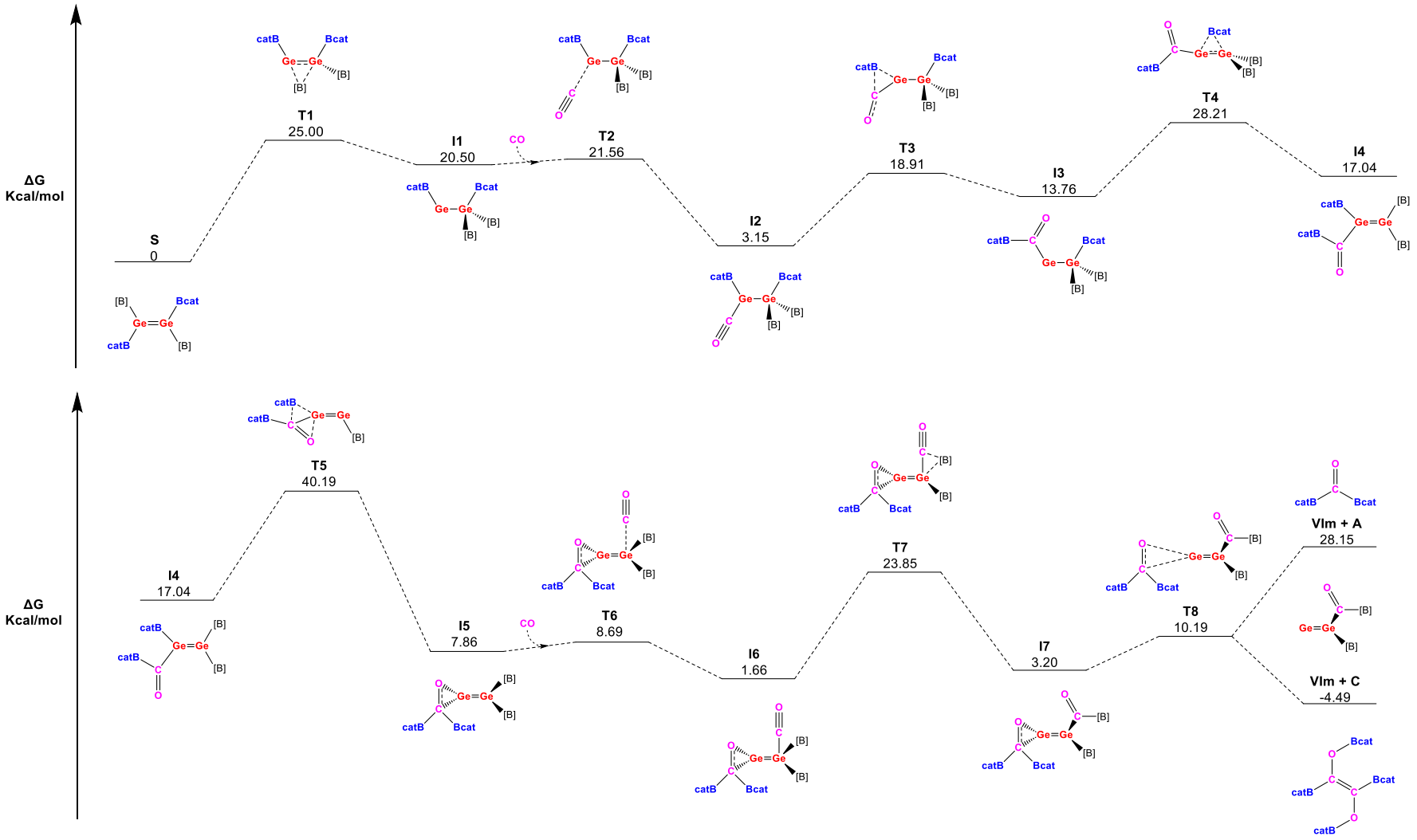

Figure 5.6: Proposed mechanism from **3** (**S**) to vinylic intermediate **VIm** with Gibbs free energies in kcal mol^{-1} relative to **3.** First half of the mechanism from **S** to **I4** (top) and second half from **I4** to **VIm** (bottom).

Digermene reactivity with CO

Initial investigation focused on the conversion of **3** with CO to form the reduced vinylic intermediate, where the formation of diboron(4) species catBB(NDippCH)$_2$ **4** provides compelling evidence supporting the occurrence of a reductive elimination processes at the Ge centre. Direct formation of a CO complex with **3** is precluded due to its planar geometry, which results in incompatible π/π* frontier molecular orbitals for bonding/back-bonding interactions. Migration of a boryl group, a process that is common to boryl and more broadly in boron chemistry along with disilene chemsirty,[2–5] facilitates the formation of the mixed valence intermediate **I1**. **I1** contains a tetravalent germanium centre bound to a divalent germanium centre that adopts carbenic frontier molecular orbitals (**Figure 5.7**). This allows for a bonding interaction involving donation from the CO lone pair into the Ge vacant p-orbital, and a back bonding interaction between the lone pair on Ge into the π* orbital. Adduct formation proceeds via a near barrierless transition due to reduced steric bulk at the divalent germanium centre (1.07Kcal mol^{-1}) to form **I2**.[6]

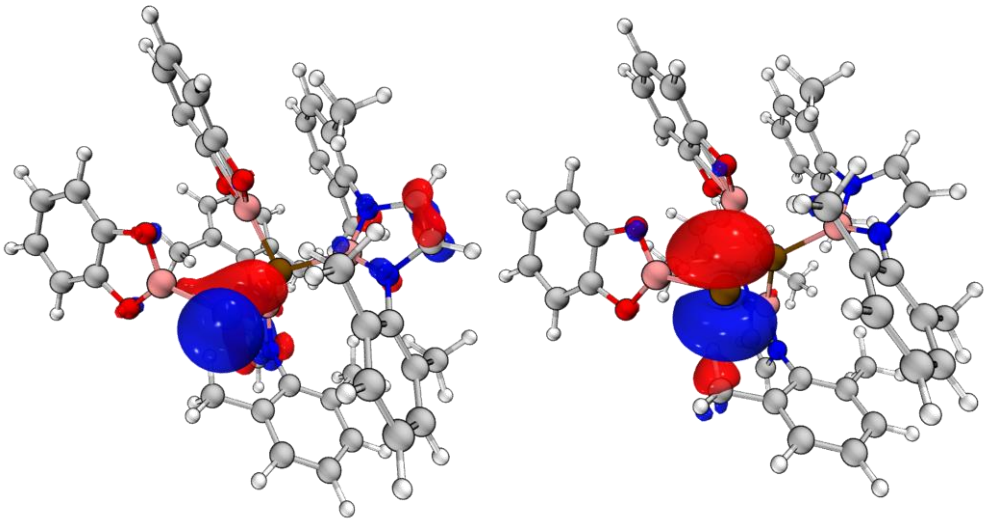

Figure 5.7: Frontier molecular orbitals of **I1** (left) HOMO and (right) LUMO

Insertion of the CO into the Ge-B bond at the Ge(I) centre is then possible, as seen previously with M–[B] systems, forming the mixed valence Ge(I)/Ge(II) boron-acyl compound

I3.[7–11] The Bcat unit then migrates from the germyl fragment across the Ge-Ge unit forming the Ge(II) intermediate **I4** in a endergonic process. Partial reductive elimination of the dibora-carbonyl fragment $(CatB)_2CO$ to give the side on bound intermediate **I5** occurs with a modest barrier of 23.15 kcal mol^{-1}. This is the highest point on the energy surface. This unit adopts a trans bent geometry with the two carbenic fragments forming a donor-acceptor interaction.[12] This interaction can be clearly visualised through the NOCV deformation densities with the donor iso-surfaces in purple and acceptor iso-surfaces in green (**Figure 5.8**). The trans-bent geometry of the digermene orbitals are then conducive to the binding of a second CO molecule (**I6**) via a near barrierless process (0.81 kcal mol^{-1}) due to the low steric bulk in the CO direction of attack. The reaction then proceeds through insertion of the CO into the boryl–Ge bond to give the boron-acyl intermediate **I7**.

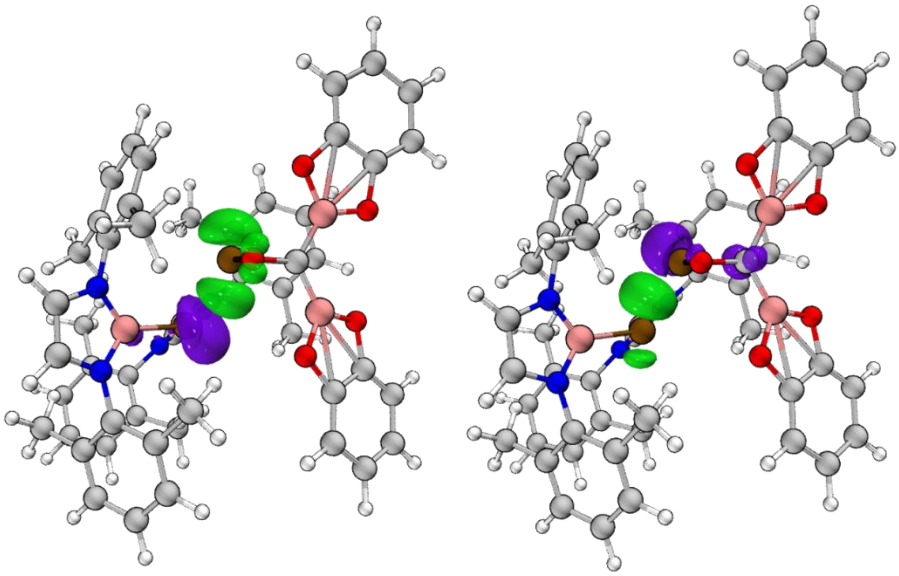

Figure 5.8: NOCV deformation densities: Pair 1 involves the donation from the bis(boryl)germylene lone pair to the vacant P orbital on the Bcat germylene,-51.3 kcal mol^{-1} (left). Pair 2 involves the donation from the Bcat germylene lone pair to the vacant P orbital on the bis(boryl)germylene, -28.3 kcal mol^{-1} (right).

The $(Bcat)_2CO$ fragment (**A)** is then released in an endergonic process (28.15 kcal mol^{-1} **IVm + A**) however; this fragment can rearrange to form a carbene (**B**) which subsequentially dimerizes resulting in an overall exergonic process to the vinylic intermediate (**VIm + C** -4.49 kcal

mol^{-1}). The Bcat containing by-product could not be experimentally verified but is expected to be **C** (**Scheme 5.3**).

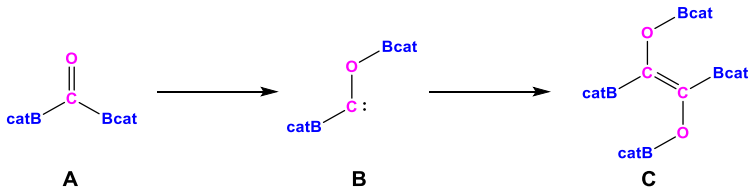

Scheme 5.3: Conversion of byproduct $(Bcat)_2CO$ (**A**) to carbene **B** and **C**

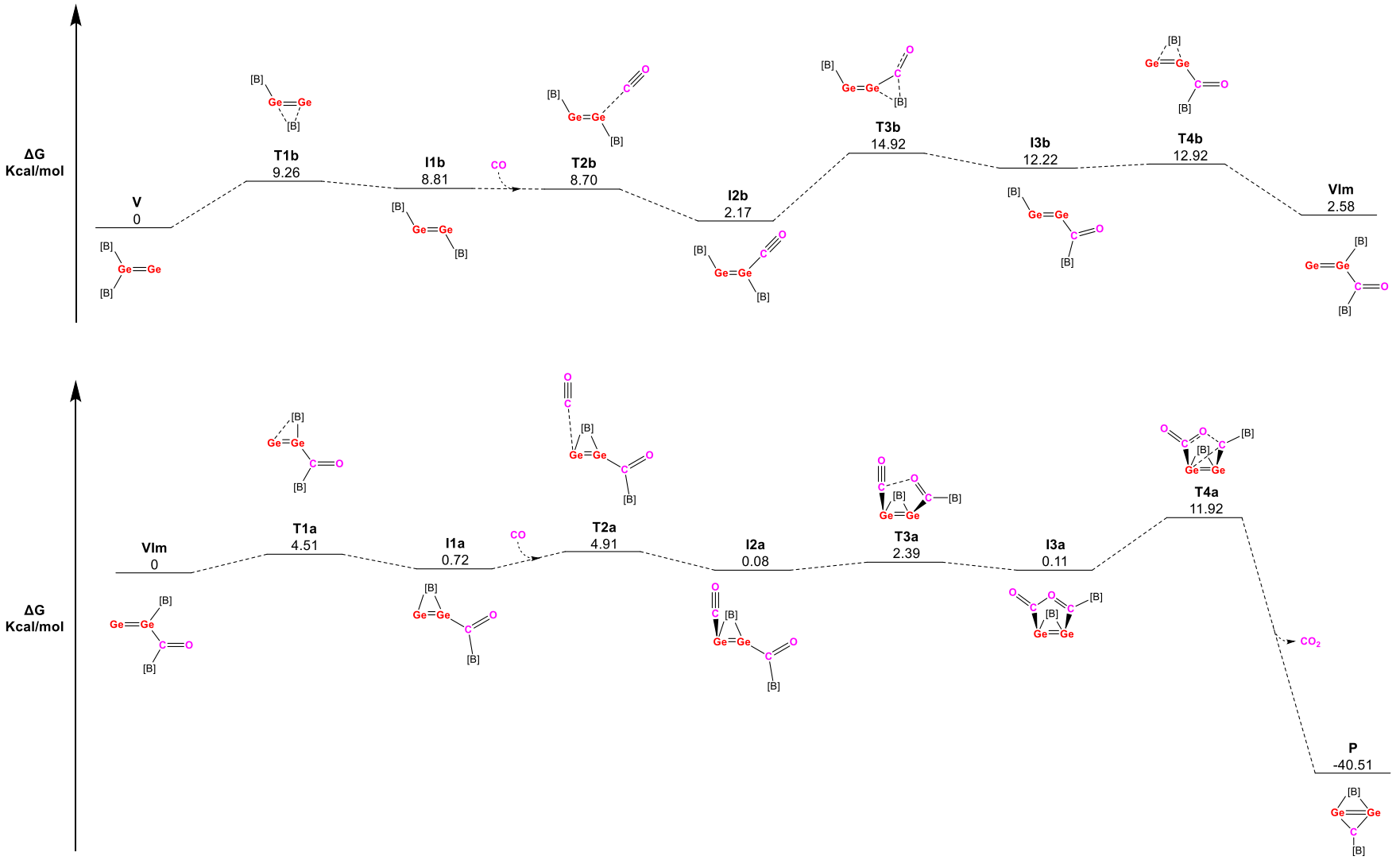

Figure 5.9: Proposed mechanism from vinylidene **III** (**V**) to vinylic intermediate **VIm**, with Gibbs free energies in kcal mol^{-1} relative to **VIm** (top)**.** Proposed mechanism from vinylic intermediate **VIm** to product **P** (**5**), with Gibbs free energies in kcal mol^{-1} relative to **VIm** (bottom)**.**

Vinylidene reactivity with CO

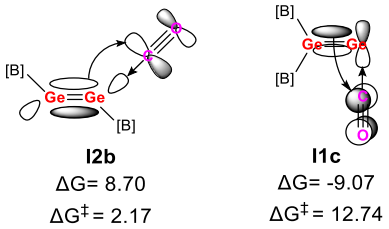

I2b
ΔG= 8.70
$\Delta G^{\ddagger}$ = 2.17

I1c
ΔG= -9.07
$\Delta G^{\ddagger}$ = 12.74

Figure 5.10: Two different binding modes for CO for different isomers of $([B]Ge)_2$ with thermodynamic data in kcal mol^{-1}

Direct coordination to the trivalent germanium with the vinylidene **III** is orbitally infeasible, but bonding instead can occur on the monovalent germanium centre perpendicular to the Ge–Ge bond using the LUMO (vacant P orbital) and HOMO π bonding orbital in order to back-bond. This geometry is challenging to approach due to the Dipp groups shrouding this site, preventing facile binding (**Figure 5.11**). The digermyne (**I1b**) has a more accessible CO binding site with the vacant orbital pointing towards the least sterically congested region (**Figure 5.10**) and the vinylidene compound **III** (**V**) has been shown to have a small barrier to interconversion (9 kcal mol^{-1}).[1] **I1b** binds a CO molecule to form the digermyne carbonyl complex **I2b** which is 2.17 kcal mol^{-1} above the starting vinylidene (**V**)**.** In **I2b**, the binding of CO also aligns the boryl group and CO molecules on the same Germanium (Ge) centre. This configuration primes **I2b** for potential insertion into the Ge–B bond providing a gateway for further reactivity. **I1c** Is however, thermodynamically favoured (ΔG = -9.06 kcal mol^{-1}) but with a larger activation barrier ($\Delta G^{\ddagger}$ = 12.74 kcal mol^{-1}) due to the significant conformational change needed to accommodate the CO binding. This leads us to propose that the divergent reactivity of vinylidene **III** at low and high temperature regimes originates from different CO binding modes. At low temperatures, **I2b** forms as the kinetic product due to a lower barrier to binding. At higher temperatures, the more stable **I1c** becomes accessible and subsequently undergoes unknown reactions, leading to the experimentally observed unidentified reaction products.

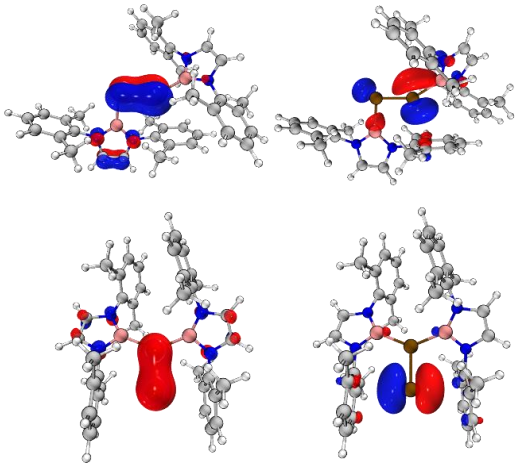

Figure 5.11: Fronter molecular orbitals of digermyne **I1b** (top left HOMO, top right LUMO) and Vinylidene **V** (bottom left HOMO, bottom right LUMO)

Insertion of CO to the Boryl–Ge bond in **I2b** leads to boron-acyl intermediate **I3b**. This intermediate then rearranges to form the common vinylic intermediate **VIm** in a near barrierless process (0.69 kcal mol^{-1}) to be overall endergonic by 2.58 kcal mol^{-1}. In keeping with the proposition this is a kinetic pathway, the surface from **V** to **VIm** is relatively flat with the highest point being **T2b**, 14.92 kcal mol^{-1} above the surface.

Formation of the common product

Analogously with the vinyladine **III**, coordination of CO to **VIm** is challenging due to steric shrouding of the monovalent Ge centre. When investigating the migration of the boryl, it was found the bridged intermediate **I1a** was near isoenergetic with **VIm**. **I1a** demonstrates more accessible orbitals for CO binding, with a vacant p-type orbital accepting the CO lone pair and a π-bonding Ge–Be orbital enabling back bonding (**Figure 5.12**). This leads to the CO binding perpendicular to the Ge–B–Ge plane (**I2a**). Cyclisation can then occur through the boryl carbonyl group approaching the bound CO forming the intermediate **I3a** containing a 5 membered Ge–Ge–C–O–C ring. Remarkably, the reaction surface from **VIm** to **I3a** exhibits an exceptionally flat profile, with each intermediate closely aligned in energy, making them effectively isoenergetic with one another, and with barriers measuring less than 5 kcal mol^{-1}.

In the final step, CO_2 is released from **I3a**, closing the ring and forming the product (**P**) in a single step. The CO_2 release provides a large driving force and is a highly exergonic process (-40.00 kcal mol^{-1}). The overall thermodynamics of the reaction of the digermene **2** (**S**) to product **5** (**P**) is -45.00 kcal mol^{-1} with a maximum height above the surface of 40.19 kcal mol^{-1} being the partial reductive elimination of bis-B_{Cat} carbonyl. The overall thermodynamic barrier of the conversion of vinylidene **III** (**V**) to **5** (**P**) is 37.93 kcal mol^{-1} with a maximum above the surface of 14.92kcal mol^{-1} (**T2b**) being the binding of CO to **I1b**.

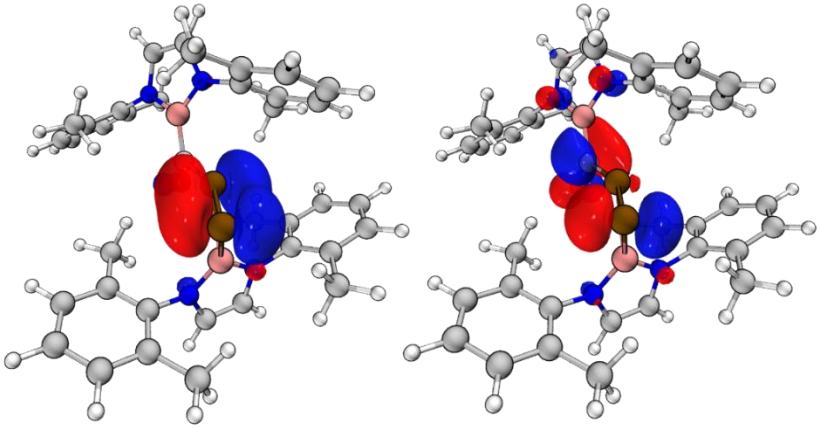

Figure 5.12: Frontier molecular orbitals of **I2a**, HOMO (left) and LUMO (right)

Conclusion

This mechanistic profile demonstrates a plethora of different binding modes of low valent Ge systems with CO and how the unique orbital morphologies can dictate the course of the reaction. Future work would focus on gathering of adequate characterisation data on product **5**, and investigating the reactivity of **3** with other CO analogues to see how the reactivities differ.

Methods

All computational work reported here was performed using ORCA (Revision 5.0.4) unless otherwise specified[13–15]. All geometries were first optimised using the meta-generalized-gradient approximation (mGGA) functional R2-SCAN[16], which was employed in conjunction with the Def2-TZVPPm basis set,[17] with the D4 dispersion correction, and the employing the geometrical counterpoise correction gCP5 (together known as the R2SCAN-3c method).[18] Alongside this, the Conductor-like Continuum Polarization Model (CPCM) was used to approximate benzene solvation. The nature of the stationary points (minima) was confirmed by full frequency calculations, and are characterized by zero imaginary frequencies or a single imaginary frequency along the reaction coordinate. Intrinsic reaction coordinate (IRC) calculations where also performed on each transition state to confirm they linked the proposed intermediates. EDA-NOCV analysis was performed using the ORCA programme.[19–22]

References

1. Rit, A., Campos, J., Niu, H. & Aldridge, S. A stable heavier group 14 analogue of vinylidene. *Nature Chemistry 2016 8:11* **8**, 1022–1026 (2016).
2. Mkhalid, I. A. I., Barnard, J. H., Marder, T. B., Murphy, J. M. & Hartwig, J. F. C-H activation for the construction of C-B bonds. *Chem Rev* **110**, 890–931 (2010).
3. Hillman, M. E. D. The Carbonylation of Organoboranes. I. The Carbonylation of Trialkylboranes. A Novel Synthesis of Trialkylcarbinols. *J Am Chem Soc* **84**, 4715–4720 (1962).
4. Neeve, E. C., Geier, S. J., Mkhalid, I. A. I., Westcott, S. A. & Marder, T. B. Diboron(4) Compounds: From Structural Curiosity to Synthetic Workhorse. *Chem Rev* **116**, 9091–9161 (2016).
5. Negishi, E. ichi. Chemistry of organoborates. *J Organomet Chem* **108**, 281–324 (1976).
6. Fujimori, S. & Inoue, S. Main group carbonyl complexes. *Communications Chemistry 2020 3:1* **3**, 1–4 (2020).
7. Shere, H., Hill, M. S., Pécharman, A. F. & Mahon, M. F. Reactivity of a magnesium diboranate with organic nitriles. *Dalton Trans.* **50**, 1283–1292 (2021).
8. Wang, B., Kang, X., Nishiura, M., Luo, Y. & Hou, Z. Isolation, structure and reactivity of a scandium boryl oxycarbene complex. *Chem Sci* **7**, 803–809 (2015).
9. Lu, W., Hu, H., Li, Y., Ganguly, R. & Kinjo, R. Isolation of 1,2,4,3-Triazaborol-3-yl-metal (Li, Mg, Al, Au, Zn, Sb, Bi) Derivatives and Reactivity toward CO and Isonitriles. *J Am Chem Soc* **138**, 6650–6661 (2016).
10. Frank, R. *et al.* Cobalt Boryl Complexes: Enabling and Exploiting Migratory Insertion in Base-Metal-Mediated Borylation. *Angew. Chem. Int. Ed.* **54**, 9586–9590 (2015).
11. Li, S. *et al.* Rare Earth Metal Boryl Complexes: Synthesis, Structure, and Insertion of a Carbodiimide and Carbon Monoxide. *Angew. Chem. Int. Ed.* **50**, 6360–6363 (2011).
12. Power, P. P. Main-group elements as transition metals. *Nature* **463** 171–177 (2009)
13. Neese, F. & Wiley, J. The ORCA program system. *Wiley Interdiscip Rev Comput Mol Sci* **2**, 73–78 (2012).
14. Neese, F. Software update: the ORCA program system, version 4.0. *Wiley Interdiscip Rev Comput Mol Sci* **8**, e1327 (2018).
15. Neese, F., Wennmohs, F., Becker, U. & Riplinger, C. The ORCA quantum chemistry program package. *Journal of Chemical Physics* **152**, 224108 (2020).
16. Furness, J. W., Kaplan, A. D., Ning, J., Perdew, J. P. & Sun, J. Accurate and Numerically Efficient r2SCAN Meta-Generalized Gradient Approximation. *Journal of Physical Chemistry Letters* **11**, 8208–8215 (2020).
17. Weigend, F. & Ahlrichs, R. Balanced basis sets of split valence, triple zeta valence and quadruple zeta valence quality for H to Rn: Design and assessment of accuracy. *Physical Chemistry Chemical Physics* **7**, 3297–3305 (2005).
18. Grimme, S., Hansen, A., Ehlert, S. & Mewes, J. M. R2SCAN-3c: A 'swiss army knife' composite electronic-structure method. *Journal of Chemical Physics* **154**, 64103 (2021).
19. Mitoraj, M. & Michalak, A. Applications of natural orbitals for chemical valence in a description of bonding in conjugated molecules. *J Mol Model* **14**, 681–687 (2008).
20. Mitoraj, M. & Michalak, A. Donor-acceptor properties of ligands from the natural orbitals for chemical valence. *Organometallics* **26**, 6576–6580 (2007).
21. Jerabek, P. & Frenking, G. Comparative bonding analysis of N_2 and P_2 versus tetrahedral N_4 and P_4. *Theoretical Chemistry Accounts 2014 133:3* **133**, 1–9 (2014).
22. Mitoraj, M. P., Michalak, A. & Ziegler, T. A combined charge and energy decomposition scheme for bond analysis. *J Chem Theory Comput* **5**, 962–975 (2009).

Statement of Authorship

Title of Paper	A planar per-borylated digermene
Publication Status	Published
Publication Details	Xiongfei Zheng, Agamemnon E. Crumpton, Mathias A. Ellwanger, Simon Aldridge, Dalton Trans., 2023,52, 16591-16595

Student Confirmation

Student Name:	Agamemnon Elvis Crumpton
Contribution to the Paper	Performed DFT calculations on the structures within the manuscript, investigated these compounds with energy decomposition analysis and contributed to the discussion of the quantum chemical calculations in the manuscript. In the unpublished work, I performed the DFT calculations elucidating the mechanism, solved the X-ray structure for the product and wrote this section.
Signature 	Date 15/04/2024

Supervisor Confirmation

Supervisor name and title: Professor Simon Aldridge	
Supervisor comments I can confirm that the candidate's contribution to this paper is as described above.	
Signature 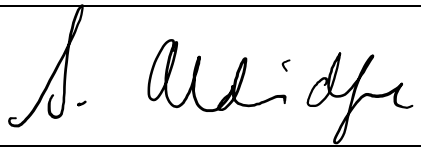	Date 18/4/2024

Chapter 6 - Coordination and Homologation of CO at Al(I): Mechanism and Chain growth, Branching, Isomerization and Reduction

Andreas Heilmann, Matthew M. D. Roy, Agamemnon E. Crumpton, Liam P. Griffin, Jamie Hicks, Jose M. Goicoechea*, and Simon Aldridge*

Published in the Journal of the American Chemical Society: J. Am. Chem. Soc. 2022, 144, 28, 12942–12953

Author contributions

Andreas Heilmann: Synthesised the novel compounds, collected characterisation data and lead crystallographer.

Matthew M. D. Roy: Carried out preliminary investigations.

Agamemnon E. Crumpton: Performed the quantum chemical calculations.

Liam P. Griffin: Optimised synthesis one of the novel compounds.

Jamie Hicks: Advised on synthetic chemistry and crystallographer.

Jose M. Goicoechea: Corresponding author.

Simon Aldridge: Corresponding author.

Manuscript was written by Simon Aldridge and Andreas Heilmann with contribution to the discussion of the quantum chemical calculations by Agamemnon E. Crumpton.

Abstract

Homologation of carbon monoxide is central to the heterogeneous Fischer Tropsch Process for the production of hydrocarbon fuels. C–C bond formation has been modelled by homogeneous systems, with $[C_nO_n]^{2-}$ fragments (n = 2-6) formed by two-electron reduction being commonly encountered. Here we show that four- or six-electron reduction of CO can be accomplished by the use of anionic aluminium(I) ('aluminyl') compounds, to give both topologically linear and branched C_4/C_6 chains. We show that the mechanism for homologation relies on the highly electron-rich nature of the aluminyl reagent, and on an unusual mode of interaction of the CO molecule, which behaves primarily as a Z-type ligand in initial adduct formation. The formation of $[C_6O_6]^{4-}$ from $[C_4O_4]^{4-}$ shows for the first time a solution-phase CO homologation process that brings about chain branching via complete C-O bond cleavage, while comparison of the linear

$[C_4O_4]^{4-}$ system with the $[C_4O_4]^{6-}$ congener formed under more reducing conditions, models the net conversion of C–O bonds to C–C bonds in the presence of additional reductant.

Introduction

The assembly of complex molecules from carbon monoxide via C–C bond formation represents a fundamental chemical challenge that has key relevance to the production of hydrocarbon fuels via the heterogeneous Fischer-Tropsch Process.[1] Although employed industrially since 1925, the mechanism for the conversion of mixtures of CO and H_2 to short-to-medium chain alkane products through the formation of C–C bonds remains the subject of significant debate.[2] C=C bond formation to yield alkenes represents a competing homologation process, and the product mixture typically also includes oxygenated species along with methane - an undesirable reduction product produced without accompanying C–C bond formation. The idealized ratio of H_2:CO (ca. 2:1; eqn 1, typically with $10 < n < 20$) reflects the importance of the reductant (H_2) in generating the desired alkane products. The much lower proportion of dihydrogen in the coal-derived synthesis gas ('Syn Gas') feedstock is typically rectified through application of the Water Gas Shift reaction.[3]

$$(2n + 1)\ H_2 \ + \ n\ CO \longrightarrow C_nH_{2n+2} \ + \ n\ H_2O$$

Equation 6.1: Fisher Tropsch homologation chemistry

The amenability of homogeneous systems to small molecule characterization techniques has driven the investigation of organometallic compounds capable of modelling the homologation of CO via C–C bond formation.[4] Prominent examples include *d*-block metal compounds (mirroring the use of heterogeneous transition metal catalysts such as iron and cobalt in the Fischer-Tropsch process),[5-17] with examples derived from low-valent *s*-, *p*-,[18-33] and *f*-block compounds[34-50] having also been reported (e.g. **I**-**VII**, Figure 6.1). Prevalent among the homologation products formed via reduction processes are cyclic systems of the type $[C_nO_n]^{2-}$ (n = 3, 4, 6) and the related ethynediolate system $[C_2O_2]^{2-}$,[6-8,11,18,20-23,29,40,41,44-48] formed by a formal two-electron reduction process, although a number of systems featuring longer linear

chains of carbon atoms have also been reported (Figure 6.1).[14,17,22,25,31,33,34,36,37,42,49] Within this sphere, a small number of studies have emerged which demonstrate the potential for control of homologation processes at a constant oxidation level: the selective formation of $[C_nO_n]^{2-}$ (n = 2, 3 or 4) by the cooperative action of U(III) or Mg(I) centres has been shown to be influenced by the steric bulk of ancillary ligands,[21,48] and the stepwise growth of C_3 chains by the addition of CO has been demonstrated at d-block metal systems derived from metal carbonyl precursors.[17] Very recently the formation of C_4 or C_5 chains using aluminium(I) systems has been demonstrated with the product formed appearing to reflect the nuclearity of the metal reagent.[33]

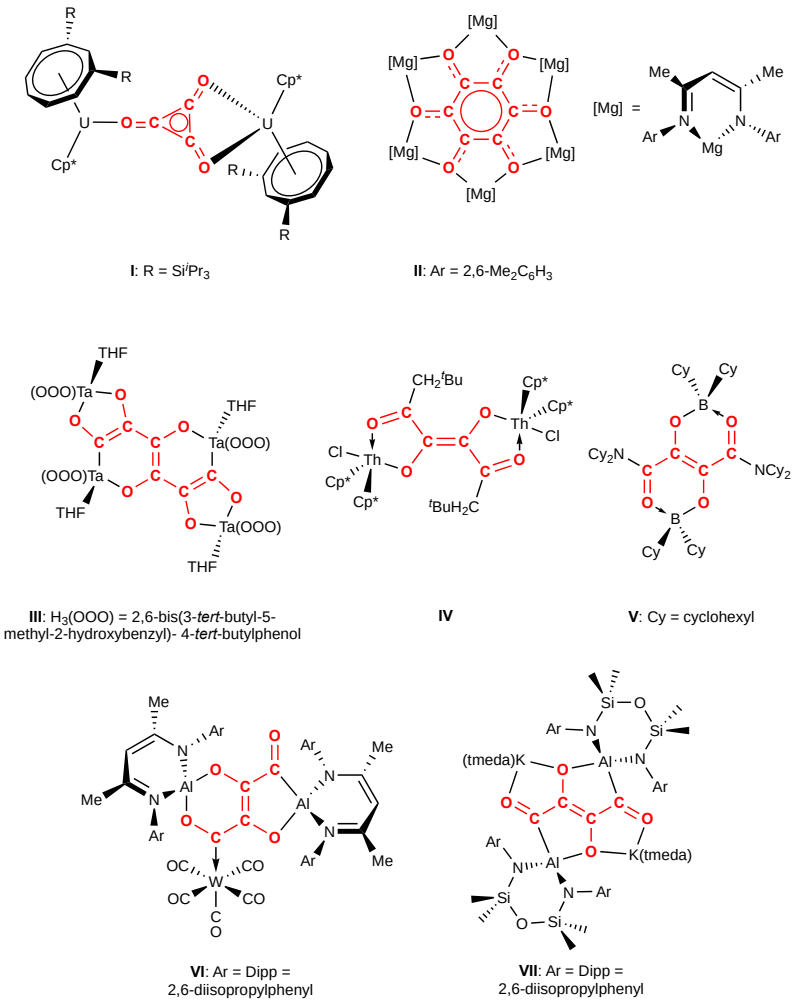

Figure 6.1: Selected examples of CO homologation relevant to the current study.

We have been developing the chemistry of electron-rich aluminium ('aluminyl') compounds - stabilized by NON supporting ligands (4,5-bis(2,6-diisopropylanilido)-2,7-di-tert-butyl-9,9-dimethylxanthene; **Figure 6.2**).[51,52] Such systems have been shown to be capable of the cleavage of C–H,[51] C–C,[53] and C–O bonds in arene substrates,[54] and to allow access to reactive terminal imide species which can cleave the CO bond in carbon monoxide.[55] Systems such as $K_2[(NON)Al]_2$ ($[\mathbf{1}\text{-K}]_2$) have also shown strongly reducing capabilities towards oxygen-containing substrates,[56] and here we report on the reactivity of aluminyl compounds towards CO. We show that homologation to give the known $[C_4O_4]^{4-}$ fragment occurs with both mono- and dinuclear systems, a finding rationalized computationally through a rate-determining C=C bond forming dimerization process. The initial interaction of the CO molecule at aluminium is unusual, in that it behaves primarily as a Z-type ligand, reflecting the highly electron-rich nature of the aluminyl reagent. Subsequent formation of $[C_6O_6]^{4-}$ from $[C_4O_4]^{4-}$ shows for the first time a solution-phase CO homologation process that brings about chain branching via complete C-O bond cleavage. In addition, comparison of the linear $[C_4O_4]^{4-}$ system with the (unprecedented) $[C_4O_4]^{6-}$ congener formed under more reducing conditions, models the conversion of C–O bonds to C–C bonds in the presence of additional reductant.

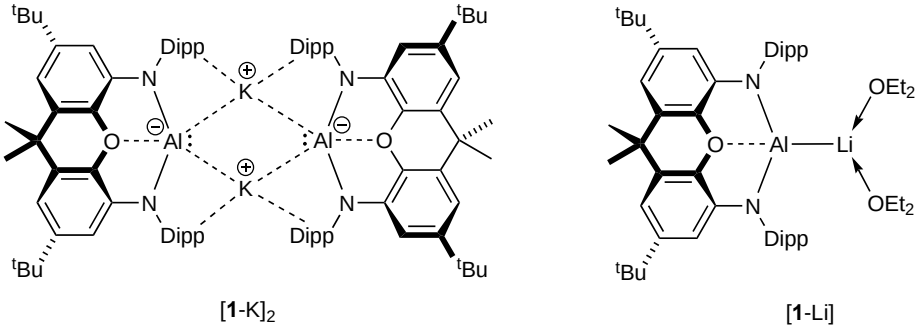

Figure 6.2: Aluminyl compounds central to the current study: dimeric potassium aluminyl compound $K_2[(NON)Al]_2$, $[\mathbf{1}\text{-K}]_2$, and monomeric lithium analogue $(Et_2O)_2LiAl(NON)$, $[\mathbf{1}\text{-Li}(OEt_2)_2]$.

Results and Discussion

Synthesis of $[C_4O_4]^{4-}$ and $[C_6O_6]^{4-}$ via CO homologation.

The reaction of potassium aluminyl compound [**1**-K]$_2$[51] with CO (ca. 1.5 atm) in benzene over 16 h at ca. 35 °C (followed by recrystallization from toluene) leads to the isolation of the orange crystalline product $[K(C_7H_8)]_2[\{(NON)Al\}_2(C_4O_4)]$, [**2**-K$(C_7H_8)]_2$, which has been characterized by standard spectroscopic and micro-analytical methods (**Scheme 6.1** and **Figure 6.3**). [**2**-K$(C_7H_8)]_2$ can be shown by X-ray crystallography to feature a centrosymmetric structure in which two [(NON)Al] units are bridged by a $[C_4O_4]$ fragment and two K^+ counterions (which each interact with the π system of a Dipp group of one NON ligand and an additional toluene molecule; **Figure 6.3**).

Overall charge balance implies that the bridging unit is $[C_4O_4]^{4-}$, a finding consistent with the presence in the (dimeric) aluminyl starting material of two Al(I) reductants, i.e. with four-electron reduction of four molecules of CO. To a first approximation, C–C distances within the $[C_4O_4]^{4-}$ unit reflect the presence of two C–C single bonds (1.507(1) Å) and a central C=C double bond (1.373(1) Å), while the C–O distances (1.383(1)/1.233(1) Å) are consistent with C–O single bonds linked to the central carbon atoms (i.e. C(2)) and C=O double bonds involving the Al-bound carbons C(1).

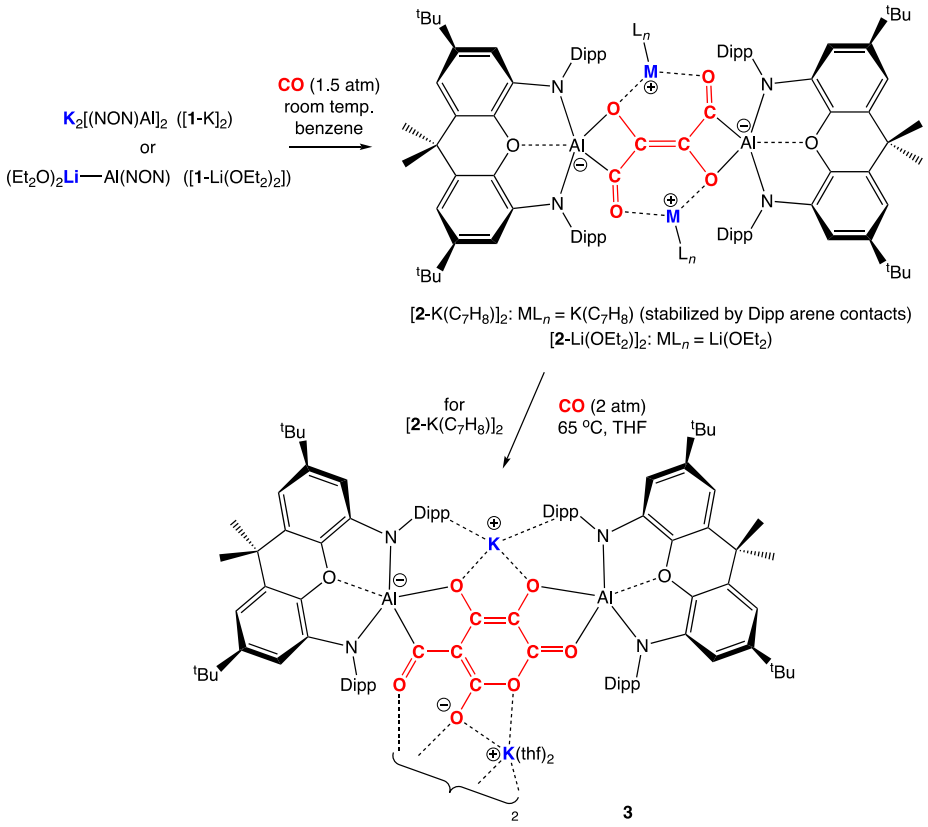

Scheme 6.1: Homologation of CO by aluminyl compounds yielding products containing $[C_4O_4]^{4-}$ or $[C_6O_6]^{4-}$ fragments. Four electron reduction of CO by $[1\text{-K}]_2$ or 2 equivalents of $[1\text{-Li(OEt}_2)_2]$ to give $[2\text{-K(C}_7\text{H}_8)]_2$/$[2\text{-Li(OEt}_2)]_2$, featuring the topologically linear $[C_4O_4]^{4-}$ fragment; onwards reaction of $[2\text{-K(C}_7\text{H}_8)]_2$ with CO to yield the $[C_6O_6]^{4-}$ system, 3.

Four-carbon homologation has some literature precedent. In terms of a metal-bound ligand system, the C/O skeleton bears some resemblance connectivity-wise to the enedione diolate $[R_2C_4O_4]^{2-}$ system reported by Marks and co-workers, derived from insertion of two molecules of CO into a thorium(IV) alkyl bond (**IV**),[34,36] and to the mixed d-block/Al systems reported by Crimmin et al. (**VI**).[17] Structurally, however it is most closely related to Stephan's B/N functionalized system $Cy_2N\{C_4O_4(BCy_2)_2\}NCy_2$ derived from the trapping of CO by a combination of $LiNCy_2$ and $ClBCy_2$, and which also features a C(=O)–C(–O)=C(–O)–C(=O) skeleton (**V**).[31] In addition, a similar C_4 system was reported very recently by Coles and co-workers (**VII**).[33]

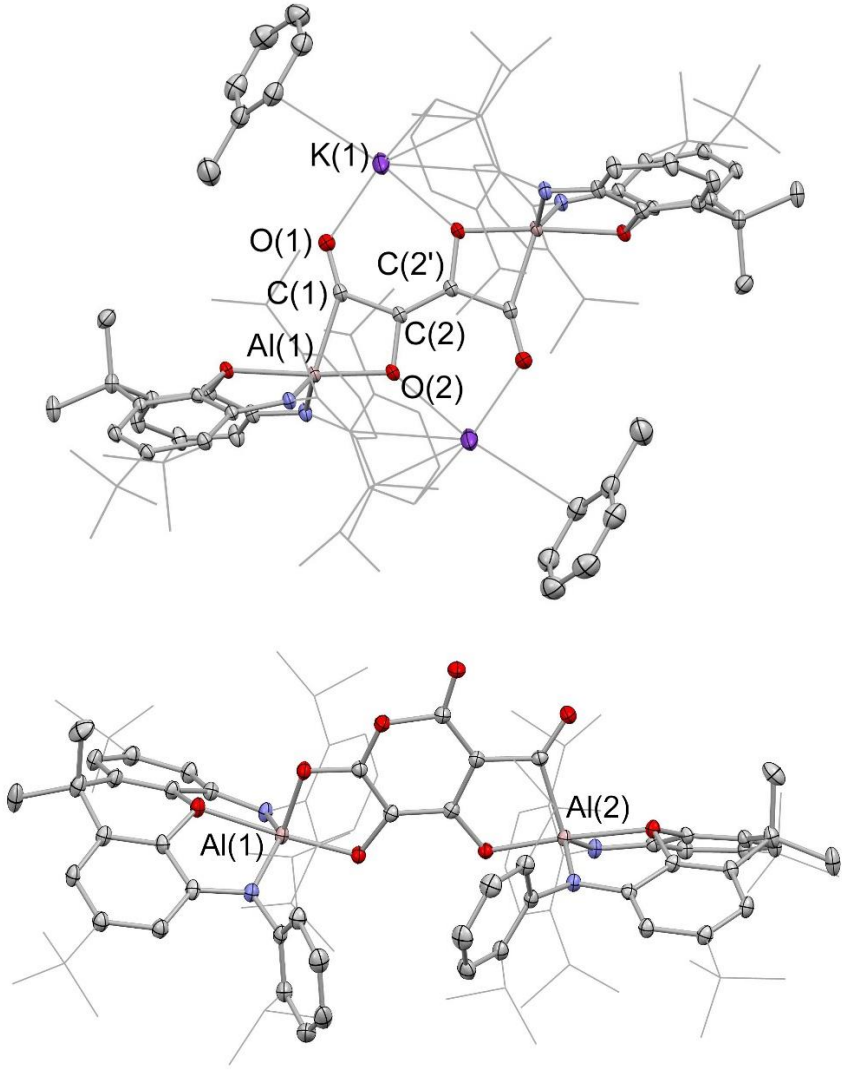

Figure 6.3: Molecular structures of (upper) $[K(C_7H_8)]_2[\{(NON)\ Al\}_2(C_4O_4)]$, [**2**-$K(C_7H_8)]_2$ and (lower) the anionic component of the asymmetric unit of $K[K(THF)_2][\{(NON)Al\}_2(C_6O_6)]$, **3**, in the solid state as determined by X-ray crystallography. Hydrogen atoms omitted and selected groups represented in wireframe format for clarity; thermal ellipsoids drawn at the 50% probability level. Key metrical parameters are listed in **Table 6.1**.

The isolated yield of [**2**-$K(C_7H_8)]_2$ obtained from [**1**-K]$_2$ and CO is low (ca. 10 %), and *in situ* ^{1}H NMR monitoring is consistent with the formation of other (NON)Al-containing species under these reaction conditions. Hypothesizing that this is due to the formation of other homologation products of the type $[C_nO_n]^{4-}$, we sought (i) to probe the reactivity of isolated samples of [**2**-$K(C_7H_8)]_2$ with CO under more forcing conditions, to see if homologation could be driven towards longer C–C-bonded chains; and (ii) to investigate if greater control of the delivery of the carbon monoxide (and with it the product distribution) could be achieved by the use of alternative CO-containing reagents.Targeting the second of these objectives, we

employed $Fe(CO)_5$ as a labile (and readily soluble) source of the CO molecule in reactions with [**1**-K]$_2$. Reaction with four equivalents of $Fe(CO)_5$ in benzene-d_6 in the presence of the crown ether 12-crown-4 (to aid crystallization), leads to the formation of [**2**-K(12-c-4)]$_2$, the solid-state structure of which is very closely related to that of [**2**-K(C_7H_8)]$_2$ (see Supporting Information). While the potential involvement of the iron centre in $Fe(CO)_5$ in this chemistry cannot be ruled out, it is noteworthy that conversion to the same $[C_4O_4]^{4-}$ fragment via this approach is markedly higher (20-30 %) than that obtained using gaseous CO.

Table 6.1: Key metrical parameters for aluminium complexes containing $[C_4O_4]^{n-}$ ions (n = 2, 4, 6).

	$[C_4O_4]^{4-}$			**$[C_4O_4]^{6-}$**	**$[C_4O_4]^{2-}$**
d/Å	[**2**-K(C_7H_8)]$_2$	[**2**-K(THF)]$_2$	[**2**-Li(OEt_2)]$_2$	[**4**-K_2(BEt_3)]$_2$	**5**
C–C	1.507(1) 1.373(1)	1.525(4) 1.489(3) 1.376(3)	1.482(5) 1.357(4)	1.481(3) 1.377(4)	1.438(2) 1.461(2)
C–O	1.233(1) 1.383(1)	1.213(4) 1.247(3) 1.373(3) 1.381(3)	1.246(5) 1.391(4)	1.382(3) 1.440(3)	1.257(2) 1.265(2)
Al–C	2.038(1)	2.053(2) 2.041(3)	2.063(4)	2.008(2)	n/a
Al–O	1.871(1)	1.872(2) 1.860(2)	1.877(2)	1.874(2)	1.933(1) 1.994(1)

The possibility for assembling $[C_nO_n]^{4-}$ chains with n > 4 was probed via the reaction of [**2**-K(C_7H_8)]$_2$ with CO at higher temperatures/pressures. Use of 2 atm pressure in THF-d_8 at ca. 65 ^oC over 4 d leads to quantitative conversion by ^1H NMR (through a single identifiable intermediate species) to a single product featuring two inequivalent NON ligands, and which can be shown by X-ray crystallography to be K[K(THF)$_2$] [{(NON)Al}$_2$(C_6O_6)], (**3**; **Figure 6.3**). **3** features a $[C_6O_6]^{4-}$ fragment formed by the assimilation of two further equivalents of CO, and which presents distinct (O,O and C,O) coordination modes at the two aluminium centres. The geometry of the $[C_6O_6]^{4-}$ group is unique, featuring a six membered pyran core, with the mono-branched nature of the six-carbon chain implying that C–C bond formation is also accompanied by complete cleavage of one of the C–O bonds. While the homologation of CO by highly

reducing molecular species to give linear or cyclic products has literature precedent, to our knowledge, the formation of *branched* carbon chains in this fashion, with accompanying cleavage of the exceptionally strong C-O bond is unprecedented. Examples of branched-chain carbon skeletons have been reported previously - but only via subsequent derivatization reactions of linear CO-derived chains with electrophiles such as CO_2 or MeI.[50]

Mechanistic studies: CO coordination and C–C/C=C bond formation.

While the two-electron reduction of CO by a number of main group compounds to give systems of the type $[C_nO_n]^{2-}$ has been reported,[18,20-23,29] four-electron processes yielding the topologically linear $[C_4O_4]^{4-}$ fragment have more limited literature precedent.[31,33] We were therefore keen to probe the mechanism of this transformation through both experimental and quantum chemical methods. As a key mechanistic principle, we first set out to determine whether the dimeric nature of the aluminyl reagent, [**1**-K]$_2$, is critical in driving the formation of the (four-electron reduction) product, $[C_4O_4]^{4-}$.

[**1**-K]$_2$ has been shown by DOSY NMR measurements to retain a dinuclear structure in solution in arene solvents. With this in mind, we targeted the reactivity of CO with related aluminyl compounds known to possess a mononuclear structure. The reaction of the (monomeric) lithium aluminyl complex $(Et_2O)_2$LiAl(NON) ([**1**-Li$(OEt_2)_2$])[57] with CO was therefore probed under similar conditions. Intriguingly, this chemistry leads to the formation of a very similar dinuclear product, [**2**-Li(OEt_2)]$_2$, featuring an analogous $[C_4O_4]^{4-}$ fragment, and two encapsulated Li^+ counter-ions each ligated by two of the oxygen atoms of the $[C_4O_4]^{4-}$ unit and an additional molecule of diethyl ether. The structural metrics relating to the $Al_2(C_4O_4)$ unit (**Table 6.1**) are very similar to those measured for [**2**-K(C_7H_8)]$_2$, being consistent with a centrosymmetric four-carbon chain incorporating two C–C and one C=C bonds. Moreover, the formation of [**2**-Li(OEt_2)]$_2$ from [**1**-Li$(OEt_2)_2$] in this manner (in greater conversion to [**2**-K(C_7H_8)]$_2$, 40 vs. 10 %) suggests that the state of aggregation of the aluminyl reagent is not critical in

determining the stoichiometry of this carbon-containing product. This observation is consistent with the mechanism proposed by Marks and co-workers for the formation of $[Cp^*_2Th\{OC(CH_2{}^tBu)C(O)\}]_2$, in which the central C=C bond is postulated as being constructed in the final mechanistic step through the dimerization of two mono-metallic carbene units (themselves accessed by bending of a coordinated ketene ligand).[36] Coles has also proposed that the dimerization of a dioxocarbene moiety is the final step in the formation of an ethenetraolate ligand, $[C_2O_4]^{4-}$.[58]

In the case of the (NON)Al-derived systems presented here, this hypothesis is consistent with the results of mechanistic calculations carried out using Density Functional Theory - for a model system in which the backbone ^{t}Bu and Dipp ^{i}Pr groups are replaced by Me, and the cation is omitted for computational efficiency (**Figure 6.4**). The rate-determining step for the lowest energy pathway is found to involve dimerization of two carbene fragments, with these each being derived from the coupling of two molecules of CO. Kinetically, the transition state energy for the C=C forming step is located ca. 34 kcal mol^{-1} above the starting materials (and ca. 37 kcal mol^{-1} above the preceding singlet carbene intermediate). This barrier height reflects, at least in part, the sterically encumbered (and anionic) nature of the two NON-supported fragments being brought together, and presumably underpins the relatively low yields associated with systems such as [**2**-K(C_7H_8)]$_2$ (and the possibility for forming longer C-based chains via carbene/CO coupling).[33]

In terms of the initial interaction of the CO molecule(s) with the (model) [(NON')Al]$^-$ unit, we find that end-on approach of CO perpendicular to the AlN_2 plane in a manner analogous to that determined for CO-adducts of isoelectronic silylene systems, $X_2Si{\cdot}CO$,[59] does not correspond to a local minimum on the potential energy surface. Rather, reflecting the nucleophilic nature of the aluminyl reagent, the approach of the carbon monoxide unit gives rise to a bent Al–C–O unit, and the predominant orbital interaction involves electron donation

from Al to the π* orbital of CO. For the model C-bound bis (carbonyl) adduct $[(NON')Al(CO)_2]^-$, the HOMO (**Figure 6.5**) defines a three-centre interaction involving the aluminium-centred lone pair and the π* orbitals of the two carbonyl ligands. Moreover, ETS-NOCV analysis determines that this three-centre 'backbonding' interaction accounts for the majority (261 kcal mol^{-1}) of the orbital interaction energy (ΔE_{orb}).[60] By contrast, the complementary 3-centre interaction, involving donation from the CO lone pairs to the Al-centred p_π-orbital accounts for only 25 kcal mol^{-1}. By means of comparison, a related ETS-NOCV analysis on the mono-carbonyl adduct of a cationic borole (in which the CO ligand behaves primarily as a σ-donor) yields 26 kcal mol^{-1} (back-bonding to CO) and 106 kcal mol^{-1} (sigma donation from CO).[61] As such, the primary role of the CO donors in $[(NON')Al(CO)_2]^-$ is strongly suggested to be as Z-type ligands.

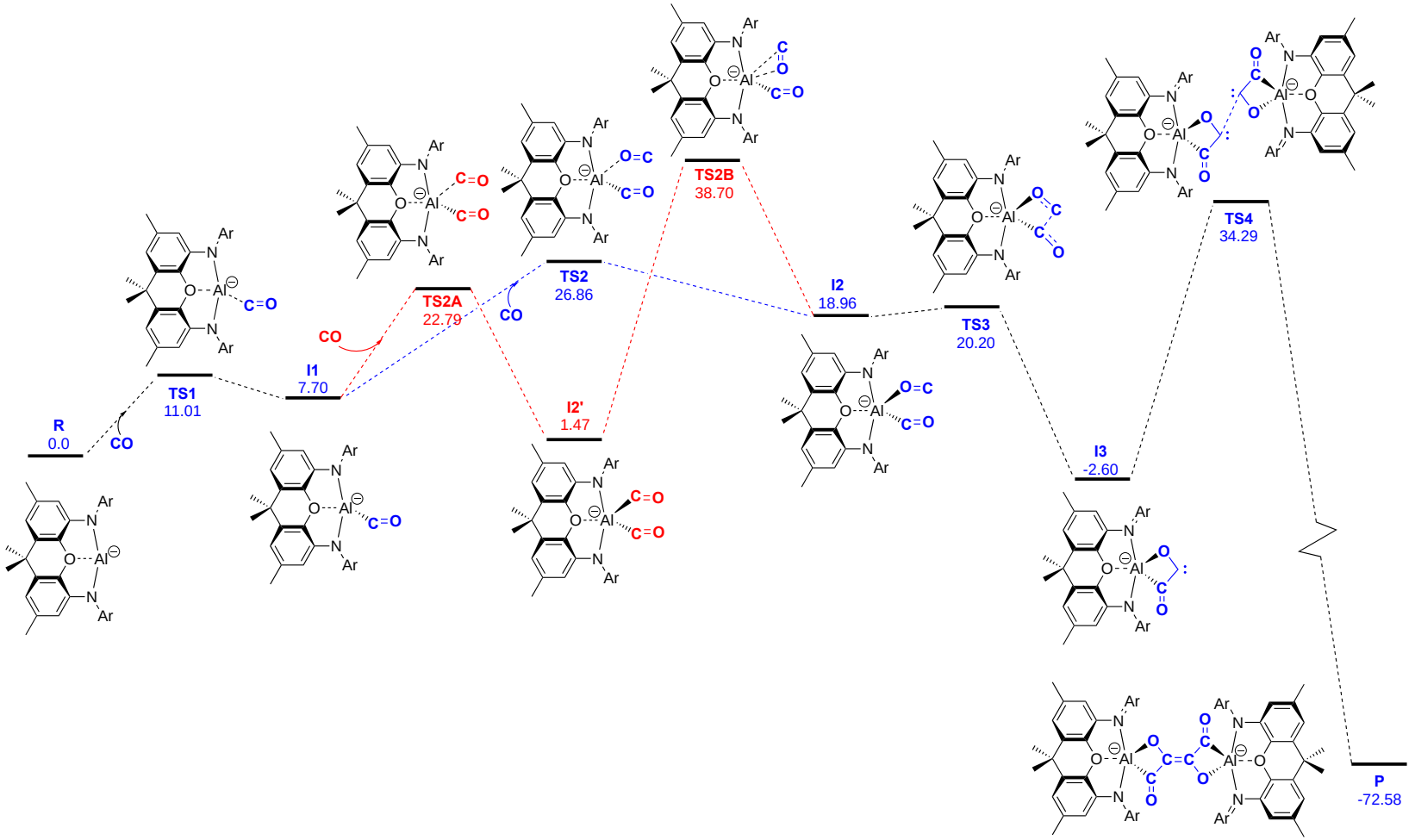

Figure 6.4: Proposed mechanism for CO homologation. The lowest energy pathway (blue) involves iso-carbonyl binding of one molecule of CO (**I2**); the alternative (higher barrier) pathway shown in red involves binding of the second CO through carbon (**I2'**) then isomerization to **I2**. (Calculations carried out at the B3LYP/def2-TZVP//B3LYP/def2-SVP level with solvation modelled with CPCM (benzene), and backbone ^{t}Bu groups replace by Me for computational efficiency).

While bis-*C*-ligated adduct, $[(NON')Al(CO)_2]^-$ (**I2'**) represents the lowest energy form of the dicarbonyl species, onward transformation into carbene intermediate **I3** necessarily involves rotation of one of the CO ligands to generate the isomeric species $[(NON')Al(CO)(OC)]^-$ (**I2**) featuring one isocarbonyl donor.[62] The barrier to this isomerization within the coordination sphere of aluminium (ca. 40.2 kcal mol^{-1}) is found to be significantly higher than that for simple dissociation/re-association. Moreover, while **I2** is ca. 17.5 kcal mol^{-1} higher in energy than **I2'**, it is capable of undergoing a very facile C–C coupling to generate carbene intermediate **I3** which is lower in energy than either of the carbonyl adducts.

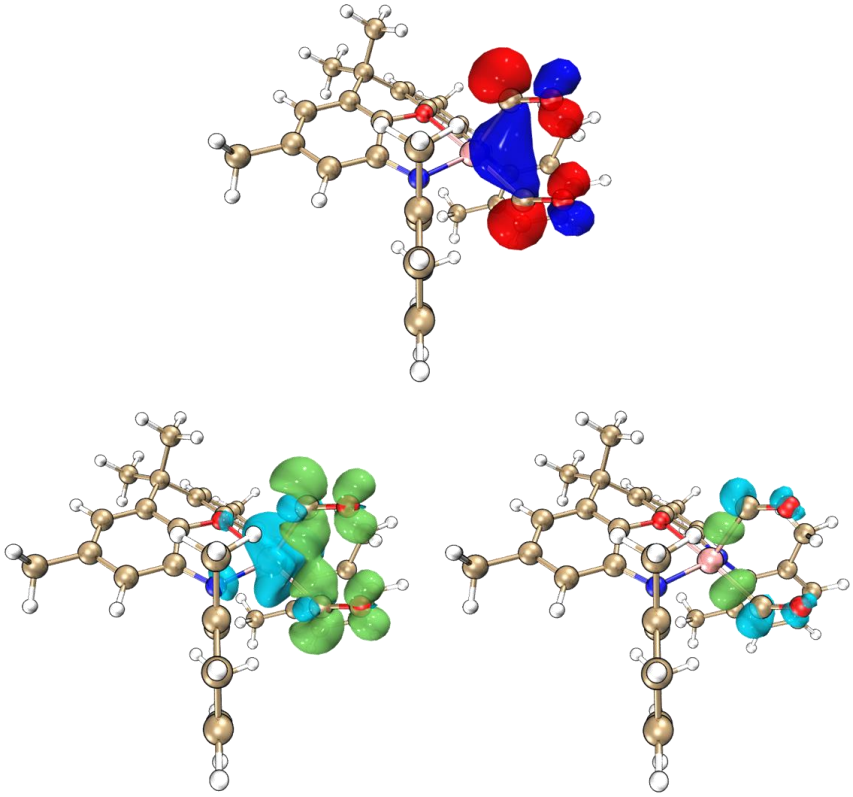

Figure 6.5: (upper) HOMO of the model C-bound bis(carbonyl) adduct $[(NON')Al(CO)_2]^-$ (shading denotes phasing of wavefunction); (lower) predominant orbital interactions determined by ETS-NOCV methods for the binding of the two carbonyl ligands (shading denotes deformation densities: blue/green - depletion/enhancement of electron density).

Interestingly, although C=C bond formation represents the key thermodynamic driving force for the overall homologation reaction (with the final dimerization process being energetically downhill by ca. 70 kcal mol^{-1}), experimental evidence for the *lability* of the central C=C bond in $[C_4O_4]^{4-}$ systems can be obtained from the reactions of isolated samples of [**2**-

$K(C_7H_8)]_2$ with alkali metal hydroborate reagents. In the case of the reaction with Li[^{s}Bu$_3$BH] in benzene/THF, simple cation metathesis is observed, generating $[Li(THF)]_2$ [{(NON)Al}$_2$(C_4O_4)], [**2**-Li(THF)]$_2$, the structure of which closely resembles both [**2**-K(C_7H_8)]$_2$ and [**2**-Li(OEt_2)]$_2$ (see Supporting Information). However, thermolysis with K[Et_3BH] at ca. 65-70 °C in the same solvent system leads to 70 % conversion over a period of 14 d to a new species, the apparently analogous potassium salt [**2**-K(THF)]$_2$. The structure of this species, however, can be shown by X-ray crystallography to feature the alternative *syn* disposition of substituents about the central C=C double bond (**Scheme 6.2** and **Figure 6.6**).[33] The C=C/C–C and C=O/C–O bond lengths within the carbon chain are not significantly different from the *anti* form, but the [**2**-K(THF)]$_2$ units are linked in the solid state via bridging K^+ cations into tetra-aluminium 'dimer of dimers' (see Supporting Information). The lower solubility of this aggregate presumably drives the *anti*-to-*syn* isomerization process.

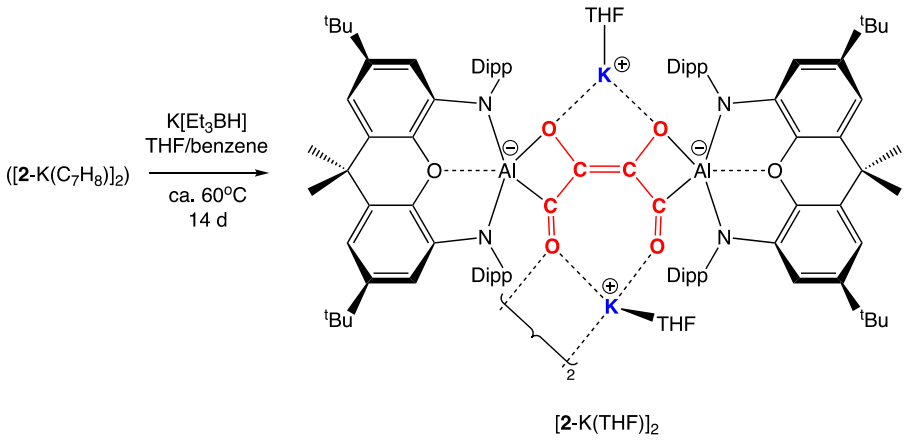

Scheme 6.2: Isomerization of $[C_4O_4]^{4-}$: anti to syn isomerization of the $[C_4O_4]^{4-}$ fragment in the presence of K[Et_3BH] in benzene/THF at ca. 60°C.

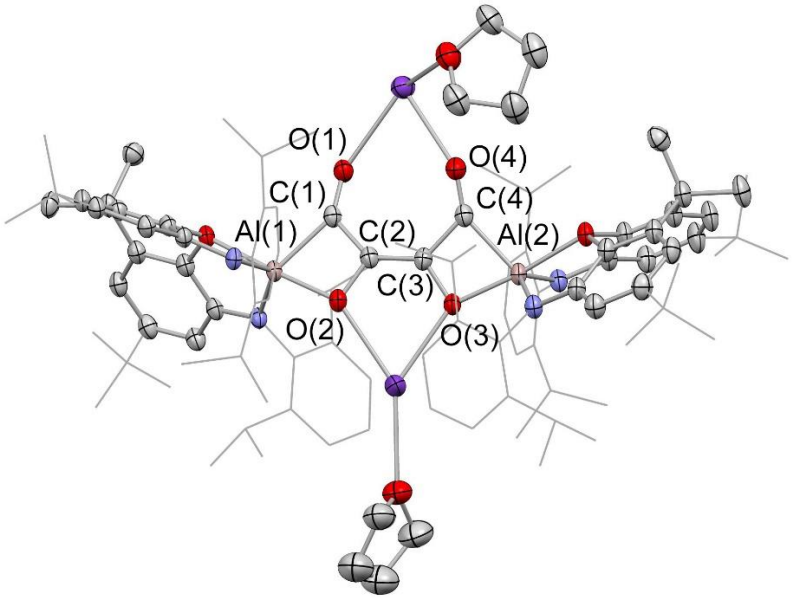

Figure 6.6: Molecular structure of $[K(THF)]_2[\{(NON)Al\}_2(C_4O_4)]$, [**2**-$K(THF)]_2$ in the solid state as determined by X-ray crystallography, showing dimeric unit analogous to [**2**-$K(C_7H_8)]_2$. Further aggregation into 'dimer of dimers' shown in Figure **S 6.2** . Hydrogen atoms omitted and selected groups represented in wireframe format for clarity; thermal ellipsoids drawn at the 50% probability level. Key metrical parameters are listed in **Table 6.1**.

Kinetically, both heat and the presence of additional K^+ cations can be shown to be necessary for the transformation to occur. C=O/C=C conjugation within the $[C_4O_4]^{4-}$ unit (manifested through resonance structures featuring a central C(2)–C(2') single bond) presumably lowers the barrier to rotation about the central C=C double bond, and allows mechanistically for the *anti*-to-*syn* isomerization process.

$[C_4O_4]^{6-}$ and $[C_4O_4]^{2-}$ systems: synthesis and structural comparisons.

While *isolated* samples of [**2**-$K(C_7H_8)]_2$ are resistant to further reduction by the hydride component of Li[^{s}Bu_3BH] or K[Et_3BH], the addition of K[Et_3BH] to a mixture of [**1**-$K]_2$/CO in benzene/THF *in situ* allows a more reduced product to be obtained. In this case, the reaction leads to evolution of dihydrogen (as judged by ^{1}H NMR spectroscopy) and the formation of the further reduced species $K_4[\{(NON)Al\}_2(C_4O_4)(BEt_3)_2]$ ([**4**-$K_2(BEt_3)]_2$), containing an unprecedented formally hexa-anionic $[C_4O_4]^{6-}$ chain (**Scheme 6.3** and **Figure 6.7**). Mechanistically, the fact that isolated samples of [**2**-$K(C_7H_8)]_2$ are not reduced (either chemically or electrochemically) suggests that the formation of ([**4**-$K_2(BEt_3)]_2$ involves a reduction event which occurs *prior* to the dimerization of the carbene intermediate **I3**.

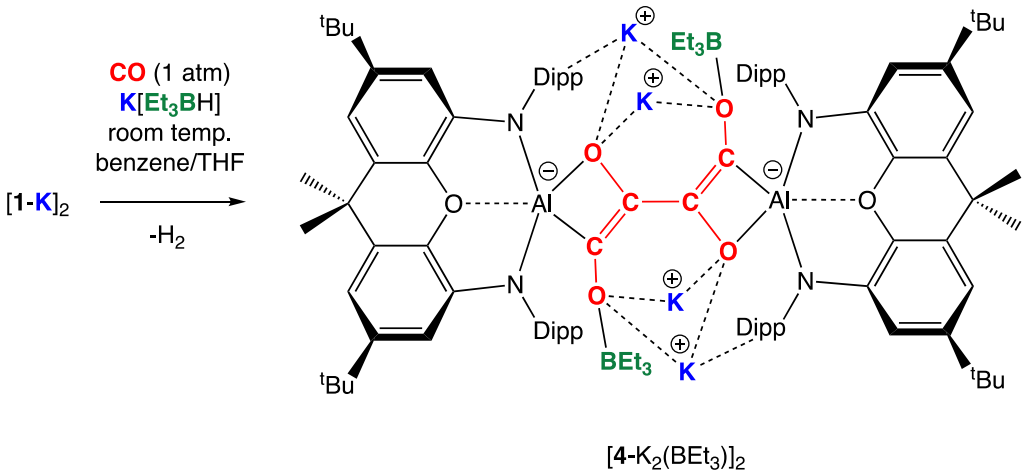

Scheme 6.3: Synthesis of a dialuminium system containing the $[C_4O_4]^{6-}$ fragment: synthesis of $K_4[\{(NON)Al\}_2(C_4O_4)(BEt_3)_2]$, $[4\text{-}K_2(BEt_3)]_2$, via the reaction of $[1\text{-}K]_2$ with CO in the presence of the hydride source $K[Et_3BH]$.

$[\mathbf{4}\text{-}K_2(BEt_3)]_2$ is extremely reactive, particularly in solution, and has limited solubility in compatible solvents; as such, it can be characterized by ^1H NMR spectroscopy and X-ray crystallography only. The centro-symmetric structure revealed crystallographically reveals four K^+ cations encapsulated by a combination of O-atom and aryl π system ligation. Two molecules of triethylborane are also incorporated into the molecular framework, bound to the terminal O-atoms of the $[C_4O_4]^{6-}$ chain. The central C–C distance is consistent with a single bond (1.481(3) Å) and the two terminal CC linkages feature bond lengths (1.377(4) Å) reflective of a C=C bond within an enolate functionality. The C–O distances (1.382(3) and 1.440(3) Å) are consistent with single bonds. As such, the structural metrics for $[\mathbf{4}\text{-}K_2(BEt_3)]_2$ are consistent with a system based around a butadiene-tetraolate skeleton, C(–O)=C(–O)–C(–O)=C(–O).

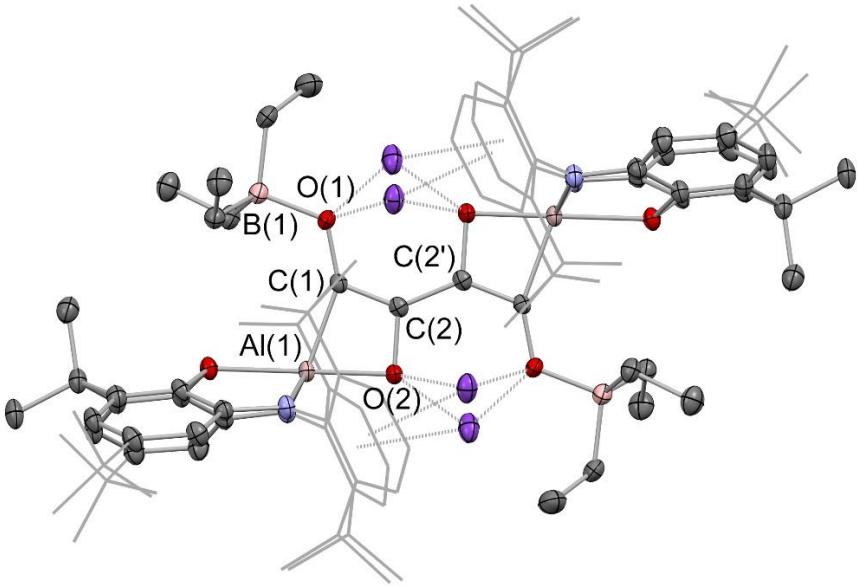

Figure 6.7: Molecular structure of [**4**-$K_2(BEt_3)$]$_2$ in the solid state as determined by X-ray crystallography. Hydrogen atoms omitted and selected groups represented in wireframe format for clarity; thermal ellipsoids drawn at the 50% probability level. Key metrical parameters are listed in **Table 6.1**.

To allow for a complete structural comparison of the series of systems of the type $[C_4O_4]^{n-}$ (n = 2, 4, 6) within the same aluminium coordination sphere, we also targeted the corresponding $[C_4O_4]^{2-}$ (squarate) system. Such systems have been synthesized in the past by homologation of CO using metal centres (or combinations of metal centres) capable of effecting a two-electron reduction.[20,44] In our hands, however, dimeric Al(II) systems such as (NON)Al-Al(NON)[51] do not react with CO under either thermal or photolytic conditions, presumably reflecting the stronger nature of the metal-metal bond, compared (for example) to dimeric Mg(I) reductants.[20-22] For structural comparison, we therefore examined alternative synthetic approaches involving the reactions of pre-formed squarate salts $M_2[C_4O_4]$ with the readily available Al(III) iodide precursor (NON)AlI. In the event, (NON)Al(C_4O_4)Al(NON) (**5**) is most easily accessed by combining the disilver salt of squaric acid, $Ag_2[C_4O_4]$ with (NON)AlI in Et_2O. **5** has been characterized by standard spectroscopic and analytical methods, and by X-ray crystallography (**Figure 6.8**). Its molecular structure features a planar carbocyclic $[C_4O_4]^{2-}$ ligand bridging between the two aluminium centres. The carbon-containing fragment closely resembles those reported previously,[20,44] featuring C–C and C–O distances of 1.438(2)/1.461(2) and 1.257(2)/1.265(2) Å, respectively, consistent with the presence of a delocalized π system involving all four CO units, albeit with the four-fold symmetry of the free squarate ion being

disrupted by chelation to the aluminium centres. The two different Al–O distances (1.933(1) and 1.994(1) Å) reflect a geometry at aluminium which is between square pyramidal and trigonal bipyramidal (= 0.55), with the longer bond length being associated with the axial O-donor (assuming the TBP limit).

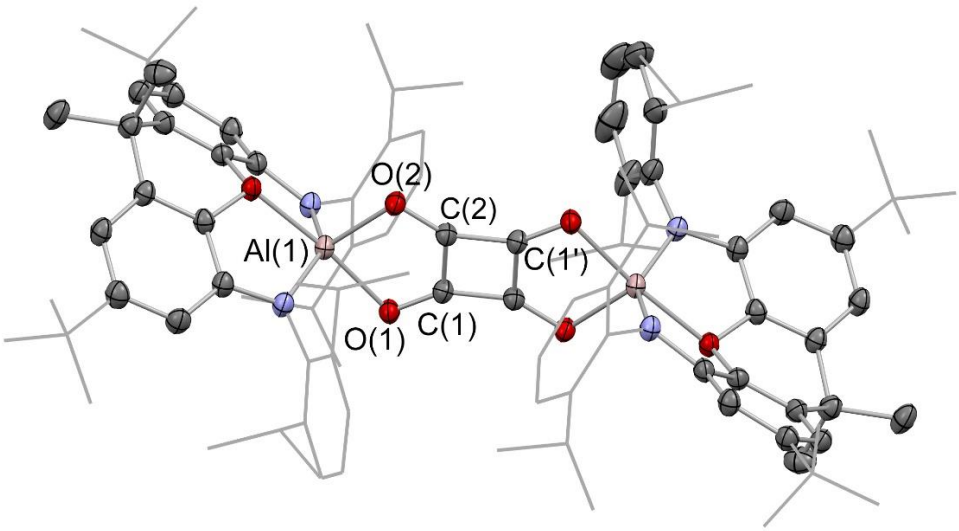

Figure 6.8: Molecular structure of the dialuminium-supported $[C_4O_4]^{2-}$ compound $\{(NON)Al\}_2(C_4O_4)$, **5**, in the solid state as determined by X-ray crystallography. Hydrogen atoms omitted and selected groups represented in wireframe format for clarity; thermal ellipsoids drawn at the 50% probability level. Key metrical parameters are listed in **Table 6.1**.

The availability of structural data for **5**, [**2**-$K(C_7H_8)]_2$ and [**4**-$K_2(BEt_3)]_2$ provides a unique opportunity to probe the effects on the carbon/oxygen aggregate of stepwise (formal) reduction of the carbocyclic fragment (**Figure 6.9**) - notwithstanding the fact that both (experimentally) chemical and electrochemical oxidation or reduction of [**2**-$K(C_7H_8)]_2$ are not facile. The two π-electron squarate dianion has been described as possessing a 'moderate' aromaticity,[63] a factor which underpins the prevalence of this planar carbocycle in four-carbon systems derived from two-electron reduction processes of CO.[20,44] In the case of **5**, DFT calculations imply that an alternative (linear) isomer featuring a chain of four –C(=O)– units (akin to a doubly oxidized form of [**2**-$K(C_7H_8)]_2$) is not an energetic minimum, rearranging to give a system featuring a bridging ethynediolate fragment ($[OCCO]^{2-}$), and two aluminium-bound CO ligands (which even then lies ca. 10.8 kcal mol^{-1} above the squarate form; see Supporting Information). The topologically linear butenedione diolate structure associated with the more heavily reduced $[C_4O_4]^{4-}$ tetra-anion avoids the formation of a Huckel 4π anti-aromatic

carbocycle derived from the addition of an additional pair of electrons to the LUMO of the squarate system. An alternative carbocyclic isomer featuring a more pronounced rectangular 'squarate' core (akin to the Jahn-Teller distorted structure of the related 4π electron system cyclobutadiene)[64] is found to lie significantly higher in energy (by > 48 kcal mol^{-1}).

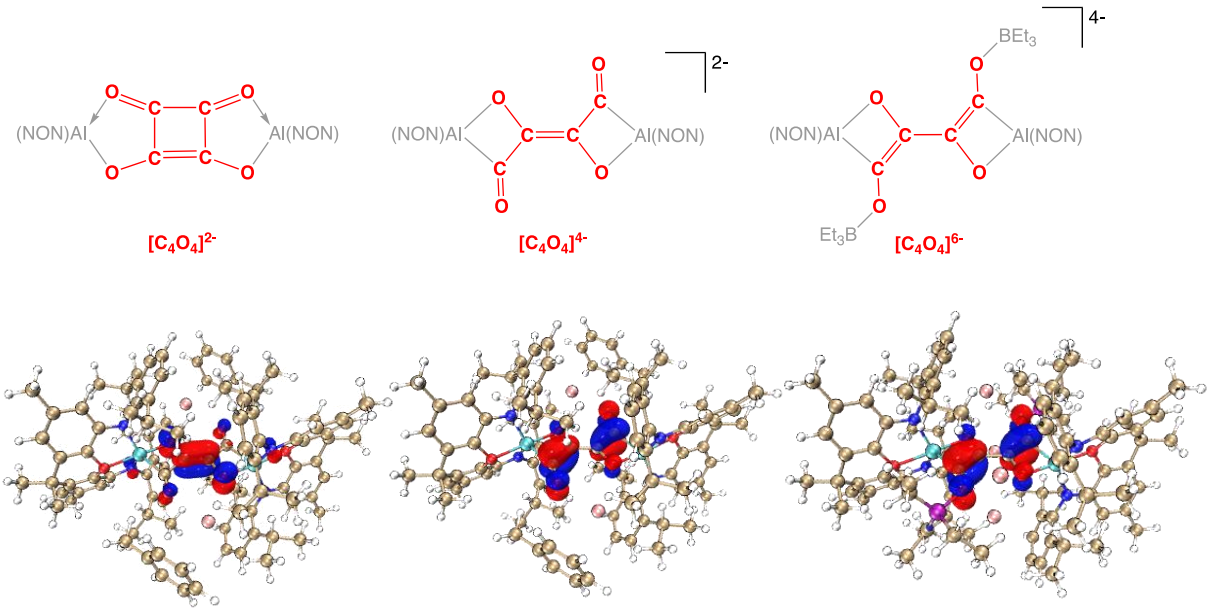

Figure 6.9: Comparison of the structures of the $[C_4O_4]^{n-}$ fragments within **5**, [**2**-K(C_7H_8)]$_2$ and [**4**-K_2(BEt_3)]$_2$: (upper) important resonance structures of $[C_4O_4]^{2-}$, $[C_4O_4]^{4-}$ and $[C_4O_4]^{6-}$ fragments; (lower) Key frontier orbitals: HOMO-1 and LUMO of [**2**-K(C_7H_8)]$_2$ and HOMO of [**4**-K_2(BEt_3)]$_2$

The HOMO-1 of [**2**-K(C_7H_8)]$_2$ (**Figure 6.9** (lower)), corresponds to a π-bonding orbital across the central CC linkage of the $[C_4O_4]^{4-}$ ligand. The formal addition of a further pair of electrons would then generate the $[C_4O_4]^{6-}$ hexa-anion which adopts a butadienetetraolate structure, via reduction of the enedione component to the corresponding bis(enolate). The structural changes associated with the CC and CO linkages on transitioning from $[C_4O_4]^{4-}$ to $[C_4O_4]^{6-}$ are consistent with the form of the LUMO of [**2**-K(C_7H_8)]$_2$ (and the HOMO of [**4**-K_2(BEt_3)]$_2$), which features out-of phase π interactions in the terminal CO and central CC units (**Figure 6.9**).

The overall transition from $[C_4O_4]^{2-}$ to $[C_4O_4]^{4-}$ to $[C_4O_4]^{6-}$ is characterized by net bond cleavage (C–C/C–O bonds: 11 to 10 to 9) consistent (at a simplistic level) with successive filling of anti-bonding molecular orbitals. Comparison between the closely related $[C_4O_4]^{4-}$ and $[C_4O_4]^{6-}$ fragments in [**2**-K(C_7H_8)]$_2$ and [**4**-K_2(BEt_3)]$_2$, respectively, reflects the net conversion of C–O bonds to C–C bonds in the presence of additional reductant. The roles of the $[Et_3BH]^-$ reagent in

bringing about this transformation (acting as both a source of electrons and of the BEt_3 fragment bound at C–O^-) suggest that it acts as a surrogate for H_2 in the Fischer-Tropsch Process.[2]

Conclusions

We have shown here that four- or six-electron reduction of CO can be accomplished by the use of anionic aluminium(I) ('aluminyl') compounds of the type $M_n[(NON)Al]_n$ to give topologically linear or branched C_4/C_6 chains, depending on reaction conditions. The mechanism for homologation to the $[C_4O_4]^{4-}$ system proceeds via rate-limiting formation of the central C=C double bond from two carbene fragments, and rationalizes the synthesis of this system from both monomeric (M = Li) and dimeric (M = K) precursors. Initial adduct formation with CO relies on the highly electron-rich nature of the aluminyl reagent, which drives an unusual (primarily Z-type) mode of interaction of the CO molecule with the metal centre. The onward formation of $[C_6O_6]^{4-}$ from $[C_4O_4]^{4-}$ demonstrates for the first time a homogeneous process which brings about chain branching via complete C-O bond cleavage. Comparison of the linear $[C_4O_4]^{4-}$ system with the $[C_4O_4]^{6-}$ congener formed under more reducing conditions, reflects the net conversion of C–O bonds to C–C bonds in the presence of additional reductant.

Characterizing data

General considerations

All manipulations were carried out using standard Schlenk line or dry-box techniques under an atmosphere of argon or dinitrogen. Et_2O and THF were distilled from sodium or potassium and benzophenone. All other solvents were degassed by sparging with argon and dried by passing through a column of the appropriate drying agent. NMR spectra were measured in benzene-d_6 (which was dried over potassium) or THF-d_8 (which was dried over CaH_2), with the solvent then being distilled under reduced pressure and stored under argon in Teflon valve ampoules. NMR samples were prepared under argon in 5 mm Wilmad 507-PP tubes fitted with J. Young Teflon valves. ^1H and $^{13}C\{^1H\}$ NMR spectra were recorded on Bruker Avance III HD nanobay 400 MHz, Bruker Avance III 500 MHz, or Bruker NEO 600 MHz spectrometers at ambient temperature and referenced internally to residual proteo-solvent (^1H) or solvent (^{13}C) resonances and are reported relative to tetramethylsilane (δ = 0 ppm). Assignments were confirmed using two-dimensional ^1H-^1H and ^{13}C-^1H NMR correlation experiments. Chemical shifts are quoted in δ (ppm) and coupling constants in Hz. Elemental analyses were carried out by Elemental Microanalysis Ltd, Okehampton, Devon, UK. **NON**AlI[66a], K_2[**NON**Al]$_2$[66a], [Li(OEt$_2$)$_2$][**NON**Al][66b] and Ag_2(squarate)[67] were prepared according to literature methods. All other reagents were used as received.

Synthesis of novel compounds

Complete details of synthetic methods and characterizing data, crystallographic information are details of quantum chemical studies are provided in the Supporting Information. Starting materials NONAlI,[51a] K_2[NONAl]$_2$,[51a] [Li(OEt$_2$)$_2$] [NONAl][57] and Ag_2(squarate)[65] were prepared according to literature methods. All other reagents were used as received.

[K(C$_7$H$_8$)]$_2$[{(NON)Al}$_2$(C$_4$O$_4$)], ***[2-K(C$_7$H$_8$)]$_2$****:*

To a 25 mL reaction bomb was added [1-K]$_2$ (250 mg, 0.34 mmol) and benzene (7.5 mL). The resulting mixture was degassed twice using the freeze-pump-thaw method, and sealed under

vacuum. The bomb was then warmed to 307 K in an oil bath, and after a few minutes the headspace was charged with CO (1.5 atm, ca. 1.2 mmol). After sealing the vessel, the mixture was vigorously shaken for 30 s, and subsequently allowed to stand undisturbed at 307 K for 16 h. Recrystallization from toluene led to the formation of small orange crystals of [2-K(C_7H_8)]$_2$·4(C_7H_8); isolated yield of single crystals: 37 mg, 11 %. Anal. Calc. for $C_{98}H_{124}Al_2K_2N_4O_6$ + 1.5 toluene: C 75.57, H 7.95, N 3.25; found: C 75.52, H 8.04, N 3.22. ^{1}H NMR (400 MHz, THF-d_8) δ 7.07 – 6.95 (m, 6H, Dipp-Ar-C*H*), 6.42 (d, *J* = 1.9 Hz, 2H, XA-C*H*^{1}), 5.62 (d, *J* = 1.9 Hz, 2H, XA-C*H*^{3}), 3.30 – 3.14 (m, 4H, C*H*Me$_2$), 1.73 (s, 3H, C(C*H*$_3$)$_2$), 1.56 (s, 3H, C(CH$_3$)$_2$), 1.11 (d, *J* = 6.8 Hz, 6H, CH(C*H*$_3$)$_2$), 1.04 (s, 18H, C(C*H*$_3$)$_3$), 0.86 (d, *J* = 6.8 Hz, 6H, CH(C*H*$_3$)$_2$), 0.68 (d, *J* = 6.8 Hz, 6H, CH(C*H*$_3$)$_2$), 0.43 (d, *J* = 6.8 Hz, 6H, CH(C*H*$_3$)$_2$). ^{13}C NMR (126 MHz, THF-d_8) δ 148.2 (Dipp-*o*-*C*), 147.8 (*C*^{t}Bu), 147.6 (Dipp-*o*-*C*), 146.8 (XA-*C*N), 144.8 (Dipp-*i*-*C*), 142.5 (XA-*C*O), 133.8 (*C*CMe$_2$), 131.3 (C(=O)*C*O), 129.2 (C_6H_6), 125.4 (Dipp-Ar-*C*H), 125.2 (Dipp-Ar-*C*H), 123.6 (Dipp-*m*-*C*H), 111.0 (XA-*C*^{3}H), 105.3 (XA-*C*^{1}H), 37.9 (*C*CMe$_2$), 35.5 (*C*Me$_3$), 32.6 (C(*C*H$_3$)$_2$), 32.2 (C(*C*H$_3$)$_3$), 29.1 (*C*H(CH$_3$)$_2$), 28.5 (*C*H(CH$_3$)$_2$), 26.3 (CH(*C*H$_3$)$_2$), 25.5* (CH(*C*H$_3$)$_2$), 24.7 (CH(*C*H$_3$)$_2$), 24.5 (CH(*C*H$_3$)$_2$), 23.8 (C(*C*H$_3$)$_2$). *Overlapped with solvent signal – located in HSQC and HMBC. Due to quadrupolar broadening the resonance associated with the Al-*C*(=O) group was not observed in the range -30 to 300 ppm. The corresponding signal is measured for the related derivative [2-K(12-crown-4)]$_2$ at 296.2 ppm.

[K(12-c-4)]$_2$[{(NON)Al}$_2$(C_4O_4)], ***[2-K(12-c-4)]$_2$:***

(Method 1): To a suspension of [2-K(C_7H_8)]$_2$ (15 mg, 0.009 mmol) in benzene-d_6 (0.5 ml) was added a solution of 12-crown-4 in toluene (0.18 mL, 0.1 M, 0.018 mmol, 2.05 equiv.) and the reaction mixture heated at 358 K for 2 h. Volatiles were removed under vacuum and the product was obtained as an orange powder. Yield 13 mg, 80 % (quantitative by NMR). (Method 2): To a solution of [1-K]$_2$ (0.120 g, 0.163 mmol) in toluene (5 mL) was added a solution of 12-crown-4 in toluene (3.2 mL of a 0.1 M solution, 0.320 mmol). The resulting red solution was stirred at room temperature for 5 min, before addition of Fe(CO)$_5$ (22 µL, 0.161 mmol). The resulting dark red solution was stirred overnight. Removal of volatiles yields a yellow oil which can be dissolved in

minimal benzene and stored at room temperature overnight to yield single crystals of [2-K(12-c-4)]$_2$·4(C_6H_6) suitable for X-ray crystallography. Isolated yield of single crystals ca. 5 mg, 20% (30 % by NMR). ^{1}H NMR (600 MHz, THF-d_8) δ 7.01 (t, *J* = 7.0 Hz, 2H, Dipp-*p*-C*H*), 6.96 (d, *J* = 7.0 Hz, 4H, Dipp-*m*-C*H*), 6.40 (d, *J* = 2.0 Hz, 2H, XA-C*H*^{1}), 5.59 (d, *J* = 1.9 Hz, 2H, XA-C*H*^{3}), 3.60 (s, 16H, 12-crown-4), 3.42 – 3.34 (m, 2H, C*H*Me$_2$), 3.14 (sept., *J* = 6.9 Hz, 2H, C*H*Me$_2$), 1.73 (s, 3H, C(C*H*$_3$)$_2$), 1.58 (s, 3H, C(C*H*$_3$)$_2$), 1.24 (d, *J* = 6.7 Hz, 6H, CH(C*H*$_3$)$_2$), 1.03 (s, 18H, C(C*H*$_3$)$_3$), 0.79 (d, *J* = 6.8 Hz, 6H, CH(C*H*$_3$)$_2$), 0.77 (d, *J* = 6.8 Hz, 6H, CH(C*H*$_3$)$_2$), 0.33 (d, *J* = 6.8 Hz, 6H, CH(C*H*$_3$)$_2$). ^{13}C NMR (151 MHz, THF-d_8) δ 296.2 (Al*C*O), 147.7 (Dipp-*o*-*C*), 147.5 (Dipp-*o*-*C*), 147.4 (*C*^{t}Bu), 146.9 (XA-*C*N), 145.2 (Dipp-*i*-*C*), 142.7 (XA-*C*O), 134.1 (*C*CMe$_2$), 130.8 (C(=O)*C*O), 125.9 (Dipp-*m*-*C*H), 125.1 (Dipp-*p*-*C*H), 123.1 (Dipp-*m*-*C*H), 111.4 (XA-*C*^{3}H), 105.3 (XA-*C*^{1}H), 70.5 (O*C*H$_2$), 37.8 (*C*Me$_2$), 35.4 (*C*(CH$_3$)$_3$), 32.2 (C(*C*H$_3$)$_3$), 32.0 (C(*C*H$_3$)$_2$), 29.4 (*C*HMe$_2$), 28.7 (*C*HMe$_2$), 26.5 (CH(*C*H$_3$)$_2$), 25.0 (CH(*C*H$_3$)$_2$), 24.6 (CH(*C*H$_3$)$_2$), 24.3 (CH(*C*H$_3$)$_2$), 23.6 (C(*C*H$_3$)$_2$).

[Li(OEt$_2$)][{(NON)Al}$_2$(C$_4$O$_4$)], [2-Li(OEt$_2$)]$_2$ and [Li(THF)]$_2$[{(NON)Al}$_2$(C$_4$O$_4$)], ***[2-Li(THF)]$_2$****:*

Ether adduct: (Method 1) A solution of [1-Li] (15 mg, 0.017 mmol) in C_6D_6 (0.5 mL) was degassed twice using the freeze-pump-thaw method. The headspace was then charged with CO (2 bar) and briefly shaken. ^{1}H NMR reveals formation of a mixture of products, including [2-Li(OEt$_2$)]$_2$ in ca. 40% yield. Upon concentration (to ca. 1/3 volume) and standing for two days, X-ray quality crystals of [2-Li(OEt$_2$)]$_2$ formed.

(Method 2) [2-K(C_7H_8)]$_2$ (30 mg, 0.018 mmol) and LiI (5 mg, 2.1 equiv.) were dissolved in Et$_2$O (15 mL) and briefly heated to 318 K in a sealed ampoule, leading to a colour change from orange to yellow. The mixture was allowed to cool to room temperature and the resulting cloudy mixture was filtered onto benzene (8 mL). After mixing, the solution was concentrated until it turned turbid (ca. 5 mL). At this point a sample (0.2 mL) was taken and diluted with C_6D_6 (0.3 ml) and a ^{1}H NMR spectrum measured. The resulting spectrum shows the presence of a single species, which has the same spectroscopic signals as those obtained using method 1 in a J. Young's NMR tube. ^{1}H NMR (400 MHz, C_6D_6) δ 6.67 (d, *J* = 2.0 Hz, 2H, XA-C*H*^{1}), 6.00 (d, *J* = 2.0 Hz, 2H, XA-C*H*^{3}), 3.72 (sept, *J* = 6.9 Hz, 2H), 1.70 (s, 3H, C(C*H*$_3$)$_2$), 1.61 (s, 3H, C(C*H*$_3$)$_2$), 1.52 (d, *J* = 6.9 Hz, 6H,

$CH(CH_3)_2$), 1.19 (s, 18H, $C(CH_3)_3$), 0.36 (d, *J* = 6.9 Hz, 6H, $CH(CH_3)_2$). Samples of $[2\text{-}Li(OEt_2)]_2$ lose Et_2O under continuous vacuum. Dissolution in THF-d_8, however, yields spectroscopic signals indistinguishable from samples of $[2\text{-}Li(THF)]_2$ prepared as set out below.

THF adduct: A solution containing $[2\text{-}K(C_7H_8)]_2$ (ca. 20 mg, 0.012 mmol) was prepared as described above and $Li[HB^sBu_3]$ (1 mL of a 1 M solution in THF) was added. The mixture was heated at 307 K for 16 h affording small yellow crystals. Analytically pure samples can be obtained by recrystallization from minimal benzene or THF and washing with THF. Isolated yield of single crystals: 7 mg, 30% over last step. Anal. Calc. for $C_{106}H_{140}Al_2Li_2N_4O_8$ + 1.75 THF: C 75.73, H 8.66, N 3.13; found: C 75.13, H 8.66, N 3.21. ^{1}H NMR (400 MHz, C_6D_6) δ 7.25 (m, 6H, Dipp-Ar-C*H*), 6.70 (d, *J* = 2.0 Hz, 2H, XA-C*H*^{1}), 6.05 (d, *J* = 2.0 Hz, 2H, XA-C*H*^{3}), 3.77 (sept, *J* = 6.9 Hz, 2H, C*H*Me_2), 3.70 (s, m, 4H, THF), 3.41 (sept, *J* = 6.9 Hz, 2H, C*H*Me_2), 1.69 (s, 3H, $C(CH_3)_2$), 1.60 (s, 3H, $C(CH_3)_2$), 1.58 (d, *J* = 6.9 Hz, 6H, $CH(CH_3)_2$), 1.32 (m, 4H, THF), 1.21 (s, 18H, $C(CH_3)_3$), 1.15 (overlapping d, *J* = 6.9 Hz, 12H, $CH(CH_3)_2$), 0.36 (d, *J* = 6.9 Hz, 6H, $CH(CH_3)_2$). ^{13}C NMR (151 MHz, C_6D_6) δ 147.8 (*C*^{t}Bu), 147.2 (Dipp-*o*-*C*), 146.3 (Dipp-*o*-*C*), 145.7 (XA-*C*^{4}), 143.6 (Dipp-*i*-*C*), 141.4 (XA-*C*O), 133.1 (*C*CMe_2), 125.8 (Dipp-*p*-*C* and Dipp-*m*-*C*), 123.0 (Dipp-*m*-*C*), 111.3 (XA-*C*^{3}H), 106.4 (XA-*C*^{1}H), 68.6 (THF-*C*O), 37.0 (*C*Me_2), 35.0 (*C*Me_3), 32.1 ($C(CH_3)_2$), 31.9 ($C(CH_3)_3$), 29.5 (*C*HMe_2), 28.2 (*C*HMe_2), 26.3 ($CH(CH_3)_2$), 25.4 (THF), 24.1 ($CH(CH_3)_2$), 23.9 ($CH(CH_3)_2$), 23.2 ($C(CH_3)_2$), 23.2 ($CH(CH_3)_2$). Due to quadrupolar broadening (and overlap with the solvent) the resonances associated with the $[C_4O_4]^{4-}$ fragment were not observed in the range -30 to 300 ppm. The corresponding signals are measured for the related derivative $[2\text{-}K(12\text{-crown-}4)]_2$ at 130.8 and 296.2 ppm. ^{7}Li NMR (156 MHz, C_6D_6) δ 0.61.

K[K(THF)$_2$][{(NON)Al}$_2$(C$_6$O$_6$)], ***3****:*

$[2\text{-}K(C_7H_8)]_2$ (25 mg, 0.015 mmol) was suspended in THF-d_8 (0.5 mL) in a J. Youngs NMR tube and degassed twice using the freeze-pump-thaw method. The headspace was then charged with CO (2 atm) and heated at 339 K for 4 d. During this time $[2\text{-}K(C_7H_8)]_2$ dissolved and a colour change from yellow to red to orange was observed. ^{1}H NMR monitoring shows quantitative conversion to a single product. After concentrating the solution to a quarter of its original, small pale orange

plates formed at the surface of the solution. Anal. Calc. for $C_{108}H_{140}Al_2K_2N_4O_{10}$ + 2 THF: C 72.16, H 8.14, N 2.90; found: C 72.13, H 8.06, N 2.55. ^{1}H NMR (600 MHz, THF-d_8) δ 7.43 (t, *J* = 7.6 Hz, 2H, Dipp-*p*-C*H*), 7.32 (t, *J* = 7.6 Hz, 2H, Dipp-*p*-C*H*), 7.25 (dd, *J* = 7.8, 1.6 Hz, 2H, Dipp-*m*-C*H*), 7.16 (dd, *J* = 7.6, 1.6 Hz, 2H, Dipp-*m*-C*H*), 7.09 (dd, *J* = 7.8, 1.6 Hz, 2H, Dipp-*m*-C*H*), 7.00 (dd, *J* = 7.7, 1.6 Hz, 2H, Dipp-*m*-C*H*), 6.49 (d, *J* = 1.9 Hz, 2H, XA-C^1*H*), 6.42 (d, *J* = 1.9 Hz, 2H, XA-C^1*H*), 5.36 (d, *J* = 1.9 Hz, 2H, XA-C^3*H*), 5.34 (d, *J* = 1.9 Hz, 2H, XA-C^3*H*), 3.46 – 3.36 (overlapping sept., 4H, C*H*Me$_2$), 3.32 (sept., *J* = 7.2 Hz, 2H, C*H*Me$_2$), 3.16 (sept., *J* = 6.9 Hz, 2H, C*H*Me$_2$), 1.75 (s, 3H, C(C*H*$_3$)$_2$), 1.73 (s, 3H, C(C*H*$_3$)$_2$), 1.57 (s, 3H, C(C*H*$_3$)$_2$), 1.54 (s, 3H, C(C*H*$_3$)$_2$), 1.20 (d, *J* = 7.0 Hz, 6H, CH(C*H*$_3$)$_2$), 1.03 (s, 18H, C(C*H*$_3$)$_3$), 1.00 (s, 18H, C(C*H*$_3$)$_3$), 0.95 (d, *J* = 6.9 Hz, 6H, CH(C*H*$_3$)$_2$), 0.87 (d, *J* = 6.7 Hz, 6H, CH(C*H*$_3$)$_2$), 0.83 (d, *J* = 6.8 Hz, 6H, CH(C*H*$_3$)$_2$), 0.80 (d, *J* = 6.7 Hz, 6H, CH(C*H*$_3$)$_2$), 0.73 (d, *J* = 6.7 Hz, 6H, CH(C*H*$_3$)$_2$), 0.68 (d, *J* = 6.8 Hz, 6H, CH(C*H*$_3$)$_2$), 0.51 (d, *J* = 6.8 Hz, 6H, CH(C*H*$_3$)$_2$). ^{13}C NMR (151 MHz, THF-d_8) δ = 258.6 (C_6O_6), 173.5 (C_6O_6), 169.0 (C_6O_6), 156.2 (C_6O_6), 149.4 (Dipp-*o*-*C*), 149.1 (Dipp-*o*-*C*), 148.0 (Dipp-*o*-*C*), 147.6 (*C*^{t}Bu), 147.5 (Dipp-*o*-*C*), 147.3 (*C*^{t}Bu), 146.1 (XA-*C*^{4}), 145.8 (Dipp-*i*-*C*), 145.7 (Dipp-*i*-*C*), 145.6 (XA-*C*^{4}), 142.7 (XA-*C*O), 141.5 (XA-*C*O), 133.7 (*C*CMe$_2$), 133.3 (*C*CMe$_2$), 129.2 (free C_6H_6), 127.4 (Dipp-*p*-*C*H), 127.3 (Dipp-*p*-*C*H), 127.2 (Dipp-*m*-*C*H), 126.2 (Dipp-*m*-*C*H), 124.4 (Dipp-*m*-*C*H), 123.8 (Dipp-*m*-*C*H), 118.2 (C_6O_6), 111.3 (XA-*C*^{3}H), 110.5 (C_6O_6), 106.5 (XA-*C*^{1}H), 105.9 (XA-*C*^{1}H), 37.9 (*C*Me$_2$), 37.8 (*C*Me$_2$), 35.5 (*C*Me$_3$), 35.4 (*C*Me$_3$), 32.2 (C(*C*H$_3$)$_3$), 32.1 (C(*C*H$_3$)$_3$), 32.1 (C(*C*H$_3$)$_2$), 32.0 (C(*C*H$_3$)$_2$), 29.2 (*C*HMe$_2$), 28.8 (*C*HMe$_2$), 28.1 (*C*HMe$_2$), 28.0 (*C*HMe$_2$), 26.2 (CH(*C*H$_3$)$_2$), 26.1 (CH(*C*H$_3$)$_2$), 26.0 (CH(*C*H$_3$)$_2$), 25.3 (CH(*C*H$_3$)$_2$), 25.2 (CH(*C*H$_3$)$_2$), 24.9 (CH(*C*H$_3$)$_2$), 22.9 (C(*C*H$_3$)$_2$), 22.9 (C(*C*H$_3$)$_2$).

$K_4[\{(NON)Al\}_2(C_4O_4)(BEt_3)_2]$, ***[4-$K_2$(BEt$_3$)]$_2$****:*

To a stirred solution containing [1-K]$_2$ (220 mg, 0.30 mmol), benzene (6.6 mL), and CO (ca. 1.5 bar) in a 25 mL reaction bomb was added K[HBEt$_3$] (1.5 mL of a 1M solution in THF, 1.5 mmol). After 24 h, the solution was concentrated to a fifth of its original volume under reduced pressure. Prolonged standing led to the formation of colourless extremely sensitive crystals of [4-K_2(BEt$_3$)]$_2$. Yield 12 mg, 4%. ^{1}H NMR (400 MHz, THF-d_8) δ 7.27 (br s, 6H, Dipp-Ar-C*H*), 6.36 (br s, 2H, XA-C*H*^{1}), 5.28 (s, 2H, XA-C*H*^{3}), 3.79 (br s, 2H, C*H*Me$_2$), 3.47 (sept, J = 6.6 Hz, 2H, C*H*Me$_2$),

1.68 (s, 6H, C(CH_3)$_2$), 1.28 (br s, 6H, CH(CH_3)$_2$), 1.00 (s, 18H, C(CH_3)$_3$), 0.80 (d, *J* = 6.6 Hz, 13H), 0.57 (t, *J* = 7.7 Hz, 9H, BCH_2CH_3), 0.06 (q, *J* = 7.7 Hz, 6H, BCH_2CH_3). Due to the low solubility and stability of this compound in solution, no satisfactory ^{11}B and ^{13}C spectra could be obtained.

[(NON)Al]$_2$(C_4O_4), ***5****:*

(NON)AlI (500 mg, 0.60 mmol, 2.0 eq) and $Ag_2(C_4O_4)$ (110 mg, 0.33 mmol) were suspended in Et_2O (10 mL) and the reaction mixture refluxed at 308 K for 48 h in the dark. Volatiles were removed in vacuo and the residue extracted into toluene (15 mL), filtered, and layered with hexane (15 mL). Upon standing for several days, crystals of 5 suitable for single crystal X-ray diffraction were obtained. Yield 180 mg, 39 %. Anal. Calc. for $C_{98}H_{124}Al_2N_4O_6$ + 0.5 hexane: C 78.21, H 8.51, N 3.61; found 78.08, H 8.76, N 3.34. ^{1}H NMR (400 MHz, C_6D_6) δ 7.20 (m, 2H, Dipp-*p*-C*H*), 7.14 (m, 4H, Dipp-*p*-C*H*), 6.72 (d, *J* = 1.9 Hz, 2H, XA-CH^1), 5.98 (d, *J* = 1.9 Hz, 2H, XA-CH^3), 3.54 (sept, *J* = 6.8 Hz, 4H, C*H*Me_2), 1.58 (s, 6H, C(CH_3)$_2$), 1.15 (s, 18H, C(CH_3)$_3$), 1.06 (d, *J* = 6.8 Hz, 12H, CH(CH_3)$_2$), 0.91 – 0.83 (br s, 12H, CH(CH_3)$_2$). ^{13}C NMR (126 MHz, C_6D_6) δ = 194.0 (C_4O_4), 148.9 (*C*^{t}Bu), 147.0 (Dipp-*o*-*C*), 144.4 (XA-*C*N), 141.0, 140.8 (Dipp-*i*-*C*, XA-*C*O), 133.3 (*C*CMe_2), 127.0 (Dipp-*p*-*C*), 125.1 (Dipp-*m*-*C*), 112.1 (XA-*C*^{3}H), 108.2 (XA-*C*^{1}H), 37.2 (*C*Me_2), 35.1(*C*Me_3), 31.7 (C(*C*H_3)$_3$), 28.4 (*C*HMe_2), 26.4 (br, C(*C*H_3)$_2$), 25.4 (CH(*C*H_3)$_2$), 24.7(CH(*C*H_3)$_2$).

Crystallographic Data

General details

Single-crystal X-ray diffraction data for all compounds were collected on an Oxford Diffraction/Agilent SuperNova diffractometer equipped with a 135 mm Atlas CCD area detector. Crystals were selected under Paratone-N oil, mounted on MiTeGen Micromount loops and quench-cooled using an Oxford Cryosystems open flow N2 cooling device.[68] Data were collected at 150 K using mirror monochromated Cu Kα radiation (λ = 1.5418 Å; Oxford Diffraction Supernova). Data collected were processed using the CrysAlisPro package, including unit cell parameter refinement and inter-frame scaling (which was carried out using SCALE3 ABSPACK within CrysAlisPro).[69] Equivalent reflections were merged and diffraction patterns processed with the CrysAlisPro suite.[70] Structures were solved ab initio from the integrated intensities using SHELXT[5] and refined on F2 using SHELXL[71] with the graphical interface OLEX2[72] or XSeed[73]. Selected crystallographic data are summarised in ables **ST 6.1** and **ST 6.2**, and full details are given in the supplementary deposited CIF files (CCDC 2114859-2114865 and 2118134). These data can be obtained free of charge from the Cambridge Crystallographic Data Centre via http://www.ccdc.cam.ac.uk/data_request/cif.

Table of Crystallographic data

ST 6.1: Crystallographic data for CO homologation and related compounds.

Compound	**$[2\text{-}K(C_7H_8)]_2$**	**$[2\text{-}K(12\text{-}c\text{-}4)]_2$**	**$[2\text{-}Li(OEt_2)]_2$**	**$[2\text{-}Li(THF)]_2$**
Formula	$C_{140}H_{172}Al_2K_2N_4O_6$	$C_{138}H_{180}Al_2K_2N_4O_{14}$	$C_{118}H_{156}Al2Li_2N_4O_8$	$C_{118}H_{152}Al_2Li_2N_4O_8$
Fw (g mol^{-1})	2138.97	2251.01	1826.30	1822.27
Cell setting	triclinic	monoclinic	triclinic	monoclinic
Space group	P -1	P 2_1/n	P -1	P 2_1/c
a (Å)	11.9812(2)	14.9714(3)	12.9738(12)	21.0096(3)
b (Å)	14.1102(3)	24.1421(4)	13.1913(12)	19.3474(3)
c (Å)	18.7841(3)	18.3072(3)	17.1181(15)	26.6821(4)
α (°)	95.810(2)	90	70.273(8)	90
β (°)	96.5580(10)	103.748(2)	84.966(7)	98.5930(10)
γ (°)	97.410(2)	90	82.504(7)	90
V (Å^3)	3106.71(10)	6427.4(2)	2731.1(4)	10724.0(3)
Z	1	2	1	4
ρ_{calc} (g cm^{-3})	1.143	1.163	1.110	1.129
Radiation, λ (Å)	Cu K_α, 1.54184	Cu K_α, 1.54184	Cu K_α, 1.54184	Cu K_α, 1.54184
μ (mm^{-1})	1.238	1.267	0.670	0.682
Reflections collected	75174	46647	19852	88487
Independent reflections	12904	13283	9799	22269
$R_{(int)}$	0.026	0.0402	0.0592	0.0523
Parameters	808	936	673	1311
R_1 (all data)	0.0405	0.0760	0.1354	0.0686
R_1 (I >2σ(I))	0.0368	0.0569	0.0670	0.0452
wR_2 (all data)	0.1068	0.1684	0.1854	0.1231
wR_2 (I >2σ(I))	0.1029	0.1516	0.1500	0.1090
GooF	1.048	1.075	0.996	1.009
T	150(2)	150.06(15)	150.01(10)	150.01(10)
CCDC ref	2114863	2114865	2114859	2114862

ST 6.2: Crystallographic data for CO homologation and related compounds.

Compound	**[2-K(THF)]$_2$**	**3**	**[4-K$_2$(BEt$_3$)]$_2$**	**5**
Formula	$C_{240}H_{336}Al_4K_4N_8O_{23}$	$C_{240}H_{348}Al_4K_4N_8O_{26}$	$C_{122}H_{166}Al_2B_2K_4N_4O_6$	$C_{110.40}H_{149.60}Al_2N_4O_6$
Fw (g mol^{-1})	3965.47	4025.56	2016.56	1682.69
Cell setting	triclinic	monoclinic	triclinic	monoclinic
Space group	P -1	C 2/c	P -1	P 2$_1$/c
a (Å)	15.1682(5)	43.9642(13)	12.1088(5)	17.8436(4)
b (Å)	19.7249(6)	13.9217(3)	13.4265(6)	17.7254(2)
c (Å)	20.7358(4)	39.0993(10)	19.2028(7)	18.2264(5)
α (°)	79.886(2)	90	101.260(3)	90
β (°)	71.094(2)	102.525(3)	94.270(3)	118.887(3)
γ (°)	75.739(3)	90	113.177(4)	90
V (Å^3)	5657.3(3)	23361.5(11)	2774.8(2)	5047.5(2)
Z	1	4	1	2
ρ_{calc} (g cm^{-3})	1.164	1.145	1.207	1.107
Radiation, λ (Å)	Cu K$_\alpha$, 1.54184	Cu K$_\alpha$, 1.54184	Cu K$_\alpha$, 1.54184	Cu K$_\alpha$, 1.54184
μ (mm^{-1})	1.355	1.328	2.008	0.673
Reflections collected	92463	88466	42687	66822
Independent reflections	23286	24207	10348	10527
R$_{(int)}$	0.0671	0.0550	0.0836	0.0438
Parameters	1434	1332	650	585
R$_1$ (all data)	0.1000	0.0751	0.0853	0.0598
R$_1$ (I >2σ(I))	0.0700	0.0539	0.0527	0.0502
wR$_2$ (all data)	0.2231	0.1562	0.1467	0.1503
wR2 (I >2σ(I))	0.1936	0.1402	0.1256	0.1382
GooF	1.035	1.031	1.023	1.028
T	150.01(10)	150.00(10)	150.01(10)	150.01(10)
CCDC ref	2114861	2118134	2114860	2114864

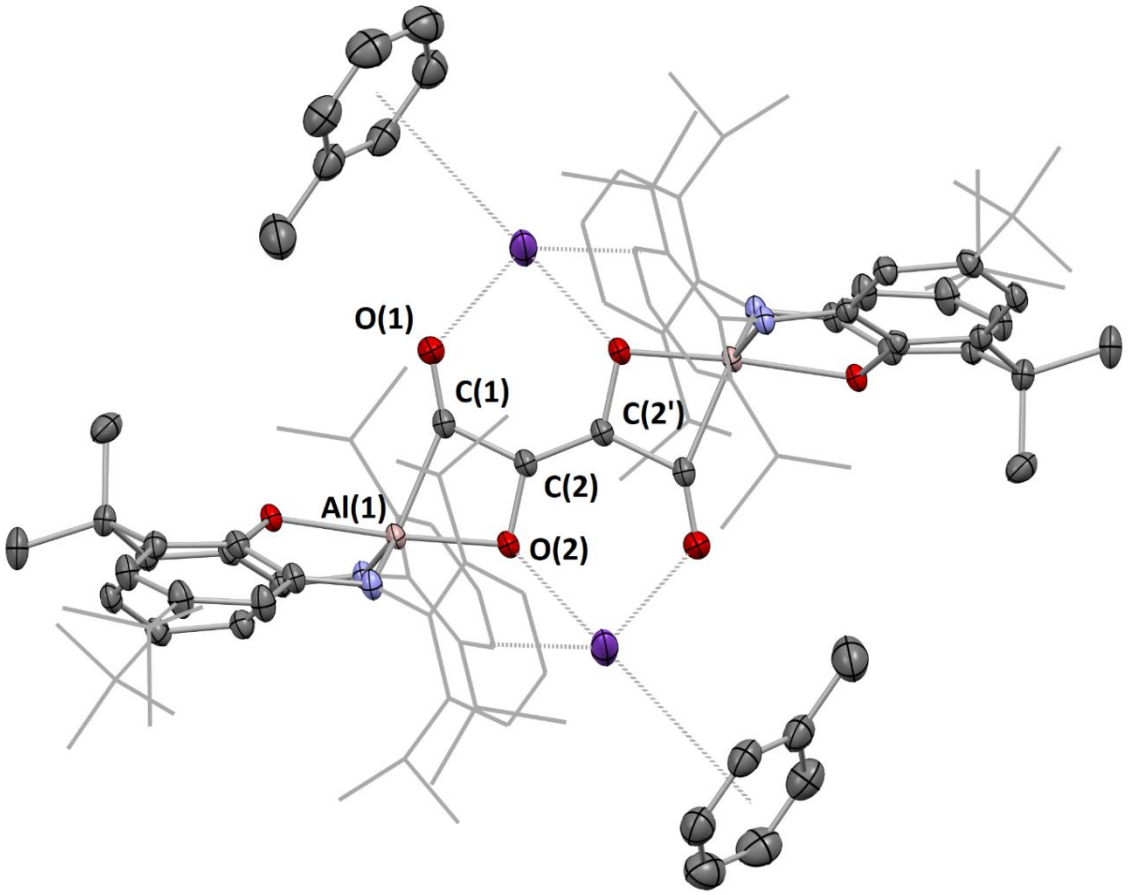

S 6.1: Molecular structure of [**2**-K(C_7H_8)]$_2$ in the solid state as determined by single crystal diffraction. Thermal ellipsoids have been set at 50% probability. Hydrogen atoms have been omitted and selected groups are shown in wireframe for clarity.

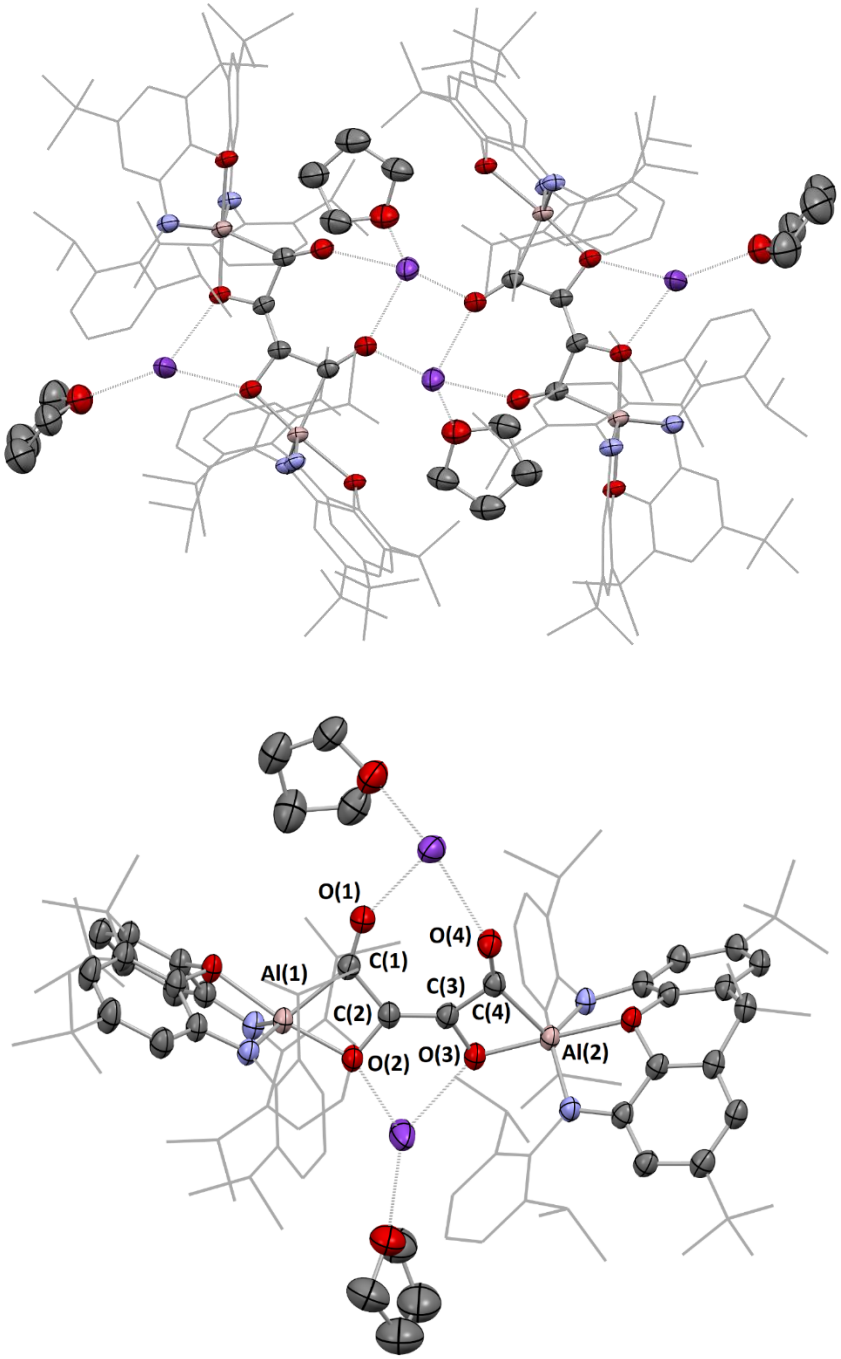

S 6.2: Molecular structure of [**2**-K(THF)]$_2$ (top) and the asymmetric unit (bottom) in the solid state as determined by single crystal diffraction. Thermal ellipsoids have been set at 50% probability. Hydrogen atoms have been omitted and selected groups are shown in wireframe for clarity.

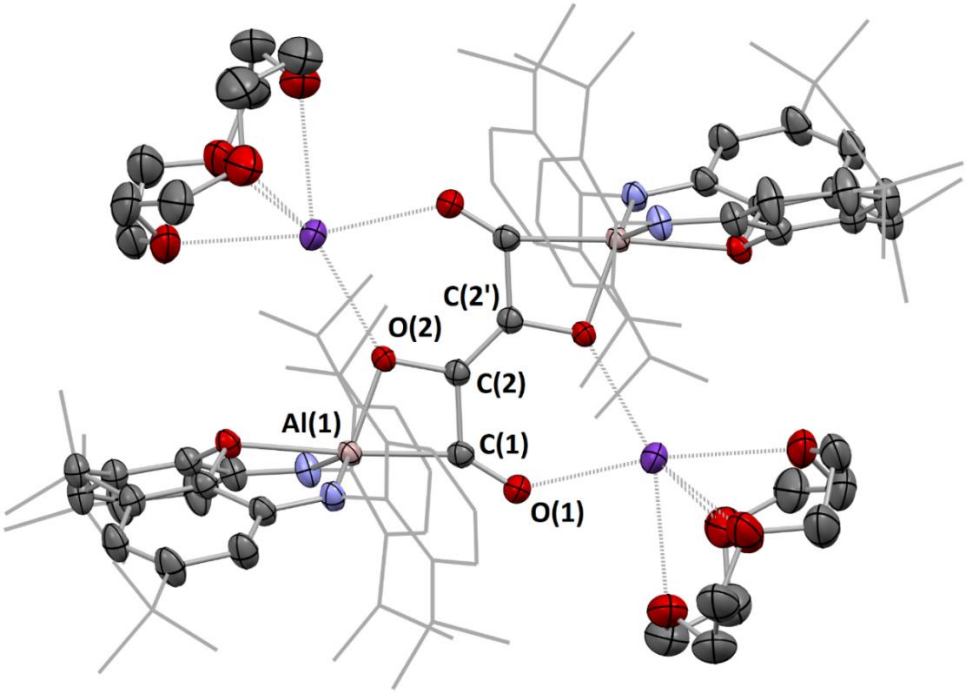

S 6.3: Molecular structure of [**2**-K(12-crown-4)]$_2$ in the solid state as determined by single crystal diffraction. Thermal ellipsoids have been set at 50% probability. Hydrogen atoms have been omitted and selected groups are shown in wireframe for clarity.

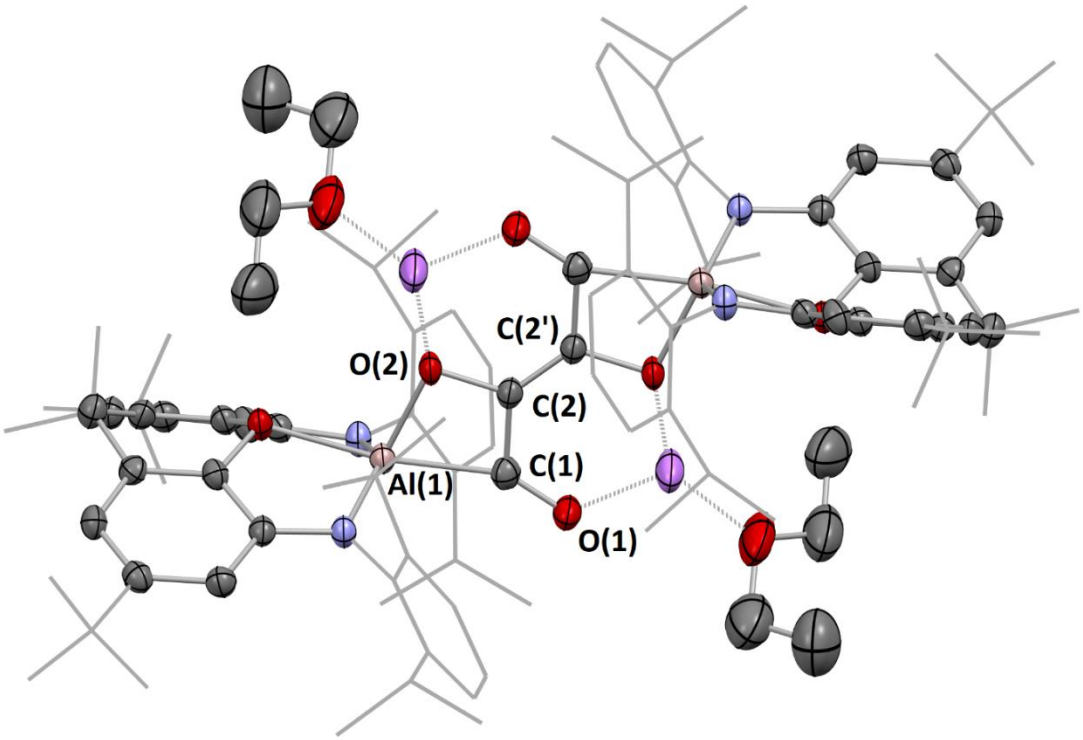

S 6.4: Molecular structure of [**2**-Li(OEt$_2$)]$_2$ in the solid state as determined by single crystal diffraction. Thermal ellipsoids have been set at 50% probability. Hydrogen atoms have been omitted and selected groups are shown in wireframe for clarity.

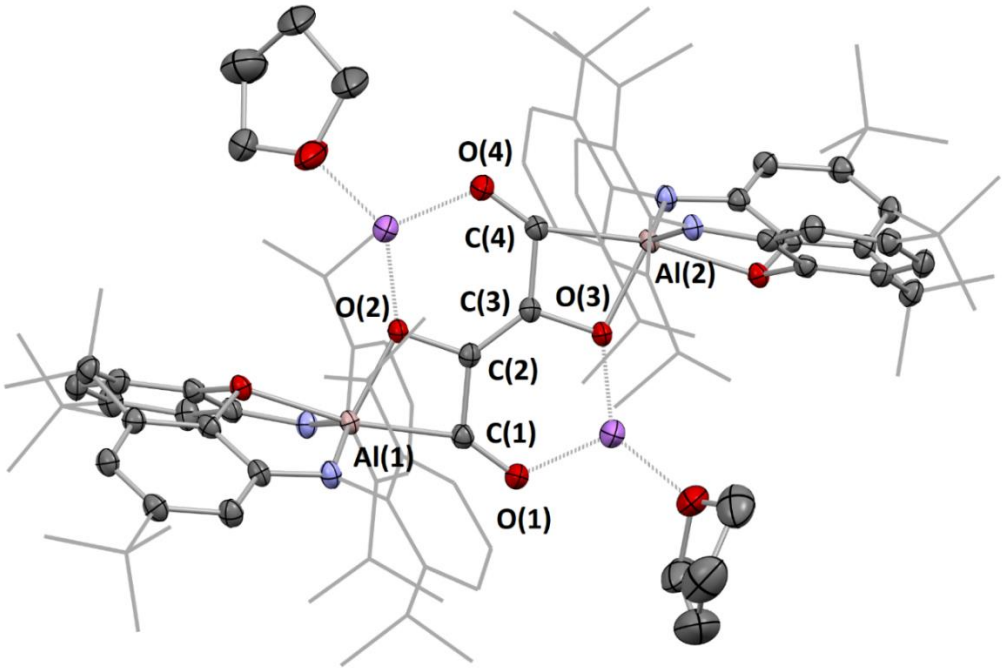

S 6.5: Molecular structure of [**2**-Li(THF)]$_2$ in the solid state as determined by single crystal diffraction. Thermal ellipsoids have been set at 50% probability. Hydrogen atoms have been omitted and selected groups are shown in wireframe for clarity.

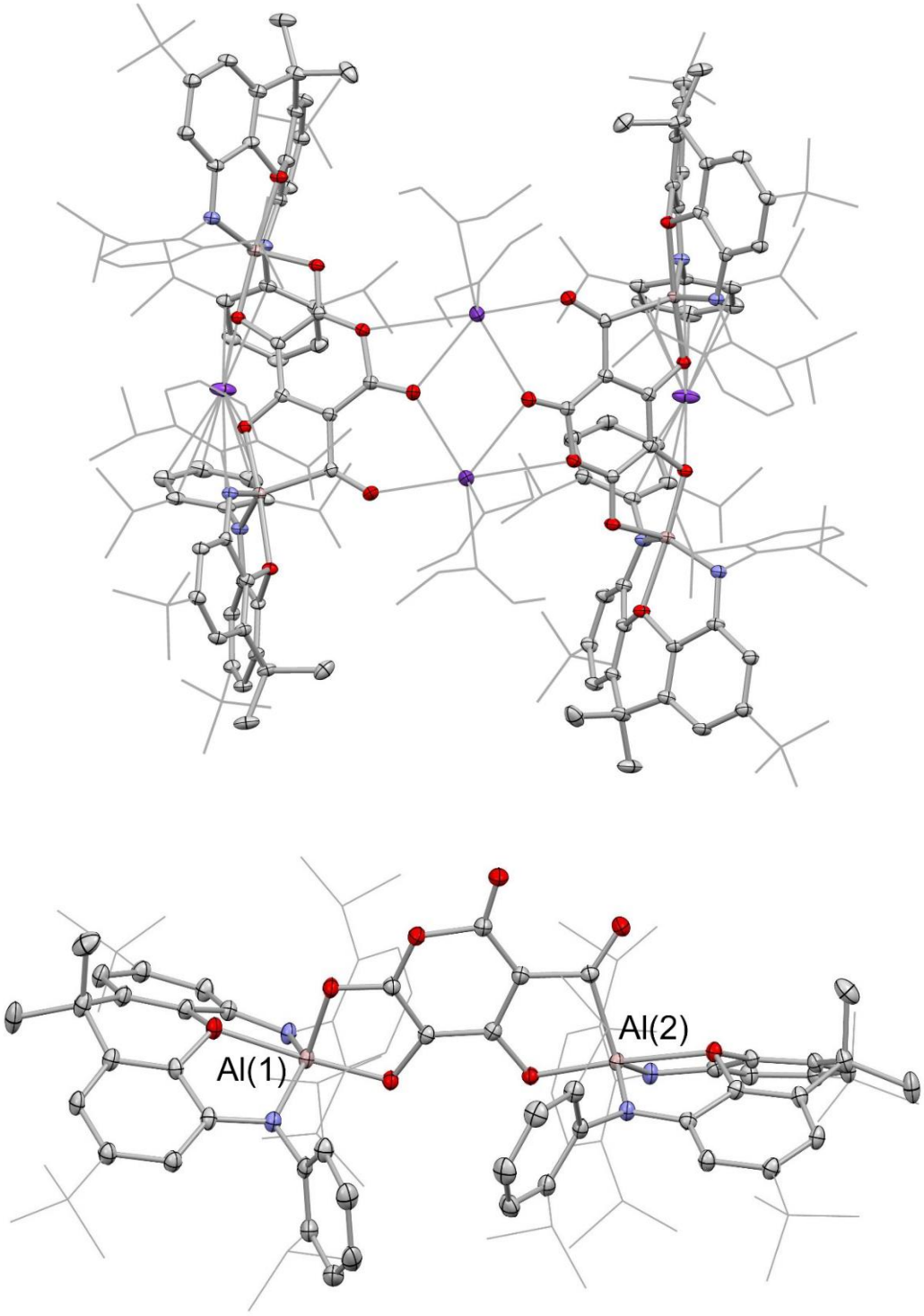

S 6.6: Molecular structure of **3** (top) and the anionic component of the asymmetric unit (bottom) in the solid state as determined by single crystal diffraction. Thermal ellipsoids have been set at 50% probability. Hydrogen atoms have been omitted and selected groups are shown in wireframe for clarity.

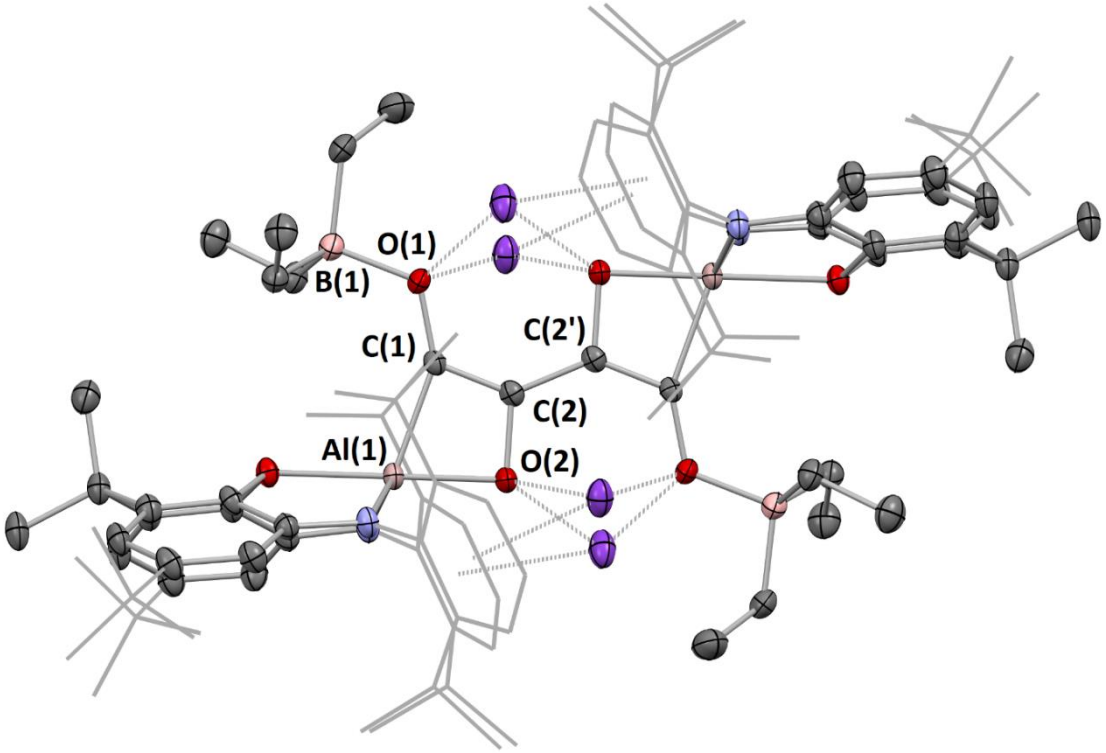

S 6.7: Molecular structure of [**4**-$K_2(BEt_3)]_2$ in the solid state as determined by single crystal diffraction. Thermal ellipsoids have been set at 50% probability. Hydrogen atoms have been omitted and selected groups are shown in wireframe for clarity

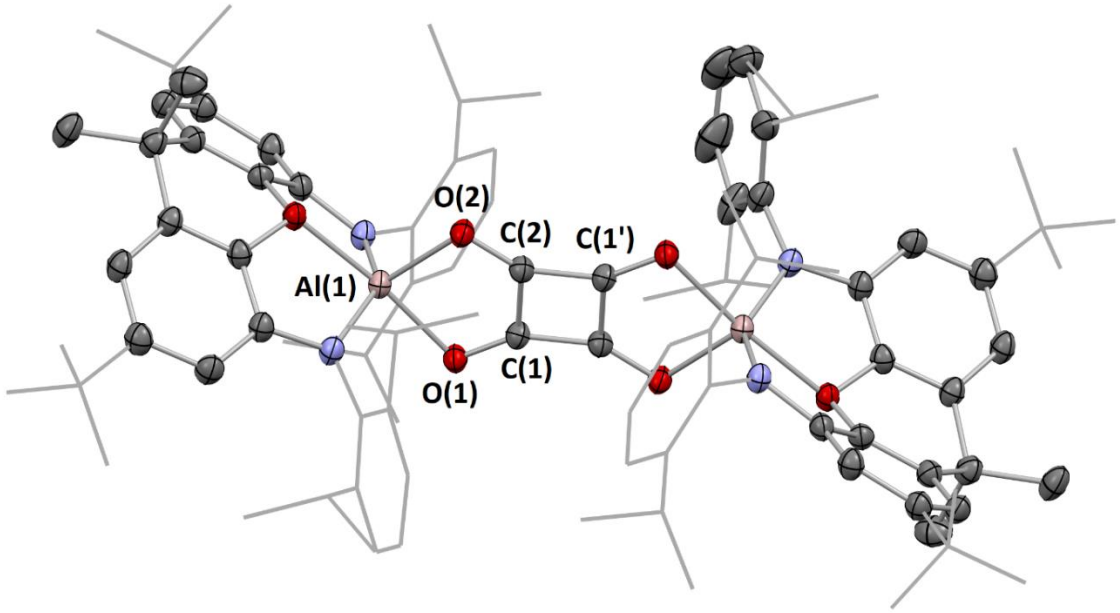

S 6.8: Molecular structure of **5** in the solid state as determined by single crystal diffraction. Thermal ellipsoids have been set at 50% probability. Hydrogen atoms have been omitted and selected groups are shown in wireframe for clarity.

Computational details

General details

All computational work reported here was carried out using density functional theory (DFT). Geometry optimisations for model compounds **A – F** and toluene were performed with Gaussian16 (Revision C.01)[73] and for model compounds **G – J**, **R**, **P**, **TS1– TS4**, **I1 – I3** and carbon monoxide using ORCA (Revision 5.0.2).[74] Calculations were performed for model systems with simplified ligands to reduce computational cost. In all cases the tBu groups on the xanthene backbone were replaced by methyl substituents. Further, the Dipp groups were replaced with Ph groups for compounds **G – J**, or with ortho-Xylyl groups for compounds **R**, **P**, **TS1 – TS4**, **I1 – I3**.

Molecular orbitals

Different isomers of the $[C_4O_4]^{2-}$ and $[C_4O_4]^{4-}$ containing compounds **A – E** were initially scoped using the B3LYP exchange correlation functional,[75-78] with Def-SVP basis sets,[79,80] and Grimme's empirical dispersion correction (GD3BJ).[81,82] Integration grid accuracy was set at ultrafine. The nature of stationary points found (minima) was confirmed by full frequency calculations. Further geometry optimizations were performed for synthetically viable species **A**, **E** and **F** using the B3LYP exchange correlation functional and Def-TZVP basis set, with Grimme's empirical dispersion correction (GD3BJ).

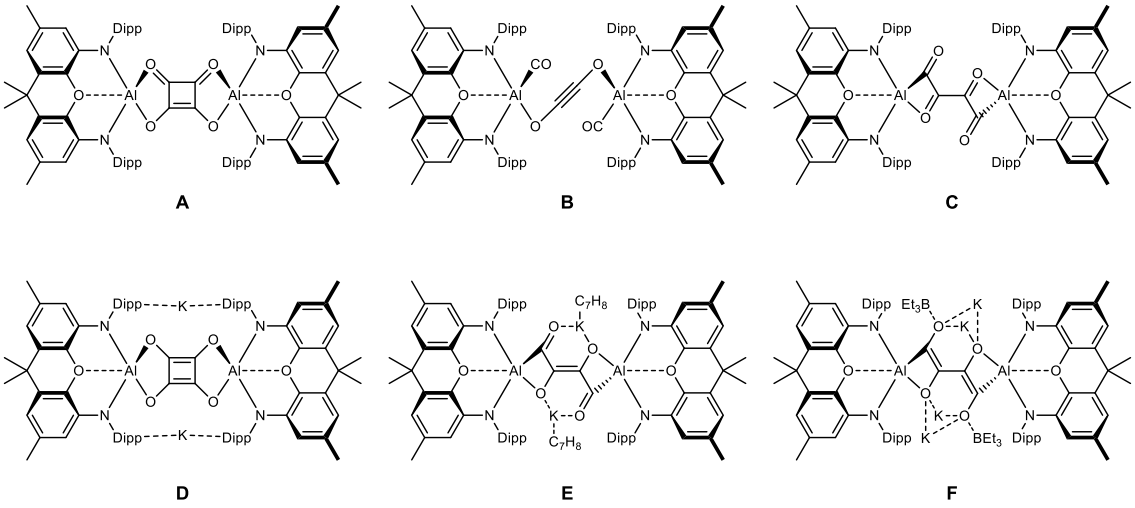

S 6.9 Model compounds **A** – **F**

ST 6.3: Sum of electronic and thermal enthalpies at 298.15 K and 1 atm calculated at the SVP level for model compounds **A** - **F**.

	Enthalpy (Hartrees)	Relative to C/E (kJ mol^{-1})
A	-4488.762327	-335.933
B	-4488.651576	-45.156
C	-4488.634377	0
Toluene	-271.262744	
D	-5688.581626	
D + 2 Toluene	-6231.107114	213.0488
E	-6231.188260	0
F	-7412.923916	

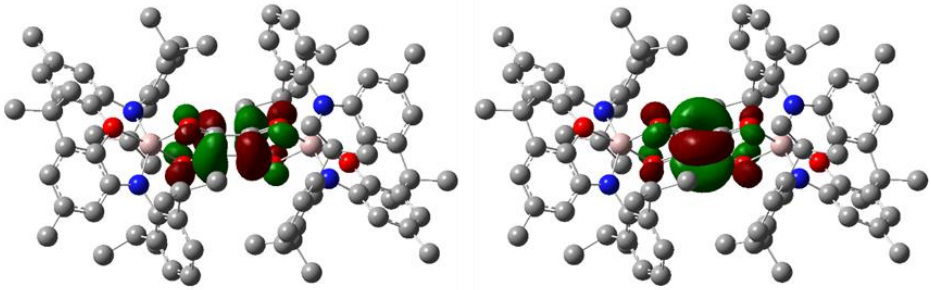

LUMO+1, -7.32767930E-02 Hartree

LUMO, -8.94303358E-02 Hartree

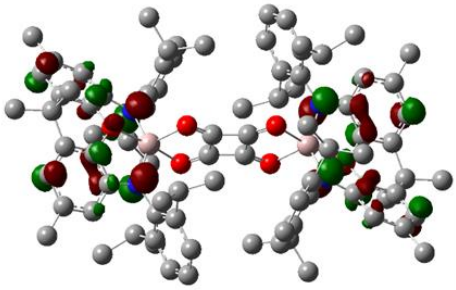

HOMO, -2.00482134E-01 Hartree

S 6.10: Selected frontier molecular orbitals for **A** calculated at the TZVP level. (Iso-value 0.04)

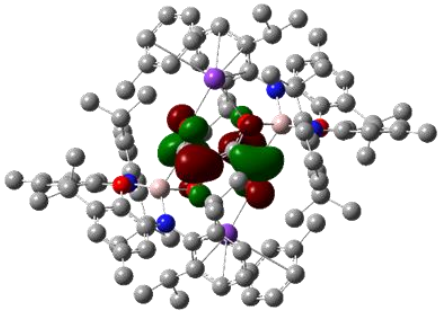

LUMO, -6.44873297E-02 Hartree

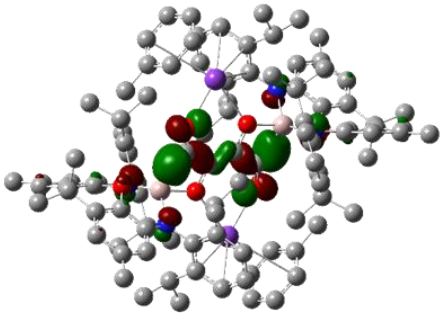

HOMO, -1.69247574E-01 Hartree

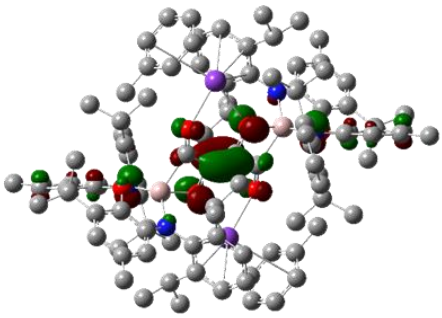

HOMO-1, -1.79567181E-01 Hartree

S 6.11: Selected frontier molecular orbitals for **E** calculated at the TZVP level. (Iso-value 0.04)

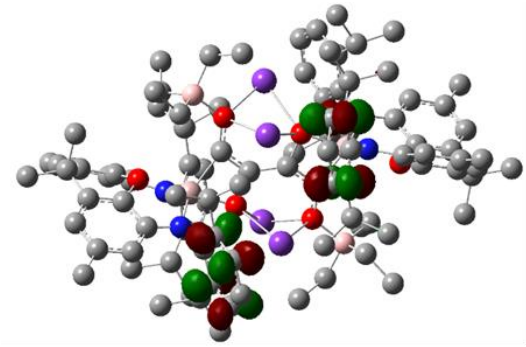

LUMO, -2.85128860E-02 Hartree

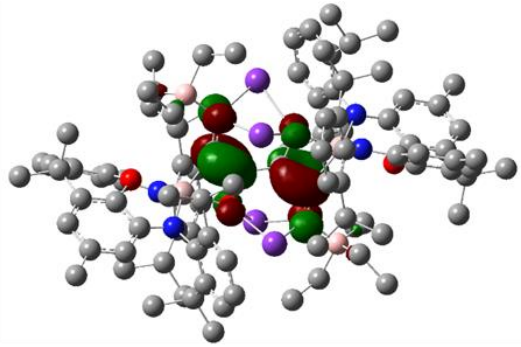

HOMO, -1.45382664E-01 Hartree

S 6.12: Selected frontier molecular orbitals for **F** calculated at the TZVP level. (Iso-value 0.04)

Mechanistic studies

Mechanistic studies were performed with the ORCA (Revision 5.0.2) programme using the B3LYP exchange correlation functional, [75-78] with Def-SVP basis sets,[79,80] and Grimme's empirical dispersion correction (GD3BJ).[81,82] In all cases the tBu groups on the xanthene backbone were replaced by methyl substituents. Further, the Dipp groups were replaced with P ortho-Xylyl groups. The nature of stationary points found (minima) was confirmed by full frequency calculations with transitions states containing a single imaginary frequency corresponding to the reaction coordinate. Further single point calculations were performed using the B3LYP exchange correlation functional and Def-TZVP basis set to get final energies.

The mechanism for the formation of **P** (Figure **S 6.13**) is proposed to proceed through initial binding of CO in a bent fashion via the C atom (**I1**) with a second CO binding in reverse orientation via the O atom (**I2**). An isomerisation then occurs (**TS3**) to a carbene (**I3**) which can then dimerize to form **P**, the observed homologation product. Dimerization (**TS4**) is the rate determining step with a moderate high barrier due to the large steric bulk and electrostatic repulsion of the anionic fragments. This moderate high barrier is consistent with the experimental findings, that heating is required and low yields are observed.

Through the course of this mechanistic investigation a range of binding modes were considered (Figure **S 6.14**), with the bent CO binding (**H**) being the lowest in energy for the initial binding of CO. Attempts to coordinate CO to the vacant p-orbital on Al in a linear fashion did not converge to a stable structure.

When binding two CO molecules, an energetic minimum was found featuring two Al bound C atoms (**I2'**). However, we propose that the isomeric system **I2** is the relevant intermediate in the transformation from **R** to **P** with **I2'** being an unproductive intermediate. The conversion between **I1** and **I2'** is somewhat reversible due to the moderate barrier and small ΔG, and as such the conversion of **I2** to **I2'** is proposed to proceed via **I1** not via direct rotational interconversion, as the barrier (**TS2B**) is significantly higher in energy. Binding of an isocarbonyl

ligand OC to form **I2** is energetically unfavourable with respect to **I2'**; however onward isomerisation to carbene system **I3** is near barrier-less with **I3** lying downhill of both **R** and **I2'**. ETS-NOCV (using the implementation in multiwfn wavefunction analysis package)[90] was used to further investigate the binding of the two CO molecules in **I2** and **I2'**. This analysis revealed that the binding of CO involves two main interactions; the dominant interaction involves the CO π* symmetry orbitals and the lone pair on the aluminium to form a multicentre bond (Figures **S 6.15** and **S 6.16**). This bonding motif was also found to support reverse binding of CO in **I2** with only a modest decrease in the NOCV pair energy.

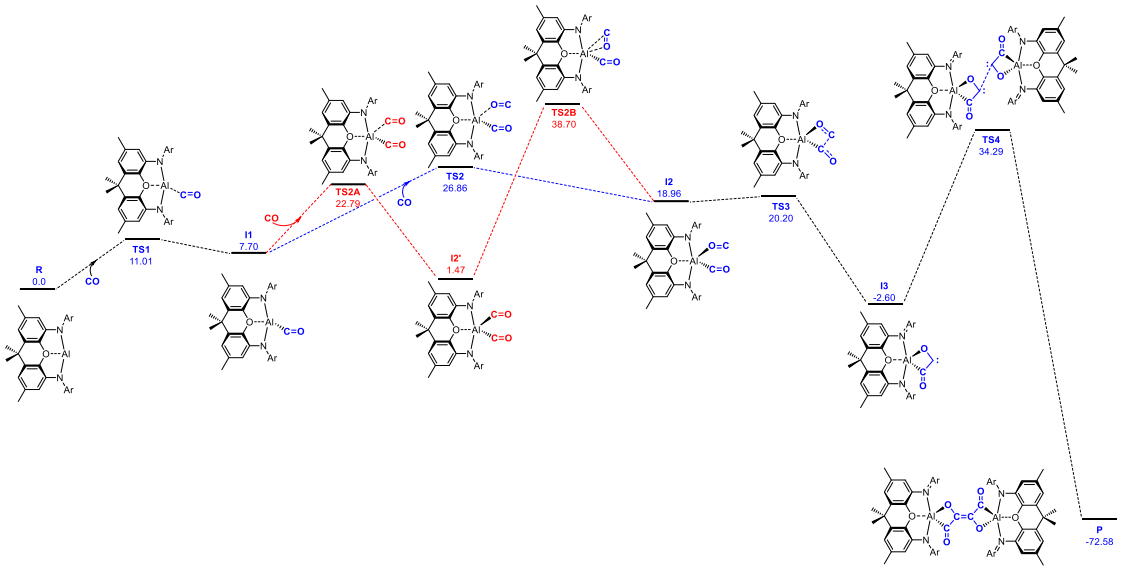

S 6.13: Proposed mechanism for CO homologation at B3LYP/def2-TZVP//B3LYP/def2-SVP with solvation modelled with CPCM(Benzene). Pathway in blue representing lowest energy pathway with reverse binding of CO (**I2**); pathway in red in a representing the prior binding of a second CO through carbon (**I2'**) then isomerization to **I2**

CO binding studies

To investigate the mechanism of CO activation different binding modes of one or two CO molecules to the aluminium centre were calculated (**G – J**) using the using the B3LYP exchange correlation functional,[77-80] with 6-31G(d) Pople basis sets[86,87] and DFT-D4 dispersion.[88] Further mechanistic work (**R, P**, **TS1– TS4**, **I1 – I3**) was performed using the B3LYP exchange correlation functional,[77-80] with Def-SVP basis sets,[79,80] DFT-D4 dispersion and LR-CPCM (benzene) solvent modelling,[89] with single point energies being performed with the Def-TZVP basis set. The transition state structures (saddle points) were confirmed by having a single imaginary frequency.

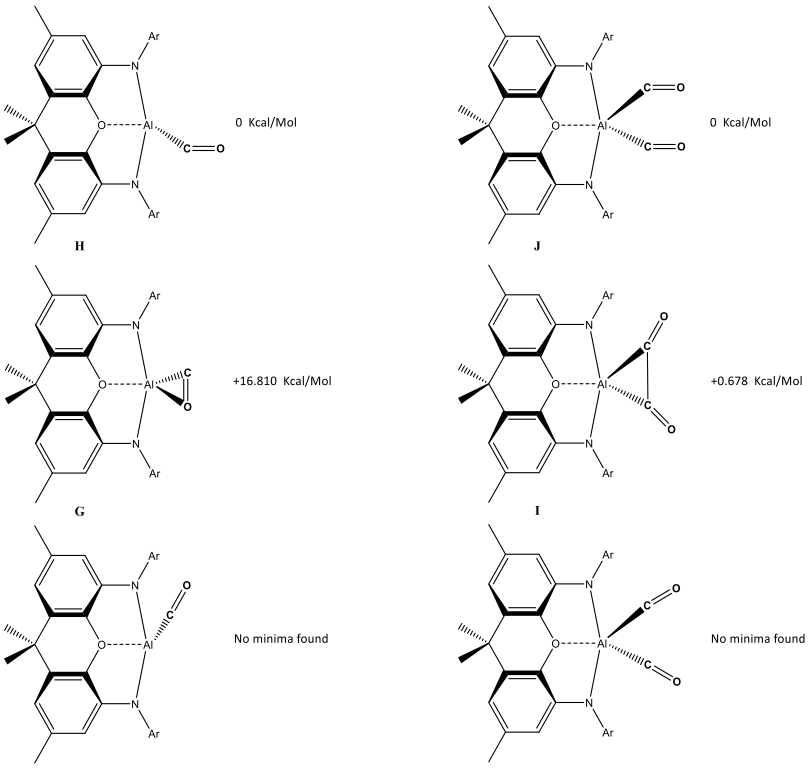

S 6.14: Different possible isomers of coordination of one and two CO molecules and their relative energies.

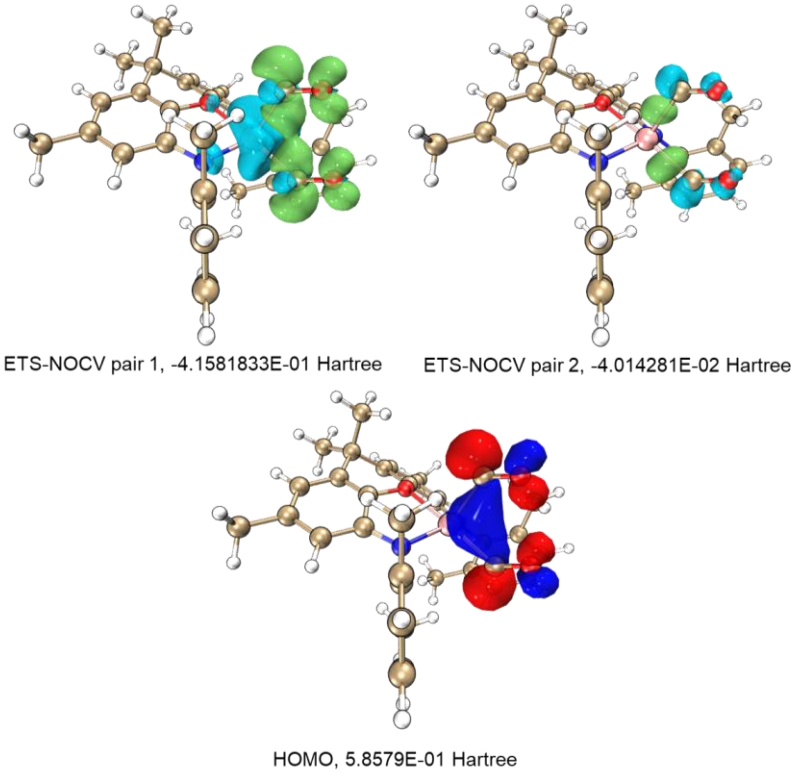

S 6.15: Selected frontier molecular orbitals and ETS-NOCV pair densities for **I2** calculated at the 6-31G(d) level. (Iso-value 0.05 and 0.005 for Molecular orbitals and pair densities respectively)

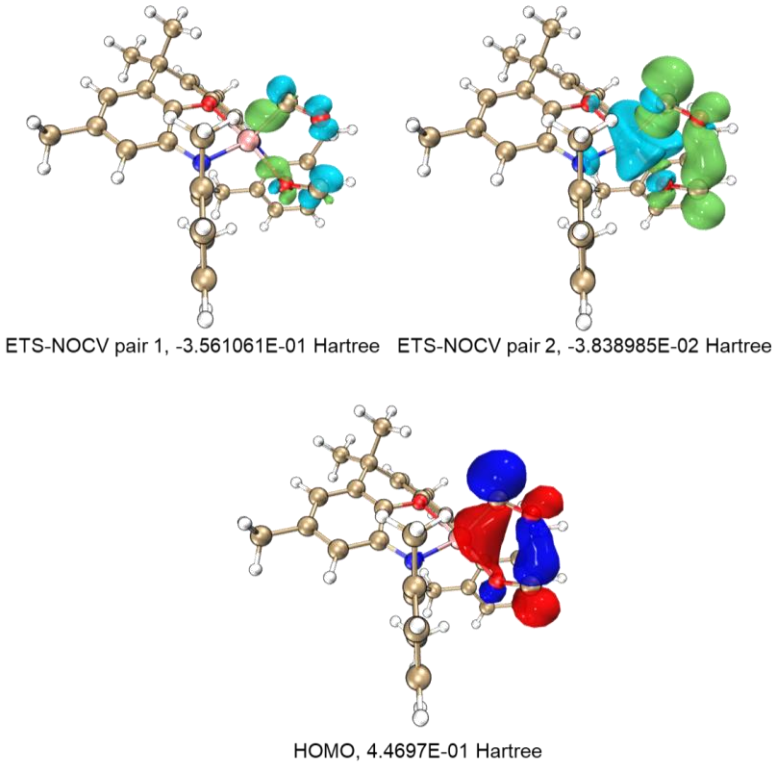

S 6.16: Selected frontier molecular orbitals and ETS-NOCV pair densities for **I2** calculated at the 6-31G(d) level. (Iso-value 0.04 and 0.005 for Molecular orbitals and pair densities respectively)

References

1 Schulz, H. Short history and present trends of Fischer−Tropsch synthesis. *Appl. Catal*. *A* **1999**, *186*, 3-12. DOI: 10.1016/S0926-860X(99)00160-X.

2 Van Santen, R. A., Ciobıca, I. M., van Steen, E.; Ghouri, M. M. Mechanistic Issues in Fischer−Tropsch Catalysis, 1st ed., Elsevier Inc.: Amsterdam, 2011; 54, pp 127−187. ISBN: 978-0-12-387772-7.

3 Kaneko, T., Derbyshire, F., Makino, E., Gray, D., Tamura, M.; Li, K. Coal Liquefaction. Ullmann's Encyclopedia of Industrial Chemistry. Weinheim: Wiley-VCH (2012). ISBN: 978-3-527-32943-4.

4 For a recent review, see Kong, R. Y.; Crimmin, M. R. Cooperative strategies for CO homologation. *Dalton Trans.* **2020**, *49*, 16587-16597. DOI: 10.1039/D0DT01564D.

5 Manriquez, J. M.; McAlister, D. R.; Sanner, R. D.; Bercaw, J. E. Reduction of carbon monoxide promoted by alkyl and hydride derivatives of permethylzirconocene. *J. Am. Chem. Soc.* **1978**, *100*, 2716-2724. DOI: 10.1021/ja00477a025.

6 Bianconi, P. A.; Williams, I. D.; Engeler, M. P.; Lippard, S. J. Reductive coupling of two carbon monoxide ligands to form a coordinated alkyne. *J. Am. Chem. Soc.* **1986**, *108*, 311–313. DOI: 10.1021/ja00262a030.

7 Bianconi, P. A.; Vrtis, R. N.; Rao, C. P.; Williams, I. D.; Engeler, M. P.; Lippard, S. J. Reductive coupling of carbon monoxide ligands to form coordinated bis(trimethylsiloxy)ethyne in seven-coordinate niobium(I) and tantalum(I) [$M(CO)_2(dmpe)_2Cl$] complexes. *Organometallics* **1987**, *6*, 1968–1977. DOI: 10.1021/ om00152a023.

8 Coffin, V. L.; Brennen, W.; Wayland, B. B. Thermodynamic studies of competitive adduct formation: single- and double-insertion reactions of carbon monoxide with rhodium octaethylporphyrin dimer. *J. Am. Chem. Soc.* **1988**, *110*, 6063-6069. DOI: 10.1021/ja00226a022.

9 Vrtis, R. N.; Rao, C. P.; Bott, S. G.; Lippard, S. J. Synthesis and stabilization of tantalum-coordinated dihydroxyacetylene from two reductively coupled carbon monoxide ligands. *J. Am. Chem. Soc.* **1988**, *110*, 7564–7566. DOI: 10.1021/ja00230a062.

10 Wayland, B. B.; Sherry, A. E.; Coffin, V. L. Selective reductive coupling of carbon monoxide. *J. Chem. Soc., Chem. Commun.* **1989**, 662-663. DOI: 10.1039/C39890000662.

11 Protasiewicz, J. D.; Lippard, S. J. Vanadium-promoted reductive coupling of carbon monoxide and facile hydrogenation to form cis-disiloxyethylenes. *J. Am. Chem. Soc.* **1991**, *113*, 6564-6570. DOI: 10.1021/ja00017a030.

12 Cummins, C. C.; Van Duyne, G. D.; Schaller, C. P.; Wolczanski, P. T. Carbonylation of zirconium complex [tert-$Bu_3SiNH]_3ZrH$ and x-ray structure study of [tert-$Bu_3SiNH]_3ZrCH_3$. *Organometallics* **1991**, *10*, 164-171. DOI: 10.1021/om00047a044.

13 Miller, A. J. M.; Labinger, J. A.; Bercaw, J. E. Reductive coupling of carbon monoxide in a rhenium carbonyl complex with pendant Lewis acids. *J. Am. Chem. Soc*. **2008**, *130*, 11874–11875. DOI: 10.1021/ja805108z.

14 Watanabe, T.; Ishida, Y.; Matsuo, T.; Kawaguchi, H. Reductive coupling of six carbon monoxides by a ditantalum hydride complex. *J. Am. Chem. Soc.* **2009**, *131*, 3474–3475. DOI: 10.1021/ja9007276.

15 Buss, J. A.; Agapie, T. Four-electron deoxygenative reductive coupling of carbon monoxide at a single metal site. *Nature* **2016**, *529*, 72-75. DOI: 10.1038/nature16154.

16 Sharpe, H. R.; Geer, A. M.; Taylor, L. J.; Gridley, B. M.; Blundell, T. J.; Blake, A. J.; Davies, E. S.; Lewis, W.; McMaster, J.; Robinson, D.; Kays, D. L. Selective reduction and homologation of carbon monoxide by organometallic iron complexes. *Nature Commun.* **2018**, *9*, 3757. DOI: 10.1038/s41467-018-06242-w.

17 (a) Kong, R. Y.; Crimmin, M. R. Carbon Chain Growth by Sequential Reactions of CO and CO_2 with [$W(CO)_6$] and an aluminum(I) Reductant. *J. Am. Chem. Soc.* **2018**, *140*, 13614−13617. DOI: 10.1021/jacs.8b09761. See also: (b) Kong, R. Y. Kong, Batuecas, M.; Crimmin, M. R. Reactions of aluminium(I) with transition metal carbonyls: scope, mechanism and selectivity of CO homologation. *Chem. Sci.* **2021**, *12*, 14845-14854. DOI: 10.1039/ D1SC04940B. (c) Batuecas, M.; Kong, R. Y.; White, A. J. P.; Crimmin, M. R. *Angew. Chem. Int. Ed.* **2022**, *61*, e202202241. DOI: 10.1002/anie.202202241.

18 Lalrempuia, R.; Kefalidis, C. E.; Bonyhady, S. J.; Schwarze, B.; Maron, L.; Stasch, A.; Jones, C. Activation of CO by hydrogenated magnesium(I) dimers: sterically controlled formation of ethenediolate and cyclopropanetriolate complexes *J. Am. Chem. Soc.* **2015**, *137*, 8944−8947. DOI: 10.1021/jacs.5b06439.

19 Anker, M. D.; Hill, M. S.; Lowe, J. P.; Mahon, M. F. Alkaline-earth-promoted CO homologation and reductive catalysis. *Angew. Chem. Int. Ed.* **2015**, *54*, 10009-10011. DOI: 10.1002/ anie.201505851.

20 Yuvaraj, K.; Douair, I.; Paparo, A.; Maron, L.; Jones, C. Reductive trimerization of CO to the deltate dianion using activated magnesium(I) compounds. *J. Am. Chem. Soc.* **2019**, *141*, 8764–8768. DOI: 10.1021/jacs.9b04085.

21 Yuvaraj, K.; Douair, I.; Jones, D. D. L.; Maron, L.; Jones, C. Sterically controlled reductive oligomerisations of CO by activated magnesium(I) compounds: deltate vs. ethenediolate formation. *Chem. Sci*. **2020**, *11*, 3516–3522. DOI: 10.1039/D0SC00836B.

22 Paparo, A.; Yuvaraj, K.; Matthews, A. J. R.; Douair, I.; Maron, L.; Jones, C. Reductive hexamerization of CO involving cooperativity between magnesium(I) reductants and $[Mo(CO)_6]$: synthesis of well-defined magnesium benzenehexolate complexes. *Angew. Chem. Int. Ed.* **2021**, *60*, 630-634. DOI: 10.1002/ anie.202009523.

23 Liu, H.-Y.; Schwamm, R. J.; Neale, S. E.; Hill, M. S.; McMullin, C. L.; Mahon, M. F. Reductive dimerization of CO by a Na/Mg(I) Diamide. *J. Am. Chem. Soc.* **2021**, *143*, 17851-17856. DOI: 10.1021/jacs.1c09467.

24 Wang, X.; Zhu, Z.; Peng, Y.; Lei, H.; Fettinger, J.C.; Power, P.P. Room-temperature reaction of carbon monoxide with a stable diarylgermylene. *J. Am. Chem. Soc*. **2009**, *131*, 6912–6913. DOI: 0.1021/ja9017286.

25 Braunschweig, H.; Dellermann, T.; Dewhurst, R. D.; Ewing, W. C.; Hammond, K.; Jimenez-Halla, J. O. C.; Kramer, T.; Krummenacher, I.; Mies, J.; Phukan, A. K.; Vargas, A. Metal-free binding and coupling of carbon monoxide at a boron–boron triple bond. *Nature Chem.* **2013**, *5*, 1025-1028. DOI: 10.1038/ nchem.1778.

26 Majumdar, M.; Omlor, I.; Yildiz, C. B.; Azizoglu, A., Huch, V.; Scheschkewitz, D. Reductive cleavage of carbon monoxide by a disilenide. *Angew. Chem. Int. Ed.* **2015**, *54*, 8746–8750. DOI: 10.1002/anie.201503455.

27 Anker, M. D.; Kefalidis, C. D.; Yang, Y.; Fang, J.; Hill, M. S.; Mahon, M. F.; Maron, L. Alkaline earth-centered CO homologation, reduction, and amine carbonylation. *J. Am. Chem. Soc.* **2017**, *139*, 10036-10054. DOI: 10.1021/jacs.7b04926.

28 Shi, X.; Hou, C.; Zhou, C.; Song, Y.; Cheng, J. A molecular barium hydrido complex stabilized by a super-bulky hydrotris(pyrazolyl)borate ligand. *Angew. Chem. Int. Ed.* **2017**, *56*, 16650-16653. DOI: 10.1002/anie.201709344.

29 Protchenko, A. V.; Vasko, P.; Do, D. C. H.; Hicks, J.; Fuentes, M. Á.; Jones, C.; Aldridge, S. Reduction of carbon oxides by an acyclic silylene: reductive coupling of CO. *Angew. Chem. Int. Ed.* **2019**, *58*, 1808-1812. DOI: 10.1002/anie.201812675.

30 Wang, Y.; Kostenko, A.; Hadlington, T. J.; Luecke, M.-P.; Yao, S.; Driess, M. Silicon-mediated selective homo- and heterocoupling of carbon monoxide. *J. Am. Chem. Soc.* **2019**, *141*, 626-634. DOI: 10.1021/jacs.8b11899.

31 Xu, M.; Qu, Z.-W.; Grimme, S.; Stephan, D. W. Lithium dicyclohexylamide in transition-metal-free Fischer−Tropsch chemistry. *J. Am. Chem. Soc.* **2021**, *143*, 634-638. DOI: 10.1021/ jacs.0c11482.

32 Yuvaraj, K.; Jones, C. Reductive coupling of CO with magnesium anthracene complexes: formation of magnesium enediolates. *Chem. Commun.* **2021**, *57*, 9224-9227. DOI: 10.1039/ D1CC03890G.

33 Evans, M. J.; Gardiner, M. G.; Anker, M. D.; Coles, M. P. Extending chain growth beyond $C_1 \rightarrow C_4$ in CO homologation: aluminyl promoted formation of the $[C_5O_5]^{5-}$ ligand. *Chem. Commun.* **2022**, in press. DOI: 10.1039/D2CC01554D.

34 Fagan, P. J.; Manriquez, J. M.; Marks, T. J.; Day, V. W.; Vollmer, S. H.; Day, C. S. Carbon monoxide activation by f-element organometallics. An unusually distorted, carbene-like dihaptoacyl and CO tetramerization. *J. Am. Chem. Soc.* **1980**, *102*, 5393-5396. DOI: 10.1021/ja00536a048.

35 Fagan, P. J.; Moloy, K. G.; Marks, T. J. Carbon monoxide activation by organoactinides. Migratory carbon monoxide insertion into metal-hydrogen bonds to produce polynuclear formyls. *J. Am. Chem. Soc.* **1981**, *103*, 6959-6962. DOI: 10.1021/ja00413a032.

36 Evans, W. J.; Wayda, A. L.; Hunter, W. E.; Atwood, J. L. Organolanthanoid activation of carbon monoxide: single and multiple insertion of CO into t-butyl lanthanoid bonds; X-ray crystallographic identification of a new bonding mode for a bridging enedione diolate ligand formed by formal coupling of four CO molecules. *J. Chem. Soc., Chem. Commun.* **1981**, 706-708. DOI: 10.1039/C39810000706.

37 Evans, W. J.; Grate, J. W.; Hughes, L. A.; Zhang, H.; Atwood, J. L. Reductive homologation of CO to a ketenecarboxylate by a low-valent organolanthanide complex—synthesis and X-ray crystal-

structure of $[(C_5Me_5)_4Sm_2(O_2CCCO)(THF)]_2$. *J. Am. Chem. Soc*. **1985**, *107*, 3728–3730. DOI: 10.1021/ja00298a060.

38 Radu, N. S.; Engeler, M. P.; Gerlach, C. P.; Tilley, T. D.; Rheingold, A. L. Isolation of the first d^0 metalloxy ketene complexes via "double insertion" of carbon monoxide into thorium-silicon bonds. *J. Am. Chem. Soc*. **1995**, *117*, 3621-3622. DOI: 10.1021/ ja00117a035.

39 Ferrence, G. M.; McDonald, R.; Takats, J. Stabilization of a discrete lanthanide(II) hydrido complex by a bulky hydridotris(pyrazolyl)borate ligand. *Angew. Chem. Int. Ed.* **1999**, *38*, 2233-2237. DOI: 10.1002/(SICI)1521-3773(19990802)38:15< 2233::AID-ANIE2233>3.0.CO;2-X.

40 Summerscales, O. T.; Cloke, F. G. N.; Hitchcock, P. B.; Green, J. C.; Hazari, N. Reductive cyclotrimerization of carbon monoxide to the deltate dianion by an organometallic uranium complex. *Science* **2006**, *311*, 829–831. DOI: 10.1126/science.1121784.

41 Summerscales, O. T.; Cloke, F. G. N.; Hitchcock, P. B.; Green, J. C.; Hazari, N. Reductive cyclotetramerization of CO to squarate by a U(III) complex: the X-ray crystal structure of $[(U(\eta\text{-}C_8H_6\{(SiPr_3)\text{-}Pr\text{-}i\text{-}1,4\}_2)(\eta\text{-}C_5Me_4H)]_2(\mu\text{-}\eta^2\text{:}\eta^2\text{-}C_4O_4)$. *J. Am. Chem. Soc.* **2006**, *128*, 9602–9603. DOI: 10.1021/ja063222r.

42 Evans, W. J.; Lee, D. S.; Ziller, J. W.; Kaltsoyannis, N. Trivalent $[(C_5Me_5)_2(THF)Ln]_2(\mu\text{-}\eta^2\text{:}\eta^2\text{-}N_2)$ complexes as reducing agents including the reductive homologation of CO to a ketene carboxylate, $(\mu\text{-}\eta^4\text{-}O_2C\text{–}C\text{=}C\text{=}O)^{2-}$. *J. Am. Chem. Soc*. **2006**, *128*, 14176–14184. DOI: 10.1021/ja0640851.

43 Werkema, E. L.; Maron, L.; Eisenstein, O.; Andersen R. A. Reactions of Monomeric $[1,2,4\text{-}(Me_3C)_3C_5H_2]_2CeH$ and CO with or without H_2: An Experimental and Computational Study. *J. Am. Chem. Soc.* **2007**, *129*, 2529-2541. DOI: 10.1021/ja066482h.

44 Frey, A. S.; Cloke, F. G. N.; Hitchcock, P. B.; Day, I. J.; Green, J. C.; Aitken, G. Mechanistic studies on the reductive cyclooligomerisation of CO by U(III) mixed sandwich complexes; the molecular structure of $[U(\eta\text{-}C_8H_6\{Si^iPr_3\text{-}1,4\}_2)(\eta\text{-}Cp^*)]_2(\mu\text{-}\eta^1\text{:}\eta^1\text{-}C_2O_2)$. *J. Am. Chem. Soc.* **2008**, *130*, 13816–13817. DOI: 10.1021/ja8059792.

45 Arnold, P. L.; Turner, Z. R.; Bellabarba, R. M.; Tooze, R. P. Carbon monoxide coupling and functionalisation at a simple uranium coordination complex. *Chem. Sci.* **2011**, *2*, 77–79. DOI: 10.1039/C0SC00452A.

46 Mansell, S. M.; Kaltsoyannis, N.; Arnold, P. L. Small molecule activation by uranium tris(aryloxides): experimental and computational studies of binding of N_2, coupling of CO, and deoxygenation insertion of CO_2 under ambient conditions. *J. Am. Chem. Soc.* **2011**, *133*, 9036-9051. DOI: 10.1021/ja2019492.

47 Gardner, B. M.; Stewart, J. C.; Davis, A. L.; McMaster, J.; Lewis, W.; Blake, A. J.; Liddle, S. T. Homologation and functionalization of carbon monoxide by a recyclable uranium complex. *Proc. Natl. Acad. Sci. U. S. A.* **2012**, *109*, 9265-9270. DOI: 10.1073/pnas.1203417109.

48 Tsoureas, N.; Summerscales, O. T.; Cloke, F. G. N.; Roe, S. M. Steric effects in the reductive coupling of CO by mixed-sandwich uranium(III) complexes. *Organometallics* **2013**, *32*, 1353. DOI: 10.1021/om301045k.

49 Wang, B.; Luo, G.; Nishiura, M.; Luo, Y.; Hou, Z. Cooperative trimerization of carbon monoxide by lithium and samarium boryls. *J. Am. Chem. Soc.* **2017**, *139*, 16967-16973. DOI: 10.1021/jacs.7b10108.

50 Simler, T.; McCabe, K. N.; Maron, L.; Nocton, G. CO reductive oligomerization by a divalent thulium complex and CO_2-induced functionalization. 2021/10/29. ChemRxiv, Cambridge. DOI: 10.26434/chemrxiv-2021-vsjxz (accessed 2022/06/22).

51 (a) Hicks, J.; Vasko, P.; Goicoechea, J. M.; Aldridge, S. Synthesis, structural and reaction chemistry of a nucleophilic aluminyl anion. *Nature* **2018**, *557*, 92-95. DOI: 10.1038/s41586-018-0037-y. (b) Hicks, J.; Vasko, P.; Goicoechea, J. M.; Aldridge, S. The aluminyl anion: a new generation of aluminium nucleophile. *Angew. Chem. Int. Ed.* **2021**, *60*, 1702-1711. DOI: 10.1002/ anie.202007530.

52 (a) Schwamm, R. J.; Anker, M. D.; Lein, M.; Coles, M. P. Reduction vs. addition: the reaction of an aluminyl anion with 1,3,5,7-cyclooctatetraene. *Angew. Chem. Int. Ed.* **2019**, *58*, 1489-1493. DOI: 10.1002/anie.201811675. (b) Kurumada, S.; Takamori, S.; Yamashita, M. An alkyl-substituted aluminium anion with strong basicity and nucleophilicity. *Nature Chem.* **2020**, *12*, 36-39. DOI: 10.1038/s41557-019-0365-z. (c) Schwamm, R. J.; Coles, M. P.; Hill, M. S.; Mahon, M. F.; McMullin, C. L.; Rajabi, N. A.; Wilson, A. S. S. A stable calcium alumanyl. *Angew. Chem. Int. Ed.* **2020**, *59*, 3928-3932. DOI: 10.1002/anie.201914986. (d) Koshino, K.; Kinjo, R. Construction of σ-Aromatic AlB_2 Ring via Borane Coupling with a Dicoordinate Cyclic (Alkyl)(Amino)Aluminyl Anion. *J. Am. Chem. Soc.* **2020**, *142*, 9057-9062. DOI: 10.1021/jacs.0c03179. (e) Grams, S.; Eyselein, J.; Langer,

J.; Färber, C.; Harder S. Boosting low-valent aluminum(I) reactivity with a potassium reagent. *Angew. Chem. Int. Ed.* **2020**, *59*, 15982-15986. DOI: 10.1002/anie.202006693.

53 Hicks, J.; Vasko, P.; Goicoechea, J. M.; Aldridge, S. Reversible, room-temperature C-C bond activation of benzene by an isolable metal complex. *J. Am. Chem. Soc.* **2019**, *141*, 11000-11003. DOI: 10.1021/jacs.9b05925.

54 Hicks, J.; Vasko, P.; Heilmann, A.; Goicoechea J. M.; Aldridge, S. Arene C-H activation at aluminium(I): *meta* selectivity driven by the electronics of S_NAr chemistry. *Angew. Chem. Int. Ed.* **2020**, *59*, 20376-20380. DOI: 10.1002/anie.202008557.

55 Heilmann, A.; Hicks, J.; Vasko, P.; Goicoechea, J. M.; Aldridge, S. Carbon monoxide activation by a molecular aluminium imide: C-O Bond cleavage and C-C bond formation. *Angew. Chem. Int. Ed.* **2020**, *59*, 4897-4901. DOI: 10.1002/anie.201916073.

56 Hicks, J.; Heilmann, A.; Vasko, P.; Goicoechea, J. M.; Aldridge, S. Trapping and reactivity of a molecular aluminium oxide ion. *Angew. Chem. Int. Ed.* **2019**, *58*, 17265-17268. DOI: 10.1002/anie.201910509.

57 Roy, M. M. D.; Hicks, J.; Vasko, P.; Heilmann, A.; Baston, A.-M.; Goicoechea, J. M.; Aldridge, S. Probing the extremes of covalency in M–Al bonds: lithium and zinc aluminyl compounds. *Angew. Chem. Int. Ed*. **2021**, *60*, 22301-22306. DOI: 10.1002/anie.202109416.

58 Anker, M. D.; McMullin, C. L.; Rajabi, N. A.; Coles, M. P. Carbon–carbon bond forming reactions promoted by aluminyl and alumoxane anions: introducing the ethenetetraolate ligand. *Angew. Chem. Int. Ed.* **2020**, *59*, 12806-12810. DOI: 10.1002/ anie.202005301.

59 (a) Ganesamoorthy, C.; Shoening, J.; Wölper, C.; Song, L.; Schreiner, P. R.; Schulz, S. *Nature. Chem.* **2020**, *12*, 608-614. DOI: 10.1038/s41557-020-0456-x. (b) Reiter, D.; Holzner, R.; Porzelt, A.; Frisch, P.; Inoue, S. *Nature Chem.* **2020**, *12*, 1131-1135. DOI: 10.1038/s41557-020-00555-4. See also: (c) Fujimori, S.; Inoue, S. Carbon monoxide in main-group chemistry. *J. Am. Chem. Soc.* **2022**, *144*, 2034-2050. DOI: 10.1021/jacs.1c13152.

60 ETS-NOCV: Mitoraj, M. P.; Michalak, A.; Ziegler, T. A combined charge and energy decomposition scheme for bond analysis. *J. Chem. Theory Comput.* **2009**, *5*, 962–975. DOI: 10.1021/ct800503d. The ETS method partitions the interaction energy between two fragments according to:
$\Delta E_{int} = \Delta E_{prep} + \Delta E_{orb} + \Delta E_{Pauli} + \Delta E_{elstat}$
ΔE_{orb} (the orbital interaction term) represents the interactions between the occupied molecular orbitals on one fragment and the unoccupied molecular orbitals of the other fragment, as well as the mixing of occupied and virtual orbitals within the same fragment.

61 Heitkemper, T.; Sindlinger, C. P. A cationic NHC-supported borole. *Chem.-Eur. J.* **2020**, *26*, 11684-11689. DOI: 10.1002/ chem.202001916.

62 For a previous example of a transformation of CO proceeding through an O-bound adduct, see for example: Berkefeld, E.; Piers, W. E.; Parvez, M.; Castro, L.; Maron, L.; Eisenstein, O. Carbon monoxide activation via O-Bound CO using decamethylscandocinium–hydridoborate ion pairs. *J. Am. Chem. Soc.* **2012**, *134*, 10843-10851. DOI: 10.1021/ja300591v.

63 Schleyer, P. v. R.; Najafian, K.; Kiran, B.; Jiao, H. Are oxocarbon dianions aromatic? *J. Org. Chem.* **2000***, 65,* 426-431. DOI: 10.1021/jo991267n.

64 Kollmar, H.; Staemmler, V. A theoretical study of the structure of cyclobutadiene. *J. Am. Chem. Soc.* **1977**, *99*, 3583–3587. DOI: 10.1021/ja00453a009.

65 Hill-Cousins, J. T.; Pop, I.; Pileio, G.; Stevanato, G.; Håkansson, P.; Roy, S. S.; Levitt, M. H.; Brown, L. J.; Brown, R. C. D.; Synthesis of an isotopically labeled naphthalene derivative that supports a long-lived nuclear singlet state. *Org. Lett.* **2015**, *17*, 2150-2153.DOI: 10.1021/acs.orglett.5b00744.

66 a)Hicks, J.; Vasko, P.; Goicoechea, J. M.; Aldridge, S. Synthesis, structure and reaction chemistry of a nucleophilic aluminyl anion. *Nature*, **2018**, *557*, 92-95. b) Roy, M. M. D.; Hicks, J.; Vasko, P.; Heilmann, A.; Baston, A.-M.; Goicoechea, J. M.; Aldridge, S. Probing the Extremes of Covalency in M−Al bonds: Lithium and Zinc Aluminyl Compounds. *Angew. Chem. Int. Ed.* **2021**, *60*, 22301. c) Cruz, C. A.; Emslie, D. J. H; Harrington, L. E.; Britten, J. F.; Robertson, C. M. Extremely Stable Thorium(IV) Dialkyl Complexes Supported by Rigid Tridentate 4,5-Bis(anilido)xanthene and 2,6-Bis(anilidomethyl)pyridine Ligands. *Organometallics* **2007** *26* (3), 692-701

67 Hill-Cousins, J. T.; Pop, I.; Pileio, G.; Stevanato, G.; Håkansson, P.; Roy, S. S.; Levitt, M. H.; Brown, L. J.; Brown, R. C. D. Synthesis of an Isotopically Labeled Naphthalene Derivative That Supports a Long-Lived Nuclear Singlet State. *Organic Letters*, **2015**, *17*, (9), 2150-2153.

68 Cosier, J.; Glazer, A. M. A nitrogen-gas-stream cryostat for general X-ray diffraction studies. *J. Appl. Cryst.* **1986**, *19*, 105-107.

69 CrysAlisPro, Agilent Technologies, Version 1.171.39.46.

70 Sheldrick, G. M. SHELXT - Integrated space-group and crystal-structure determination. *Acta Crystallogr., Sect. A: Found. Adv.,* **2015**, *71*, 3–8.
71 Sheldrick, G. M. Crystal structure refinement with SHELXL. *Acta Crystallogr., Sect. C: Struct.Chem.,* **2015**, *71*, 3–8.
72 Dolomanov, O. V.; Bourhis, L. J.; Gildea, R. J.; Howard, J. A. K.; Puschmann, H. OLEX2: a complete structure solution, refinement and analysis program. *J. Appl. Cryst.* **2009**, *42*, 339-341.
73 Barbour, L. J. X-Seed — A Software Tool for Supramolecular Crystallography. *J. Supramol. Chem.* **2001**, 1189–1191.
74 van der Sluis, P.; Spek, A. L. BYPASS: an effective method for the refinement of crystal structures containing disordered solvent regions. *Acta Cryst.,* **1990**, *A46*, 194-201.
75 Spek, A. L. PLATON SQUEEZE: a tool for the calculation of the disordered solvent contribution to the calculated structure factors. *Acta Cryst.*, **2015**, *C71*, 9-18.
76 Gaussian16, Revision C.01, Frisch, M. J.; Trucks, G. W.; Schlegel, H. B.; Scuseria, G. E.; Robb, M. A.; Cheeseman, J. R. ; Scalmani, G.; Barone, V.; Petersson, G. A.; Nakatsuji, H.; Li, X.; Caricato, M.; Marenich, A. V.; Bloino, J.; Janesko, B. G.; Gomperts, R.; Mennucci, B.; Hratchian, H. P.; Ortiz, J. V.; Izmaylov, A. F. ; Sonnenberg, J. L.; Williams-Young, D.; Ding, F.; Lipparini, F.; Egidi, F; Goings, J.; Peng, B.; Petrone, A.; Henderson, T.; Ranasinghe, D.; Zakrzewski, V. G.; Gao, J.; Rega, N.; Zheng, G.; Liang, W.; Hada, M.; Ehara, M.; Toyota, K.; Fukuda, R.; Hasegawa, J.; Ishida, M.; Nakajima, T.; Honda, Y.; Kitao, O.; Nakai, H. ; Vreven, T.; Throssell, K.; Montgomery, Jr., J. A.; Peralta, J. E.; Ogliaro, F.; Bearpark, M. J.; Heyd, J. J.; Brothers, E. N.; Kudin, K. N.; Staroverov, V. N.; Keith, T. A.; Kobayashi, R.; Normand, J. ; Raghavachari, K.; Rendell, A. P.; Burant, J. C.; Iyengar, S. S.; Tomasi, J.; Cossi, M.; Millam, J. M.; Klene, M.; Adamo, C.; Cammi, R.; Ochterski, J. W.; Martin, R. L.; Morokuma, K.; Farkas, O.; Foresman, J. B.; Fox, D. J. Gaussian, Inc., Wallingford CT, **2019**.
77 a) Neese, F. The ORCA program system, Wiley Interdiscip. Rev.: Comput. Mol. Sci. **2012**, 2, 73–78. b) Neese, F. Software update: the ORCA program system, version 4.0, Wiley Interdiscip. Rev.: Comput. Mol. Sci. **2017**, 8, e1327. c) Neese, F.; Wennmohs, F.; Becker, U.; Riplinger, C. The ORCA quantum chemistry program package, J. Chem. Phys. **2020**, 152, 224108.
78 Becke, A. D.; Density-functional thermochemistry. III. The role of exact exchange. *J. Chem. Phys.* **1993**, *98*, 5648–5652.
79 Lee, C.; Yang, W.; Parr, R. G. Development of the Colle-Salvetti correlation-energy formula into a functional of the electron density. *Phys. Rev. B*, **1988**, *37*, 785–789.
80 Vosko, S. H.; Wilk, L.; Nusair, M. Accurate spin-dependent electron liquid correlation energies for local spin density calculations: a critical analysis. *Can. J. Phys.* **1980**, *58*, 1200–1211.
81 Stephens, P. J.; Devlin, F. J.; Chabalowski, C. F., Frisch, M. J. Ab Initio Calculation of Vibrational Absorption and Circular Dichroism Spectra Using Density Functional Force Fields. *J. Phys. Chem.* **1994**, *98*, 45, 11623–11627.
82 Schaefer, A.; Huber, C.; Ahlrichs, R. Fully optimized contracted Gaussian basis sets of triple zeta valence quality for atoms Li to Kr. *J. Chem. Phys.* **1994**, *100*, 5829–5835.
83 Schaefer, A.; Horn, H.; Ahlrichs, R. Fully optimized contracted Gaussian basis sets for atoms Li to Kr. *J. Chem. Phys.* **1992**, *97*, 2571–2577.
84 Grimme, S.; Antony, J.; Ehrlich, S.; Krieg, H. A consistent and accurate ab initio parametrization of density functional dispersion correction (DFT-D) for the 94 elements H-Pu. *J. Chem. Phys.* **2010**, *132*, 154104–154119.
85 Grimme, S.; Ehrlich, S.; Goerigk, L. Effect of the damping function in dispersion corrected density functional theory. *J. Comput. Chem.* **2011**, *32*, 1456–1465.
86 Pople, J. A.; Segal, G. A. Approximate Self-Consistent Molecular Orbital Theory. III. CNDO Results for AB2 and AB3 Systems. J. Chem. Phys. **1965**, 43, 136.
87 Pople, J. A.; Segal, G. A. Approximate Self-Consistent Molecular Orbital Theory. II. Calculations with Complete Neglect of Differential Overlap. J. Chem. Phys. **1966**, 44, 3289.
88 Grimme, S. A generally applicable atomic-charge dependent London dispersion correction. J. Chem. Phys. **2019**, 150, 154122
89 Cammi, R.; Mennucci, B.; Tomasi, J.; Fast Evaluation of Geometries and Properties of Excited Molecules in Solution: A Tamm-Dancoff Model with Application to 4-Dimethylaminobenzonitrile. J. of Phys. Chem. A. **2000,** 104(23), 5631.
90 a) Tian Lu, Feiwu Chen, Multiwfn: A Multifunctional Wavefunction Analyzer, J. Comput. Chem. **2012**, 33, 580-592. b) Tian Lu, Feiwu Chen, Calculation of Molecular Orbital Composition, Acta Chim. Sinica, **2011**, 69, 2393-2406

Alternate mechanistic pathways (unpublished)

Through the investigation of the mechanism of CO homologation we propose the rate determining step to be the dimerization of two carbenes to form the final product. As discussed in chapter 4 the geometry created when two carbenes come together to dimerize depends on the whether the carbenes are singlet or triplet in nature.[1] The effect of this is that the trajectory of approach of the two **I3** moieties has to be from above where a significant degree of steric bulk lies in order to maximise overlap between the lone pair and the vacant orbital (**Figure 6.10**).

Alternate mechanism

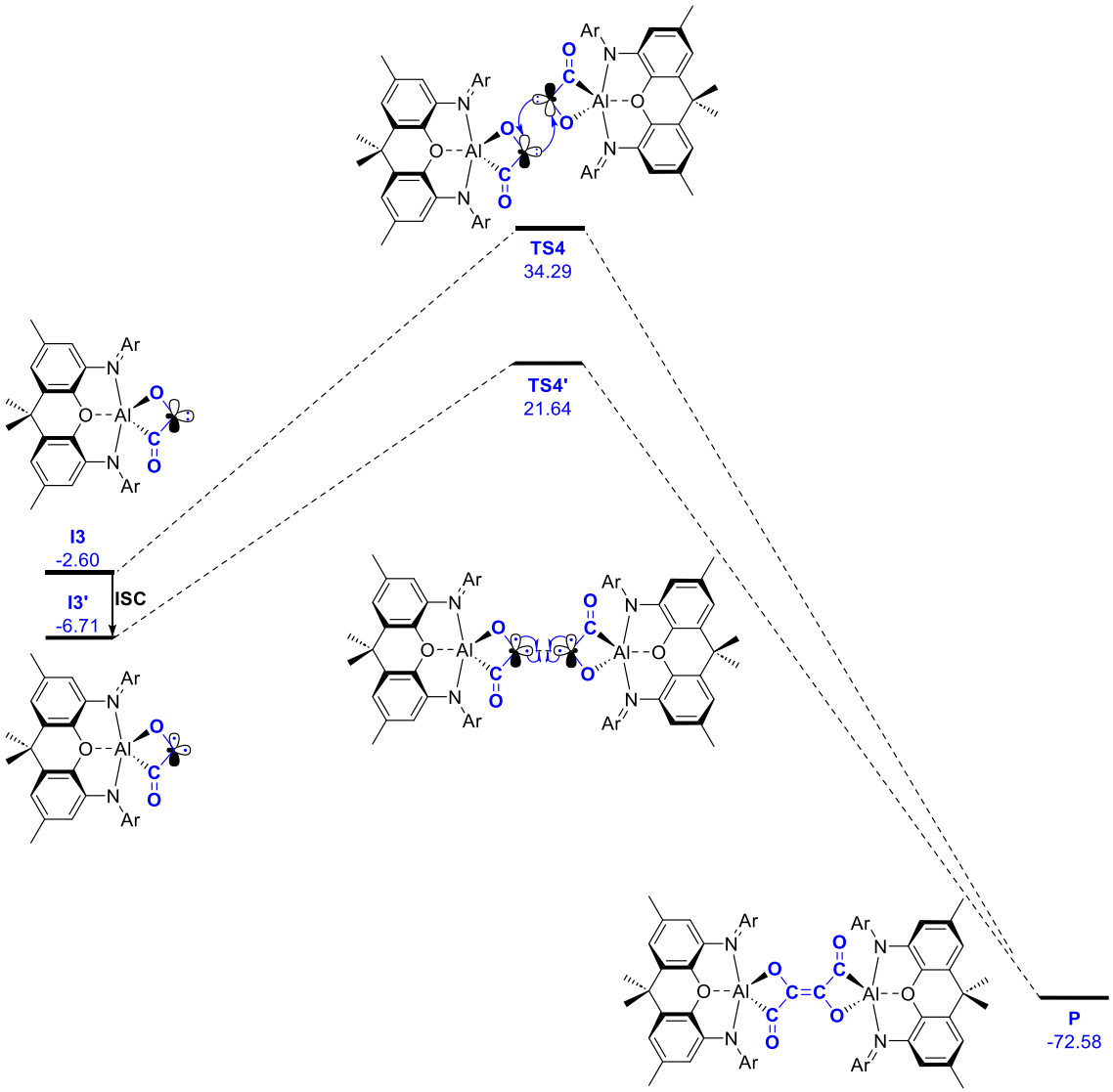

Figure 6.10: Alternate mechanistic pathway from **I3** to **P** via triplet carbene **I3'**

P is an alkene and is naturally planar in nature, indicating it would be best formed by two triplet carbenes (**I3'**). Given the modest barrier in **TS4** the barrier for the recombination of

two triplet carbenes (**I3'**) was calculated (**TS4'**). This demonstrated a significant decrease from 34.3 to 21.6 kcal mol^{-1} (with respect to starting materials). Two effects contribute to this change. Firstly, **TS4'** benefits from improved energetic orbital overlap, with respect too **TS4** which has an energetic overlap of the HOMO/LUMO gap (2.18 eV) in **I3**. In contrast, for **I3'** carbenes, homoleptic recombination occurs with perfect energetic overlap, as the orbital energies are inherently the same, with the pairing energy of the electron serving as the only energetic penalty. This effectively reduces the overall energetic cost of recombination lowering the barrier height. The second factor is the special overlap of the orbitals. Triplet recombination (**TS4'**) can occur through direct approach thus reduced steric profile of the attack. In contrast in **TS4,** carbene **I3** must attack from the top, a sterically more congested site, and perfect special overlap is pitted against steric repulsion thus leading to an increased energetic cost (**Figure 6.10**). A triplet intermediate could also pose a potential explanation for the poor yields, given the inherent reactivity of triplet carbenes leading to side reactions supported by the observation of broad shifts in numerous products during the in-situ NMR spectrum.

While this triplet recombination is convenient way to reduce the barrier height, its feasibility must be carefully scrutinised. In order to move from a singlet to triplet carbene, a formally forbidden transformation, intersystem crossing must occur (ISC), this process is aided by the presence and proximity of Al and K in the system (due to spin orbit coupling).[2] Two approaches to achieve singlet to triplet conversion could be conceived, either by photoexcitation or thermally.

Photoexcitation

When examining the carbene **I3** a small degree of stabilisation from adjacent groups is observed, due to the π accepting carbonyl group and weakly σ donating oxygen atom, leading to a small calculated HOMO/LUMO gap of 2.18 eV.[3,4] Further to this the excited states of **I3**, calculated using time-dependent DFT (TD-DFT), reveal a small S1 transition between the lone pair to the vacant porbital of 0.789 eV with a T1 of 0.254 eV (**Figure 6.11**). This is well within the energy that could be acquired through a photoexcitation, in fact it is in the IR wavelengths (visible light

is from 1.63-3.26 eV). The $\Delta E_{S1\text{-}T1}$ is however, larger than would be traditionally be ideal (0.535 eV vs < 0.37 eV) for ISC along with both orbitals being of the same type so ISC is not predicted to be fast by El-Sayeds rules.[5–7] A better energy match is the S2 and T2 ($\Delta E_{S2\text{-}T2}$ = 0.035 eV) which corresponds to the transition from the lone pair to the π^* manifold of the xanthene with subsequent relaxation to the T1 (**Figure 6.12**). The S2 state is 1.941 eV above the ground state which is in the red-orange range of the visible spectrum which does reflect the colour of the solution phase reaction.

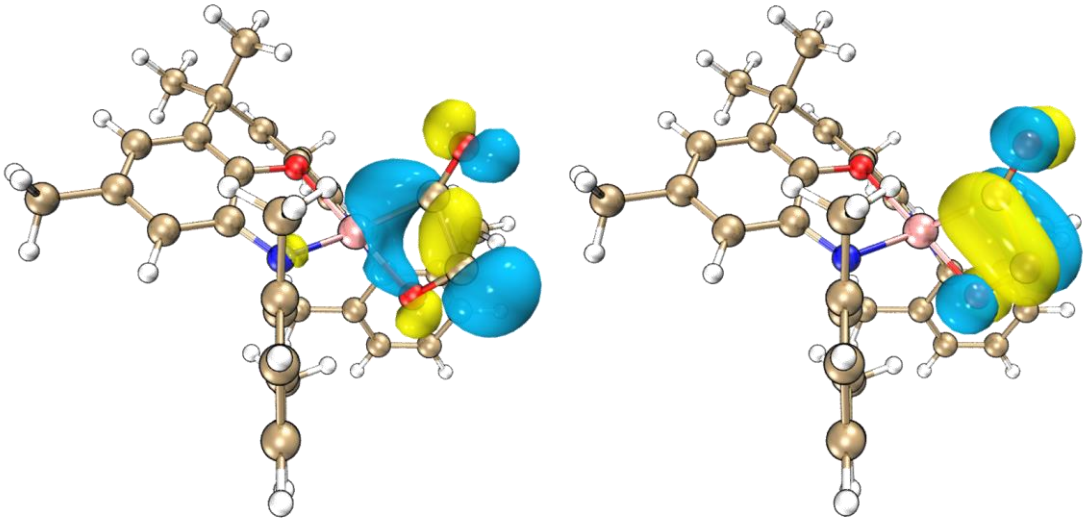

Figure 6.11: NTOs for the transition to S1 of **I3**, (left) donor orbital (right) acceptor orbital.

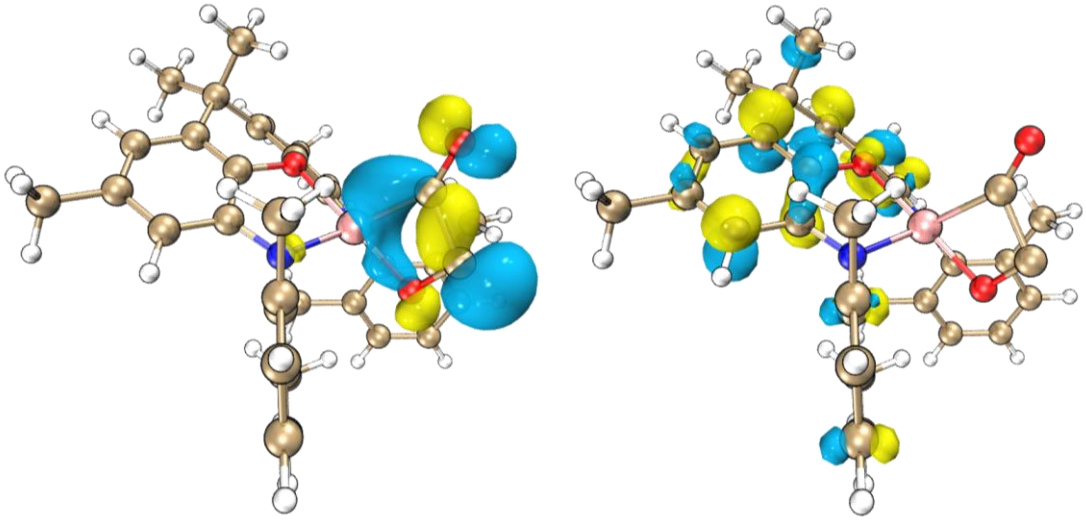

Figure 6.12: NTOs for the transition to S2 of **I3**, (left) donor orbital (right) acceptor orbital.

Thermal conversion

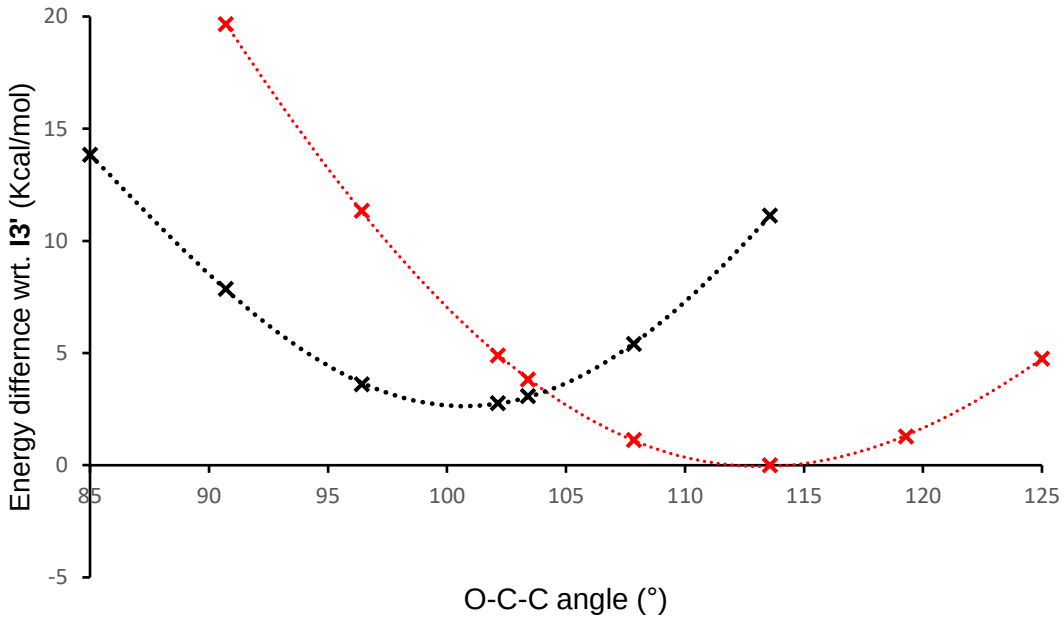

Figure 6.13: Graph of O-C-C angles of carbenes **I3** (black) and **I3'** (red) vs energy with respect to **I3'.**

Conversion between the singlet and triplet states could also be achieved thermally if the energy surfaces overlap sufficiently well. The optimised geometry of the triplet sate of **I3'** is calculated to lie 3.53 kcal mol^{-1} below that of the singlet sate **I3**. Geometrically, there is minimal variation between these states, with the C-C-O angle showing the most significant difference, ranging from 100.3° to 113.7°. This is consistent with expectations, as a triplet carbene (**I3'**) is anticipated to exhibit a closer-to-linear arrangement. When the C-C-O bond angles are scanned for both the **I3** and **I3'** carbenes they can see to overlap at 104.1° (**Figure 6.13**). This has previously been used to estimate the thermal ISC crossing barrier which would be 0.656 kcal mol^{-1}, a value that could be easily overcome at room temperature. [8,9]

Conclusions

In conclusion, the alternative pathway for T4 utilizing the small singlet-triplet gap of the carbenes **I3** and **I3'** significantly reduces the barrier height. The transformation of **I3** between its singlet and triplet states can occur through probable pathways initiated by both thermal and photo processes. This suggests that the change in mechanism is not merely a convenience for

lowering the barrier height, but rather a rational alteration. Further investigations using EPR spectroscopy in situ could provide experimental evidence for the triplet intermediate.

Methods

Mechanistic studies were performed with the ORCA (Revision 5.0.2) programme [10–12] using the B3LYP exchange correlation functional[13–15], with Def-SVP basis sets,[16] and Grimme's empirical dispersion correction (D4) [17]and CPCM solvation for benzene.[18] In all cases the tBu groups on the xanthene backbone were replaced by methyl substituents. Further, the Dipp groups were replaced with P ortho-Xylyl groups. The nature of stationary points found (minima) was confirmed by full frequency calculations with transitions states containing a single imaginary frequency corresponding to the reaction coordinate. Further single point calculations were performed using the B3LYP exchange correlation functional and Def-TZVP basis set to get final energies.[16] TD-DFT was performed on **I3** to examine the excited sates and natural transition orbitals were generated with the ORCA programme.[19]

References

1. Hanusch, F., Groll, L. & Inoue, S. Recent advances of group 14 dimetallenes and dimetallynes in bond activation and catalysis. *Chem Sci* **12**, 2001–2015 (2021).
2. Marian, C. M. Understanding and Controlling Intersystem Crossing in Molecules. *Annu Rev Phys Chem* (2021).
3. Martin, D., Melaimi, M., Soleilhavoup, M. & Bertrand, G. A brief survey of our contribution to stable carbene chemistry. *Organometallics* **30**, 5304–5313 (2011).
4. Kumar Kushvaha, S., Mishra, A., Roesky, H. W. & Chandra Mondal, K. Recent Advances in the Domain of Cyclic (Alkyl)(Amino) Carbenes. *Chem Asian J* **17**, e202101301 (2022).
5. El-Sayed rules. *The IUPAC Compendium of Chemical Terminology* (2008).
6. Chen, R. *et al.* Promoting Singlet/triplet Exciton Transformation in Organic Optoelectronic Molecules: Role of Excited State Transition Configuration. *Scientific Reports 2017 7:1* **7**, 1–11 (2017).
7. Aizawa, N. *et al.* Delayed fluorescence from inverted singlet and triplet excited states. *Nature* **609**, 502–506 (2022).
8. Geise, C. M. *et al.* Computational and experimental studies of the effect of substituents on the singlet-triplet energy gap in phenyl(carbomethoxy)carbene. *Journal of Organic Chemistry* **67**, 3079–3088 (2002).
9. Costa, P. *et al.* Light and Temperature Control of the Spin State of Bis(p-methoxyphenyl)carbene: A Magnetically Bistable Carbene. *J Am Chem Soc* **138**, 1622–1629 (2016).
10. Neese, F. & Wiley, J. The ORCA program system. *Wiley Interdiscip Rev Comput Mol Sci* **2**, 73–78 (2012).
11. Neese, F., Wennmohs, F., Becker, U. & Riplinger, C. The ORCA quantum chemistry program package. *Journal of Chemical Physics* **152**, 224108 (2020).
12. Neese, F. Software update: the ORCA program system, version 4.0. *Wiley Interdiscip Rev Comput Mol Sci* **8**, e1327 (2018).
13. Becke, A. D. Density-functional thermochemistry. III. The role of exact exchange. *J Chem Phys* **98**, 5648–5652 (1993).
14. Stephens, P. J., Devlin, F. J., Chabalowski, C. F. & Frisch, M. J. Ab Initio calculation of vibrational absorption and circular dichroism spectra using density functional force fields. *Journal of Physical Chemistry* **98**, 11623–11627 (1994).
15. Lee, C., Yang, W. & Parr, R. G. Development of the Colle-Salvetti correlation-energy formula into a functional of the electron density. *Phys Rev B* **37**, 785 (1988).
16. Weigend, F. & Ahlrichs, R. Balanced basis sets of split valence, triple zeta valence and quadruple zeta valence quality for H to Rn: Design and assessment of accuracy. *Physical Chemistry Chemical Physics* **7**, 3297–3305 (2005).
17. Caldeweyher, E. *et al.* A generally applicable atomic-charge dependent London dispersion correction. *Journal of Chemical Physics* **150**, 154122 (2019).
18. Barone, V. & Cossi, M. Quantum calculation of molecular energies and energy gradients in solution by a conductor solvent model. *J. Phys. Chem. A.* **102**, 1995–2001 (1998).
19. Petrenko, T., Kossmann, S. & Neese, F. Efficient time-dependent density functional theory approximations for hybrid density functionals: Analytical gradients and parallelization. *Journal of Chemical Physics* **134**, 54116 (2011).

Statement of Authorship

Title of Paper	Coordination and homologation of CO at Al(I): mechanism and chain growth, branching, isomerization and reduction
Publication Status	Published
Publication Details	*Andreas Heilmann, Matthew M. D. Roy, Agamemnon E. Crumpton, Liam P. Griffin, Jamie Hicks, Jose M. Goicoechea, and Simon Aldridge, J. Am. Chem. Soc.* 2022, 144, 28, 12942–12953

Student Confirmation

Student Name:	Agamemnon Elvis Crumpton	
Contribution to the Paper	Performed DFT calculations on the structures within the manuscript, investigated the mechanism of activation of CO, performed energy decomposition analysis on the binding situations of CO and contributed to the discussion of the quantum chemical calculations in the manuscript. In the unpublished work, I performed the DFT calculations elucidating the mechanism and wrote this section.	
Signature 		Date 15/04/2024

Supervisor Confirmation

Supervisor name and title: Professor Simon Aldridge	
Supervisor comments I can confirm that the candidate's contribution to this paper is as described above.	
Signature 	Date 18/4/2024

Chapter 7 - Modulating Hydrogen Shuttling in Ammonia by Neutral and Cationic Boron-containing Frustrated Lewis Pairs (FLPs)

Agamemnon E. Crumpton, Andreas Heilmann and Simon Aldridge*

Published in Angewandte Chemie: Angew. Chem. Int. Ed. 2024, e202406440.

Author contributions

Agamemnon E. Crumpton: Synthesised the novel compounds, collected characterisation data, performed the quantum chemical calculations and lead crystallographer.

Andreas Heilmann: Crystallographer.

Simon Aldridge: Corresponding author.

Manuscript was written by Simon Aldridge and Agamemnon Crumpton.

Abstract

Xanthene-backbone FLPs featuring secondary borane functions –B(Ar^X)H (where Ar^X = C_6F_5 (Ar^F) or C_6Cl_5 (Ar^{Cl})) have been targeted through reactions of the dihydroboranes $Me_2S{\cdot}BAr^XH_2$ with [4,5-Xanth(PR_2)Li]$_2$ (R = Ph, ^{i}Pr), and investigated in the synthesis of related cationic systems via hydride abstraction. The reactivity of these systems (both cationic and charge neutral) with ammonia have been probed, with a view to probing the potential for proton shuttling via N–H bond 'activation.' We find that in the case of four-coordinate boron systems (cationic or change neutral), the N–H linkage remains intact, supported by a NH···P hydrogen bond which is worth up to 17 kcal mol^{-1} thermodynamically, and enabled by planarization of the flexible xanthene scaffold. For cationic three coordinate systems, N-to-P proton transfer is viable, driven by the ability of the boron centre to stabilise the $[NH_2]^-$ conjugate base through N-to-B π bonding. This proton transfer can be shown to reversible in the presence of excess ammonia, depending on the nature of the B-bound Ar^X group. It is viable in the case of C_6F_5 substituents, but is prevented by the more sterically encumbering and secondary donor-stabilising capabilities of the C_6Cl_5 substituent.

Introduction

In the realm of homogeneous catalysis and carbon-free fuel applications, the activation of ammonia (NH_3) has emerged as a valuable pursuit, driven by its high energy density and annual global production exceeding 176 million tonnes.[1,2] Despite the notable success of transition metal complexes in activating and transforming a wide range of E–H bonds, however, NH_3 activation poses a unique challenge due to its inclination to form stable Werner-ammine coordination complexes,[3] and the prohibitive gas-phase N–H bond dissociation energy of 99.4 kcal mol^{-1}.[4]

A significant area of recent research effort in small molecule activation has centred around alternative approaches based on main group element compounds.[5,6] Notably, Bertrand has employed cyclic (alkyl)(amino)carbenes (CAACs) to effect NH_3 activation through insertion into the N–H bond, offering direct comparison with the limited number of *d*-block systems capable of oxidative addition.[7–15] More recent developments have explored alternative pathways, such as single-electron transfer from a dithiolene zwitterion or a Bi(II) complex,[16,17] as well as the thermoneutral and reversible splitting of NH_3 by Goicoechea and colleagues using a geometrically constrained phosphine.[18] Another ground-breaking contribution has come from Breher and co-workers, who demonstrated catalytic NH_3 transfer through a 'masked' frustrated Lewis pair (FLP) comprised of a phosphorus ylid and an aluminium Lewis acid.[19]

We have been interested in the chemistry of FLPs based on a xanthene backbone, and featuring phosphine Lewis base and borane Lewis acid components in the 4- and 5-positions (**Figure 7.1**).[20–22] In the case of systems such as Xanth($PMes_2$)(BAr^F_2), featuring both triaryl-borane and -phosphine functionalities, simple adduct formation is observed with ammonia via N→B bond formation. FLP systems featuring secondary borane units, –B(Ar)H, have been implicated in novel patterns of chemical reactivity,[23] and we were interested in targeting xanthene compounds of the type Xanth(PR_2){$B(Ar^X)H$} (R = Ph, ^{i}Pr; Ar^X = Ar^F, C_6F_5 or Ar^{Cl}, C_6Cl_5).[24–29] We hypothesized that the H-substituent, while sterically less encumbering, would offer a chemical handle through which to modulate reactivity, for example via hydride abstraction to

generate related boron-centred cations. In particular, we wanted to probe this approach to modulate N-to-P hydrogen shuttling via N–H bond 'activation.' These studies, and the influence of the boron-bound aryl substituent thereon, are reported in this manuscript.

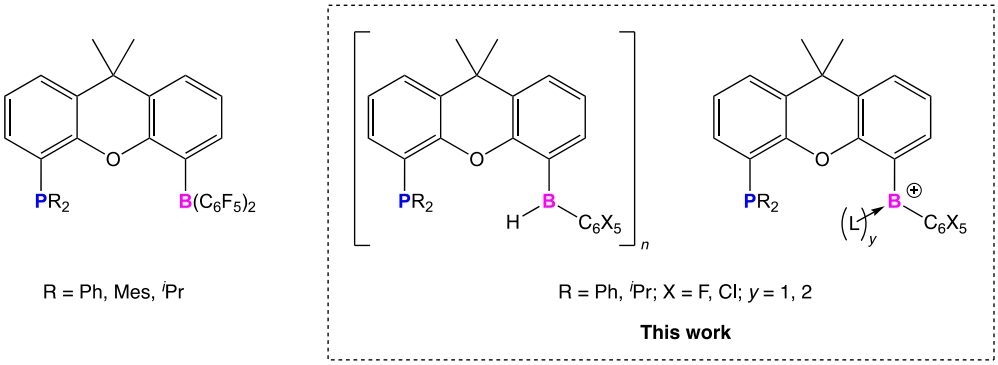

Figure 7.1: 4,5-Disubstituted xanthene derived FLPs relevant to the current study. [13]

Results and Discussion

Syntheses of xanthene -supported secondary borane/phosphines

The reactions of the lithio-xanthene phosphines $[4,5\text{-Xanth}(PR_2)Li]_n$ (R = Ph, n = 2; R = ^{i}Pr, n = 4) with perhaloaryl-substituted boranes $Me_2S{\cdot}(C_6X_5)BH_2$ (X = F, Cl) in toluene (**Scheme 7.1**) lead to essentially quantitative conversion in each case to the anionic borates **1a**-**d** (in ca. 55-75% isolated yields after recrystallization from hexanes). These complexes exhibit diagnostic triplet ^{11}B resonances (at δ_B = -20.3, -26.7, -19.6, and -26.1 ppm for **1a**-**d** respectively; $^1J_{BH} \approx 75$ Hz), typical of tetracoordinate boron hydrides, with the signals for the Ar^{Cl} derivatives (**1a**/**c**) shifted downfield of the Ar^F variants (**1b**/**d**).[24,30] Consistently, the ^{11}F NMR spectra of C_6F_5-containing compounds **1b**/**d** show splittings between the *meta* and *para* C–F resonances indicative of a tetrahedral geometry at boron ($\Delta\delta_{m,p}$ = 2.75, 3.12 ppm for **1b**/**d**, respectively).[31] Single-crystal X-ray diffraction studies confirm the connectivity implied by the spectroscopic data, and reveal coordination of the Li^+ cation by multiple donor sites (P, O, C, H, Cl/F), both intra- and

intermolecular, leading to an overall oligomeric structure in each case (**Figure 7.2**, **C** and Figure **S 7.3-S 7.5**).

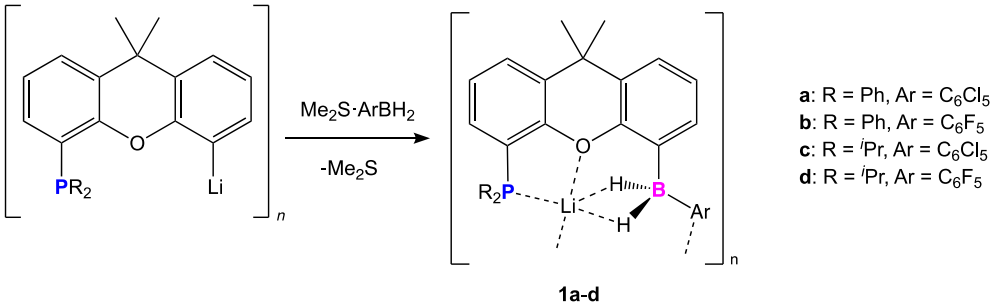

Scheme 7.1: Syntheses of lithium dihydroborates **1a-d** via the reactions of $[4,5\text{-Xanth}(PR_2)Li]_n$ (R = Ph, n = 2;R = ^{i}Pr, n = 4) with $Me_2S\cdot(C_6X_5)BH_2$ (X = F, Cl).

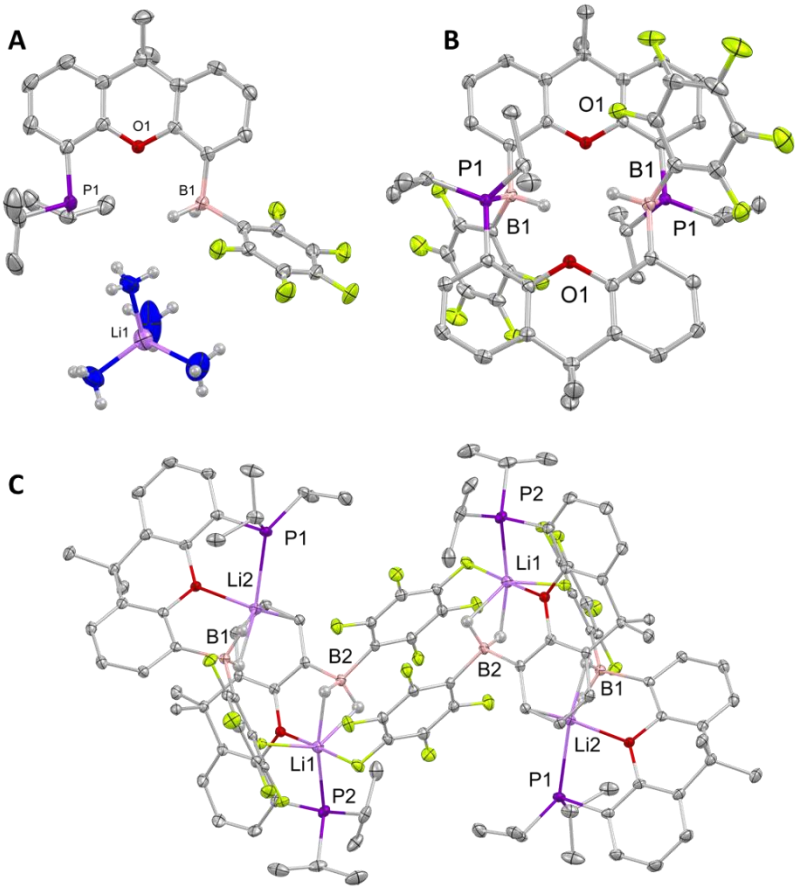

Figure 7.2: Molecular structures of (A) **1c**, (B) **2c** and (C) **3c** in the solid state as determined by X-ray crystallography. Most H atoms omitted for clarity; thermal ellipsoids drawn at the 50% probability level (**1c**, **3c**) or the 30% level (**2c**). Key bond lengths (Å) and angles (°): **1c** P(2)-Li(2) 2.575(3), P(1)-Li(1) 2.519(3), O(1)-Li(1) 2.029(3), O(2)-Li(2) 2.044(3), B(2)-Li(2) 2.274(4), B(1)-Li(1) 2.282(4); **1b** P(1)···Li(1), O(1)···Li(1)6.472(4), 5.197 B(1)···Li(1) 4.969; **1c** P(1)-B(1') 1.9895(18), C(14)-P(1)-B(1')-C(2') 178.44(9)

The encapsulation of the Li cation within these phosphine/dihydroborate aggregates appears to have chemical (in addition to structural) implications, offering a potential explanation for the lack of reactivity of **1a-d** towards mild hydride abstraction reagents such as Me_3SiCl.[32]

When each of **1a**-**d** is exposed to NH_3 (at 1 bar and 20°C), however, crystalline solids are formed which can be shown by single crystal X-ray diffraction to feature the well separated anion/cation pairs, $[Li(NH_3)_n][Xanth(PR_2)\{BH_2(C_6X_5)\}]$, **2a**-**d** (**a**, n =2; **b**, n = 3; **c**, n = 4). The Li^+ ion is coordinated by NH_3 ligands (n = 2 - 4) depending on the nature of the B-bound aryl group (**Figure 7.2**, **A**), in a manner familiar from ammoniate chemistry.[33,34] Removal of the NH_3 atmosphere leads to NH_3 uptake being rapidly reversed, with visible bubbling from the crystalline material and re-dissolution being complete within 5 min to regenerate **1a**-**d** (**Scheme 7.2**).

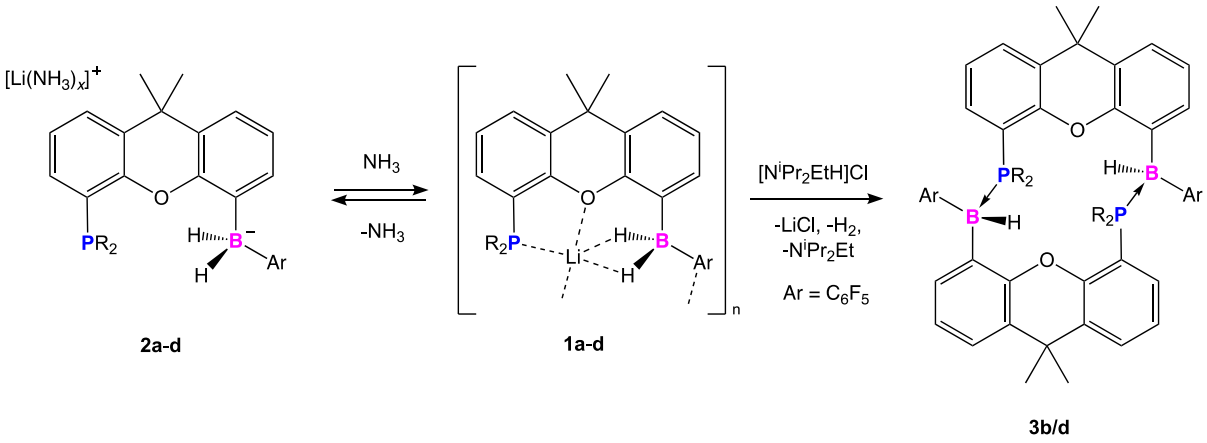

Scheme 7.2: De-aggregation of lithium dihydroborates **1a**-**d** via ammonia uptake/coordination at Li^+; use of the weak, sterically encumbered acid $[N^iPr_2EtH]^+$ to effect LiH removal and formation of the (dimeric) secondary borane/phosphine complexes **3b**/**d** (for Ar = C_6F_5)

The cleavage of **1a**-**d** in the presence of amine donors and the possibility to access the target systems $Xanth(PR_2)\{BH(C_6X_5)\}$ (R = Ph, ^{i}Pr; X = F, Cl) by protic removal of the additional boron-bound hydride, led us to examine the reactivity of **1a**-**d** towards $[N^iPr_2EtH]Cl$. At room temperature these reactions lead to immediate effervescence, and in the cases of Ar^F-substituted systems **1b** and **1d**, the phosphine/borane products **3b**/**d** crystallize from a benzene solution. X-ray crystallography reveals that these two products are "head-to-tail" dimers of the P/B FLPs, with the phosphine donor of one molecule being bound to the borane function of the other, and vice versa (**Figure 7.2**, **B**). These systems are resolutely insoluble in compatible solvents, and cannot therefore be characterized in solution; both react with water (or water-containing solvents) via proto-deboronation, leading to loss of the borane function in the 5-position. C_6Cl_5-containing systems **1a**/**c** also react with $[N^iPr_2EtH]Cl$ but in these cases an intractable mixture of P-/B-containing products results. We hypothesize that this is due to the

additional steric and electronic demands of the C_6Cl_5 group (see below), which prevent dimerization, meaning that the putative (monomeric) FLPs Xanth(PR_2){$BH(C_6Cl_5)$} (R = Ph, ^{i}Pr) remain in solution and are subject to further chemical attack (e.g. by [N^{i}Pr$_2$EtH]Cl).[24]

Ammonia adducts

Due to the insolubility of **3b**/**d** and the difficulty in accessing **3a**/**c** cleanly, we looked to pre-install the NH_3 molecule within the FLP frameworks directly via the reactions of **1a**-**d** with the parent ammonium cation $[NH_4]^+$ (as the Cl^- salt). This approach leads to the quantitative conversion of Xanth(PR_2){$BH(C_6X_5)\cdot NH_3$} (R = Ph, ^{i}Pr; X = F, Cl), **4a**-**d** (**Scheme 7.3**). These ammonia adducts are each characterized by a broad single resonance in the ^{11}B NMR spectrum (at δ_B = -9.1, -12.5, -10.5 and -13.5 ppm respectively), which taken together with a small magnitude of $\Delta\delta_{m,p}$ in the ^{19}F spectra of **4b**/**d** (4.85 and 4.89 ppm), are strongly indicative of a 4-coordinate boron centre bearing a single hydride. The N–H resonances in the respective ^{1}H NMR spectra are significantly shifted downfield (δ_H = 3.64, 3.42, 3.86 and 3.56 ppm) relative to free NH_3 (δ_H =-0.14 in C_6D_6).[35] Previous work has shown that amine adducts of $B(C_6F_5)_3$ result in NH resonances that are downfield shifted upon the formation of hydrogen-bonded complexes, and the extent of this shift depends on the nature of the associated hydrogen bond acceptor.[36,37] Comparison with the chemical shift of $B(C_6F_5)_3\cdot NH_3$ itself (2.67 ppm in benzene-d_6) implies that the **4a**-**d** feature additional NH···X interactions, and X-ray crystallography reveals close contacts (2.6033(6), 2.6613(6) and 2.5974(6) Å for **4a-c**) featuring near-linear NH···P units (176.93(8), 169.67(11) and 173.34(15)°; **Figure 7.3**).[38–41], Previously detected gas phase NH···P interactions, are characterized by much longer (calculated) bond lengths.[38,41–43]

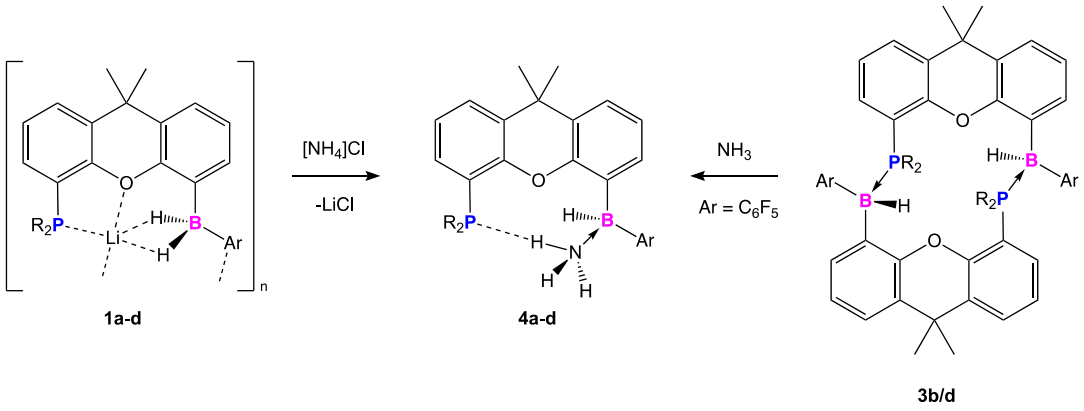

Scheme 7.3: Formation of ammonia adducts **4a**-**d** via protonolysis or substitution chemistry.

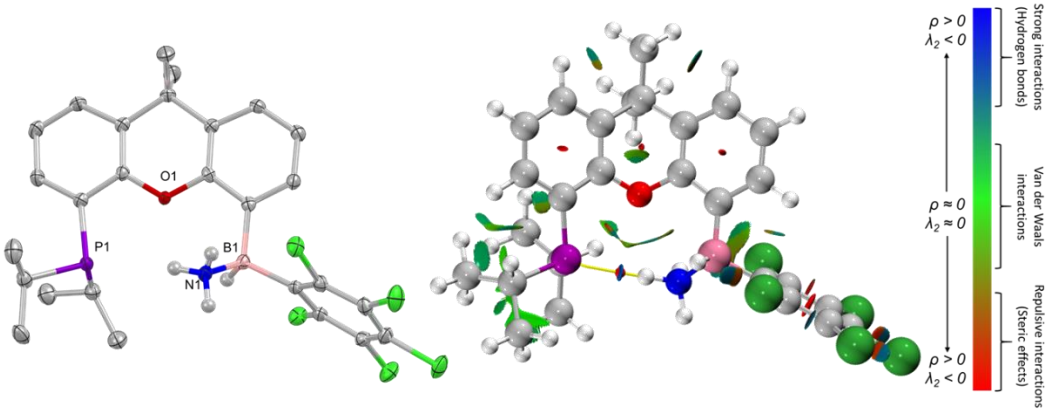

Figure 7.3: (left) Molecular structure of **4c** in the solid state as determined by X-ray crystallography. Most H atoms omitted for clarity; thermal ellipsoids drawn at the 50% probability level. Key bond lengths (Å) and angles (°): B(1)-N(1) 1.611(4), N(1)H···P(1) 2.5974(6), N(1)-H···P(1) 173.34(15), xanthene fold angle 0.45(10) ; (right) NCI plots of **4c**. The range of $\lambda_2 \times \rho(r)$ used for the plots is −0.03 to +0.02 au at s = 0.3 au, QTAIM bond path in yellow with critical point in red.

Structurally characterised examples of NH···P hydrogen bonds are surprisingly scarce, with very few displaying the favourable close-to-linear alignment of the three atoms seen in **4a**-**c**.[38,41,44–47] The xanthene backbone in all three cases **4a**-**c** displays a near planar geometry (xanthene fold angles of **4a** = 5.67(6) °, **4b** = 4.97(7) ° and **4c** = 0.45(10) °), rather than being puckered , thereby increasing the distance between the P and B substituents, which allows for accommodation of the close-to-linear NH···P unit. Density functional theory (DFT) calculations allow visualisation of hydrogen bonding through Non Covalent Interaction (NCI) plots,[48] and for **4a**-**c** these reveal unequivocal H-bonding regions between the P and N–H fragments (see **Figure 7.3**, right for **4c**). Examination by the QT-AIM method reveals a bond critical point (BCP) in each case, lying between the P and N–H units, with a density of ca. 0.02 a.u. and a potential energy (ca. -0.011 a.u.), consistent with other reported calculations of hydrogen bonds.[49–51] Second-

order perturbation theory using the Natural Bonding Orbitals (NBO) basis defines a hydrogen bond strength of 15.1/14.2 kcal mol^{-1} for the $^{i}Pr_2P$-containing systems (**4c**/**d**), with the Ph_2P variants being weaker 4.6/3.1 kcal mol^{-1} (**4a**/**b**),[52] as expected based on the relative pK_as of the phosphines. Nonetheless, the hydrogen bonds in **4a-d** surpass previously calculated interactions for N–H···P systems.[53]

Reactivity of NH_3 in an FLP context: proton shuttling

To increase the Lewis acidity of the boron centre in **4a**-**d** (and by extension the Brønsted acidity of the coordinated ammonia molecule), hydride abstraction from boron was effected using $[Ph_3C][Al(OC(CF_3)_3)_4]$ (**Scheme 7.4**).[54] The resulting cations each give rise to an ^{11}B resonance at ca. 40 ppm (41.2, 39.3, 41.7 and 39.7 for **5a**-**d**, respectively), indicative of 3-coordinate boron. Transfer of an N–H proton to phosphorus is evident in the ^{31}P NMR spectrum, with the resonance shifted downfield of **4a**-**d** (and displaying a doublet coupling pattern) consistent with the formation of a P–H unit (δ_P = -3.0, -2.7, 20.3 and 25.5 ppm for **5a**-**d**, respectively). In addition, the NH protons give rise to two distinct signals in a 1:1 ratio, implying hindered rotation around the B–N bond. Single-crystal X-ray diffraction data was obtained for **5a** (but only by the use of the alternative $[B(C_6F_5)_4]^-$ counter-ion), which confirms that the boron centre is indeed planar (sum of angles = 359.99 °;**Figure 7.4**, left), with B=N double bond character implied by the short B–N distance of 1.383(3) Å.[55]Another structural feature apparent for **5a** in the solid state is the alignment of the Ar^{Cl} group orthogonal to the N–B–C–C plane (91.2(3), 83.9(15) °). While steric constraints are certainly important orientationally, the use of second-order perturbation theory also allows a donor/acceptor interaction to be identified between the two *ortho* chlorines and the boron centre, with a cumulative magnitude of 14.8 (for **5a**) or 14.5 kcal mol^{-1} (for **5c**); the equivalent F-to-B interactions in **5b**/**d** are much weaker (< 2 kcal mol^{-1}).[56] The effect of donation from the *ortho* chlorines is further seen in the calculated B–N Wiberg bond indices (WBIs) with **5a**/**c** possessing lower double bond character (1.196, 1.188) than **5b**/**d** (1.223, 1.234). While individual Cl→B interactions are weak, the WBI of 0.056 that they cumulatively contribute,

signals an additional feature relevant to Ar^{Cl} groups that helps to explain their reactivity (see below).[57]

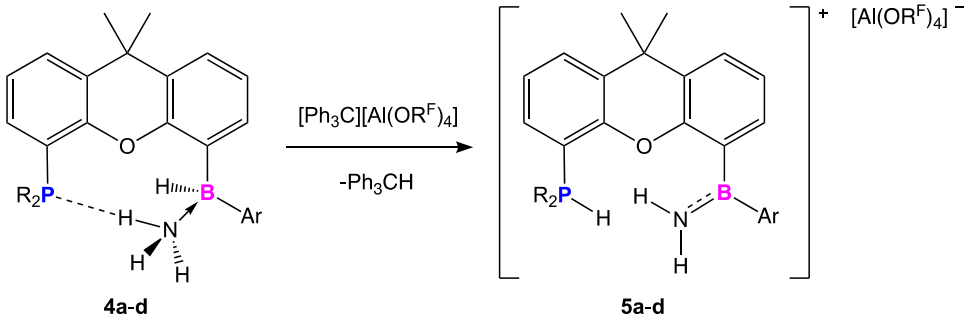

Scheme 7.4: N-to-P proton migration in **4a**-**d**, triggered by hydride abstraction at boron.

The accumulated data therefore suggest that the splitting of the coordinated ammonia molecule in **4a**-**d** on hydride abstraction (i.e. N–H to P–H conversion) reflects increased acidity within the NH_3 moiety on conversion of a four-coordinate borane adduct to a three coordinate borenium cation, $-BAr^{F/Cl}(NH_3)^+$, and the potential for stabilization of the conjugate amide base (NH_2^-) through π-bond formation with the three-coordinate boron centre in **5a**-**d** (augmented by Cl→B donation in the case of the Ar^{Cl} derivatives).

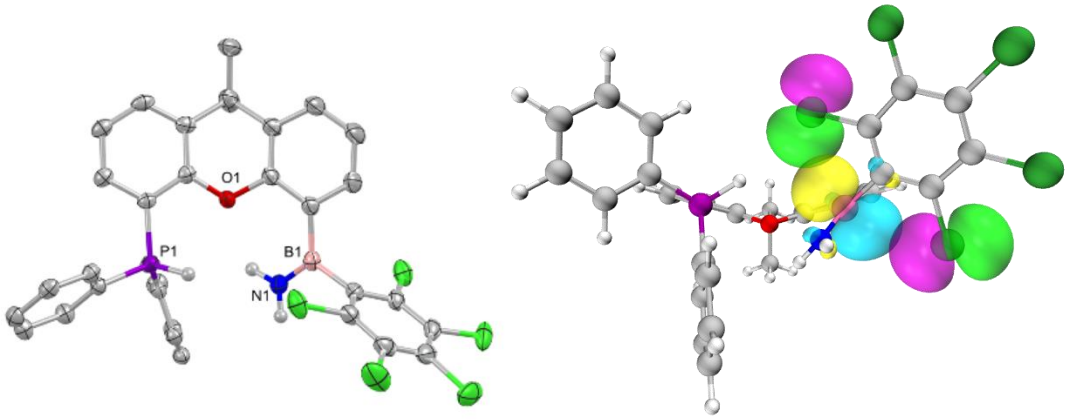

Figure 7.4: (left) Molecular structure of **5a** in the solid state as determined by X-ray crystallography. Most H atoms omitted for clarity; thermal ellipsoids drawn at the 50% probability level. Key bond lengths (Å) and angles (°): B(1)-N(1) 1.383(3), Cl(1A)-B(1) 3.095(3), Cl(5A)-B(1) 2.990(2), Cl(1B)-B(1) 3.110(15), Cl(5B)-B(1) 3.031(15), N(1)–B(1)–C(14)–C(28) plane to Ar^{Cl} 91.2(3), 83.9(15), xanthene fold angle 30.95(7) (right) Natural orbitals from the second order perturbation theory analysis with isosurface values of 0.05 (a.u.). The Cl donor p orbitals are shown in magenta/green and the accepting vacant p orbital on boron in yellow/cyan.

With a view to exploring the reversibility of N-to-P proton transfer, the reactivity of **5a**-**d** to additional ammonia was probed. Exposure to NH_3 (at 1 bar pressure) leads to an immediate

colour change from yellow to colourless (for the C_6F_5 systems) or pale yellow (for Ar = C_6Cl_5). Two different reaction pathways are revealed, depending on the nature of the boron-bound aryl groups (**Scheme 7.5** and **Figure 7.5**). In the cases of the C_6Cl_5 systems **5a**/**c**, the reaction products (**7a**/**c**) give rise to ^{11}B resonances at (δ_B = 39.0/38.9 ppm, respectively) indicative of three-coordinate boron. The doublet resonance in the ^{31}P spectrum of both **5a** and **c** collapses to a singlet and is shifted downfield (to δ_P = -18.7/-11.1 ppm for **7a**/**c**). The solid-state structure of **7a** could be determined by X-ray crystallography, showing a structure very similar to the cationic component of **5a**, but with deprotonation of the P–H unit having occurred (sum of angles at phosphorus: **7a** = 304.4 °; **5a** = 332.8 °, **Figure 7.5** left). Crystallization of the co-product $[NH_4][Al(OR^F)_4]$ was also possible, consistent with the hypothesis the added NH_3 had effected deprotonation of the phosphonium function.

By contrast, in the cases of the C_6F_5 systems **5b**/**d**, the products (**6b**/**d**) are characterized by ^{11}B resonances at δ_B = -3.9 and 3.2 ppm, respectively, with $\Delta\delta_{m,p}(^{19}F)$ values of 7.75/7.70 ppm, consistent a tetrahedral boron centre. As with **7a**/**c** the doublet resonance in the ^{31}P NMR spectrum collapses into a singlet and is shifted downfield (to δ_P = -18.9/-12.5 ppm for **6b**/**d**, respectively). Additionally, the presence of coordinated NH_3 in **6b**/**d** is signalled by a very broad 6H ^1H NMR resonance at δ_H = 1.44/1.98 ppm. A single-crystal diffraction study carried out on **6b** confirms the formation of a boronium cation, featuring two boron-bound NH_3 ligands, balanced by a $[Al(OR^F)_4]^-$ counter-anion (the asymmetric unit features two complete anion/cation pairs). The structure also features a N–H···P hydrogen bond analogous to those found in compounds of type **4** with short H···P contacts of 2.6897(10)/2.54(5) Å and N–H···P angles of 162.4(3)/169.0(40). Use of Second Order Perturbation Theory allows energies of 16.2/16.8 kcal mol^{-1} to be estimated for these interactions (for **6b**/**d**, respectively). With a broader perspective, the formation of **6b**/**d** in this manner provides evidence for reversal of N–H activation in the presence of excess NH_3.

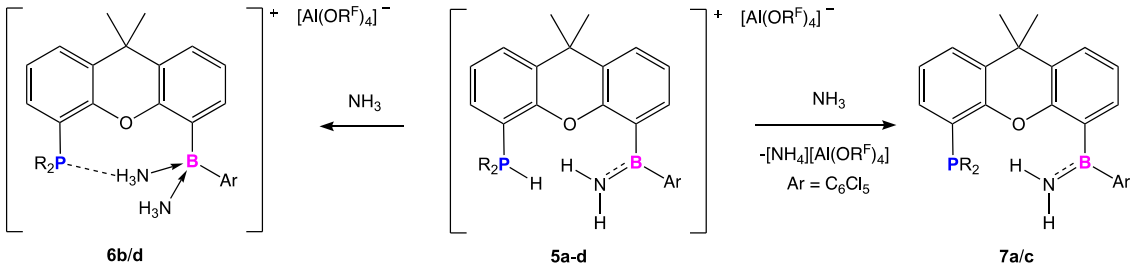

Scheme 7.5: Divergent reactivity of C_6F_5/C_6Cl_5-substituted systems **5b/d** and **5a/c** towards additional ammonia leading to the formation of boronium (**6b/d**) and borane products (**7a/c**).

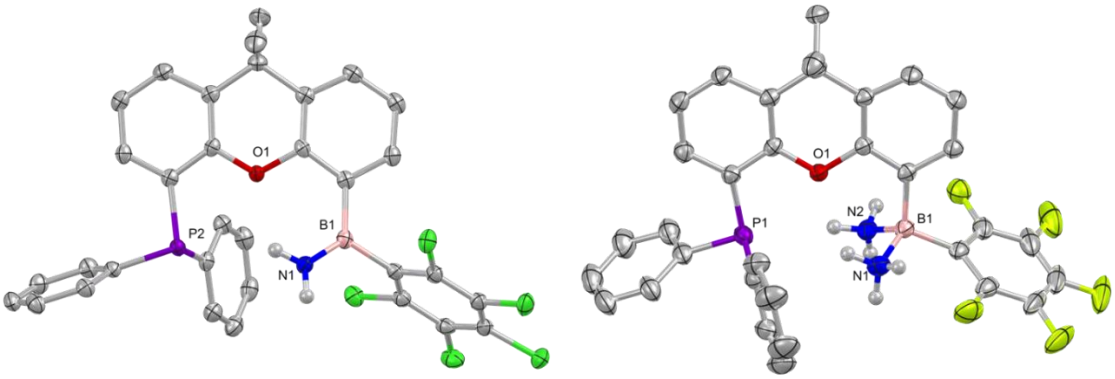

Figure 7.5: Molecular structures of **7a** (left) and **6b** (right) in the solid state as determined by X-ray crystallography. Most H atoms omitted for clarity and thermal ellipsoids drawn at the 50% probability level. Key bond lengths (Å) and angles (°): **7a** N(1)-B(1) 1.375(2), xanthene fold 15.55(5); **6b** N(3)H···P(2) 2.6897(10), N(2)H···P(1) 2.54(5), N(3)-H···P(2) 162.4(3), N(3)-H···P(2) 169(4).

DFT calculations were carried out to illuminate the different reaction pathways from **4a-d** (plus ammonia) in the presence of different B-bound aryl groups. Energetic barriers for the intramolecular activation of NH_3 following hydride abstraction are calculated to be very small (ca. 1 kcal mol^{-1} for the conversion of **4a-d** to **5a-d**, **Figure 7.6**). In similar fashion, the reverse reaction (H^+ transfer from P to NH_2) is also found to be very facile upon coordinating a second NH_3 molecule at boron (3.7, 3.5 kcal mol^{-1} for **5b/d** to **6b/d**, **Figure 7.6**). Pre-organization of the NH_3···P unit, through hydrogen bonding, aligns the phosphine lone pair and the N–H σ^* orbital. When the Lewis acidity of the system is changed, by the removal of a hydride (to form a cationic boron centre), shuttling of a proton is extremely facile, as orbital alignment has already been achieved and the N–H bond has been weakened. Shutting of protons in this manner could be likened to the N–H–N hydrogen bond motifs in enzymatic reactions.[58,59]

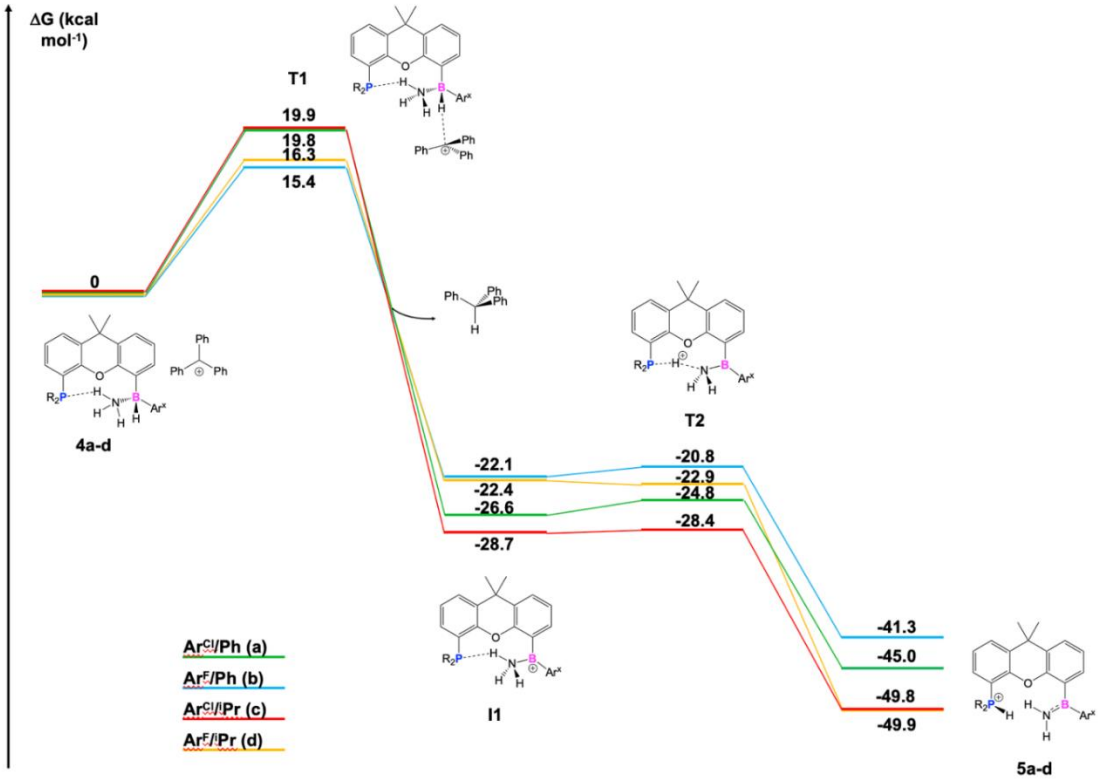

Figure 7.6: Mechanism for the conversion of **4a-d** (S) to **5a-d** (I2), all energies in kcal mol^{-1} and given with respect to **4a-d** (I2).

The formation of different products from systems of type **5** (viz., **6b**/**d** or **7a**/**c**) depends crucially on the role of additional NH_3, i.e. whether it acts as a base or a ligand coordinating at boron. Coordination of NH_3 is calculated to be a higher energy pathway (by 1-2 kcal mol^{-1}) for the C_6Cl_5 systems due to a combination of enhanced steric and Cl-to-B interactions above and below the borane plane (**Figure 7.7**). Conversely, the approach of NH_3 towards the phosphonium unit leading to deprotonation appears to be more facile. The activation barrier for attack at the phosphonium unit is 15.7 kcal mol^{-1} for the P^iPr_2 system (i.e. **5a** to **7a**) compared to 17.5 kcal mol^{-1} for coordination at the borane; for the PPh_2 analogue (**5c**) the barriers to approach to the P–H or borane units are very similar (19.3 mol^{-1} for **3T** and 20.5 kcal mol^{-1} for **T3**). The by-product morphology is crucial to ensure the reaction is exergonic for **5c** to **7c**, with the $[NH_4]^+$ cation gaining considerable stability from the coordination of three NH_3 molecules (ca. 13 kcal mol^{-1}) and resulting in deprotonation being the lowest energy pathway (Supplementary Table ST10). The boronium product is likely not favoured due too steric crowding of the tetracoordinate boron with the bulky Ar^{Cl} group.

For the Ar^F systems (**5b/d-6b/d**) the barriers for both processes were found to be much smaller (**5b-6b**, 12.7; **5b-7b**, 12.5; **5d-6d**, 15.2; **5d-7d** 17.3 kcal mol^{-1}, **Figure 7.7**) due to reduced steric effects and little donor stabilization at boron from the *ortho* fluorine atoms; the boronium products are also thermodynamically more favourable in both cases (**5b-6b**, -10.8; **5b-7b**, -2.0; **5d-6d**, -1.7; **5d-7d** 6.9 kcal mol^{-1}).

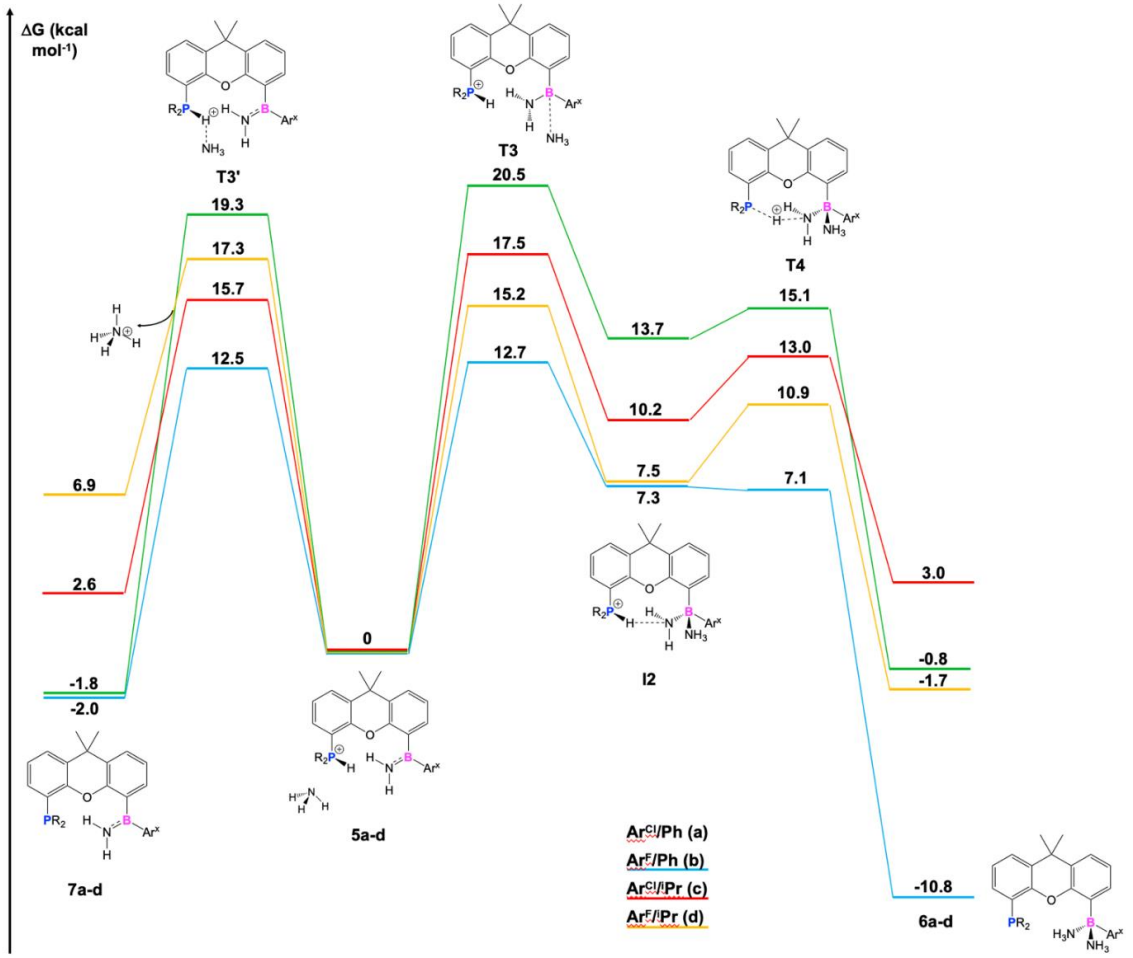

Figure 7.7: Mechanism for the conversion of **5a-d** (I2) to either **6a-d** (P1) or **7a-d** (1P), all energies in kcal mol^{-1} and given with respect to **5a-d** (I2).

Conclusions

Xanthene-backbone FLPs featuring the 2° borane functions –B(Ar^F)H and –B(Ar^{Cl})H can be synthesized in good yield through reactions of the dihydroboranes Ar^XBH_2 with [4,5-Xanth(PR_2)Li]$_2$ (R = Ph, ^{i}Pr), and have been investigated as precursors for related cationic systems via hydride abstraction. The reactivity of these systems with ammonia has been examined, in order to probe the potential for proton shuttling via N–H bond cleavage. In the case of four-

coordinate boron systems (both cationic and charge neutral), the N–H linkage remains intact, supported by strong, close-to-linear NH···P hydrogen bonds, enabled in turn by planarization of the flexible xanthene scaffold. For cationic three coordinate systems, N-to-P proton transfer is viable, driven by the ability of the borane to stabilise the $[NH_2]^-$ conjugate base through N-to-B π bonding. This proton transfer can be shown to be reversible in the presence of excess ammonia, depending on the nature of the B-bound Ar^X group. It is viable in the case of C_6F_5 substituents, but is prevented by the more sterically encumbering and secondary donor-stabilising capabilities of the C_6Cl_5 substituent.

Characterization data

General considerations

All manipulations were carried out using Schlenk line or glovebox techniques under an atmosphere of argon or dinitrogen. Solvents were dried by passage through activated alumina towers, degassed before use and stored over 3 Å molecular sieves. NMR spectra were measured in C_6D_6, d^8-toluene of d2-Dichlormethane which were dried over 3 Å molecular sieves, with the solvent stored under nitrogen in a Teflon valve ampoule. NMR samples were prepared under nitrogen in 5 mm Wilmad 507-PP tubes fitted with J. Young Teflon NMR spectra were measured on a Bruker Avance III HD Nanobay 400 MHz NMR spectrometer equipped with a 9.4 T magnet or a Bruker Avance III NMR 500 MHz NMR spectrometer. ^1H and ^{13}C NMR spectra were referenced internally to residual proteo-solvent (^1H) or solvent (^{13}C) resonances and are reported relative to tetramethylsilane (δ = 0 ppm). Variable temperature ^{31}P spectra were referenced relative to an internal standard of Ph_2P-Xan-H in d^8-toluene. Chemical shifts are quoted in δ (ppm) and coupling constants in Hz. FTIR spectra were recorded on a Bruker Alpha spectrometer with Platinum-ATR module. Elemental analyses were carried out by London Metropolitan University. Tritylium tetrafluoroborate, sec-butyllithium, Tetramethylethylenediamin, 9,9-dimethylxanthene, hexachlorobenzene and HCl in diethyl ether solution was used as received from sigma Aldrich. Ph_2P-xan-Li,[60] Tritylium $[Al(OC(CF_3)_3)_4]$,[61] Tritylium $[B(C_6F_5)_4]$[62] and $Ar^FBH_2{\cdot}SMe_2$ [32] were prepared according to literature procedure.

NH4Cl, $Ar^{Cl}BH_2{\cdot}SMe_2$[32] and $^{i}Pr_2$P-xan-Li [60] were prepared according to modified literature procedures outlined below.

Modified procedures

NH_4Cl:

To a solution of HCl (2 M, 100 mL) in diethyl ether, NH_3 and N_2 was blown over the surface in a Schlenk flask at 0°C for 10 minutes. The solution was then filtered and the resulting white solid washed with 3 x 3 mL of diethyl ether. The solid was then dried to a pressure of 0.1 Mbar in vacuo with an additional liquid Nitrogen Pre-trap to collect any sublimed NH_4Cl. This was stored under a dry argon atmosphere. Yield: 8.76 g (47.5%)

$Ar^{Cl}BH_2{\cdot}SMe_2$:

To a slurry of C_6Cl_6 (10 g, 35.11 mmol) nbuli (2.5 M, 14 mL, 35.11 mmol) was added dropwise at -78°C under vigorous stirring. The dark cloudy solution was then slowly warmed to -40°C where all the precipitate dissolves. The solution was then cooled back to -78°C and Borane dimethyl sulfide complex (5 mL, 52.67 mmol) was added all at once. The solution was then stirred for a further 15 minutes at -78°C then was warmed to room temperature and stirred for a further 2 hours. TMSCl (10 mL 70.22 mmol) was then added dropwise and the resulting suspension filtered via canula and volatiles removed in vacuo. The orange solid was used without further purification. Yield: 9.90 g (87 %). **Spectroscopic data: $^{1}H\{^{11}B\}$** NMR (500 MHz, CD_2Cl_2) δ 2.91 (s, 1H, B-H), 2.32 (s, 6H, SMe_2). **^{11}B** NMR (160 MHz, CD_2Cl_2) δ -10.92 (t, *J* = 111.7 Hz, B-H). **^{13}C** NMR (126 MHz, CD_2Cl_2) δ 138.8(C-BH), 132.3(o), 131.5(p), 131.1(m), 24.2(SMe_2). **Elemental microanalysis** $C_8H_8BCl_5S(C_4H_{10}O)_{0.1}$ calc: C 30.42 % H 2.74 % found: C 30.63 % H 2.41 %

iPr_2P-xan-Li:

To a solution of 9,9-dimethylxanthene (10 g , 47.56 mmol) and Tetramethylethylenediamine (7.1 mL 47.56 mmol) in diethyl ether (50 mL), sec-butyllithium (1.4 M, 37.4 mL, 52.32 mmol) was added dropwise at -78°C. The dark red solution was stirred at -78°C for 1 hour then warmed to room temperature where it was stirred for a further 18 hours. Diisopropylphosphine chloride

(7.6 mL, 47.56 mmol) was added dropwise at -78°C where it was stirred for 15 minutes then warmed to room temperature and stirred for a further 18 hours. Solvents where then removed in vacuo and extracted into dichloromethane (65 mL) and filtered via canula. Solvents were then removed in vacuo, redissolved in diethyl ether (50 mL) where the solution was cooled to -78°C and n-butyllithium (2.5M 26 ml, 65 mmol) was then added dropwise. The solution was stirred at -78°C for 1 hour then warmed to room temperature where it was stirred for a further 18 hours. The solution was then filtered via canula and the pale-yellow solid washed with n-hexanes (4 x 30 mL) until colourless. Solid was then dried in vacuo and used without further purification. Yield: 12.44 g (64 %). **Spectroscopic data** ^{1}**H** NMR (400 MHz, C_6D_6) δ 8.2 (dt, *J* = 6.47, 2.03 Hz, 1H ArH), 7.3 (dd, *J* = 7.69, 1.65 Hz, 1H, ArH), 7.2 – 7.1 (m, 1H, ArH), 7.0 (dt, *J* = 7.60, 2.11 Hz, 1H, ArH), 6.9 (q, *J* = 7.55 Hz, 2H, ArH), 1.9 – 1.8 (m, 1H, CH), 1.8 (s, 3H, Xan-CH_3), 1.6 (s, 3H, Xan-CH_3), 1.1 – 1.0 (m, 1H, CH), 1.0 (dd, *J* = 15.03, 6.82 Hz, 3H, $CHCH_3$), 0.7 (dd, *J* = 14.65, 6.86 Hz, 3H, $CHCH_3$), 0.6 – 0.5 (m, 6H, $CHCH_3$). ^{7}**Li** NMR (156 MHz, C_6D_6) δ 3.2 (d, *J* = 27.90 Hz, Li-P). ^{31}**P** NMR (162 MHz, C_6D_6) δ -22.5 (q, *J* = 28.65 Hz, P-Li). ^{13}**C** NMR (101 MHz, C_6D_6) δ 159.6 (Ar), 154.4 (d, *J* = 16.19 Hz, Ar), 144.2 (d, *J* = 7.23 Hz, Ar), 130.3 (dd, *J* = 60.55, 3.36 Hz, Ar), 124.4 (d, *J* = 4.03 Hz, Ar), 121.4, 120.3 (d, *J* = 13.16 Hz, Ar), 34.6 (CH), 34.3 (Xan-CH_3), 34.2 (Xan-CH_3), 22.8 (d, *J* = 11.02 Hz, CH), 20.6 (d, *J* = 6.63 Hz, $CHCH_3$), 19.9 (d, *J* = 7.28 Hz, $CHCH_3$), 19.7 (d, *J* = 3.90 Hz, $CHCH_3$), 19.2 (d, *J* = 19.30 Hz, $CHCH_3$), 15.6 (d, *J* = 2.86 Hz, $CHCH_3$).**Elemental microanalysis**: $C_{21}H_{26}LiOP$ 0.5($C_4H_{10}O$) calc: C 74.78 %, H 8.46 %. found: C 74.47 %, H 8.19 %.

Synthesis of novel compounds

1a-d

*General procedure A for (**1a-d**):*

Toluene (50 ml) was added dropwise to R_2P-xan-Li (2.5 mmol, 1 equiv.) and Ar^xBH_2 (2.5 mmol, 1 equiv.) at -78 °C under vigorous stirring. The resulting solution was stirred at -78°C for 10 minutes and then the reaction was warmed to room temperature and stirred for a further 6 hours. Full conversion to products seen by NMR spectroscopy.

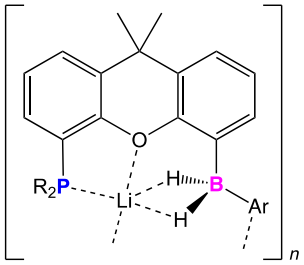

a: R = Ph, Ar = C_6Cl_5
b: R = Ph, Ar = C_6F_5
c: R = ^{i}Pr, Ar = C_6Cl_5
d: R = ^{i}Pr, Ar = C_6F_5

1a-d

Compound **1a-d**

1a:

Following **General Procedure A** with $Ar^{Cl}BH_2$ and Ph_2-xan-Li on the scale described, the resulting clear orange solution was filtered via canula to remove trace white solid and concentrated to incipient crystallisation. Storge at -30°C overnight resulted in crystals suitable for X-ray diffraction. Crystals where washed with cold (-78°C) diethyl ether to remove oily residue. Yield: 1210 mg (73 %). **Spectroscopic data:** ^{1}**H** NMR (500 MHz, C_6D_6) δ 7.43 (tt, *J* = 6.6, 2.3 Hz, 4H, ArH), 7.18 (dd, *J* = 7.8, 1.6 Hz, 1H, ArH), 7.13 – 7.06 (m, 2H, ArH), 7.03 (td, *J* = 4.1, 1.5 Hz, 8H, ArH), 6.82 (t, *J* = 7.6 Hz, 1H, ArH), 3.14 (q, *J* = 76.0 Hz, 2H, BH_2), 1.42 (s, 6H, Xan(CH_3). ^{7}**Li** NMR (156 MHz, C_6D_6) δ 1.5. ^{11}**B** NMR (128 MHz, C_6D_6) δ -20.3 (t, *J* = 75.4 Hz, BH_2). ^{31}**P** NMR (202 MHz, C_6D_6) δ -25.4. ^{13}**C** NMR (126 MHz, C6D6) δ 156.5 (Ar), 156.3 (Ar), 154.4 (Ar), 139.2 (Ar), 135.0 (Ar), 134.9 (Ar), 133.7 (Ar), 133.6 (Ar), 133.2 (Ar), 131.0 (Ar), 129.9 (Ar), 129.2 (Ar), 129.1 (Ar), 128.4 (Ar), 125.4 (Ar), 124.9 (Ar), 124.8 (Ar), 121.8 (Ar), 121.7 (Ar), 121.0 (Ar), 35.3 (Xan-CH_3) 29.9 (Xan-C). **Elemental microanalysis** $C_{33}H_{24}BCl_5LiOP$ 0.5($C_4H_{10}O$) calc: C 60.09% H 4.18% found: C 60.31% H 4.36%

1b:

Following **General Procedure A** with Ar^FBH_2 and Ph_2-xan-Li on the scale described, the resulting clear yellow solution was filtered via canula to remove trace white solid and concentrated to incipient crystallisation. Storge at -30°C overnight resulted in crystals suitable for X-ray diffraction. Crystals were washed with cold (-78°C) diethyl ether to remove oily residue. Yield: 956 mg (65 %). **Spectroscopic data:** ^{1}H NMR (500 MHz, C_6D_6) ^{1}**H** NMR (500 MHz, C_6D_6) δ 7.44 – 7.37 (m, 2H, ArH), 7.14 – 7.00 (m, 11H, ArH), 6.95 (dd, *J* = 7.8, 1.7 Hz, 1H, ArH), 6.82 (dt, *J* = 16.6,

7.5 Hz, 2H, ArH), 2.51 (q, *J* = 80.3 Hz, 2H,BH_2), 1.35 (s, 6H,Xan-CH_3). **^{7}Li** NMR (156 MHz, C_6D_6) δ 1.0. **^{11}B** NMR (160 MHz, C_6D_6) δ -26.7 (t, *J* = 76.1 Hz, BH_2). **^{19}F** NMR (470 MHz, C_6D_6,) δ -132.87 (d, *J* = 22.7 Hz, ArF-o), -161.19 (t, *J* = 20.5 Hz,ArF-p), -163.94 (ddd, *J* = 29.3, 20.3, 9.7 Hz,ArF-m). **^{31}P** NMR (202 MHz, C_6D_6) δ -24.4. **^{13}C** NMR (126 MHz, C_6D_6) δ 155.6 (Ar), 155.4 (Ar), 154.3 (Ar), 134.0 (Ar), 133.8 (Ar), 133.8 (Ar), 133.7 (Ar), 133.1 (Ar), 133.0 (Ar), 132.9 (Ar), 130.1 (Ar), 129.9 (Ar), 129.0 (Ar), 128.9 (Ar), 128.4 (Ar), 125.1 (Ar), 124.9 (Ar), 122.7 (Ar), 122.1 (Ar), 122.0 (Ar), 35.2 (Xan- CH_3), 29.8 (Xan-C). **Elemental microanalysis** $C_{33}H_{24}BF_5LiOP$ 0.5($C_4H_{10}O$) calc: C 68.10% H 4.74% found: C 68.22% H 4.72%

1c:

Following **General Procedure A** with $Ar^{Cl}BH_2$ and $^{i}Pr_2P$ -xan-Li on the scale described, the resulting cloudy orange solution was heated to 100°C upon which the precipitate dissolved. The solution then was filtered via canula to remove trace white solid and was then concentrated to a third of the original volume in vacuo where the addition of hexanes (5 mL) leads to precipitation of a white crystalline solid. Storge at room temperature overnight resulted in crystals suitable for X-ray diffraction. Yield: 834 mg (56 %). **Spectroscopic data: ^{1}H** NMR (500 MHz, C_6D_6) δ 7.24 (dd, *J* = 7.6, 1.7 Hz, 1H, ArH), 7.15 – 7.10 (m, 1H, ArH), 6.94 – 6.81 (m, 3H, ArH), 6.60 (t, *J* = 7.9 Hz, 1H, ArH), 2.77 (q, *J* = 75.8 Hz, 2H, BH_2), 1.74 (dq, *J* = 13.6, 6.9 Hz, 2H, CH), 1.43 (s, 6H, Xan-CH_3), 0.87 (dd, *J* = 16.2, 7.0 Hz, 6H, $CHCH_3$), 0.70 (dd, *J* = 13.9, 7.0 Hz, 6H, $CHCH_3$). **^{7}Li** NMR (156 MHz, C_6D_6) δ 1.3. **^{11}B** NMR (128 MHz, C_6D_6) δ -19.6 (t, *J* = 75.8 Hz, BH_2). **^{31}P** NMR (202 MHz, C_6D_6) δ -12.8. **^{13}C** NMR (126 MHz, C_6D_6) δ 156.1 (Ar), 156.0 (Ar), 153.7 (Ar), 139.1 (Ar), 134.1 (Ar), 133.1 (Ar), 131.2 (Ar), 130.6 (Ar), 130.6 (Ar), 130.2 (Ar), 125.3 (Ar), 123.9 (Ar), 121.7 (Ar), 118.9 (Ar), 35.0 (XanCH_3), 31.0 (Xan-C), 22.9 (CH), 19.4 ($CH2CH_3$), 19.3 ($CH2CH_3$), 19.0 ($CH2CH_3$), 18.9 ($CH2CH_3$). **Elemental microanalysis** $C_{27}H_{28}BCl_5LiOP$ 0.5(C_7H_8) calc: C 57.19%H 5.04% found: C 57.58% H 5.04%

1d:

Following **General Procedure A** with $Ar^{F}BH_2$ and $^{i}Pr_2P$ -xan-Li on the scale described, the resulting cloudy orange solution was heated to 100°C upon which the precipitate dissolved. The solution

then was filtered via canula to remove trace white solid and then concentrated to a third of the original volume in vacuo where the addition of hexanes (5 mL) leads to precipitation of a white crystalline solid. Storge at room temperature overnight resulted in crystals suitable for X-ray diffraction. Yield: 854 mg (66 %). **Spectroscopic data:** ^{1}**H** NMR (500 MHz, C_6D_6) δ 7.25 – 7.18 (m, 1H, ArH), 7.15 (s, 1H, ArH), 7.07 – 6.97 (m, 2H, ArH), 6.96 – 6.88 (m, 2H, ArH), 2.51 (q, *J* = 74.5 Hz, 2H, ArH), 1.79 (dp, *J* = 13.6, 6.8 Hz, 2H, CH), 1.37 (s, 6H, XanCH_3), 0.92 (dd, *J* = 15.7, 6.9 Hz, 6H, $CHCH_3$), 0.79 (dd, *J* = 14.1, 7.0 Hz, 6H, $CHCH_3$). ^{7}**Li** NMR (156 MHz, C_6D_6) δ 1.2. ^{11}**B** NMR (160 MHz, C_6D_6) δ -26.1. (t, *J* = 76.5 Hz, BH_2) ^{19}**F** NMR (470 MHz, C_6D_6) δ -132.95 (d, *J* = 28.6 Hz, ArF-o), -161.00 (t, *J* = 20.4 Hz, ArF-p), -164.12 (ddd, *J* = 26.9, 20.2, 9.9 Hz, ArF-m).^{31}**P** NMR (202 MHz, C_6D_6) δ -12.8. ^{13}**C** NMR (126 MHz, C_6D_6) δ 156.3 (Ar), 156.1 (Ar), 154.2 (Ar), 134.0 (Ar), 134.0 (Ar), 133.2 (Ar), 130.6 (Ar), 130.5 (Ar), 129.9 (Ar), 128.4 (Ar), 127.7 (Ar), 125.2 (Ar), 124.1 (Ar), 122.2 (Ar), 119.8 (Ar), 35.1 (Xan-CH_3), 30.1 (Xan-C), 23.0 (CH), 19.2 ($CH2CH_3$), 19.1 ($CH2CH_3$), 19.1 ($CH2CH_3$), 19.0 ($CH2CH_3$). **Elemental microanalysis** $C_{27}H_{28}BF_5LiOP$ calc: C 63.31% H 5.51% found: C 63.37% H 5.78%

2a-d

*General procedure for **2a-d**:*

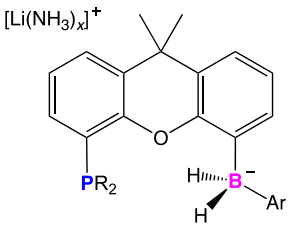

2a-d

Compound **2a-d**

To an NMR tube fitted with a J. Young's valve **1a-d** (10 mg) was dissolved in d6-bezene and degassed by three freeze-pump-thaw cycles where 1.5 Bar of NH_3 was added. Crystals immediately formed for **2a-c**. These where characterised by X-ray crystallography but

spontaneously (and rapidly) loose NH_3 when not exposed to an atmosphere of NH_3 leading to all attempts at elemental micro analysis to fail. Spectroscopically these samples are identical to the starting material. While solid precipitate formed from [$^{i}Pr_2$P-xan-BAr$^{Cl}H_2$]Li when exposed to pressures of NH_3 no crystalline sample could be obtained for single crystal X-ray diffraction.

3b/d

All of the 4 systems were reacted with diisopropylethylamine chloride however the Ar^{Cl} systems only show decomposition to proteo ligand.

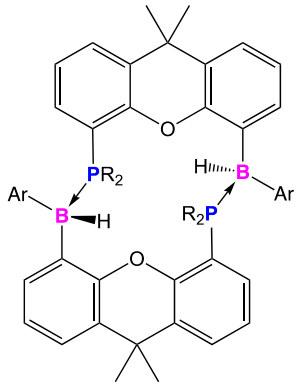

3b/d

Compound **3b/d**

3b:

To an NMR tube fitted with a J. Young's valve **1b** (10 mg, 8.74 µmol) was dissolved in d6-bezene and diisopropylethylamine chloride (1.5 mg, 8.74 µmol) was added with immediate evolution of H_2 gas. After 15 minutes crystals suitable for X-ray crystallography where obtained. All attempts to dissolve these crystals failed or resulted in decomposition. Yield 7 mg (71 %).

Spectroscopic data: Elemental microanalysis $(C_{33}H_{23}BF_5OP)_2(C_6H_6)_{0.5}$ calc: C 70.72 % H 4.49 % found: C 71.12 % H 4.38 %

3d:

To an NMR tube fitted with a J. Young's valve **1d** (10 mg, 9.91 µmol) was dissolved in d6-bezene and diisopropylethylamine chloride (1.6 mg, 9.91 µmol) was added with immediate evolution of H_2 gas. After 15 minutes crystals suitable for X-ray crystallography where obtained. All attempts

to dissolve these crystals failed or resulted in decomposition. Yield 5 mg (51 %). **Spectroscopic data: Elemental microanalysis** $(C_{27}H_{27}BF_5OP)_2(C_6H_6)_{0.25}$ calc: C 65.35 % H 5.48 % found: C 65.50 % H 5.77 %

4a-d

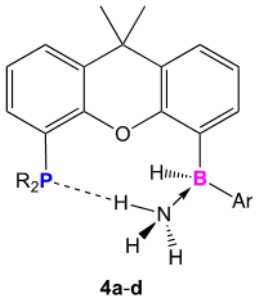

4a-d

Compound 4a-d

4a:

Following **General Procedure A** with $Ar^{Cl}BH_2$ and Ph_2-xan-Li on the scale described, the resulting clear orange solution was filtered via canula onto NH_4Cl (267.5 mg, 5 mmol, 2 equiv.). The resulting suspension was placed in an ultrasonic bath while leaving the system open to an oil bubbler (as H_2 gas is evolved). Reaction progression is evidenced by the evolution of gas. When bubbling is no longer seen, the reaction has reached completion. This is heavily dependent upon quality of NH_4Cl. The solution was then filtered via canula and concentrated to incipient crystallisation. Storage at room temperature overnight results in crystals suitable for X-ray diffraction. Yield: 786 mg (47 %). **Spectroscopic data:** ^{1}**H** NMR (500 MHz, C_6D_6) δ 7.50 (ddt, *J* = 8.2, 6.0, 1.5 Hz, 2H, ArH), 7.43 (td, *J* = 7.8, 1.7 Hz, 2H,ArH), 7.20 (dd, *J* = 7.8, 1.6 Hz, 1H, ArH), 7.16 – 7.12 (m, 2H, ArH), 7.12 (dd, *J* = 5.2, 1.6 Hz, 3H, ArH), 7.12 – 7.05 (m, 2H, ArH), 6.99 – 6.91 (m, 2H, ArH), 6.85 – 6.78 (m, 2H, ArH), 3.92 (s, 1H, BH), 3.64 (s, 3H, NH_3), 1.56 (s, 3H, Xan-CH_3), 1.39 (s, 3H, Xan-CH_3). ^{11}**B** NMR (160 MHz, C_6D_6) δ -9.1 (br BH). ^{31}**P** NMR (202 MHz, C_6D_6) δ -19.2. ^{13}**C** NMR (126 MHz, C_6D_6) δ 153.7 (Ar), 153.5 (Ar), 153.4 (Ar), 138.5 (Ar), 136.7 (Ar), 135.2 (Ar), 134.3 (Ar), 134.1 (Ar), 134.0 (Ar), 133.2 (Ar), 132.3 (Ar), 131.8 (Ar), 131.5 (Ar), 131.0 (Ar), 129.6 (Ar), 129.3 (Ar), 129.2 (Ar), 129.1 (Ar), 129.0(Ar), 128.4 (Ar), 124.4 (Ar), 123.9 (Ar), 123.5 (Ar), 123.4

(Ar), 34.5 (Xan-CH_3), 33.4 (Xan-CH_3), 32.1 (Xan-C). **Elemental microanalysis** $C_{33}H_{26}BCl_5LiNOP$ 0.5(C_7H_8) calc: C 61.09% H 4.21% N 1.95% found: C 61.07% H 3.84% N 1.85%

4b:

Following **General Procedure A** with Ar^FBH_2 and Ph_2-xan-Li on the scale described, the resulting clear yellow solution was filtered via canula onto NH_4Cl (267.5 mg, 5 mmol, 2 equiv.). The resulting suspension was placed in an ultrasonic bath while leaving the system open to an oil bubbler (as H_2 gas is evolved) for 1 hour then stirred for a further 3 hours. This reaction is highly sensitive to time spent in the ultrasonic bath - prolonged periods (c. 3 hours of sonication) causes decomposition to proteo ligand. The solution was then filtered via canula and volatiles removed in vacuo. The white oily solid was extracted into hexanes (75 mL), filtered via canula and concentrated to incident crystallisation. Storge at -30°C overnight resulted in crystals suitable for X-ray diffraction. Yield: 534 mg (36 %). **Spectroscopic data: ^{1}H** NMR (500 MHz, C_6D_6) δ 7.35 (ddt, *J* = 8.3, 6.6, 2.0 Hz, 2H, ArH), 7.25 – 7.19 (m, 2H, ArH), 7.20 (dt, *J* = 3.1, 1.5 Hz, 2H, ArH), 7.18 (dd, *J* = 7.7, 1.7 Hz, 1H, ArH), 7.07 (dt, *J* = 6.0, 1.6 Hz, 6H, ArH), 7.05 (d, *J* = 3.6 Hz, 1H, ArH), 6.88 – 6.75 (m, 2H, ArH), 3.42 (s, 4H, BH/NH_3), 1.54 (s, 3H, Xan-CH_3), 1.46 (s, 3H, Xan-CH_3). **^{11}B** NMR (160 MHz, C_6D_6) δ -12.5 (br BH). **^{19}F** NMR (470 MHz, C_6D_6) δ -133.95 (dd, *J* = 24.9, 9.7 Hz, ArF-o), -159.15 (t, *J* = 20.8 Hz,ArF-p), -164.20 (ddd, *J* = 24.4, 19.8, 9.4 Hz, ArF-m). **^{31}P** NMR (202 MHz, C_6D_6) δ -19.5. **^{13}C** NMR (126 MHz, C_6D_6) δ 153.7 (Ar), 153.7 (Ar), 153.6 (Ar), 135.7 (Ar), 135.7 (Ar), 134.4 (Ar), 134.3 (Ar), 134.1 (Ar), 133.5 (Ar), 133.4 (Ar), 132.3 (Ar), 131.0 (Ar), 131.0 (Ar), 129.6 (Ar), 129.2 (Ar), 129.1 (Ar), 129.0 (Ar), 129.0 (Ar), 128.9 (Ar), 124.8 (Ar), 123.9 (Ar), 123.5 (Ar), 123.1 (Ar0, 123.0 (Ar), 34.5 (Ar), 33.0 (Ar), 32.1 (Ar). **Elemental microanalysis** $C_{33}H_{26}BF_5LiNOP$ 0.5(C_7H_8) calc: C 68.99% H 4.76% N 2.2% found: C 68.66% H 4.52% N 2.17%

4c:

Following **General Procedure A** with $Ar^{Cl}BH_2$ and $^iPr_2P$ -xan-Li on the scale described, the resulting cloudy orange solution was heated to 100°C upon which the precipitate dissolved. The solution then was filtered via canula onto NH_4Cl (267.5 mg, 5 mmol, 2 equiv.). The resulting suspension was placed in an ultrasonic bath while leaving the system open to an oil bubbler (as

H_2 gas is evolved). The reaction can be seen to be finished when no more gas is evolved, this process is heavily dependent on the quality of the NH_4Cl. The solution was then filtered via canula and concentrated to incipient crystallisation. Storage at room temperature overnight results in crystals suitable for X-ray diffraction. Yield: 865 mg (57 %). **Spectroscopic data: ^{1}H** NMR (500 MHz, C_6D_6) δ 7.24 (dd, *J* = 7.7, 1.6 Hz, 1H, ArH), 7.14 – 7.11 (m, 1H, ArH), 7.06 (tt, *J* = 5.3, 1.9 Hz, 1H, ArH), 6.97 (dt, *J* = 9.7, 7.5 Hz, 2H, ArH), 6.83 (dd, *J* = 7.2, 1.6 Hz, 1H, ArH), 4.26 (s, 1H, BH), 3.86 (s, 3H, NH_3), 2.12 – 2.02 (m, 1H, $CHCH_3$), 1.94 (td, *J* = 7.1, 3.6 Hz, 1H, $CHCH_3$), 1.57 (s, 3H, Xan-CH_3), 1.43 (s, 3H, Xan-CH_3), 1.15 (ddd, *J* = 40.0, 14.5, 7.0 Hz, 6H, CH_3), 1.05 – 0.95 (m, 6H, CH_3). **^{11}B** NMR (160 MHz, C_6D_6) δ -10.5 (br BH). **^{31}P** NMR (202 MHz, C_6D_6) δ -9.0. **^{13}C** NMR (126 MHz, C_6D_6) δ 154.5 (Ar), 154.4 (Ar), 153.2 (Ar), 138.6 (Ar), 133.2 (Ar), 131.8 (Ar), 131.5 (Ar), 131.0 (Ar), 131.0 (Ar), 130.7 (Ar), 130.7 (Ar), 124.5 (Ar), 123.8 (Ar), 122.7 (Ar), 121.1 (Ar), 121.0 (Ar), 34.5 (Xan-CH_3), 33.4 (Xan-CH_3), 32.8 (Xan-C), 25.2 (CH), 25.1 (CH), 21.4 ($PCHCH_3$), 20.9 (d, *J* = 7.0 Hz, $PCHCH_3$), 20.6 (d, *J* = 16.0 Hz, $PCHCH_3$), 19.9 (d, *J* = 17.7 Hz, $PCHCH_3$), 19.8 (d, *J* = 8.7 Hz, $PCHCH_3$), 18.5 (d, *J* = 4.4 Hz, $PCHCH_3$). **Elemental microanalysis** $C_{27}H_{30}BCl_5LiNOP$ 0.5(C_7H_8) calc: C 56.39% H 5.28% N 2.16% found: C 56.02% H 4.84% N 2.16%

4d:

Following **General Procedure A** with Ar^FBH_2 and $^iPr_2P$-xan-Li on the scale described, the resulting cloudy orange solution was heated to 100°C upon which the precipitate dissolved and was filtered via canula onto NH_4Cl (267.5 mg, 5 mmol, 2 equiv.) The resulting suspension was placed in an ultrasonic bath while leaving the system open to an oil bubbler (as H2 gas is evolved) for 1 hour then stirred for a further 3 hours. This reaction is highly sensitive to time spent in the ultrasonic bath - prolonged periods (c. 3 hours of sonication) causes decomposition to proteo ligand. The solution was then filtered via canula and volatiles removed in vacuo. The resulting white cloudy oil was dissolved into a minimal amount of benzene (10 mL) and lyophilised. The resulting white powder was extracted in hexanes and solvents were removed in vacuo. Crystals suitable for X-ray diffraction could not be obtained. Yield: 1132 mg (86.8 %). **Spectroscopic data: ^{1}H** NMR (500 MHz, C_6D_6) δ 7.25 (dd, *J* = 7.7, 1.6 Hz, 1H, ArH), 7.19 (dd, *J* = 7.7, 1.7 Hz, 1H, ArH),

7.07 – 7.01 (m, 2H, ArH), 6.99 – 6.90 (m, 2H, ArH), 3.89 (s, 1H, br, BH) 3.56 (s, 3H, NH_3), 2.01 (h, *J* = 6.9 Hz, 1H CH), 1.89 (pd, *J* = 7.0, 3.8 Hz, 1H, CH), 1.59 (s, 3H Xan-CH_3), 1.42 (s, 3H, Xan-CH_3), 1.12 (dd, *J* = 14.5, 7.1 Hz, 3H, $ChCH_3$), 1.04 (dd, *J* = 14.9, 6.8 Hz, 3H, $ChCH_3$), 0.96 – 0.86 (m, 6H, $ChCH_3$) **^{11}B** NMR (160 MHz, C_6D_6) δ -13.5 (br BH). **^{19}F** NMR (470 MHz, C_6D_6) δ -132.86 (dd, *J* = 24.8, 9.9 Hz, ArF-o), -159.13 (t, *J* = 20.4 Hz, ArF-p), -164.02 (ddd, *J* = 24.6, 20.1, 9.7 Hz,ArF-m). **^{31}P** NMR (202 MHz, C_6D_6) δ -9.5 (br). **^{13}C** NMR (126 MHz, C_6D_6) δ 154.6 (Ar), 154.5 (Ar), 153.5 (Ar), 133.3 (Ar), 131.0 (Ar), 131.0 (Ar), 130.7 (Ar), 130.7 (Ar), 128.4 (Ar), 124.7 (Ar), 123.8 (Ar), 122.6 (Ar), 120.9 (Ar), 120.8 (Ar), 34.5 (Xan-CH_3), 34.0 (Xan-CH_3), 31.5 (Xan-C), 24.7 (d, *J* = 10.5 Hz, $PCHCH_3$), 21.0 (d, *J* = 7.2 Hz, $PCHCH_3$), 20.4 (d, *J* = 15.4 Hz, $PCHCH_3$), 19.9 (d, *J* = 11.9 Hz, $PCHCH_3$), 19.7 (d, *J* = 19.2 Hz, $PCHCH_3$), 18.21 (d, *J* = 3.8 Hz, $PCHCH_3$). **Elemental microanalysis** $C_{27}H_{30}BCl_5LiNOP$ 0.5(C_6H_6) calc: C 64.30% H 5.94% N 2.50% found: C 63.96% H 5.87% N 2.51%

5a-d

A variety of anions where used when exploring the abstraction of the hydride but the Krossing anion ($[Al(OC(CF_3)_3)_4]$) produced the most spectroscopically clean material. All anions are spectroscopically identical for the cationic product, with the exception of BF_4 which varies only slightly, but with varying degree of side reactions occurring from the reaction of the borenium intermediate. Reactions with all anions were performed analogously.

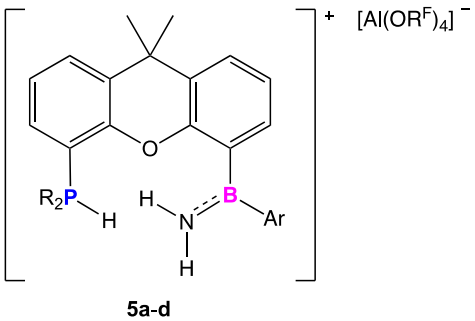

5a-d

Compound **5a-d**

5a:

To an NMR tube fitted with a J. Young's valve **4a** (10 mg, 0.015 mmol) of and Tritylium $[Al(OC(CF_3)_3)_4]$ (14.5 mg, 0.015 mmol) where dissolved in ODFB. Volatiles were removed in vacuo and the resulting solid washed with hexanes twice (0.1 mL) and then redissolved in d2-

Dichloromethane. Yield quantitative by NMR spectroscopy. Crystals could be obtained for the $[B(C_6F_5)_4]^-$ salt (**5a'**) prepared in the analogues manor with $[Ph_3C][B(C_6F_5)_4]$. Spectroscopic data was identical with the addition of the resonances from the $[B(C_6F_5)_4]^-$ anion in place of the $[Al(OC(CF_3)_3)_4]^-$ anion. Crystals were obtained by layering a solution of **5a'** with pentane. Isolated yield of **5a'** 0.5 mg (3 %). **Spectroscopic data:** ^{1}**H** NMR (500 MHz, CD_2Cl_2) δ 8.84 (d, *J* = 512.4 Hz, 1H, PH), 8.08 (d, *J* = 7.8 Hz, 1H, ArH), 8.01 – 7.95 (m, 2H, ArH), 7.80 (td, *J* = 7.9, 3.6 Hz, 4H, ArH), 7.71 – 7.54 (m, 5H, ArH), 7.45 (td, *J* = 7.9, 3.2 Hz, 1H, ArH), 7.35 – 7.32 (m, 1H, ArH), 7.19 (d, *J* = 7.6 Hz, 1H, ArH), 7.13 – 7.06 (m, 1H, ArH), 4.36 (s, 1H, NH), 4.30 (s, 1H, NH), 1.77 (s, 6H, Xan-CH_3). ^{11}**B** NMR (160 MHz, CD_2Cl_2) δ 41.2. ^{19}**F** NMR (470 MHz, CD_2Cl_2) δ -75.69 ($Al(OC(CF_3)_3)_4$). ^{27}**Al** NMR (104 MHz, CD_2Cl_2) δ 34.6.^{31}**P** NMR (202 MHz, CD_2Cl_2) δ -3.0 (d, *J* = 513.7 Hz). ^{13}**C** NMR (126 MHz, CD_2Cl_2) δ 154.4 (Ar), 153.0 (Ar), 144.4 (Ar), 137.2 (Ar), 136.1 (Ar), 135.0 (Ar), 134.2 (Ar), 133.7 (Ar), 133.5 (Ar), 132.3 (Ar), 131.8 (Ar), 131.6 (Ar), 128.4 (Ar), 128.2 (Ar), 128.0 (Ar), 126.2 (Ar), 125.7 (Ar), 125.2 (Ar), 122.9 (Ar), 120.5 (Ar), 118.2 (Ar), 114.0 (d, *J* = 90.2 Hz, Ph-P), 101.1 (d, *J* = 92.9 Hz, Xan-P), 35.3 (Xan-C), 31.8 (Xan-CH_3). **Accurate mass** $C_{33}H_{25}BCl_5NOP+$ calc: 668.0204 m/z found: 668.0216 m/z

5b:

To an NMR tube fitted with a J. Young's valve **4b** (10 mg, 0.017 mmol) of and Tritylium $[Al(OC(CF_3)_3)_4]$ (16.5 mg, 0.017 mmol) where dissolved in ODFB. Volatiles were removed in vacuo and the resulting solid washed with hexanes twice (0.1 mL) and then redissolved in d2-Dichloromethane. Yield quantitative by NMR spectroscopy. **Spectroscopic data:** ^{1}**H** NMR (500 MHz, CD_2Cl_2) δ 8.40 (d, *J* = 498.8 Hz, 1H, PH), 8.05 (d, *J* = 7.8 Hz, 1H, ArH), 7.90 – 7.86 (m, 3H, ArH), 7.71 (td, *J* = 7.8, 3.6 Hz, 4H, ArH), 7.62 – 7.53 (m, 6H, ArH), 7.40 (td, *J* = 7.8, 3.4 Hz, 1H, ArH), 7.02 (ddd, *J* = 15.0, 7.7, 1.5 Hz, 1H, ArH), 4.93 (s, 1H, NH), 4.67 (s, 1H, NH), 1.76 (s, 6H, Xan-CH_3). ^{11}**B** NMR (160 MHz, CD_2Cl_2) δ 39.3. ^{19}**F** NMR (470 MHz, CD_2Cl_2) δ -75.71 ($Al(OC(CF_3)_3)_4$), -131.31 (ddd, *J* = 21.7, 10.3, 3.3 Hz, ArF-o), -150.61 – -151.41 (m, ArF-p), -161.75 – -161.90 (m, ArF-m). ^{27}**Al** NMR (104 MHz, CD_2Cl_2) δ 34.6. ^{31}**P** NMR (202 MHz, CD_2Cl_2) δ -2.7 (d, *J* = 508.3 Hz). ^{13}**C** NMR (126 MHz, CD_2Cl_2) δ 153.4 (Ar), 150.4 (Ar), 144.0 (Ar), 136.40 (Ar), 136.0 (Ar), 133.7 (Ar),

133.6 (Ar), 133.5 (Ar), 133.3 (d, *J* = 5.8 Hz, ArF), 133.1 (d, *J* = 9.0 Hz, ArF), 132.2 (Ar), 131.0 (Ar), 130.9 (Ar), 128.7 (Ar), 127.9 (Ar), 125.5 (d, *J* = 14.2 Hz, ArF), 125.2 (Ar), 121.2 (q, *J* = 292.3 Hz, CF_3), 113.2 (d, J = 90.5 Hz, Ph-P), 100.1 (d, J = 92.0 Hz, Xan-P), 34.6 (Xan-C), 31.9 (Xan-CH3). Accurate mass C33H25BF5NOP+ calc: 588.1682 m/z found: 588.1674 m/z

5c:

To an NMR tube fitted with a J. Young's valve **4c** (10 mg, 0.0165 mmol) of and Tritylium $[Al(OC(CF_3)_3)_4]$ (16.2 mg, 0.0165 mmol) where dissolved in ODFB. Volatiles were removed in vacuo and the resulting solid washed with hexanes twice (0.1 mL) and then redissolved in d2-Dichloromethane. Yield quantitative by NMR spectroscopy. **Spectroscopic data: ^{1}H** NMR (500 MHz, CD_2Cl_2) δ 8.02 (d, *J* = 7.8 Hz, 1H, ArH), 7.62 (dd, *J* = 7.6, 1.9 Hz, 1H, ArH), 7.52 (td, *J* = 7.8, 3.1 Hz, 1H, ArH), 7.40 (ddd, *J* = 11.9, 7.8, 1.5 Hz, 1H, ArH), 7.19 (td, *J* = 7.9, 1.6 Hz, 2H, ArH), 7.09 (dt, *J* = 473.0, 6.7 Hz, 1H, PH), 5.06 (s, 1H, NH), 4.90 (s, 1H, NH), 2.95 (dh, *J* = 10.0, 7.0 Hz, 2H, PCH), 1.72 (s, 6H, Xan-CH_3), 1.51 (dd, *J* = 20.1, 7.0 Hz, 6H, PCHCH_3), 1.39 (dd, *J* = 19.5, 7.1 Hz, 6H). **^{11}B** NMR (160 MHz, CD_2Cl_2) δ 41.7. **^{19}F** NMR (470 MHz, CD_2Cl_2) δ -75.70 ($Al(OC(CF_3)_3)_4$). **^{27}Al** NMR (104 MHz, CD_2Cl_2) δ 34.6. **^{31}P** NMR (202 MHz, CD_2Cl_2) δ 20.3 (d, *J* = 460.5 Hz, PH). **^{13}C** NMR (126 MHz, CD_2Cl_2) δ 154.7 (Ar), 153.2 (Ar), 144.4 (Ar), 135.3 (Ar), 135.2 (Ar), 135.0 (Ar), 134.6 (Ar), 134.0 (Ar), 132.4 (Ar), 130.1 (Ar), 129.4 (Ar), 128.4 (Ar), 128.2 (Ar), 126.1 (Ar), 125.7 (Ar), 121.7 (q, *J* = 291.8 Hz,CF_3), 98.4 (d, *J* = 79.1 Hz, Xan-P), 35.4 (Xan-C), 31.4 (Xan-CH_3), 21.5 (d, *J* = 43.6 Hz, PCH), 17.6 (d, *J* = 1.9 Hz, PCHCH_3), 17.2 (d, *J* = 3.1 Hz, PChCH_3). **Accurate mass** $C_{27}H_{29}BF_5NOP$+ calc: 600.0517m/z found: 600.0459m/z

5d:

To an NMR tube fitted with a J. Young's valve **4d** (10 mg, 0.019 mmol) of and Tritylium $[Al(OC(CF_3)_3)_4]$ (18.7 mg, 0.015 mmol) where dissolved in ODFB. Volatiles were removed in vacuo and the resulting solid washed with hexanes twice (0.1 mL) and then redissolved in d2-Dichloromethane. Yield quantitative by NMR spectroscopy. **Spectroscopic data: ^{1}H** NMR (500 MHz, CD_2Cl_2) δ 7.81 (dt, *J* = 7.9, 1.2 Hz, 1H, ArH), 7.41 (dd, *J* = 5.8, 3.6 Hz, 1H, ArH), 7.28 (td, *J* = 7.8, 3.1 Hz, 1H, ArH), 7.20 – 7.12 (m, 3H, ArH), 6.16 (dt, *J* = 466.2, 6.9 Hz, 1H, PH), 5.15 (s, 1H,

NH), 4.90 (s, 1H, NH), 2.67 (dh, *J* = 9.8, 7.1 Hz, 2H, PCH), 1.53 (s, 6H, Xan-CH_3), 1.22 (dd, *J* = 20.2, 7.1 Hz, 6H, $PCHCH_3$), 1.09 (dd, *J* = 19.7, 7.1 Hz, 6H, $PCHCH_3$). **^{11}B** NMR (160 MHz, CD_2Cl_2) δ 39.7.(br) **^{19}F** NMR (470 MHz, CD_2Cl_2) δ -75.69 ($Al(OC(CF_3)_3)_4$) , -131.29 (ddd, *J* = 22.4, 10.0, 3.5 Hz, ArF-o), -150.38 (t, *J* = 19.9 Hz, ArF-p), -161.20 – -161.37 (m, ArF-m). **^{27}Al** NMR (104 MHz, CD_2Cl_2) δ 34.6. **^{31}P** NMR (202 MHz, CD2Cl2) δ 25.5 (d, J = 478.2 Hz, PH). **^{13}C** NMR (126 MHz, CD_2Cl_2) δ 153.6 (Ar), 150.6 (Ar), 144.0 (Ar), 135.3 (d, *J* = 2.3 H, ArF), 134.1 (d, *J* = 5.4 Hz, ArF), 132.2 (Ar), 131.1 (d, *J* = 6.9 Hz), 128.9 (Ar), 127.9 (Ar), 127.9 (Ar), 127.7 (Ar), 127.6 (Ar), 125.3 (t, *J* = 6.3 Hz, ArF), 121.3 (q, *J* = 290.9 Hz, CF_3), 97.5 (d, *J* = 79.5 Hz, Xan-P), 34.7 (Xan-C), 31.6 (Xan-CH_3), 20.8 (d, *J* = 43.5 Hz, PCH), 17.0 (d, *J* = 1.9 Hz, $PCHCH_3$), 16.5 (d, *J* = 3.0 Hz, $PCHCH_3$). **Accurate mass** $C_{27}H_{29}BF_5NOP+$ calc: 520.1995 m/z found: 520.1980 m/z

6b/d

All reactivity done with the Krossing anion as produced the most spectroscopically clean material however analogous systems could be prepared using BArF (C_6F_6 and $C_6H_3(CF_3)_2$). The side product for the ArCl systems are the ammonium Non-coordinating anion salt which have been crystallographic ally characterised for BArF[20] and Krossing anions.

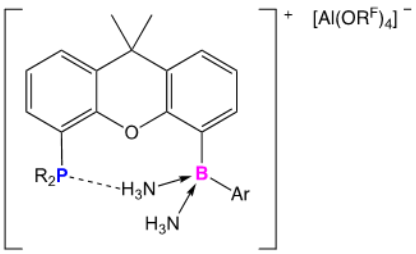

6b/d

Compound **6b/d**

6b:

An NMR tube fitted with a J. Young's valve containing **5b** (10 mg, 6.43 µmol) in d_2-dichloromethane (0.5 mL) was degassed by three freeze-pump-thaw cycles, and NH_3 added (to ca. 1.5 bar pressure). After 5 min, volatiles were removed in vacuo and the resulting solid extracted into benzene (0.6 mL). Crystals suitable for X-ray diffraction could be obtained by heating the sample to 100°C followed by slow cooling to room temperature. Conversion was

quantitative by NMR spectroscopy. Isolated yield 1 mg (10 %). **Spectroscopic data: ^{1}H** NMR (500 MHz, CD_2Cl_2) δ 7.63 (dd, *J* = 7.9, 1.6 Hz, 1H), 7.56 – 7.39 (m, 8H), 7.37 – 7.30 (m, 2H), 7.27 – 7.24 (m, 1H), 7.16 (d, *J* = 7.7 Hz, 1H), 7.04 (t, *J* = 7.6 Hz, 1H), 6.68 (ddd, *J* = 7.3, 5.5, 1.6 Hz, 1H), 6.56 (d, *J* = 7.3 Hz, 1H), 1.69 (s, 6H), 1.44 (s, 6H). **^{11}B** NMR (160 MHz, CD_2Cl_2) δ -3.9. **^{19}F** NMR (470 MHz, CD_2Cl_2) δ -75.72, -134.76 (dd, *J* = 23.8, 9.1 Hz, ArF-o), -153.36 (t, *J* = 20.4 Hz, ArF-p), -161.11 (td, *J* = 22.5, 8.2 Hz, ArF-m). **^{27}Al** NMR (104 MHz, CD_2Cl_2) δ 34.6. **^{31}P** NMR (202 MHz, CD_2Cl_2) δ -18.9 (br m PPh). **^{13}C** NMR (126 MHz, CD_2Cl_2) δ 152.9 (Ar), 152.0 (d, *J* = 16.3 Hz, ArP), 149.3 (Ar), 144.4 (Ar), 134.1 (Ar), 133.9 (Ar), 133.5 (Ar), 133.0 (Ar), 132.7 (Ar), 130.9 (Ar), 130.9 (Ar), 130.7 (Ar), 130.4 (Ar), 129.9 (Ar), 129.9 (Ar), 129.2 (Ar), 129.2 (Ar), 128.5 (Ar), 128.3 (Ar), 128.2 (Ar), 126.9(Ar), 125.3 (Ar), 124.9 (Ar), 122.9 (d, *J* = 290.3 Hz, CF_3), 121.2 (d, *J* = 2.1 Hz), 34.7 (Xan-C), 32.5 (Xan-CH_3). **Accurate mass** $C_{27}H_{26}BCl_5OP(NH_3)$+ calc: 588.1682 m/z found: 588.1674 m/z $C_{27}H_{26}BCl_5OP(NH_3)_2$+ calc: 605.1947 found: 605.1997

6d:

An NMR tube fitted with a J. Young's valve containing **5d** (10 mg, 6.73 µmol) in d_2-dichloromethane was degassed by three freeze-pump-thaw cycles, and NH_3 added (to ca. 1.5 bar pressure).After 5 mins, conversion was quantitative by NMR spectroscopy. **Spectroscopic data: ^{1}H** NMR (500 MHz, CD_2Cl_2) δ 7.62 (dd, *J* = 7.8, 1.5 Hz, 1H, ArH), 7.53 (dd, *J* = 7.8, 1.6 Hz, 1H, ArH), 7.42 (ddd, *J* = 7.6, 3.6, 1.5 Hz, 1H, ArH), 7.28 – 7.25 (m, 1H, ArH), 7.08 (t, *J* = 7.6 Hz, 1H, ArH), 6.62 (d, *J* = 7.2 Hz, 1H, ArH), 2.32 (ddq, *J* = 10.5, 7.0, 3.5 Hz, 2H, PCH), 1.98 (s, 6H, br NH_3), 1.65 (s, 6H, Xan-CH_3), 1.18 (dd, *J* = 16.5, 7.0 Hz, 6H, $PCHCH_3$), 0.99 (dd, *J* = 13.0, 6.9 Hz, 6H, $PCHCH_3$). **^{11}B** NMR (160 MHz, CD_2Cl_2) δ -3.3. **^{19}F** NMR (470 MHz, CD_2Cl_2) δ -75.70 ($Al(OC(CF_3)_3)_4$), -135.14 (dd, *J* = 23.4, 9.3 Hz, ArF-o), -153.27 (t, *J* = 19.9 Hz, ArF-p), -160.97 (m, ArF-m). **^{27}Al** NMR (104 MHz, CD_2Cl_2) δ 34.6. **^{31}P** NMR (202 MHz, CD_2Cl_2) δ -12.5 (br m, $PCHCH_3$). **^{13}C** NMR (126 MHz, CD_2Cl_2) δ 154.7 (Ar), 154.6 (Ar), 153.5 (Ar), 149.2 (Ar), 144.5 (Ar), 132.8 (Ar), 132.2 (Ar), 132.2 (Ar), 131.8 (Ar), 131.1 (Ar), 128.5 (Ar), 128.3 (Ar), 127.9 (Ar), 127.0 (Ar), 124.9 (Ar), 124.7 (Ar), 121.7 (q, *J* = 291.5 Hz, CF_3), 119.5 (Ar), 119.5 (Ar), 35.1 (Xan-C), 31.4 (Xan-CH_3), 24.0 (d, *J* = 4.1 Hz, PCH), 20.3 (d, *J* = 16.3 Hz, $PCHCH_3$), 19.5 (d, *J* = 7.5 Hz, $PCHCH_3$). **Accurate mass**

$C_{27}H_{26}BF_5OP(NH_3)$+ calc: 520.1995 m/z found: 520.1980 m/z $C_{27}H_{26}BF_5OP(NH_3)_2$+ calc: 537.2260 m/z found: 537.2279 m/z

7a/c

All reactivity done with the Krossing anion as produced the most spectroscopically clean material however analogous systems could be prepared using BArF (C_6F_6 and $C_6H_3(CF_3)_2$). The side product for the ArCl systems are the ammonium Non-coordinating anion salt which have been crystallographic ally characterised for BArF[20] and Krossing anions.

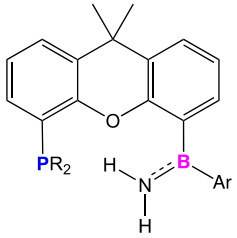

7a/c

Compound **7a/c**

7a:

An NMR tube fitted with a J. Young's valve containing **5a** (10 mg, 6.11 µmol) in d2-dichloromethane was degassed by three freeze-pump-thaw cycles and NH_3 added (to ca. 1.5 bar pressure). After 5 min, volatiles were removed in vacuo and the resulting solid extracted into hexanes (0.6 mL). Crystals suitable for X-ray diffraction were obtained by slow evaporation of the solvent. Conversion was quantitative by NMR spectroscopy. Isolated yield 0.5 mg (12 %). **Spectroscopic data:** ^{1}**H** NMR (500 MHz, CD_2Cl_2) δ 7.43 (ddd, *J* = 7.4, 5.4, 1.7 Hz, 2H, ArH), 7.29 – 7.21 (m, 8H, ArH), 7.17 – 7.14 (m, 2H, ArH), 6.96 (t, *J* = 7.7 Hz, 1H, ArH), 6.89 (t, *J* = 7.5 Hz, 1H, ArH), 6.82 (dd, *J* = 7.4, 1.8 Hz, 1H, ArH), 6.63 (ddd, *J* = 7.5, 4.4, 1.6 Hz, 1H, ArH), 4.42 (s, 2H, NH_2), 1.58 (s, 6H, Xan-CH_3). ^{11}**B** NMR (160 MHz, CD_2Cl_2) δ 39.0. ^{31}**P** NMR (202 MHz, CD_2Cl_2) δ -18.7. ^{13}**C** NMR (126 MHz, CD_2Cl_2) δ 155.5 (Ar), 152.9 (d, *J* = 17.8 Hz, ArP), 149.1 (Ar), 144.4 (Ar), 137.0 (Ar), 136.3 (Ar), 134.5 (Ar), 134.3 (Ar), 134.2 (Ar), 133.0 (Ar), 132.9 (Ar), 131.6 (Ar), 130.5 (Ar), 130.5 (Ar), 130.1 (Ar), 129.8 (Ar), 129.4 (Ar), 129.1 (Ar), 128.1 (Ar), 125.2 (Ar), 124.1 (Ar), 123.6 (Ar), 122.9 (Ar), 120.5 (Ar), 118.2 (Ar), 34.6 (Xan-C), 33.0 (Xan-CH_3). **Accurate mass** $C_{33}H_{24}BCl_5NOP$

(+H$^+$) calc: 668.0204 m/z found: 668.0216 m/z $C_{33}H_{24}BCl_5NOP$ (+Na$^+$) calc: 690.0023 m/z found: 689.9995 m/z

7c:

An NMR tube fitted with a J. Young's valve containing **5c** (10 mg, 6.39 μmol) in d_2-dichloromenthane was degassed by three freeze-pump-thaw cycles, and NH_3 added (to ca. 1.5 bar pressure). After 5 mins, conversion was quantitative by NMR spectroscopy. **Spectroscopic data:** **^{1}H** NMR (500 MHz, CD_2Cl_2) δ 7.96 (d, *J* = 11.5 Hz, 1H, ArH), 7.54 (dd, *J* = 7.4, 2.1 Hz, 1H, ArH), 7.50 (dd, *J* = 7.8, 1.6 Hz, 1H, ArH), 7.26 – 7.24 (m, 1H, ArH), 7.19 – 7.16 (m, 1H,ArH), 7.04 – 6.94 (m, 2H, Arh), 4.65 (s, 2H, NH_2), 2.19 (hept, *J* = 6.9 Hz, 2H, PCH), 1.66 (s, 5H, Xan-CH_3), 1.15 (dd, *J* = 15.0, 6.9 Hz, 6H, PCHCH_3), 0.98 (dd, *J* = 11.8, 6.9 Hz, 6H, PCHCH_3). **^{11}B** NMR (160 MHz, CD_2Cl_2) δ 38.9. **^{31}P** NMR (202 MHz, CD_2Cl_2) δ -11.1 (br m, PCHCH_3). **^{13}C** NMR (126 MHz, CD_2Cl_2) δ 155.8 (Ar), 154.4 (d, *J* = 17.3 Hz, ArP), 149.1 (Ar), 144.4 (Ar), 137.2 (Ar), 134.5 (Ar), 132.9 (Ar), 131.8 (d, *J* = 2.9 Hz, ArP), 131.6 (Ar), 130.5 (Ar), 130.1 (Ar), 129.9 (Ar), 128.5 (Ar), 128.3 (Ar), 127.7 (Ar), 127.5 (Ar), 127.0 (Ar), 126.7 (Ar), 125.7 (Ar), 123.3 (Ar), 122.0 (Ar), 121.7 (q, *J* = 291.3 Hz, ArB), 34.7 (Xan-C), 33.0 (Xan-CH_3), 23.3 (d, *J* = 11.1 Hz, PCH), 19.9 (d, *J* = 17.6 Hz, PCHCH_3), 19.1 (d, *J* = 9.1 Hz, PCHCH_3). **Accurate mass** $C_{27}H_{28}BF_5NOP$ (+H$^+$) calc: 600.0517 m/z found: 600.0499 m/z $C_{27}H_{28}BF_5NOP$ (+Na$^+$) calc: 622.0336 found: 622.0322 m/z

Crystallographic Data

Methods

All data was collected wither on the Rigaku XtaLAB Synergy-DW VHF equip with a PhotonJet-R dual wavelength rotating anode and HyPix-Arc 150° detector or Oxford Diffraction/Agilent SuperNova. Crystals were prepared with Paratone-N or perfluorinated oil, mounted on MiTeGen Micromount loops, and quench-cooled with an Oxford Cryosystems open flow N2 cooling device ([63]). Specific data collection details are in Table 1. Data processing involved CrysAlisPro: unit cell refinement, SCALE3 ABSPACK inter-frame scaling, merging equivalent reflections, and diffraction pattern processing.[64] Structures were solved using SHELXT and refined with SHELXL in OLEX2 ([65–67]). Crystallographic data is in supplementary CIF files () available free via the Cambridge Crystallographic Data Centre: http://www.ccdc.cam.ac.uk/data_request/cif."

Table of Crystallographic data

	015aec22	*022aec22*	*025aec22*	*027aec22*	*029aec22*	*056aec22*	*104aec23*
Formula	$C_{33}H_{33}BF_5LiN_3OP$	$C_{27}H_{28}BF_5LiOP$	$C_{42}H_{39}BCl_5LiN_2OP$	$C_{33}H_{26}BCl_5NOP$	$C_{42}H_{32}BF_5OP$	$C_{54}H_{54}B_2F_{10}O_2P_2$	$C_{120}H_{124}B_4Cl_{20}Li_4O_4P_4$
M.W	631.34	512.21	813.72	671.58	689.45	1008.53	2534.06
Space group	monoclinic	monoclinic	monoclinic	monoclinic	triclinic	monoclinic	monoclinic
Hall	P 1 21/c 1	P 1 21/n 1	P 1 21/c 1	P 1 21/c 1	P -1	I 1 2/a 1	P 1 21/c 1
a	13.3098(2)	17.2474(2)	10.6749(2)	9.40120(10)	11.5649(4)	16.6941(2)	13.67992(6)
b	15.5776(2)	17.9679(2)	13.8975(3)	10.91110(10)	12.0658(4)	14.2199(2)	20.92142(8)
c	15.0661(2)	17.3091(2)	27.5888(6)	30.2143(4)	13.4546(6)	21.6439(3)	21.82302(10)
α	90	90	90	90	80.152(3)	90	90
β	90.8660(10)	104.1860(10)	91.045(2)	97.4410(10)	66.187(4)	111.254(2)	101.1316(4)
γ	90	90	90	90	84.052(3)	90	90
V	3123.37(7)	5200.51(11)	4092.24(15)	3073.21(6)	1691.08(11)	4788.54(13)	6128.31(5)
Z	4	8	4	4	2	4	2
T	150.00(18)	150.00(17)	150.01(13)	150.01(18)	150.01(19)	150.02(16)	150.0(3)
Reflns used	12302	17554	14194	13442	9066	12469	30998
Reflns number	34885	42417	39998	35573	38277	28353	51787
mu	1.31	1.41	0.429	5.022	0.143	1.53	4.98
Radiation	Cu K\a	Cu K\a	Mo K\a	Cu K\a	Mo K\a	Cu K\a	Cu K\a
λ	1.54184	1.54184	0.71073	1.54184	0.71073	1.54184	1.54184
Paramaters	419	677	490	386	453	326	731
R_{all}	0.0472	0.0532	0.0625	0.0388	0.1026	0.0425	0.0327
R_{gt}	0.0357	0.0421	0.0419	0.0294	0.0537	0.0332	0.0294
wR	0.0898	0.1201	0.0995	0.0744	0.1147	0.0897	0.0778
R_{av}	0.0453	0.0461	0.036	0.0439	0.0588	0.0379	0.0352
Goof	1.045	1.023	1.033	1.018	1.028	1.035	1.029

	124aec23	*136aec23*	*138aec23*	*155aec23*	*206aecah21*	*217ekek17*	*268aecah22*
Formula	$C_{27}H_{40}BF_5LiN_4OP$	$C_{34}H_{38}BCl_5NOP$	$C_{84}H_{104}Li_4O_4P_4$	$C_{33}H_{26}BF_5NOP$	$C_{80}H_{64}B_2F_{10}Li_2O_2P_2$	$C_{78}H_{92}Li_2O_8P_2$	$C_{139}H_{104}B_4Cl_{20}Li_4O_2P_2$
M.W	580.35	695.68	1329.31	589.33	1344.75	1233.41	1371.05
Space group	orthorhombic	monoclinic	monoclinic	monoclinic	monoclinic	triclinic	triclinic
Hall	P 21 21 21	P 1 21/n 1	P 1 21/n 1	P 1 21/c 1	P 1 21/n 1	P -1	P -1
a	9.52360(10)	11.73510(10)	12.92050(10)	9.21967(5)	12.6620(3)	16.8986(3)	12.9435(3)
b	13.15580(10)	10.81520(10)	23.6455(2)	10.14618(5)	22.6035(4)	22.9407(3)	13.6814(3)
c	25.1337(2)	26.7388(3)	24.9528(2)	29.27277(16)	24.2600(5)	19.4446(3)	20.3154(6)
α	90	90	90	90	90	90	82.442(2)
β	90	91.5290(10)	104.7860(10)	94.1297(5)	97.740(2)	115.0824(19)	72.847(2)
γ	90	90	90	90	90	90	66.829(2)
V	3149.02(5)	3392.41(6)	7370.93(11)	2731.19(3)	6880.1(3)	6827.2(2)	3159.76(15)
Z	4	4	4	4	4	4	1
T	150.00(10)	100.01(10)	100.00(10)	99.99(10)	150.01(10)	150	150.0(3)
refIns_used	50510	58283	46045	51119	13572	32734	16121
refIns_number	78192	142428	187131	118903	41998	70587	35777
mu	1.253	4.561	1.323	1.446	1.202	1.012	4.883
Radiation	Cu K\a	Cu K\a	Cu K\a	Cu K\a	Cu K\a	Cu K\a	Cu K\a
λ	1.54184	1.54184	1.54184	1.54184	1.54184	1.54184	1.54184
Paramaters	390	456	889	382	975	811	829
R_{all}	0.0289	0.0576	0.0763	0.0502	0.0791	0.069	0.0541
R_{gt}	0.0279	0.0545	0.0541	0.0492	0.061	0.0604	0.0432
wR	0.076	0.1132	0.153	0.1213	0.1879	0.1713	0.1204
R_{av}	0.0505	0.0642	0.0637	0.0314	0.037	0.034	0.0366
Goof	1.04	1.215	1.029	1.064	1.024	0.9781	1.021

	286aec23_auto	*431aec23_auto*	*454aec23_auto*
Formula	$C_{57}H_{25}B_2Cl_5F_{20}NOP$	$C_{52}H_{35}AlBF_{41}N_2O_5P$	$C_{36}H_{26}BCl_5FNOP$
M.W	1349.62	1615.58	726.61
Space group	triclinic	monoclinic	triclinic
Hall	P -1	P 1 21/c 1	P -1
a	10.33900(10)	28.14400(10)	11.53470(10)
b	11.91420(10)	14.13700(10)	12.12430(10)
c	25.1093(2)	31.7506(2)	13.81540(10)
α	100.1410(10)	90	66.4380(10)
β	94.0840(10)	104.3190(10)	70.7880(10)
γ	102.0230(10)	90	76.3720(10)
V	2959.12(5)	12240.21(13)	1660.24(3)
Z	2	8	2
T	100.00(10)	100.00(10)	100.00(10)
reflns_used	44403	69041	37254
reflns_number	70394	152714	58860
mu	3.429	2.165	4.74
Radiation	Cu K\a	Cu K\a	Cu K\a
λ	1.54184	1.54184	1.54184
Paramaters	829	2582	461
R_{all}	0.0389	0.0946	0.0294
R_{gt}	0.0356	0.0835	0.0274
wR	0.0997	0.2485	0.0747
R_{av}	0.0323	0.0457	0.0363
Goof	1.061	1.062	1.043

Additional X-ray structures

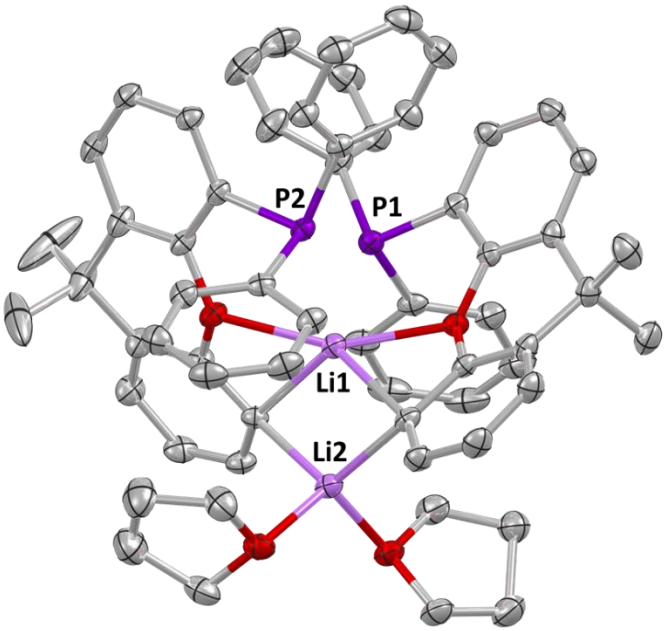

S 7.1: Molecular structure of Ph_2P-xan-Li (217ekek17), most H atoms and solvent omitted for clarity; thermal ellipsoids drawn at the 50%

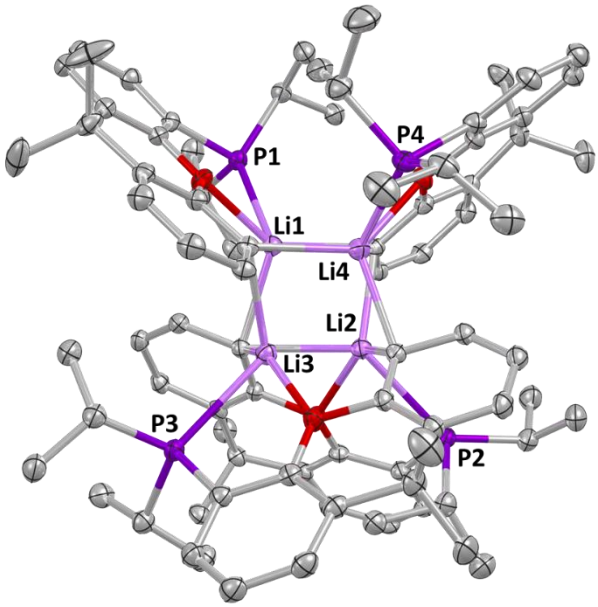

S 7.2: Molecular structure of $^{i}Pr_2P$-xan-Li (138aec22), most H atoms omitted for clarity; thermal ellipsoids drawn at the 30%

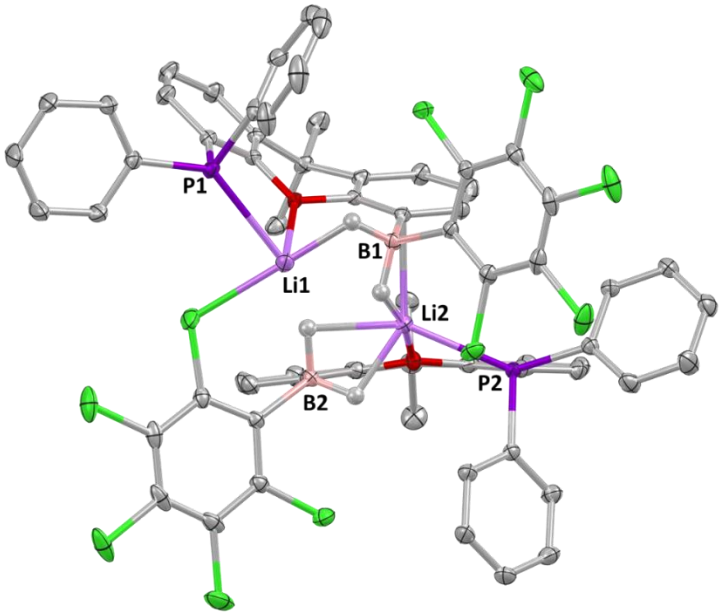

S 7.3: Molecular structure of **1a** (268aecah22), most H atoms omitted for clarity; thermal ellipsoids drawn at the 50%

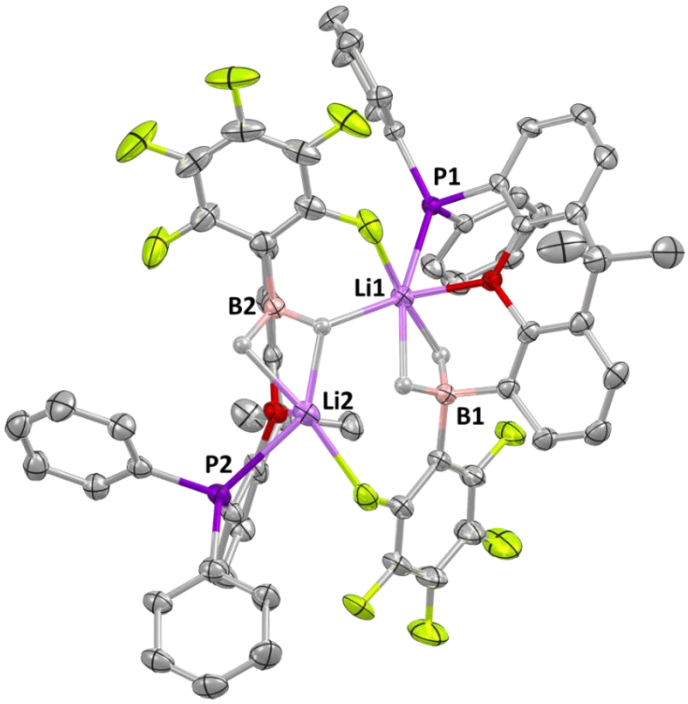

S 7.4: Molecular structure of **1b** (206aecah21), most H atoms omitted for clarity; thermal ellipsoids drawn at the 50%

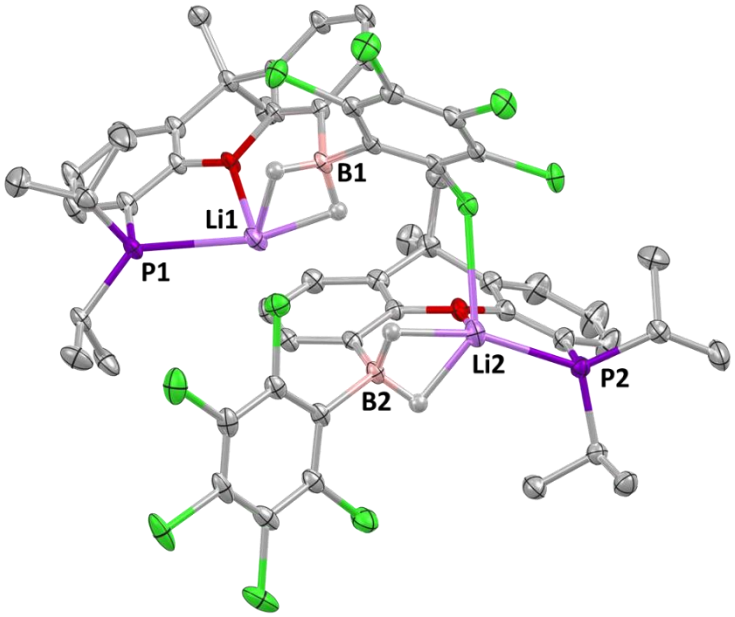

S 7.5: Molecular structure of **1c** (104aec23), most H atoms omitted for clarity; thermal ellipsoids drawn at the 50%

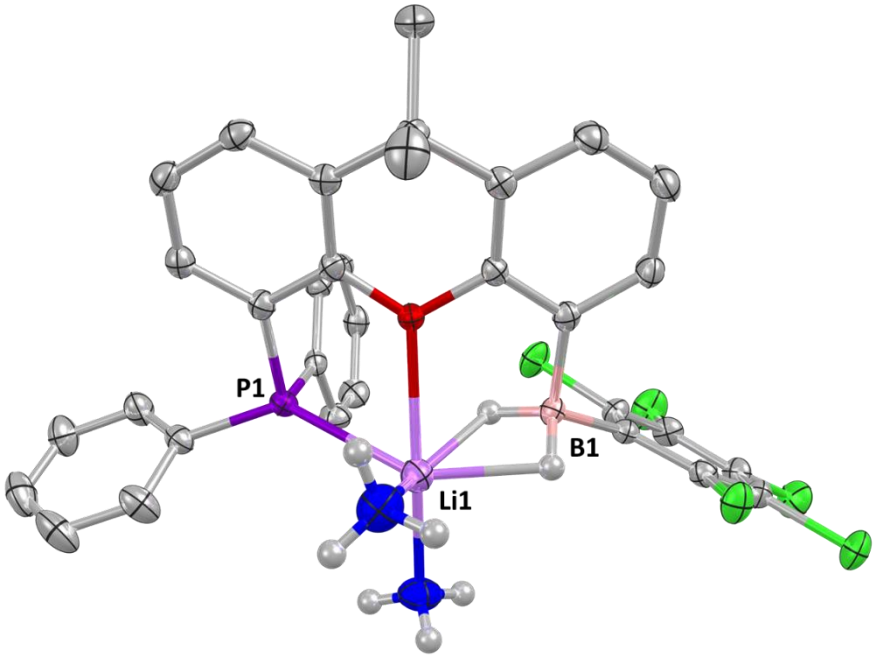

S 7.6: Molecular structure of **2a** (025aec22), most H atoms omitted for clarity; thermal ellipsoids drawn at the 50%

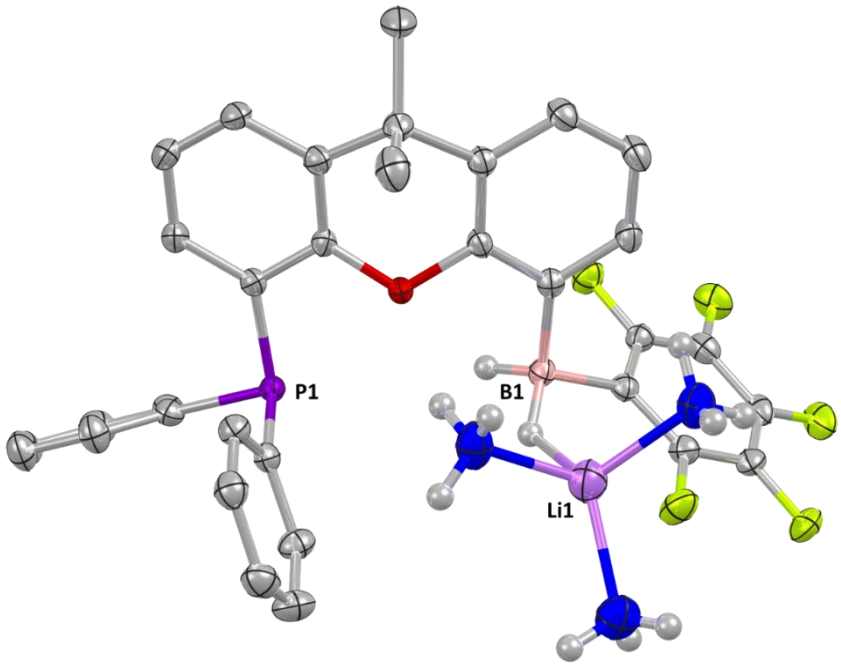

S 7.7: Molecular structure of **2b** (015aec22), most H atoms omitted for clarity; thermal ellipsoids drawn at the 50%

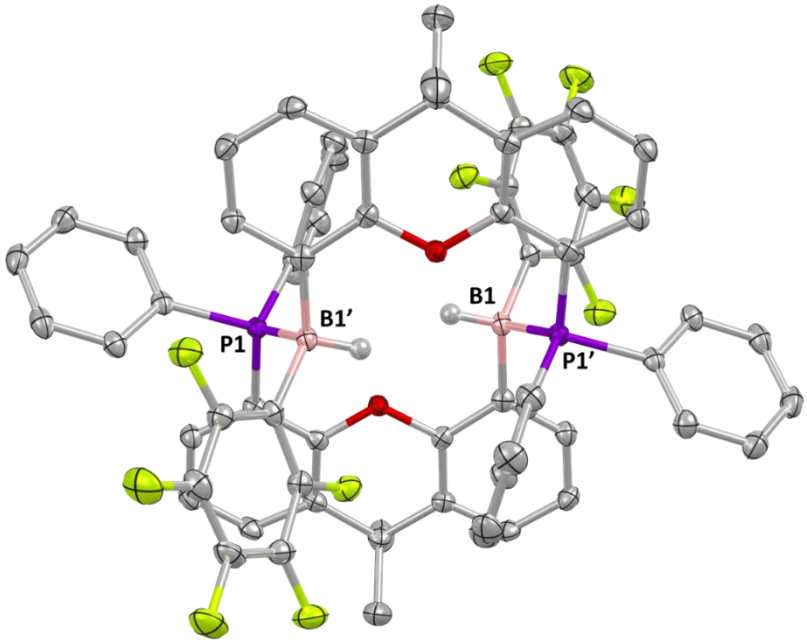

S 7.8: Molecular structure of **3a** (029aec22), most H atoms omitted for clarity; thermal ellipsoids drawn at the 50%

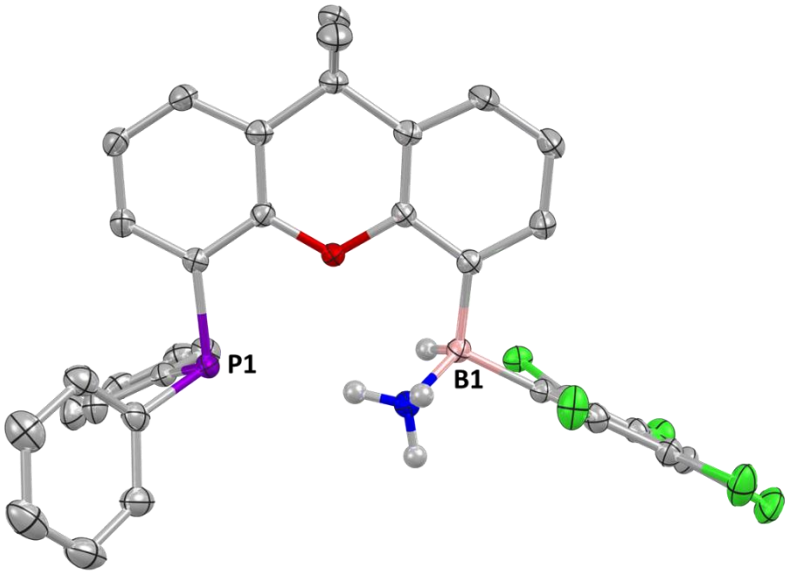

S 7.9: Molecular structure of **4a** (027aec22), most H atoms omitted for clarity; thermal ellipsoids drawn at the 50%

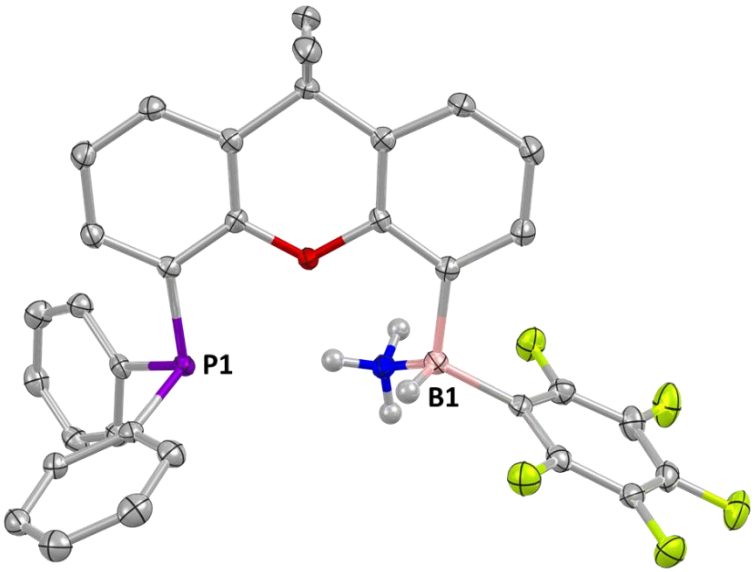

S 7.10: Molecular structure of **4b** (155aec23), most H atoms omitted for clarity; thermal ellipsoids drawn at the 50%

DFT

Methods

All calculations performing with the ORCA (Revision 5.0.4) program.[68–70] All compounds where first optimised using the meta-generalized-gradient approximation (mGGA) functional R2-SCAN[71] in conjunction with the Def2-TZVPPm basis set[72] with the D4 dispersion correction[73], and employing the geometrical counterpoise correction gCP[74] (together known as the R2SCAN-3c method)[72]. Frequency calculations were performed to confirm the nature of minima or saddle points by none or one imaginary frequency respectively. Frequency calculations were also used to generate simulated IR spectra using the Avogadro visualiser.[75] Single point calculations where then performed using the ωB97x range separated hybrid functional[76,77] with the D4 dispersion correction alongside the Def2-QZVP basis set[78,79] and solvation of benzene with the conductor-like polarizable continuum model, CPCM for CH_2Cl_2.[80]

Bonding analysis

QTAIM/NCI

Bonding analysis was performed on the wavefunctions using the Multiwfn(QTAIM/NCI) and NBO7 programmes.[81–83] To investigate the presence of Hydrogen bonding second order perturbation theory was performed to look for the donor acceptor interactions between the phosphorus lone pair and the N-H orbitals. To further investigate this topology analysis in the atoms and molecules framework (QTAIM)[84] was performed to investigate the nature/existence of a bond critical point (BCP) between the P-H-N and this was superimposed on the non-covalent indicator (NCI) surface.[85] These showed the BCP lines up with the blue regions on the NCI surface indicative of hydrogen bonding (**S 7.11**, **S 7.12**, **S 7.13**, **S 7.14**, **S 7.15**).[86]

ST 7.1: Parameters associated with the NH···P hydrogen bonds: Total NH···P being the SOPT energy in Kcal/mol, WBI of the H-P "bond" and the following values at the H-P bond critical point ρ (electron density a.u.), K (kentic energy, a.u.), V (potencial energy, a.u.), E (total energy, a.u), ∇2 (Laplacian, a.u.) and ELF

	4a	***4b***	***4c***	***4d***	***6b***	***6d***
Total NH···P	4.62	14.96	15.65	3.1	16.8	16.21
WBI	0.0182	0.0549	0.058	0.0129	0.0708	0.0636
ρ	0.014502	0.020750	0.021348	0.012731	0.021005	0.021005
K	-0.000229	0.001153	0.001274	-0.000521	0.001263	0.001263
V	-0.007788	-0.011238	-0.011594	-0.006726	-0.011057	-0.011057
E	0.000229	-0.001153	-0.001274	0.000521	-0.001263	-0.001263
∇^2	0.032986	0.035726	0.036181	0.031074	0.034128	0.034127
ELF	0.086887	0.165698	0.172549	0.070123	0.179846	0.179847

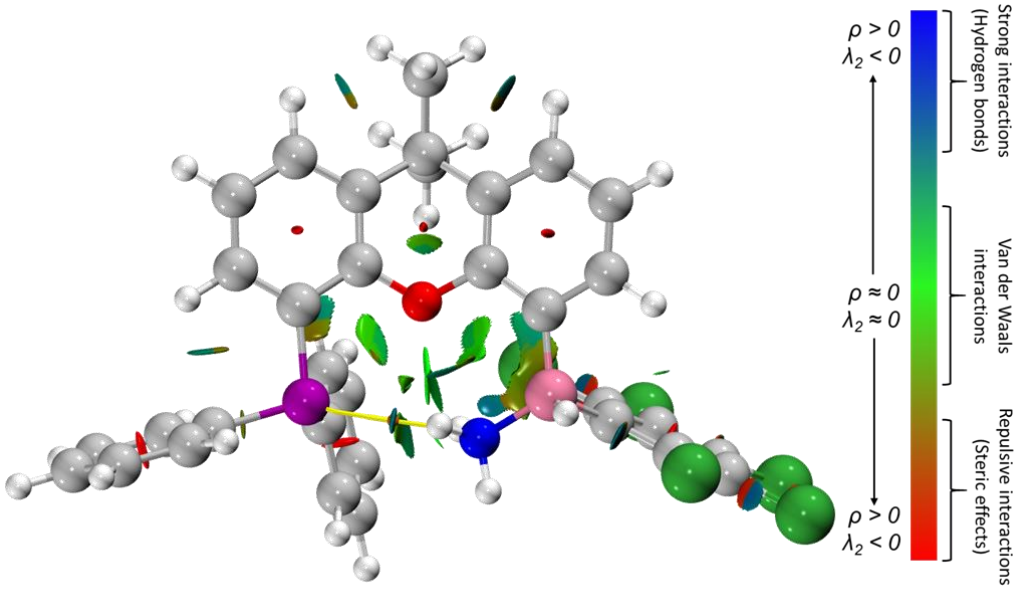

S 7.11: NCI plots of the **4a**, the range of $\lambda_2 \times \rho(r)$ used for the plots is −0.03 to +0.02 au at s = 0.3 au, QTAIM bond path in yellow with critical point in orange.

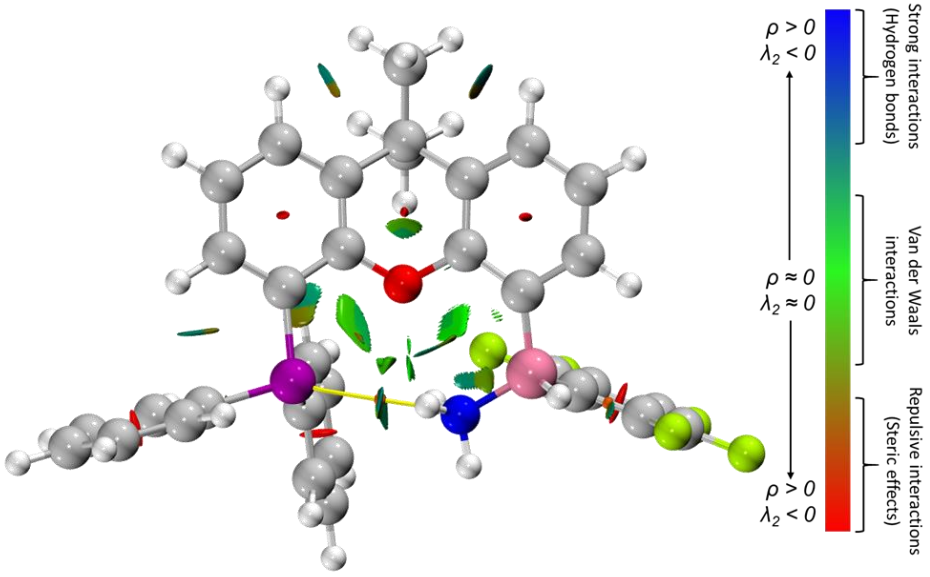

S 7.12: NCI plots of the **4b**, the range of $\lambda_2 \times \rho(r)$ used for the plots is −0.03 to +0.02 au at s = 0.3 au, QTAIM bond path in yellow with critical point in orange.

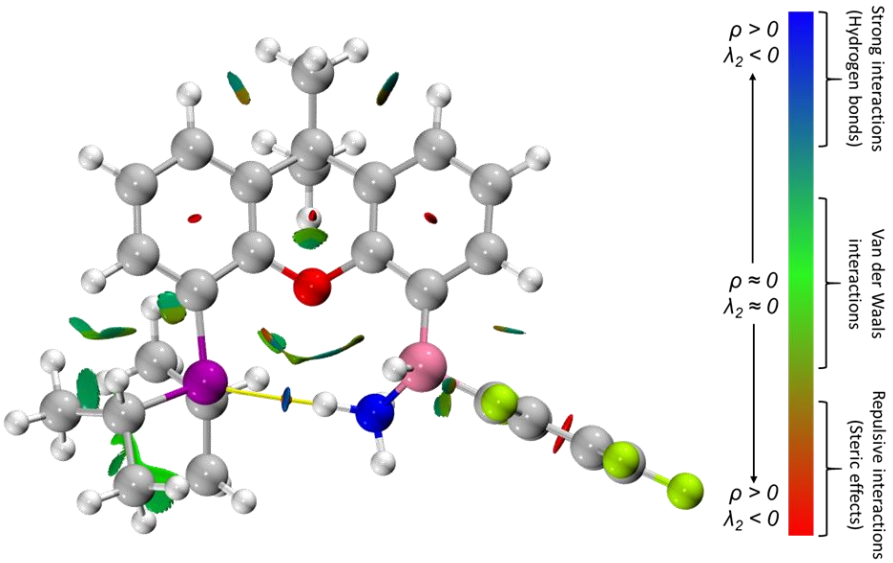

S 7.13: NCI plots of the **4d**, the range of $\lambda_2 \times \rho(r)$ used for the plots is −0.03 to +0.02 au at s = 0.3 au, QTAIM bond path in yellow with critical point in orange.

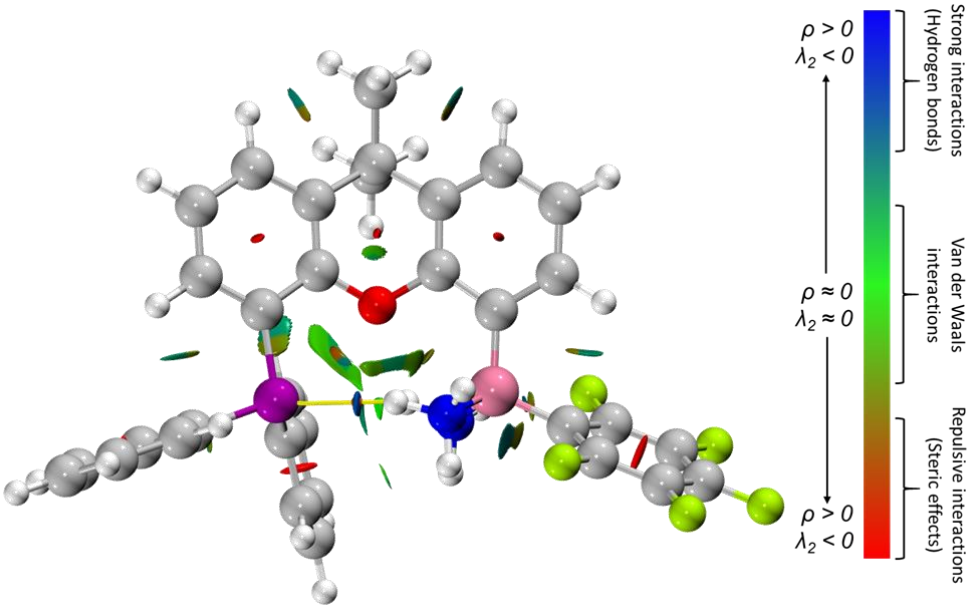

S 7.14: NCI plots of the **6b**, the range of $\lambda_2 \times \rho(r)$ used for the plots is −0.03 to +0.02 au at s = 0.3 au, QTAIM bond path in yellow with critical point in orange.

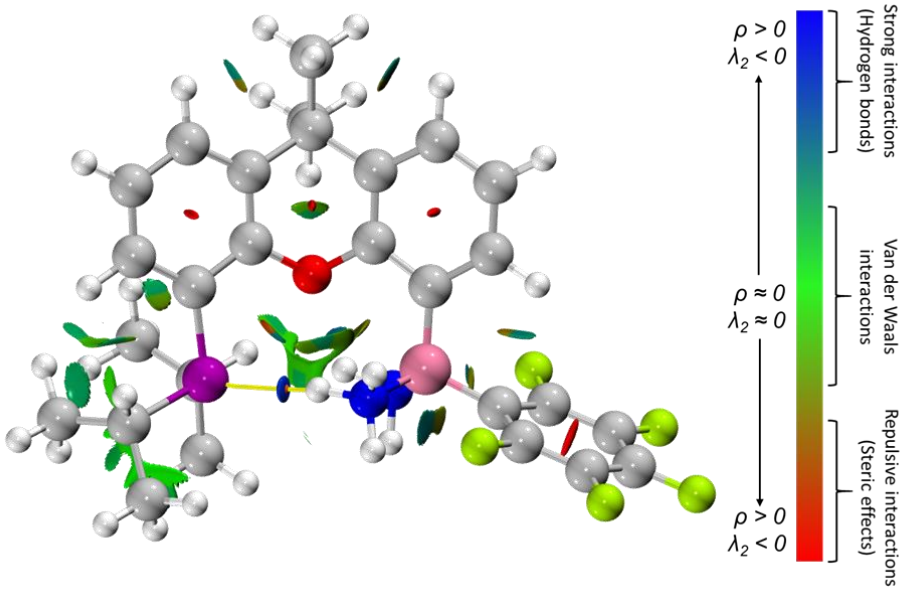

S 7.15: NCI plots of the **6d**, the range of $\lambda_2 \times \rho(r)$ used for the plots is −0.03 to +0.02 au at s = 0.3 au, QTAIM bond path in yellow with critical point in orange.

NBO

Second order perturbation theory was also used to investigate the donation of the ortho Cl groups into the vacant boron P orbital. These orbitals being visualised with the donor orbital and the acceptor orbital in figures **S 7.16**, **S 7.17**, **S 7.18**, **S 7.19**, **S 7.20** and **S 7.21** showing clearly the ortho Cl groups play an important role in the stabilisation of the LUMO. This was extended to the series of $B(C_6Cl_5)_x(C_6F_5)_y$ that has been previously studied experimentally and it too showed this ortho- stabilisation that could account for the observed reduced electrophilicity of $R_2B(C_6Cl_5)$ fragments.

ST 7.2: Parameters associated with the X···B donation: Total X···B being the SOPT energy in Kcal/mol, the N→B SOPT energy in Kcal/mol and WBI for the N-B bond. WBI for X···B ~0

	5a	***5b***	***5c***	***5d***
Total Cl···B	14.81	1.63	14.47	0
N→B	123.73	124.25	119.91	126.92
WBI N/B	1.1957	1.2233	1.1876	1.2339
WBI X1/B	0.0321	0.0314	0.0049	0.007
WBI X1/B	0.0248	0.0252	0.0046	0.0056
WBI X/B total	0.0569	0.0566	0.0095	0.0126

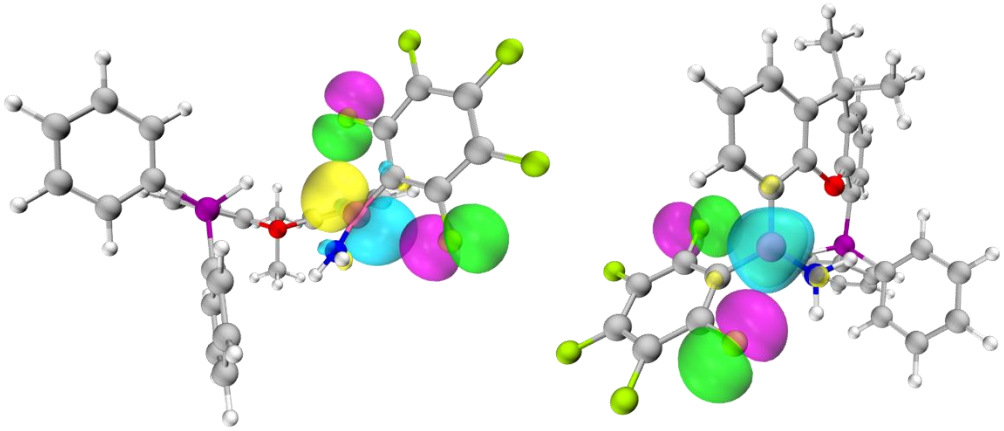

S 7.16: NBO orbitals for **5b** demonstrating the lack of overlap. The F donor P orbitals (magenta/green) and the accepting vacant P orbital on boron (yellow/cyan).

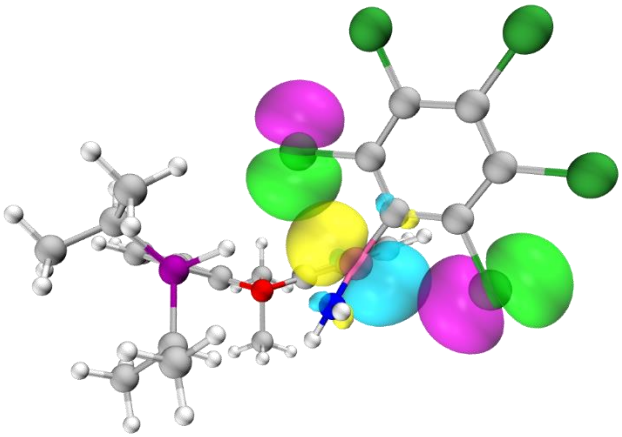

S 7.17: NBO orbitals from the SOPT for **5c**. The Cl donor P orbitals (magenta/green) and the accepting vacant P orbital on boron (yellow/cyan).

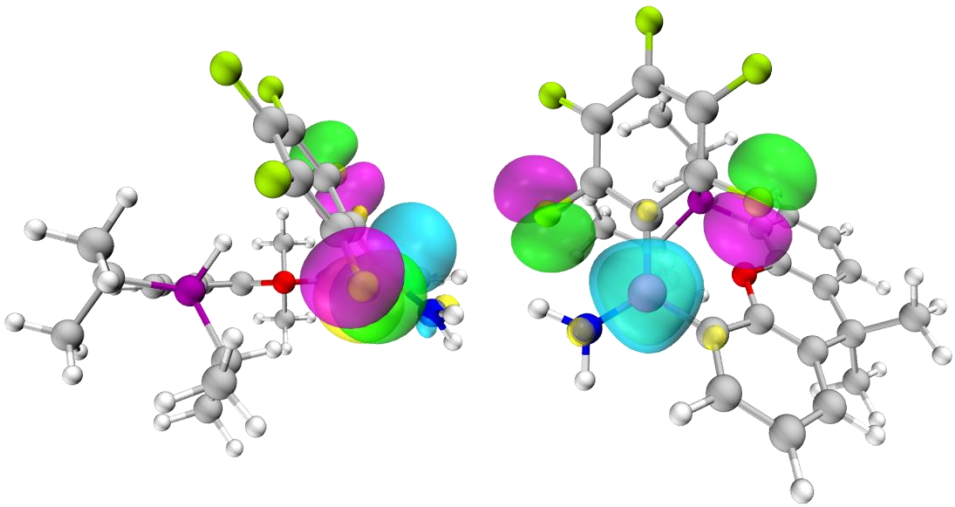

S 7.18 :NBO orbitals for **5d** demonstrating the lack of overlap The F donor P orbitals (magenta/green) and the accepting vacant P orbital on boron (yellow/cyan).

ST 7.3: interaction energies X···B interaction in selection of Ar_3B: Total SOPT of all X···B interactions and Averaged X···B interactions per Ar^x ring all in Kcal/mol

	$B(C_6Cl_5)(C_6F_5)_2$	$B(C_6Cl_5)_2(C_6F_5)$	$B(C_6Cl_5)_3$	$B(C_6F_5)_3$
Total Cl···B	23.37	31.97	59.54	N/A
Average Cl···B	23.37	15.985	19.84667	N/A
Total F···B	0.53	0	N/A	0
Average F···B	0.265	0	N/A	0

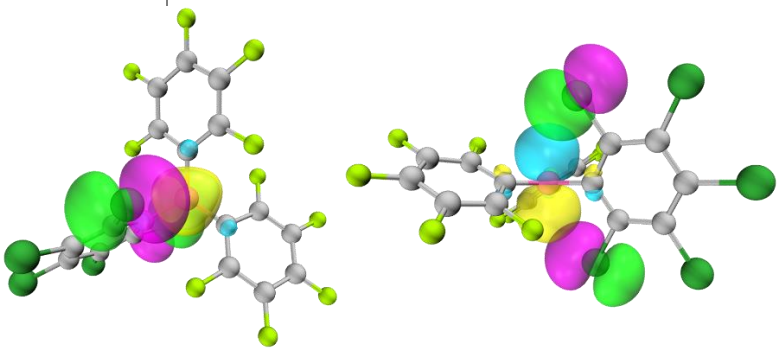

S 7.19: NBO orbitals from the SOPT for **$B(C_6Cl_5)(C_6F_5)_2$**. The F donor P orbitals (magenta/green) and the accepting vacant P orbital on boron (yellow/cyan).

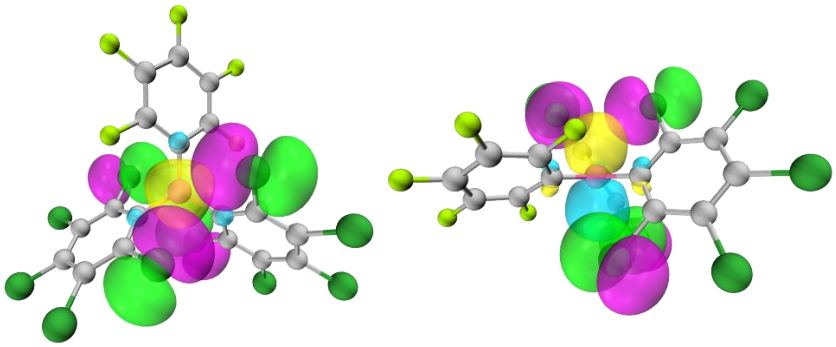

S 7.20: NBO orbitals from the SOPT for **$B(C_6Cl_5)_2(C_6F_5)$**. The F donor P orbitals (magenta/green) and the accepting vacant P orbital on boron (yellow/cyan).

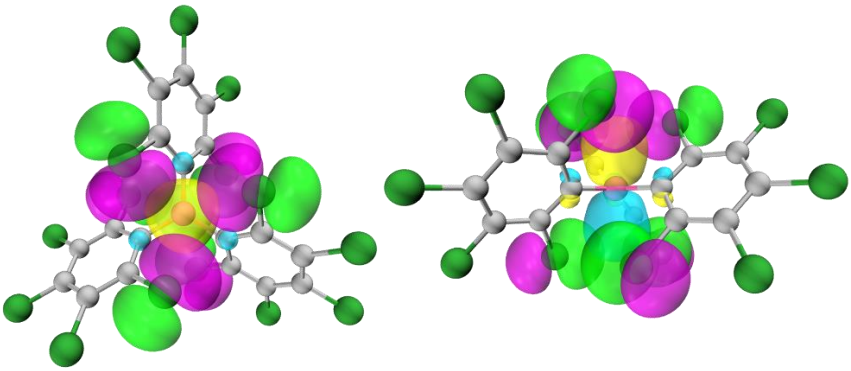

S 7.21: NBO orbitals from the SOPT for **$B(C_6Cl_5)_3$**. The F donor P orbitals (magenta/green) and the accepting vacant P orbital on boron (yellow/cyan).

Mechanistic studies

NH_3 activation mechanism (**4** to **5**)

Mechanistic studies were performed on the activation of ammonia by **4a-d** upon the abstraction of hydride via the trityl cation. This process is outlined below (**S 7.22**)with **4a-d** (S) undergoing a modest barrier to hydride abstraction (T1) then a near barrierless transition to **5a-d** (T2).

ST 7.4: Table of Gibbs free energy values for the conversion of **4a** (S) to **5a** (I2). E is the total energy in Hartree; ΔG(S) is the Gibbs free energy with respect to **4a** (S) in kcal/mol and ΔG_R the Gibbs free energy for the conversion of X to Y or barrier hight with respect to reactant.

	S	*T1*	*I1*	*T2*	*I2*
E	-4071.48	-4804.73	-4070.72	-4070.71	-4070.74
ΔG(S)	0	19.79803	-26.591	-24.801	-44.9751
ΔG_R		19.79803	-26.591	1.789936	-18.3841

ST 7.5: Table of Gibbs free energy values for the conversion of **4b** (S) to **5b** (I2). E is the total energy in Hartree; ΔG(S) is the Gibbs free energy with respect to **4b** (S) in kcal/mol and ΔG_R the Gibbs free energy for the conversion of X to Y or barrier hight with respect to reactant.

	S	*T1*	*I1*	*T2*	*I2*
E	-2269.76	-3003.01	-2268.98	-2268.98	-2269.01
ΔG(S)	0	15.36061	-22.0526	-20.774	-41.306
ΔG_R		15.36061	-22.0526	1.278594	-19.2535

ST 7.6: Table of Gibbs free energy values for the conversion of **4c** (S) to **5c** (I2). E is the total energy in Hartree; ΔG(S) is the Gibbs free energy with respect to **4c** (S) in kcal/mol and ΔG_R the Gibbs free energy for the conversion of X to Y or barrier hight with respect to reactant.

	S	*T1*	*I1*	*T2*	*I2*
E	-3845.08	-4578.32	-3844.31	-3844.31	-3844.35
ΔG(S)	0	19.93078	-28.7383	-28.3613	-53.3236
ΔG_R	0	19.93078	-28.7383	0.377013	-24.5854

ST 7.7: Table of Gibbs free energy values for the conversion of **4d** (S) to **5d** (I2). E is the total energy in Hartree; ΔG(S) is the Gibbs free energy with respect to **4d** (S) in kcal/mol and ΔG_R the Gibbs free energy for the conversion of X to Y or barrier hight with respect to reactant.

	S	*T1*	*I1*	*T2*	*I2*
E	-2043.35	-2776.61	-2042.58	-2042.58	-2042.62
ΔG(S)	0	16.27443	-22.3724	-22.8544	-49.9449
ΔG_R		16.27443	-22.3724	-0.482	-27.5725

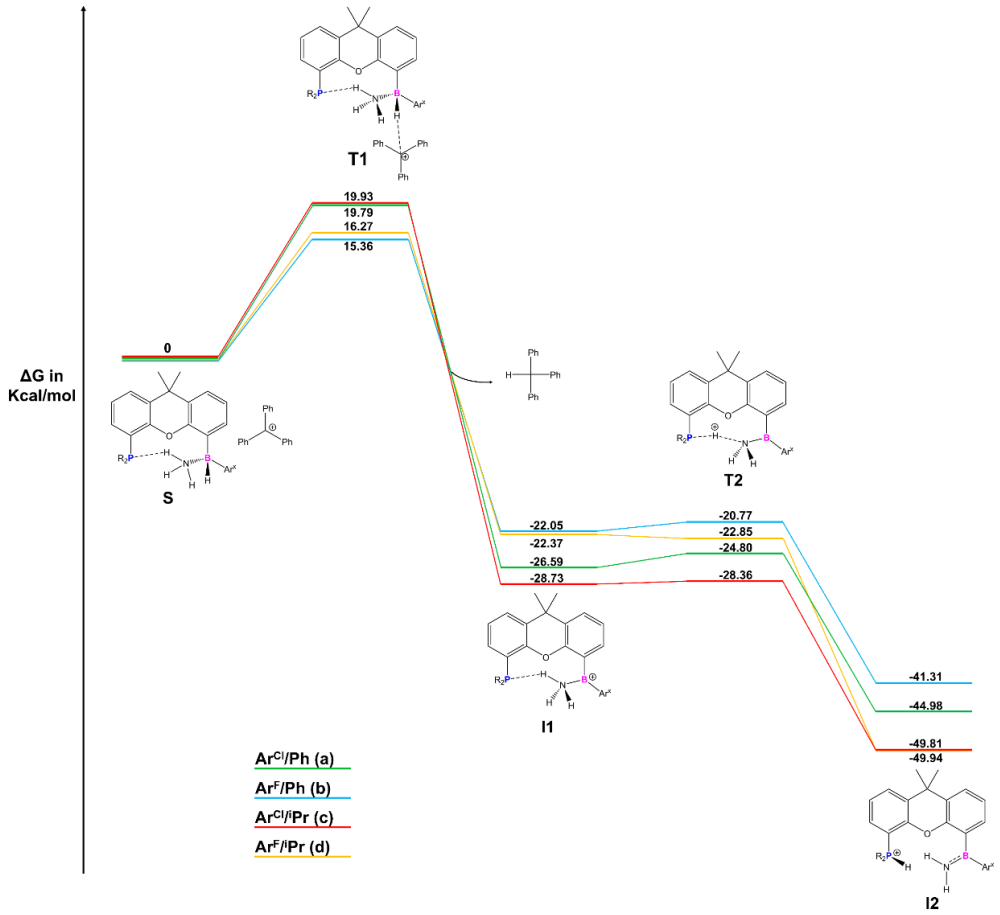

S 7.22: Mechanism for the conversion of **4a-d** (S) to **5a-d** (I2), all energies in Kcal/mol energy with respect to **4a-d** (S).

Addition of NH_3 mechanism (**5** to either **6** or **7**)

In order to rationalise the difference in product distribution from the addition of ammonia from **5a-d** (I2) to either **6b/d** (P1) or **7a/c** (1P). It can be seen the Ar^{Cl} systems uniformly have higher barriers for either process due too the increased steric contains of the group, and this follows to the favouring of the less sterically encumbered product **7a/c** (1P). A secondary factor could be the ortho-Cl donating effect where the trigonal planar boron centre gains additional stabilisation relative to the Ar^{F} groups which have a endergonic transformation to **7b/d** (1P). Differences in the Phosphine group seem to be most impactful upon the reverse N-H activation in the relative energies of **6a-d** (P1), with the more basic iPr phosphine being less exergonic in this transformation.

ST 7.8: Table of Gibbs free energy values for the conversion of **5a** (I2) to either **6a** (P1) or **7a** (1P). E is the total energy in Hartree; ΔG(S) is the Gibbs free energy with respect to **4a** (S) in kcal/mol; ΔG(I2) is the Gibbs free energy with respect to **5a** (I2) in kcal/mol and ΔG_R the Gibbs free energy for the conversion of X to Y or barrier hight with respect to reactant.

	1P	*3T*	*I2*	*T3*	*I3*	*T4*	*P1*
E	-4070.31	-4127.31	-4070.74	-4127.31	-4127.32	-4127.32	-4127.35
ΔG(S)	-46.817	-25.7213	-44.9751	-24.4944	-31.2329	-29.9017	-46.6433
ΔG(I2)	-1.8419	19.25378	0	20.48071	13.74212	15.07338	-1.66826
ΔG_R	-1.8419	19.25378	0	20.48071	13.74212	1.331253	-15.4104

ST 7.9: Table of Gibbs free energy values for the conversion of **5b** (I2) to either **6b** (P1) or **7b** (1P). E is the total energy in Hartree; ΔG(S) is the Gibbs free energy with respect to **4b** (S) in kcal/mol; ΔG(I2) is the Gibbs free energy with respect to **5b** (I2) in kcal/mol and ΔG_R the Gibbs free energy for the conversion of X to Y or barrier hight with respect to reactant.

	1P	*3T*	*I2*	*T3*	*I3*	*T4*	*P1*
E	-2268.58	-2325.59	-2269.01	-2325.59	-2325.6	-2325.6	-2325.63
ΔG(S)	-43.3353	-28.8482	-41.306	-28.6019	-34.0018	-34.202	-52.1317
ΔG(I2)	-2.02925	12.45777	0	12.70414	7.304213	7.103992	-10.8257
ΔG_R	-2.02925	12.45777	0	12.70414	7.304213	-0.20022	-18.1299

ST 7.10: Table of Gibbs free energy values for the conversion of **5c** (I2) to either **6c** (P1) or **7c** (1P). The process seems to be endergonic however, when the NH_3 coordinated NH_4 is considered (1P*) the process is very exergonic. E is the total energy in Hartree; ΔG(S) is the Gibbs free energy with respect to **4c** (S) in kcal/mol; ΔG(I2) is the Gibbs free energy with respect to **5c** (I2) in kcal/mol and ΔG_R the Gibbs free energy for the conversion of X to Y or barrier hight with respect to reactant.

	*1P**	*1P*	*3T*	*I2*	*T3*	*I3*	*T4*	*P1*
E		-3843.91	-3900.92	-3844.35	-3900.92	-3900.93	-3900.93	-3900.94
ΔG(S)	-61.7132	-47.2299	-34.1197	-49.811	-32.322	-39.6323	-36.8399	-46.7733
ΔG(I2)	-11.9022	2.58110	15.69124	0	17.48898	10.17863	12.97102	3.037651
ΔG_R	-11.9022	2.58110	15.69124	0	17.48898	10.17863	2.792399	-7.14097

ST 7.11: Table of Gibbs free energy values for the conversion of **5d** (I2) to either **6d** (P1) or **7d** (1P). E is the total energy in Hartree; ΔG(S) is the Gibbs free energy with respect to **4d** (S) in kcal/mol; ΔG(I2) is the Gibbs free energy with respect to **5d** (I2) in kcal/mol and ΔG_R the Gibbs free energy for the conversion of X to Y or barrier hight with respect to reactant.

	1P	*3T*	*I2*	*T3*	*I3*	*T4*	*P1*
E	-2042.18	-2099.2	-2042.62	-2099.2	-2099.21	-2099.21	-2099.22
ΔG(S)	-43.0595	-32.6612	-49.9449	-34.7614	-42.4659	-39.0809	-50.7473
ΔG(I2)	6.88541	17.28374	0	15.18357	7.479025	10.86398	-0.80238
ΔG_R	6.88541	17.28374	0	15.18357	7.479025	3.384955	-8.28141

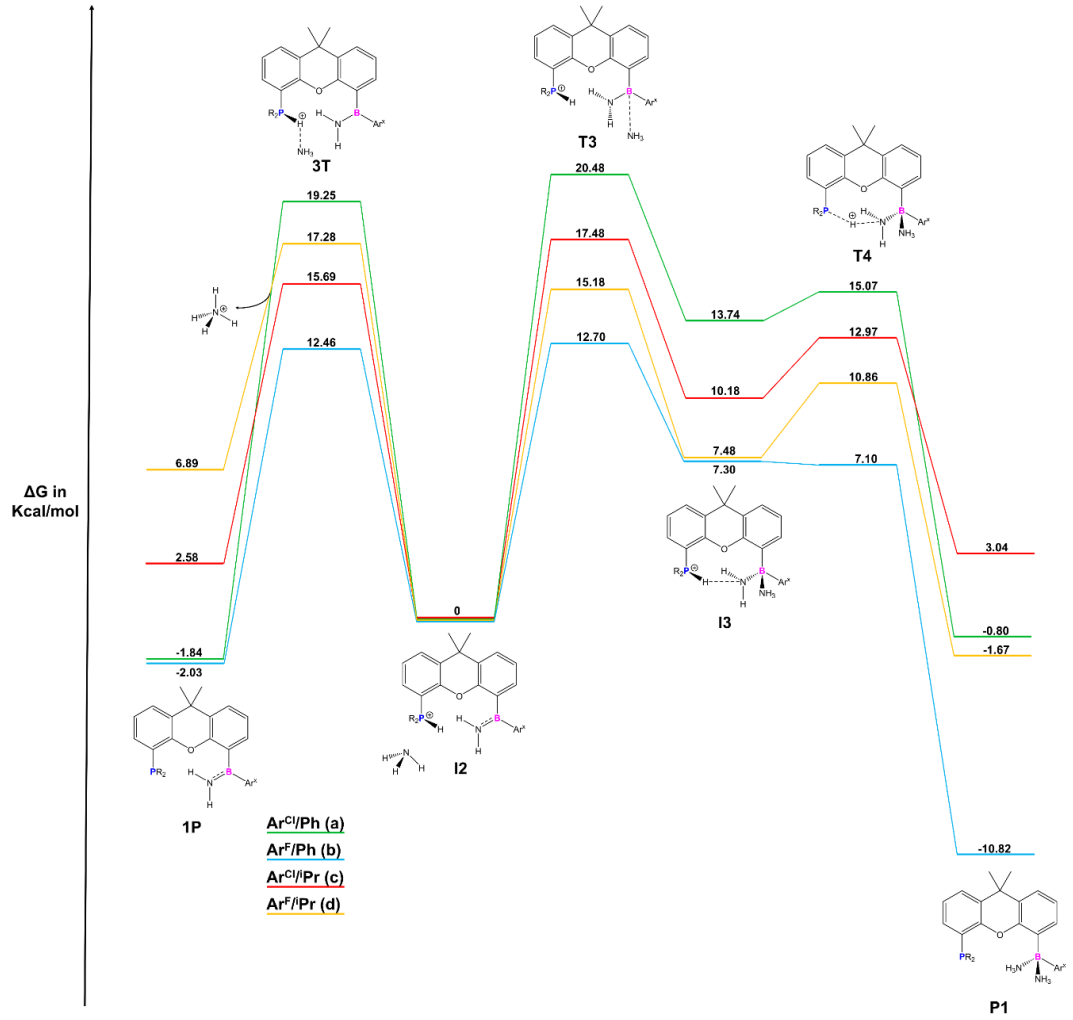

S 7.23 Mechanism for the conversion of **5a-d** (I2) to either **6a-d** (P1) or **7a-d** (1P), all energies in Kcal/mol energy with respect to **5a-d** (I2).

Alternate pathways

As ammonia is acting as both a ligand and a base, the alternate conversion from **5a-d** (I2) to **6a-d** (P1) was envisioned using ammonia as a proton transfer reagent. This was found to be much less energetically efficient with the barriers being an order of magnitude higher.

ST 7.12 Table of Gibbs free energy values for the alternate conversion of **5a** (I2) to **6a** (P1) with use of ammonia as a proton transfer reagent**.** This data is between I3 and **6a** (P1). E is the total energy in Hartree; ΔG(S) is the Gibbs free energy with respect to **4a** (S) in kcal/mol; ΔG(I3) is the Gibbs free energy with respect to intermediate I3 in kcal/mol and ΔG_R the Gibbs free energy for the conversion of X to Y or barrier hight with respect to reactant.

	I3	*T4_1*	*I4*	*T4_2*	*P1*	*T4*
E	-4127.32	-4183.9	-4126.89	-4183.93	-4127.35	-4127.32
ΔG(S)	-31.2329	-8.19472	-42.8576	-28.1604	-47.9746	-29.9017
ΔG(I3)	0	23.03823	-11.6247	3.072586	-16.7416	1.331253
ΔG_R	0	23.03823	-11.6247	14.69728	-16.7416	1.331253

ST 7.13: Table of Gibbs free energy values for the alternate conversion of **5b** (I2) to **6b** (P1) with use of ammonia as a proton transfer reagent**.** This data is between I3 and **6b** (P1). E is the total energy in Hartree; ΔG(S) is the Gibbs free energy with respect to **4b** (S) in kcal/mol; ΔG(I3) is the Gibbs free energy with respect to intermediate I3 in kcal/mol and ΔG_R the Gibbs free energy for the conversion of X to Y or barrier hight with respect to reactant.

	I3	*T4_1*	*I4*	*T4_2*	*P1*	*T4*
E	-2325.6	-2382.18	-2325.17	-2382.21	-2325.63	-2325.6
ΔG(S)	-34.0018	-13.0704	-46.0962	-32.0473	-51.9315	-34.202
ΔG(I3)	0	20.93138	-12.0944	1.954516	-17.9297	-0.20022
ΔG_R	0	20.93138	-12.0944	14.04889	-17.9297	-0.20022

ST 7.14: Table of Gibbs free energy values for the alternate conversion of **5c** (I2) to **6c** (P1) with use of ammonia as a proton transfer reagent**.** This data is between I3 and **6c** (P1). E is the total energy in Hartree; ΔG(S) is the Gibbs free energy with respect to **4c** (S) in kcal/mol; ΔG(I3) is the Gibbs free energy with respect to intermediate I3 in kcal/mol and ΔG_R the Gibbs free energy for the conversion of X to Y or barrier hight with respect to reactant.

	I3	*T4_1*	*I4*	*T4_2*	*P1*	*T4*
E	-3900.93	-3957.5	-3900.49	-3957.53	-3900.94	-3900.93
ΔG(S)	-39.6323	-13.3716	-43.0247	-28.5278	-49.5657	-36.8399
ΔG(I3)	0	26.26075	-3.39238	11.10459	-9.93337	2.792399
ΔG_R		26.26075	-3.39238	14.49696	-9.93337	2.792399

ST 7.15: Table of Gibbs free energy values for the alternate conversion of **5d** (I2) to **6d** (P1) with use of ammonia as a proton transfer reagent**.** This data is between I3 and **6d** (P1). E is the total energy in Hartree; ΔG(S) is the Gibbs free energy with respect to **4d** (S) in kcal/mol; ΔG(I3) is the Gibbs free energy with respect to intermediate I3 in kcal/mol and ΔG_R the Gibbs free energy for the conversion of X to Y or barrier hight with respect to reactant.

	I3	*T4_1*	*I4*	*T4_2*	*P1*	*T4*
E	-2099.21	-2155.79	-2098.77	-2155.81	-2099.22	-2099.21
ΔG(S)	-42.4659	-16.8361	-45.804	-29.9275	-54.1323	-39.0809
ΔG(I3)	0	25.62981	-3.33812	12.53836	-11.6664	3.384955
ΔG_R	0	25.62981	-3.33812	15.87648	-11.6664	3.384955

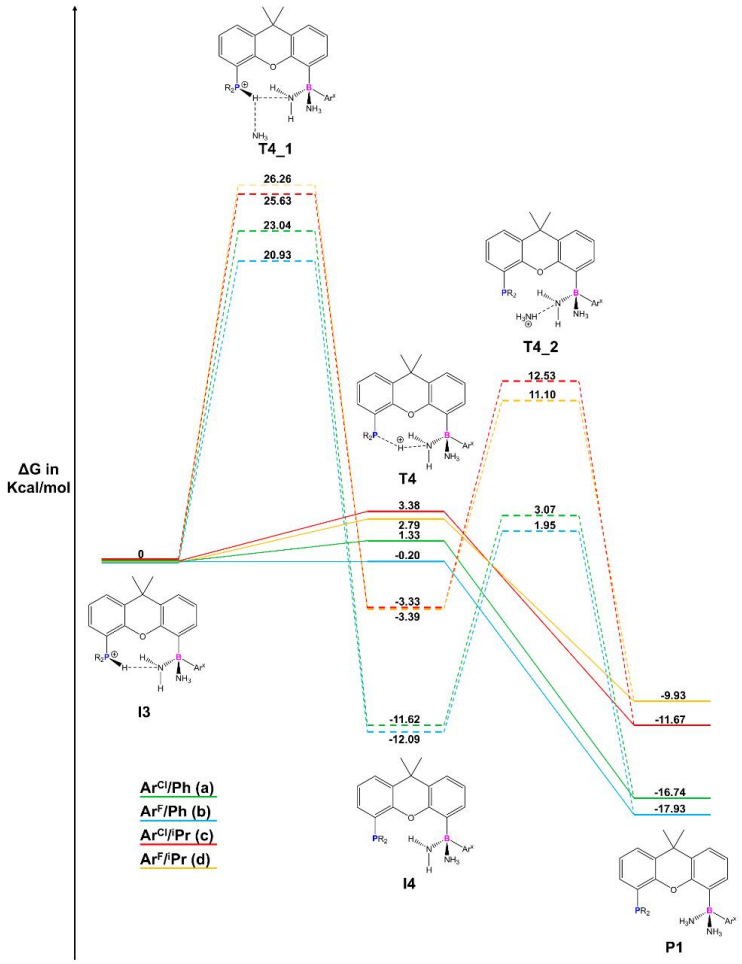

S 7.24: Mechanism for the alternate conversion of **5a-d** (I2) to either **6a-d** (P1) with use of ammonia as a proton transfer reagent**.** This data is between I3 and **6a-d** (P1) and all energies in Kcal/mol energy with respect to intermediate I3.

An alternative pathway to convert **7a-d** (1P) to **6a-d** (P1) was investigated using ammonia as a proton transfer reagent, but this process was found to be kinetically infeasible due to barriers in excess of 40Kcal/mol.

ST 7.16 Table of Gibbs free energy values for the alternate conversion of **7a** (1P) to **6a** (P1) with use of ammonia as a proton transfer reagent**.** E is the total energy in Hartree; ΔG(S) is the Gibbs free energy with respect to **4a** (S) in kcal/mol; ΔG(1P) is the Gibbs free energy with respect to **7a** (1P) in kcal/mol and ΔG_R the Gibbs free energy for the conversion of X to Y or barrier hight with respect to reactant.

	1P	*4T*	*I1*	*5T*	*P1*
E	-4070.31	-4127.32	-4070.72	-4127.31	-4127.35
ΔG(S)	-46.817	-8.39163	-18.0124	-21.7861	-46.6433
ΔG(1P)	0	38.42535	28.80457	25.03084	0.173649
ΔG_R	0	38.42535	28.80457	-3.77373	-28.6309

ST 7.17: Table of Gibbs free energy values for the alternate conversion of **7b** (1P) to **6b** (P1) with use of ammonia as a proton transfer reagent**.** E is the total energy in Hartree; ΔG(S) is the Gibbs free energy with respect to **4b** (S) in kcal/mol; ΔG(1P) is the Gibbs free energy with respect to **7b** (1P) in kcal/mol and ΔG_R the Gibbs free energy for the conversion of X to Y or barrier hight with respect to reactant.

	1P	*4T*	*I1*	*5T*	*P1*
E	-2268.58	-2325.59	-2268.98	-2325.59	-2325.63
ΔG(S)	-43.3353	-6.11735	-13.474	-25.0958	-52.1317
ΔG(1P)	0	37.21791	29.86126	18.23951	-8.79647
ΔG_R	0	37.21791	29.86126	-11.6218	-38.6577

ST 7.18: Table of Gibbs free energy values for the alternate conversion of **7c** (1P) to **6c** (P1) with use of ammonia as a proton transfer reagent**.** E is the total energy in Hartree; ΔG(S) is the Gibbs free energy with respect to **4c** (S) in kcal/mol; ΔG(1P) is the Gibbs free energy with respect to **7c** (1P) in kcal/mol and ΔG_R the Gibbs free energy for the conversion of X to Y or barrier hight with respect to reactant.

	1P	*4T*	*I1*	*5T*	*P1*
E	-3843.91	-3900.91	-3844.31	-3900.9	-3900.94
ΔG(S)	-47.2299	-6.92229	-20.1597	-22.2525	-46.7733
ΔG(1P)	0	40.30757	27.07013	24.9774	0.456549
ΔG_R	0	40.30757	27.07013	-2.09273	-26.6136

ST 7.19: Table of Gibbs free energy values for the alternate conversion of **7d** (1P) to **6d** (P1) with use of ammonia as a proton transfer reagent**.** E is the total energy in Hartree; ΔG(S) is the Gibbs free energy with respect to **4d** (S) in kcal/mol; ΔG(1P) is the Gibbs free energy with respect to **7d** (1P) in kcal/mol and ΔG_R the Gibbs free energy for the conversion of X to Y or barrier hight with respect to reactant.

	1P	*4T*	*I1*	*5T*	*P1*
E	-2042.18	-2099.18	-2042.58	-2099.18	-2099.22
ΔG(S)	-43.0595	-4.32705	-13.7939	-23.9397	-50.7473
ΔG(1P)	0	38.73246	29.26563	19.11979	-7.68779
ΔG_R	0	38.73246	29.26563	-10.1458	-36.9534

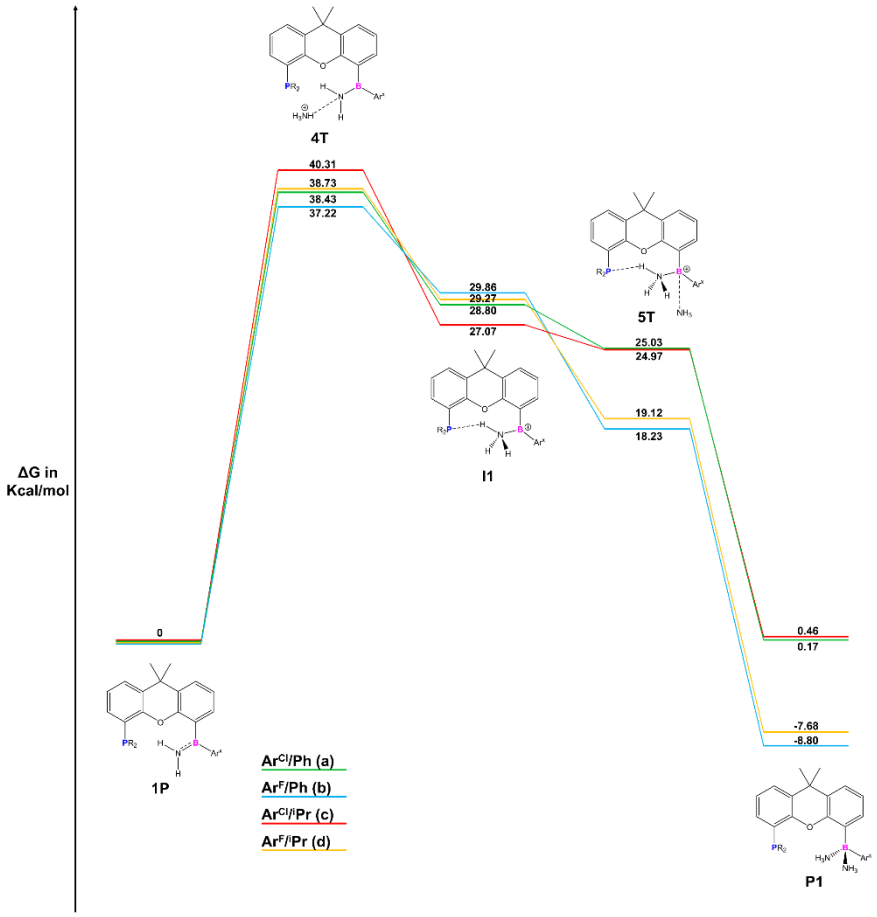

S 7.25: Mechanism for the conversion of **7a-d** (1P) to **6a-d** (P1) using ammonia as a proton transfer reagent, all energies in Kcal/mol energy with respect to **7a-d** (1P).

References

1. B. David, F. Armstrong, P. Bowen, D. Fowler, J. Irvine, L. Murciano, Ammonia: Zero-Carbon Fertiliser, Fuel and Energy Store, POLICY BRIEFING, London 2020.
2. Van der Vlugt, J. I. Advances in selective activation and application of ammonia in homogeneous catalysis. *Chem Soc Rev* **39**, 2302–2322 (2010).
3. Werner, A. Coordination chemistry. *Z. Anorg. Chem. 3* **3**, 267–300 (1893).
4. Bezdek, M. J., Guo, S. & Chirik, P. J. Coordination-induced weakening of ammonia, water, and hydrazine X-H bonds in a molybdenum complex. *Science* **354**, 730–733 (2016).
5. Hansmann, M. M. & Bertrand, G. Transition-Metal-like Behavior of Main Group Elements: Ligand Exchange at a Phosphinidene. *J Am Chem Soc* **138**, 15885–15888 (2016).
6. Weetman, C. & Inoue, S. The Road Travelled: After Main-Group Elements as Transition Metals. *ChemCatChem* **10**, 4213–4228 (2018).
7. Frey, G. D., Lavallo, V., Donnadieu, B., Schoeller, W. W. & Bertrand, G. Facile splitting of hydrogen and ammonia by nucleophilic activation at a single carbon center. *Science* **316**, 439–441 (2007).
8. Zhao, J., Goldman, A. S. & Hartwig, J. F. Oxidative addition of ammonia to form a stable monomeric amido hydride complex. *Science* **307**, 1080–1082 (2005).
9. Braun, T. Oxidative addition of NH3 to a transition-metal complex: A key step for the metal-mediated derivatization of ammonia? *Angew. Chem. Int. Ed.* **44**, 5012–5014 (2005).
10. Fafard, C. M., Adhikari, D., Foxman, B. M., Mindiola, D. J. & Ozerov, O. V. Addition of ammonia, water, and dihydrogen across a single Pd-Pd bond. *J Am Chem Soc* **129**, 10318–10319 (2007).
11. Morgan, E., MacLean, D. F., McDonald, R. & Turculet, L. Rhodium and iridium amido complexes supported by silyl pincer ligation: Ammonia N-H bond activation by a [PSiP]Ir complex. *J Am Chem Soc* **131**, 14234–14236 (2009).
12. Koelliker, R. & Milstein, D. Facile Cleavage of Ammonia. *Angew. Chem. Int. Ed. in English* **30**, 707–709 (1991).
13. Hulley, E. B., Bonanno, J. B., Wolczanski, P. T., Cundari, T. R. & Lobkovsky, E. B. Pnictogen-hydride activation by (silox)3Ta (silox = tBu3SiO); Attempts to circumvent the constraints of orbital symmetry in N2 activation. *Inorg Chem* **49**, 8524–8544 (2010).
14. Nakajima, Y., Kameo, H. & Suzuki, H. Cleavage of Nitrogen–Hydrogen Bonds of Ammonia Induced by Triruthenium Polyhydrido Clusters. *Angew. Chem. Int. Ed.* **45**, 950–952 (2006).
15. Salomon, M. A., Jungton, A. K. & Braun, T. Activation of ethylene and ammonia at iridium: C–H versus N–H oxidative addition. *Dalton Trans.* 7669–7677 (2009).
16. Wang, Y. *et al.* Activation of Ammonia by a Carbene-Stabilized Dithiolene Zwitterion. *J Am Chem Soc* **144**, 16325–16331 (2022).
17. Yang, X. *et al.* Radical Activation of N-H and O-H Bonds at Bismuth(II). *J Am Chem Soc* **144**, 16535–16544 (2022).
18. Abbenseth, J. *et al.* Thermoneutral N−H Bond Activation of Ammonia by a Geometrically Constrained Phosphine. *Angewandte Chemie* **133**, 23817–23821 (2021).
19. Krämer, F., Paradies, J., Fernández, I. & Breher, F. nature chemistry A crystalline aluminium-carbon-based ambiphile capable of activation and catalytic transfer of ammonia in non-aqueous media. *Nature Chemistry* **16**, 63–69 (2024).
20. Vasko, P. *et al.* Reversible C−H Activation, Facile C−B/B−H Metathesis and Apparent Hydroboration Catalysis by a Dimethylxanthene-Based Frustrated Lewis Pair. *Chem. Eur. J.* **24**, 10531–10540 (2018).
21. Mo, Z., Rit, A., Campos, J., Kolychev, E. L. & Aldridge, S. Catalytic B-N Dehydrogenation Using Frustrated Lewis Pairs: Evidence for a Chain-Growth Coupling Mechanism. *J Am Chem Soc* **138**, 3306–3309 (2016).
22. Mo, Z. *et al.* Facile Reversibility by Design: Tuning Small Molecule Capture and Activation by Single Component Frustrated Lewis Pairs. *J Am Chem Soc* **137**, 12227–12230 (2015).
23. Légaré, M. A., Courtemanche, M. A., Rochette, É. & Fontaine, F. G. Metal-free catalytic C-H bond activation and borylation of heteroarenes. *Science* **349**, 513–516 (2015).
24. Ashley, A. E. *et al.* Separating Electrophilicity and Lewis Acidity: The Synthesis, Characterization, and Electrochemistry of the Electron Deficient Tris(aryl)boranes $B(C6F5)_{3-n}(C_6Cl_5)_n$ (n = 0-3). *J. Am. Chem. Soc* **133**, 14727–14740 (2011).

25. Zhao, H., Reibenspies, J. H. & Gabbaï, F. P. Lewis acidic behavior of $B(C_6Cl_5)_3$. *Dalton Trans.* **42**, 608–610 (2012).
26. Zaher, H. *et al.* Structural and theoretical studies of intermolecular dihydrogen bonding in $[(C_6F_5)_2(C_6Cl_5)B]$–H···H–[TMP]. *Chem. Commun.* **49**, 9755–9757 (2013).
27. Lawrence, E. J., Blagg, R. J., Hughes, D. L., Ashley, A. E. & Wildgoose, G. G. A Combined "Electrochemical–Frustrated Lewis Pair" Approach to Hydrogen Activation: Surface Catalytic Effects at Platinum Electrodes. *Chem. Eur. J.* **21**, 900–906 (2015).
28. Blagg, R. J. *et al.* Novel B(Ar')2(Ar'') hetero-tri(aryl)boranes: a systematic study of Lewis acidity. *Dalton Trans.* **45**, 6032–6043 (2016).
29. Blagg, R. J. & Wildgoose, G. G. H_2 activation using the first 1 : 1 : 1 hetero-tri(aryl)borane. *RSC Adv* **6**, 42421–42427 (2016).
30. Singaram, B., Cole, T. E. & Brow, H. C. Addition Compounds of Alkali-Metal Hydrides. 26. Facile Reaction of Borinic Esters with Lithium Monoethoxyaluminohydride To Form Lithium Dialkylborohydrides1esters R2BOMe2. *Organometallics* **3**, 1520–1523 (1984).
31. Massey, A. G. & Park, A. J. Perfluorophenyl derivatives of the elements : VII. further studies on tris(pentafluorophenyl)boron. *J Organomet Chem* **5**, 218–225 (1966).
32. Blagg, R. J. *et al.* Novel $B(Ar')_2(Ar'')$ hetero-tri(aryl)boranes: a systematic study of Lewis acidity. *Dalton Trans.* **45**, 6032 (2016).
33. Neufeld, R., Michel, R., Schçne, A. & Stalke, D. Introducing aHydrogen-BondD onori nto aW eakly Nucleophilic Brønsted Base:A lkali MetalH examethyldisilazides (MHMDS, M = Li, Na,K,R band Cs) with Ammonia. doi:10.1002/chem.201600833.
34. Michel, R., Herbst-Irmer, R. & Stalke, D. Unprecedented CpLi ammoniacates. *Organometallics* **29**, 6169–6171 (2010).
35. Shima, T., Yang, J., Luo, G., Luo, Y. & Hou, Z. Dinitrogen Activation and Hydrogenation by C5Me4SiMe3-Ligated Di- And Trinuclear Chromium Hydride Complexes. *J Am Chem Soc* **142**, 9007–9016 (2020).
36. Mountford, A. J. *et al.* Intra-and Intermolecular N−H, F−C Hydrogen-Bonding Interactions in Amine Adducts of Tris(pentafluorophenyl)borane and alane. (2005).
37. Fuller, A.-M. *et al.* The synthesis, molecular structure and supramolecular architecture of complexes between the ammonia adduct of tris(pentafluorophenyl)boron and a series of mono and polydentate hydrogen-bond acceptors †. (2008.
38. Hasegawa, M. & Noda, H. Distribution of hydrogen bond angles in molecular crystals. *Nature* **254**, 212–212 (1975).
39. Shahi, A. & Arunan, E. Why are Hydrogen Bonds Directional? *Indian Academy of Sciences. Special Issue on CHEMICAL BONDING* **128**, 1571–1577 (2016).
40. Steiner, T. he Hydrogen Bond in the Solid State. *Angew. Chem. Int. Ed.* **41**, 1433–7851 (2002).
41. Arunan, E. *et al.* Defining the hydrogen bond: An account (IUPAC Technical Report). *Pure and Applied Chemistry* **83**, 1619–1636 (2011).
42. Møller, K. H., Hansen, A. S. & Kjaergaard, H. G. Gas Phase Detection of the NH−P Hydrogen Bond and Importance of Secondary Interactions Published as part of The J. Phys. Chem. A. virtual special issue "Spectroscopy and Dynamics of Medium-Sized Molecules and Clusters: Theory, Experiment, and Applications." (2015).
43. Hansen, A. S., Du, L. & Kjaergaard, H. G. Positively charged phosphorus as a hydrogen bond acceptor. *Journal of Physical Chemistry Letters* **5**, 4225–4231 (2014).
44. Matano, Y. *et al.* Monophosphaporphyrins: Oxidative π-Extension at the Peripherally Fused Carbocycle of the Phosphaporphyrin Ring. (2008).
45. Andrieu, J., Baldoli, C., Maiorana, S., Poli, R. & Richard, P. Chiral α-P,N Ligands From a Diastereoselective Ph 2 PH Addition to (η 6-Benzaldimine)tricarbonylchromium Complexes. Eur. J. Org. Chem. 2909–2914 (1999).
46. Durran, S. E., Elsegood, M. R. J., Hammond, S. R. & Smith, M. B. Flexible κ4-PNN'O-tetradentate ligands: synthesis, complexation and structural studies. *Dalton Trans.* **39**, 7136–7146 (2010).
47. Kammerer, S., Neumann, B., Köhler, B., Mayer, P. & Lorenz, I. P. Rhodium(III), Palladium(II) and Rhenium(I) Complexes with 7-(Diphenylphosphine)-indole and -indolate. *Z Anorg Allg Chem* **639**, 1173–1180 (2013).
48. Johnson, E. R. *et al.* Revealing noncovalent interactions. *J Am Chem Soc* **132**, 6498–6506 (2010).
49. Bader, R. F. W. Molecular Fragments or Chemical Bonds *Acc Chem Res* **8**, 34–40 (1975).
50. Bader, R. F. W. Atoms in Molecules. *Acc Chem Res* **18**, 9–15 (1985).

51. Emamian, S., Lu, T., Kruse, H. & Emamian, H. Exploring Nature and Predicting Strength of Hydrogen Bonds: A Correlation Analysis Between Atoms-in-Molecules Descriptors, Binding Energies, and Energy Components of Symmetry-Adapted Perturbation Theory. *J Comput Chem* **40**, 2868–2881 (2019).
52. Glendening, E. D., Landis, C. R. & Weinhold, F. NBO 7.0: New vistas in localized and delocalized chemical bonding theory. *J Comput Chem* **40**, 2234–2241 (2019).
53. Gilli, P., Pretto, L., Bertolasi, V. & Gilli, G. Predicting Hydrogen-Bond strengths from Acid-Base molecular properties. the pKa slide rule: Toward the solution of a Long-Lasting problem. *Acc Chem Res* **42**, 33–44 (2009).
54. Krossing, I., Brands, H., Feuerhake, R. & Koenig, S. New reagents to introduce weakly coordinating anions of type $Al(ORF)_4^-$: synthesis, structure and characterization of Cs and trityl salts. *J Fluor Chem* **112**, 83–90 (2001).
55. Maier, A., Hofmann, M., Pritzkow, H. & Siebert, W. A Planar, Aromatic bicyclo-Tetraborane(4). *Angew. Chem. Int. Ed* **41**, (2002).
56. Ara, I., Forniés, J., García-Monforte, M. A., Martín, A. & Menjón, B. Synthesis and Characterization of Pentachlorophenyl–Metal Derivatives with d0 and d10 Electron Configurations. *Chem. Eur. J.* **10**, 4186–4197 (2004).
57. Lu, T. & Chen, F. Bond order analysis based on the laplacian of electron density in fuzzy overlap space. *J. Phys. Chem. A.* **117**, 3100–3108 (2013).
58. Shan, S. O. & Herschlag, D. [11] Hydrogen bonding in enzymatic catalysis: Analysis of energetic contributions. *Methods Enzymol* **308**, 246–276 (1999).
59. Dajnowicz, S. *et al.* Direct evidence that an extended hydrogen-bonding network influences activation of pyridoxal 5'-phosphate in aspartate aminotransferase. *Journal of Biological Chemistry* **292**, 5970–5980 (2017).
60. Vasko, P. *et al.* Reversible C−H Activation, Facile C−B/B−H Metathesis and Apparent Hydroboration Catalysis by a Dimethylxanthene-Based Frustrated Lewis Pair. *Chem. Eur. J.* **24**, 10531–10540 (2018).
61. Krossing, I., Brands, H., Feuerhake, R. & Koenig, S. New reagents to introduce weakly coordinating anions of type $Al(ORF)_4$ À : synthesis, structure and characterization of Cs and trityl salts.
62. Song, F., Cannon, R. D., Lancaster, S. J. & Bochmann, M. Activator effects in metallocene-based alkene polymerisations: unexpectedly strong dependence of catalyst activity on trityl concentration. *J Mol Catal A Chem* **218**, 21–28 (2004).
63. Cosier, J. & Glazer, A. M. A Nitrogen-Gas-Stream Cryostat for General X-ray Diffraction Studies. *J. Appl. Cryst* **19**, 105–107 (1986).
64. CrysAlisPro v.1.171.42.70a, Agilent Technologies 2011.
65. Sheldrick, G. M. Crystal structure refinement with SHELXL. *Acta Crystallogr C Struct Chem* **71**, 3–8 (2015).
66. Sheldrick, G. M. SHELXT - Integrated space-group and crystal-structure determination. *Acta Crystallogr A* **71**, 3–8 (2015).
67. Dolomanov, O. V., Bourhis, L. J., Gildea, R. J., Howard, J. A. K. & Puschmann, H. OLEX2: A complete structure solution, refinement and analysis program. *J Appl Crystallogr* **42**, 339–341 (2009).
68. Neese, F. & Wiley, J. The ORCA program system. *Wiley Interdiscip Rev Comput Mol Sci* **2**, 73–78 (2012).
69. Neese, F. Software update: the ORCA program system, version 4.0. *Wiley Interdiscip Rev Comput Mol Sci* **8**, e1327 (2018).
70. Neese, F., Wennmohs, F., Becker, U. & Riplinger, C. The ORCA quantum chemistry program package. *Journal of Chemical Physics* **152**, 224108 (2020).
71. Furness, J. W., Kaplan, A. D., Ning, J., Perdew, J. P. & Sun, J. Accurate and Numerically Efficient r2SCAN Meta-Generalized Gradient Approximation. *Journal of Physical Chemistry Letters* **11**, 8208–8215 (2020).
72. Grimme, S., Hansen, A., Ehlert, S. & Mewes, J. M. R2SCAN-3c: A "swiss army knife" composite electronic-structure method. *Journal of Chemical Physics* **154**, 64103 (2021).
73. Caldeweyher, E. *et al.* A generally applicable atomic-charge dependent London dispersion correction. *Journal of Chemical Physics* **150**, 154122 (2019).
74. Kruse, H. & Grimme, S. A geometrical correction for the inter- and intra-molecular basis set superposition error in Hartree-Fock and density functional theory calculations for large systems. *Journal of Chemical Physics* **136**, 154101 (2012).

75. Hanwell, M. D. *et al.* Avogadro: An advanced semantic chemical editor, visualization, and analysis platform. *J Cheminform* **4**, 1–17 (2012).
76. Chai, J. Da & Head-Gordon, M. Systematic optimization of long-range corrected hybrid density functionals. *Journal of Chemical Physics* **128**, (2008).
77. Chai, J. Da & Head-Gordon, M. Long-range corrected hybrid density functionals with damped atom–atom dispersion corrections. *Physical Chemistry Chemical Physics* **10**, 6615–6620 (2008).
78. Weigend, F. & Ahlrichs, R. Balanced basis sets of split valence, triple zeta valence and quadruple zeta valence quality for H to Rn: Design and assessment of accuracy. *Physical Chemistry Chemical Physics* **7**, 3297–3305 (2005).
79. Weigend, F. Accurate Coulomb-fitting basis sets for H to Rn. *Physical Chemistry Chemical Physics* **8**, 1057–1065 (2006).
80. Barone, V. & Cossi, M. Quantum calculation of molecular energies and energy gradients in solution by a conductor solvent model. *J. Phys. Chem. A.* **102**, 1995–2001 (1998).
81. E. D. Glendening, et al. NBO7. (2018).
82. Lu, T. & Chen, F. Multiwfn: A multifunctional wavefunction analyzer. *J Comput Chem* **33**, 580–592 (2012).
83. Glendening, E. D., Landis, C. R. & Weinhold, F. NBO 7.0: New vistas in localized and delocalized chemical bonding theory. *J Comput Chem* **40**, 2234–2241 (2019).
84. Cortés-Guzmán, F. & Bader, R. F. W. Complementarity of QTAIM and MO theory in the study of bonding in donor-acceptor complexes. *Coord Chem Rev* **249**, 633–662 (2005).
85. Johnson, E. R. *et al.* Revealing noncovalent interactions. *J Am Chem Soc* **132**, 6498–6506 (2010).
86. Contreras-García, J., Yang, W. & Johnson, E. R. Analysis of hydrogen-bond interaction potentials from the electron density: Integration of noncovalent interaction regions. *J. Phys. Chem. A.* **115**, 12983–12990 (2011).

Statement of Authorship

Title of Paper	Modulating Hydrogen Shuttling in Ammonia by Neutral and Cationic Boron-Containing Frustrated Lewis Pairs (FLPs)
Publication Status	Submitted
Publication Details	*Submitted to Angewandte Chemie 04/04/2024*

Student Confirmation

Student Name:	Agamemnon Elvis Crumpton	
Contribution to the Paper	Performed synthesis, DFT calculations and Xray crystallography on the compounds within the manuscript. I wrote the initial draft of the manuscript and helped with the later revisions.	
Signature 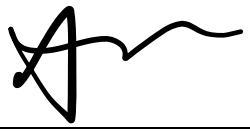		Date 15/04/2024

Supervisor Confirmation

Supervisor name and title: Professor Simon Aldridge	
Supervisor comments I can confirm that the candidate's contribution to this paper is as described above.	
Signature 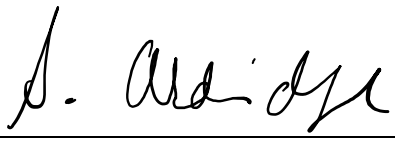	Date 18/4/2024

Chapter 8 - Leveraging Non-Covalent Interactions for the Binding of CO by a Weakly Lewis Acidic Borane

Agamemnon E. Crumpton, Caitilín McManus and Simon Aldridge*

Submitted to the Journal of the American Chemical Society

Author contributions

Agamemnon E. Crumpton: Synthesised the novel compounds, collected characterisation data, performed the quantum chemical calculations and lead crystallographer.

Caitilín McManus: Crystallographer.

Simon Aldridge: Corresponding author.

Manuscript was written by Simon Aldridge and Agamemnon E. Crumpton.

Abstract

Previous examples of boron carbonyl complexes exploit very high Lewis acidity, a low oxidation state boron centre or extensive ligand back-donation in order to capture CO. By contrast, here we report a boron carbonyl complex featuring a very weakly Lewis acidic borane characterized by an acceptor number (13.6), only marginally higher than that reported for $B(NMe_2)_3$. Encapsulation of the CO guest within a flexible supramolecular binding pocket augments binding through non-covalent interactions, critically via dispersion forces.

$\{(Ph_2P)xanth\}_3B$ has been synthesised in a two-step process from $[xanth(PPh_2)Li(thf)]_2$ and features a solid-state structure in which two of the three B-bound $xanth(PPh_2)$ units are projected above the BC_3 plane, generating an *up*,*up*,*down* conformation. Quantum chemical methods and consideration of intramolecular non-covalent interactions, however, reveal that the alternative *up*,*up*,*up* conformation, characterized by a cage-like geometry, is favoured significantly *in silico* (by ca. 33.0 kcal mol^{-1}). The combination of a Lewis acid and three Lewis basic sites within the $\{(Ph_2P)xanth\}_3B$ cage suggests strong binding of polar protic guests such as H_2O and NH_3 in solution through both donor/acceptor and hydrogen bonding interactions. Crystallographic and quantum chemical studies confirm this hypothesis and a binding hierarchy

H_2O < $MeNH_2$ < NH_3 is established reflecting a combination of donor strength and complementarity of H-bond architecture.

On the other hand, the binding of weakly polar non-protic guests such as CO would be expected to be precluded on the basis of the very weakly Lewis acidic nature of the boron centre determined by the Guttman-Beckett method. Exposure of {(Ph_2P)xanth}$_3$B to CO under very mild conditions (1 bar, 25°C) however, reversibly yields {(Ph_2P)xanth}$_3$B·CO, a borane carbonyl adduct featuring a central BCO moiety shrouded by xanth(PPh_2) moieties. Geometric factors (orientation of the P- and O-donors; P···C and O···C distances) in both the solid state and calculated structures rule out significant P- or O-donation into the CO π* orbital (i.e. binding via an FLP-type mechanism). Structural and spectroscopic properties of {(Ph_2P)xanth}$_3$B·CO (a C–O bond length not statistically different from that of free CO, a blue shifted carbonyl stretching frequency and an upfield shifted carbonyl ^{13}C NMR resonance) imply that σ-donation from CO to boron dominates the OC–B interaction. This hypothesis is supported by EDA-NOCV analysis which shows that the OC–B σ bond accounts for 74.2% of the total orbital interaction energy with back-bonding from the B–C σ bonds accounting for only 16.5%.

Structural characterization of a series of related host-guest complexes featuring B-bound MeCN, ^{t}BuNC or CN^- guests showcases the ability of {(Ph_2P)xanth}$_3$B to encapsulate substrates by modulating the shape and size of the pocket to the guest. Consistently, we find that dispersion forces are critical to substrate binding, especially in the context of an overall free energy of binding for {(Ph_2P)xanth}$_3$B·CO which is marginally exergonic at room temperature (ΔG_{298} = -1.3 kcal mol^{-1} (expt), -2.3 kcal mol^{-1} (calc)). Alternative binding modes in which the B-bound CO guest is located either inside or outside the host cage differ in energy by 59.5 kcal mol^{-1}.

Introduction

Transition metal complexes are central to numerous widely-employed catalytic processes, in a large part due to their partially filled *d*-orbital manifold and facile oxidation state switching.[1,2] The availability of frontier orbitals of both σ and π symmetry allows for the synergistic binding (and activation) of key ambiphilic small molecule substrates, such as CO, H_2 and alkenes. While *d*-block compounds (particularly of the Platinum Group Metals) are therefore integral to current catalytic protocols, issues of scarcity, toxicity and geopolitics have led to the emergence of metal-free systems as alternative paradigms for small molecule capture and activation.[3,4] Moulding the electronic structure of such systems to bind molecules such as CO has therefore attracted significant interest.[5–7] Within this field, boron carbonyls represent a landmark development, as such complexes have been shown to mimic the bonding of CO in transition metal complexes.[8–11]

The simple borane-carbonyl complex, $H_3B{\cdot}CO$ has been known since 1937, characterised by its blue-shifted carbonyl stretching vibration, characteristic of a σ-dominated bonding interaction.[12–15] A handful of other simple borane carbonyl adducts have since been structurally characterised,[16–32] focusing, at least initially, on the use of electron-withdrawing perfluoroalkyl groups at boron.[29,30] These systems, however, are typically not formed directly via CO coordination, but rather via the solvolysis of the parent borate. Given the primary role of CO in these complexes as a σ-donor, recent work has focused on enhancing the Lewis acidity of the borane. To this end, boro-cations and anti-aromatic boroles have been employed to bind gaseous CO.[23,32] Sindlinger and co-workers have even reported a cationic borole system (**Figure 8.1**, E) which gives rise to a red-shifted carbonyl stretching vibration (with respect to free CO) indicative of back-bonding from the filled π type orbitals of the borole scaffold.[31] In parallel with these investigations, the emergence of Frustrated Lewis Pair (FLP) chemistry has led to the discovery of a number of mixed Lewis acid/base systems displaying reactivity towards carbon

monoxide.[3,4,33] These FLPs offer the possibility for the synergistic binding of CO between the acceptor and donor moieties involving a pseudo back-bonding interaction from the Lewis base component. [34,35]

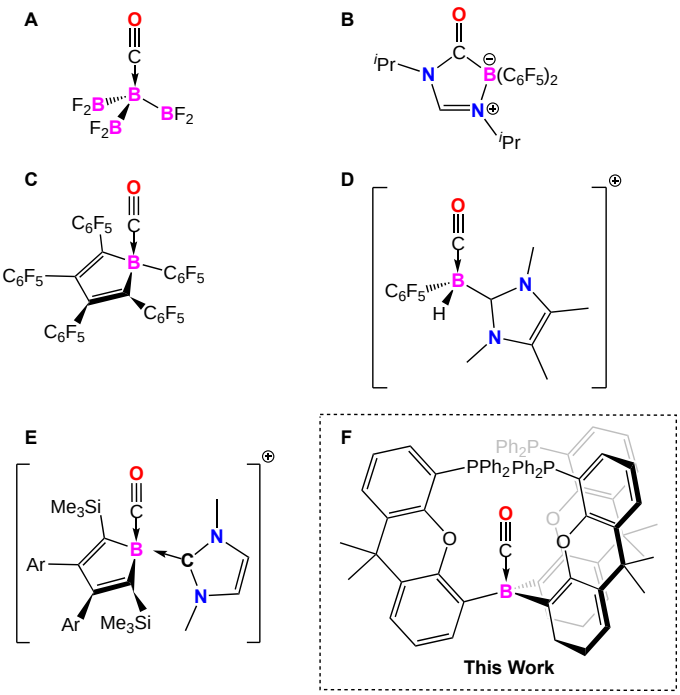

Figure 8.1: Selected examples of CO complexation by boron-containing systems.

Molecular encapsulation is a fundamental process in Nature, exemplified by endocytosis in cells and enzyme activity within binding pockets.[36,37] While transition metal systems are central to industrial processes, enzymes offer unparalleled efficacy and specificity,[35] and the search for enzyme-mimetic systems has led to the development of synthetic molecular cages that mimic biological functions.[38,39] These supramolecular cages, feature customizable cavities that bind guest molecules through weak non-covalent interactions.[38] The selective encapsulation of these cages can enhance stability,[40] enable gas separation[41] and catalyse reactions,[42–44] among other applications.[45–47]

In the current study we report a unique mode of stabilisation of a boron carbonyl complex using a very weakly Lewis acidic borane, via encapsulation of the substrate within a flexible supramolecular binding pocket. This draws inspiration from Nature to augment binding

through non-covalent interactions and in doing so impart an unprecedented degree of stability on a carbonyl host-guest complex.

Results and Discussion

Synthesis of cage-like molecular host

{(Ph_2P)xanth}$_3$B (**2**) was synthesised via a two-step process from [xanth(PPh_2)Li(thf)]$_2$ (**Scheme 8.1**). The initial step involves the reaction of [xanth(PPh_2)Li(thf)]$_2$ with $Me_2S{\cdot}BHBr_2$ from -78°C to room temperature in toluene to give Li[{(Ph_2P)xanth}$_3$BH] (**1**). **1** features a cage-like arrangement based on a tetrahedral hydroborate core, with the encapsulated lithium ion coordinated by three phosphine donors (**Figure 8.2**). Retention of this structure in benzene-d_6 solution is implied by the ^{31}P NMR spectrum which shows a 1:1:1:1 quartet at δ_P = -17.5 ppm, consistent with a single phosphine environment on the NMR timescale and coupling to ^{7}Li (I = 3/2). In the second step, removal of the encapsulated LiH moiety was achieved through reaction with the weak acid [^{i}Pr$_2$EtNH]Cl at 100°C in toluene, a process which liberates H_2 (together with ^{i}Pr$_2$EtN and LiCl; **Scheme 8.1**). Using this methodology, {(Ph_2P)xanth}$_3$B (**2**) could be isolated in 55-60 % overall yield (for the two steps), and crystals suitable for SCXRD could be obtained from toluene solution at 25°C.

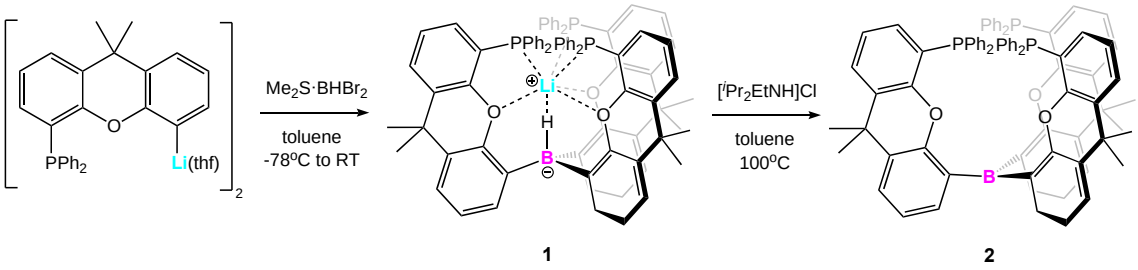

Scheme 8.1: Two-step synthesis of **2**: initial reaction of [xanth(PPh_2)Li(thf)]$_2$ with $Me_2S{\cdot}BHBr_2$ to give intermediate **1**, followed by removal of LiH using [^{i}Pr$_2$NH(Et)]Cl.

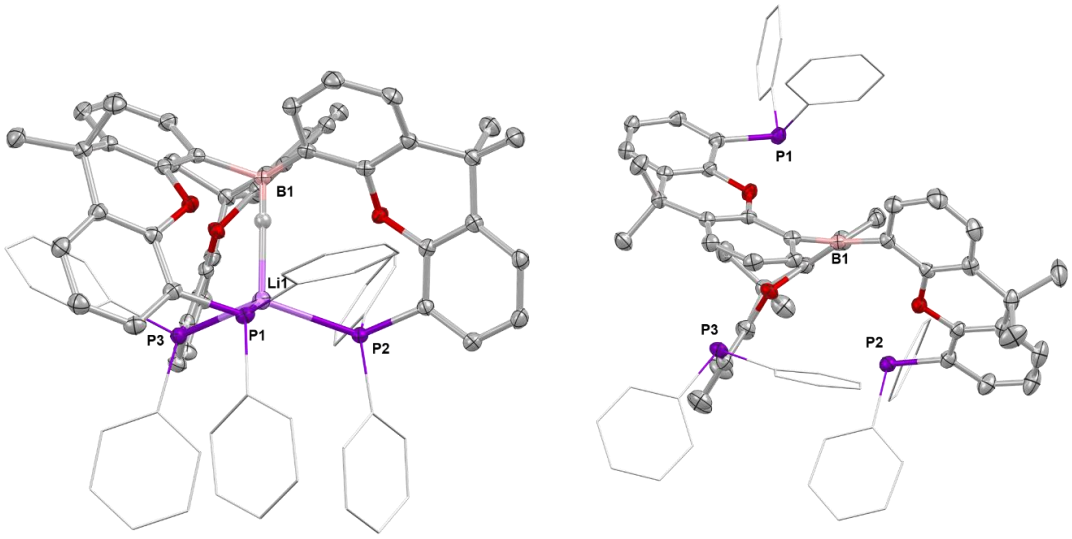

Figure 8.2: Molecular structures of **1** (left) and **2** (right) in the solid state as determined by X-ray crystallography. Ellipsoids set to 50% probability, phenyl groups shown in wireframe format and most hydrogen atoms omitted for clarity. Key bond lengths (Å) and angles (°): (for **1**) B–H 1.0000(12), Li–H 1.8679(19), P–Li 2.560(2), 2.567(2), 2.598(2); (for **2**) B–C 1.560(2), 1.572(2), 1.575(2), C–B–C 116.2(1), 118.0(1), 125.7(1).

The solid-state structure of **2** reveals the expected planar tri-coordinate boron centre (sum of angles at B(1), 359.9°) with the torsional alignment of the B-bound aryl groups generating a conformation in which two xanth(PPh_2) units are projected above the BC_3 plane, and the third points downwards (*up*,*up*,*down* conformation; **Figure 8.2**). The ^{31}P NMR spectrum reveals a single signal at δ_P = -18.3 ppm, implying either rapid fluxional exchange on the NMR timescale at room temperature, or the adoption of a more symmetrical structure in benzene-d_6 solution.

DFT analysis (using the R2SCAN-3c method) was employed to investigate the relative energies of different conformations of **2**, in particular the *up*,*up*,*down* form seen in the solid state and an alternative *up,up*,*up* arrangement featuring all three xanth(PPh_2) units projected in the same direction. These quantum chemical results reveal that the *up*,*up*,*up* conformation, characterized by a cage-like geometry, is favoured significantly *in silico* (by ΔG = 33.0 kcal mol^{-1} cf. the *up*,*up*,*down* conformation). The energy difference can be attributed primarily to enhanced intramolecular non-covalent interactions (NCI, Figure **S 8.8**-**SS 8.11**), particularly between the -PPh_2 units and the xanthene backbone in the 'closed cage' conformation.[48] This

large energetic preference implies that **2** is likely to exist in solution exclusively as the cage-like *up*,*up*,*up* conformation, with the contrasting form found in the solid state presumably resulting from enhanced *inter*molecular interactions enabled by the more open conformation.

Binding of protic guest molecules

The energetic preference for a cage-like conformation for **2** and the presence of a Lewis acid acceptor and three Lewis base donor functions within the scaffold, suggests that their deployment in convergent fashion could be used to trap ambiphilic guest molecules (as in formal LiH host/guest species, **1**). As such, **2** proves to be a highly effective scavenger of trace water, leading to the formation of $\{(Ph_2P)xanth\}_3B{\cdot}OH_2$ (**3**; **Figure 8.3**). Bulk preparation of **3** and crystallisation from hexanes yields crystals suitable for SCXRD (**Figure 8.4**). The structure shows a H_2O unit bound within the cage, with the protons of the water molecule directed towards two of the phosphine units, consistent with the presence of OH···P hydrogen bonding interactions (2.34(2) and 2.31(2) Å). The retention of these interactions in solution is indicated by the downfield shifted nature of the H_2O ^{1}H NMR resonance (δ_H = 10.69 ppm).[49] Given the propensity of **2** to form **3** even with trace amounts of water, a reliable method to remove water was sought. Heating **3** under vacuum for 24 h yielded no change by *in situ* ^{1}H NMR monitoring, but the addition of P_2O_5 to a toluene solution of **3** and heating at 80°C for 48 h yields complete conversion to **2**.

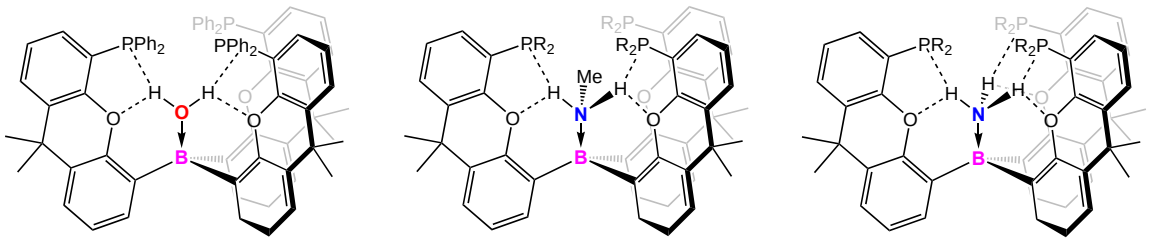

3

4: R = Ph
6: R = ^{i}Pr

5: R = Ph
7: R = ^{i}Pr

Figure 8.3: Binding of protic guest molecules by 2 and its iPr2P– analogue.

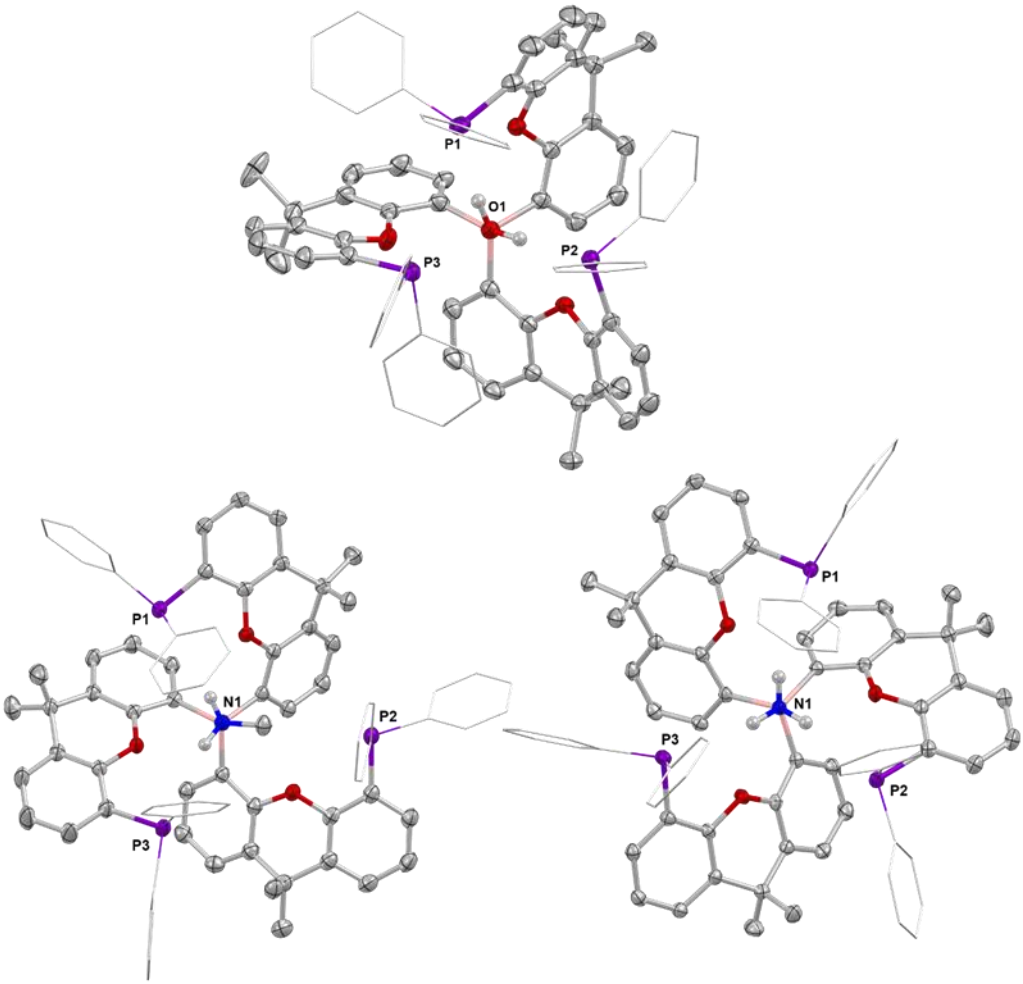

Figure 8.4: Molecular structures of 3 (upper), 4 (lower left) and 5 (lower right) in the solid state as determined by X-ray crystallography. Ellipsoids set to 50% probability, phenyl groups shown in wireframe format and most hydrogen atoms omitted for clarity. Key bond lengths (Å): (for 3) B–O 1.588(2), P···H 2.31(2), 2.34(2); O···H 2.47(2), 2.58(2); (for 4) B–N 1.649(2), P···H 2.88(2), 3.09(2); O···H 2.20(3), 2.40(2); (for 5) B–N 1.627(2), P···H 3.1819(4), 2.6651(5), 2.7987(5); O···H 2.2949(9), 2.3353(12), 2.3055(11).

By extension of the binding of water in **3**, the reaction of **2** with other protic donor molecules was investigated. **2** reacts immediately with $MeNH_2$ to form $\{(Ph_2P)xanth\}_3B{\cdot}NH_2Me$ (**4**), characterized by a very similar ^{31}P NMR shift to that of **3** (both -19.6 ppm). SCXRD studies indicate a similar overall structure to **3**, albeit featuring a more distorted cage geometry with one xanthene unit being rotated to accommodate the bulkier $MeNH_2$ guest (∠N–B–(xanthene plane) 161.7(1), 145.7(1), 146.0(1)°; **Figure 8.4**). The NH···P contacts are notably longer (2.88(2) and 3.09(3) Å) than the OH···P interactions in **3**, reflecting both the structural distortion of the cage and the poorer hydrogen bond donor capabilities of $MeNH_2$ (over H_2O). Short NH···O

contacts (2.20(3) and 2.40(2) Å) are also observed featuring the ether function of the xanthene units, implying that instead of two strong hydrogen bonds in **3**, four weaker interactions are possible in **4**. Informatively, it is found that **3** can readily be converted to **4** via the addition of excess $MeNH_2$, revealing that despite the structural distortion and weaker H-bonds, the overall binding of $MeNH_2$ is stronger than that of H_2O.

Given that the tri-xanthene cage moiety of **2** features three hydrogen bond acceptors, the binding of NH_3 was explored. Exposure of **2** to 1 bar of NH_3 leads to immediate conversion to the NH_3 adduct $\{(Ph_2P)xanth\}_3B{\cdot}NH_3$ (**5**), as determined by in situ ^{31}P NMR spectroscopy (new signal at δ_P = -21.7 ppm). Crystals suitable for SCXRD were obtained and the structure reveals the expected binding motif (**Figure 8.4**), featuring a relatively short N–B distance (1.627(2) vs 1.649(2) Å for **4**) and a combination of both NH···P (3.1819(4), 2.6651(5), 2.7987(5) Å) and NH···O interactions (2.2949(9), 2.3353(12), 2.3055(11) Å); lower left **Figure 8.4**). Immediate conversion to **5** was also observed upon the addition of NH_3 to **3** or **4**, indicating stronger binding of NH_3, presumably due to the third proton capable of hydrogen bonding interactions.

In order to better understand the binding of protic guest donors by **2**, DFT calculations were carried out and Energy Decomposition Analyses employed to quantify the different contributions to the host-guest interactions. Use of the sobEDA method returns free energies of binding of -10.2, -21.9 and -25.4 kcal mol^{-1} for the H_2O, $MeNH_2$ and NH_3 adducts **3**-**5**, in accordance with the relative strengths of guest binding determined experimentally. ETS-NOCV analysis was used to decompose the orbital component into the most significant orbital deformation densities.[50–52] Intuitively, the primary pair density associated with each system is the donor/acceptor bond between the lone pair at N/O and the vacant orbital at B boron (**Figure 8.5**). As expected, the more nucleophilic nitrogen donors give rise to significantly stronger donor/acceptor interactions (**3**, -50.3; **4**, -76.0; **5**, -76.2 kcal mol^{-1}).[53] Secondary interactions constitute 27, 22 and 19 % of the total orbital interaction for **3**-**5**, respectively (**3**, -18.7; **4**, -21.8;

5, -18.8 kcal mol^{-1}). While each of **3**-**5** displays pair densities associated with charge movement from the protons to the E–B bond, only **3** gives rise to a pair density that could unequivocally be designated as a true hydrogen bond (**Figure 8.5**, pair 2).[54] Second order perturbation theory within NBO,[55] was used to further quantify the magnitude of the host-guest interactions in **3**-**5**. Accordingly, **3** features an OH···P hydrogen bond of 22.5 kcal mol^{-1} with minimal OH···O interactions, while **4** and **5** have much weaker interactions, individually <10 kcal mol^{-1} (**4**, 8.8 kcal mol^{-1}; **5**, 7.37 kcal mol^{-1}). This finding concurs with the experimental observation (based on crystallographic and NMR data) that N/OH···P hydrogen bonding is most significant in the case of H_2O adduct **3**.

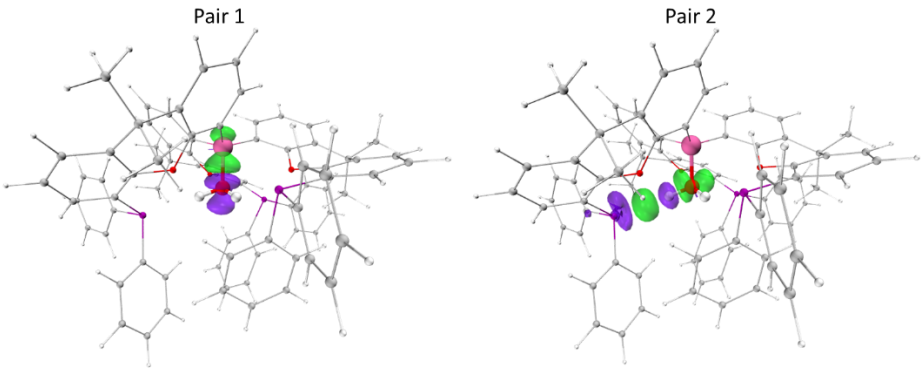

Figure 8.5: NOCV pair deformation densities for complex **3**, with iso-surfaces set to 0.005 for pair 1 and 0.002 a.u for pairs 2. Key: green, electron gain; purple, electron depletion.

Variation of cage substituents

In order to explore potential effects relating to the phosphine substituents, the synthesis of corresponding $^{i}Pr_2P$– variant was attempted. A synthetic route analogous to that used to synthesise **1** resulted in a complex reaction mixture that resisted further purification. An alternative procedure, involving the reaction of [xanth(P^{i}Pr$_2$)Li]$_4$ with BBr_3 also generated a mixture of products; in this case, however, addition of $MeNH_2$ led to the formation of a single product {($^{i}Pr_2P$)xanth}$_3$B·NH_2Me (**6**), which allows for direct comparison with its Ph_2P– counterpart. Crystals suitable for SCXRD were obtained from benzene at 25°C and the structure was found to be analogous to **4** with two units in the asymmetric unit (**Figure 8.6**).

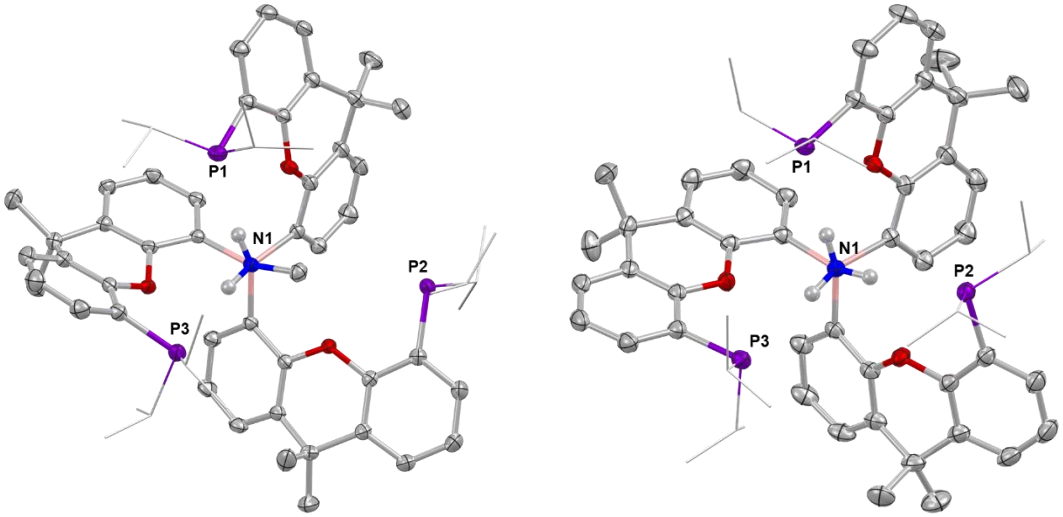

Figure 8.6: Molecular structures of **6** (left) and one of the two independent molecules in the asymmetric unit of **7** (right) in the solid state as determined by X-ray crystallography. Ellipsoids set to 50% probability, isopropyl groups shown in wireframe format and most hydrogen atoms omitted for clarity. Key bond lengths (Å): (for **6**) B–N 1.622(2), 1.625(2), P···H 2.62(2), 2.62(2), 2.57(2), 2.57(2); O···H 2.26(2), 2.35(2), 2.37(2), 2.25(2); (for **7**) B–N 1.609(2), P···H 2.7588(5), 2.6112(5), 2.5749(7); O···H 2.3154(10), 2.3233(9), 2.3557(11).

While the B–N separation is slightly shorter for **6** than for **4** (1.622(2)/1.625(2) vs 1.649(2) Å), the NH···P distances are markedly shorter for the $^{i}Pr_2P$– variant (2.57(2), 2.57(2), 2.62(2) and 2.62(2) Å), as might be predicted by increased phosphine basicity.[56] Shorter NH···O interactions are also seen (2.25(2), 2.37(2), 2.26(2) and 2.35(2) Å), although whether this is due to the tighter geometry afforded by the shorter NH···P distances or vice versa is difficult to deconvolute. The $MeNH_2$ guest is less labile within **6** than **4**. No reaction is observed on addition of NH_3 to **6** at 25°C, while heating at 80°C for 72 h leads only to 40% $MeNH_2/NH_3$ substitution. Despite this, single crystals of the ammonia adduct {($^{i}Pr_2P$)xanth}$_3$B·NH_3 (**7**), could be isolated and SCXRD employed to confirm the geometry of the product (**Figure 8.6**). Here too, shorter NH···P distances are determined (2.7588(5), 2.6112(5), 2.5749(7) Å) compared to the Ph_2P-analogue **5**, consistent with stronger hydrogen bonding interactions.

The poorer conversion of **6** into **7** (cf. **4** into **5**) is likely attributed to the tighter binding of $MeNH_2$, facilitated by stronger hydrogen bonding interactions, which offer an increased kinetic barrier to the exchange process. EDA-NOCV analyses reveal N–B donor/acceptor pairs

which amount to -79.6 kcal mol^{-1} for compound **6** and 80.8 kcal mol^{-1} for compound **7**, i.e. values which are very similar to those observed for **4** (-76.0 kcal mol^{-1}) and **5** (-76.2 kcal mol^{-1}). On the other hand, the strengths of the respective hydrogen bonds, calculated using second-order perturbation theory, are significantly enhanced for compounds **6** (18.8 kcal mol^{-1}) and **7** (18.6 kcal mol^{-1}) (cf. 8.8 and 7.3 kcal mol^{-1} for **4** and **5**) corroborating the shorter NH···P distances determined through crystallography.

Binding of carbon monoxide and related molecules

While the combination of a Lewis acid and three Lewis basic sites within **2** might be expected to be optimal for binding substrates such as NH_3, the binding of weakly polar non-protic guests such as CO would be expected to be precluded on the basis of an acceptor number of 13.6 (determined by the Guttman-Beckett method), which is only marginally higher than those reported for $B(NMe_2)_3$ (9.1) and $B(O^tBu)_3$ (11.8).[57] Exposure of **2** to CO (1 bar) at 25°C in *ortho*-difluorobenzene, however, yields small colourless crystals, which can be shown by SCXRD to contain $\{(Ph_2P)xanth\}_3B{\cdot}CO$ (**8**; **Figure 8.7**), a borane carbonyl adduct featuring a central BCO moiety shrouded by xanthene phosphine moieties (**Figure 8.8**). The solid-state structure features two molecules in the asymmetric unit each featuring a near linear B–C–O unit (177.7(2)° and 174.7(2)°), and the B–C bond lengths (both 1.619(3) Å) fall within the range of previous borane-carbon monoxide adducts.

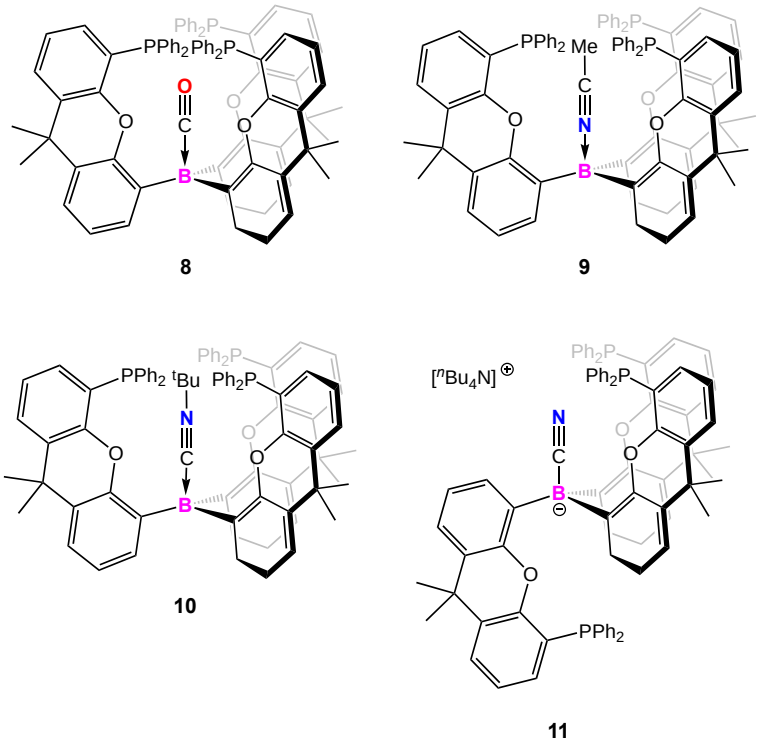

Figure 8.7: Adducts of **2** formed with CO (**8**), MeCN (**9**), ^{t}BuNC (**10**) and CN^- (**11**).

The phosphine donors are remote from the carbon atom of the CO guest, with separations of ca. 3.5 Å (3.564(2), 3.629(2), 3.715(2), 3.551(2), 3.717(2) and 3.841(2) Å), i.e. over double the sum of the respective covalent radii (1.73 Å) and even in excess of the sum of the Van der Waals radii (3.5 Å).[58] In addition, the orientations of the phosphine groups suggest that the lone pairs are directed towards the xanthene backbone, rather than the CO guest; these metrical data (together with a ^{31}P NMR shift only slightly up-field from that of **2** (-21.8 ppm)) effectively precludes the possibility of an FLP mode of CO binding. The capture of CO between the donor and acceptor units, as seen with other FLP systems, is typically accompanied by a large downfield shift of the ^{31}P resonance.

The C–O bond lengths measured for **8** (1.117(3), 1.122(3) Å) are not statistically different from that of free CO (1.1281 Å),[16–28,59,60] and the IR stretching frequency (2178.7 cm^{-1}) falls within the range previously reported for borane-CO complexes. As such, it is indicative of σ-dominated bonding with minimal back-bonding, similar to that of so-called "non-classical" transition metal carbonyl complexes.[12,16–28,59] This is further corroborated by the CO ^{13}C NMR resonance at 171.7

ppm, which is shifted up-field compared to that of free CO (184.1 ppm). EDA-NOCV analysis carried out on **8** in an attempt to quantify the relative magnitudes of bonding and back-bonding interactions. Consistently, the OC–B σ bond accounts for 74.2% of the total orbital interaction energy with back-bonding accounting for only 16.5%; back-bonding occurs to both CO π* orbitals with electron density being transferred from the B–C σ bonds (**Figure 8.9**).

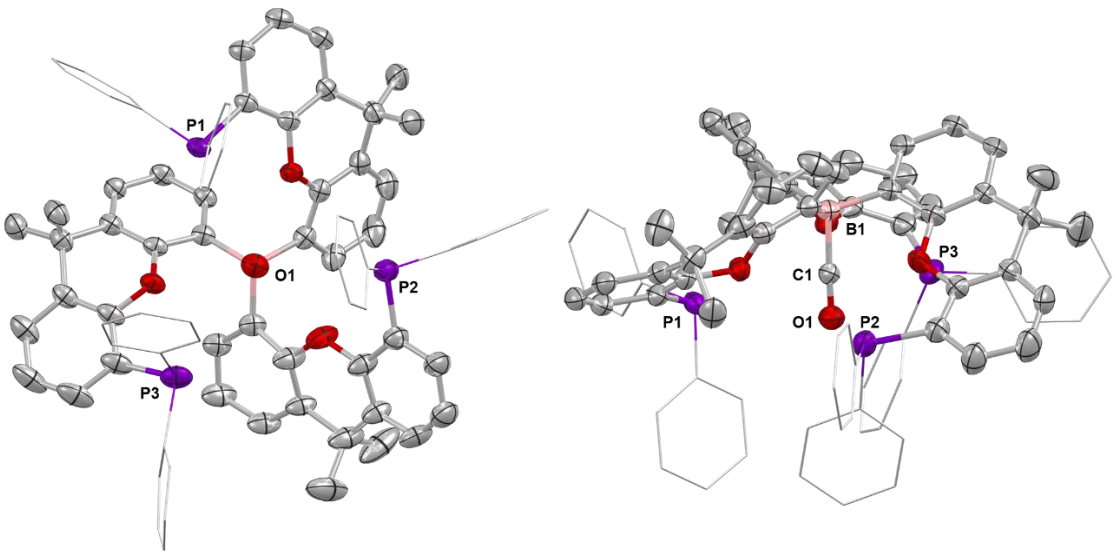

Figure 8.8: Molecular structure of one of the two independent molecules in the asymmetric unit of **8** in the solid state as determined by X-ray crystallography (top and side views). Ellipsoids set to 50% probability, isopropyl groups shown in wireframe format and most hydrogen atoms omitted for clarity. Key bond lengths (Å) and angles (°): B–C(O) 1.619(3), 1.619(3), C–O 1.117(3), 1.122(3), P···C(O) 3.564(2), 3.629(2), 3.715(2), 3.551(2), 3.717(2), 3.841(2), O···C(O) 2.699(2), 2.818(2), 2.711(3), 2.770(2), 2.754(2), 2.739(2), B–C–O 177.7(2), 174.4(2).

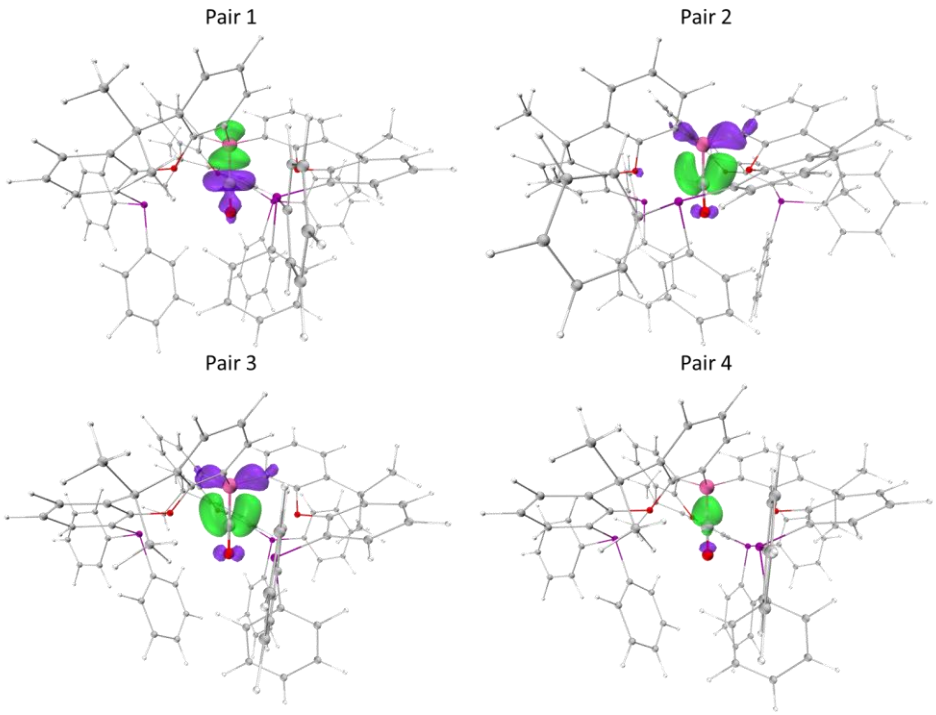

Figure 8.9: NOCV pair deformation densities for carbonyl complex **8**, iso-surface set to 0.005 for pair 1 and 0.002 a.u for pairs 2-4. Key: green, electron gain; purple, electron depletion.

The reaction of **8** with CO is reversible: **2** is regenerated on removal of the CO atmosphere. In solution the release of CO can be driven at elevated temperatures, and VT-NMR measurements allow for the determination of ΔH and ΔS from a van't Hoff plot. The values obtained for ΔH (-10.9 kcal mol^{-1}) and ΔS (3.21 cal mol^{-1} K^{-1}) for the release of CO align well with the corresponding DFT-calculated values (assuming a closed cage *up*, *up*, *up* conformation for **2**): ΔH_{calc} = -12.7 kcal mol^{-1}; ΔS_{calc} = 3.5 cal mol^{-1} K^{-1}.

The capture of a range of related guest molecules/anions by **2** was also investigated: ^{t}BuNC, MeCN and CN^{-} (as the $[^{n}Bu_4N]^{+}$ salt) (**Figure 8.7**). **2** takes up acetonitrile in benzene leading to complete conversion to {(Ph_2P)xanth}$_3$B·NCMe (**9**); as with CO, complete removal of acetonitrile is observed under continuous vacuum. The structure of **9** in the solid state, elucidated by SCXRD, contains a single molecule in the asymmetric unit featuring a linear B–N–C–C unit (∠B–N–C, 176.5(2)°; ∠N–C–C, 179.2(2)°; **Figure 8.10**), and long P···N distances (ca. 4 Å). The CN stretching vibration (at 2356.0 cm^{-1}) is significantly higher than that of uncoordinated acetonitrile (2253 cm^{-1}),[61] implying that the bonding interaction is dominated by σ donation, as

with carbonyl complex **8**. Consistently, EDA-NOCV calculations on **9** show that the total orbital interaction energy is dominated by σ donation (71.0 %) with only 11.9% being derived from π back bonding from the B–C σ bonds. This reduction in back bonding is consistent with the acetonitrile being a poorer π acceptor.

With the more sterically demanding tert-butyl isocyanide, formation of the corresponding host-guest complex is less facile: heating to 80 °C for 18 h is required for full conversion to {(Ph_2P)xanth$\}_3$B·CN^{t}Bu (**10**). The binding of ^{t}BuNC also appears to be less reversible than with CO or MeCN, with no release of the guest molecule observed under continuous vacuum. The structure of **10** determined by SCXRD features a crystallographically imposed linear B–C–N–C unit (**Figure 8.10**), and wide P···C separations (3.947(2), 3.966(2), Å). The CN stretching frequency at 2284.5 cm^{-1} (as determined by IR spectroscopy) is also higher than that of free ^{t}BuNC (2140 cm^{-1}), [22] indicating that here too the bonding is predominantly driven by σ interactions. EDA-NOCV confirms that **10** features the smallest proportion of the back bonding, 10.2% (77% σ donation), implying that tert-butyl isocyanide is a weaker π acceptor in this context than acetonitrile and CO).[62] Assimilation of the cyanide anion by **2** also requires more forcing conditions: reaction with tetrabutylammonium cyanide in benzene requires heating at 80 °C for 18 h to generate [^{n}Bu$_4$N][{(Ph_2P)xanth$\}_3$B·CN] (**11**). The structure of **11** in solution is much less symmetrical than the other adducts, as indicated by ^{1}H (three xanthene backbone methyl group signals) and ^{31}P NMR spectroscopy (three phosphine resonances at -18.0, -20.2 and -23.7 ppm). Consistently, SCXRD reveals not the cage geometry seen for all other host-guest species, but an adduct based on the alternative *up*, *up*, *down* conformer of the host **2** (**Figure 8.10**).

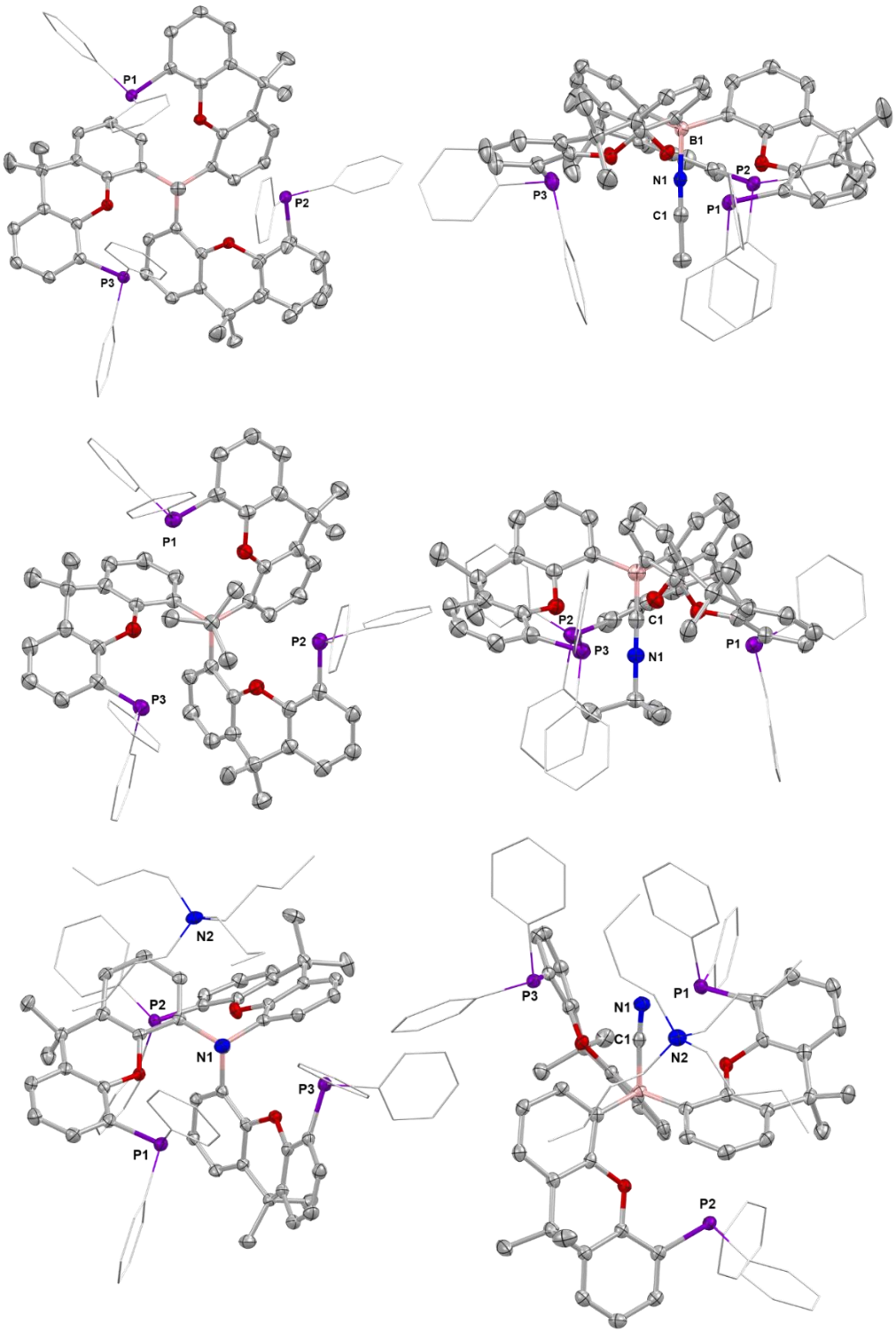

Figure 8.10: Molecular structure of **9** (upper), one of the two independent molecules in the asymmetric unit of **10** (centre) and **11** (lower) in the solid state as determined by X-ray crystallography (top and side views of each). Ellipsoids set to 50% probability, isopropyl groups shown in wireframe format and most hydrogen atoms omitted for clarity. Key bond lengths (Å) and angles (°): (for **9**) B–N 1.591(3), C–N 1.138(2), P···N 3.943(1), 4.032(1), 4.081(1), O···N 2.828(2), 2.834(2), 2.945(2), B–N–C 176.5(2), N–C–C 179.2(2); (for **10**) B–C(N) 1.619(12), 1.523(12), C–N 1.094(12), 1.194(10), P···C(N) 3.947(2), 3.966(2), O···C(N) 2.804(4), 2.832(3), B–C–N 180.0, 180.0, C–N–C 180.0, 180.0; (for **11**) B–C(N) 1.625(4), C–N 1.148(3), P···C(N) 3.733(3), 3.777(2), O···C(N) 2.908(3), 3.049(3), B–C–N 173.4(3).

Quantum chemical analysis of CO binding

Previous examples of boron-centred carbonyl complexes have leveraged very high Lewis acidity, a low oxidation state boron centre or extensive ligand back-donation in order to facilitate binding of CO. **2** demonstrates none of these features - it is a very modest Lewis acid offering a small degree of ligand back-donation.[16–28,59] Hypothesising that stabilisation in this case might be afforded by secondary interactions with the shrouding xanthene groups, a series of calculations was carried on **8** and the related adducts **9**-**11**. A combination of geometric factors (orientation of the P- and O-donors; P···C and O···C distances) in both the solid state and calculated structures of **8** and Second Order Perturbation Theory/NOCV analyses rule out significant P- or O-donation into the CO π^* orbital i.e. binding via an FLP-type mechanism. As such, the potential role(s) of non-covalent interactions in stabilising host-gest complexes were probed. This was achieved by consideration of **8**-**11**, together with model systems in which the guest is bound outside the cage (**8'** - **11'**; **Figure 8.11**). In the case of **8** and **8'**, the binding of CO is only thermodynamically viable within the host cage. The value of $\Delta\Delta G$ (59.5 kcal mol^{-1}) calculated for binding outside the cage (vs. within it) implies that the stabilisation of the host-guest complex from non-covalent interactions within the host cavity is very significant (**Table 8.1**). To further probe the differences in the binding within (**8-11**) and outside the cage (**8'-11'**) energy decomposition analysis was performed using SobEDA method.

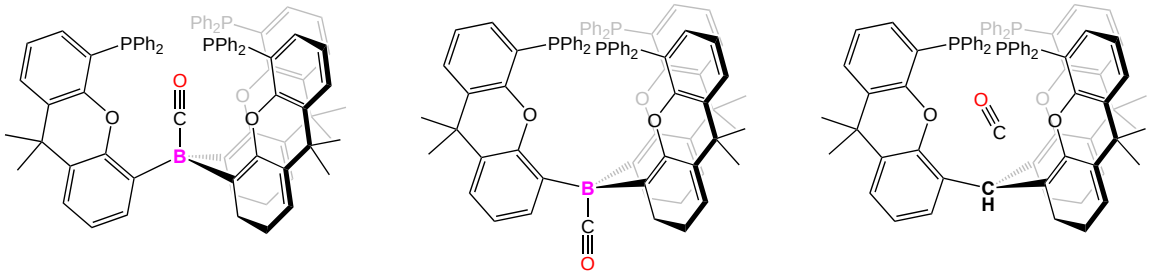

8 **8'** **8***

Figure 8.11: Binding of CO inside the cage (8, left), binding outside the cage (8', middle) and as a host guest interaction with the modified cage with C instead of B (8*, right).

Table 8.1: Decomposition of the host-guest interactions in **8**-**11** and **8'**-**11'** using the sobEDA approach.[63]

	8	**8'**	**Δ[b]**	**9**	**9'**	**Δ[b]**	**10**	**10'**	**Δ[b]**	**11**	**11'**	**Δ[b]**
Gibbs free energy of binding ΔG_B[a]	-2.3	53.7	-59.5	-7.0	55.8	-62.8	-10.2	46.5	-56.7	-0.9	19.4	-20.3
Total interaction energy (ΔE_{int})	-34.2	-4.7	-29.5	-51.7	-14.4	-37.3	-66.4	-24.0	-42.4	-88.9	-70.0	-18.9
Electrostatic (ΔE_{elst})	-76.4	-66.6	-9.8	-103.4	-74.4	-29.0	-120.7	-80.1	-40.6	-95.6	-96.0	0.4
Exchange-repulsion (ΔE_{xrep})	211.3	237.5	-26.2	202.4	217.8	-15.4	230.6	242.5	-11.9	235.5	259.2	-23.7
Orbital (ΔE_{orb})	-115.1	-113.0	-2.1	-104.0	-100.8	-3.2	-125.5	-118.6	-6.9	-159.1	-155.7	-3.4
Coulomb correlation (ΔE_c)	-54.0	-62.5	8.5	-46.7	-57.0	10.3	-50.8	-67.9	17.1	-69.8	-77.4	7.6
DFT correlation (ΔE_{DFTc})	-52.9	-61.9	9.0	-44.4	-55.9	11.5	-46.1	-65.9	19.8	-68.7	-76.8	8.1
Dispersion correction (ΔE_{dc})	-1.1	-0.6	-0.5	-2.3	-1.1	-1.2	-4.8	-2.0	-2.76	-1.1	-0.6	-0.5

[a] Energies given in kcal mol^{-1}; [b] Defined as ΔE for compound **n** minus ΔE for compound **n'**.

The SobEDA approach[63] decomposes the interaction energy between fragments (in this case the substrate/guest and cage/host) into chemically intuitive electrostatic (ΔE_{elst}), exchange repulsion (ΔE_{xrep}), orbital interaction (ΔE_{orb}) and Coulomb correlation terms (ΔE_c), such that ΔE_{int} = ΔE_{elst} + ΔE_{xrep} + ΔE_{orb} + ΔE_c. The total interaction energy between the cage host and CO guest fragments (in their geometries as found in the host-guest complex) in **8'** is 29.5 kcal mol^{-1} less favourable when compared to **8** . This corresponds to a moderate decrease in the attractive ΔE_{elst} ($\Delta\Delta E_{elst}$ = 9.7 kcal mol^{-1}) when comparing **8'** to **8**, that could be attributed to the loss of interactions between the (weakly) polar CO molecule with the electron rich and deficient regions within cage. The repulsive ΔE_{xrep} term increases for **8'** compared to **8**, which can be rationalised by pyramidalization at boron which pushes the xanthene groups together when the guest molecule is bound *outside* the cage, increasing the degree of steric repulsion. By contrast, when binding occurs within the cage the xanthene groups are pushed apart effectively opening the cage, and reducing the steric clash (**Figure 8.12**).

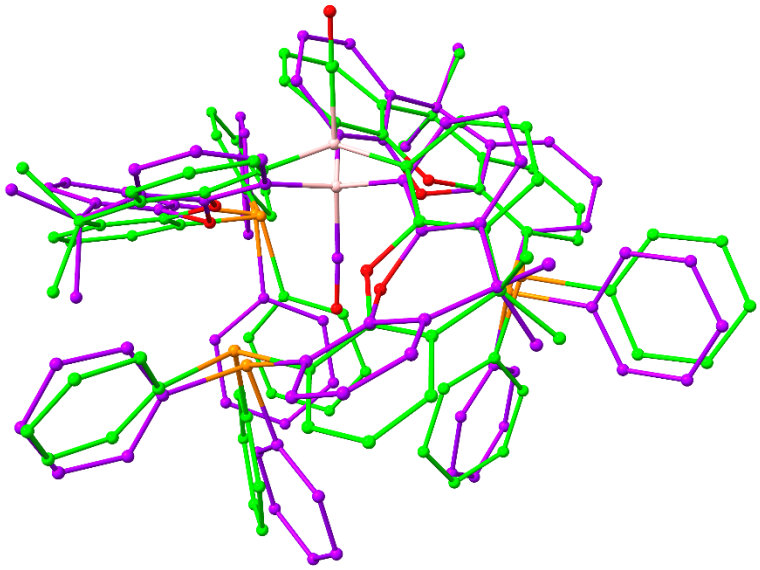

Figure 8.12: Geometries of optimised structures **8** (purple) and **8'** (green) overlapped to demonstrate the effects on the cage architecture on pyramidalization of the boron centre.

The attractive ΔE_{orb} term stays approximately the same (between **8'** and **8**), as might be expected given that this term is dependent on orbital overlap, which is more-or-less consistent between binding inside or outside the cage. The Coulomb correlation term (ΔE_c) can be can be

decomposed further into dispersion (ΔE_{dc}) and DFT correlation (ΔE_{DFTc}) terms. Interpreting the overall chemical meaning of ΔE_c for directly bonded systems is challenging because the ΔE_{DFTc} term reflects a mix of short-range (electronic repulsion) and medium-range (dispersion) interactions, an inherent limitation of the employed DFT functional hence we examine the 'pure' host/guest system **8*** below. [63]

The sobaEDA analysis was also carried out on the other host-guest complexes, with **9** and **10** displaying the same trend with the attractive ΔE_{elst} term increasing (from **9'**/**10'** to **9**/**10**) with the magnitude of this change increasing substantially more than in the case of **8'**/**8** due to the greater dipole moments of acetonitrile and tert-butyl isocyanide. [64–66] The ΔE_{xrep} term follows the same trend as with **8'** – **8**, reflecting a decrease in steric repulsion however, the magnitude of this term decreases as the steric bulk of the substrate increases offsetting the pyramidalization effects.

As an alternative approach, the effects of secondary interactions on the stabilisation of the host-guest complex were probed by examining the CH (for boron) substituted system **8*** (**Figure 8.11**), in which the CO guest is bound solely by non-covalent interactions. Incorporation of CO within this system is associated with a slightly exothermic value of ΔH (-1.1 kcal mol^{-1}). **8*** features no direct donor/acceptor bond between the host and guest, which allows for re-partitioning of the chemically unintuitive ΔE_{DFTc} term in the modified SobEDAw method.[63] In SobEDAw ΔE_{DFTc} is redistributed into the ΔE_{xrep} and the ΔE_{dc} terms giving a a dispersion term which is more comparable to that calculated by Symmetry-adapted perturbation theory (SAPT); the interaction energy is reformulated instead as $\Delta E_{int} = \Delta E_{elst} + \Delta E_{xrep} + \Delta E_{orb} + \Delta E_{dc}$. This approach delivers a value for ΔE_{int} of -8.5 kcal mol^{-1}, with the dominating attractive interaction being the dispersion contribution (ΔE_{dc} = -19.8 kcal mol^{-1}). As such, the importance of dispersion interactions in host binding within the cage architecture of systems of this type is amply demonstrated. The smallest term, as anticipated due to limited orbital overlap between CO and

the cage, is the ΔE_{orb} term (-4.9 kcal mol^{-1}). The ΔE_{elst} term is calculated to be -7.7 kcal mol^{-1}, reflecting the minor electrostatic interactions between the weakly polar CO guest and the cage; this value is similar in magnitude to the difference in ΔE_{elst} between **8** and **8'** (-9.8 kcal mol^{-1}).

Conclusions

{(Ph$_2$P)xanth}$_3$B (**2**) has been synthesised in good yield (55-60%) via a two-step process from [xanth(PPh$_2$)Li(thf)]$_2$, and features a solid-state structure in which two of the three B-bound xanth(PPh$_2$) units are projected above the BC$_3$ plane, generating an *up*,*up*,*down* conformation. On the other hand, quantum chemical methods reveal that the alternative *up*,*up*,*up* conformation, characterized by a cage-like geometry, is favoured significantly *in silico* (by ca. 33.0 kcal mol^{-1}) due to enhanced intramolecular non-covalent interactions. The combination of a Lewis acid and three Lewis basic sites within the {(Ph$_2$P)xanth}$_3$B cage might be expected to facilitate strong binding of polar protic guests in solution through a combination of donor/acceptor and hydrogen bonding interactions. Crystallographic and quantum chemical studies confirm this hypothesis and a binding hierarchy H$_2$O < MeNH$_2$ < NH$_3$ is established reflecting the interplay between the Lewis base donor strength and the complementarity of the H-bond architecture.

By contrast, the assimilation by **2** of weakly polar non-protic guests such as CO would be expected to be precluded on the basis of an acceptor number determined by the Guttman-Beckett method (13.6) which is only marginally higher than that reported for B(NMe$_2$)$_3$. Exposure of **2** to CO under very mild conditions (1 bar, 25°C) however, reversibly yields {(Ph$_2$P)xanth}$_3$B·CO (**8**), a borane carbonyl adduct featuring a central BCO moiety shrouded by xanth(PPh$_2$) moieties. Geometric factors (notably the orientation of the P- and O-donors and the P···C and O···C distances) in both the solid state and calculated structures effectively rule out significant P- or O-donation into the CO π^* orbital (i.e. binding via an FLP-type mechanism). Structural and spectroscopic properties of **8** (a C–O bond length not statistically different from that of free CO,

a blue shifted carbonyl stretching frequency and an upfield shifted carbonyl ^{13}C NMR resonance) imply that σ-donation from CO to boron dominates the OC–B interaction. This hypothesis is supported by EDA-NOCV analysis which shows that the OC–B σ bond accounts for 74.2% of the total orbital interaction energy with back-bonding from the B–C σ bonds accounting for only 16.5%.

Structural characterization of a series of related host-guest complexes featuring B-bound MeCN, ^{t}BuNC or CN^- guests showcases the ability of $\{(Ph_2P)xanth\}_3B$ to encapsulate substrates by modulating the shape and size of the pocket to the guest. Consistently, we find that dispersion forces are critical to substrate binding, especially in the context of an overall free energy of binding for $\{(Ph_2P)xanth\}_3B{\cdot}CO$ which is marginally exergonic at room temperature (ΔG_{298} = -1.3 kcal mol^{-1} (expt), -2.3 kcal mol^{-1} (calc)). Alternative binding modes in which the B-bound CO guest is located either inside or outside the host cage differ in energy by 59.5 kcal mol^{-1}.

Characterization data

General Considerations

All manipulations were carried out using Schlenk line or glovebox techniques under an atmosphere of argon or dinitrogen. Solvents were dried by passage through activated alumina towers, degassed before use and stored over K. NMR spectra were measured in C_6D_6 or d^8-toluene which were dried over 3 Å molecular sieves, with the solvent stored under nitrogen in a Teflon valve ampoule. CO was stored in a Teflon valve ampoule over P_2O_5. NMR samples were prepared under nitrogen in 5 mm Wilmad 507-PP tubes fitted with J. Young Teflon NMR spectra were measured on a Bruker Avance III HD Nanobay 400 MHz NMR spectrometer equipped with a 9.4 T magnet or a Bruker Avance III NMR 500 MHz NMR spectrometer. ^1H and ^{13}C NMR spectra were referenced internally to residual proteo-solvent (^1H) or solvent (^{13}C) resonances and are reported relative to tetramethylsilane (δ = 0 ppm). Variable temperature ^{31}P spectra were referenced relative to an internal standard of Ph_2P-Xan-H in d^8-toluene. Chemical shifts are quoted in δ (ppm) and coupling constants in Hz. FTIR spectra were recorded on a Bruker Alpha spectrometer with Platinum-ATR module. Elemental analyses were carried out by London Metropolitan University, when measuring prosperous containing compounds carbon % can be artificially lowered.[67] Ph_2P-xan-Li and *$^iPr_2P$-xan-Li were prepared according to literature procedure.*[68] [DIEPAH][CL] was made via modified literature procedure using dry HCL in Et_2O.[69]

Synthesis of novel compounds

1 *- $(Ph_2P\text{-}xan)_3BH\text{-}Li$*

Toluene (50 ml) was added dropwise to Ph2P-xan-Li (500 mg, 1.250 mmol) and Dibromoborane dimethyl sulfide complex (300 mg, 1.283 mmol) at -78 °C under vigorous stirring. The resulting solution was stirred at -78°C for 30 minutes and then the reaction was warmed to room temperature and stirred for a further 16 hours. The cloudy solution was then heated to 100°C and filtered via canula where the resulting solution was concentrated to the point of incipient

crystallisation. storage of this solution overnight at -30°C resulted in very large cubic crystals which were washed with Et2O. Yield: 456 mg (91%) crystals suitable for X-ray diffraction could be obtained by recrystallisation from benzene at room temperature. **Spectroscopic data:** **^{1}H** NMR (500 MHz, C6D6) δ 7.26 – 7.18 (m, 9H, ArH), 7.06 (t, J = 7.5 Hz, 3H, ArH), 6.90 (t, J = 7.2 Hz, 12H, ArH), 6.82 (t, J = 7.5 Hz, 6H, ArH), 6.79 – 6.67 (m, 12H, ArH), 6.55 (t, J = 7.6 Hz, 6H, ArH), 4.42 – 2.95 (m, 1H, BH), 1.60 (s, 9H, Xan-CH_3), 1.39 (s, 9H, Xan-CH_3). **^{7}Li** NMR (156 MHz, C6D6) δ -1.1. **^{11}B** NMR (160 MHz, C6D6) δ -16.7 (d, J = 70.4 Hz). **^{31}P** NMR (202 MHz, C6D6) δ -17.5 (q, J = 47.3 Hz). **^{13}C** NMR (126 MHz, C6D6) δ 155.9, 154.4, 135.7, 135.2, 135.2, 135.1, 135.0, 133.3, 132.9, 132.6, 132.6, 132.6, 132.5, 131.6, 128.6, 127.5, 123.4, 122.7, 121.9, 120.6, 35.2 (Xan-CH_3), 34.8 (Xan-CH_3), 26.4 (Xan-C). **Elemental Microanalysis:** $C_{81}H_{67}BLiO_3P_3$+0.5(Et_2O) calc; C 80.19% H 6.1% found; 80.24 % 6.12 %.

2 - $(Ph_2P\text{-}xan)_3B$

Toluene (25 ml) was added dropwise to **1** (200 mg, 0.167 mmol) and [DiPEAH][CL] under vigorous stirring and then heated to 100°C for 2 hours. The resulting solution was then cooled to 2°C and left to stand for 6 hours where it was then filtered from unreacted [DiPEAH][CL] and the and volatiles were removed in vacuo. The resulting solid was washed with hexanes and extracted into toluene where it was concentrated to incipient crystallisation. Storge at -30°C overnight resulted in crystals suitable for X-ray diffraction. yield: 125 mg (62.8%).

Special Procedure A

Some degree of contamination with the water bound product is always seen, in order to get clean material for further reaction further purification is needed. $(Ph_2P\text{-}xan)_3B$ (25 mg, 0.0210 mmol) and P_2O_5 (25 mg, 0.0881 mmol) is added to an NMR tube fitted with a J. Young's valve and dissolved in toluene and heated at 50°C for 3 hours with regular agitation. The solution is then filtered through a syringe filter with solvents removed in vacuo. This was then used for subsequent reaction **Spectroscopic data:** **^{1}H** NMR (500 MHz, C6D6) δ 7.27 (dd, J = 7.5, 1.9 Hz,

3H, ArH), 7.09 – 7.05 (m, 9H, ArH), 6.97 – 6.87 (m, 21H, ArH), 6.86 – 6.74 (m, 15H, ArH), 1.52 (s, 18H, Xan-CH_3). **^{31}P** NMR (162 MHz, C6D6) δ -18.3. **^{13}C** NMR (126 MHz, C6D6) δ 156.6, 155.6, 139.6, 139.5, 138.4, 134.3, 134.1, 133.4, 132.0, 129.5, 129.3, 128.6, 128.4, 126.2, 123.3, 123.3, 34.9 (Xan-C), 30.8 (Xan-CH_3). No ^{11}B resonance could be found likely due to it being very broad. **Mass:** $C_{81}H_{66}BO_3P_3$ ($+K^+$) calc; 1229.3950 m/z, reported; 1229.3994 m/z **Elemental analysis:** $C_{81}H_{66}BO_3P_3$ calc: C 82.01 % H 5.65 % found: C 79.14 % H 5.75 %.

3 - (Ph_2P-xan)$_3$B-OH_2

Method A

To an NMR tube fitted with a J. Young's valve of **2** (prepared by Special Procedure A) or any of its adducts (bar NH_3 or Methyl amine) is dissolved in C_6D_6 and any trace water is added (for example wet methanol). Quantitative conversation is seen in all cases.

Method B

To a solution of Ph2P-xan-Li (500 mg, 1.250 mmol) in toluene (50 mL) at -78°C was added dropwise a solution of boron tribromide (1 M in Toluene, 0.833 mmol, 0.83 mL). The resulting solution was stirred for 1 hour at -78°C then was allowed to warm to room temperature where it was stirred for a further 16 hours. Bench methanol (24 mmol, 1 mL) was then added (as a water surrogate) and the resulting cloudy solution becomes clear. Volatiles were removed in vacuo and the sticky white powder is extracted into toluene and the product is filtered. Volatiles were once again removed in vacuo. Yield: 324 mg (64.3 %) crystals suitable for X-ray diffraction could be obtained through recrystallisation in hexanes and storage at -30°C over the course of 2 days. **Spectroscopic data:** **^{1}H** NMR (500 MHz, C6D6) δ 10.69 (q, J = 2.3 Hz, 2H, H_2O), 7.31 – 7.27 (m, 3H, ArH), 7.22 (dd, J = 7.6, 1.8 Hz, 3H, ArH), 7.02 (t, J = 8.3 Hz, 6H, ArH), 6.94 (dd, J = 7.4, 1.7 Hz, 3H, ArH), 6.89 – 6.77 (m, 24H, ArH), 6.74 (t, J = 7.6 Hz, 3H, ArH), 6.63 (t, J = 7.5 Hz, 6H, ArH), 1.64 (s, 9H, Xan-CH_3), 1.37 (s, 9H, Xan-CH_3). **^{11}B** NMR (160 MHz, C6D6) δ 0.00. **^{31}P** NMR (202 MHz, C6D6) δ -19.6. **^{13}C** NMR (126 MHz, C6D6) δ 155.4, 135.0, 134.9, 134.8, 132.8, 132.8, 132.7,

132.7, 131.9, 128.8, 128.6, 128.6, 126.5, 123.2, 123.0, 122.6, 35.0 (Xan-CH_3), 34.7 (Xan-CH_3), 25.3 (Xan-C). **Mass:** $C_{81}H_{68}BO_4P_3$ ($+H^+$) calc; 1209.4496 m/z, reported; 1209.4521 m/z **Elemental analysis:** $C_{81}H_{66}BO_3P_3$ calc: C 80.83 % H 5.73 % found: C 80.45 % H 5.93 %.

4 *- $(Ph_2P\text{-}xan)_3B\text{-}NH_2Me$*

Method A

To an NMR tube fitted with a J. Young's valve of **2** (prepared by Special Procedure A) or any of its adducts (bar NH_3) is dissolved in C_6D_6, 1 drop of methylamine solution in THF(1M) was added. Quantitative conversation is seen in all cases.

Method B

To a solution of Ph2P-xan-Li (500 mg, 1.250 mmol) in toluene (50 mL) at -78°C was added dropwise a solution of boron tribromide (1 M in Toluene, 0.833 mmol, 0.83 mL). The resulting solution was stirred for 1 hour at -78°C then was allowed to warm to room temperature where it was stirred for a further 16 hours. Methyl amine (1 M in THF, 5 mmol, 5 ML) was then added and the resulting cloudy solution becomes less turbid. Volatiles were removed in vacuo and the sticky white powder is extracted into toluene and the product is filtered. Volatiles were once again removed in vacuo. Yield: 212 mg (41.6 %) crystals suitable for X-ray diffraction could be obtained through recrystallisation in benzene at room temperature. **Spectroscopic data:** **^{1}H** NMR (500 MHz, C6D6) δ 7.26 (dd, J = 7.4, 1.8 Hz, 3H, ArH), 7.20 (ddd, J = 9.8, 7.7, 1.8 Hz, 6H, ArH), 7.09 – 6.91 (m, 26H, ArH and NH_2), 6.87 (ddt, J = 7.6, 5.7, 1.6 Hz, 9H, ArH), 6.76 (td, J = 7.6, 5.3 Hz, 6H, ArH), 2.47 (t, J = 6.3 Hz, 3H, NCH_3), 1.61 (s, 9H, Xan-CH_3), 1.40 (s, 9H, Xan-CH_3). **^{11}B** NMR (160 MHz, C6D6) δ 0.3. **^{31}P** NMR (202 MHz, C6D6) δ -19.6. **^{13}C** NMR (126 MHz, C6D6) δ 155.9, 138.2, 138.1, 137.2, 134.3, 134.1, 133.5, 133.4, 133.1, 132.7, 129.8, 128.6, 128.4, 126.9, 125.7, 124.0, 123.9, 123.8, 123.5, 123.2, 35.0 (Xan-CH_3) , 33.8 (Xan-CH_3), 30.4 (NCH_3), 28.3 (Xan-C). **Mass:** $C_{82}H_{71}BNO_3P_3$ ($+H^+$) calc; 1222.4813 m/z, reported; 1222.4862m/z **Elemental analysis:** $C_{81}H_{66}BO_3P_3$ calc: C 80.95 % H 5.91 % N 1.11 % found: C 80.86 % H 6.07 % N 1.19 %.

5 - *(Ph_2P-xan)$_3$B-NH_3*

Method A

To an NMR tube fitted with a J. Young's valve **2** (prepared by Special Procedure A) or any of its adducts is dissolved in C_6D_6 degassed by three freeze-pump-thaw cycles where 1 bar of NH_3 was added. Quantitative conversation is seen in all cases.

Method B

To a solution of Ph2P-xan-Li (500 mg, 1.250 mmol) in toluene (50 mL) at -78°C was added dropwise a solution of boron tribromide (1M mL in Toluene, 0.833 mmol, 0.83 mL). The resulting solution was stirred for 1 hour at -78°C then was allowed to warm to room temperature where it was stirred for a further 16 hours. Bench methanol (24 mmol, 1 mL) was then added (as a water surrogate) and the resulting cloudy solution becomes clear. Volatiles were removed in vacuo and the sticky white powder is extracted into toluene and the product is filtered. Ammonia gas is then bubbled through the solution for 15 mins and then is concentrated to incipient crystallisation where it is stored at 30°C overnight to produce crystalline material. Yield 242 mg (48.1 %). Crystals suitable for X-ray crystallography was produced through recrystallisation from benzene at room temperature. **Spectroscopic data**: **^{1}H** NMR (400 MHz, C6D6) δ 7.24 – 7.14 (m, 9H, ArH), 7.12 (dd, J = 6.9, 1.7 Hz, 6H, ArH), 7.01 – 6.76 (m, 30H, ArH), 6.71 (t, J = 7.6 Hz, 3H, ArH), 6.70 (s, 3H, NH3), 1.50 (s, 9H, Xan-CH_3), 1.33 (s, 9H, Xan-CH_3).**^{11}B** NMR (128 MHz, C6D6) δ -4.7. **^{31}P** NMR (202 MHz, C6D6) δ -21.7. **^{13}C** NMR (126 MHz, C6D6) δ 154.4 (d, J = 8.2 Hz, Ph-P), 136.5 (d, J = 10.9 Hz, PhP), 136.1 (d, J = 10.9 Hz, Ph-P), 134.4, 132.8, 132.6, 132.5, 132.3, 131.7, 131.2, 127.8, 127.7, 127.7, 127.4, 127.2, 126.0, 122.4, 122.1, 122.1, 121.8, 33.7 (Xan-C), 30.9 (Xan-CH_3), 29.5 (Xan-CH_3). **Mass:** $C_{81}H_{69}BNO_3P_3$ ($+H^+$) calc; 1208.4656 m/z, reported; 1208.4679 m/z **Elemental analysis:** $C_{81}H_{69}BNO_3P_3$ calc: C 80.89 % H 5.82 % N 1.12 % found: C 80.08 % H 6.00 % N 1.32 %.

8 - *(Ph_2P-xan)$_3$B-CO*

Preparation

To an NMR tube fitted with a J. Young's valve **2**, (prepared by Special Procedure A), is dissolved in *ortho*difluorobenzene and degassed by three freeze-pump-thaw cycles where 1 bar of CO was added. Crystals suitable for X-ray diffraction are formed upon standing. Quantitative conversation is seen in this concentration. Upon removal of solvent in vacuo complete conversion back to **2** is seen.

VT NMR

To an NMR tube fitted with a J. Young's valve **2**, (prepared by Special Procedure A) is dissolved in C_7D_8 (d_8-toluene) with Ph_2P-xanthH used as an internal standard. Under this concentration full conversion is not seen. **Spectroscopic data**: **^{1}H** NMR (500 MHz, C6D6) δ 7.26 (dd, J = 7.7, 1.7 Hz, 3H, ArH), 7.11 (t, J = 7.3 Hz, 12H, ArH), 7.05 (q, J = 6.9 Hz, 6H, ArH), 6.98 (d, J = 6.1 Hz, 6H, ArH), 6.91 (dd, J = 5.7, 1.8 Hz, 3H, ArH), 6.88 – 6.72 (m, 18H, ArH), 1.56 (s, 9H, Xan-CH_3), 1.05 (s, 9H, Xan-CH_3). **^{11}B** NMR (160 MHz, C6D6) δ -14.8. **^{31}P** NMR (162 MHz, C6D6) δ -21.8. **^{13}C** NMR (126 MHz, C6D6) δ 171.7 (CO), 155.6, 155.6, 155.5, 140.8 (d, J = 15.9 Hz, Ph-P), 136.9 (d, J = 17.3 Hz, Ph-P), 135.1, 134.2, 134.0, 133.7, 133.5, 132.5, 129.9, 128.8, 128.7, 127.6, 126.9, 125.7 (d, J = 18.6 Hz, Ph-P), 125.1, 124.1, 123.3, 35.0 (Xan-CH_3), 34.5 (Xan-CH_3), 27.5(Xan-C). **IR:** C-O stretch: 2178.7 cm^{-1} **Mass:** $C_{82}H_{69}BNO_4P_3$ ($+K^+$) calc; 1257.3899 m/z, reported; 1257.3896 m/z

9 - *(Ph_2P-xan)$_3$B-NCMe*

To an NMR tube fitted with a J. Young's valve **2,** (prepared by Special Procedure A) is dissolved in C_6D_6 and Acetonitrile solution (0.1 in d6-benzene M, 0.0210 mmol, 0.21 mL) is added. Crystal suitable for X-ray diffraction were obtained upon standing. Quantitative conversation is seen. Upon removal of solvent in vacuo complete conversion back to **2** is seen. **Spectroscopic data**: **^{1}H** NMR (500 MHz, C6D6) δ 7.32 (dd, J = 7.7, 1.7 Hz, 3H, ArH), 7.21 (dd, J = 7.4, 1.7 Hz, 3H, ArH), 7.18 (d, J = 1.7 Hz, 3H, ArH), 7.15 – 6.99 (m, 18H), 6.87 – 6.76 (m, 15H, ArH), 6.74 (t, J = 7.6 Hz,

3H, ArH), 1.65 (s, 9H, Xan-CH_3), 1.34 (s, 9H, Xan-CH_3), 0.60 (s, 3H, NC-CH_3 (overlapped with free MeCN)). **^{11}B** NMR (160 MHz, C6D6) δ -5.3. **^{31}P** NMR (202 MHz, C6D6) δ -19.7. **^{13}C** NMR (126 MHz, C6D6) δ 156.8 , 140.5 (d, J = 16.8 Hz, PhP), 140.4 (d, J = 19.1 Hz, PhP), 137.9 (Me-CN) 135.8, 134.3, 134.1, 133.8, 133.2 (d, J = 2.8 Hz, PhP), 133.0, 132.9, 129.5, 128.6 (d, J = 4.6 Hz, PhP), 127.4, 126.8, 124.4, 124.3, 123.8, 123.3, 123.1, 115.9, 35.1 (Xan-CH_3), 34.7 (Xan-CH_3), 27.0 (Xan-C), 0.1 (NC-CH_3 (overlapped with free MeCN)). **IR:** C-N stretch: 2356.0 cm^{-1} **Mass:** $C_{83}H_{69}BNO_3P_3$ ($+H^+$) calc; 1232.4656 m/z, reported; 1232.4268 m/z

10 - $(Ph_2P\text{-}xan)_3B\text{-}CN^tBu$

To an NMR tube fitted with a J. Young's valve **2**, (prepared by Special Procedure A) is dissolved in toluene and tert-Butyl isocyanide solution (1 M in toluene, 0.2 mmol, 0.2 mL) is added. The solution was then heated at 80°C for 18 hours where quantitative conversation can be seen. Solvent was then removed in vacuo and redissolved in C_6D_6. Crystals suitable for X-ray diffraction were obtained by slow evaporation of solvent into silicon oil over the course of a week. **Spectroscopic data**: **^{1}H** NMR (500 MHz, C6D6) δ 7.26 – 7.17 (m, 9H, ArH), 7.11 (d, J = 5.6 Hz, 3H, ArH), 7.01 (dp, J = 8.6, 2.7 Hz, 21H, ArH), 6.94 – 6.89 (m, 9H, ArH), 6.72 (dt, J = 16.8, 7.5 Hz, 6H, ArH), 1.55 (s, 9H, Xan-CH_3), 1.26 (s, 9H, Xan-CH_3), 0.52 (s, 9H, CN-^{t}Bu). **^{11}B** NMR (160 MHz, C6D6) δ -16.2. **^{31}P** NMR (202 MHz, C6D6) δ -22.0. **^{13}C** NMR (126 MHz, C6D6) δ 158.3, 158.12(N-C), 157.1 , 142.0 (d, J = 18.7 Hz, PhP), 139.3 (d, J = 18.8 Hz, PhP), 136.6, 136.2, 134.7 (d, J = 3.3 Hz, PhP), 133.7, 133.6, 133.4, 133.3, 129.5, 128.6, 127.5 (d, J = 5.5 Hz, PhP), 126.3, 124.1, 124.0, 123.7, 123.5, 123.2, 35.3 (Xan-CH_3), 34.0 ($C(CH_3)_3$), 30.2 (Xan-C), 28.1 (Xan-CH_3), 24.8 (CN-^{t}Bu). **IR:** C-O stretch: 2284.5 cm^{-1} **Mass:** $C_{86}H_{75}BNO_3P_3$ ($+H^+$) calc; 1274.5126 m/z, reported; 1274.5138 m/z

11 - $[(Ph_2P\text{-}xan)_3B\text{-}CN][TBA]$

In order to prevent the formation of HCN gas, a modified preparation of **2** is used. **2** (25 mg, 0.0210 mmol) and P_2O_5 (25, 0.0881 mmol mg) is added to an NMR tube fitted with a J. Young's valve and dissolved in toluene and heated at 50°C for 3 hours with regular agitation. The solution

is then filtered through a syringe filter into a vial and LiH (10 mg, 1.26 mmol) is added and agitated for 15 minutes. The resulting suspension is filtered through a syringe filter into an NMR tube fitted with a J. Young's valve with Tetrabutylammonium cyanide (5.64 mg, 0.0210 mmol). The solution was then heated at 80°C for 18 hours where quantitative conversation can be seen and solvents are removed in vacuo. Crystals suitable for X-ray diffraction where obtained through heating a suspension of **11** till it fully dissolved and slow cooling the solution to room temperature. **Spectroscopic data**: **^{1}H** NMR (500 MHz, C6D6) δ 9.75 (d, J = 6.9 Hz, 2H, ArH), 8.72 (s, 2H, ArH), 7.93 (t, J = 6.6 Hz, 3H, ArH), 7.62 (t, J = 6.7 Hz, 3H, ArH), 7.52 (d, J = 7.4 Hz, 2H, ArH), 7.45 (t, J = 6.9 Hz, 5H, ArH), 7.37 (t, J = 7.1 Hz, 3H, ArH), 7.25 (ddd, J = 22.0, 14.6, 7.2 Hz, 6H, ArH), 7.19 – 7.12 (m, 4H, ArH), 7.10 (s, 6H, ArH), 7.14 – 7.03 (m, 3H, ArH), 7.03 – 6.89 (m, 3H, ArH), 6.79 – 6.61 (m, 5H, ArH), 6.34 (t, J = 7.3 Hz, 1H, ArH), 2.66 – 2.59 (m, 8H, N-*CH_2*), 1.71 (d, J = 3.5 Hz, 6H, Xan-*CH_3*), 1.60 (s, 3H, Xan-*CH_3*), 1.30 (s, 3H, Xan-*CH_3*), 1.08 (p, J = 7.5 Hz, 8H, CH_2-*CH_2*-CH_2), 0.99 (p, J = 7.1 Hz, 11H, CH_2-*CH_2*-CH_3), 0.91 (s, 3H), 0.73 (t, J = 7.2 Hz, 12H, CH_2-*CH_3*). **^{11}B** NMR (128 MHz, C6D6) δ -13.58. **^{31}P** NMR (202 MHz, C6D6) δ -18.0, -20.2, -23.7. **^{13}C** NMR (126 MHz, C6D6) δ 155.5 (CN), 154.4, 154.0, 142.3, 141.4, 140.8, 139.5, 139.4, 138.9, 137.2, 136.7, 136.6, 136.1, 134.3, 134.2, 133.8, 133.7, 133.6, 133.4, 133.3, 132.7, 132.5, 132.4, 131.3, 129.0, 127.2, 126.1, 125.6, 125.5, 125.3, 123.3, 121.4, 121.1, 121.0, 120.6, 120.5, 120.2, 56.8 (N-*CH_2*), 35.0(Xan-*CH_3*), 33.5 (Xan-*CH_3*), 33.1(Xan-*CH_3*), 29.6 (Xan-*C*), 27.8 (Xan-*C*), 27.6 (Xan-*C*), 22.9 (CH_2-*CH_2*-CH_2), 18.5 (CH_2-*CH_2*-CH_3), 12.7 (CH_2-*CH_3*). **Mass:** $C_{82}H_{66}BNO_3P_3$ (-) calc; 1216.4354 m/z, reported; 1216.4397 m/z

6 - (iPr2P-xan)$_3$B-NH$_2$Me

To a solution of ^{i}Pr2P-xan-Li (500 mg, 1.504 mmol) in toluene (50 mL) at -78°C was added dropwise a solution of boron tribromide (1M mL in Toluene, 1.00 mmol, 1 mL). The resulting solution was stirred for 1 hour at -78°C then was allowed to warm to room temperature where it was stirred for a further 16 hours. Methyl amine (1 M in THF, 5 mmol, 5 ML) was then added and the resulting cloudy solution becomes less turbid. Volatiles were removed in vacuo and the

sticky white powder is extracted into toluene and the product is filtered. Volatiles were once again removed in vacuo. Yield: 432 mg (84.6 %). Crystals suitable for X-ray diffraction could be obtained through recrystallisation in benzene at room temperature. **Spectroscopic data**: **^{1}H** NMR (500 MHz, C_6D_6) δ 7.99 (s, 1H, NH), 7.62 (s, 1H,NH), 7.45 – 7.39 (m, 1H, ArH), 7.35 – 7.30 (m, 3H, ArH), 7.09 (dt, *J* = 7.51, 2.25 Hz, 3H, ArH), 7.03 – 6.88 (m, 6H, ArH), 6.82 (t, *J* = 7.53 Hz, 3H, ArH), 3.48 (d, *J* = 6.02 Hz, 3H, NCH_3), 2.47 – 2.28 (m, 3H, CH), 1.84 (pd, *J* = 7.04, 3.10 Hz, 3H, CH), 1.67 (s, 9H, Xan-CH_3), 1.58 (s, 9H, Xan-CH_3), 1.23 (q, *J* = 7.02 Hz, 2H, CH_2CH_3), 1.05 – 0.91 (m, 18H, CH_2CH_3), 0.69 – 0.54 (m, H, CH_2CH_3).**11B** NMR (160 MHz, C6D6) δ -1.4. **31P** NMR (202 MHz, C6D6) δ -12.0. **13C** NMR (126 MHz, C6D6) δ 155.0, 136.8, 131.7, 130.5, 130.1, 128.8, 128.0, 126.1, 123.4, 122.9, 121.7, 116.4, 34.5 (Xan-C), 31.3 (Xan-CH_3), 31.3 (Xan-CH_3), 24.5 (CH), 24.4 (CH), 23.7 (CH), 23.6(CH), 23.5 (NCH_3), 20.8 (CH_3), 20.6(CH_3), 20.0(CH_3), 19.9(CH_3), 19.9(CH_3), 19.8(CH_3), 19.8(CH_3), 19.7(CH_3), 19.6(CH_3), 18.4(CH_3), 18.3(CH_3). **Mass:** $C_{64}H_{83}BNO_3P_3$ ($+H^+$) calc; 1018.5752 m/z, reported; 1018.5775 m/z. **Elemental analysis:** $C_{64}H_{83}BNO_3P_3$ calc: C 76.12 % H 8.20 % N 1.32 % found: C 75.48 % H 8.03 % N 1.27 %

7 - (iPr2P-xan)$_3$B-NH$_3$

To an NMR tube fitted with a J. Young's valve **6** (25 mg, 0.0246 mmol) is dissolved in C_6D_6 degassed by three freeze-pump-thaw cycles where 1 bar of NH_3 was added. The solution was then heated at 80°C for 72 hours. Crystals suitable for X-ray diffraction could be obtained through slow evaporation of the solvent into silicon oil over a week. In all cases <50% conversation is seen and **6** co-crystallises and separation is not possible. NMR and mass data from product mixture. ^{1}H NMR could not be assigned as overlaps significantly with the ($^{i}Pr_2$P-xan)$_3$B-MeNH$_3$, especially in the ^{i}Pr region of the spectrum. **Spectroscopic data**: **^{11}B** NMR (128 MHz, C6D6) δ -5.3. **^{31}P** NMR (162 MHz, C6D6) δ -12.9. **Mass:** $C_{63}H_{81}BNO_3P_3$ ($+K^+$) calc; 1042.5154 m/z, reported; 1042.5148 m/z (mass of **6** also observed)

Spectroscopic Data

CO NMR

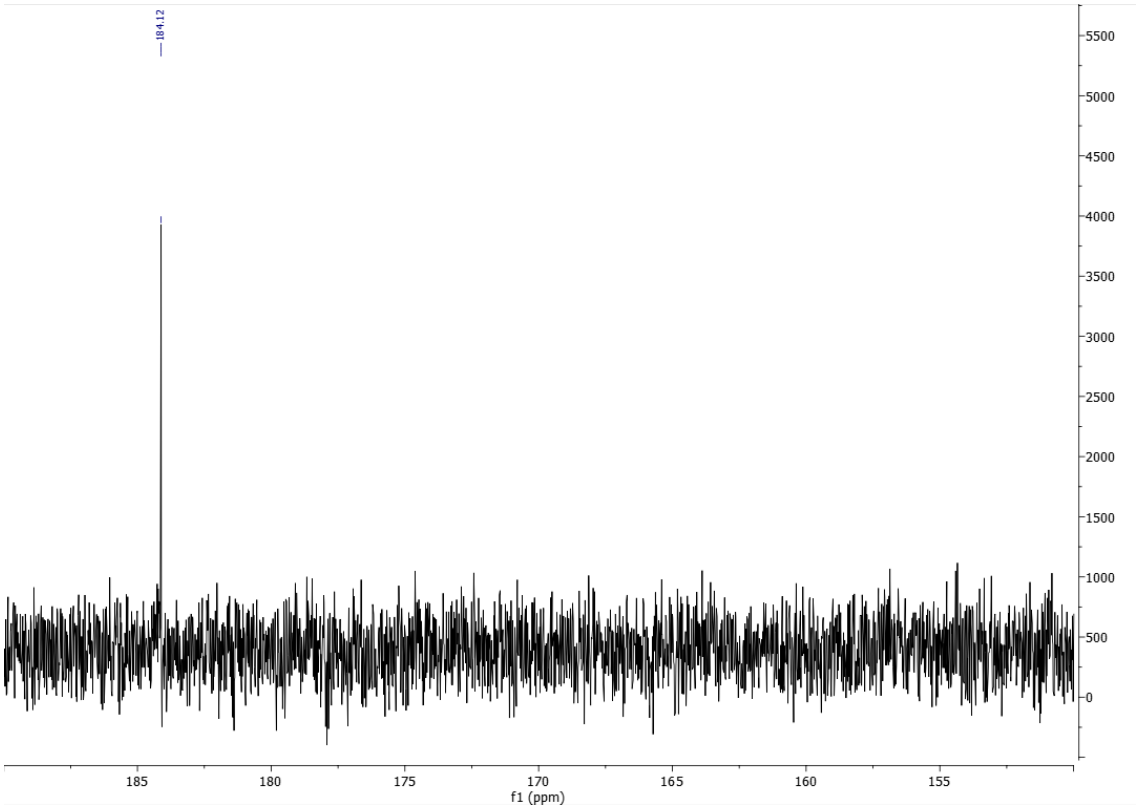

S 8.1 ^{13}C NMR of CO dissolved in d6-Benzene using a 2 s relaxation delay (standard Brucker pulse sequence) after 3000 scans

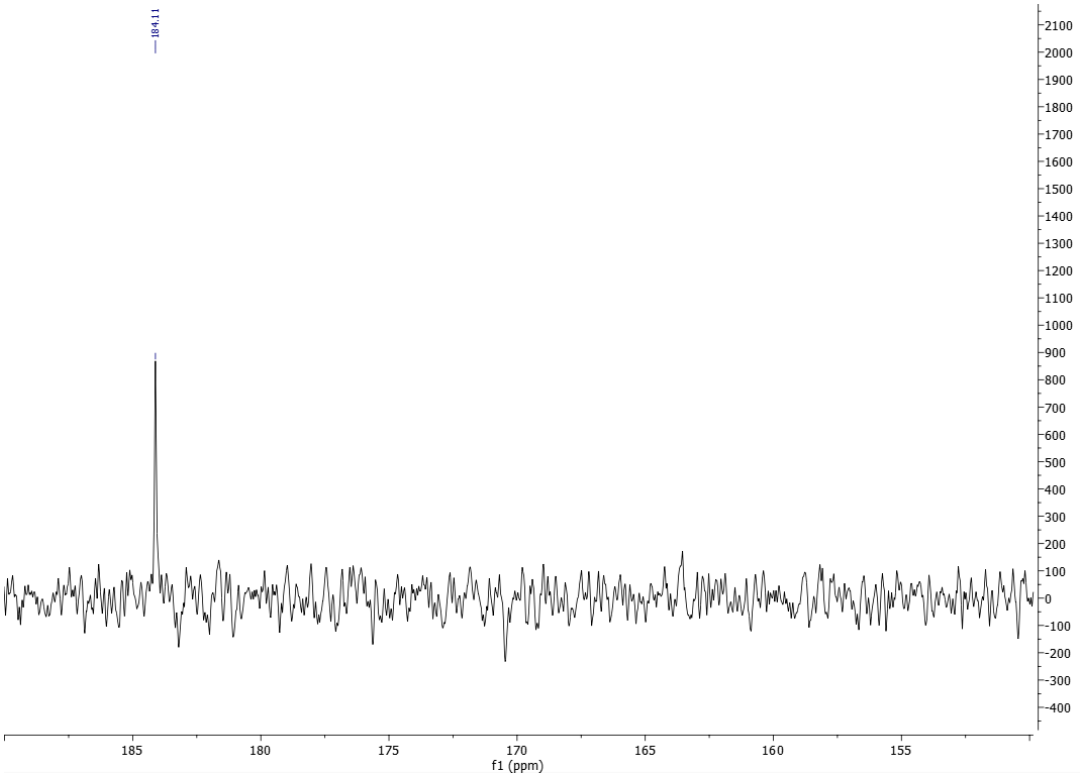

S 8.2: ^{13}C NMR of CO dissolved in d6-Benzene using shortened 0.10 s delay after 3000 scans

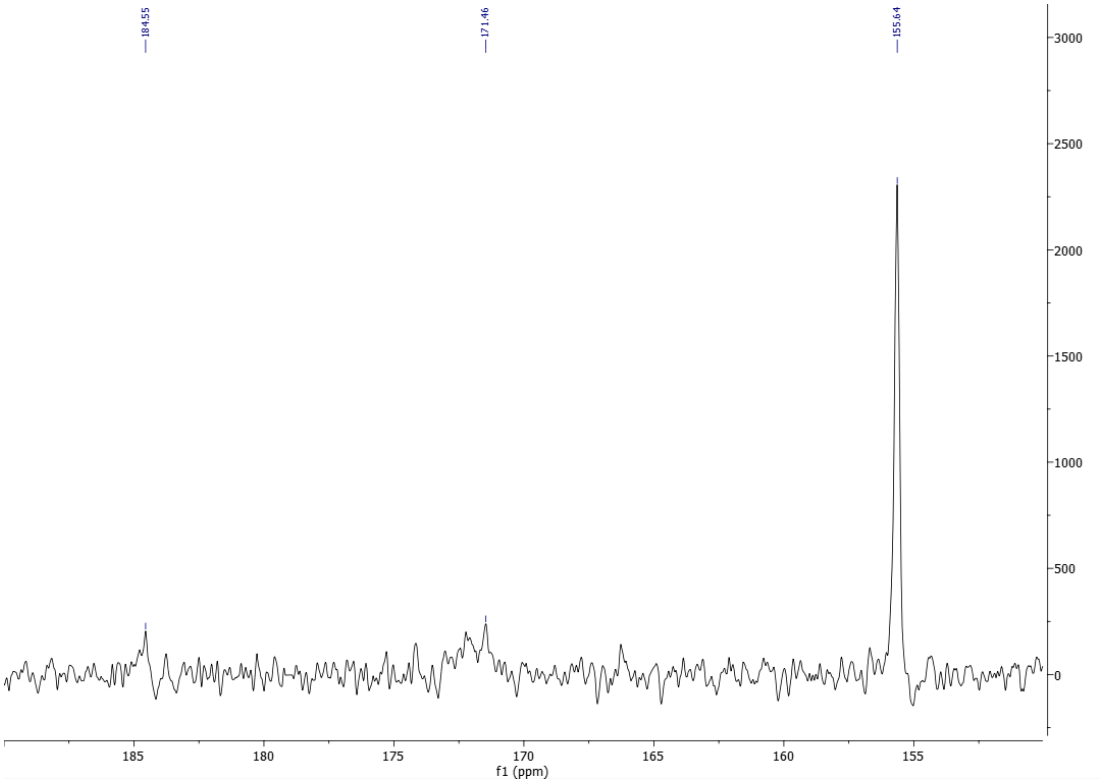

S 8.3: ^{13}C NMR of **2** dissolved in d6-Benzene using a 2 s relaxation delay (standard Brucker pulse sequence) after 10,000 scans

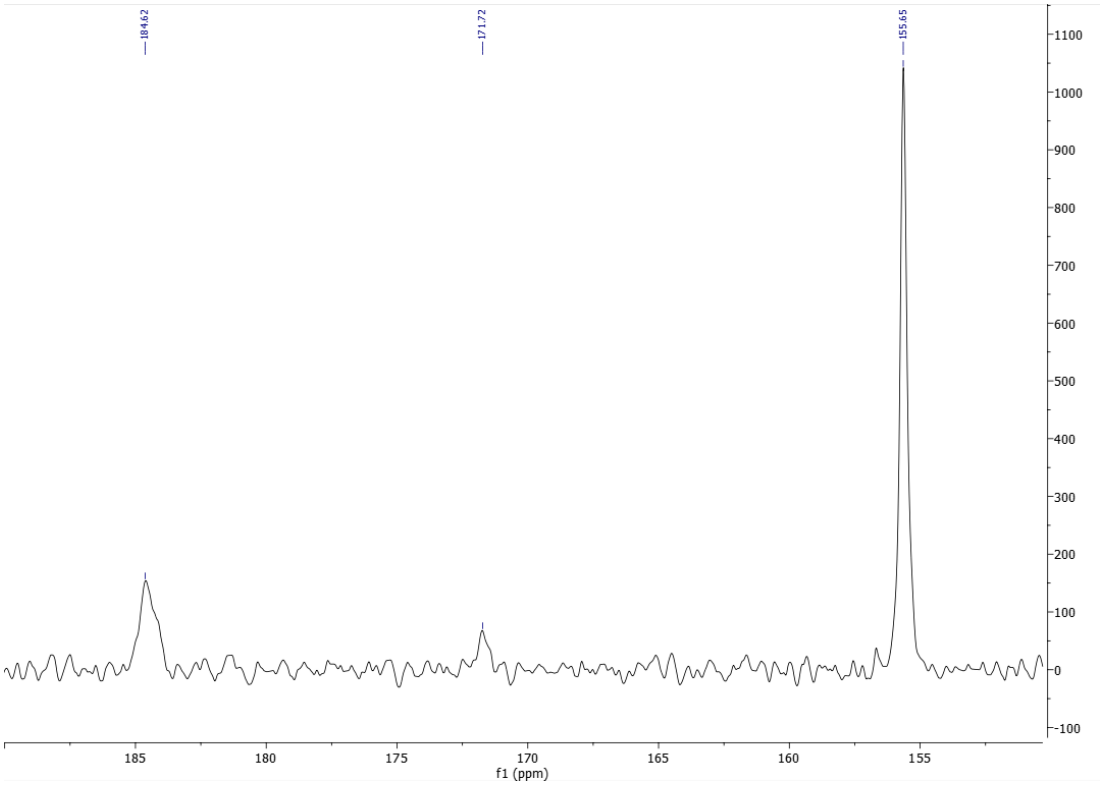

S 8.4: ^{13}C NMR of **2** dissolved in d6-Benzene using shortened 0.10 s delay after 100,000 scans

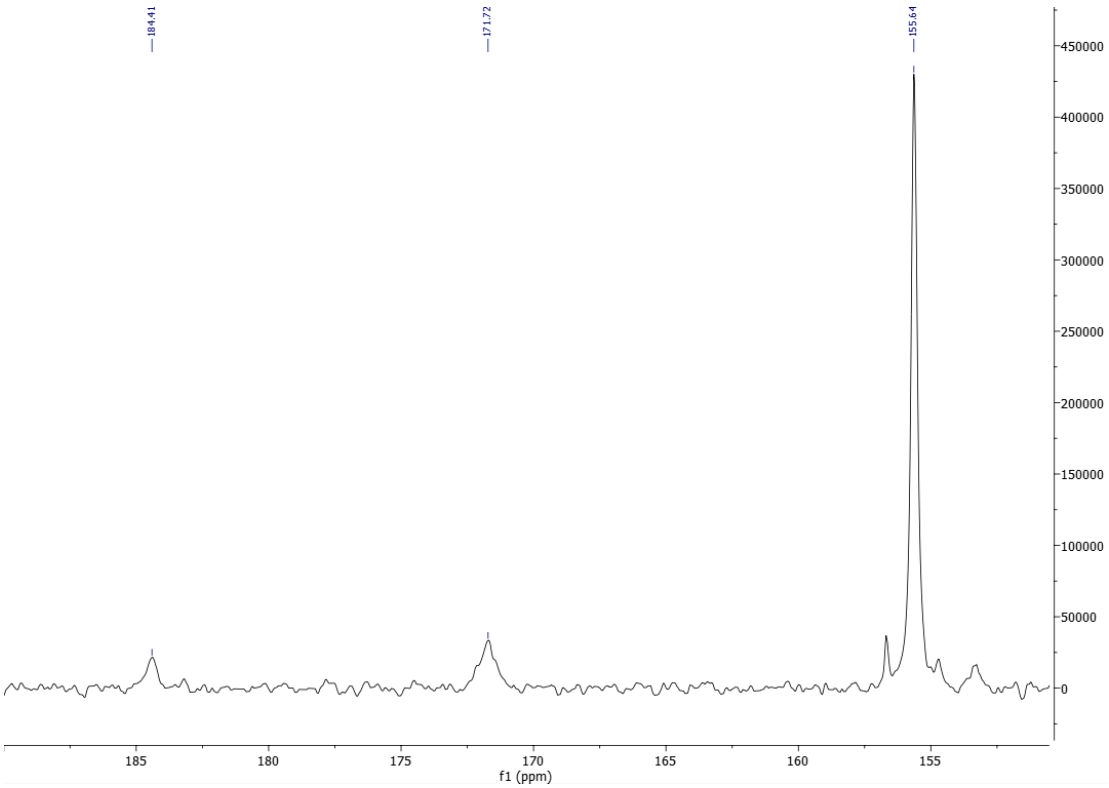

S 8.5: ^{13}C NMR of **2** dissolved in d6-Benzene using shortened 0.10 s delay after 250,000 scans with more concentrated sample (35 mg per 0.5 mL of C6D6). Trace (Ph2P-xan)3BOH_2 can be seen around the resonance at 155.64 ppm.

In order to find the broad ^{13}C CO resonance we employed the fact CO is bound to a quadrupolar $^{11/10}B$ nuclei and used a short T1 experiment (0.16 s delay) in the region of interest as the ^{13}C nuclei should relax much quicker. The standard Bruker ^{13}C experiment (2 s relaxation delay) does not yield a strong free CO or bound CO resonance after 10 hours (**S 8.3**) however, using the shortened T1 delay a resonance can be observed at 171.72 ppm with free CO also visible at 184.41 ppm after 100,000 scans (**S 8.4**). In order to get a clearer spectrum, the same region was probed on a more concentrated sample for 250,000 scans (**S 8.5**). The resonance at 171.72 is clearly distinguishable to free CO (**S 8.1**, **S 8.2**), and is shifted upfield consistent with the CO IR stretch indicating a strengthening of the C-O bond.

VT NMR

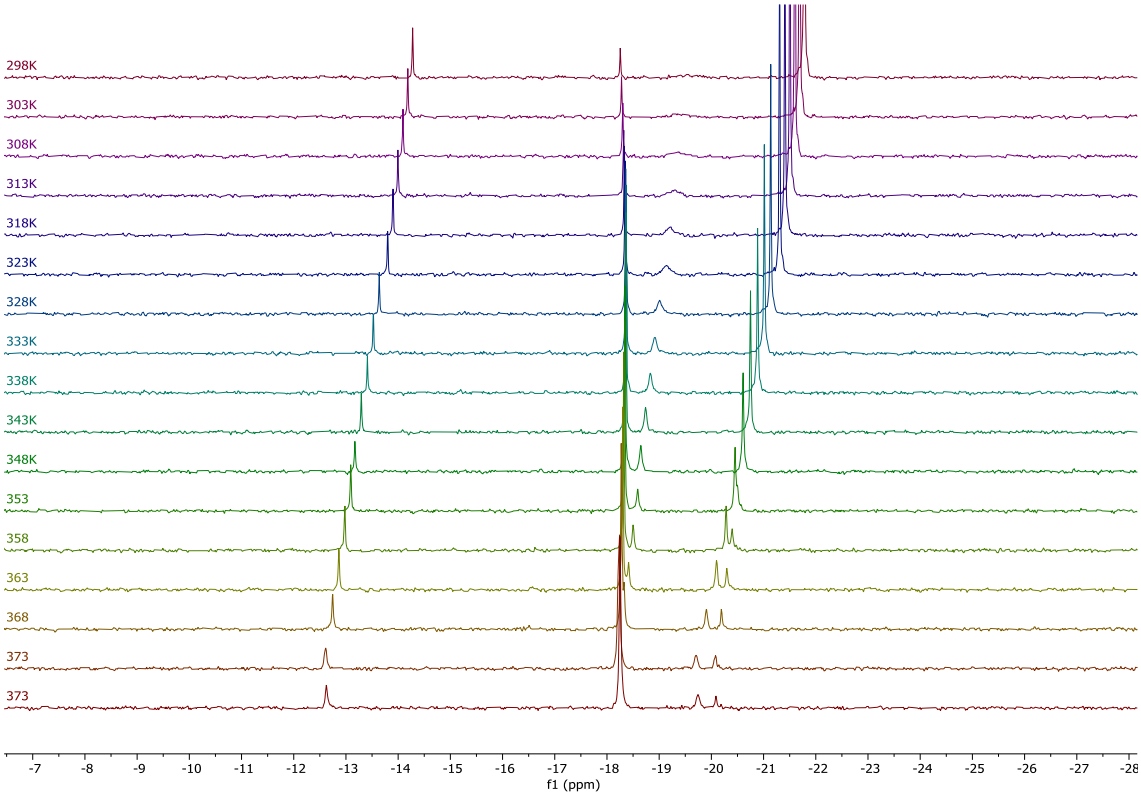

S 8.6 ^{31}P VT NMR from 298-373K of CO uptake of **2**

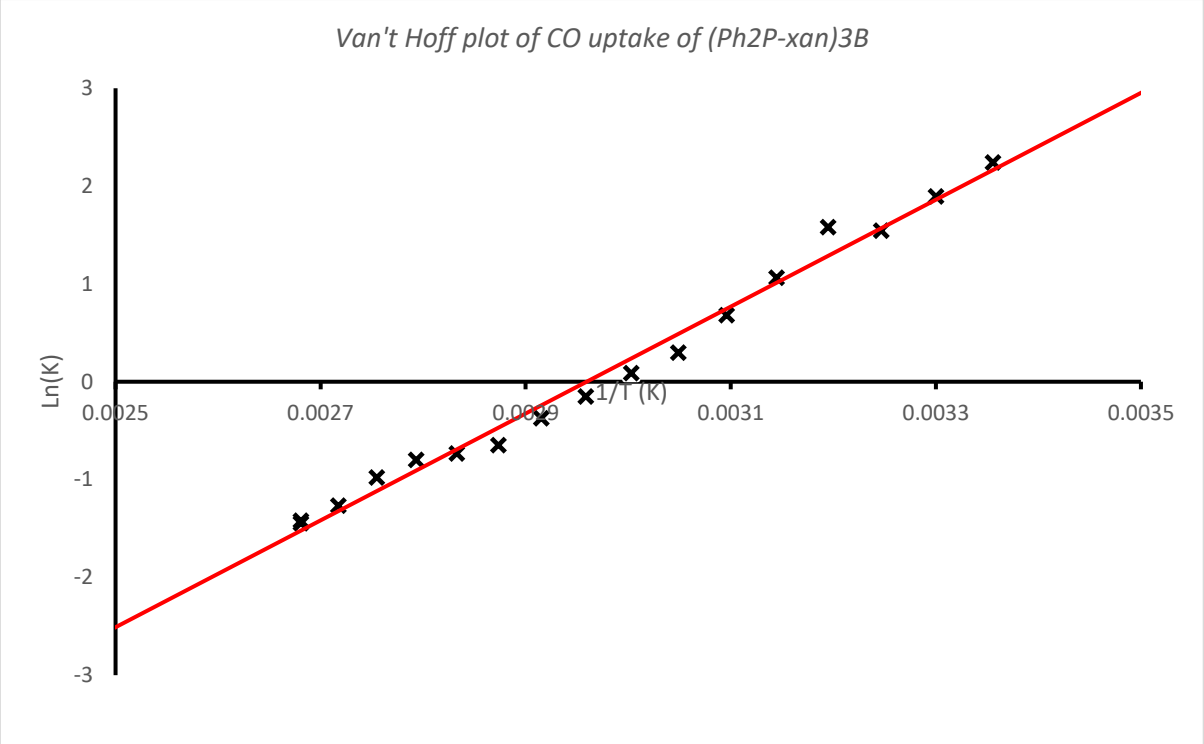

S 8.7: Van't Hoff plot of CO uptake of **2** with ΔH of -10.86 Kcal/mol and a ΔS of -32.12 cal/mol

Crystallographic Data

Methods

All data was collected wither on the Rigaku XtaLAB Synergy-DW VHF equip with a PhotonJet-R dual wavelength rotating anode and HyPix-Arc 150° detector or Oxford Diffraction/Agilent SuperNova. Crystals were prepared with Paratone-N or perfluorinated oil, mounted on MiTeGen Micromount loops, and quench-cooled with an Oxford Cryosystems open flow N2 cooling device ([70]). Specific data collection details are in Table 1. Data processing involved CrysAlisPro:[71] unit cell refinement, SCALE3 ABSPACK inter-frame scaling, merging equivalent reflections, and diffraction pattern processing. Structures were solved using SHELXT and refined with SHELXL in OLEX2 ([72–74]). Crystallographic data is in supplementary CIF files (2321565,2321566, 2321567, 2321568, 2322595 and 2322556) available free via the Cambridge Crystallographic Data Centre: http://www.ccdc.cam.ac.uk/data_request/cif."

X-ray tables

Name	*123aec23*	*134aeccm21*	*153aec23*	*156aec23*	*157aec23*	*163aec23*	*194aec23*	*280aec23*	*301aec23*	*330aec23*	*332aec23*
chemical formula	$C_{93}H_{81}BNO_3P_3$	$C_{81}H_{66}BO_3P_3$	$C_{82}H_{71}BNO_3P_3$	$C_{81}H_{68}BO_4P_3$	$C_{95}H_{83}BLiO_3P_3$	$C_{64}H_{83}BNO_3P_3$	$C_{66}H_{84}BNO_3P_3$	$C_{82}H_{66}BO_4P_3$	$C_{86}H_{75}BNO_3P_3$	$C_{98}H_{102}BN_2O_3P_3$	$C_{83}H_{69}BNO_3P_3$
Molecular weight	1364.3	1191.05	1222.11	1209.07	1383.27	1018.03	1043.06	1219.06	1274.19	1459.53	1232.11
Space group system	triclinic	triclinic	triclinic	monoclinic	triclinic	monoclinic	monoclinic	triclinic	trigonal	monoclinic	triclinic
Space group (Hall)	P -1	P -1	P -1	P 1 21/n 1	P -1	P 1 21/n 1	C 1 2/c 1	P -1	P 3 1 c	P 1 21 1	P -1
a	12.1687(2)	15.1342(4)	10.97770(10)	12.08526(4)	12.41167(6)	11.55435(4)	41.6461(8)	11.90675(7)	19.1556(4)	12.53360(10)	11.2305(2)
b	13.4038(3)	15.2088(4)	14.3258(2)	15.08018(5)	12.60674(7)	49.6560(2)	11.7710(2)	13.32636(10)	19.1556(4)	21.26540(10)	14.9413(2)
c	24.8061(6)	15.7792(4)	21.8808(3)	38.06644(12)	23.43695(12)	20.45834(8)	24.2165(5)	43.7452(2)	28.8526(5)	15.29760(10)	21.0548(2)
α	85.415(2)	101.097(2)	81.6380(10)	90	95.7034(4)	90	90	82.2865(5)	90	90	92.3870(10)
β	85.545(2)	102.429(2)	77.8480(10)	94.2325(3)	92.7202(4)	99.5935(4)	90.411(2)	89.6844(5)	90	93.4700(10)	94.8310(10)
γ	64.878(2)	94.734(2)	70.2100(10)	90	93.8046(4)	90	90	69.1539(6)	120	90	109.9740(10)
V	3647.30(15)	3451.27(16)	3154.99(7)	6918.61(4)	3635.60(3)	11573.66(8)	11871.0(4)	6421.44(8)	9168.7(4)	4069.82(5)	3299.28(8)
Z	2	2	2	4	2	8	8	4	4	2	2
T (K)	150.00(10)	150.00(16)	100.00(10)	100.00(10)	100.00(10)	100.01(10)	150.01(10)	100.00(10)	100.00(10)	100.00(10)	99.99(10)
Unique reflections	25340	14826	54774	199490	129526	167096	17235	122492	19949	66623	39694
Collected reflections	63406	37317	139362	338660	163951	400055	43339	293614	71726	120883	84732
Mu	1.161	1.154	1.28	1.169	1.166	1.284	1.264	1.265	0.896	1.072	1.229
Radiation	Cu K\a	Cu K\a	Cu K\a	Cu K\a	Cu K\a	Cu K\a	Cu K\a	Cu K\a	CuK\a	Cu K\a	Cu K\a
λ	1.54184	1.54184	1.54184	1.54184	1.54184	1.54184	1.54184	1.54184	1.54184	1.54184	1.54184
Parameters	972	799	826	890	1002	1351	659	1946	568	975	870
R_{all}	0.0523	0.0516	0.0497	0.0394	0.0326	0.0418	0.0473	0.0623	0.0783	0.0407	0.0501
R_{gt}	0.0384	0.0402	0.0441	0.0356	0.0321	0.0365	0.0387	0.0554	0.0612	0.0388	0.0443
wR	0.1011	0.1058	0.1231	0.0991	0.0821	0.0989	0.1043	0.1456	0.1735	0.1009	0.1236
R_{int}	0.043	0.0413	0.0333	0.035	0.0229	0.0362	0.0331	0.0368	0.0406	0.0835	0.0435
goof	1.012	1.041	1.032	1.028	1.038	1.022	1.03	1.058	0.996	1.024	1.028

DFT

General procedure

All calculations performing with the ORCA (Revision 5.0.4) program.[75–77] All compounds where first optimised using the meta-generalized-gradient approximation (mGGA) functional R2-SCAN[78] in conjunction with the Def2-TZVPPm basis set[79] with the D4 dispersion correction[80], and employing the geometrical counterpoise correction gCP[81] (together known as the R2SCAN-3c method)[79]. Frequency calculations were performed to confirm the nature of minima by the lack of imaginary frequencies. Frequency calculations were also used to generate simulated IR spectra using the Avogadro visualiser.[82] Single point calculations where then performed using the ωB97x range separated hybrid functional[83,84] with the D4 dispersion correction alongside the Def2-TZVP basis set[85,86] and solvation of benzene with the conductor-like polarizable continuum model, CPCM for Benzene.[87]

Weak bonding analysis

Bonding analysis was performed on the wavefunctions using the Multiwfn(QTAIM/NCI) and NBO7 programmes.[55,88,89] In order to visualise the weak interactions causing the assembly of the cage conformation and its ability to accept molecules into the pocket non-covalent indicator [90] (NCI) surface coupled with the topological bond critical paths and bond critical points (BCP) from the atoms and molecules framework (QTAIM) [91] was used.

Analysis of the NCI surface reveals why the cage conformation is favoured in both the iPr and Ph systems (-11.91 and -32.67 ΔG Kcal/mol respectively) increased Van der Waal regions, shown by the green isosurfaces, between the xanthene backbone groups than with the open conformation. Supporting this analysis, the increased presence bond critical paths linking the adjacent xanthene backbones indicating more intramolecular bonding regions. This difference can be seen to be less prevalent for the iPr cage with the open conformation still maintaining a significant number of intramolecular interaction regions.

Blue regions on the NCI surface can be seen in the case of the protic bond systems (NH_3, H_2O and $MeNH_2$) which are indicative of hydrogen bonding.[92] Second order perturbation theory (SOPT) within NBO also identified these hydrogen bonding interactions. For the CO analogues a shroud of Van der Waal interactions surrounding the central molecule with bonding critical points indicating the importance of weak forces in the formation of these complexes.

Weak interactions are also prevalent in the CO analogues with Van der Waal regions shrouding the complexed molecule linked by a number of bond paths.

ST 8.1: NBO Second order perturbation theory values for the EH···P interaction in Kcal/mol. EH···P (1) is the first hydrogen bond, EH···P (2) is the second hydrogen bond, total is the sum of the hydrogen bonds to phosphorus in the species

	3	***5***	***4***	***7***	***6***
EH···P (1)	22.48	7.37	1.3	18.56	14.89
EH···P (2)		5.61	8.84	12.52	18.79
EH···P (3)				8.42	
total	22.48	12.98	10.14	39.5	33.68

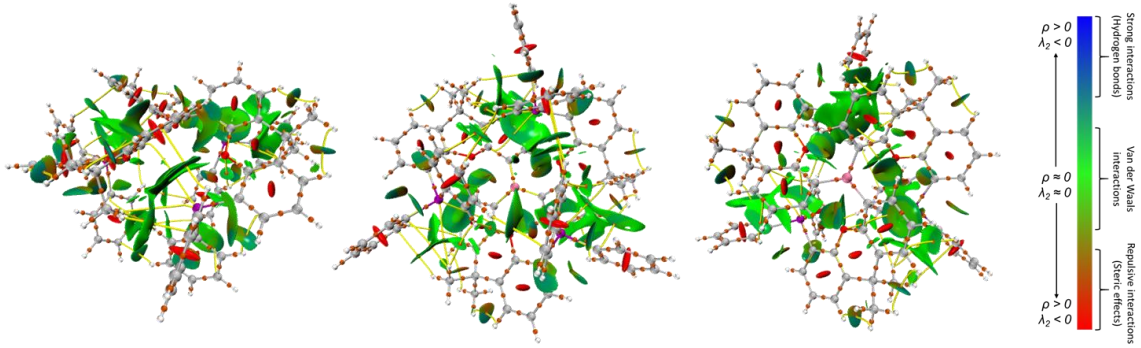

S 8.8: NCI of Free **2** in cage conformation with the isosurface of 0.5 a.u, BGR from -0.03 to 0.02, QTAIM bond paths in yellow and BCPs in orange.

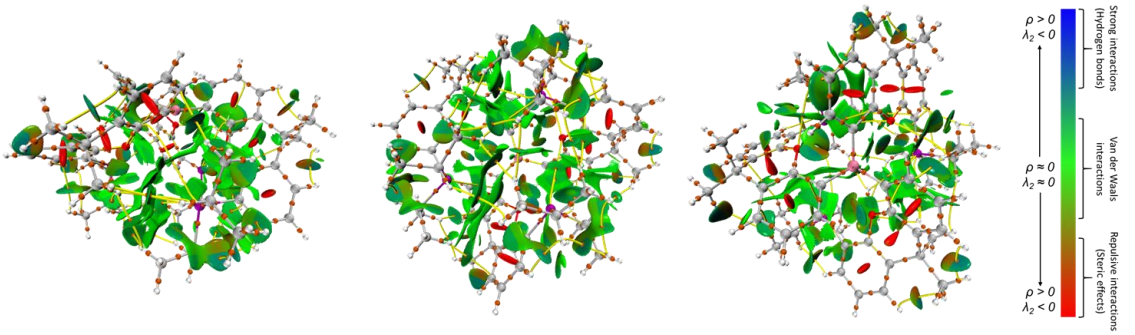

S 8.9: NCI of Free (^{i}Pr2P-xan)$_3$B in cage conformation with the isosurface of 0.5 a.u, BGR from -0.03 to 0.02, QTAIM bond paths in yellow and BCPs in orange.

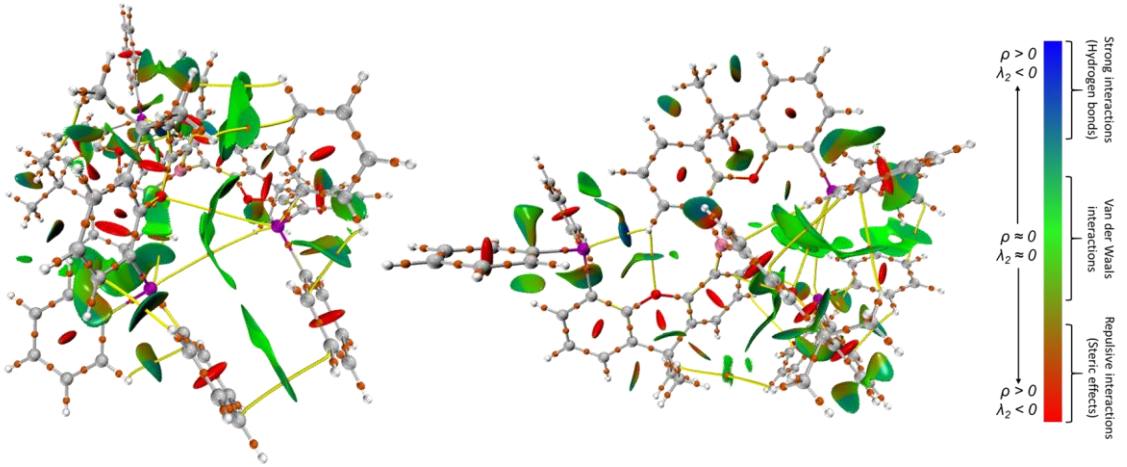

S 8.10: NCI of Free cage, **2** in open conformation with the isosurface of 0.5 a.u, BGR from -0.03 to 0.02, QTAIM bond paths in yellow and BCPs in orange.

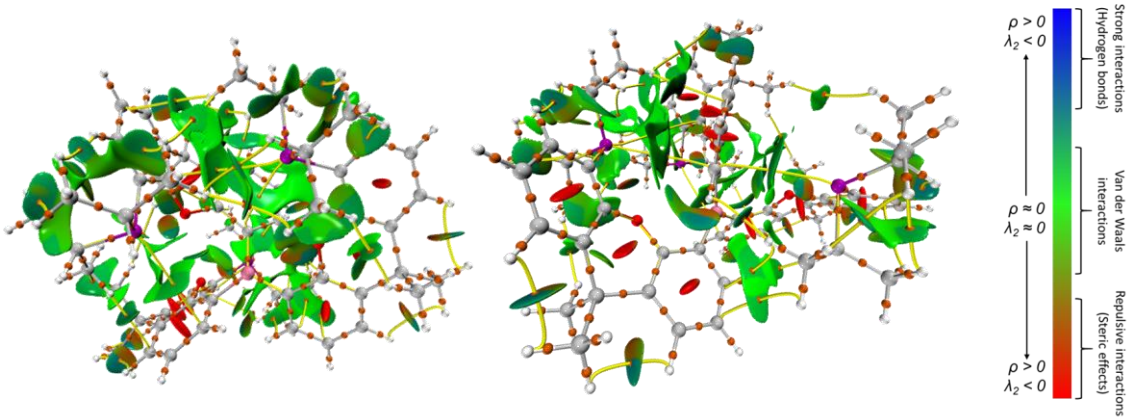

S 8.11: NCI of Free (^{i}Pr$_2$P-xan)$_3$B in open conformation with the isosurface of 0.5 a.u, BGR from -0.03 to 0.02, QTAIM bond paths in yellow and BCPs in orange.

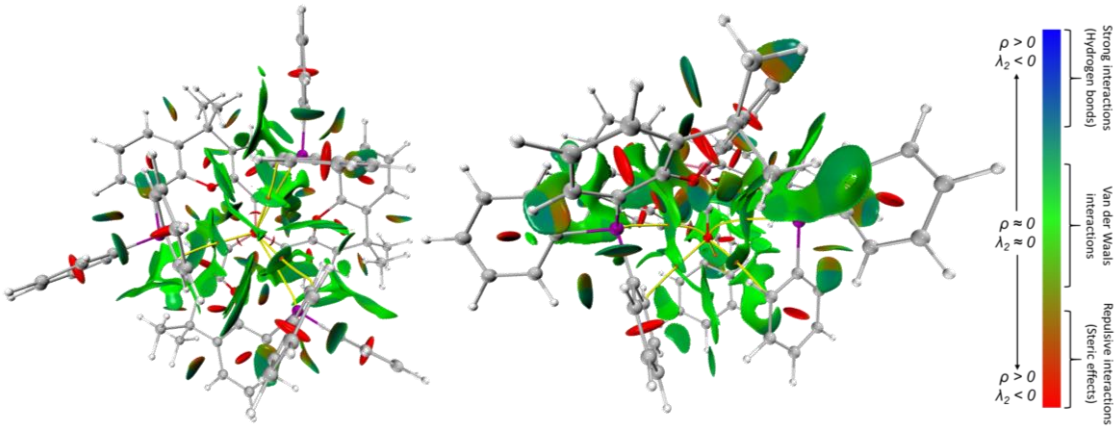

S 8.12: NCI of complex **8** with the isosurface of 0.5 a.u, BGR from -0.03 to 0.02, QTAIM bond paths in yellow and BCPs in orange.

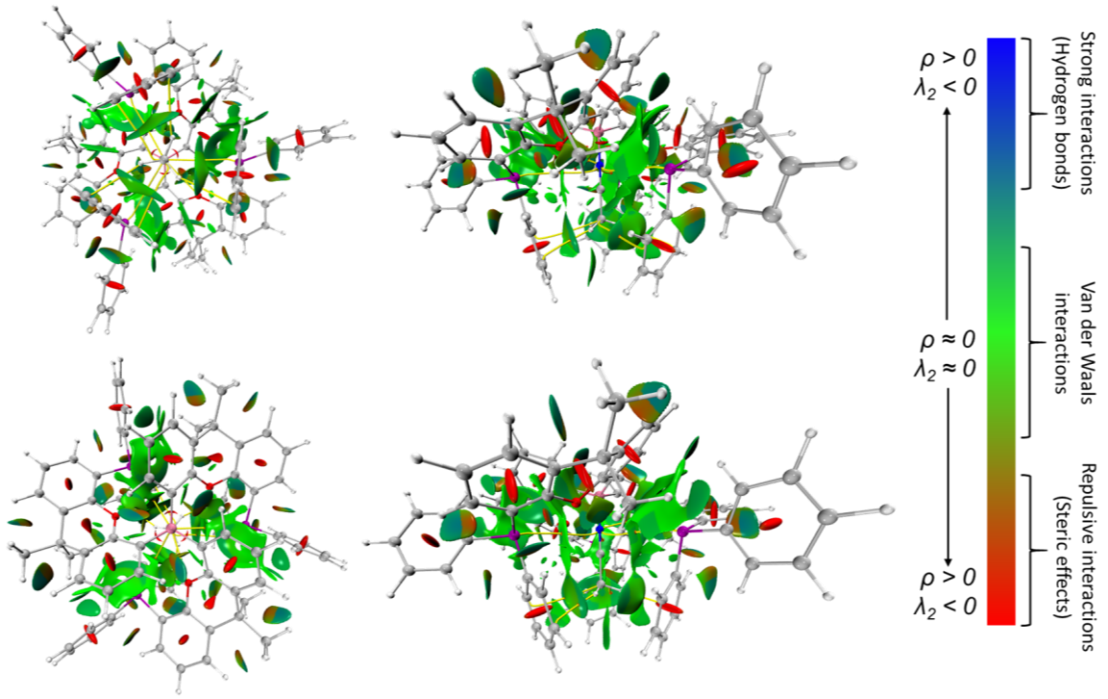

S 8.13: NCI of complex **9** with the isosurface of 0.5 a.u, BGR from -0.03 to 0.02, QTAIM bond paths in yellow and BCPs in orange.

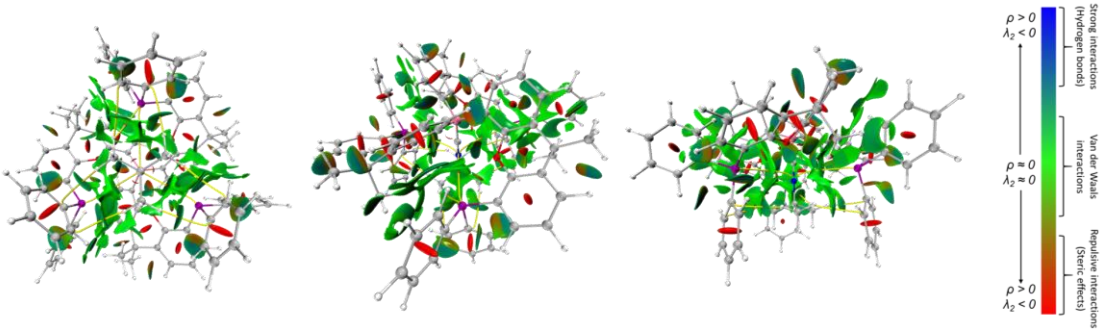

S 8.14: NCI of complex **10** with the isosurface of 0.5 a.u, BGR from -0.03 to 0.02, QTAIM bond paths in yellow and BCPs in orange.

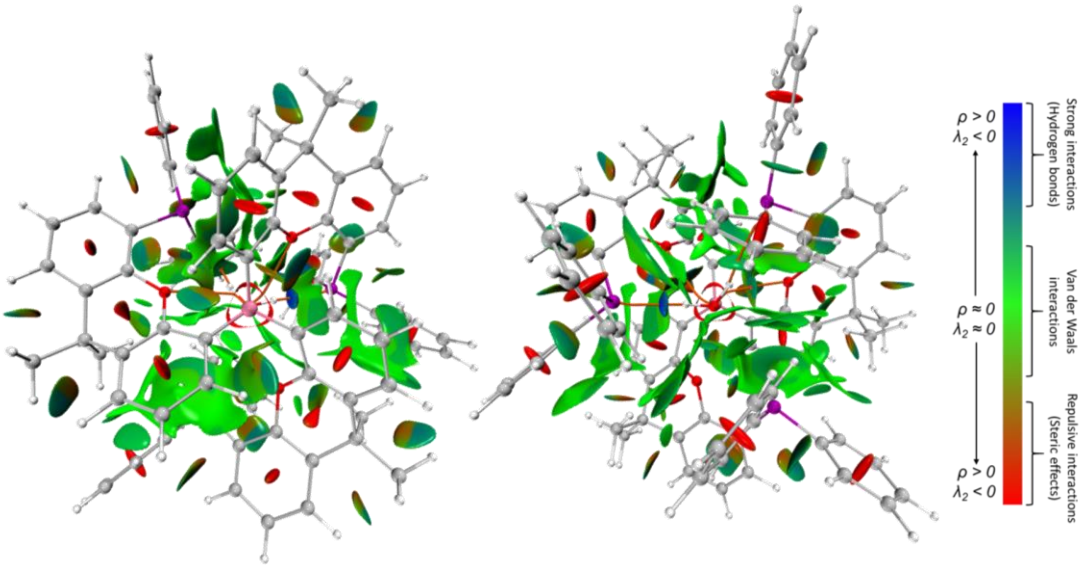

S 8.15: NCI of complex **3** with the isosurface of 0.5 a.u, BGR from -0.03 to 0.02, QTAIM bond paths in yellow and BCPs in orange.

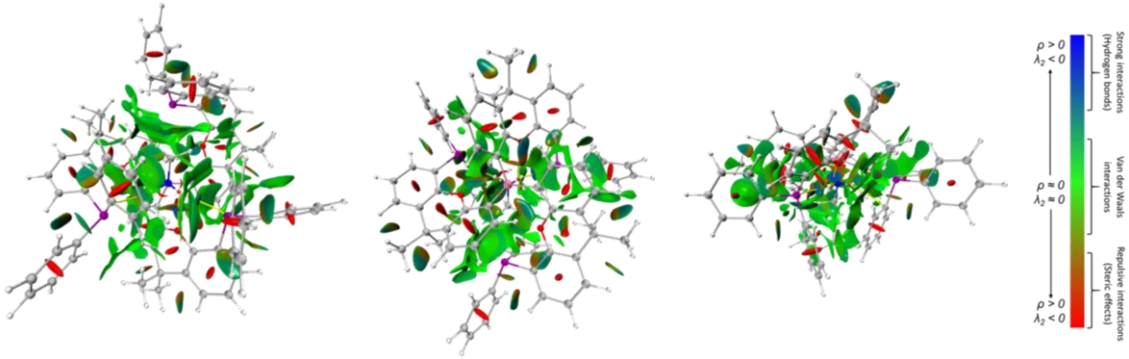

S 8.16: NCI of complex **4** with the isosurface of 0.5 a.u, BGR from -0.03 to 0.02, QTAIM bond paths in yellow and BCPs in orange.

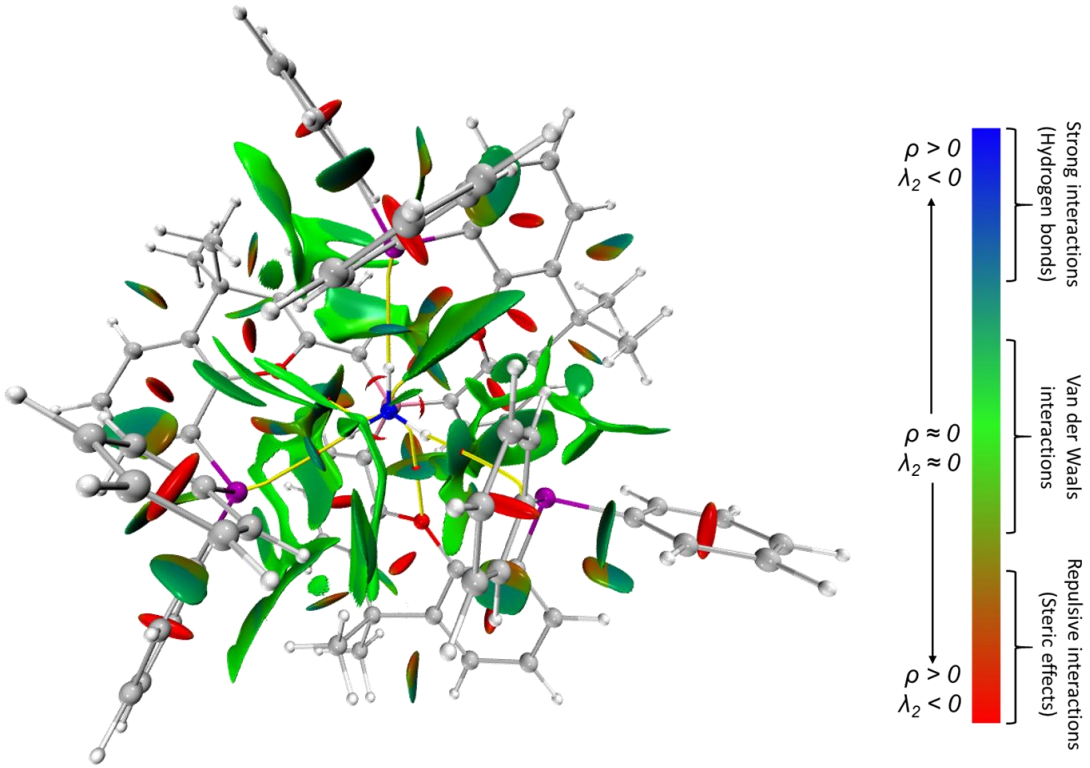

S 8.17: NCI of complex **5** with the isosurface of 0.5 a.u, BGR from -0.03 to 0.02, QTAIM bond paths in yellow and BCPs in orange.

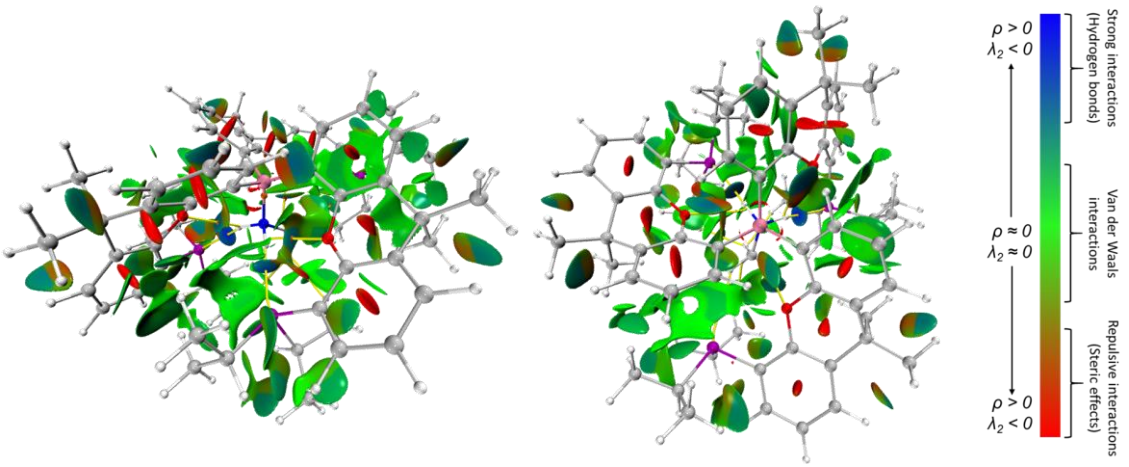

S 8.18: NCI of complex **6** with the isosurface of 0.5 a.u, BGR from -0.03 to 0.02, QTAIM bond paths in yellow and BCPs in orange.

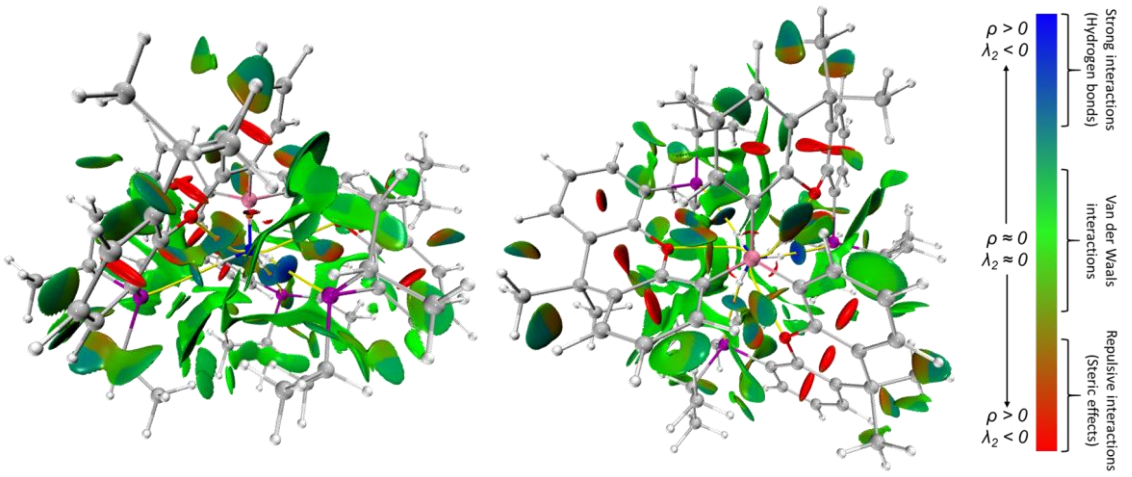

S 8.19: NCI of complex **7** with the isosurface of 0.5 a.u, BGR from -0.03 to 0.02, QTAIM bond paths in yellow and BCPs in orange.

Energy Decomposition analysis

In order to further investigate the binding of molecules to the B(XanPPh2)3 cage DFT calculations were performed on each complex. Energy Decomposition analysis (EDA) can be used to break down the interactions between two fragment wavefunctions into more chemically intuitive quantities.[93] Two complementary EDA methods where employed here; SobEDA was used to split the interaction into electrostatic (E_{ES}), exchange-repulsion ($E_{X\text{-}R}$, linked to steric repulsion and Pauli repulsion), orbital (E_{Orb}, orbital overlap effects) and coulomb correlation (E_{cc}, DFT and dispersion). [94] Extended Transition State - Natural Orbitals for Chemical Valence (ETS-NOCV) analysis was then used as a complementary technique in order to decompose the Orbital component into the most significant orbital deformation densities that make up the orbital component.[95,96]

The repulsive $E_{X\text{-}R}$ term scales as expected with the steric bulk of the bound molecule with water having the smallest and tbunc complex having the largest. The magnitude of the E_{Orb} and E_{ES} terms are very similar (within 1-2kcal) the CO analogues whereas the protic donors have slightly larger deviation with E_{ES} being larger than E_{orb} (with a difference of ~15kcal/mol) fitting with the occurrence of more electrostatic interactions between the phosphine and oxygen donors and the polarised E-H bonds. The trend for the Orb of the protic donors follows the

nucleophilicity of the lone pair. For the CO analogues the iso-nitrile is significantly more nucleophilic than the nitrile and thus has a higher Orb however, CO would be expected to show the smallest Orb as it is the least nucleophilic but doesn't. The overall interaction energies however follow the expected trend.

Breaking down the Orb into deformation density pairs shows leads to figures (**S 8.20**, **S 8.21**, **S 8.22**, **S 8.23**, **S 8.24** and **S 8.25**) where the purple regions are donating electron density into the green regions with the eigenvalue corresponding to the amount of transferred electron density. The difference between the nitrile and the CO is related to the σ donating ability with the CO being a better σ donor but the π back bonding in the CO complex is almost double that of the iso-nitrile and nitrile. This back bonding occurring between the B-C bonds and the π* orbitals. The protic complex's all show a primary E_{orb} deformation density pair associated with the lone pair and the vacant P orbital on boron, with the other pair densities comprising of a mixture of E-H back bonding (E-H σ* to B-C σ) and hydrogen bonding from the phosphines to the E-H bond. The water complex demonstrates the clearest hydrogen bond with this corroborated by the second order perturbation theory which puts this hydrogen bond at 22.48kcal. The ammonia complex shows just backdonation in the NOCV however SOPT indicates two hydrogen bonds of 7.37 and 5.61 kcal/mol. The methyl amine shows both hydrogen bonding and backdonation in the NOCV with SOPT confirming this with a H bond of 8.84kcal. The EDA would predict that the methylamine binds stronger however the Gibbs free energy of binding is larger for the ammonia complex likely due to the large distortion of the cage upon binding of the $MeNH_2$.

The ^{i}Pr cage system displays increased hydrogen bonding when compared to the Ph system as seen by significantly larger hydrogen bonding interaction (39.50 vs 12.98 Kcal/mol for the NH_3 complexes) as expected for a more basic phosphine.[56] The Gibbs free energy of binding

is larger for the ammonia complex as with the Ph system but incomplete conversion is attributed to a large kinetic barrier.

ST 8.2: Table of results from sobEDA with all values in Kcal/mol along with Gibbs free energy of formation (ΔGF) in Kcal/mol.

	8	**9**	**10**	**3**	**5**	**4**	**7**	**6**
Gibbs free energy of binding ΔG_B	-2.27	-6.96	-10.16	-10.23	-25.38	-21.88	-20.35	-29.47
Total interaction energy	-34.17	-51.67	-66.44	-46.24	-65.79	-72.51	-73.87	-71.59
Electrostatic (ΔE_{ES})	-76.35	-103.37	-120.7	-81.76	-108.47	-124.3	-131.78	-119.66
Exchange (ΔE_X)	-116.7	-109.49	-129.3	-82.37	-114.81	-121.3	-129.81	-128.74
Pauli repulsion (ΔE_R)	327.96	311.88	359.85	230.14	311.22	335.9	351.97	343.78
Exchange-repulsion (ΔE_{XR})	211.26	202.39	230.55	147.77	196.41	214.6	222.16	215.04
Orbital (ΔE_{orb})	-115.08	-104.01	-125.49	-72.32	-98.79	-101.71	-107.77	-108.02
DFT correlation (ΔE_{DFTc})	-52.92	-44.38	-46.06	-38.66	-53.34	-58.48	-53.92	-57.34
Dispersion correction (ΔE_{dc})	-1.08	-2.31	-4.75	-1.27	-1.61	-2.63	-2.56	-1.62
Coulomb correlation (ΔE_c)	-54	-46.69	-50.8	-39.93	-54.94	-61.1	-56.49	-58.95

ST 8.3: Table of results from EDA-NOCV with all values in Kcal/mol. The NOCV pairs with the largest 4 eigenvalues.

		pair 1 (E_{orb1})		**pair 2 (E_{orb2})**		**pair 3 (E_{orb3})**		**pair 4 (E_{orb4})**	
	Total	eigenvalue	energy	eigenvalue	energy	eigenvalue	energy	eigenvalue	energy
3	-68.908	0.520376	-50.256	0.204207	-5.171	0.122998	-4.350	0.118998	-2.492
5	-95.097	0.628502	-76.216	0.14806	-3.796	0.144957	-4.015	0.130867	-3.126
4	-97.786	0.634393	-75.979	0.15877	-4.34	0.143403	-4.258	0.117546	-2.959
9	-99.088	0.582712	-70.346	0.211771	-5.91	0.211249	-5.899	0.169625	-8.107
10	-121.474	0.681344	-93.782	0.222287	-6.177	0.221822	-6.157	0.173991	-7.593
8	-112.619	0.64694	-83.526	0.305397	-9.495	0.299321	-9.106	0.171388	-7.46
7	-104.21	0.633548	-80.843	0.17822	-4.743	0.158678	-3.874	0.14064	-4.981
6	-104.132	0.640261	-79.61	0.187142	-5.164	0.157003	-4.256	0.144139	-5.128

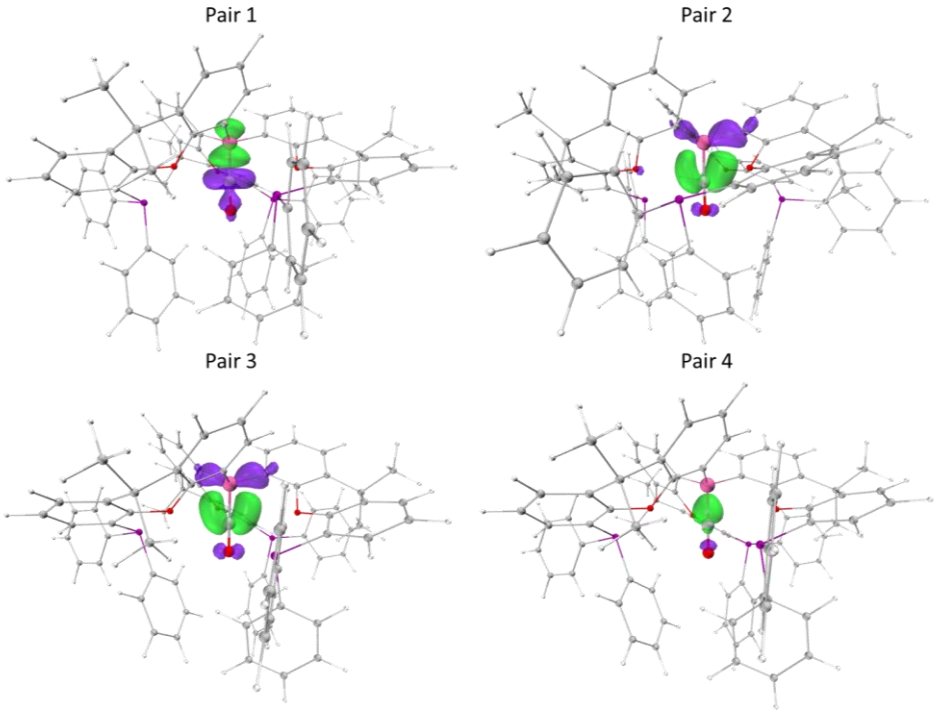

S 8.20: NOCV pair deformation densities for complex **8,** isosurface set to 0.005 for pair 1 and 0.002 a.u for pairs 2-4. Electron donation can be seen to go from purple to green.

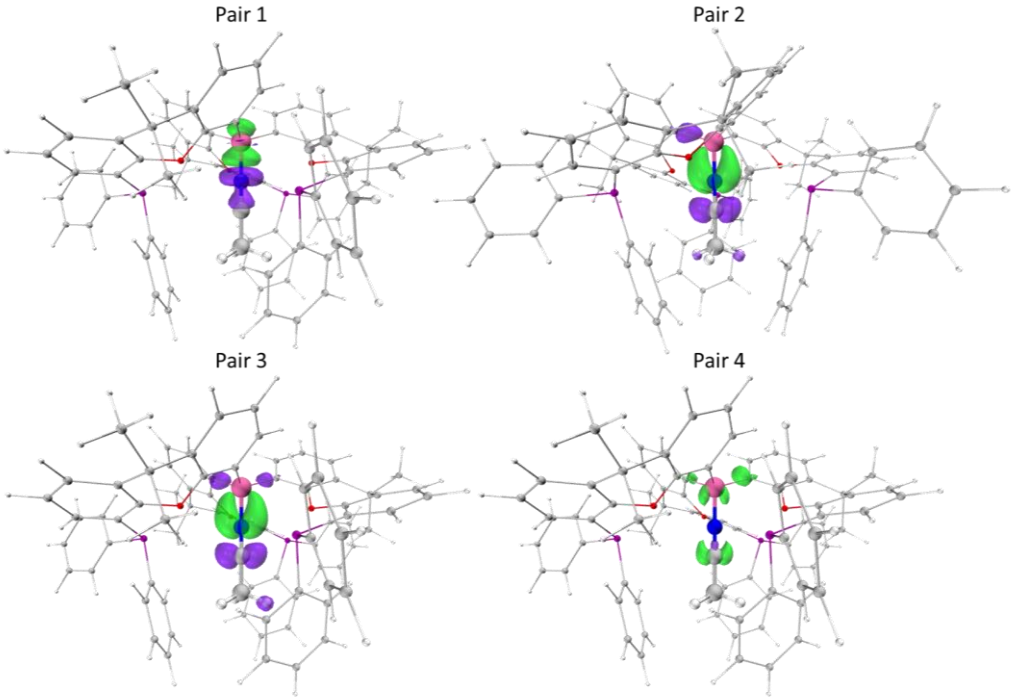

S 8.21: NOCV pair deformation densities for complex **9,** isosurface set to 0.005 for pair 1 and 0.002 a.u for pairs 2-4. Electron donation can be seen to go from purple to green.

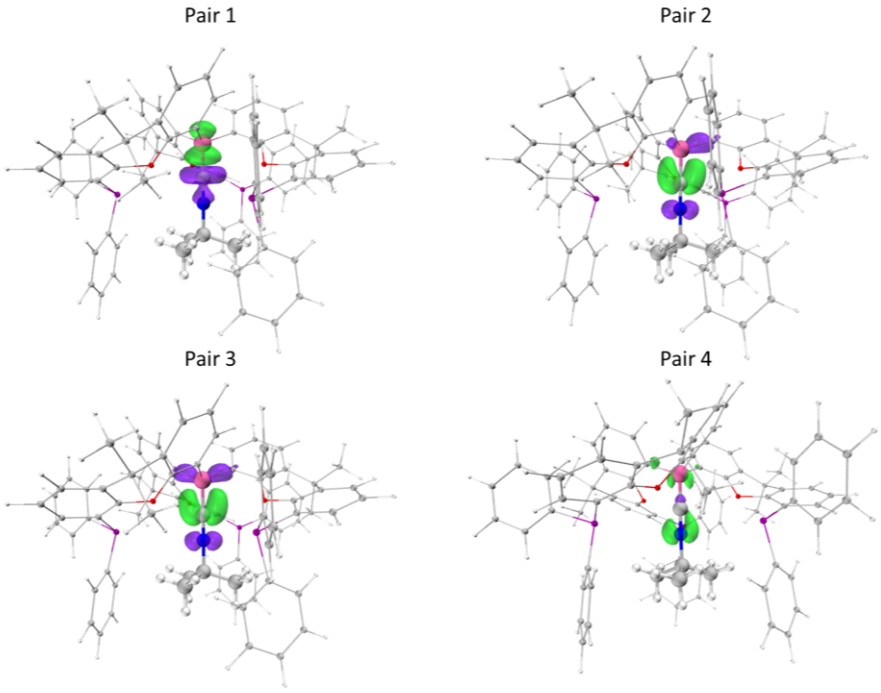

S 8.22: NOCV pair deformation densities for complex **10**, isosurface set to 0.005 for pair 1 and 0.002 a.u for pairs 2-4. Electron donation can be seen to go from purple to green.

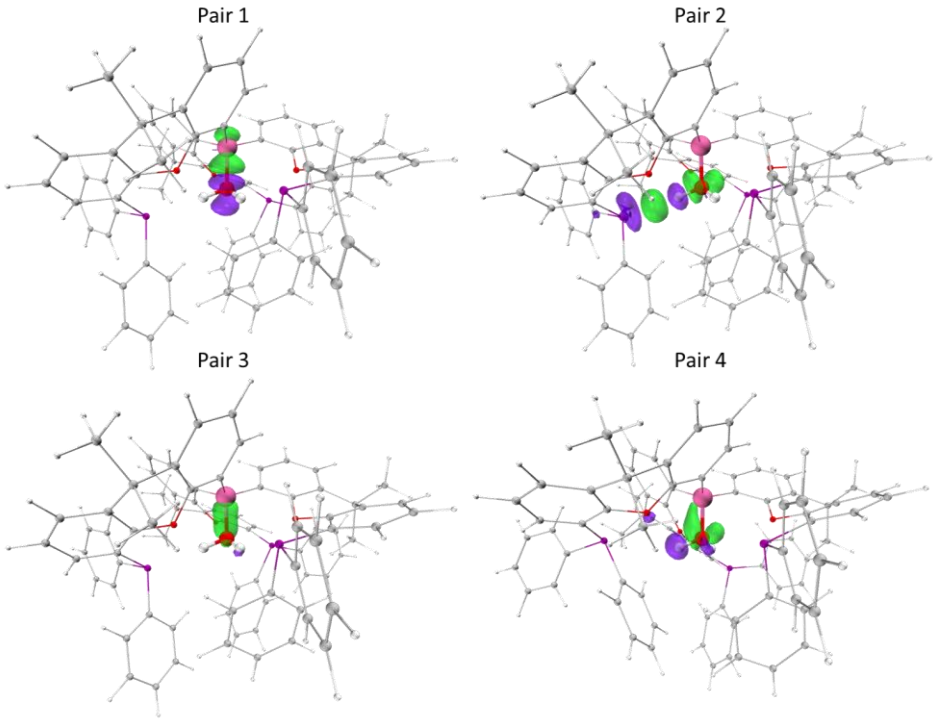

S 8.23: NOCV pair deformation densities for complex **3,** isosurface set to 0.005 for pair 1 and 0.002 a.u for pairs 2-4. Electron donation can be seen to go from purple to green.

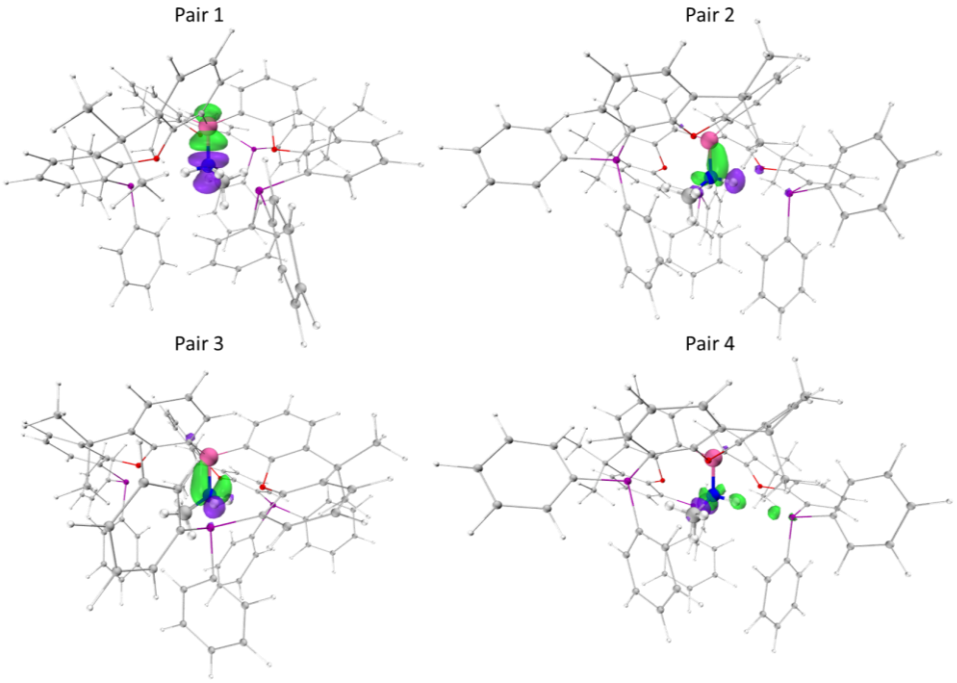

S 8.24: NOCV pair deformation densities for complex **4,** isosurface set to 0.005 for pair 1 and 0.002 a.u for pairs 2-4. Electron donation can be seen to go from purple to green.

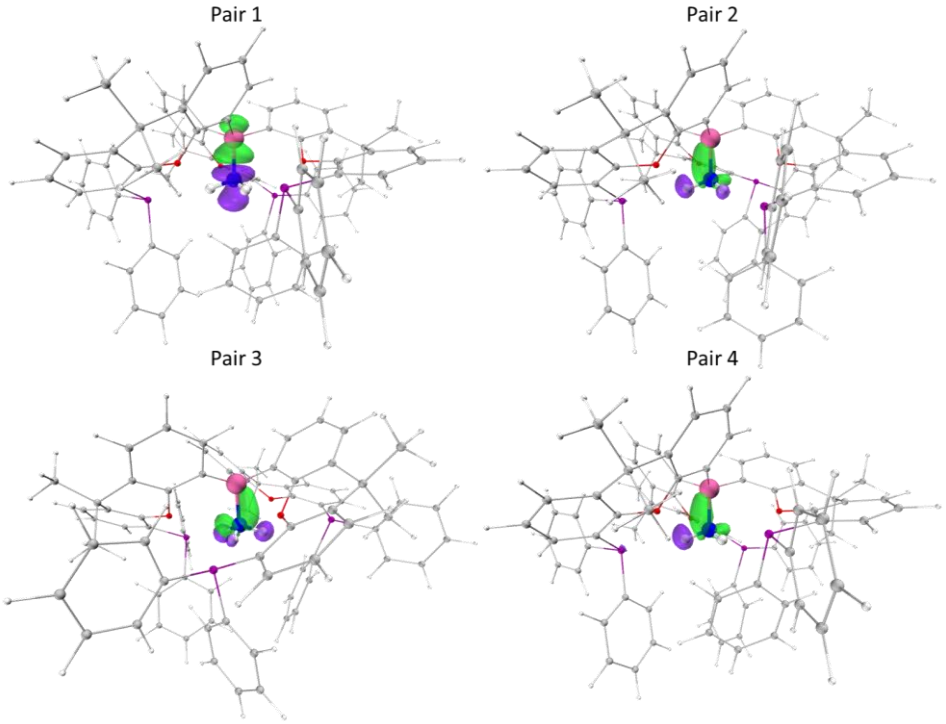

S 8.25: NOCV pair deformation densities for complex **5,** isosurface set to 0.005 for pair 1 and 0.002 a.u for pairs 2-4. Electron donation can be seen to go from purple to green.

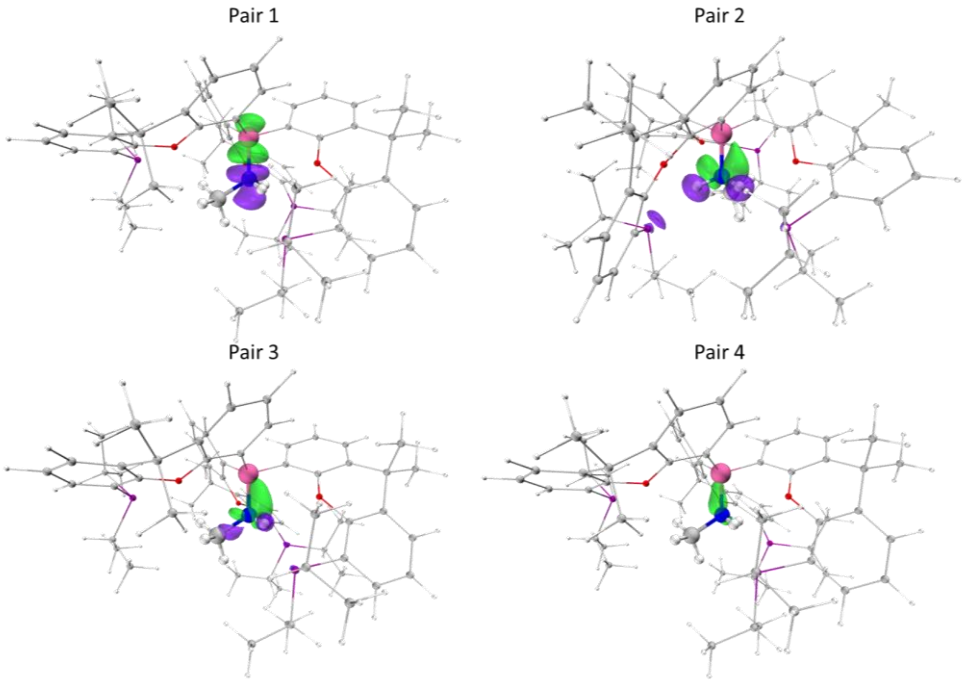

S 8.26: NOCV pair deformation densities for complex **6,** isosurface set to 0.005 for pair 1 and 0.002 a.u for pairs 2-4. Electron donation can be seen to go from purple to green.

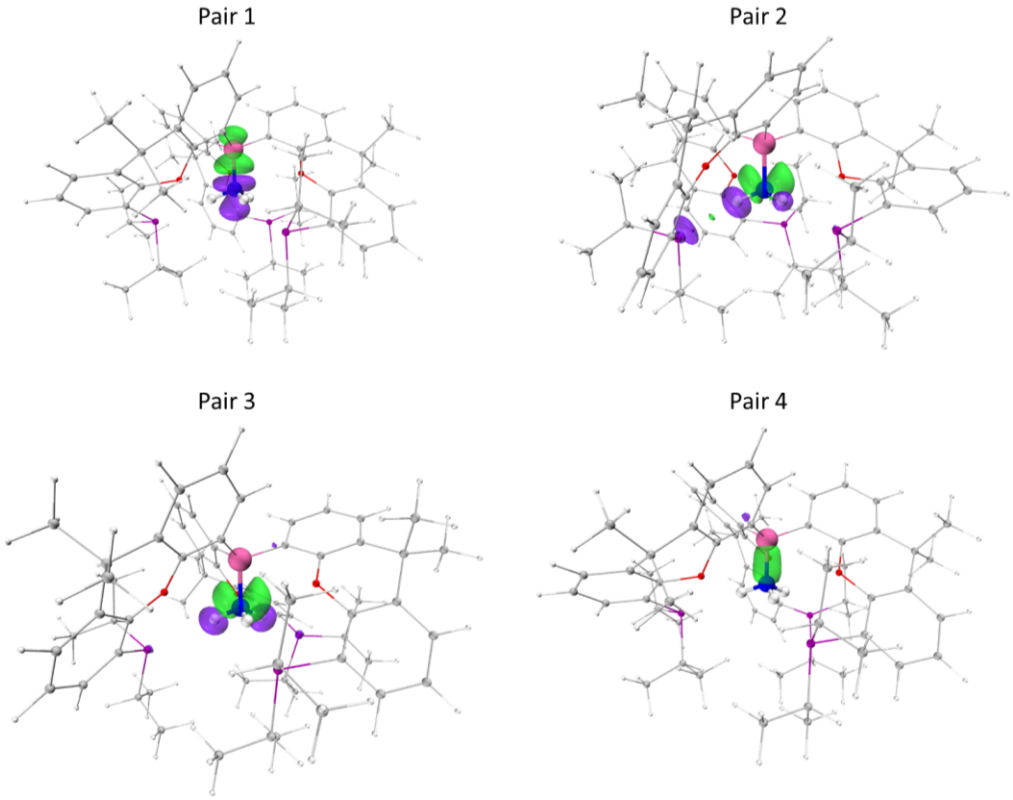

S 8.27: NOCV pair deformation densities for complex **7**, isosurface set to 0.005 for pair 1 and 0.002 a.u for pairs 2-4. Electron donation can be seen to go from purple to green.

Reverse Binding studies

In order to examine the effect of the cage architecture on the binding of various substrates, the binding of the substrates outside the cage was investigated. All systems freely optimised, however during optimisation dissociation was overserved for **3** and **9** so these systems where constrained at the same bond length as the internally bound systems.

While **8-11** displayed a similar ΔE_{orb} for the binding within and outside the cage this is not true of the protic systems (**3-7**). This can be attributed to the greater effect of hydrogen bonding for these systems which is accounted for through the ΔE_{orb} term. Much more significant changes in the ΔG_B are also seen for the protic systems, with the stability afforded by the cage architecture exceeding 120 kcal mol^{-1}. The ΔE_{elst} term is also found to play a greater role in the protic systems, as might be expected by more polar substrates. While in **8-11** a change in the ΔE_{xrep} is seen to greatly stabilise the internally bound systems, however, this is not the case in the protic systems likely due to the greater degree of rearrangement within the cage framework to accommodate the required number of hydrogen bonding interactions.

ST 8.4: Table of sobEDA decomposition values for **3-7** and **3'-7',** units in kcal mol^{-1}

	3	**3'**	**Δ**	**4**	**4'**	**Δ**	**5**	**5'**	**Δ**	**6**	**6'**	**Δ**	**7**	**7'**	**Δ**
Gibbs free energy of binding ΔG_B	-10.23	64.84	-75.07	-21.88	65.97	-87.84	-25.38	67.86	-93.24	-20.35	85.60	-105.95	-29.47	93.19	-122.66
Total interaction energy	-46.24	-14.02	-32.22	-72.51	-30.61	-41.90	-65.79	-27.77	-38.02	-73.87	-27.62	-46.25	-71.59	-25.67	-45.92
Electrostatic (ΔE_{elst})	-81.76	-71.16	-10.60	-124.30	-72.52	-51.78	-108.47	-76.56	-31.91	-131.78	-67.72	-64.06	-119.66	-74.09	-45.57
Exchange-repulsion (ΔE_{xrep})	147.77	171.14	-23.37	214.60	162.13	52.47	196.41	175.19	21.22	222.16	154.45	67.71	215.04	172.94	42.10
Orbital (ΔE_{orb})	-72.32	-66.26	-6.06	-101.71	-66.95	-34.76	-98.79	-73.26	-25.53	-107.77	-61.44	-46.33	-108.02	-70.56	-37.46
Coulomb correlation (ΔE_c)	-39.93	-47.74	7.81	-61.10	-53.27	-7.83	-54.94	-53.15	-1.79	-56.49	-52.90	-3.59	-58.95	-53.95	-5.00
DFT correlation (ΔE_{DFTc})	-38.66	-47.11	8.45	-58.48	-51.93	-6.55	-53.34	-52.34	-1.00	-53.92	-51.54	-2.38	-57.34	-53.12	-4.22
Dispersion correction (ΔE_{dc})	-1.27	-0.63	-0.64	-2.63	-1.34	-1.29	-1.61	-0.81	-0.80	-2.56	-1.37	-1.19	-1.62	-0.84	-0.78

ST 8.5: Table of sobEDA decomposition values for **8-11** and **8'-11',** units in kcal mol^{-1}

	8	**8'**	**Δ**	**9**	**9'**	**Δ**	**10**	**10'**	**Δ**	**11**	**11'**	**Δ**
Gibbs free energy of binding ΔG_B	-2.27	53.73	-59.50	-6.96	55.82	-62.77	-10.16	46.49	-56.65	-0.88	19.36	-20.25
Total interaction energy	-34.17	-4.67	-29.5	-51.67	-14.43	-37.24	-66.44	-24.03	-42.41	-88.91	-69.96	-18.95
Electrostatic (ΔE_{elst})	-76.35	-66.64	-9.71	-103.37	-74.43	-28.94	-120.7	-80.11	-40.59	-95.57	-96.01	0.44
Exchange-repulsion (ΔE_{xrep})	211.26	237.47	-26.21	202.39	217.77	-15.38	230.55	242.54	-11.99	235.54	259.17	-23.63
Orbital (ΔE_{orb})	-115.08	-113	-2.08	-104.01	-100.82	-3.19	-125.49	-118.61	-6.88	-159.05	-155.7	-3.35
Coulomb correlation (ΔE_c)	-54	-62.5	8.5	-46.69	-56.96	10.27	-50.8	-67.85	17.05	-69.83	-77.41	7.58
DFT correlation (ΔE_{DFTc})	-52.92	-61.92	9	-44.38	-55.87	11.49	-46.06	-65.86	19.8	-68.74	-76.82	8.08
Dispersion correction (ΔE_{dc})	-1.08	-0.58	-0.5	-2.31	-1.08	-1.23	-4.75	-1.99	-2.76	-1.09	-0.6	-0.49

ST 8.6: Table of EDA-NOCV decomposition values for **3-11** and **3'-11'**, eigenvalues are unitless and energies are in kcal mol^{-1}

		pair 1 (E_{orb1})		**pair 2 (E_{orb2})**		**pair 3 (E_{orb3})**		**pair 4 (E_{orb4})**	
	Total	eigenvalue	energy	eigenvalue	energy	eigenvalue	energy	eigenvalue	energy
3	-68.908	0.520376	-50.256	0.204207	-5.171	0.122998	-4.35	0.118998	-2.492
3'	-65.016	0.537999	-50.751	0.138071	-4.596	0.125929	-2.19	0.115288	-2.79
4	-95.097	0.628502	-76.216	0.14806	-3.796	0.144957	-4.015	0.130867	-3.126
4'	-72.64	0.637984	-61.724	0.133333	-4.363	0.098267	-1.343	0.098197	-1.341
5	-97.786	0.634393	-75.979	0.15877	-4.34	0.143403	-4.258	0.117546	-2.959
5'	-65.767	0.62852	-54.653	0.130122	-3.762	0.097503	-1.346	0.091144	-1.227
6	-104.132	0.640261	-79.61	0.187142	-5.164	0.157003	-4.256	0.144139	-5.128
6'	-60.313	0.619893	-50.2	0.122374	-3.241	0.092276	-1.191	0.085517	-1.051
7	-104.21	0.633548	-80.843	0.17822	-4.743	0.158678	-3.874	0.14064	-4.981
7'	-69.947	0.612548	-59.647	0.127987	-4.017	0.095745	-1.239	0.095031	-1.245
8	-112.619	0.64694	-83.526	0.305397	-9.495	0.299321	-9.106	0.171388	-7.46
8'	-110.562	0.710748	-80.084	0.322081	-9.899	0.321591	-9.875	0.173675	-7.921
9	-99.088	0.582712	-70.346	0.211771	-5.91	0.211249	-5.899	0.169625	-8.107
9'	-98.948	0.624549	-73.645	0.217473	-5.832	0.217395	-5.828	0.177035	-9.06
10	-121.474	0.681344	-93.782	0.222287	-6.177	0.221822	-6.157	0.173991	-7.593
10'	-116.249	0.75276	-92.579	0.234551	-6.126	0.234246	-6.112	0.181092	-8.346
11	-140.83	0.743028	-109.392	0.200718	-9.619	0.160081	-3.982	0.159655	-3.971
11'	-136.816	0.815478	-110.506	0.208395	-10.015	0.162977	-3.488	0.162812	-3.482

References

1. Richard Catlow, C., Davidson, M., Hardacre, C. & Hutchings, G. J. Catalysis making the world a better place. *Philosophical Transactions of the Royal Society A: Mathematical, Physical and Engineering Sciences* **374**, (2016).
2. Fan, J. H., Omura, A. & Roca, E. Geopolitics and rare earth metals. *Eur J Polit Econ* **78**, 102356 (2023).
3. Stephan, D. W. & Erker, G. Frustrated Lewis Pair Chemistry: Development and Perspectives. *Angew. Chem. Int. Ed.* **54**, 6400–6441 (2015).
4. Jupp, A. R. & Stephan, D. W. New Directions for Frustrated Lewis Pair Chemistry. *Trends Chem* **1**, 35–48 (2019).
5. Power, P. P. Main-group elements as transition metals. *Nature* **463**, 171–177 (2010).
6. Reiter, D., Holzner, R., Porzelt, A., Frisch, P. & Inoue, S. Silylated silicon–carbonyl complexes as mimics of ubiquitous transition-metal carbonyls. *Nature Chemistry* **12**, 1131–1135 (2020).
7. Ganesamoorthy, C. *et al.* A silicon–carbonyl complex stable at room temperature. *Nature Chemistry 2020 12:7* **12**, 608–614 (2020).
8. Cotton, F. A. Proposed Nomenclature for Olefin-Metal and Other Organometallic Complexes. *J. Am. Chem. Soc.* 90 6230–6232 (1968).
9. Spessard, G. O. & Miessler, G. L. *Organometallic Chemistry SECOND EDITION*. Oxford University Press. (2010).
10. Klerk, A. de. Fischer–Tropsch Process. *Kirk-Othmer Encyclopedia of Chemical Technology* 1–20 (2013).
11. Dry, M. E. The Fischer–Tropsch process: 1950–2000. *Catal Today* **71**, 227–241 (2002).
12. Lupinetti, A. J., Frenking, G. & Strauss, S. H. Nonclassical metal carbonyls: Appropriate definitions with a theoretical justification. *Angew. Chem. Int. Ed.* **37**, 2113–2116 (1998).
13. Burg, A. B. & Schlesinger, H. I. Hydrides of Boron. VII. Evidence of the Transitory Existence of Borine (BH3): Borine Carbonyl and Borine Trimethylammine. *J Am Chem Soc* **59**, 780–787 (1937).
14. Spielman, J. R. & Burg, A. B. Further Studies of the Tetraborane Carbonyl B4H8CO. *Inorg Chem* **2**, 1139–1145 (1963).
15. Kranenburg, M. *et al.* New Diphosphine Ligands Based on Heterocyclic Aromatics Inducing Very High Regioselectivity in Rhodium-Catalyzed Hydroformylation: Effect of the Bite Angle. *Organometallics* **14**, 3081–3089 (1995).
16. Zheng, X., Zulkifly, I., Heilmann, A., McManus, C. & Aldridge, S. Colorimetric Metal-Free Detection of Carbon Monoxide: Reversible CO Uptake by a BNB Frustrated Lewis Pair. *Angew. Chem. Int. Ed.* **60**, 16416–16419 (2021).
17. Chen, C. *et al.* The [(NHC)B(H)C6F5]+ Cations and Their [B](H)−CO Borane Carbonyls. *Angew. Chem. Int. Ed.* **59**, 21460–21464 (2020).
18. Dahcheh, F., Martin, D., Stephan, D. W. & Bertrand, G. Synthesis and Reactivity of a CAAC–Aminoborylene Adduct: A Hetero-Allene or an Organoboron Isoelectronic with Singlet Carbenes. *Angew. Chem. Int. Ed.* **53**, 13159–13163 (2014).
19. Braunschweig, H. *et al.* Multiple complexation of CO and related ligands to a main-group element. *Nature* **522**, 327–330 (2015).
20. Wang, H., Wu, L., Lin, Z. & Xie, Z. Synthesis, structure and reactivity of a borylene cation $[(NHSi)_2B(CO)]+$ stabilized by three neutral ligands. *J Am Chem Soc* **139**, 13680–13683 (2017).
21. Jeffery, J. C., Norman, N. C., Pardoe, J. A. J. & Timms, P. L. Synthesis and structures of carbonyl adducts of the boranes $B(BX_2)_3$ (X = F, Cl). *Chem. Commun.* 2367–2368 (2000)
22. Jacobsen, H. *et al.* Lewis Acid Properties of Tris(pentafluorophenyl)borane. Structure and Bonding in L-B(C6F5)3 Complexes. *Organometallics* **18**, 1724–1734 (1999).
23. Fukazawa, A. *et al.* Reaction of pentaarylboroles with carbon monoxide: an isolable organoboron carbonyl complex. *Chem Sci* **3**, 1814–1818 (2012).
24. Finze, M. *et al.* Tris(trifluoromethyl)borane carbonyl, (CF3)3BCO - Synthesis, physical, chemical and spectroscopic properties, gas phase, and solid state structure. *J Am Chem Soc* **124**, 15385–15398 (2002).
25. Knoth, W. H. Chemistry of Boranes. XXXI. 1,10-Bis(hydroxymethyl)octachlorodecaborate(2—). *J Am Chem Soc* **89**, 4850–4852 (1967).
26. Gerken, M., Pawelke, G., Bernhardt, E. & Willner, H. Syntheses and Characterization of $(C_2F_5)_3BCO$ and $(C_3F_7)_3BCO$. *Chem. Eur. J.* **16**, 7527–7536 (2010).

27. Heitkemper, T. & Sindlinger, C. P. A Cationic NHC-Supported Borole. *Chem. Eur. J.* **26**, 11684–11689 (2020).
28. Sajid, M. *et al.* Carbonylation reactions of intramolecular vicinal frustrated phosphane/borane lewis pairs. *J Am Chem Soc* **135**, 18567–18574 (2013).
29. Jeffery, J. C., Norman, N. C., Pardoe, J. A. J. & Timms, P. L. Synthesis and structures of carbonyl adducts of the boranes $B(BX_2)_3$ (X = F, Cl). *Chem. Commun.* 2367–2368 (2000).
30. Finze, M. *et al.* Tris(trifluoromethyl)borane carbonyl, $(CF_3)_3BCO$ - Synthesis, physical, chemical and spectroscopic properties, gas phase, and solid state structure. *J Am Chem Soc* **124**, 15385–15398 (2002).
31. Heitkemper, T. & Sindlinger, C. P. A Cationic NHC-Supported Borole. *Chem. Eur. J.* **26**, 11684–11689 (2020).
32. Chen, C. *et al.* The $[(NHC)B(H)C_6F_5]^+$ Cations and Their [B](H)−CO Borane Carbonyls. *Angew. Chem. Int. Ed.* **59**, 21460–21464 (2020).
33. Stephan, D. W. Frustrated Lewis pair chemistry of CO. *Chem Soc Rev* **52**, 4632–4643 (2023).
34. Dureen, M. A. & Stephan, D. W. Reactions of boron amidinates with CO2 and CO and other small molecules. *J Am Chem Soc* **132**, 13559–13568 (2010).
35. Sajid, M., Kehr, G., Daniliuc, C. G. & Erker, G. Formylborane Formation with Frustrated Lewis Pair Templates. *Angew. Chem. Int. Ed.* **53**, 1118–1121 (2014).
36. Conner, S. D. & Schmid, S. L. Regulated portals of entry into the cell. *Nature* **422**, 37–44 (2003).
37. Stank, A., Kokh, D. B., Fuller, J. C. & Wade, R. C. Protein Binding Pocket Dynamics. *Acc Chem Res* **49**, 809–815 (2016).
38. Montà-González, G., Sancenón, F., Martínez-Máñez, R. & Martí-Centelles, V. Purely Covalent Molecular Cages and Containers for Guest Encapsulation. *Chem Rev* **122**, 13636–13708 (2022).
39. Kuah, E., Toh, S., Yee, J., Ma, Q. & Gao, Z. Enzyme Mimics: Advances and Applications. *Chemistry - A European Journal* **22**, 8404–8430 (2016).
40. Galan, A. & Ballester, P. Stabilization of reactive species by supramolecular encapsulation. *Chem Soc Rev* **45**, 1720–1737 (2016).
41. Little, M. A. & Cooper, A. I. The Chemistry of Porous Organic Molecular Materials. *Adv Funct Mater* **30**, (2020).
42. Song, Z. *et al.* Enzyme-mimetic self-catalyzed polymerization of polypeptide helices. *Nature Communications* **10**, 1–7 (2019).
43. Li, W. L. & Head-Gordon, T. Catalytic Principles from Natural Enzymes and Translational Design Strategies for Synthetic Catalysts. *ACS Cent Sci* **7**, 72–80 (2021).
44. Breslow, R. & Dong, S. D. Biomimetic reactions catalyzed by cyclodextrins and their derivatives. *Chem Rev* **98**, 1997–2011 (1998).
45. Cram, D. J., Katz, H. E. & Dicker, I. B. Host-Guest Complexation. 31. A Transacylase Partial Mimic. *J Am Chem Soc* **106**, 4987–5000 (1984).
46. Warmuth, R. Reactions Inside Carcerands. *Molecular Encapsulation: Organic Reactions in Constrained Systems* 227–268 (2010)
47. Yu, Y., Yang, J. M. & Rebek, J. Molecules in Confined Spaces: Reactivities and Possibilities in Cavitands. *Chem* **6**, 1265–1274 (2020).
48. Elmer, L.-M. *et al.* The Chemistry of a Non-Interacting Vicinal Frustrated Phosphane/Borane Lewis Pair. *Chemistry - A European Journal* **23**, 6056–6068 (2017).
49. Fulmer, G. R. *et al.* NMR chemical shifts of trace impurities: Common laboratory solvents, organics, and gases in deuterated solvents relevant to the organometallic chemist. *Organometallics* **29**, 2176–2179 (2010).
50. Mitoraj, M. & Michalak, A. Applications of natural orbitals for chemical valence in a description of bonding in conjugated molecules. *J Mol Model* **14**, 681–687 (2008).
51. Mitoraj, M. P., Michalak, A. & Ziegler, T. A combined charge and energy decomposition scheme for bond analysis. *J Chem Theory Comput* **5**, 962–975 (2009).
52. Michalak, A., Mitoraj, M. & Ziegler, T. Bond orbitals from chemical valence theory. *J. Phys. Chem. A.* **112**, 1933–1939 (2008).
53. Darwent, deB. National Standard Reference Data Series. *NationalBureau of Standards* 31 1–52 (1970).
54. Mitoraj, M. P., Kurczab, R., Boczar, M. & Michalak, A. Theoretical description of hydrogen bonding in oxalic acid dimer and trimer based on the combined extended-transition-state energy

decomposition analysis and natural orbitals for chemical valence (ETS-NOCV). *J Mol Model* **16**, 1789–1795 (2010).
55. Glendening, E. D., Landis, C. R. & Weinhold, F. NBO 7.0: New vistas in localized and delocalized chemical bonding theory. *J Comput Chem* **40**, 2234–2241 (2019).
56. Gilli, P., Pretto, L., Bertolasi, V. & Gilli, G. Predicting Hydrogen-Bond strengths from Acid-Base molecular properties. the pKa slide rule: Toward the solution of a Long-Lasting problem. *Acc Chem Res* **42**, 33–44 (2009).
57. Beckett, M. A., Strickland, G. C., Holland, J. R. & Varma, K. S. A convenient n.m.r. method for the measurement of Lewis acidity at boron centres: correlation of reaction rates of Lewis acid initiated epoxide polymerizations with Lewis acidity. *Polymer (Guildf)* **37**, 4629–4631 (1996).
58. Cordero, B. *et al.* Covalent radii revisited. *Dalton Trans.* 2832–2838 (2008)
59. Burg, A. B. & Schlesinger, H. I. Hydrides of Boron. VII. Evidence of the Transitory Existence of Borine (BH_3): Borine Carbonyl and Borine Trimethylammine. *J Am Chem Soc* **59**, 780–787 (1937).
60. Gilliam, R., Johnson, C. M. & Gordy, W. Microwave Spectroscopy in the Region from Two to Three Millimeters Phys. Rev. **78**, 140 (1950)
61. Bruce, M. R. M. & Tyler, D. R. Electronic Structure and Photochemistry of the (η 5-C_5H_5)2TiI2Complex. *Organometallics* **4**, 528–533 (1985).
62. Wang, J., Li, G., Li, Q. S., Xie, Y. & King, R. B. Isocyanide versus nitrile ligands and methyl versus trifluoromethyl substituents in metal carbonyl chemistry. *Polyhedron* **47**, 165–172 (2012).
63. Lu, T. & Chen, Q. Simple, Efficient, and Universal Energy Decomposition Analysis Method Based on Dispersion-Corrected Density Functional Theory. *J. Phys. Chem. A.* **127**, 7023–7035 (2023).
64. Scuseria, G. E., Miller, M. D., Jensen, F. & Geertsen, J. The dipole moment of carbon monoxide. *J Chem Phys* **94**, 6660–6663 (1991).
65. Kisiel, Z., Białkowska-Jaworska, E., Desyatnyk, O., Pietrewicz, B. A. & Pszczółkowski, L. The Gas-Phase Electric Dipole Moments of the Symmetric Top Tertiary Butyl Molecules tBuX, X=F, Cl, Br, I, CN, and NC. *J Mol Spectrosc* **208**, 113–120 (2001).
66. Alston Steiner, P. & Gordy, W. Precision measurement of dipole moments and other spectral constants of normal and deuterated methyl fluoride and methyl cyanide. *J Mol Spectrosc* **21**, 291–301 (1966).
67. Holtkamp, P. Schwabedissen, J. Neumann, B. Stammler, H.-G. Koptyug, I. V. Zhivonitko, V. V. Mitzel, N. W. *A Zwitterionic Phosphonium Stannate(II) via Hydrogen Splitting by a Sn/P Frustrated Lewis-Pair and Reductive Elimination*. *Chem. Eur. J.* **26**, 17381 (2020)
68. Crumpton, A. E. Heilmann, A. Aldridge, S. Angew. Chem. Int. Ed. (2024).
69. Protonenacceptoren, S., Bei, H. & Dehydrohalogenierungsreaktionen, A.-U. Spezifische Protonenacceptoren als Hilfsbasen bei Alkylierungs- und Dehydrohalogenierungsreaktionen. *Chem Ber* **91**, 380–392 (1958).
70. Cosier, J. & Glazer, A. M. A Nitrogen-Gas-Stream Cryostat for General X-ray Diffraction Studies. *J. Appl. Cryst* **19**, 105–107 (1986).
71. CrysAlisPro v.1.171.42.70a, Agilent Technologies 2011.
72. Sheldrick, G. M. SHELXT - Integrated space-group and crystal-structure determination. *Acta Crystallogr A* **71**, 3–8 (2015).
73. Sheldrick, G. M. Crystal structure refinement with SHELXL. *Acta Crystallogr C Struct Chem* **71**, 3–8 (2015).
74. Dolomanov, O. V., Bourhis, L. J., Gildea, R. J., Howard, J. A. K. & Puschmann, H. OLEX2: A complete structure solution, refinement and analysis program. *J Appl Crystallogr* **42**, 339–341 (2009).
75. Neese, F. & Wiley, J. The ORCA program system. *Wiley Interdiscip Rev Comput Mol Sci* **2**, 73–78 (2012).
76. Neese, F. Software update: the ORCA program system, version 4.0. *Wiley Interdiscip Rev Comput Mol Sci* **8**, e1327 (2018).
77. Neese, F., Wennmohs, F., Becker, U. & Riplinger, C. The ORCA quantum chemistry program package. *Journal of Chemical Physics* **152**, 224108 (2020).
78. Furness, J. W., Kaplan, A. D., Ning, J., Perdew, J. P. & Sun, J. Accurate and Numerically Efficient r2SCAN Meta-Generalized Gradient Approximation. *Journal of Physical Chemistry Letters* **11**, 8208–8215 (2020).
79. Grimme, S., Hansen, A., Ehlert, S. & Mewes, J. M. R2SCAN-3c: A 'swiss army knife' composite electronic-structure method. *Journal of Chemical Physics* **154**, 64103 (2021).

80. Caldeweyher, E. *et al.* A generally applicable atomic-charge dependent London dispersion correction. *Journal of Chemical Physics* **150**, 154122 (2019).
81. Kruse, H. & Grimme, S. A geometrical correction for the inter- and intra-molecular basis set superposition error in Hartree-Fock and density functional theory calculations for large systems. *Journal of Chemical Physics* **136**, 154101 (2012).
82. Hanwell, M. D. *et al.* Avogadro: An advanced semantic chemical editor, visualization, and analysis platform. *J Cheminform* **4**, 1–17 (2012).
83. Chai, J. Da & Head-Gordon, M. Systematic optimization of long-range corrected hybrid density functionals. *Journal of Chemical Physics* **128**, (2008).
84. Chai, J. Da & Head-Gordon, M. Long-range corrected hybrid density functionals with damped atom–atom dispersion corrections. *Physical Chemistry Chemical Physics* **10**, 6615–6620 (2008).
85. Weigend, F. & Ahlrichs, R. Balanced basis sets of split valence, triple zeta valence and quadruple zeta valence quality for H to Rn: Design and assessment of accuracy. *Physical Chemistry Chemical Physics* **7**, 3297–3305 (2005).
86. Weigend, F. Accurate Coulomb-fitting basis sets for H to Rn. *Physical Chemistry Chemical Physics* **8**, 1057–1065 (2006).
87. Barone, V. & Cossi, M. Quantum calculation of molecular energies and energy gradients in solution by a conductor solvent model. *J. Phys. Chem. A.* **102**, 1995–2001 (1998).
88. E. D. Glendening, et al. W. NBO7. (2018).
89. Lu, T. & Chen, F. Multiwfn: A multifunctional wavefunction analyzer. *J Comput Chem* **33**, 580–592 (2012).
90. Johnson, E. R. *et al.* Revealing noncovalent interactions. *J Am Chem Soc* **132**, 6498–6506 (2010).
91. Cortés-Guzmán, F. & Bader, R. F. W. Complementarity of QTAIM and MO theory in the study of bonding in donor-acceptor complexes. *Coord Chem Rev* **249**, 633–662 (2005).
92. Contreras-García, J., Yang, W. & Johnson, E. R. Analysis of hydrogen-bond interaction potentials from the electron density: Integration of noncovalent interaction regions. *J. Phys. Chem. A.* **115**, 12983–12990 (2011).
93. Zhao, L., von Hopffgarten, M., Andrada, D. M. & Frenking, G. Energy decomposition analysis. *Wiley Interdiscip Rev Comput Mol Sci* **8**, e1345 (2018).
94. Lu, T. & Chen, Q. Simple, Efficient, and Universal Energy Decomposition Analysis Method Based on Dispersion-Corrected Density Functional Theory. *J. Phys. Chem. A.* **127**, 7023–7035 (2023).
95. Altun, A., Neese, F. & Bistoni, G. Effect of Electron Correlation on Intermolecular Interactions: A Pair Natural Orbitals Coupled Cluster Based Local Energy Decomposition Study. *J Chem Theory Comput* **15**, 215–228 (2019).
96. Mitoraj, M. P., Michalak, A. & Ziegler, T. A combined charge and energy decomposition scheme for bond analysis. *J Chem Theory Comput* **5**, 962–975 (2009).

Statement of Authorship

Title of Paper	Leveraging Non-Covalent Interactions for the Binding of CO by a Weakly Lewis Acidic Borane
Publication Status	Submitted
Publication Details	*Submitted to JACS 18/4/2024*

Student Confirmation

Student Name:	Agamemnon Elvis Crumpton
Contribution to the Paper	Performed synthesis, DFT calculations and Xray crystallography on the compounds within the manuscript. I wrote the initial draft of the manuscript and helped with the later revisions.
Signature 	Date 15/04/2024

Supervisor Confirmation

Supervisor name and title: Professor Simon Aldridge	
Supervisor comments I can confirm that the candidate's contribution to this paper is as described above.	
Signature 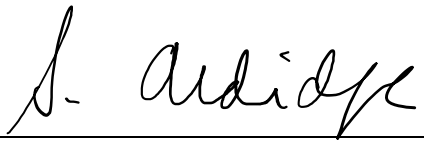	Date 18/4/2024

Chapter 9 - Summary, Outlook and Conclusions

This thesis has explored a range of novel systems within main group chemistry, including and examination of the interactions of some of these with NH_3 and CO. In this exploration, we have observed unique bonding behaviour, such as that in $Ni(BeCp)_6$, and enzymatic like stabilisation such as those found in $(Ph_2P\text{-xan})_3B$. Based on these findings, there are several areas ripe for further investigation. A summary of each chapter and areas for further investigation are outlined below.

Chapter 2: Metathesis at $[Be–Be]^{2+}$: A Route to a Nucleophilic Beryllyl

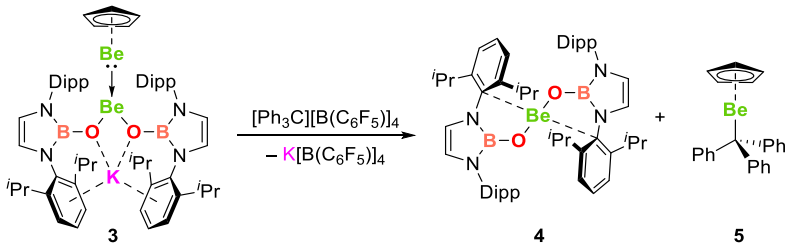

Scheme 9.1: Reactivity of complex **3** with $[CPh_3][B(C_6F_5)_4]$, a source of the organic electrophile $[CPh_3]^+$.

In this chapter, ligand metathesis of CpBeBeCp (**1**) is demonstrated, leading to the formation of Cp*BeBeCp (**2**) and $[K\{(HCDippN)_2BO\}_2]BeBeCp$ (**3**).[1] This work effectively triples the number of documented Be–Be bonds and introduces heteroleptic species, offering new avenues to explore Be-Be bonding variations with different substituents. DFT calculations reveal that **2** retains bonding characteristics similar to **1**, as anticipated due to the minor degree ligand modification. By contrast, **3** demonstrates significantly altered bonding, with its inter-beryllium ELF surface transitioning from a symmetric disk, typical of covalent bonds, to a hemispherical lobe, suggestive of donor-acceptor interactions. Basin analysis of the ELF surface highlights disparate contributions from each Be center to the bond (Be_{Cp} 1.67 e^- and Be_{NHBO} 0.24 e^-), hinting at a pronounced donor-acceptor contribution to bonding. QTAIM analysis further underscores this discrepancy, notably in the absence of a non-nuclear attractor (NNA) between the two Be centres in **3**, a feature observed in both **1** and **2**, as well as in all known Mg(I) dimers.[2,3]

Examination of the Bader charges reveals a marked contrast between the Be_{Cp} centre (+0.19) and the Be_{NHBO} centre (+1.62), providing further evidence for a donor-acceptor relationship between an electron-rich $Be_{Cp}(0)$ and an electron-poor $Be_{NHBO}(II)$ center. This interaction is further evidenced by the reactivity of **3** with $[Ph_3C][B(C_6F_5)_4]$, which cleaves the Be-Be bond, yielding $(HCDippN)_2BO\}_2Be$ (**4**) and Ph_3CBeCp (**5**) (**Scheme 9.1**). This showcases the nucleophilic nature of the BeCp fragment alongside the stability of the Be(II) species (**4**). This chapter not only broadens the spectrum of known beryllium-beryllium bonded species but also expandes the range of Be-Be interaction mechanisms, setting the stage for advanced studies and potential applications of heteroleptic beryllium complexes in the field of synthetic chemistry.

A wide range of future work is possible in this emerging area of group 2 chemistry. However, focusing on systems related to those explored in this chapter, the mixed group 2, $[K\{(HCDippN)_2BO\}_2]AeBeCp$ systems could be investigated. These systems might be synthesised by leveraging the nucleophilic character in **3** and reacting with the $(HCDippN)_2BO\}_2Ae$ fragment. It would be interesting to see if the extent of polarisation of this bond could be increased, as might be predicted, by employing the less electronegative elements as group 2 is decreased. Exploring these avenues could significantly enrich our understanding of group 2 element-element interactions, potentially unlocking new chemical behaviour and applications in materials science and even catalysis.

Chapter 3: A stable hexavalent nickel complex

In this chapter, we present the synthesis and detailed characterisation of the pioneering hexavalent nickel complex, $Ni(BeCp)_6$, together with the iron complex $Fe(BeCp)_2(CO)_4$, both synthesised from the recently introduced precursor CpBeBeCp.[1] Analysis of $Fe(BeCp)_2(CO)_4$ offers a platform to compare the BeCp against other potent σ-donors by examining the CO stretching frequencies associated with the trans CO, showcasing the trans effect. Remarkably,

the CO stretching frequencies in $Fe(BeCp)_2(CO)_4$ show the most pronounced hypsochromic shift, underscoring the exceptional electron-donating capacity of the BeCp ligand.

The $Ni(BeCp)_6$ complex deviates from conventional geometries, adopting an atypical C_{3v} configuration in its solid state rather than a more conventional O_h. Quantum chemical calculations affirm the lower energy of the C_{3v} structure's, with the O_h form being energetically less favourable by 46 kcal mol^{-1}. $Ni(BeCp)_6$ is notable for its inverse ligand field splitting, a consequence of the interplay between the electron-rich metal and electron-poor ligands. Further examination of the bonding in the C_{3V} geometry reveals a toroidal region in the ELF surface surrounding the central nickel atom which is mirrored in the residual electron density map in the SCXRD derived structure. We propose that this toroidal region of electron density is due to the aromatic stabilisation afforded by this system. Indeed, a number of computational techniques were used to probe this phenomenon (ACID, EDDB, NICS, QTAIM, ELF and ANDP) and all indicate that this complex displays aromatic characteristics. Through this exploration we not only reveal a unique stabilisation mechanism for $Ni(BeCp)_6$, but also highlight the critical impact of highly reduced metal centres on bonding motifs, offering new perspectives for the study and application of complex metal-ligand interactions in chemistry.

Naturally there are numerous areas for future work generating M-BeCp bonds across the periodic table. However, investigating the isoelectronic systems adjacent to Ni such as $[Co(BeCp)_6]^-$ and $[Cu(BeCp)_6]^+$, would offer an opportunity to observe the effect of the overall charge of the system on the aromatic stabilisation afforded by the BeCp framework and the broader ramifications this might have on the stability and geometry of the system.

Chapter 4: Synthesis of homo-metallic heavier hnalogues of cyclobutene and the cyclobutadiene dianion

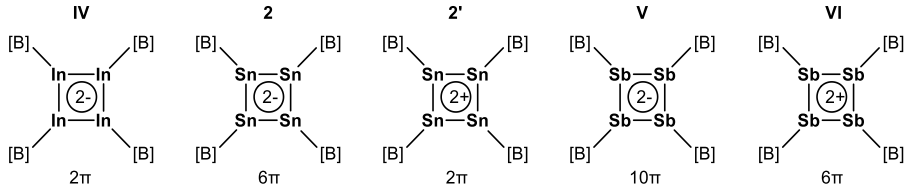

Figure 9.1: Heavier analogues of CBD

In this chapter, we report a 6 π Sn_4 analogue of the cyclobutadiene dianion (**Figure 9.1**, **2**), characterized by its slightly puckered geometry and investigate this system computationally for potential aromaticity.[4] NICS calculations indicate the non-aromatic nature of **2**, while a (theoretical) 2 π dicationic species (**Figure 9.1**, **2'**) is predicted to exhibit aromaticity. The lack of aromaticity in **2** is attributed to localized double bond character and anionic charges, as revealed by NRT analysis. Efforts to synthesize **2'** through oxidation of **2** led to decomposition, resulting in the formation of previously described Sn_6 clusters.

A previously reported $[(bory)_4In)_4]^{-2}$ CBD analogue (**Figure 9.1**, **IV**), which is isoelectronic with **2'**, highlights the potential for aromaticity in heavier CBD analogues.[5] This suggests that further investigation into potentially aromatic heavy CBD analogues could be fruitful, particularly through computational studies. For instance, exploring the Sb_4 CBD dianion analogue (**Figure 9.1**, **V**), which theoretically possesses aromaticity with 10 π electrons, and the CBD dicationic species (**Figure 9.1**, **VI**), isoelectronic with **2** and containing 6 π electrons, would be insightful. Should these systems exhibit indications of aromaticity upon computational analysis, they may present intriguing synthetic targets.

Chapter 5: A planar per-borylated digermene

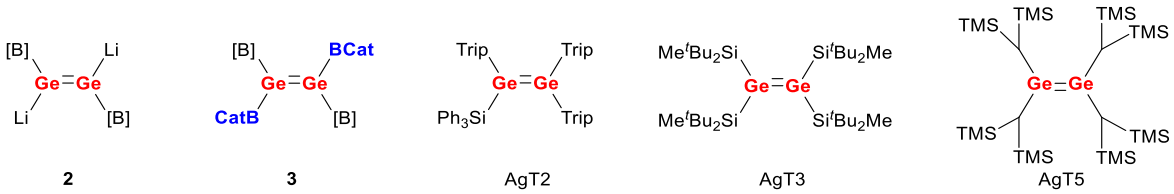

Figure 9.2: A series of digermene systems investigated by EDA

In this chapter, a planer per-borylated digermene is reported, deviating from the typical *trans* bent geometries typically observed for of dimetallenes.[6] This rare geometric nonconformity was investigated through the framework of the CGMT model via computational studies of the decomposition of a series of dimetallenes into either triplet or singlet tetrylene fragments. Both the NEDA and EDA-NOCV frameworks were considered, with the EDA-NOCV framework overly favouring radical recombination (as also found in chapter 2). The NEDA decomposition analysis indicated that the bonding in systems **2**, **3**, and **AgT3**, is best characterized by the recombination of two triplet fragments (**Figure 9.2**). **AgT3** is reported to adopt a twisted geometry, which is attributed to greater triplet character by the authors and is confirmed by this analysis. [7]

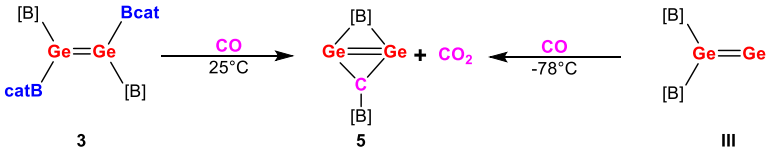

Scheme 9.2: Reaction of **3** and **III** with CO to form **5**

In further studies the reaction of **3** with CO was shown to yield the reduced species **5** (**Scheme 9.2**). The same product was identified from the low temperature reaction of vinylidene **III** with CO leading to the proposal of a common intermediate in these reactions.[8] The mechanism was studied *in silico*, and is proposed to via a 12-step process involving the migratory-insertion of CO into both of the boryl and catecholborane fragments via a number of CO binding modes. While this reaction is remarkable, the characterisation data on the products is incomplete precluding publication in a stand-alone report. This poses a natural vector for

further study, but alongside this identification of the higher temperature product of the vinylidene **III** with CO and investigating the energetic landscape to reach this (in comparison to the low temperature product **5**) would greatly enhance this study.

Chapter 6: Coordination and homologation of CO at Al(I): mechanism and chain growth, branching, isomerization and reduction

In this chapter, the synthesis of CO homologated products deriving from the NON aluminyl anion are reported with the mechanism for this process being probed *in silico*.[9] This mechanism is proposed to go via a CO bound as a Z type ligand due to the electron rich nature of the aluminyl anion, allowing binding as an isocarbonyl donor facilitating the generation of a transient carbene species. This carbene is proposed to undergo dimerisation to the observed C_4 homologation product with this process being reported to go via a singlet carbene with a moderate reaction barrier.

Further computational studies have been undertaken indicating this transient carbene species has an extremely small singlet-triplet gap, with the triplet species being of lower energy. Both the photo- and thermal- interconversion were considered, with both being deemed possible. Mechanistically a triplet carbene drastically reduces the barrier to dimerisation, along with explaining the broad NMR signals seen in the in-situ spectra.

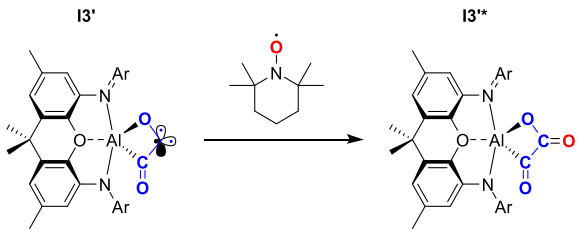

Scheme 9.3: Reaction of **I3'** with TEMPO

Experimental proof for these transient triplet radicals could be obtained by in-situ EPR spectra. In order to help characterise the method of singlet-triplet interconversion, the EPR must be collected in the absence of light and at different temperatures. Additionally, a radical trap,

such as TEMPO, could be added to the reaction mixture to generate **I3'*** which could be isolated and prove further evidence for this alternative pathway (**Scheme 9.3**).[10]

Chapter 7: Modulating Hydrogen Shuttling in Ammonia by Neutral and Cationic Boron-containing Frustrated Lewis Pairs (FLPs)

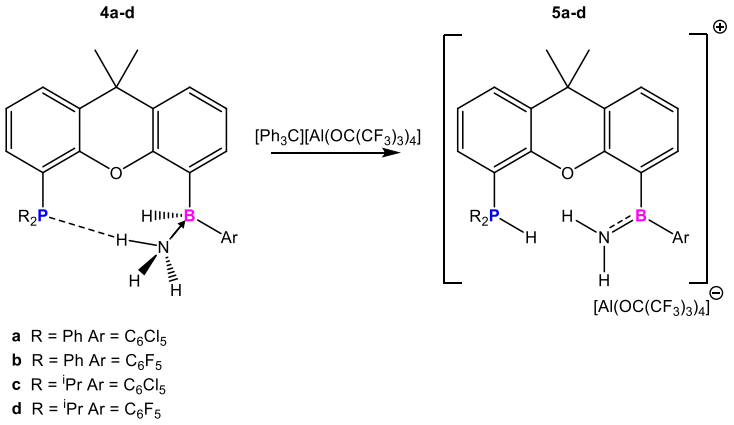

Scheme 9.4: Reaction of **4a-d** with $[Ph_3C][Al(OC(CF_3)_3)_4]$

In this chapter, the synthesis of a series of a series of FLP systems featuring boranes bearing either Ar^{Cl} and Ar^{F} groups, and their reactivity with NH_3 is reported. A series of the NH_3 coordinated xanthene phosphine boranes **4a-d** are synthesised. **4a-d** exhibit rare NH···P hydrogen bonding, which is proposed to pre-activate the N–H bond predisposing it towards activation. This is reminiscent of encounter complexes in H_2 activation within FLP systems, where the geometry is pre-organised to maximise orbital overlap before activation.[11,12] Upon abstraction of the hydride, using trityl reagents (**Scheme 9.4**), immediate N–H activation occurs to form **5a-d**, which is calculated to occur in a near barrierless process.

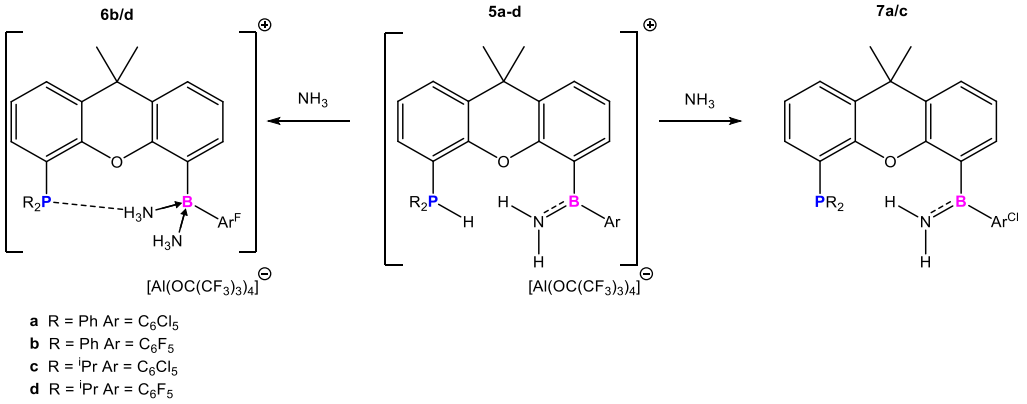

Scheme 9.5: Reaction of **5a-d** with NH_3

Upon exposure to NH_3, divergent reactivity in compounds **5a-d** is observed, influenced by the type of aryl group attached to boron (**Scheme 9.5**). Specifically, compounds **5b/d**, which feature the C_6F_5 group, undergo a reaction pathway involving the binding of a second NH_3 molecule and subsequent deprotonation of the phosphine, leading to the formation of the boronium products **6b/d**. In contrast, compounds **5a/c**, bearing the C_6Cl_5 group, are directly deprotonated by the added NH_3, resulting in the neutral species **7a/c**. This difference in reactivity is attributed to the donation from the lone pairs on the ortho Cl groups into the vacant p orbital of boron, rendering it less electrophilic. Consequently, this diminishes the likelihood of a second NH_3 molecule binding to the borane centre, instead prompting NH_3 to act as a base and deprotonate the phosphine. These findings underscore the delicate interplay of structure and electronics in dictating reactivity, paving the way for innovative approaches in the activation and functionalisation of small molecules.

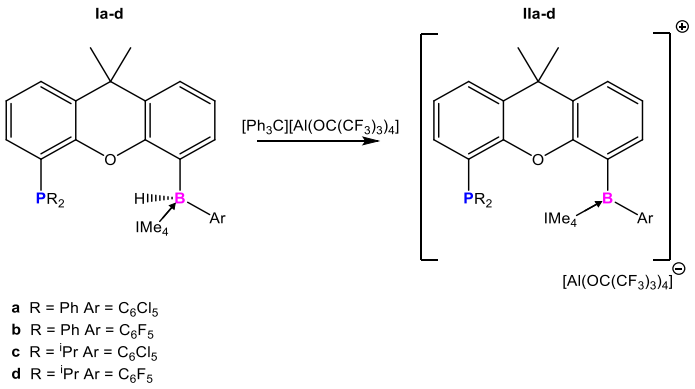

Scheme 9.6: Reaction abstracting hydride from carbene stabilised Ia-d

To further explore the reactivity of these systems, a logical next step is to investigate NH_2 transfer to various reagents. A single example of catalytic NH_2 transfer with a FLP system has thus been reported, achieving catalytic transfer to benzyl bromide, maleimides and other ring opening reactions.[13] Given their reactivity, these substrates emerge as natural choices for initial experiments. Moreover, we propose a modification in the synthesis of **4a-d** potentially incorporating a carbene to stabilise the borenium-based FLP system (**Scheme 9.6**). This adjustment could provide new insights into the system's reactivity with NH_3 and H_2, opening avenues for novel catalytic processes.

Chapter 8: Leveraging Non-Covalent Interactions for the Binding of CO by a Weakly Lewis Acidic Borane

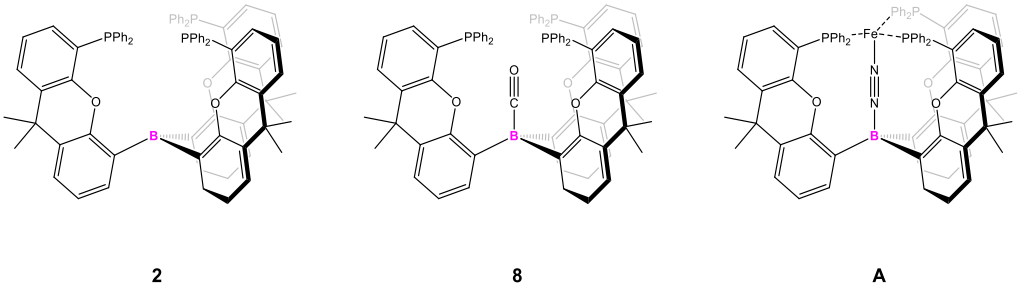

Figure 9.3: Different binding modes to xanthene derived cage **1**

In this chapter, the synthesis of novel borane xanthene phosphine-based cage systems is reported (**Figure 9.3**, **2**), designed to encapsulate a series of small molecules within the cage framework. Protic molecules such as H_2O, NH_3, and $MeNH_2$ are found to bind effectively within

the cage, primarily through hydrogen bonding mechanisms. Intriguingly, CO is also found to bind to the cage (**Figure 9.3**, **8**), displaying a bathochromically shifted CO stretch in the IR spectrum, suggesting the absence of back-bonding interactions.

Investigations into this system through computational analyses have shown that binding within the cage framework significantly enhances stabilization (CO, 59.5 kcal mol^{-1}) compared to external binding. This stabilszation arises from a combination of electrostatic and dispersion forces, underscoring the complexity of interactions within the cage framework.

Notably, this work introduces an innovative method for stabilising borane carbonyls, which have traditionally been stabilised by highly Lewis acidic boranes. [14–27] However, our Gutmann-Beckett test results, with an AN of 13.59 for compound **2**, indicate it is a comparatively weak Lewis acid. This challenges conventional approaches and opens up new avenues for the stabilization of such complexes.

The remarkable stability of the CO complexes, combined with the tripodal nature of **2**, positions it as a potentially intriguing ligand for transition metal complexes. Historically, tripodal ligands have been employed in conjunction with reduced iron systems to perform the catalytic conversion of nitrogen to ammonia.[28] However, **2**, stands out due to its significantly longer boron-phosphorus (B–P) distance compared to traditional tripodal ligands. This unique structural attribute may facilitate cooperative reactivity between the coordinated metal and the boron centre (**Figure 9.3**, **A**), opening up new avenues for catalytic applications and reactivity studies.

References

1. Boronski, J. T., Crumpton, A. E., Wales, L. L. & Aldridge, S. Diberyllocene, a stable compound of Be(I) with a Be–Be bond. *Science* **380**, 1147–1149 (2023).
2. Jones, C. Dimeric magnesium(I) β-diketiminates: a new class of quasi-universal reducing agent. *Nature Reviews Chemistry* **1**, 1–9 (2017).
3. Boronski, J. T. Alkaline earth metals: homometallic bonding. *Dalton Trans.* **53**, 33–39 (2023).
4. Zheng, X. *et al.* Synthesis of homo-metallic heavier analogues of cyclobutene and the cyclobutadiene dianion. (2022).
5. Protchenko, A. V *et al.* Electronic Delocalization in Two and Three Dimensions: Differential Aggregation in Indium "Metalloid" Clusters. *Angew. Chem. Int. Ed.* **56**, 15098–15102 (2017).
6. Zheng, X., Crumpton, A. E., Ellwanger, M. A. & Aldridge, S. A planar per-borylated digermene. *Dalton Trans.* **52**, 16591–16595 (2023).
7. Fukawa, T., Lee, V. Y., Nakamoto, M. & Sekiguchi, A. Tetrakis(di-tert-butylmethylsilyl)distannene and its anion radical. *J Am Chem Soc* **126**, 11758–11759 (2004).
8. Rit, A., Campos, J., Niu, H. & Aldridge, S. A stable heavier group 14 analogue of vinylidene. *Nature Chemistry* **8**, 1022–1026 (2016).
9. Heilmann, A. *et al.* Coordination and Homologation of CO at Al(I): Mechanism and Chain Growth, Branching, Isomerization, and Reduction. *J Am Chem Soc* **144**, 12942–12953 (2022).
10. Casal, H. L., Werstiuk, N. H. & Scaiano, J. C. The reaction of diphenylcarbene with nitroxides. *J Org Chem* **49**, 5214–5217 (2002).
11. Brown, L. C. *et al.* Frustrated Lewis pairs in ionic liquids and molecular solvents-a neutron scattering and NMR study of encounter complexes. *Chem. Commun.* **54**, 8689–8692 (2018).
12. Li, R., Dalton, / & Jupp, A. R. Evidence for the encounter complex in frustrated Lewis pair chemistry. *Dalton Trans.* **51**, 10681–10689 (2022).
13. Krämer, F., Paradies, J., Fernández, I. & Breher, F. A crystalline aluminium–carbon-based ambiphile capable of activation and catalytic transfer of ammonia in non-aqueous media. *Nature Chemistry* **16**, 63–69 (2023).
14. Zheng, X., Zulkifly, I., Heilmann, A., McManus, C. & Aldridge, S. Colorimetric Metal-Free Detection of Carbon Monoxide: Reversible CO Uptake by a BNB Frustrated Lewis Pair. *Angew. Chem. Int. Ed.* **60**, 16416–16419 (2021).
15. Burg, A. B. & Schlesinger, H. I. Hydrides of Boron. VII. Evidence of the Transitory Existence of Borine (BH3): Borine Carbonyl and Borine Trimethylammine. *J Am Chem Soc* **59**, 780–787 (1937).
16. Chen, C. *et al.* The $[(NHC)B(H)C_6F_5]^+$ Cations and Their [B](H)−CO Borane Carbonyls. *Angew. Chem. Int. Ed.* **59**, 21460–21464 (2020).
17. Dahcheh, F., Martin, D., Stephan, D. W. & Bertrand, G. Synthesis and Reactivity of a CAAC–Aminoborylene Adduct: A Hetero-Allene or an Organoboron Isoelectronic with Singlet Carbenes. *Angew. Chem. Int. Ed.* **53**, 13159–13163 (2014).
18. Braunschweig, H. *et al.* Multiple complexation of CO and related ligands to a main-group element. *Nature* **522**, 327–330 (2015).
19. Wang, H., Wu, L., Lin, Z. & Xie, Z. Synthesis, structure and reactivity of a borylene cation [(NHSi)2B(CO)]+ stabilized by three neutral ligands. *J Am Chem Soc* **139**, 13680–13683 (2017).
20. Jeffery, J. C., Norman, N. C., Pardoe, J. A. J. & Timms, P. L. Synthesis and structures of carbonyl adducts of the boranes $B(BX_2)_3$ (X = F, Cl). *Chem. Commun.* 2367–2368 (2000).
21. Jacobsen, H. *et al.* Lewis Acid Properties of Tris(pentafluorophenyl)borane. Structure and Bonding in L-$B(C_6F_5)_3$ Complexes. *Organometallics* **18**, 1724–1734 (1999).
22. Fukazawa, A. *et al.* Reaction of pentaarylboroles with carbon monoxide: an isolable organoboron carbonyl complex. *Chem Sci* **3**, 1814–1818 (2012).
23. Finze, M. *et al.* Tris(trifluoromethyl)borane carbonyl, $(CF_3)_3BCO$ - Synthesis, physical, chemical and spectroscopic properties, gas phase, and solid state structure. *J Am Chem Soc* **124**, 15385–15398 (2002).
24. Knoth, W. H. Chemistry of Boranes. XXXI. 1,10-Bis(hydroxymethyl)octachlorodecaborate(2). *J Am Chem Soc* **89**, 4850–4852 (1967).
25. Gerken, M., Pawelke, G., Bernhardt, E. & Willner, H. Syntheses and Characterization of $(C_2F_5)_3BCO$ and $(C_3F_7)_3BCO$. *Chem. Eur. J.* **16**, 7527–7536 (2010).

26. Heitkemper, T. & Sindlinger, C. P. A Cationic NHC-Supported Borole. *Chem. Eur. J.* **26**, 11684–11689 (2020).
27. Sajid, M. *et al.* Carbonylation reactions of intramolecular vicinal frustrated phosphane/borane lewis pairs. *J Am Chem Soc* **135**, 18567–18574 (2013).
28. Anderson, J. S., Rittle, J. & Peters, J. C. Catalytic conversion of nitrogen to ammonia by an iron model complex. *Nature* **501**, 84–87 (2013).